Fluorous Phase-Based Enantioselective Fluorescent Screening for Asymmetric Catalytic Reaction and Enantioselective Fluorescent Recognition of Amino Acid

Xuedan Wu

Chengdu, China

Chemistry, Bachelor of Science, Sichuan University, 2013

Organic Chemistry, Master of Art, University of Virginia, 2014

A Dissertation presented to the Graduate Faculty of the University of Virginia in Candidacy for the Degree of Doctor of Philosophy

Department of Chemistry

University of Virginia

May, 2020 Degree **will be Conferred**

Abstract

By using 1, 1'-Bi-2-naphthol (BINOL) as the chiral core, a number of fluorinated organic sensors have been developed for the fluorescent recognition of chiral molecules. This thesis has provided an application for rapid enantiomeric excess determination and high throughput catalyst screening by using a type of fluorophilic fluorescent sensor in the fluorous phase.

The excellent chiral recognition ability of the BINOL-perfluoro-diketone sensors has been expanded to a variety of chiral amino alcohols containing a secondary amine group in the fluorous phase [ef = $(I_S-I_0)/(I_R-I_0)$ value up to 100]. They also gave large nonlinear response toward the enantiomeric composition of the amino alcohols in perfluoro-hexanes (FC-72). The enantiomerically pure probes, as well as the racemic probe, were all applied to facilitate the screening of the catalysts for the asymmetric reaction of a meso-epoxide with an alkyl amine. The fluorescence-based ee measurements have been confirmed by HPLC-chiral column analysis which has validated the fluorous phase-based enantioselective fluorescent sensing method. Even with manual screening protocols, we have already discovered a condition with significantly improved enantioselectivity for the polysaccharide-catalyzed asymmetric reaction of 1,2-epoxycyclohexane with an alkyl amine. The entire procedure is automatable and also suitable for high throughput screening by using the probe.

When a novel fluorescent probe made of BINOL and coumarin was excited at λ_1 = 365 nm in a neutral buffer solution, it showed fluorescence enhancement at 465 nm in the presence of an amino acid with a very small difference between the two enantiomers. When excited at λ_2 = 467 nm, it showed highly enantioselective fluorescence enhancement at 534 nm. This allowed the determination of both concentration and enantiomeric composition of amino acids. A detailed

investigation was conducted on the reaction mechanism of the BINOL-coumarin-based fluorescent probe with amino acids. On the basis of the studies including fluorescence spectroscopy, ^{1}HNMR, UV-vis, mass spectroscopy, single crystal X-ray analysis, and molecular modeling, it was found that the distinctively different fluorescent responses of the probe toward the amino acid at the two excitation wavelengths were due to two different reaction pathways that generate different intermediates and products.

The same fluorescent probe was unexpectedly found to be highly selective at 461 nm for just one specific thiol molecule, cysteine under neutral aqueous conditions with a low applicable concentration (10 μM) and agreeable incubation temperature (37 °C) in the absence of any other additives. With interference, cysteine was selectively detectable from 1.6 μM to hundreds of μM which covered both normal and abnormal cellular cysteine concentrations of humans.

Acknowledgement

First of all, I sincerely appreciate Dr. Lin Pu for not only the support and advise from you but also your understanding and patience with me since the day I came to the US seven years ago. Since then I have been attracted by your open-minded ideas, I have been learning and growing in our lab. And I have been used to your critical thinking and I am proud to have you as my advisor who is knowledgeable, humble, and willing to help as well as to encourage me to overcome numerous difficulties. How much I wish I could have you a longer time as my lifelong advisor! My appreciation and gratitude shall also go to my research committee members, Dr. Brent Gunnoe, Dr. Ian Harrision, Dr. Robert Gillard, Dr. Jiang He and Dr. Glenn McGarvey for your academic and career advice as well as your generous guidance. I am truly thankful for the lavish help from Dr. Sen Zhang, Dr. Cassandra Fraser, Dr. Lindsay Wheeler as well as many other faculty members in the department. Additionally, I would also thank Dr. Jeff Ellena for his devoting himself into the NMR facilities and careful guidance on my works on NMR analysis, Dr. Diane Dickie for her fantastic work in analyzing all crystal-like samples I brought to her as well as many other staffs like Mrs. Susie Marshall, Dr. Ashcraft Earl, Mr. Michael Birckhead, Mr. Danny Via, and Mr. Jerry Shifflett who helped me and served in their way for the department. I am lucky to witness the growing and expanding of the department of chemistry.

Then I thank the former and current members who shared time with me in the Pu lab where under the guidance from Dr. Pu, a great number of scientists worked, collaborated, and succeeded. In light of these seniors and peers, I have been working with all my efforts as they had been doing here. Some of you worked with me, trained me, and inspired me. You are Qin Wang, Shuangxi Gu, Yuanyuan Zhu, Hui Wu, Wei Chen, Shuo Li, Shanyong Chen, Jun Ying, Chao Wang, Shifeng Nian, Xiangfeng Guo, Xuemin Duan, Wencai Huang, Zhilian Liu, Bin Zhao, Xuepeng Zhang,

Wenzeng Duan, Gengyu Du, Chaoyuan Zeng, Feng Zhao, Yifan Mao, Winnie Liu, Danny Wang, Julia Marks, Mehdi Abed.

I am also grateful to all of my friends, old and new, in chemistry department, in the university and all around the world for your kind care and priceless friendship. To name a few, you are Hongying Dong, Mingxing Zhang, Xiaofan Jia, Jingcai Ying, Cheng Qian, Guannan Chen, Yusi Hu, Bo Wei, Wucheng Nie, Su Yan, Mingxin He, Xianhao Zhang, You Chen, Yadan Fan, Yangling Li and Lin Shi. Thank you very much over and again!

Over years of living overseas, apart from my big family, I thank my dearest parents and parents in law, encouraging siblings and many other relatives for your long-time supporting on my choice in my study, career and life. I love and miss the small mountain village where I grow up but I also have to appreciate my father, Yiquan Wu, and my mother, Yuxiu Tang for your determination and efforts in providing me with opportunity to receive much better education in cities and even overseas.

Last but not the least, I thank the most significant ones, my beautiful wife and adorable daughter, Xiaoqin Zhang and Arya Wu, who came a long way to me and have been always staying with me as well as supporting me. You brought our small family infinite optimism, joy, and love. You love me for who I am and I love you two back three thousand.

To all of you, acquaintances or strangers, in these unprecedented times, thank you very much for your smiles, your warm words, your criticizing, and your trust.

Table of Contents

List of Figures

List of Schemes

List of Tables

Chapter 1

Enantioselective Fluorescent Sensor

1.1. Introduction of Chiral Molecules

A molecule or ion is called chiral if it cannot be superposed on its mirror image by any combination of rotations and translations. The two non-superimposable mirror images are referred to as enantiomers.[1] This type of geometric property is chirality that plays a primordial role in (bio)chemistry. Most biomolecules are chiral, i.e., they are encoded with a preferred handedness and thus have a stereoselective bias for specific biochemical interactions.[2] The two enantiomers are identical in most physical and chemical properties, which make it difficult to separate and probe the two enantiomers.[3] However, biologically, the enantiomers of a chiral pharmaceutical molecule function differently or even oppositely because they interacted markedly differently with the targeted chiral bio-macromolecules such as proteins, DNA, RNA, and carbohydrates in biological system.[4] A crucial step in revealing this functionality relies on the determination of the stereochemistry of these molecules. The enantiopurity of drug has been strictly inspected by health institutions due to several devastating medical incidents caused by the enantiomeric impurity of drugs over decades ago.[5, 6] Historically, these cases of enantiomers with contradictory biological activities are rare, but it's well known that racemic drugs are usually less effective and have more side effects in comparison with those under single enantiomeric forms.[7] Because enantiomerically pure drugs are more efficient in binding to biological targets than the equivalent racemic drugs or the corresponding enantiomer, in the past decades, enantioselective chemistry has been taking the dominant position in pharmaceutical,[8] pesticides

markets[9] and food science. Enantiomeric drugs have been increasingly developed for the patients due to the superiority in potency and safety. In 2006, the chiral drugs sales amount increased to 56% of the whole drug market in the US and it was expected by 2020 to reach the highest 95%.[10] According to the statistics for 2013, nine of the top ten best-selling pharmaceuticals are enantiomer-based drugs.[11] Of the new drugs approved by FDA in 2016, more than 60% are enantioenriched.[12] Chirality plays an essential role in asymmetric synthesis, biology, food science and pharmacology. Therefore, the synthesis, separation and analysis of chiral intermediates and products have gained focuses of countless scientists.

According to the Good Manufacturing Practice (GMP)[13] and the International Council for Harmonization (ICH)[14] guidelines recognized in Europe, China, Japan and United States, the impurity content of the other enantiomer cannot exceed 0.1% in registered enantiopure drugs.[15, 16] To meet the high demand in pharmaceuticals, many readily available techniques have been accommodated for rapid analysis of enantiomeric excess, including chiral HPLC, GC, NMR, circular dichroism, capillary electrophoresis, mass spectrometry, IR, UV-vis, fluorescence, rotational spectroscopy and etc.[17]

1.2. Current Chiral Analysis Techniques

Over the last decades, on the one hand, the chiroptical techniques available for the determination of the absolute configuration and enantiomeric excess have been based on the fact that the mirror symmetry of enantiomers can be broken using circularly polarized electromagnetic radiation. To analyze chiral molecules the chiroptical techniques[18] such as optical rotary dispersion (ORD), circular dichroism (CD) and vibrational optical activity (VOA) methods namely vibrational circular dichroism (VCD) and Raman optical activity (ROA) were researched and developed.[19, 20, 21]

On the other hand, at some extend the enantiomers are undistinguishable in achiral environment. Therefore, additional chiral resolving agents (CRA) are usually required to make the enantiomers separable, distinct and resolved.[22, 23] Traditionally, chiral resolving agents are often easily obtained from natural products. They act like alkaloids for the optical resolution of racemic acids and like tartaric acid for the optical resolution of racemic bases. By using the different physical properties such as the solubility of the diastereomers obtained from the reaction of racemates and the chiral resolving agents the enantiomers are separated from the racemates by recrystallization.[24] Based on the same theory, many chiral resolving agents (chiral probes) were designed, synthesized and used to induce the formation of diastereomers that have different properties which can be analyzed and separated by various techniques accordingly. In the following, a number of representative state-of-the-art techniques are discussed and evaluated based on their availability and ability in performing chiral analysis as well as enantioselective high throughput screening. XRD as an ultimate tool and judge to determine the absolute configuration of chiral molecules has its trustworthy position as well as some inevitable drawbacks.[25] It along with several chiroptical techniques will not be discussed here in this thesis since we focused more on the techniques using CRAs in order to compare with our work on using fluorescence as a competitive technique in enantioselective analysis.

1.3.1. Chiral HPLC and GC

Among all the instruments and techniques, high performance liquid chromatography (HPLC) has become universal within both the industrial and academic synthetic groups due to its high resolving power and well-developed instrumentation. Equipped with chiral columns, chiral HPLC have been established to be the standard protocol to report the enantiomeric excess (ee = ([R]-[S]) / ([R]+[S])), and takes up more than 50 % of ee determinations.[26] Developed

from common HPLC of common stationary phase such as polymer and silica, chiral HPLC uses chiral stationary phase (CSP) such as crown ethers, polysaccharides, cyclodextrins and some protein-based CSPs. Preparative chiral HPLC using chiral sorbent has enabled the separation of racemate in moderate amounts.[27] Temperature, pressure, flow rate and elution composition can be optimized to improve the separation efficiency, the progress of chiral HPLC is always marked by the discovery of new CSP materials.

In the past decades chiral CSP materials have expanded greatly intended for the separation of specific molecules that are problematic.[28] Crown ether-based CSPs have been found to be efficient for primary amines or amino acids at reversed phase conditions.[29] Some protein-based CSPs like bovine serum albumin were especially suitable for the analysis of biomolecules without derivation.[30] Many polymer CSPs fabricated through molecular imprinting or silica-gel surface coating have also been commercialized.[31, 32] Future developments of chiral HPLC will focus on discovering both general and task-specific CSP materials, reducing their production cost while increasing durability.

Cyclodextrin derivatives attached to polysiloxane are the dominant state-of-the-art CSP used currently in chiral gas chromatography (GC) technique. Chiral resolution relies on the gas-liquid interactions, including hydrogen bonding, coordination or inclusion.[33] It has been widely applied to the separation of essential oils and volatile organic compounds.[34] Notably, ionic liquid has emerged as a promising CSP material in recent years for their high stability at raised temperature and good wettability toward silica surface.[35]

1.3.2. Mass Spectrometry (MS)

Due to the superiority of mass spectrometry (MS) over other analytical methods in terms of speed, specificity and sensitivity, chiral analysis by MS has attracted much interest in recent

years.[36, 37] Chiral analysis by MS typically involves introduction of a chiral selector (CS, Aka CRA) to form diastereomers with analyte enantiomers, and comparison of the behaviors of diastereomers in MS.[38] Chiral differentiation can be achieved by comparing the relative abundances of diastereomers, the thermodynamic or kinetic constants of ion-molecule reactions of diastereomers in the gas phase, the dissociation of diastereomers in MS/MS, or the mobility of diastereomers in ion mobility mass spectrometry.

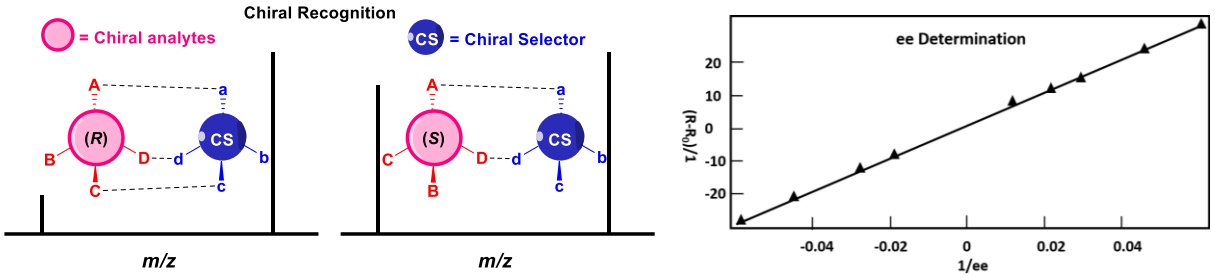

Figure 1- 1. A typical chiral MS peak distribution by using a CS and the corresponding ee determination curve by the MS peak data. Reprinted with permission from ref 38. *Copyright © 2017 Elsevier B.V. All rights reserved.*

1.3.3. Nuclear Magnetic Resonance (NMR)

Chiral analysis by NMR technique was firstly reported by *Harry Mosher et al.* at 1969 using the well-known CRA, Mosher acid (chloride) to react with chiral amine or alcohol.[39] The diastereomers formed gave a difference in chemical shift of 0.03-0.13 ppm in ^{1}H NMR and 0.11-0.71 ppm in ^{19}F NMR. However, either MTPA (methoxy(trifluoromethyl)-phenyl acetyl; Mosher)[40] or MPA (methoxyphenyl acetyl; Trost)[41] bis-esters, a drawback is the potential for diverging conversion rates in the derivatization reaction of both alcohol functionalities when two equivalents of the CRAs (kinetic resolution) are used. This effect can lead to inaccurate

enantiomeric excess values being determined. Derivatization of chiral diols with synthesized CRAs that contain either dichlorophosphine,[42] dichlorophosphate,[43] aldehyde[44] or boronic acid[45, 46, 47] functionalities avoid these limitations, as a single reagent reacts with both alcohol functionalities of the diol substrate. *James et al.* reported simple protocols by utilizing even more readily available CRAs with a three-component chiral derivatization strategy. In their methods 2-formylphenylboronic acid along with another commercially available CRA such as (*S*)-*α*-methylbenzylamine[48] or (*S*)-BINOL[49] in $CDCl_3$ were mixed with the analytes after only 10 minutes the NMR spectra were taken. In less than 90 mins in total this protocol affords diastereoisomeric iminoboronate ester complexes displaying relatively large chemical shift difference between pairs of diastereotopic resonances in their ^1H NMR spectra ($\Delta\delta$ = 0.017–0.510 ppm for the diols and $\Delta\delta$ = 0.020–0.670 ppm for the primary amines) compared to other boronic acid-based CRAs used for the analysis of chiral diols and amines.

Scheme 1- 1. NMR analysis of the enantiomeric purity of chiral diols (a) and chiral primary amines (b) by using a three-component chiral derivatization protocol.

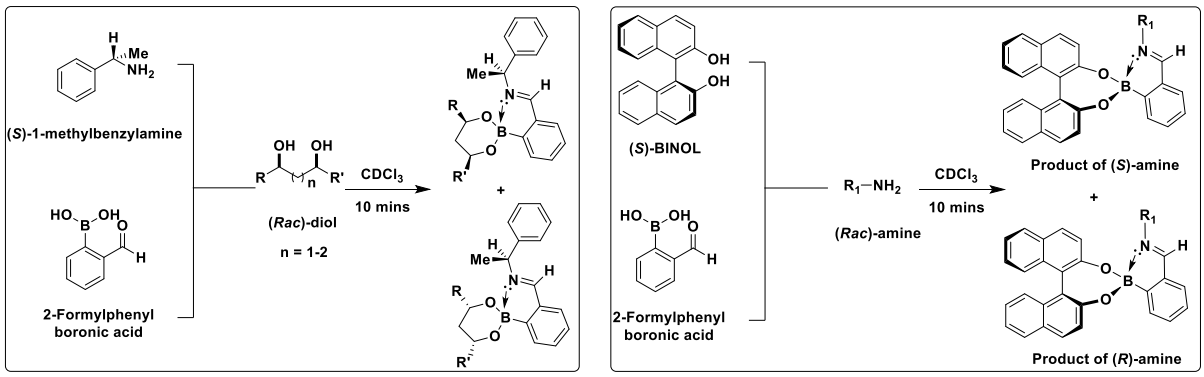

(a) (b)

The extensive spread of NMR technique has made it a popular tool to determine optical purity and absolute configuration of many kinds of compounds. Compared with chiral HPLC, it

has higher tolerance to impurities and can determine *ee* values of many samples in a single experimental setup. It is also more economical and time-efficient. Using ^{1}H, ^{19}F, or ^{31}P NMR, numerous chiral auxiliary agents, most of which are *Brønsted* acids/bases, transition metal complexes or host-guest receptors, have been explored and researched comprehensively.[50]

1.3.4. Circular Dichroism

As a remarkable representative of the chiroptical techniques circular dichroism (CD) is dichroism involving circularly polarized light. This intrinsic nature makes it a very straightforward method to determine enantiomeric excess and absolute configuration. A positive or negative CD signal is produced when two enantiomers show different absorption to left-polarized light and right-polarized light. Though having been applied to the study of chiral molecules of all types, it is in the study of biomolecules especially proteins where CD spectroscopy find most of its applications, as well as technique innovations.[51] In studying secondary structures of proteins, CD is the standard method to determine the percentage of α helix and β sheet as they shown characteristic CD spectra under 260nm.[52, 53] However, initial use of CD in enantiomeric excess determination was limited because most small chiral molecules had no good UV-vis absorption over 200 nm.

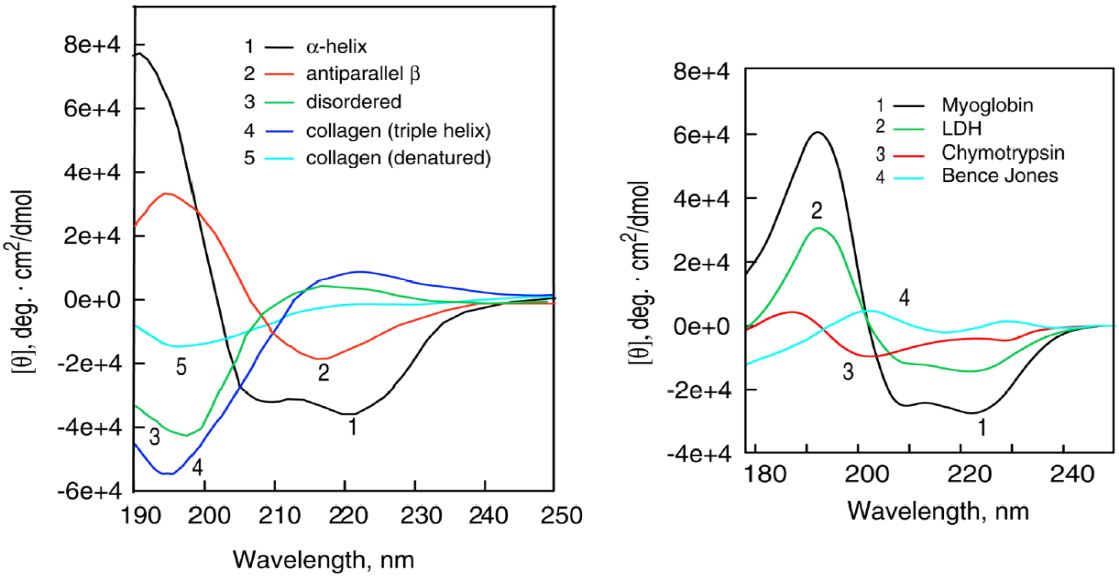

Figure 1- 2. Circular dichroism (CD) spectra of polypeptides and proteins with representative secondary structures. Adapted with permission from ref 53. *Copyright © 2007, Springer Nature*.

Researchers have developed a series of molecular sensors containing fluorophores to induce CD signals at UV-vis region for rapid enantiomeric excess determination for small chiral molecules.[54, 55, 56, 57, 58, 59] These probes are CD silent owing to free rotations at room temperature. Once they reacted with chiral amine or alcohol, rotations are restricted and the CD responses are induced with opposite *Cotton effects* observed for two enantiomers at 300-450 nm ranges.

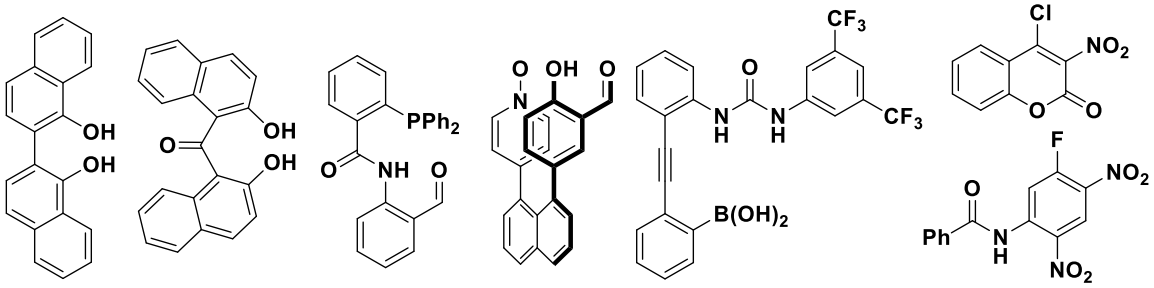

In a most recent case carried out by *Wolf et al*. an electron-deficient fluoroarene, *N*-(5-fluoro-2,4-dinitrophenyl)benzamide was synthesized via a quick one-step amidation from commercial available sources and employed for the sensing of a solution containing either (*R*)- or (*S*)-amino acids, amino alcohols, amines as well as biothiols.[59] The reaction with (*R*)- or (*S*)-enantiomers gave exactly the opposite results from 250-450 nm by various substrates. By irreversibly binding amino acids in aqueous solution with a well-defined 1:1 stoichiometry, distinct chiroptical signals were generated to allow assignment of the absolute configuration and quantification of the sample concentration and enantiomeric ratio. The UV response of the sensor was nonenantioselective and therefore allows determination of the total amount of an amino acid sample independent of the enantiomeric composition while the induced CD signals were in response to the chirality of the target compound and could be used for absolute configuration and er analysis.

Scheme 1- 2. Enantioselective sensing of amino acids, biothiols, amines, and amino alcohols with the aryl fluoride probe, *N*-(5-fluoro-2,4-dinitrophenyl) benzamide. Reprinted with permission from ref 59. *Copyright [2019] American Chemical Society.*

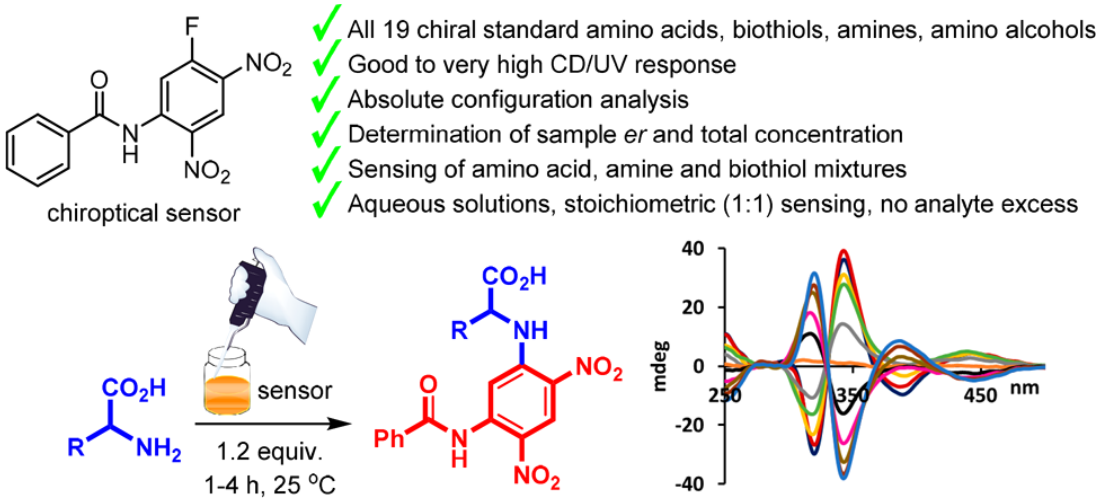

1.3.5. UV-vis Spectroscopy

UV−vis spectroscopy technique conducting quantitative ee determination has been well elaborated and notorious.[60] A chiral analyte binds to the chiral host, which results in a change in the spectroscopic signal. In many cases, the enantioselective probes require multistep synthesis, with the efficacy of the host being determined post synthesis. Such a protocol is unfavorable because of the poor spectroscopic signal and the requirement of synthesis of new probe for new substrates. This process is time-consuming and presents a bottleneck for the quantitative determination of enantiomeric excess. In contrast, enantioselective indicator displacement assays (eIDAs) have been demonstrated for the enantioselective discrimination of chiral substrates with broad functionalities.[61]

Anslyn et al. has established the eIDAs practicality over a couple of decades. For instance, a simple and general method was developed for the quantitative ee determination of nonderivatized α-amino acids with a chiral Cu(II)-diamine complex and the indicator pyrocatechol violet (PCV). Titration of Cu(II)-diamine to the indicator PCV formed a 1:1 complex that resulted in a shift of absorption maxima from 445 nm to 645 nm, accompanied by a color change from yellow to blue. Addition of enantiomeric amino acid mixtures gave colors that were in between the two enantiopure extremes and a calibration curve was used to quantify ee. It is worth noting that the ligand used in this eIDA was synthesized in one step from commercially available starting materials and required no chromatographic purification. The binding favors D-amino acids over the L-amino acids by a factor of 2.0-2.5, which can be used for rapid ee measurements.

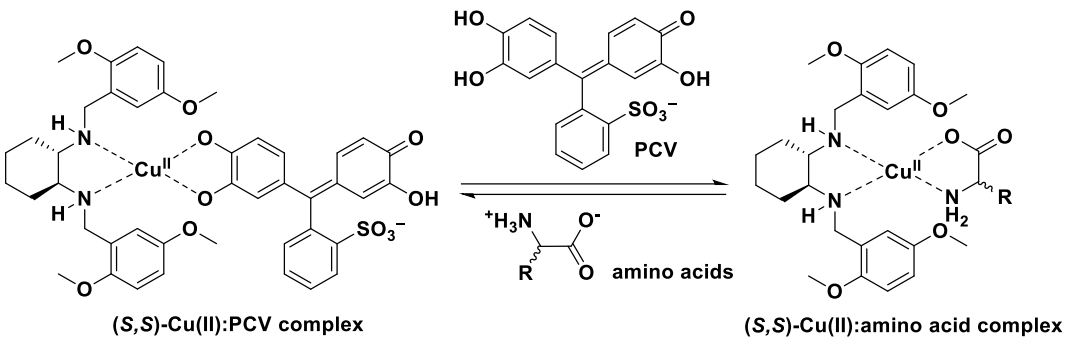

Figure 1- 3. Enantioselective indicator displacement assay (eIDA) for the ee determination of α-amino acids.

Anslyn et al. also demonstrated that the UV-vis analytical method could be streamlined by using an enantioselective indicator displacement assay (eIDA) with a dual-chamber quartz cuvette.[62] As shown in Scheme 1-3, one cuvette was filled with a methanolic aqueous solution containing the pale indicator 4-methylesculetin (ML), and the achiral host boronic acid **1**. The other cuvette was charged with the red indicator alizarin complexone (AC), and the chiral host (*S, S*)-**2**. The reversible interactions between indicators and hosts in each cuvette were found to modulate the UV signatures of the dyes (Scheme 1-3B). The corresponding equilibria were disturbed upon addition of nonracemic 2-hydroxy-3-phenylpropionic acid, which ultimately altered the UV absorbance of the two separate systems (Scheme 1-3C). The use of the dual-chamber cuvette allowed simultaneous collection of the optical changes by a single measurement. An artificial neural network analysis (ANN) of the UV data obtained with several samples of the 2-hydroxy-3-phenylpropionic acids showed that both concentration and ee of the analyte could be determined with error margins of no more than 2%. This protocol was simple and was agreeable to conditions of many synthetic organic compounds.

Scheme 1- 3. A) Dual-chamber cuvette containing the indicators ML (left) and AC (right) in 75% methanolic aqueous solution with 10 mM HEPES at pH 7.4. B) UV spectra of ML in the presence of varying amounts of 1 (blue) and of AC with varying amounts of (*S, S*)-**2** (red). C) Change in the UV absorptions in the presence of 2-hydroxy-3-phenylpropionic acids with varying ee. D) Two independent equations that correlate the absorbance (A) to $[G]_t$ and ee at wavelengths λ_1 (387 nm) and λ_2 (536 nm). Adapted with permission from ref 62. *Copyright © 2007 WILEY-VCH Verlag GmbH & Co. KGaA, Weinheim.*

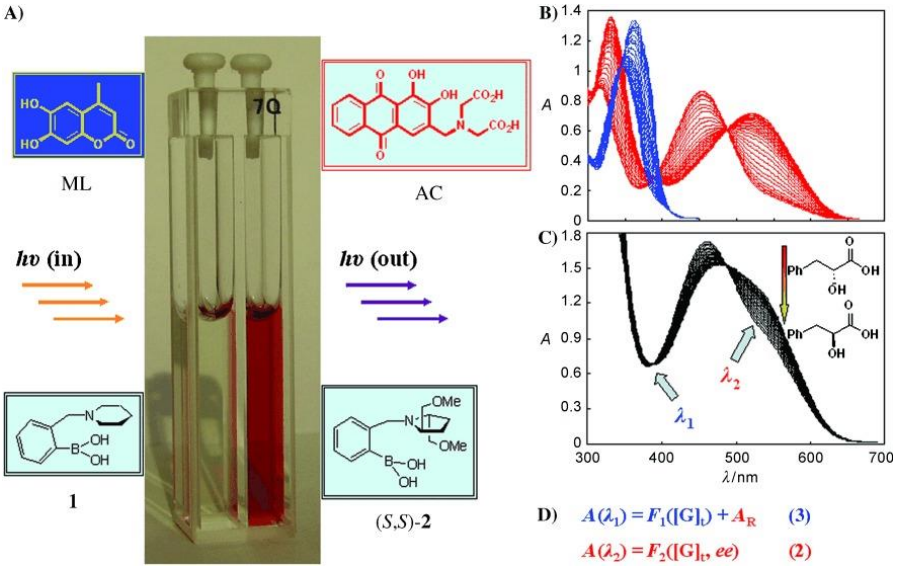

1.3.6. Rotational Spectroscopy

Broadband microwave spectroscopy is a proven tool to precisely determine molecular properties of gas-phase molecules. Microwave spectroscopy also widely known as rotational spectroscopy or molecular rotational resonance (MRR) spectroscopy is extremely sensitive to small differences in molecular structure, and as such is well suited for the differentiation of isomers.[63] Recent developments make it applicable to investigate chiral molecules. Due to the

high spectral resolution of MRR, a mixture of components, including isomers (regioisomers, diastereomers, cis–trans isomers, or isotopologues), can be resolved without the need for separation or chemometrics.[64, 65, 66, 67] The technique is suitable for research in online reaction monitoring of a stereoselective pharmaceutical process due to its advantages described above.[68] Recently, *Brooks H. Pate et al* have also enabled the MRR instrument using two strategies- three-wave mixing and chiral tagging that could be probably applied to the online reaction monitoring for enantiomers of pharmaceutical as well (Figure 1-4).[69, 70, 71] Enantiomers could be differentiated, and the enantiomeric excess and, indirectly, the absolute configuration could be determined in a rapid and molecule-selective manner.

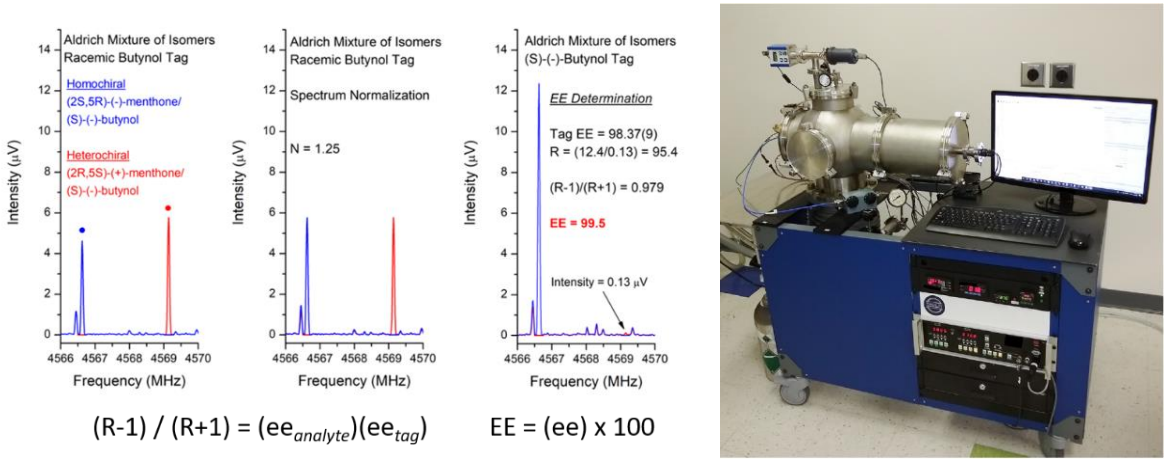

(a) (b)

Figure 1- 4. a) Determination of enantiomeric excess by rotational spectroscopy using (*S*)-(-)-butynol as the chiral tag. Adapted with permission from ref 72. b) A photograph of the MRR spectrometer used in the online stereochemical process monitoring. Adapted with permission from ref 69. *Copyright [2019] American Chemical Society.*

1.3.7. Fluorescence

Compared with many other chiral analysis techniques, fluorescence is exclusively advantageous for its ultrahigh sensitivity that has enabled single molecule detection and non-invasive nature that is suitable for *in vivo* diagnosis. It has been widely used for the sensing and imaging of ions, gases, carbohydrates, pH, protein, DNA, RNA and many other biomolcules.[73] Generally, fluorescence sensing records one of the changes in fluorescence intensity, ratio, lifetime, anisotropy or phase, either positive or negative changes. Intensity and intensity ratios are most widely used and easy to carry out, followed by lifetime sensing.[74]

1.3. Fluorescence in Chiral Analysis

Using fluorescence as a tool for chiral analysis has received a lot of attention in recent years due to its advantages in high sensitivity, real-time analysis, easy for automation and low cost.[75, 76, 77] Because chiral molecules usually only have absorptions at far-UV region, chiral hosts containing chromophores or fluorophores are required to induce emissions at UV-vis regions. In a three-point model, enantioselectivity in fluorescence originates from the different interactions of two enantiomers with chiral hosts containing fluorophores due to their difference in spatial orientations. These interactions can be non-covalent interactions like hydrogen bonding and *Van der Waals* interactions, or dynamic covalent interactions through formation of imines or boronic esters, or direct asymmetric chemical reactions. For the sensor structures that have been developed, there are inherently chiral Binaphthyl-based chemosensors, boronic ester sensors, Schiff-base derived sensors, macromolecule sensors, metal-complex sensors, polymer-based sensors and etc. *Pu et al.* have conducted a wide range of study in using 1,1'-bi-2-naphthol (BINOL) as the backbone structures for chirality sensing.[72, 78] BINOL has stable chiral configuration at room temperature and both enantiomers are commercially available with low costs. Diversified structural modifications of BINOL are easy to carry out at various positions

on its aromatic rings. The naphthol unit is a satisfactory fluorophore and has emissions at the UV-vis region. The hydroxyl groups are also good hydrogen bonding sites for incoming chiral guests.

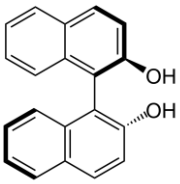

(*R*)-BINOL

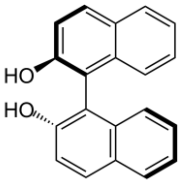

(*S*)-BINOL

1.3.1. Hydrogen Bonding (Non-covalent Interactions)

Among non-covalent bonding interactions-based sensing, hydrogen boding networks are the mostly studied ones. In an initial study, *Parker et al*. simply used BINOL to determine *ee* values of 1–phenylethylamine by observing fluorescence quenching resulted from the interaction of the amine with BINOL upon hydrogen bonding.[79, 80] Though very small difference in Stern-Volmer (K_{sv}) constants is observed for the *R* and *S* enantiomers, with $K_{sv}(R) / K_{sv}(S) = 1.09$. *Beer et al*. synthesized a probe BINOL-BODIPY by coupling two BODIPY units to (*R*)-BINOL and observed better enantioselectivity to the same amine with $K_{sv}(R) / K_{sv}(S) = 1.40$ at 540 nm.[81] In this research only the BINOL-BODIPY probe would be responsive to the amine while the bis-methyl BINOL-BODIPY was non-responsive, which validated the hydrogen bonding theory.

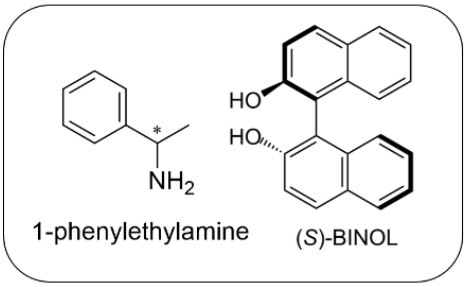

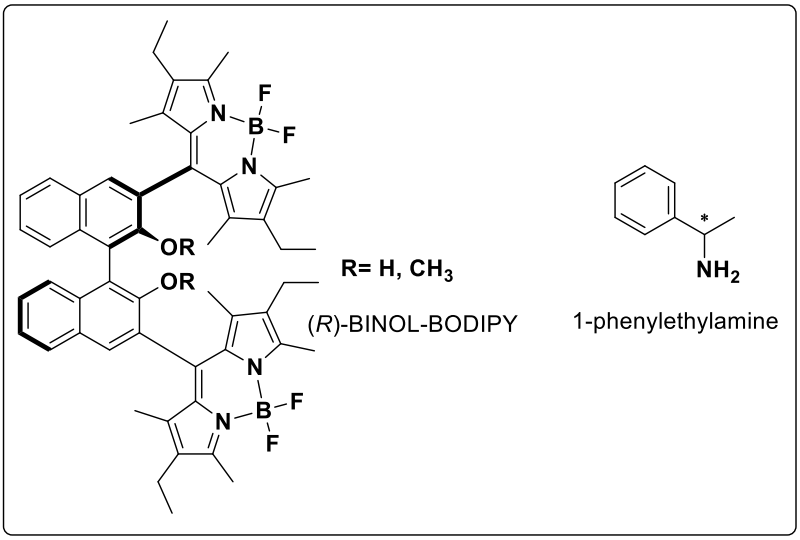

In the sensing of α-hydroxyl acids like Mandelic acid (MA), *Pu et al*. designed a BisBINOL whose fluorescence was quenched by intramolecular hydrogen bonding.[82] The 3-point binding to MA formed complex **3** whose fluorescence was restored with enantioselectivity. As shown in Figure 1-5, the addition of (*S*)-mandelic acid gave much larger fluorescence enhancement of the sensor than the addition of the *R* enantiomer. The enantiomeric fluorescence enhancement ratio *ef* [= (I_S-I_0) / (I_R-I_0)] is calculated to be 2.49 at 367 nm.

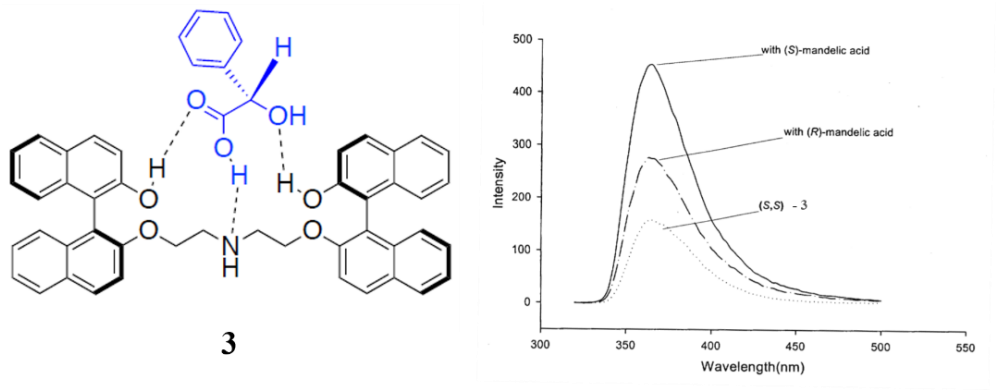

Figure 1- 5. Complex **3** formed by hydrogen bonding and Emission spectra of **3** with or without the enantiomers of mandelic acid. (λ_{ex} = 310 nm) Adapted with permission from ref 82. *Copyright [2002] American Chemical Society.*

Analogs **4** and **5** of the BisBINOL probe were synthesized in order to improve the sensitivity. As a result of the light-harvesting effect from the extended conjugation, increased fluorescence enhancements and much higher sensitivity was observed (Figure 1-6, right).[83]

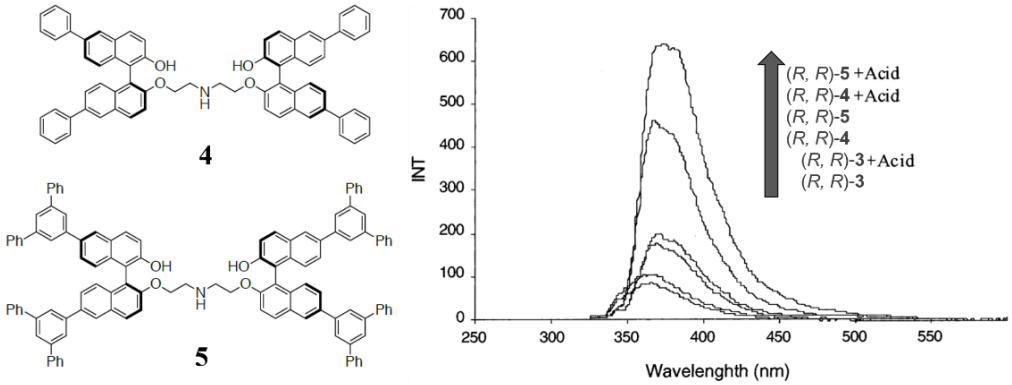

Figure 1- 6. Structures of **4** and **5** and the fluorescence spectra of **3**, **4**, and **5** with or without (*R*)-mandelic acid. (λ_{ex} = 310 nm) Adapted with permission from ref 83. *Copyright [2002] American Chemical Society.*

In another case, macrocycle **6** was synthesized to give enantioselective ratiometric response to chiral acids at 365 nm and 424 nm (Figure 1-7).[84] The hydrogen bond interaction between the chiral cavity of **6** with chiral acid is responsible for the fluorescence change. Within a certain concentration range, one enantiomer of the chiral acids can increase the fluorescence intensity of the macrocycles by 2-3-fold, while the other enantiomer scarcely enhances the fluorescence. Such unusually high enantioselective responses make these macrocycles very attractive as fluorescent sensors in determining the enantiomeric composition of the α-hydroxycarboxylic acids. They are potentially useful for the combinatorial screening of the catalysts for the asymmetric synthesis of α-hydroxycarboxylic acids.

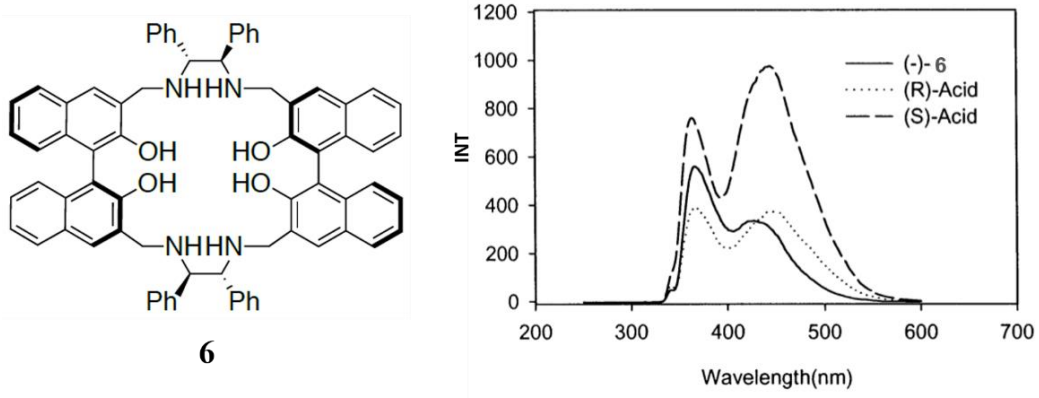

Figure 1- 7. Structures of **6** and the fluorescent emission spectra of **6** (1.0×10^{-4} M in benzene containing 2% DME) both with and without (*R*)- and (*S*)-mandelic acid (2.0×10^{-2} M). (λ_{ex} = 340 nm) Adapted with permission from ref 84. *Copyright [2002] American Chemical Society.*

Later on, a series of BINOL-based sensors were developed based on hydrogen bonding interactions between hosts and guests. An amino alcohol-based sensor **7** was also found to show

ratiometric response to a wide range of aromatic and aliphatic α-hydroxyl acids through hydrogen bonding with *ef* values up to 26.[85] Practically, both enantiomeric excess and total concentration should be determined in a real application of chiral analysis. However, the methods mentioned above are only able to give information on ee values at given concentrations. A pseudo-enantiomeric pair consisting of (*S*)-BINOL derived amino alcohol **7** and (*R)*-H8BINOL derived amino alcohol **8** were designed and synthesized accordingly.[86] The similar structures of **7** and **8** allow them give similar enantioselectivity for mandelic acid. However, as the H8BINOL is less conjugated, the emission occurs at shorter wavelength. A 1:1 mixture of **7** and **8** gives dual emission at 330 nm and 374 nm respectively. With a single measurement, the difference in fluorescence intensity at two peaks can be used to calculate enantiomeric excess, while the sum to calculate total concentration of enantiomers (Figure 1-8).

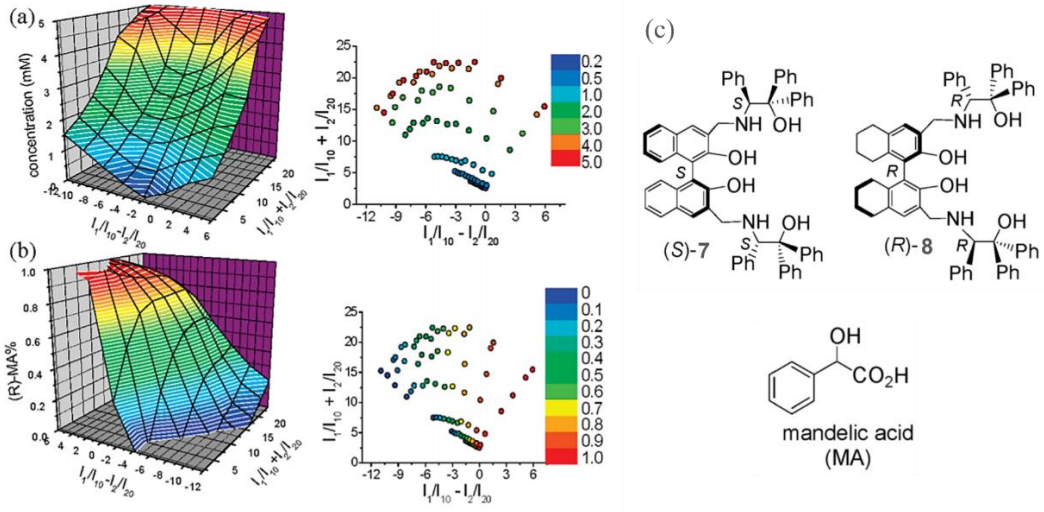

Figure 1- 8. 3D and 2D plots of I_1/I_{10} - I_2/I_{20} and I_1/I_{10} + I_2/I_{20} with (a) the MA concentration (mM) and (b) (*R*)-MA%. (c) The structures of **7**, **8**, and the analyte MA. (I_1: the fluorescent intensity of **7** + MA, I_{10}: the fluorescent intensity of **7** only; I_2: the fluorescent intensity of **8** + MA, I_{20}: the fluorescent intensity of **8** only, λ_{ex} = 290 nm) Adapted with permission from ref 86.

Copyright [2010] American Chemical Society.

Song et al. then developed a salen-based chiral fluorescence polymer sensor for enantioselective recognition of α-hydroxyl carboxylic acids by similar hydrogen bonding interactions.[87] It exhibited greater fluorescence enhancement response toward (L)-α-hydroxyl carboxylic acids, and the value of enantiomeric fluorescence difference ratio (ef) could reach as high as 8.41 for mandelic acid and 6.55 for lactic acid. The (*R*, *R*)-salen-based polymer would display bright blue fluorescence color change in the presence of (L)-α-hydroxyl carboxylic acids under a commercially available UV lamp, which could be clearly observed by the naked eyes (Figure 1-9).

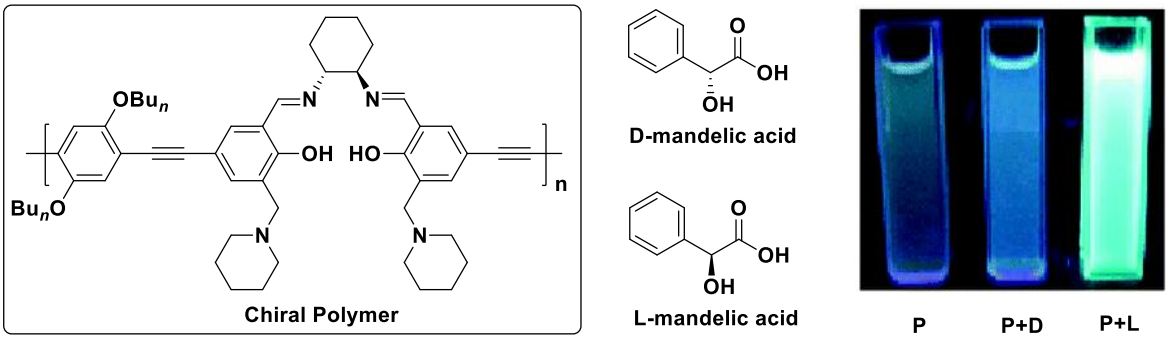

Figure 1- 9. Structures of the polymer sensor and the α-hydroxyl carboxylic acids. (inset) The fluorescence image of a solution of the polymer (5×10^{-5} mol/L) plus 15.0 equiv of MA were excited by a commercially available UV lamp (λ = 365 nm). Adapted with permission from ref 87. *Copyright [2012] American Chemical Society.*

Wolf et al. conducted a study on applying the enantiopure 1,8-diheteroarylnaphthalene derivatives for enantioselective fluorescence quenching by amino acids caused by hydrogen

bonding.[88] Except different Stern-Volmer quenching constants, different lifetimes were obtained for sensor **9** when it interacted chiral N-Boc-Proline, **10** in CH_3CN. The lifetime reduces to 7.5 ns for L-enantiomer and 6.8 ns for D-enantiomer respectively, from the original 18.8 ns (Figure 1-10).

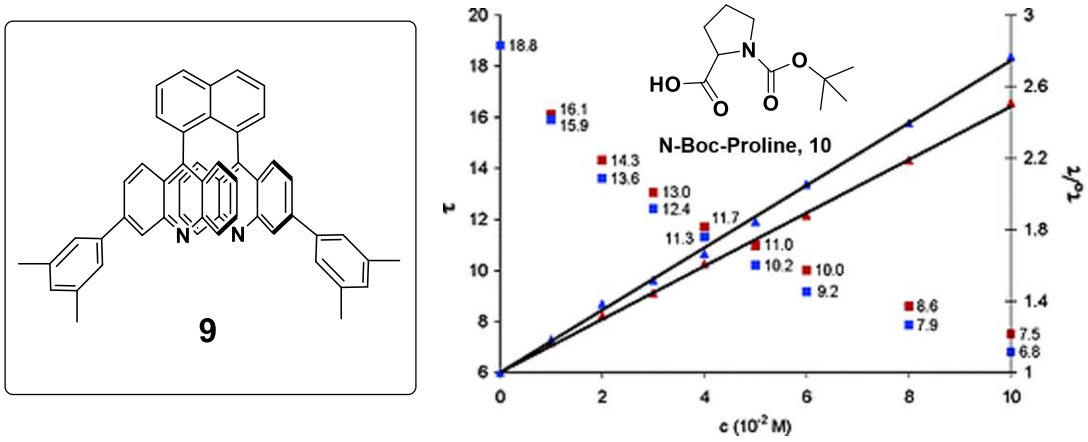

Figure 1- 10. Fluorescence lifetime titration of (+)-**9** in the presence of the enantiomers of **10** in acetonitrile. Fluorescence lifetime, τ, of (+)-9 in the presence of various amounts of (*R*)-**10** (blue box) and (*S*)-**10** (red box); ratio of the fluorescence lifetime of (+)-**9** in the absence and in the presence of (*R*)-**10** (blue triangle) and (*S*)-**10** (red triangle). Sensor **9** exhibits a single-componential decay that was fitted at 550 nm. λ_{ex} = 370 nm. Adapted with permission from ref 88. *Copyright [2006] American Chemical Society.*

Many crown ether-based receptors containing BINOL units have also been synthesized for chiral sensing. Using a furo-fused-BINOL based chiral crown ether **11**, *Karnik et al.* reported the enantioselective sensing of phenylethylamine and valine ethyl ester with 2-3 times difference in fluorescence intensity at 367 nm. The chiral molecule formed a 1:1 complex with **11** and the

association constant was calculated to be $K_R / K_S = 11.30$ for phenylethylamine and 7.02 for valine ester. [89]

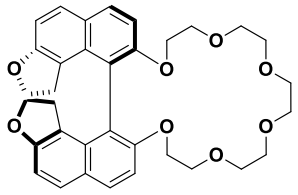

11

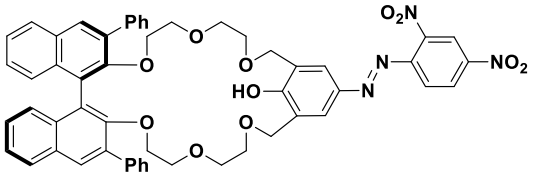

12

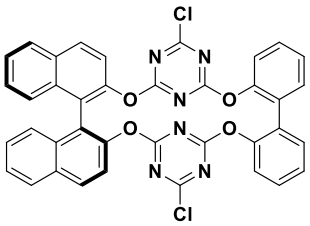

13

Hyun *et al*. designed **12** by incorporating the crown-ether as binding site, BINOL as chiral barrier and dinitrophenylazophenol as chromophore. [90] When treated with primary amino alcohols, different absorption maximum wavelengths up to 43.5 nm and binding constants up to 2.51 times (K_S / K_R) were observed in acetonitrile. The color of **12** changed from green-yellow to purple with the addition of (*R*)-phenylalaninol and to blue with the addition of the (*S*)-phenylalaninol. More recently, *Xu et al*. synthesized a triazine based crown ether **13** and achieved descent enantioselectivity toward amino acid anions. [91] Very high (5.4-fold) fluorescence enhancement was observed with the addition of D-Alanine, while little change was observed for L-Alaine.

A most recent case carried out by *Zhang et al*. involved in ion-pair and hydrogen-bond interaction was achieved by a chiral thiourea Schiff base **14** derived from (*R*, *R*)-1,2-cyclohexanediamine and tetraphenylethylene (TPE, a well-known chiral aggregation-induced emission, AIE moiety). [92] It was applied as a highly effective chiral sensor for the

enantioselective discrimination of various acids and amines with *ef* values about 10.0 in half of the cases.

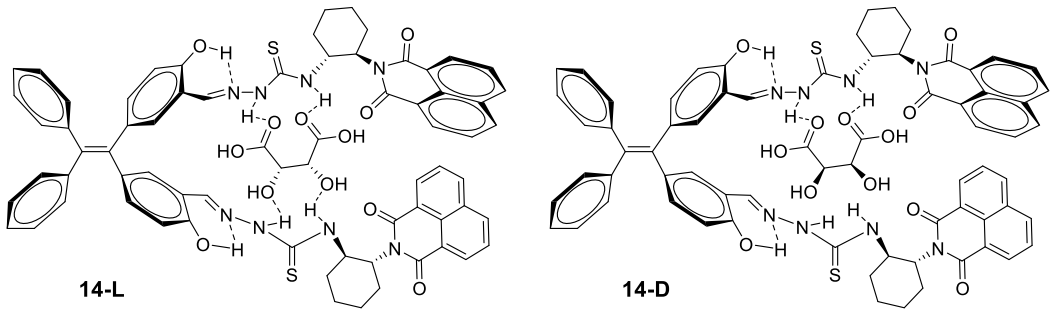

Figure 1- 11. The possible structures of the 1:1 complexation of sensor **14** between L and D-tartaric acid.

1.3.2. Reversible Covalent Interactions

Reversible (dynamic) covalent chemistry including boronate ester formation, imine formation and exchange, esterification and hemiacetal exchange and etc. [93] has been prosperous in the past decades and has demonstrated great potentials in fluorescence sensing. [94, 95, 96] Similar to supramolecular interaction, dynamic covalent interaction is also reversible, exchangeable and can reach equilibrium very soon. But it also shares the robustness of covalent chemistry, which makes it less reversible than supramolecular interaction, and in some cases, a catalyst or an additive is needed to reach a rapid equilibrium.

As the pioneers in chiral analysis, James *et al* combined two boronic acid groups to the chiral BINOL and achieved fluorescence discrimination of D- and L-monosaccharides. [97] Fluorescence of **15** was enhanced upon dual binding with glucose at pH 7.77 (phosphate 33.3% (w/w) methanol buffer) in an 1:1 fashion forming cyclic boronate ester fluorescent products or

an 1:2 fashion generating the non-cyclic boronate ester fluorescent products of **15** versus the monosaccharides.(Scheme1-4) The stronger B-O bonding makes it suitable for sensing in water minimizing the interference of its hydrogen bonding. The fluorescence enhancement ratio was 1.93 for glucose and 1.47 for fructose (D / L). Starting from their report, boronic acid motif has become the popular design in the sensing of carbohydrates, alcohols and phenols.[98, 99, 100]

Scheme 1- 4. Fluorescence recognition of glucose using boronate ester formation.

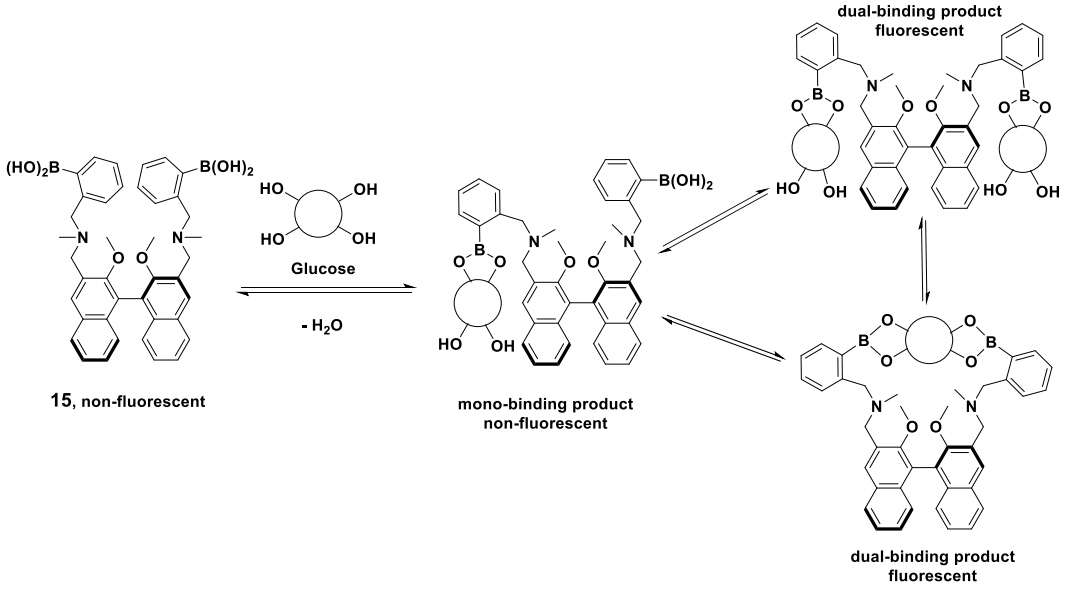

1.3.3. Covalent Bond Formation

The *Pu* group has demonstrated the usefulness of covalent substrate binding with BINOL based probes facilitated by Zn metal cation. *Huang et al*. reported using a diformyl-BINOL **16** in the presence of Zn(II) for enantioselective sensing of amines, amino alcohols and amino acids through imine formation in methanol.[101] The distinct fluorescence intensity at over 500 nm enables visual discrimination of these enantiomers under UV lamps. The formation of Schiff

bases and their complex (**17**) with Zn(II) was revealed by ESI-MS study. As a necessary component, Zn(II) was assumed to play key roles on inhibiting the excited state imine isomerization and intramolecular proton transfer and increasing rigidity of the Schiff bases formed.[102, 103]

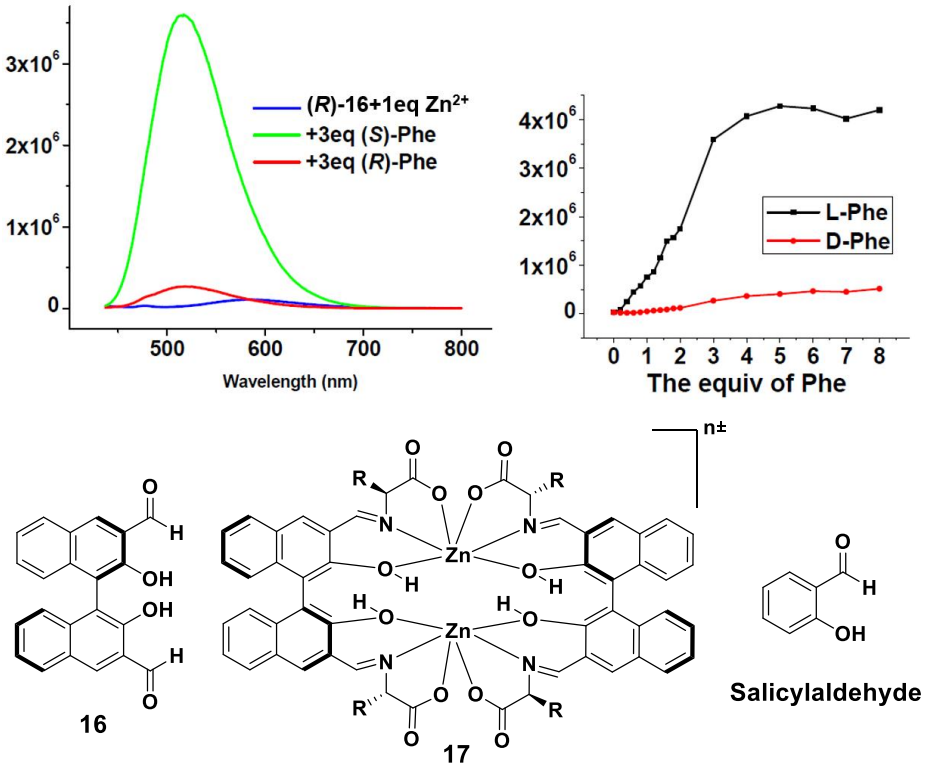

Figure 1- 12. Fluorescence spectra of (*R*)-**16**+Zn^{2+}(1 equiv) (2.0 x 10^{-5} M in methanol/1% CH_2Cl_2 with 10 equiv Bu_4NOH) with (*S*)- and (*R*)-phenylalanine (a), and $I_{515\,nm}$ versus the amino acid concentration (b). (λ_{exc}= 417 nm) Adapted with permission from ref 101. *Copyright [2014] Royal Society of Chemistry.*

Addition of the achiral salicylaldehyde (4 equiv) to the above (*R*)-**16**+Zn^{2+} system allowed the monitoring the fluorescence responses at two emission wavelengths of λ_1 = 447 nm

and λ_2 = 529 nm towards amino acids with the same excitation wavelength (λ_{exc} = 320 nm).[104] The short wavelength emission was due to the reaction of the achiral salicylaldehyde with the amino acids and Zn^{2+} which was non-enantioselective while very sensitive toward the amino acids, and the emission at long wavelength was enantioselective due to the chiral probe (*R*)-**16**. Thus, measuring the fluorescence enhancement at the two wavelengths allowed simultaneous determination of both concentration and enantiomeric composition of amino acids.

In order to further improve the enantioselectivity of the mono-BINOL aldehyde (*S*)-**16** in the fluorescent recognition of amino acids, *Zhu et al.* designed and synthesized the bisBINOL-based chiral aldehyde (*S, S*)-**19**. Under certain conditions (0.01 mM in CH_3CN, 2 equiv Zn(II)), (*S, S*)-**19** exhibited enantioselective fluorescence enhancement with various amino acids (in BICINE buffer, pH = 8.8) at λ_{em} > 500 nm, with extremely high *ef*'s [$(I_L-I_0)/(I_D-I_0)$] observed (8-199 for a variety of amino acids).[105] Cooperation of two BINOL units shown in **20** from the reaction of (*S,S*)-**19** with amino acids and Zn(II) was proposed to account for the generally high enantioselectivity in the fluorescence responses.

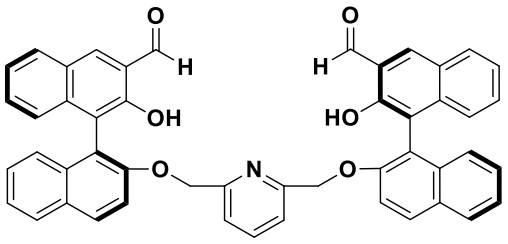

(*S,S*)-19

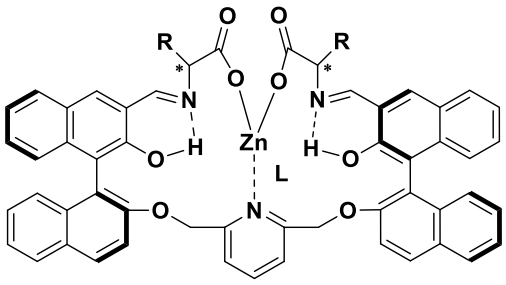

20

1.3.4. Metal Complexation

Besides Zn(II) mentioned above, some other metal ions have also been utilized for enantioselective sensing. A latest interesting study conducted by *Wang et al.* suggested the addition of Mg^{2+} was also turning on the fluorescence response of the probe **16**, 3,3′-diformyl-1,1′-bi-2-naphthol, toward chiral amino acids with high enantioselectivity at a probe concentration of 1.0×10^{-5} M in methanol/1% CH_2Cl_2 (Scheme 1-5). It was surprisingly found that the enantioselective fluorescence responses of the molecular probe in the presence of Mg^{2+} toward certain amino acids are the opposite of those in the presence of Zn^{2+}, that is, using Mg^{2+} with an L-amino acid generates much greater fluorescence enhancement than with the corresponding D-amino acid, but using Zn^{2+} with the D-amino acid gives much greater fluorescence than with the L-enantiomer.[106] Thus, simply changing the metal cation additive allows the chirality sense of the fluorescence-based molecular recognition to be easily regulated.

Scheme 1- 5. Opposite enantioselectivity of Mg(II) versus Zn(II) with **16** and a proposed reaction of (*S*)-**16** with L- and D-Met in the presence of Mg^{2+}. Reprinted with permission from ref 106. *Copyright [2020] American Chemical Society.*

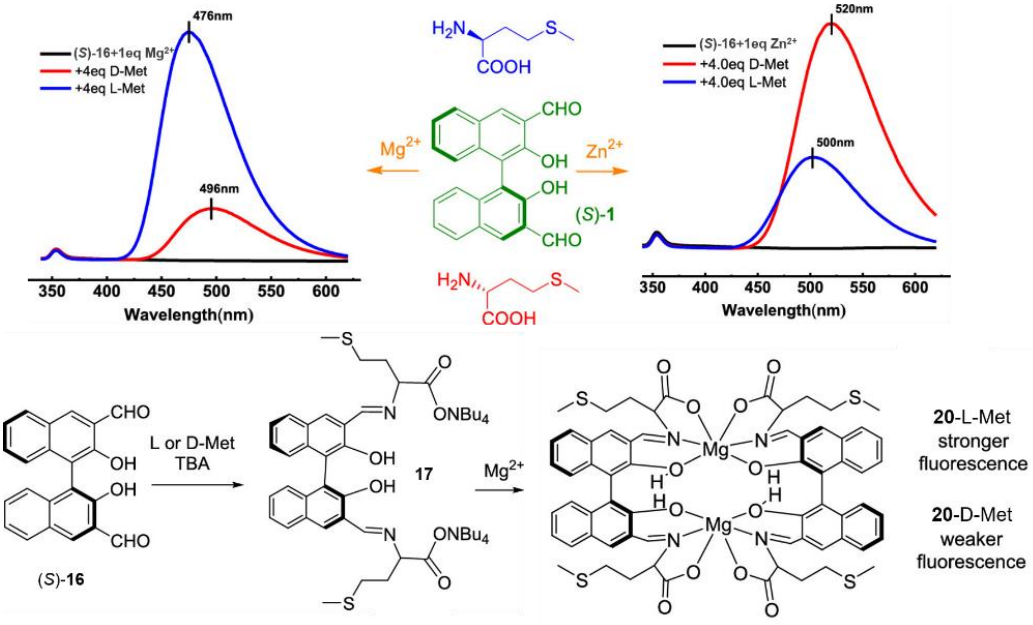

In another rare case, *Pu et al*. observed an unprecedented enantioselective gel collapsing from the gel formed by Cu(II) coordination to sensor **21** upon ultra-sonication.[107] The gel remains stable when treated with (*R*)-phenylglycinol while collapses when (*S*)-phenylglycinol was applied (Scheme 1-6). Stronger fluorescence enhancement was also observed for the (*S*)-enantiomer. And the chiral Cu(II) complex also exhibits significant enantioselective fluorescent enhancement in the presence of a variety of amino alcohols in solution. This study demonstrates that the chiral molecular gels are potentially useful for visual chiral discrimination.

Scheme 1- 6. Enantioselective response of the gel (*R*)-**21** toward (*R*)-phenylglycinol and (*S*)-phenylglycinol. Adapted with permission from ref 107. *Copyright [2010] American Chemical Society.*

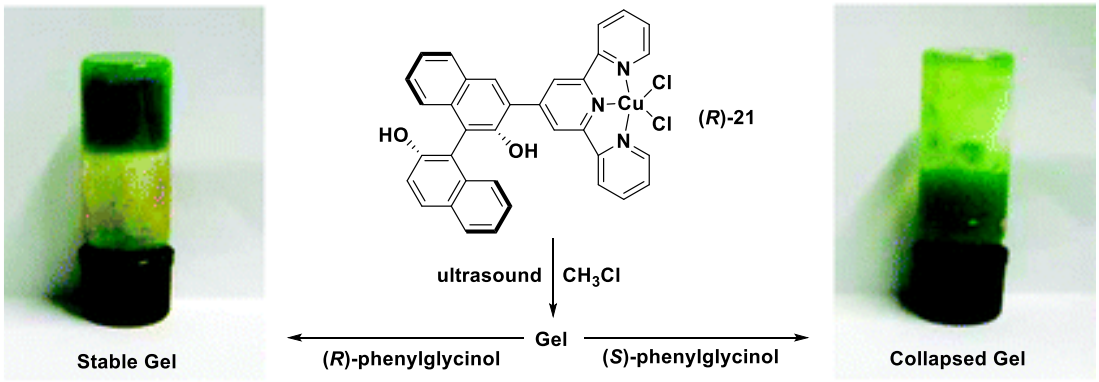

1.3.5. Novel Material-based Sensors

Besides research on the small molecular sensors, a lot of works have also been reported by accommodating chirality to novel materials like polymer, nanomaterial, MOF, and COF. By the *Pu* group several enantioselective polymer-based BINOL derivatives were designed and

synthesized recently. They exhibited very unique properties including very good amphiphilicity,[108] lower critical solution temperature (LCST),[109] water solubility,[110] emission red shift,[111] and greatly amplified enantioselectivity[112] that couldn't be achieved by simple small molecular probes. Over the last decades, by using luminescent nanomaterials and quantum dots there have been appeared a number of works in the enantioselective for chiral molecules like amino acids.[113, 114, 115, 116] Chiral binding units were linked to the surface of these materials in order to gain the ability in enantioselective discrimination.

As a new class of crystalline porous materials, metal–organic frameworks (MOFs) have attracted a great deal of interest due to their rationally manipulation and functionality at the molecular level. The exceptionally high porosity of MOFs allows applications in diverse areas such as gas storage and separation, drug delivery, bioimaging, catalysis, and chemical sensing. As a leader in the field of building a variety of MOFs, *Lin et al.* reported enantioselective sensing of various amino alcohols using the metal-organic framework (MOF) formed by coordination of Cd(II) with ligand **L**-H_4.[117] Fluorescence of MOF was quenched by amino alcohols and different Stern-Volmer constants were observed for the two enantiomers of one amino alcohol (Figure 1-13), with K_{SV} (*R*) / K_{SV} (*S*) reaching up to 3.12.

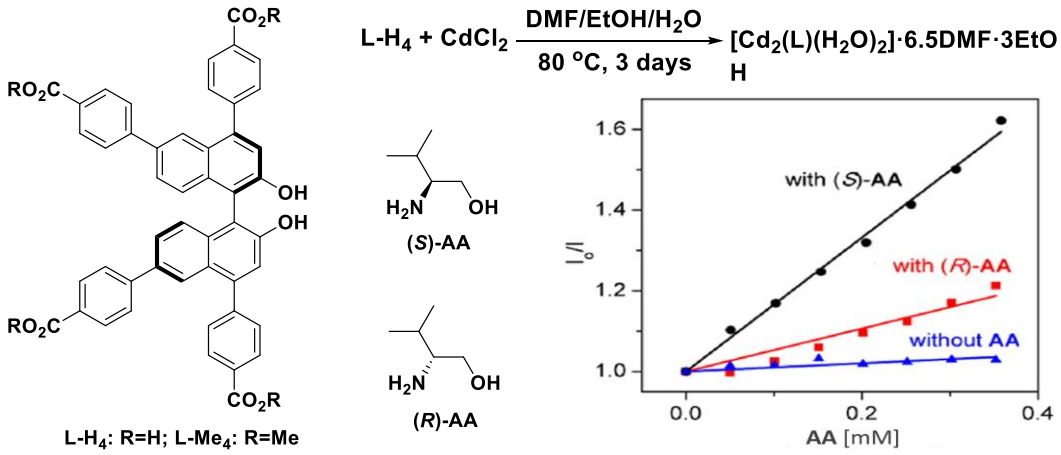

Figure 1- 13. Synthesis of the Cd(II) MOF and fluorescence quenching of the MOF by amino alcohols. Adapted with permission from ref 117. *Copyright [2012] American Chemical Society.*

Very similar with the MOFs, the covalent organic frameworks COFs are a new class of porous crystalline materials by integrating organic building blocks into predetermined networks via covalent bonds. One of their striking features lies in the tunable, designable, and functionalizable nano-space. The nano-space within COFs allows designed incorporation of different functionalities for targeted applications, such as molecule storage and separation, energy storage, optoelectronics, and catalysis; and it has also provided plenty of opportunities for enantioselective processes including asymmetric catalysis, enantioselective separation, and sensing. Among countless scientists and researchers focused on MOFs as well as COFs, the *Cui* group recently dedicating themselves in applying these frameworks and other novel materials (e.g. supramolecular coordination chiral cages) they built in enantioselective process.[118, 119, 120, 121, 122] Figure 1-14 displays some representative examples of novel structures the *Cui* group synthesized and characterized.

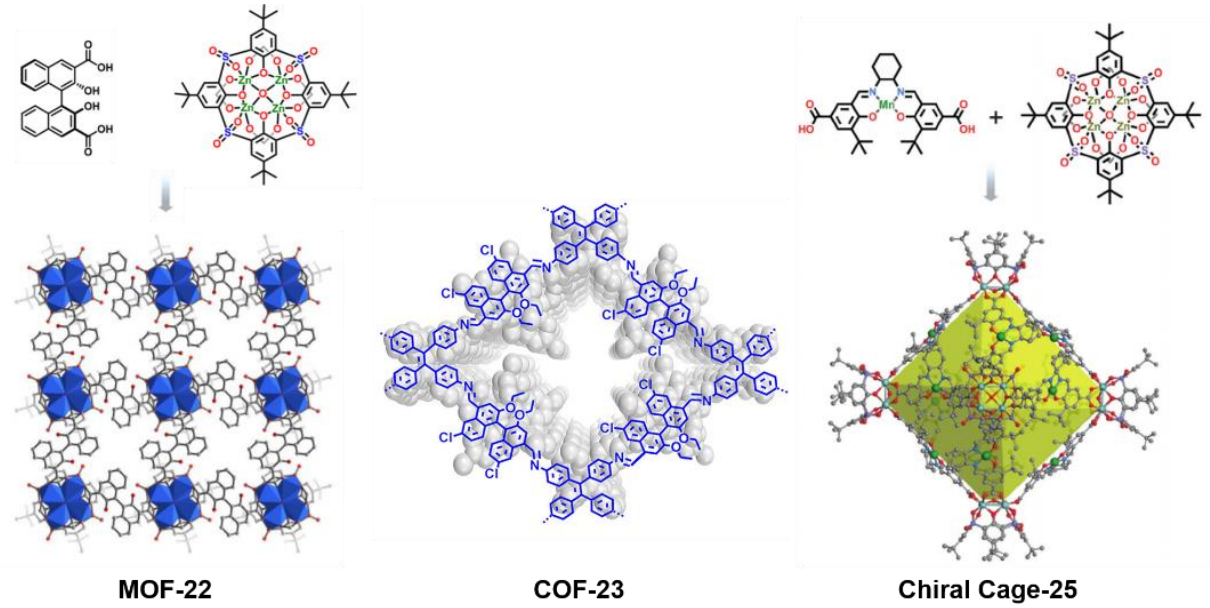

Figure 1- 14. Selective structures of recent novel materials for enantioselective processes. Adapted with permission from ref 118, 119, 121. *Copyright © 2018 WILEY-VCH Verlag GmbH & Co. KGaA, Weinheim. Copyright [2019] American Chemical Society.*

Taking an enantiopure BINOL-based linear dialdehyde and a tetrakis(4-aminophenyl)ethene as building blocks, two imine-linked chiral fluorescent COF-**23**, with a 2D layered tetragonal structure was prepared by *Cui et al.* in a latest study of enantioselective sensing with COFs.[119] The COF-**23** containing flexible tetraphenylethylene units could be readily exfoliated into ultrathin 2D nanosheets and electrospun to make free-standing nanofiber membrane. In both the solution and membrane systems, the fluorescence of COF-**23** nanosheets could be successfully quenched by the volatile chiral odor vapors like α-pinenes via enantioselective interactions with the restrained BINOL moieties, giving rise to remarkable chiral vapor COF sensors. Compared to the BINOL-based homogeneous and membrane systems, the COF-**23** nanosheets exhibited greatly enhanced sensitivity and enantioselectivity owing to the

confinement effect and the conformational rigidity of the sensing BINOL groups in the framework.

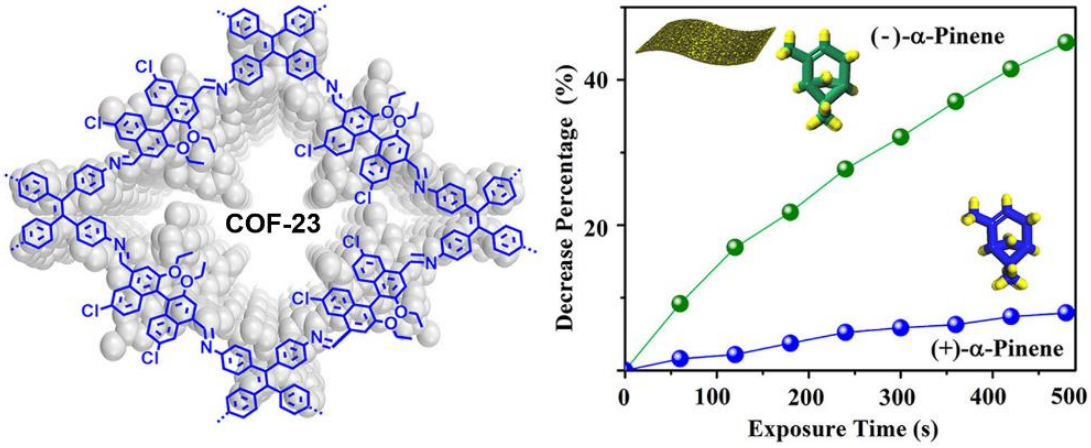

Adapted with permission from ref 119. *Copyright [2019] American Chemical Society.*

The amplified chiral discrimination of the analytes afforded by the BINOL-based COF should be utilized to design functional chiral COFs for other targeted chirality applications such as heterogeneous asymmetric catalysis, enantio-separations, and enantioselective high throughput screening for small molecule substrates via diverse signals.

1.3.6. Fluorinated Sensors

Due to the extreme electronegativity of fluorine atom, fluorination of a molecule affects nearly all of its properties, like reactivity, adsorption, distribution, metabolism, and excretion.[123] In the area of pharmaceuticals and agrochemicals, fluorination is an important method to modulate bioactivities of molecules.[124] The fluorinated drugs have been widely applied to the treatment of cancer, cardiovascular diseases, infectious diseases, nervous system diseases and etc.[118] The top-selling ones are Prozac (anti-depression), Lipitor (reductase inhibitor) and Cipro (infection treatment).

A few fluorine atoms are usually enough to change the bioactivities of a drug significantly. When the weight percentage of fluorine (wt %) in C(sp3)-F bonds within a molecule exceeds 60%, this molecules is referred to be "fluorous", a term introduced by *Horváth et al.* in 1994 as an analogue of "aqueous".[125] Fluorocarbons, which are produced by replacing all hydrogen atoms in hydrocarbons to fluorine, are fluorous solvents that are both lipophobic and hydrophobic. The most commonly used fluorous solvents are perfluorinated alkanes like perfluorohexanes (FC-72) and perfluorodecalins (PP6). Fluorous ponytail is fluoroalkyl moiety with the formula $(CH_2)_m(CF_2)_nCF_3$. Ponytail can make a molecule partially or predominantly soluble in fluorous solvent depending on its number and length. At low or room temperature, a biphasic heterogeneous system is formed between fluorous and organic solvents. However, at elevated temperature they are miscible and a single-phase homogeneous system is formed. In the past two decades, fluorous chemistry has been widely studied in the area of green chemistry, materials chemistry and biomedical systems.[126, 127, 128]

In light of the unique properties of the fluorine chemistry, *Pu et al.* developed and reported several fluorinated sensors for chiral amino alcohols, amines, and amino acids in the aprotic polar solvent, fluorous phase and (fluorous versus. non-fluorous) biphasic system with distinct differences in fluorescence[129, 130, 131, 132] or CD[133] signals.

Wang et al. found that compound **25**, prepared from 1,1′-bi-2-naphthol (BINOL), showed highly enantioselective fluorescent response in perfluorohexane (FC-72).[129] The electrophilic perfluoroalkyl ketone groups of **25** could form adducts with nucleophilic chiral amino alcohols in FC-72 to produce enantioselective fluorescence enhancement. This compound can be used for chiral recognition in a fluorous solvent, but it cannot be used in fluorous/nonfluorous biphasic systems because the amino alcohol adduct has very limited solubility in the fluorous solvent and

in a biphasic system the amino alcohol substrates prefer to stay in the original nonfluorous phase instead of getting into the fluorous phase to react with **25**. Chiral recognition in a biphasic system can simplify the application of such a fluorous phase-based fluorescent sensors in reaction screening experiments, since these experiments are generally conducted in nonfluorous solvents. It is therefore desirable to increase the fluorine content of the fluorescent probe in order to conduct the biphasic recognition.

Wang et al. designed and synthesized a novel BINOL-based aldehyde **26** containing four perfluoroalkyl groups with the incorporation of additional intramolecular hydrogen-bonding capability for the enantioselective fluorescent recognition of the *trans-1,2*-diaminocyclohexane (DACH).[131] For the first time it has demonstrated that the enantioselective fluorescent recognition can be conducted in a fluorous/organic biphasic system.

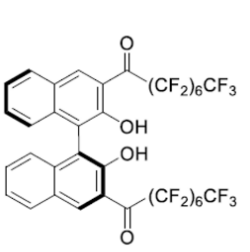

25

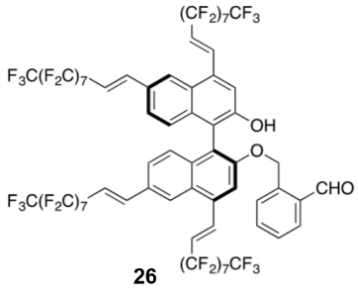

26

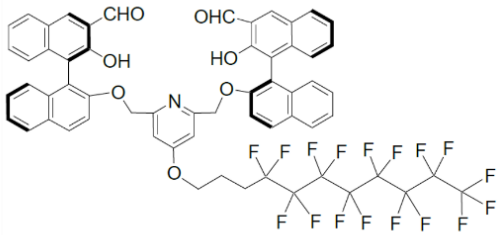

27

Latest, *Zhu et al*. introduced a perfluoroalkyl chain to the bisBINOL-based aldehyde to make the fluorinated probe (*R,R*)-**27**.[132] When a solution of (*R,R*)-**27** in a fluorous solvent 1H,1H,2H,2H-perfluoro-1-octanol (PFOH) was mixed with an aqueous solution of amino acids and Zn^{2+} in the presence of TBAOH, fluorescence of the fluorous phase in the biphasic system showed good enantioselective enhancement. The observed *ef*'s $[(I_D-I_0)/(I_L-I_0)]$ were distinctively high values. This biphasic fluorescent sensing was useful to analyze the enantiomeric

composition of the crude amino acid products generated from an enzyme-catalyzed asymmetric hydrolysis of a racemic amino acid ester.

These researches above started and accelerated the investigation of the usage of the fluorinated probes in rapid fluorescent screening of reactions that producing chiral substrates. Chiral recognition in the fluorous phase offers the advantage of minimizing the interference of other species in a screening protocol, i.e., catalyst, ligand, additive, etc., potentially giving rise to a rapid screening course of crude reaction mixtures. Overall, it minimizes the workup needed prior to the determination of ee values, and is a major advance in conducting optical ee assays.

1.4. Enantioselective High-throughput Screening (HTS)

1.4.1. Introduction of HTS

The increasing demand to highly efficient catalysts and development of computing technology has promoted the discovery of asymmetric catalysts using combinatorial methods.[134, 135] Instead of a single design, synthesis and testing cycle, HTS facilitates this process by largely multiplying each step, especially for testing and design.[136] Testing enantiomeric excess (ee) has long been limited by the efficiency of chiral HPLC, which requires the sample to have high purity and takes about 30 minutes for each run, as well as large amount of solvent consumption.[137]

1.4.2. High Performance Liquid Chromatography (HPLC)

In an early study by *Gao et al*, they used chiral HPLC to screen the substrate scopes of a single catalyst for asymmetric reduction of ketone to alcohol.[138] By dividing the ketones to several groups based on their retention times to avoid spectra overlap, they are able to measure up to eight *ee* values in a single run. But a preliminary flash chromatography is required for larger sample amounts.

In order to increase the analytical throughput, the LC columns containing smaller particles have been widespread developed and commercialized and equipped on the instruments that can operate at significantly higher pressure, allowing for the same resolution for a given separation to be achieved in significantly less time. For instance, using a column with 5 μm particles a series of alkyl benzenes analytes could be separated in 15 min while by using the same phase with just 1.7 μm particles, the alkyl benzene samples could be resolved in only 1.8 min.[139] Though the ultrafast chiral separations progressed slower, there has recently been growing interest in developing sub-2 μm particles to decrease analysis time for enantiomer resolution.[140] Where chiral separations often required upward of 20 min in the past, we are now reaching a period where these separations can be carried out in the seconds time window.[141, 142] A further study was carried out using a chemically diverse set of 50 racemic compounds including some challenging intermediates from the pharmaceutical industry. As a result, it was possible to resolve 43 of the 50 members of the set under 1 min of run time using either SFC or HPLC.[143] Unfortunately, all ultrafast HPLC separations mentioned above were achieved still with chemically pure samples, let along direct using the crude asymmetric reaction mixtures.

1.4.3. Nuclear Magnetic Resonance (NMR) Spectroscopy

As a well-established technique NMR has its intrinsic advantages such as mature instrumentations, easily accessible data analysis, and relative rapid analytical rate. *Swager et al.* reported a palladium complex with chiral pincer ligands which was capable of resolving mixtures containing 12 amine racemates using ^{19}F NMR.[144] Like this case, recent studies focus more on its application in high-throughput analysis, which enables rapid *ee* determination of many samples. *Reetz et al.* set up a flow-through NMR screening equipped with an autosampler to achieve ee measurements in a high volume that was up to 1400/24 hours.[145]

Though still limited by substrate scope, low sensitivity, line-broadening and resolution, chiral NMR is an important alternative to HPLC when chiral columns are not efficient or sample separations are difficult.

1.4.4. Mass Spectroscopy (MS)

Mass spectrometry technique has been widely studied for HTS in kinetic resolution and asymmetric transformation.[146] It doesn't need chromatographic sample purification and can achieve nano-scale *ee* determination.[147] The principle is based on using isotope labeling to make quasi-enantiomers, also known as pseudo-enantiomers, which are assumed to behave as real enantiomers in catalytic reactions but have distinct molecular weights. *Reetz et al.* used this method to screen lipase-catalyzed kinetic resolution of phenylethyl acetate. The quasi-enantiomers were mixed at exact 1:1 ratio, and peak intensity ratios in ESI-MS after reaction can be correlated to the enantiomeric excess. The results obtained are highly consistent with the GC results. Using a well-designed setup, they were able to measure more than 1000 ee values accurately within a single day for this reaction. This strategy was also applied to other reactions like enantioselective esterification or hydrolysis of esters.

Remarkably, *Pfaltz et al.* reported the use of racemic catalysts for high throughput screening in palladium catalyzed allylic substitutions starting with unequal amount (25:75) of quasi-enantiomers using ESI-MS.[148] This method opens a door for evaluating the efficiency of chiral catalyst when its enantiopure form is not readily available. However, mostly MS serves as the most sensitive detection method after chiral chromatography separation and analysis.

1.4.5. Infrared Resonance (IR)

In another example carried out by *Reetz et al., an* IR-thermographic assays is used for the screening of various kinds of reactions like salen-catalyzed hydrolysis of epoxide to diol.[149] They found that Co(II) salen is more effective than Mn(II) or Cr(II) sales. Using an infrared camera, the temperature increase caused by the reaction can be imaged overtime. In a parallel setup containing *R*, *S* and racemate epoxide separately, it is observed that (*S*)-epoxide with Co(II) salen caused highest temperature increase. IR-thermography fits well into the need of high-throughput screening. However, this method is more qualitative than quantitative as subtle differences in temperature increase cannot be resolved. Regarding endothermic reactions, "cold spots" have been created for IR imaging.[150]

1.4.6. Supercritical Fluid Chromatography (SFC)

More recently, supercritical fluid chromatography (SFC) has emerged as an ideal tool for faster separations due to superior diffusion rates and lower viscosity of supercritical CO_2. SFC is a separation technique similar to high performance liquid chromatography (HPLC) using mostly the same hardware and software as HPLC. The mobile phase is a binary or ternary mixture (usually including organic modifier such as polar solvent and additives like acid or base) with CO_2 as the main component. The separation is usually performed as a gradient elution where composition of the mobile phase is changed versus time. Most of the chiral stationary phase are still crown ethers, ligand exchange, protein-based CSPs, and the polysaccharide-based CSPs that were responsible for two-thirds of the enantiomer separations, very similar with those in the chiral HPLC columns.[151] Experts in the field agree that SFC has established itself as the preferred way of doing chiral analysis on both the analytical and preparative scales. They also say that SFC will become the norm for small-scale purifications. Increased interest in (a) the petrochemical and food industries, (b) the determination of environmental air quality, (c)

biodiesel quality control, (d) protein separations, etc. can be expected in the future.[152] A number of manufacturers and companies have been developing SFC new instrumentation with their expertise in HPLC instrumentation development. SFC is easily coupled with mass spectrometry (MS) for high-throughput analysis, purity assessment, structure characterization, impurity profiling and purification.[153] Enantiomeric excess (ee) was evaluated for two internally synthesized compound libraries using a high-throughput automated intelligent four channel parallel SFC/MS system equipped with a multiplexed ion source interface (SFC/MS-MUX).[154] The system analyzed each sample simultaneously against four chiral columns using up to six organic modifiers. A reversal of elution order was observed for several samples across multiple CSPs and modifiers. The relationship between elution order and percent enantiomeric excess (% ee) accuracy was presented for compounds exhibiting high, middle, and low % ee values. Later another report appeared that noted a raised enantioselectivity was achieved by using SFC compared with HPLC due to the modifiers used rather than from the chromatographic mode used.[155] A recent report from the *Merck Research Lab* SFC was used by them as the state-of-the-art technique for GMP analysis in support of pharmaceutical development and manufacturing activities, which largely proved the universal analysis capability in very high accuracy, precision, repeatability, sensitivity as well as enantioselectivity when it comes to chiral analytes.[13]

1.4.7. Circular Dichroism (CD)

Circular dichroism spectroscopy is inherently suited for chiral recognition task. Left- and right-circularly polarized light creates diastereomeric interactions with the chiral analyte giving rise to characteristic *Cotton effects* that could be rapidly read out by the CD instrument. *Yanagisawa et al.* developed a HTS protocol that speeds up the optimization of the $Cu(OAc)_2$-catalyzed Henry reaction between a benzaldehyde derivative and nitromethane (Figure 1-15).[156]

In this approach, chiral imidazoline-amine ligands were immobilized on a solid surface and then tested. Upon completion of the reaction, the mixtures were analyzed via continuous injections into a CD spectrophotometer. A maximum CD signal was only observed for reactions with both high yield and high enantioselectivity. This original HTS effort led to the discovery of a method that gives the desired nitroaldol product in 95% ee. The tandem use of combinatorial chemistry with CD spectroscopy allowed for the screening of experimental parameters that would otherwise be given up due to the sheer number of reactions that would need to be processed. Furthermore, the use of immobilized catalysts simplifies reaction screening because any interference of potentially CD active catalysts with the optical ee determination is eliminated. Optical methods for ee determination can have a large advantage over chromatographic methods in such cases.

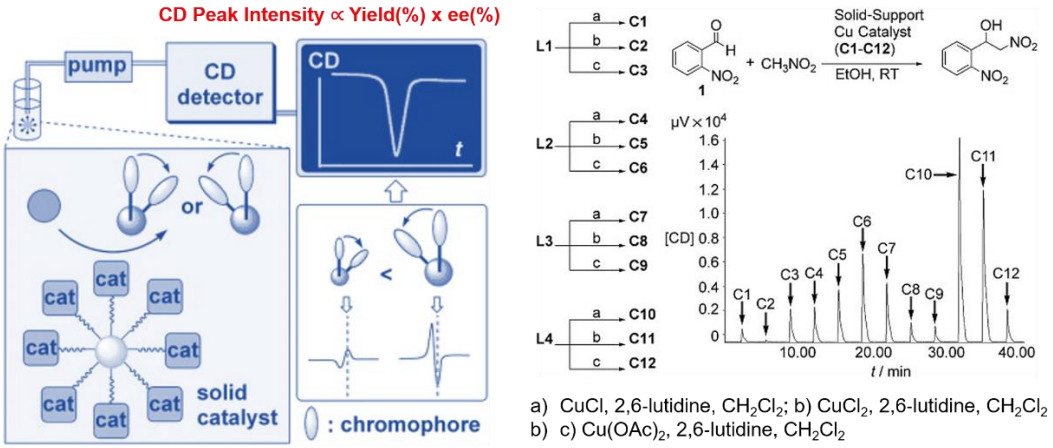

Figure 1- 15. Schematic for HTS of heterogeneous catalytic asymmetric Henry reaction with continuous injection CD spectrophotometry. Adapted with permission from ref 156. *Copyright © 2006 WILEY-VCH Verlag GmbH & Co. KGaA, Weinheim.*

Miller and *Anslyn* carried out a synergistic combinatorial and chiroptical study by applying a previously developed supramolecular CD sensing assay to speed up ongoing efforts to improve the Baeyer−Villiger oxidation shown in Figure 1-16.[157] They screened the performance of small peptide catalysts in the desymmetrization of the cyclic ketone. For determination of the absolute configuration and ee, the lactone product was subjected to methanolysis and a simple silica plug purification. The stereochemical analysis of the corresponding alcohol was achieved by CD measurements with the self-assembled complex. This approach was successful in identifying the best catalysts for this reaction and it offered significant time savings over chiral HPLC. While its ability to evaluate catalyst performance is equivalent to HPLC, even for samples with low ee. The assay reduced the time from ~30 min to just a few seconds per sample. However, the sample preparation for the CD measurements (self-assembly) usually needs one day at room temperature.

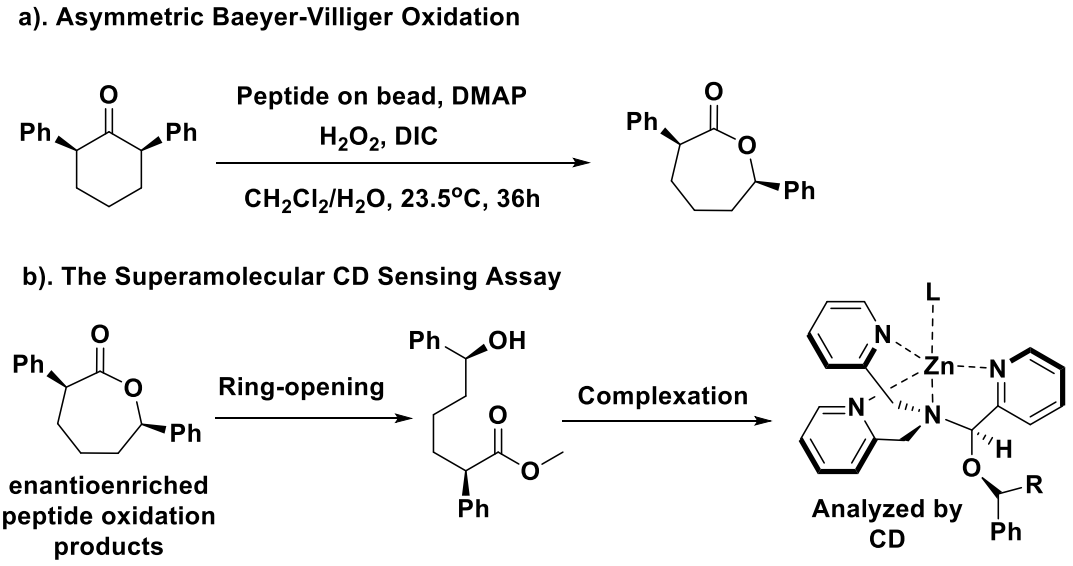

Figure 1- 16. CD Analysis of an asymmetric Baeyer−Villiger Oxidation.

Wolf et al. have also developed some well-designed sensors containing fluorophores to induce CD signals at UV-vis region for rapid *ee* determination and catalyst screening.[54, 56, 57, 58] The errors of enantiomeric excess and concentration measurements are generally below 10% to the HPLC standard. Remarkably, they demonstrated the feasibility of using CD for high-throughput chiral catalysts screening in Sharpless dihydroxylation, iridium-catalyzed hydrogenation and ketone reduction, and the allylation of isatins with a chiral boron complex, without any workup of crude reaction mixtures. However, the sample preparation for the CD measurements (self-assembly) still needs about over 20 hours at room temperature. Moreover, a CD spectrometer is much expensive than a UV-vis or fluorescence spectrometer that has a much better sensitivity with a variety of sensing modes.

1.4.8. UV-vis Spectroscopy

UV-vis has also demonstrated its value in HTS in a few cases. In an initial super HTS occasion, *Reetz et al.* picked out the best lipases from a library of 30, 000 mutant lipases that synthesize chiral acid with over 90 % *ee* compared with 2 % ee from natural lipase.[158] During screening, they use the *R* and *S* enantiomers of a chiral m-nitrophenol ester in parallel for each lipase in 96 wells and measure the absorption at 410 nm caused by the formation of nitrophenolate anion. The difference in absorption is directly related to *ee* values. In addition, most of chiral separation techniques utilizing UV-vis and UV-vis-based spectrometer as a reliable and available detector for the separated product analysis.

Anslyn et al. demonstrated that the UV-vis technique was adaptable to yield and ee analysis of a chemical reaction. (Scheme 1-7)[159] A tailored UV-vis eIDA was applied to the Sharpless asymmetric dihydroxylation (AD) of trans-stilbene. The chemo-sensing of the isolated

diol product of the AD reaction was conducted with a combination of the boronic acid hosts and the indicator. The raw UV absorbance data were collected on a 96-well plate followed by a 3-layered Multilayer Perceptron (MLP) analysis which furnished results with sufficient accuracy for HTS purposes. However, theses colorimetric protocols have their intrinsic flaw in sensitivity and substrates limitations.

Scheme 1- 7. Equilibria involved in the UV-vis enantioselective indicator displacement assay (eIDA) using a chiral host for chiral diols with pyrocatechol violet (PCV) as the indicator. ΔAbs, absorbance change; $[G]_t$, total guest concentration; ee, enantiomeric excess. Adapted with permission from ref 159. *Copyright [2009] National Academy of Sciences.*

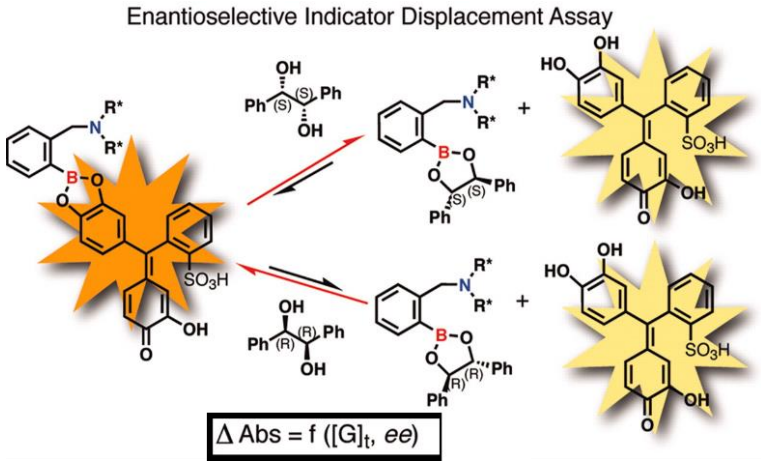

1.4.9. Fluorescence

The advances in optical protocols for quantitative enantiomeric excess determination have led to their use in a variety of high throughput screening courses for the discovery of novel asymmetric reaction. The protocols mentioned above might be competitive with the gold standard HPLC methods. While in the near future, with its superiority in accessibility, sensitivity,

diverse reading outs, and the compatibility for the existing HTS facilities, enantioselective fluorescence technique can truly be used to avoid the chiral HPLC in many instances.

As one of the earliest examples by choosing fluorescence as the optical method for asymmetric reaction discovery, *Pu et al*. developed macrocycle **28** for fluorescence detection of mandelic acid.[160] Using both enantiomers of **28**, the enantiomeric excess of a reaction crude product could be determined with a calibration curve. To demonstrate the suitability of this assay for HTS, the conversion of an aldehyde to a long-chain aliphatic group-substituted α-hydroxy ester was investigated. Subsequent hydrolysis of the methyl mandelate gave the α-hydroxy acid product that was soluble only in THF and insoluble in water and many polar/nonpolar organic solvents. The asymmetric reaction product precipitated out, avoiding the requirement for purification prior to ee analysis by the developed screening protocol (Scheme 1-8), by which the ee of the reaction was determined with the enantioselective fluorescent sensor pairs. The fluorescence-determined ee values matched well with chiral HPLC results.

Scheme 1- 8. The enantioselective fluorescent assay for asymmetric catalysis screening and the comparison of the ees from HPLC analysis with those from fluorescence measurements. Adapted with permission from ref 160. *Copyright [2005] American Chemical Society.*

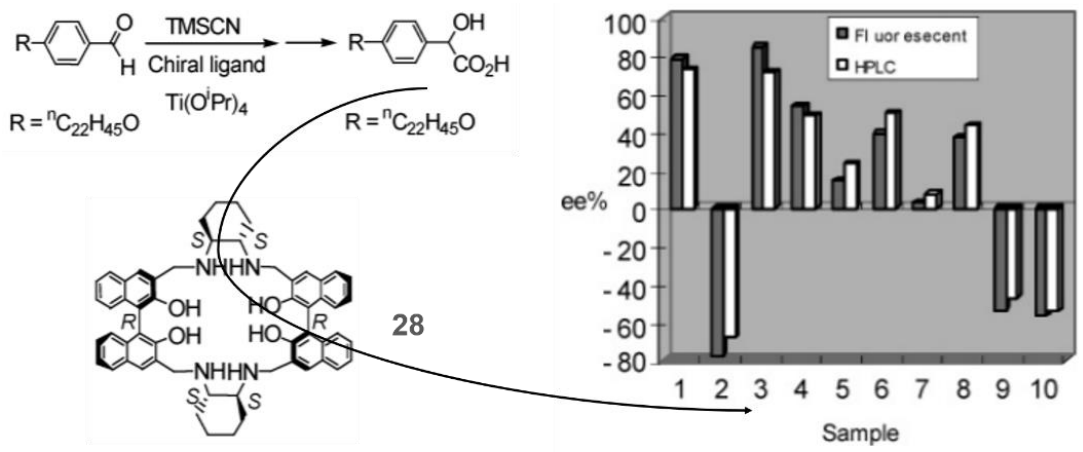

Wolf et al. used the chiral probe, 1,8-diquinolylnaphthalene *N, N'*-dioxide, **29**, for enantioselectively probing an enzyme catalytic transformation (Scheme 1-9).[161] The kinetic resolution of *trans*-1,2-diaminocyclohexane (**30**) with dimethyl malonate by *Candida antarctica* lipase (CAL) was investigated. Probe **29** exhibited enantioselective fluorescence enhancement upon formation of diastereomeric hydrogen bond adducts with the diamine enantiomers. Very small aliquots of product mixtures from fast acid/ base extraction were used to conduct the screening of the reaction. The ee values were determined from a calibration curve and verified by chiral HPLC, which required a precolumn cumbersome product derivatization. Thus, this fluorescence sensing protocol streamlined the reaction monitoring by fewer labor, time, as well as cost and it might be also amenable to other asymmetric transformations. Concentration and ee analysis of samples of **30** with this IDA gave results that differed only by several percent from the actual values.

Scheme1- 9. Enantioselective probe **29** for the screening of the kinetic resolution of *trans*-1,2-diaminocyclohexane and the comparison of the ees from HPLC analysis with those from fluorescence measurements. Adapted with permission from ref 161. *Copyright [2005] American Chemical Society.*

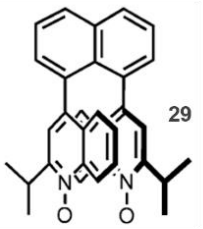

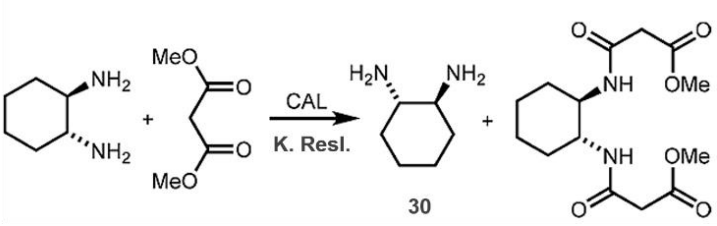

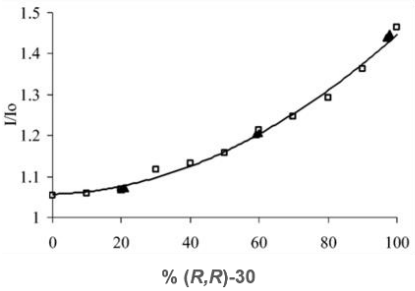

time (h)	% ee (*S*,*S*-30) by HPLC	I/I_0 [a]	% ee (*S*,*S*-30) by fluorescence sensing[a]
1.5	24	1.1287	24
2.5	44	1.1022	44
3.5	56	1.0905	50
5.0	64	1.0861	56
7.0	68	1.0686	62

The practice of a sensor first in racemic form for concentration and then in enantiopure form for enantiomeric excess analysis usually requires two tests though with the same setup.[162] However, the sensing of both unknown parameters is able to be accomplished with a single assay. *Pu et al*. introduced a well-designed eIDA based on dynamic covalent chemistry with the BINOL derived di-imine **31** formed by condensation of **16** with 2-naphthylamine. The free sensor exhibited only weak fluorescence signals under the same conditions and generated slight background noise. Imine metathesis in the presence of excess of diamine and zinc acetate gave a mixture of complex **32** and 2 equivalents of 2-naphthylamine, which served as the displaced indicator with a fluorescence emission at 427 nm that was associated to the original concentration of the chiral diamine substrates while the fluorescence intensity of **32** measured at 525 nm depends on the chirality of the diamine and provides information about the analyte enantiomeric excess. Similar results were obtained with phenylalaninol, phenylglycinol and alaninol (Scheme 1-10). [163] This protocol could be applied to determine the enantiomeric excess and total concentration of chiral amines simultaneously through dynamic imine exchange.

Scheme 1- 10. A) Preparation of compound (*R*)-**31** and B), C), D) Sensing of chiral diamine through imine exchange using **31**. Adapted with permission from ref 163. *Copyright [2015] American Chemical Society.*

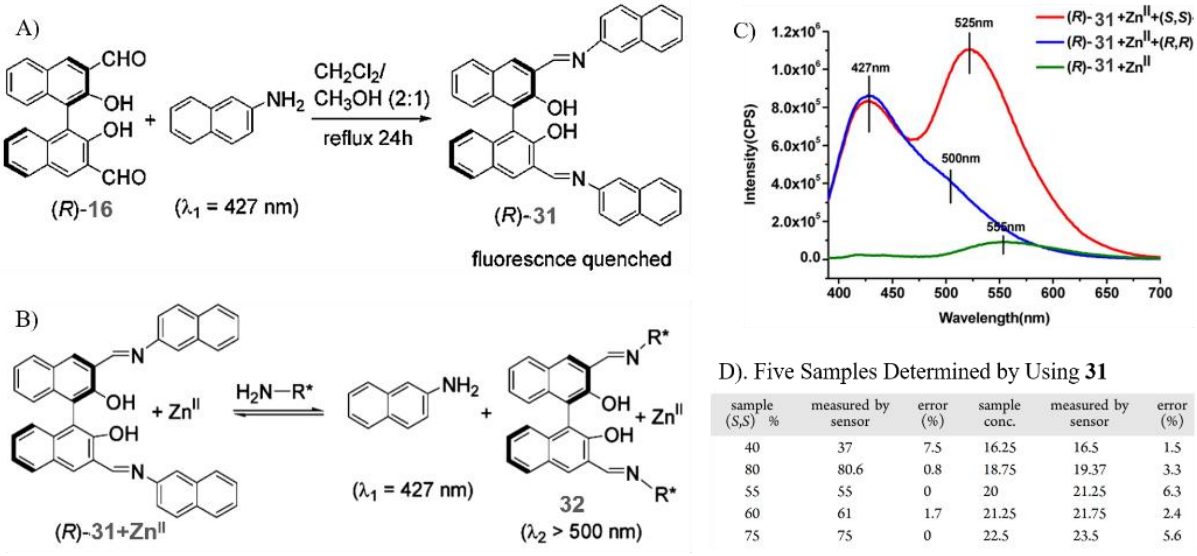

D). Five Samples Determined by Using **31**

sample (*S*,*S*) %	measured by sensor	error (%)	sample conc.	measured by sensor	error (%)
40	37	7.5	16.25	16.5	1.5
80	80.6	0.8	18.75	19.37	3.3
55	55	0	20	21.25	6.3
60	61	1.7	21.25	21.75	2.4
75	75	0	22.5	23.5	5.6

More similar works of the *Pu* group in determination of the overall concentration and the ee of chiral substrates simultaneously could be found in this review paper.[74] They have been long pioneering in the field of applying fluorescent probes in rapid chiral analysis with the simplest fashion. However, over a decade past, a real example that is one further step forward to the above preliminary researches is still awaiting.

1.5. Conclusion

Although a large number of enantioselective techniques for chiral compounds have been developed, it is still a challenge to utilizing most of them in real screening for asymmetric reactions. While chromatography remains the workhorse for determining the purity and enantiomeric excess for chiral compounds in regulated pharmaceutical work, the use of optical methods in synthetic organic reactions run in parallel has been rapidly gaining progress. These

methods are generally less accurate than HPLC, however they offer several advantages that compensate this limitation. Chromatography is inherently a serial process with uncontrollable factors and requires new methods for every new structure analyzed. Small changes in analyte structure can cause dramatic differences in enantio-selectivity of a chiral stationary phase. And usually very high chemistry purity is needed for analysis accuracy with chromatography. Optical analysis can be performed in plates and thus has many of the advantages of a parallel process. Numerous probe designs and optical assays that report ee values via circular dichroism (CD), fluorescence and UV absorbance have been developed and reported previously. Optical assays have been developed for many common functional groups created in asymmetric methodologies. The techniques are robust and ready to be employed by synthetic chemists.

Most of the chiral optical sensors including fluorescence sensors with high enantioselectivity can be used to determine ee of substrates usually only at a certain concentration, which means a separate method for determining the total concentration is needed prior to the chiral analysis. This drawback significantly limits the application of fluorescent sensors in HTS of asymmetric reactions.

The *Pu* lab has developed a series of BINOL-based chiral fluorescent sensors with very high enantioselectivity. A big subject of this thesis is to further develop and utilize those sensors and to explore protocols in the fluorous phase for ee analysis of reaction product in the crude reaction mixtures as well as for simultaneous determination of concentration and ee of chiral substrates by fluorescence. Both aspects should be very crucial processes toward the application of fluorescent sensors in the high-throughput screening of asymmetric catalysts.

1.6. References

1 Organic Chemistry (4th Edition) Paula Y. Bruice. Pearson Educational Books.

2 Brooks W.H., Guida W.C., and Daniel K.G., *Curr Top Med Chem*. **2011**, *11* (7), 760–770.

3 Challener C., *Pharmaceutical Technology*, **2015**, *39* (2), 40-41.

4 Cecilia Noguez, F. H. *Chirality* **2014**, *26*, 553.

5 Kim J.H., Scialli A.R., *Toxicol. Sci*. **2011**, *122*, 1–6.

6 Webb JF, *Canadian Medical Association Journal*. **1963**, *89*: 987–92.

7 Nguyen, L. A.; He, H.; Pham-Huy, C. *Int. J. Biomed. Sci*. **2006**, *2* (2), 85.

8 Newman, D. J.; Cragg, G. M. *J. Nat. Prod.* **2007**, *70* (3), 461.

9 Garrison AW., *Environ. Sci. Technol*. **2006**, *40* (1), 16-23.

10 Ganapathy, S. *Chiral Separation Techniques: A Practical Approach*, 3rd ed.; *John Wiley & Sons*, **2008**.

11 https://www.drugs.com/stats/top100/2013/sales (Accessed February, 2020).

12 Sanganyado E, Lu Z, Fu Q, Schlenk D, Gan J. Chiral pharmaceuticals: A review on their environmental occurrence and fate processes. *Water Research*, **2017**, *124*, 527-542.

13 Hicks MB, Regalado EL, Tan F, Gong X, Welch CJ, *Journal of Pharmaceutical and Biomedical Analysis*, **2016**, *117*, 316-324

14 Ginterová P, Znaleziona J, Knob R, Douša M, Petr J, Ševčík J, *Chemical Papers*, **2016**, 70, 1024–1030

15 Davies N.M., Teng X.W., *Adv. Pharm.*, **2003**, *1*, 242–252.

16 Announcement: FDA's policy statement for the development of new stereoisomeric drugs. *Chirality*, **1992**, *4*, 338–340.

17 Li B., Haynie D.T., Chiral drug separation, in: S. Lee (Ed.), Encyclopedia of Chemical Processing, *Taylor & Francis, New York*, **2005**, 449–458.

18 Covington CL, Raghavan V, Smuts JP, Armstrong DW, PL. Polavarapu, *Chirality*, **2017**, *29*(11), 670-676.

19 Berova N, Polavarapu PL, Nakanishi K, Woody RW. Comprehensive Chiroptical Spectroscopy: Applications in Stereochemical Analysis of Synthetic Compounds, Natural Products, and Biomolecules. Hoboken, NJ: *John Wiley & Sons*; **2012**.

20 Berova N, Polavarapu PL, Nakanishi K, Woody RW. Comprehensive Chiroptical Spectroscopy: Instrumentation, Methodologies, and Theoretical Simulations. Hoboken, NJ: *John Wiley & Sons*; **2012**.

21 Nafie LA. Vibrational Optical Activity: Principles and Applications. Hoboken, NJ: *John Wiley and Sons*; **2011**.

22 Mateos J. L. and Cram D. J., *J. Am. Chem. Soc*. **1959**, *81* (11), 2756–2762.

23 Parker, D. *Chem. Rev*., **1991**, *91*, 1441–1457

24 Pirkle, W. H.; J. R. Hauske, *J. Org. Chem*. **1977**, *42* (11), 1839.

25 Flack HD, Bernardinelli G, *Chirality*. **2008**, *20* (5), 681-90.

26 Okamoto, Y.; Ikai, T. *Chem. Soc. Rev.* **2008**, *37* (12), 2593.

27 Wellings DA., A Practical Handbook of Preparative HPLC, *Elsevier Science*, **2005**.

28 Ward, T. J.; Ward, K. D. *Anal. Chem.* **2012**, *84* (2), 626.

29 Hyun, M. H.; Han, S. C.; Lipshurtz, B. H.; Shin, Y.-J.; Welch, C. J. *J. Chromat. A*, **2001**, *910* (2), 359.

30 Berthod, A.; Liu, Y.; Bagwill, C.; Armstrong, D. W. *J. Chromat. A* **1996**, *731*, 123.

31 Fischer, L.; Mueller, R.; Ekberg, B.; Mosbach, K. *J. Am. Chem. Soc.* **1991**, *113* (24), 9358.

32 Ikai, T.; Yamamoto, C.; Kamigaito, M.; Okamoto, Y. *Polym. J.* **2006**, *38* (2), 91.

33 Schurig, V. *J. Chromatogr. A*, **1994**, *666*, 111.

34 Schurig, V. *J. Chromatogr. A*, **2001**, *906* (1–2), 275.

35 Ding, J.; Welton, T.; Armstrong, D. W. *Anal. Chem.* **2004**, *76* (22), 6819.

36 Chen X, Kang Y, Zeng S, *Chirality*, **2018**, 30, 609-618.

37 Han DQ, Yao ZP, *TrAC Trends in Analytical Chemistry*, **2020**, 123, 115763.

38 Yu X, Yao ZP, *Analytica Chimica Acta*, **2017**, 968, 1-20.

39 Dale J. A., Dull D. L. and Mosher H. S., *J. Org. Chem.* **1969**, 34 (9), 2543–2549.

40 Dale, J.A., Mosher, H.S., *J. Am. Chem. Soc*., **1973**, 95, 512–519.

41 Trost, B.M., Belletire, J.L., Godleski, S., McDougal, P.G., Balkovec, J.M., Baldwin, J.J., Christy, M.E., Ponticello, G.S., Varga, S.L. & Springer, J.P., *J. Org. Chem*., **1986**, 51, 2370–2374

42 Brunel, J.M., Faure, B., *Tetrahedron Asymmetry*, **1995**, 6, 2353–2356.

43 Garner, C.M., McWhorter, C. & Goerke, A.R., *Tetrahedron Lett*., **1997**, *38*, 7717–7720.

44 Fukui, H., Fukushi, Y. & Tahara, S., *Tetrahedron Lett*., **2003**, *44*, 4063–4065.

45 Tokles, M. & Snyder, J.K., *Tetrahedron Lett*., **1988**, *29*, 6063–6066.

46 Burgess, K. & Porte, A.M., *Angew. Chem. Int. Ed. Engl*., **1994**, *33*, 1182–1184.

47 Caselli, E., Danieli, C., Morandi, S., Bonfiglio, B., Forni, A. & Prati, F., *Org. Lett*., **2003**, *5*, 4863–4866.

48 Kelly AM, Pérez-Fuertes Y, Fossey JS, Yeste SL, Bull SD, James TD, *Nature Protocol*, **2008**, *3*, 219.

49 Pérez-Fuertes Y, Kelly AM, Fossey JS, Powell ME, Bull SD, James TD, *Nature Protocol*, **2008**, *3*, 214.

50 Wenzel, T. J. Discrimination of Chiral Compounds Using NMR Spectroscopy, Wiley-VCH: Weinheim, **2007**.

51 Ranjbar, B.; Gill, P., *Chem. Biol. Drug Des.*, **2009**, *74* (2), 101.

52 Chen, Y. H.; Yang, J. T.; Chau, K. H. *Biochemistry*, **1974**, *13* (16), 3350.

53 Greenfield NJ. *Nat Protoc*. **2006**, *1* (6), 2876–2890.

54 Bentley, K. W.; Wolf, C. *J. Am. Chem. Soc.* **2013**, *135* (33), 12200.

55 Bentley, K. W.; Zhang P.; Wolf, *Science advances*, **2016**, *2*, e1501162.

56 Bentley, K. W.; Proano, D.; Wolf, C. *Nat. Commun.* **2016**, *7*, 12539.

57 Santos, Z. A. D. L.; Wolf, C. *J. Am. Chem. Soc.* **2016**, 138 (41), 3517-13520.

58 Thanzeel FY, Balaraman K, Wolf C, *Chemistry–A European Journal*, **2019**, *25* (47), 11020-11025.

59 Thanzeel FY, Sripada A, Wolf C, *J. Am. Chem. Soc*. **2019**, *141*, 16382−16387.

60 Leung, D.; Kang, S. O.; Anslyn, E. V. *Chem. Soc. Rev*. **2012**, *41* (1), 448−479.

61 Jo, H. H.; Lin, C.-Y.; Anslyn, E. V. *Acc. Chem. Res*. **2014**, *47* (7), 2212−2221.

62 Zhu, L.; Shabbir, S. H.; Anslyn, E. V. *Chem.-Eur. J*. **2007**, *13* (1), 99−104.

63 Brown GG, Dian BC, Douglass KO, Geyer SM, Shipman ST, Pate BH. A broadband fourier transform microwave spectrometer based on chirped pulse excitation. *Rev. Sci. Instrum*., **2008**, *79*, 053103.

64 Patterson D, Schnell M, Doyle JM., *Nature*, **2013**, *497*, 475-477.

65 Patterson D, Doyle JM., *Phys. Rev. Lett*., **2013**, *111*, 023008.

66 Shubert VA, Schmitz D, Patterson D, Doyle JM, Schnell M. *Angew. Chem. Int. Ed*. **2014**, *4*, 1152-1155.

67 Shubert VA, Schmitz D, Pérez C, Medcraft C, Krin A, Domingos SR., Patterson D, Schnell M, *J. Phys. Chem. Lett*., **2016**, *7*, 341−350.

68 Domingos SR, Pérez C, Schnell M, *Annual Review of Physical Chemistry*, **2018**, *69*, 499-519.

69 Neill JL., Yang Y., Muckle MT., Reynolds RL., Evangelisti L., Sonstrom RE., Pate BH., Gupton BF., *Org. Process Res. Dev*. **2019**, *23*, 1046−1051.

70 Lobsiger S, Perez C, Evangelisti L, Lehman KK, Pate BH., *J. Phys. Chem. Lett*., **2015**, *6*, 196-200.

71 Pate, B. H.; Evangelisti, L.; Caminati, W.; Xu, Y.; Thomas, J.; Patterson, D.; Perez, C.; Schnell, M. Quantitative chiral analysis by molecular rotational spectroscopy. In Chiral Analysis: Advances in Spectroscopy, Chromatography, and Emerging Methods, 2nd ed.;Polavarapu, P., Ed.; *Elsevier*, **2018**.

72 Pate BH., Evangelisti L., West C., Mayer KJ., Sonstrom RE., Chiral Analysis of Molecules with Multiple Chiral Centers using Chiral Tag Rotational Spectroscopy, *International Symposium on Molecular Spectroscopy*, **2019**, 06 http://hdl.handle.net/2142/104388 (Accessed 2020-03)

73 Alexander, D. Introduction to Fluorescence Sensing; *Springer*, **2009**.

74 Lakowicz, J. R. Principles of fluorescence spectroscopy, 3rd ed.; *Springer*, **2006**.

75 Pu, L., *Chem. Rev*. **2004**, *104* (3), 1687.

76 Pu, L., *Acc. Chem. Res.* **2012**, *45* (2), 150.

77 Zhang, X.; Yin, J.; Yoon, J., *Chemical Reviews*, **2014**, *114*, 4918–4959.

78 Pu, L., *Acc. Chem. Res*. **2017**, *50* (4), 1032-1040

79 Iwanek W. and Mattey J., *J. Photochem. Photobiol. A Chem.*, **1992**, *76*, 209-226.

80 Parker, K. S.; A. Townshenda; Bale, S. J. *Anal. Proc. Incl. Anal. Commun.*, **1995**, *1*, 329-332.

81 Beer, G.; Daub, J.; Rurack, K. *Chem. Commun.* **2001**, 1138-1139.

82 Lin, J.; Hu, Q. S.; Xu, M. H.; Pu, L. *J. Am. Chem. Soc.* **2002**, *124* (10), 2088-2089.

83 Xu, M. H.; Lin, J.; Hu, Q. S.; Pu, L. *J. Am. Chem. Soc.* **2002**, *124* (47), 14239.

84 Lin, J.; Zhang, H. C.; Pu, L. *Org. Lett*. **2002**, *4* (19), 3297-3300.

85 Liu, H.-L.; Peng, Q.; Wu, Y.-D.; Chen, D.; Hou, X.-L.; Sabat, M.; Pu, L. *Angew. Chem. Int. Ed. Engl*. **2010**, *49* (3), 602-606.

86 Yu, S.; Pu, L. *J. Am. Chem. Soc.* **2010**, *132* (50), 17698.

87 Song F., Wei G., Wang L., Jiao J., Cheng Y., Zhu C., *J. Org. Chem*. **2012**, *77* (10), 4759-4764.

88 Mei, X.; Martin, R. M.; Wolf, C.; V, G. U. *J. Org. Chem.*, **2006**, *71*, 2854.

89 Upadhyay, S. P.; Pissurlenkar, R. R. S.; Coutinho, E. C.; Karnik, A. V., *J. Org. Chem.* **2007**, *72* (15), 5709.

90 Cho, E. N. R.; Li, Y.; Kim, H. J.; Hyun, M. H. *Chirality*, **2011**, *23*, 349.

91 Xu, K.; Jiao, S.; Yao, W.; Xie, E.; Tang, B.; Wang, C., *Chirality*, **2012**, *24*, 646.

92 Zhang X. , Yu Q. , Chen S., Dai Z, *New J. Chem*., **2018**, *42*, 4045-4051.

93 Fang, H.; Kaur, G.; Wang, B. *J. Fluoresc.* **2004**, *14* (5), 481.

94 Simpson, M. G.; Pittelkow, M.; Watson, S. P.; Sanders, J. K. M. *Chem. Rev.* **2006**, *106* (9), 3652.

95 Jin, Y.; Yu, C.; Denman, R. J.; Zhang, W. *Chem. Soc. Rev.* **2013**, *42* (16), 6634.

96 You, L.; Zha, D.; Anslyn, E. V. *Chem. Rev.* **2015**, *115* (15), 7840.

97 James, TD.; KRAS. Sandanayake, S. Shinkai, *Nature* **1995**, *374*, 345-347.

98 Bian Z., Liu A., Li Y., Fang G., Yao Q., Zhang G., Wu Z., *Analyst*, **2020**, *145*, 719-744.

99 Li Q., Kamra T., Ye L., *Chem. Commun*., **2016**, *52*, 3701-3704.

100 Chapin BM., Metola P., Vankayala SL., Woodcock HL., Mooibroek TJ., Lynch VM., Larkin JD., Anslyn EV., *J. Am. Chem. Soc.* **2017**, *139*, 15, 5568-5578.

101 Huang, Z.; Yu, S.; Wen, K.; Yu, X.; Pu, L. *Chem. Sci*. **2014**, *5* (9), 3457-3462.

102 Wang, X.; Shi, D.; Xu, Y.; Yu, S.; Zhao, F.; Wang, Y.; Hu, L.; Tian, J.; Yu, X.; Pu, L. *Tetrahedron Lett*. **2018**, *59*, 2332–2334.

103 Song, T.; Cao, Y.; Zhao, G.; Pu, L. *Inorg. Chem*. **2017**, *56*, 4395-4399.

104 Huang, Z.; Yu, S.; Zhao, X.; Wen, K.; Xu, Y.; Yu, X.; Xu, Y.; Pu, L. *Chem. Eur. J.* **2014**, *20*, 16458–16461.

105 Zhu, Y.-Y.; Wu, X.-D.; Gu, S.-X.; Pu, L., *J. Am. Chem. Soc*., **2019**, *141*, 175−181.

106 Wang X., Jiang Y., Chen Y., Yu S., Shi D., Zhao F., Chen Y., Wang Y., Huo B., Yu XQ., Pu L., *J. Org. Chem*. **2020**, *ASAP*, https://doi.org/10.1021/acs.joc.0c00064.

107 Chen, X.; Huang, Z.; Chen, S. Y.; Li, K.; Yu, X. Q.; Pu, L. *J. Am. Chem. Soc.*, **2010**, *132 (21)*, 7297-7299.

108 Nian S., Pu L., *Chemistry–A European Journal* **2017**, *23* (71), 18066-18073.

109 Nian S., Pu L., *The Journal of organic chemistry* **2018**, *84* (2), 909-913.

110 Du G., Pu L., *Organic letters* **2019**, *21* (12), 4777-4781.

111 Hu L., Wang Y., Duan P., Du Y., Tian J., Shi D., Wang X., Yu S., Yu X., Pu L., *European Journal of Organic Chemistry* **2018** (16), 1896-1901.

112 Zhang X., Wang C., Wang P., Du J., Zhang G., Pu L., *Chemical science* **2015**, *7* (6), 3614-3620

113 Wei, W.; Qu, K.; Ren, J.; Qu, X. *Chem. Sci*. **2011**, *2*, 2050-2056.

114 Song, L.; Wang, S.; Kotov, N. A.; Xia, Y. *Anal. Chem*. **2012**, *84*, 7330−7335.

115 Gao, F.; Ma, S.; Xiao, X.; Hu, Y.; Zhao, D.; He, Z. *Talanta* **2017**, *163*, 102–110.

116 Copur, F.; Bekar, N.; Zor, E.; Alpaydin, S.; Bingol, H. *Sens. Actuators: B. Chemical* **2019**, *279*, 305–312.

117 Wanderley, M. M.; Wang, C.; Wu, C. De; Lin, W. *J. Am. Chem. Soc*. **2012**, *134* (22), 9050.

118 Tan C., Jiao J., Li Z., Liu Y., Han X., Cui Y., *Angew.Chem. Int.Ed*. **2018**, *57*, 2085 –2090.

119 Wu X., Han X., Xu Q., Cui Y., *et al. J. Am. Chem. Soc*. **2019**, *141*, 17, 7081-7089.

120 Gong W., Chen X., Jiang H., Chu D., Cui Y., Liu Y., *J. Am. Chem. Soc*. **2019**, *141*, 18, 7498-7508.

121 Tan C., Yang K., Dong J., Cui Y. *et al. J. Am. Chem. Soc*. **2019**, *141*, 44, 17685-17695.

122 Yuan C., Wu X., Gao R., Han X., Liu Y., Long Y., Cui Y., *J. Am. Chem. Soc*. **2019**, *141*, 51, 20187-20197.

123 Müller, K.; Faeh, C.; Diederich, F. *Science* **2007**, *317* (5846), 1881.

124 Wang, J., Sánchez-Roselló, M., Aceña, J. L., Del Pozo, C., Sorochinsky, A. E.; Fustero, S., Soloshonok, V. A.; Liu, H. *Chem. Rev.* **2014**, *114* (4), 2432.

125 Horvath, I. T.; Rabai, R. *Science* **1994**, *266*, 72.

126 Gladysz, J.; Curran, D.; Horváth, I. *Handbook of Fluorous Chemistry*; John Wiley & Sons: Weinheim, 2005.

127 Horvath, I. T. *Acc. Chem. Res.* **1998**, *31* (10), 641.

128 Zhang, W. *Green Chem.* **2009**, *11* (7), 911.

129 Wang C., Wu E., Wu X., Xu X., Zhang G., Pu L., *Journal of the American Chemical Society* **2015**, *137* (11), 3747-3750.

130 Wang C., Anbaei P., Pu L., *Chemistry–A European Journal*, **2016**, *22* (21), 7255-7261.

131 Wang C., Wu X., Pu L., *Chemistry–A European Journal*, **2017**, *23* (45), 10749-10752.

132 Zhu YY., Wu XD., Abed M., Gu SX., Pu L., *Chemistry–A European Journal*, **2019**, *25* (33), 7866-7873.

133 Xiao M., Yu S., Chen L., Huang Z., Wen K., Xu Y., Zhao F., Yu X., Pu L., *European Journal of Organic Chemistry*, **2017** (11), 1413-1417.

134 Reetz, M. T. *Angew. Chemie Int. Ed.* **2001**, *40* (2), 284.

135 Herrera BT., Pilicer SL., Anslyn EV., Joyce LA., Wolf C., *J. Am. Chem. Soc*. **2018**, *140* (33), 10385-10401.

136 Guo, H.-M.; Tanaka, F. *J. Org. Chem.* **2009**, *74* (6), 2417-2424.

137 Schafer, W.; Bu, X.; Gong, X.; Joyce, L. A.; Welch, C. J., High-Throughput Analysis for High-Throughput Experimentation in Organic Chemistry A2, Knochel, Paul. In Comprehensive Organic Synthesis II (Second ed.), *Elsevier: Amsterdam*, **2014**; pp 28−53.

138 Gao, X.; Kagan, H. B. *Chirality* **1998**, *124*, 120.

139 Abrahim, A.; Al-Sayah, M.; Skrdla, P.; Bereznitski, Y.; Chen, Y.;Wu, N. *J. Pharm. Biomed. Anal*. **2010**, *51* (1), 131−137.

140 Catani, M.; Ismail, O. H.; Gasparrini, F.; Antonelli, M.; Pasti, L.; Marchetti, N.; Felletti, S.; Cavazzini, A. *Analyst* **2017**, *142*, 555−566.

141 Wahab, M. F.; Wimalasinghe, R. M.; Wang, Y.; Barhate, C. L.;Patel, D. C.; Armstrong, D. W. *Anal. Chem*. **2016**, *88* (17), 8821−6.

142 Ismail, O. H.; Antonelli, M.; Ciogli, A.; Villani, C.; Cavazzini, A.; Catani, M.; Felletti, S.; Bell, D. S.; Gasparrini, F. *J. Chromatogr. A*, **2017**, *1520*, 91−102.

143 Barhate, C. L.; Joyce, L. A.; Makarov, A. A.; Zawatzky, K.; Bernardoni, F.; Schafer, W. A.; Armstrong, D. W.; Welch, C. J.; Regalado, E. L. *Chem. Commun*. **2017**, *53* (3), 509−512.

144 Zhao, Y.; Swager, TM. *J. Am. Chem. Soc*. **2015**, *137* (9), 3221-3224.

145 Reetz, M. T.; Eipper, A.; Tielmann, P.; Mynott, R. *Adv. Synth. Catal*. **2002**, *344* (9), 1008.

146 Piovesana, S.; Samperi, R.; Lagan, A.; Bella, M. *Chem. A Eur. J.* **2013**, *19* (35), 11478.

147 Miller, S. M.; Samame, R. A.; Rychnovsky, S. D. *J. Am. Chem. Soc*. **2012**, *134* (50), 20318.

148 Ebner, C.; Müller, C. A.; Markert, C.; Pfaltz, A. *J. Am. Chem. Soc.* **2011**, *133* (13), 4710.

149 Reetz, M. T.; Becker, M. H.; Kühling, K. M.; Holzwarth, A. *Angew. Chemie - Int. Ed.* **1998**, *37* (19), 2647.

150 Reetz, M. T.; Becker, M. H.; Liebl, M.; Fürstner, A. *Angew. Chemie - Int. Ed.* **2000**, *39* (7), 1236.

151 Taylor LT., *Anal. Chem*. **2010**, *82*, 4925–4935.

152 Wang RQ., Ong TT., Tang W., Ng SC., *Trends in Analytical Chemistry*, **2012**, *37*, 83-100.

153 Brondz I., Ekeberg D., Bell D.S., Annino A.R., Mikhalitsyn F. *et al., J. Pharm. Biomed. Anal*., **2007**, *43*, 937.

154 Laskar, DB.; Zeng, L.; Xu, R.; Kassel, DB. *Chirality* **2008**, *20*, 885–895.

155 Wong, MW.; Holzheuer, WB.; Webster, GK. *Curr. Pharm. Anal*. **2008**, *4*, 101–105.

156 Arai, T.; Watanabe, M.; Fujiwara, A.; Yokoyama, N.; Yanagisawa, A. *Angew. Chem., Int. Ed.* **2006**, *45* (36), 5978−5981.

157 Giuliano, M. W.; Lin, C. Y.; Romney, D. K.; Miller, S. J., Anslyn, E. V., *Adv. Synth. Catal*. **2015**, *357* (10), 2301−2309.

158 Reetz, M. T.; Zonta, A.; Schimossek, K.; Jaeger, K.-E.; Liebeton, K.; Jaeger, K.-E. *Angew. Chem. Int. Ed.* **1997**, *36* (24), 2830.

159 Shabbir, S. H.; Regan, C. J.; Anslyn, E. V. *Proc. Natl. Acad. Sci. U. S. A*. **2009**, *106* (26), 10487−10492.

160 Li, Z.-B.; Lin, J.; Qin, Y.-C.; Pu, L. *Org. Lett*., **2005**, *7* (16), 3441−3444.

161 Tumambac GE., Wolf C., *Org. Lett*. **2005**, *7* (18), 4045-4048.

162 Mei, X.; Wolf, C. *J. Am. Chem. Soc*. **2006**, 128 (41), 13326−13327.

163 Wen, K.; Yu, S.; Huang, Z.; Chen, L.; Xiao, M.; Yu, X.; Pu, L. *J. Am. Chem. Soc.*, **2015**, *137* (13), 4517.

Chapter 2

Fluorous Phase-Based Enantioselective Fluorescent Screening for Asymmetric Catalytic Reactions

2.1. Introduction

Asymmetric reaction of *meso*-epoxides with amines can generate chiral amino alcohols which are useful precursors to various natural products as well as many other compounds of biological and pharmaceutical interests.[1-5] In the presence of a chiral catalyst, enantiomerically enriched amino alcohols with two chiral centers can be generated from this reaction. Among the chiral catalysts developed so far, high enantioselectivity is generally limited to the reaction of aromatic amines.[1-5] The reactions of aliphatic amines often only give low asymmetric induction except in rare cases.[6] Recently, Takeuchi reported the asymmetric reaction of 1,2-epoxycyclohexane with cyclopropylamine to generate the amino alcohol (*R*, *R*)-**1** for the synthesis of a phosphodiesterase III inhibitor (Scheme 2-1). They found that this reaction can be catalyzed by a readily available and inexpensive polysaccharide, Soyafibe S-DN, to give (*R*, *R*)-**1** with moderate enantioselectivity.[7,8] The reaction was conducted under mild conditions without the need to remove air or moisture. The catalyst Soyafibe S-DN can be simply recovered by filtration through filter paper and directly reused without further treatment with retention of the enantioselectivity. Although this method is practically useful for the synthesis of interesting pharmaceutical products, its enantioselectivity and substrate scope need to be improved. We propose to develop an enantioselective

fluorescent sensor for the recognition of the chiral secondary amino alcohols to facilitate the screening of the catalysts for this asymmetric reaction.

Scheme 2- 1. A polysaccharide-catalyzed desymmetrization of 1,2-epoxycyclohexane to form chiral amino alcohols

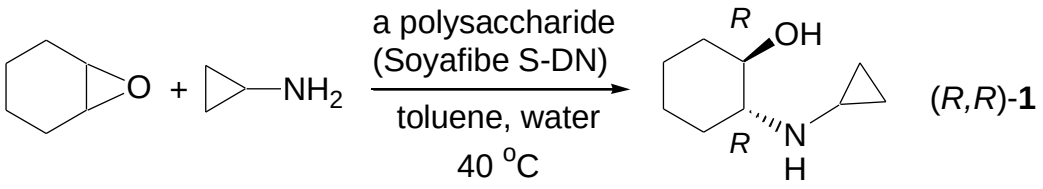

Enantioselective fluorescent sensors can provide a fast analytical method to determine the enantiomeric composition of chiral molecules and are potentially useful for high throughput screening of asymmetric reactions.[9-12] In order to minimize the interference of various reaction components on fluorescence measurement when an enantioselective fluorescent probe is used to evaluate a catalytic reaction, we have undertaken a project to investigate fluorescent recognition in highly fluorinated solvents.[13-15] Because of the lipophobic and hydrophobic properties of the highly fluorinated solvents,[16,17] fluorescent recognition in the fluorous phase should allow the measurement to be conducted away from the original reaction media in the absence of the reagents, catalysts and other species in the reaction. We have synthesized a chiral 1,1'-bi-2-naphthol (BINOL)-based compound (*S*)-**2** that contains two perfluoroalkyl ketone units.[13] This compound is soluble in perfluorohexane (FC-72) and shows enantioselective fluorescence enhancement in the presence of certain chiral amino

alcohols in the fluorous phase. Although the fluorescent response of (*S*)-**2** toward a few primary amine-based amino alcohols, its interaction with the amino alcohols like (*R, R*)-**1** containing a secondary amino group was not investigated. We therefore studied the interaction of (*S*)-, (*R*)- and *Rac*-**2** with the enantiomers of an amino alcohol containing a secondary amine group, that is (*R, R*)- and (*S, S*)-**3**, in fluorous phase and then explored the use of the fluorescent probes to evaluate the asymmetric reaction of 1,2-epoxycyclohexane with an alkyl amine catalyzed by Soyafibe S-DN in the presence of a large number of Lewis acid additives. Herein, these results are presented in this chapter.

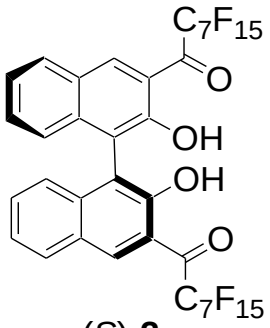

(*S*)-**2**

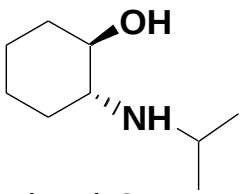

(*R,R*)-**3**

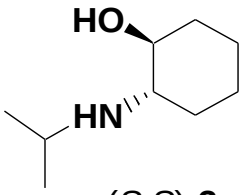

(*S,S*)-**3**

2.2. Results and Discussion

2.2.1. Fluorescent Response of (*R*)- or (*S*)-2 toward the Amino Alcohols (*R, R*)- and (*S, S*)-3

In order to develop an enantioselective fluorescent probe to facilitate the screening of catalysts for the asymmetric reaction of 1,2-epoxycyclohexane with alkyl amines, we studied the fluorescent response of (*R*)-**2** toward (*R, R*)- and (*S, S*)-**3**. In FC-72, (*R*)-**2** showed almost no fluorescence. When (*R*)-**2** (2.0×10^{-5} M) was treated with (*R, R*)-**3** (0.5 – 4 mM) in FC-72 (containing 4% Et_2O to dissolve the amino alcohol), large

fluorescence enhancement (2500 - 3000 folds) at λ = 428 nm was observed as shown in Figure 2-1a. Light yellow clear solution of the probe became white slurry with the addition of (*R*, *R*)-3. When (*R*)-2 was treated with (*S*, *S*)-3 in FC-72 under the same conditions, much smaller fluorescence enhancement (50 - 200 folds) at λ = 428 nm was observed as shown in Figure 2-1b. Light yellow solution of the probe remained clear with the addition of (*R*, *R*)-3. The excitation spectra (Figure 2-1d) for emission at 428 nm demonstrated significant differences for excitations at 280 nm as well as 350 nm when (*R*)-**2** was treated with the two amino alcohol enantiomers under the same conditions. Therefore, both of these two wavelengths could be utilized to measure the enantioselective fluorescence response in the fluorous phase. Figure 2-1c plots the fluorescence intensity at 428 nm versus the concentration of the amino alcohols. It shows that when the concentration of the amino alcohol was above 2.5 mM, there was large enantioselective fluorescence enhancement.

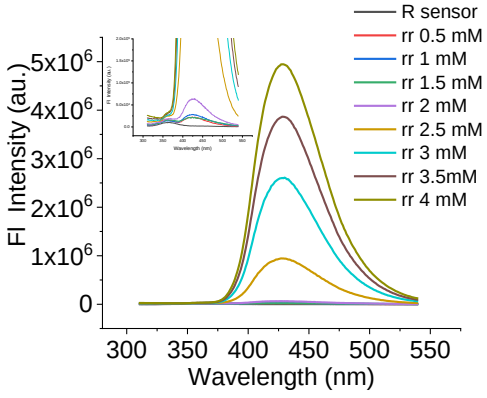

(a)

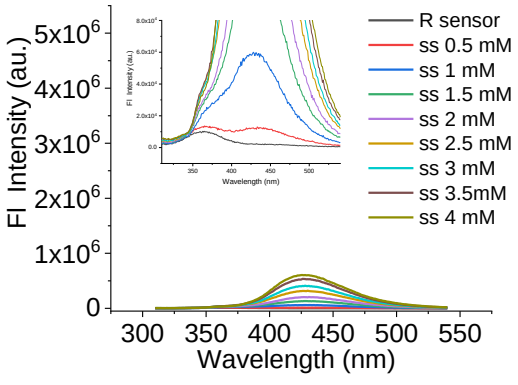

(b)

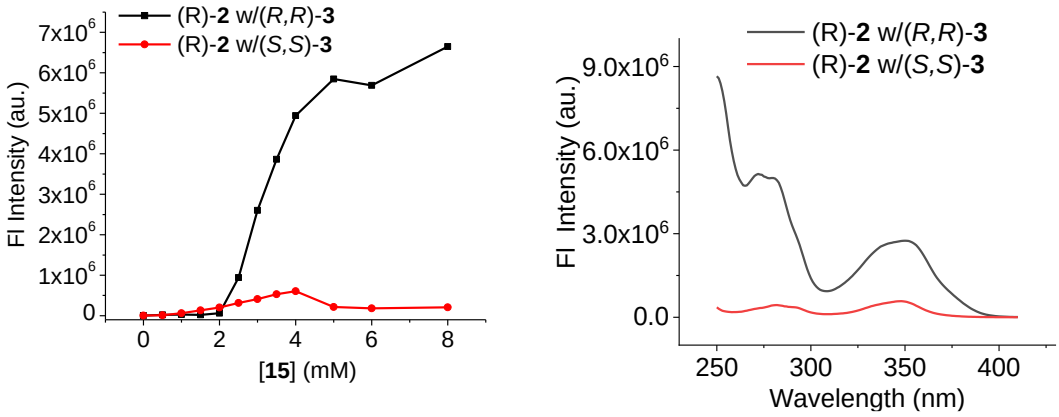

(c) (d)

Figure 2- 1. Fluorescent spectra of (*R*)-**2** with (*R, R*)-**3** (a) and (*S, S*)-**3** (b) and the fluorescent intensities of (*R*)-**2** with (*R, R*)-**3** and (*S, S*)-**3** at 428 nm (c) ([**2**] = 2.0×10^{-5} M, [**3**] = 0.5 - 8.0 mM, in FC-72/Et_2O (96/4, v) λ_{exc} = 280 nm, slit: 3/3 nm, reaction time: 2 hours), Fluorescent excitation spectra of (*R*)-2 with (*R, R*)-3 (black) and (*S, S*)-3 (red) of 428 nm (d). ([2] = 2.0×10^{-5} M, [3] = 4.0 mM, in FC-72/Et_2O (96/4, v), slit: 3/3 nm, reaction time: 2 hours)

Besides (*R*)-**2**, its enantiomer (*S*)-**2** was also used to interact with the amino alcohol of various enantiomeric composition. As shown in Figure 2-2, a mirror-image relationship was observed for the fluorescent response of (*S*)-**2** versus (*R*)-**2** toward **3** at varying ee's (enantiomeric excess = {[(*R, R*)-**3**] – [(*S, S*)-**3**]}/{[(*R, R*)-**3** + [(*S, S*)-**3**]}), which confirms the observed enantioselective fluorescent recognition. Figure 2 also shows a large non-linear effect between the fluorescence response of the probe and the ee of the chiral substrate. That is, only when one enantiomer of the amino alcohol was in excess, was there a large fluorescence enhancement. The fluorescence intensity of the

probe was also influenced by the total concentration of the amino alcohol with the higher concentration of the substrate giving higher fluorescence intensity.

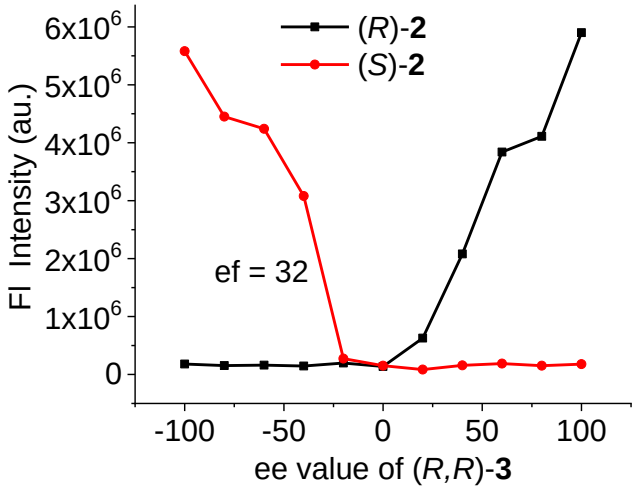

Figure 2- 2. The fluorescent intensities of (*R*)-**2** and (*S*)-**2** with **3** of various enantiomeric compositions at 428 nm ([**2**] = 2.0×10^{-5} M, [**3**] = 5 mM, in FC-72/Et_2O (96/4, v), slit: 3/3 nm, reaction time: 2 hours)

Figure 2-3 gives the photo images for the interaction of the probes (*R*)- and (*S*)-**2** (4.0×10^{-5} M) with the amino alcohols (*R, R*)- and (*S, S*)-**3** (4.0 mM) respectively in the fluorous phase under UV lamp. Strong fluorescence was observed for the interaction of (*R*)-**2** with (*R, R*)-**3** and that of (*S*)-**2** with (*S, S*)-**3**. Very little fluorescence was observed for the interaction of (*S*)-**2** with (*R, R*)-**3** and that of (*R*)-**2** with (*S, S*)-**3**. Thus, the two enantiomers of the amino alcohol can be visually discriminated by using the enantiomeric probe pair.

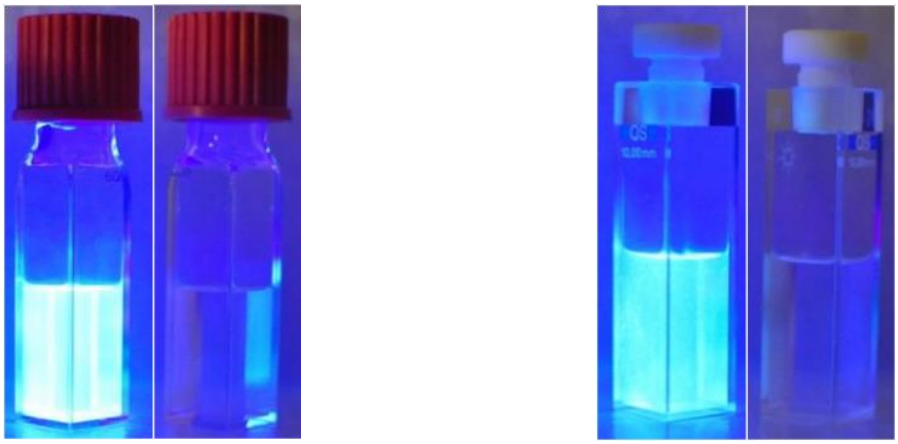

(a) (b)

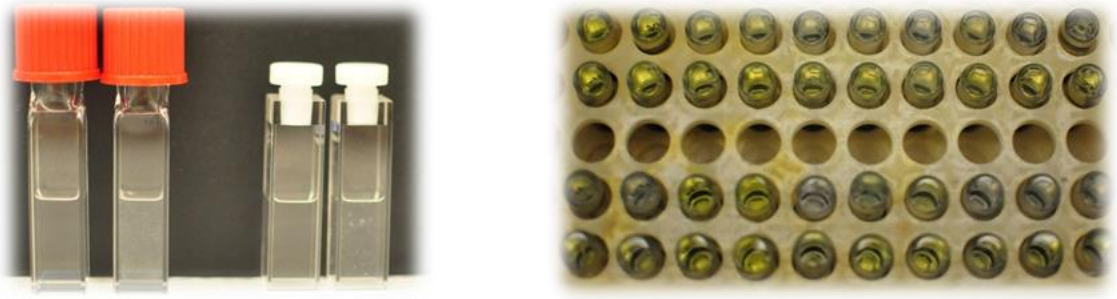

(c) (d)

Figure 2- 3. Photo images of (a) (*R*)-**2** (left) and (*S*)-**2** (right) with (*R, R*)-**3**; (b) (*S*)-**2** (left) and (*R*)-**2** (right) with (*S, S*)-**3**. ([probe **2**] = 4.0×10^{-5} M, [**3**] = 4.0 mM, in FC-72/Et_2O (98/2), under UV lamp, at 365 nm.) (c) Fluorescence recognition reactions observed in fluorescence cells by naked eyes from left to right: 1. (*S*)–**2** with (*R, R*)–**3**; 2. (*R*)–**2** with (*R, R*)–**3**; 3. (*R*)–**2** with (*S, S*)–**3**; 4. (*S*)–**2** with (*S, S*)–**3**. (d) Fluorescence recognition reactions observed in vials. Usually the colorless ones gave higher fluorescence intensities that represent amino alcohol samples with higher ee values.

2.2.2. Using Both (*R*)- and (*S*)-2 to Evaluate the Asymmetric Reaction of 1,2-Epoxycyclohexane with $^{i}PrNH_2$ to Generate the Amino Alcohol 3 Catalyzed by Soyafibe S-DN under Various Reaction Conditions

As shown in Scheme 3-1, the Soyafibe S-DN catalyzed desymmetrization of 1,2-epoxycyclohexane with an alkylamine to generate an amino alcohol with moderate ee's.[7,8] The asymmetric induction of this reaction could be attributed to the hydrogen bonding interaction between the epoxide oxygen and the hydroxyl groups of the polysaccharide catalyst. The hydrogen bonding interaction of the amine nucleophile with the polysaccharide catalyst should also be important for this catalytic process. Addition of a *Lewis* acidic metal cation could modify the interaction of the catalyst with the epoxide and amine since the *Lewis* acidic metal cation can interact with the polysaccharide hydroxyl groups, the epoxide oxygen and the amine nitrogen and modify the catalyst-substrate bindings. Therefore, we conducted a screening of a large number of metal cations in combination with Soyafibe S-DN for the asymmetric reaction of 1,2-epoxycyclohexane with $^{i}PrNH_2$ to generate the amino alcohol **3** by using the enantiomeric probe pair (*R*)- and (*S*)-**2** to quickly evaluate the reaction results (Scheme 2-2).

Scheme 2-2. Screening the reaction of 1,2-epoxycyclohexane with $^{i}PrNH_2$ to form the amino alcohol **3**.

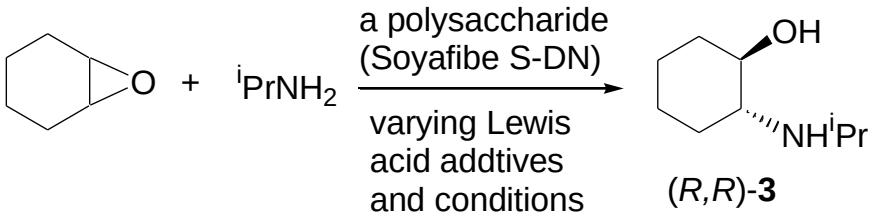

Our Phase I screening reactions were conducted in 4 mL vials with the addition of 1,2-epoxycyclohexane (0.2 mmol), $^{i}PrNH_2$ (0.2 mmol), Soyafibe S-DN (40 mg), a solvent (168 µL), H_2O (12 µL), and an additive (5 - 15 mol %) at 30 - 50 ^{o}C for 48 h. After reaction, all the reaction vials were dried under vacuum for 2 h until no solvent could be observed. The Et_2O (0.8 mL) was added at which the concentration of the desired product would be 10 mM if the yield was 100%. Then, one portion of the Et_2O solution (80 µL) was mixed with the probe (*R*)-**2** in FC-72 (2×10^{-5} M, 1.92 mL) to give fluorescence intensity I_R at 428 nm (λ_{exc} = 290 nm), and an equal amount of another portion of the Et_2O solution was mixed with the probe (*S*)-**2** in FC-72 under the same conditions to give fluorescence intensity I_S. We used the fluorescence intensities I_R-I_S and I_R+I_S as the parameters to quickly evaluate the relative catalytic efficiency and enantioselectivity of various additives and solvents.

Table 2- 1. Phase I screening results based on fluorescence intensities I_R-I_S of the enantioselective Soyafibe S-DN catalyzed reaction

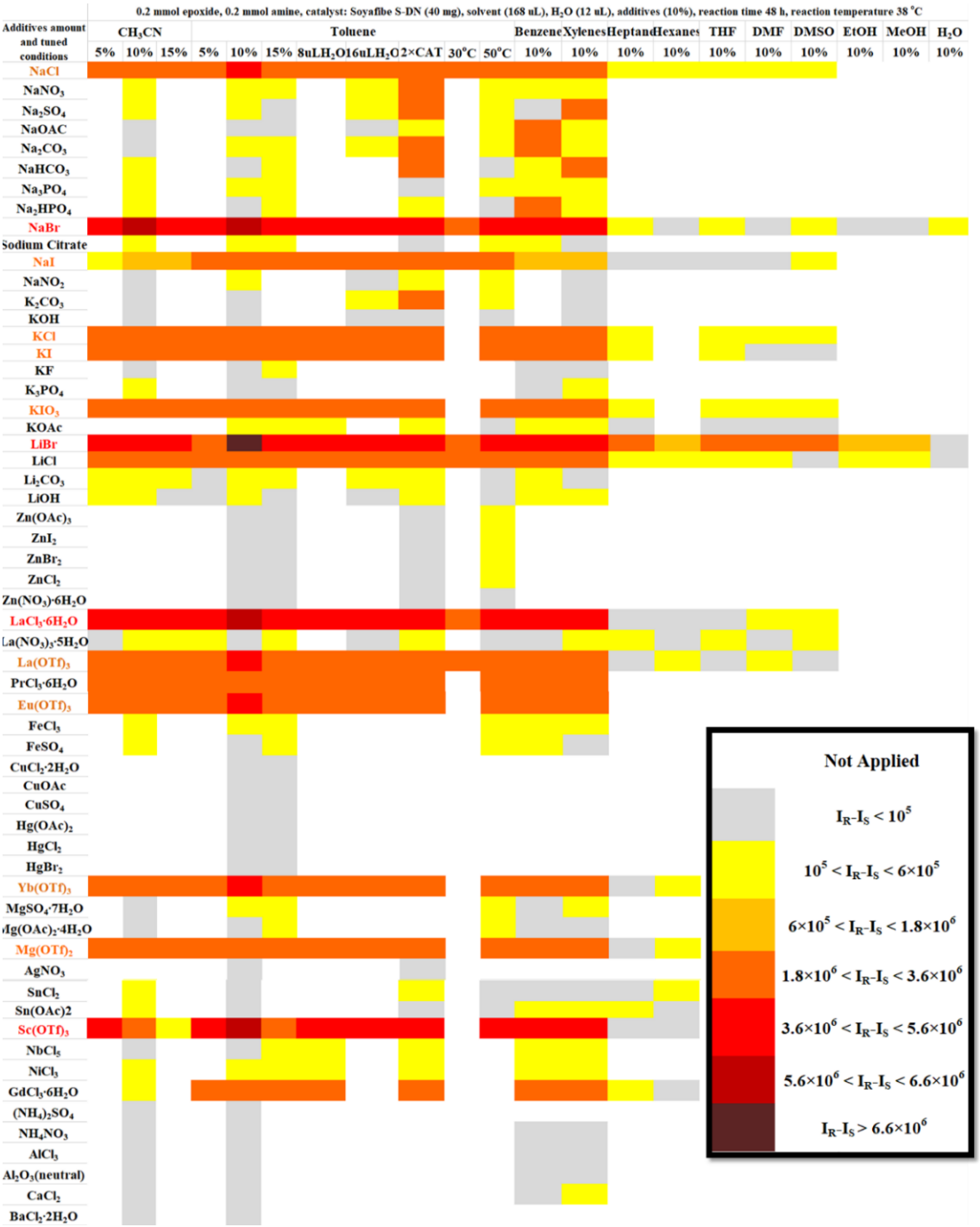

Table 2-2. Phase I screening results based on fluorescence intensities I_R+I_S of the enantioselective Soyafibe S-DN catalyzed reaction

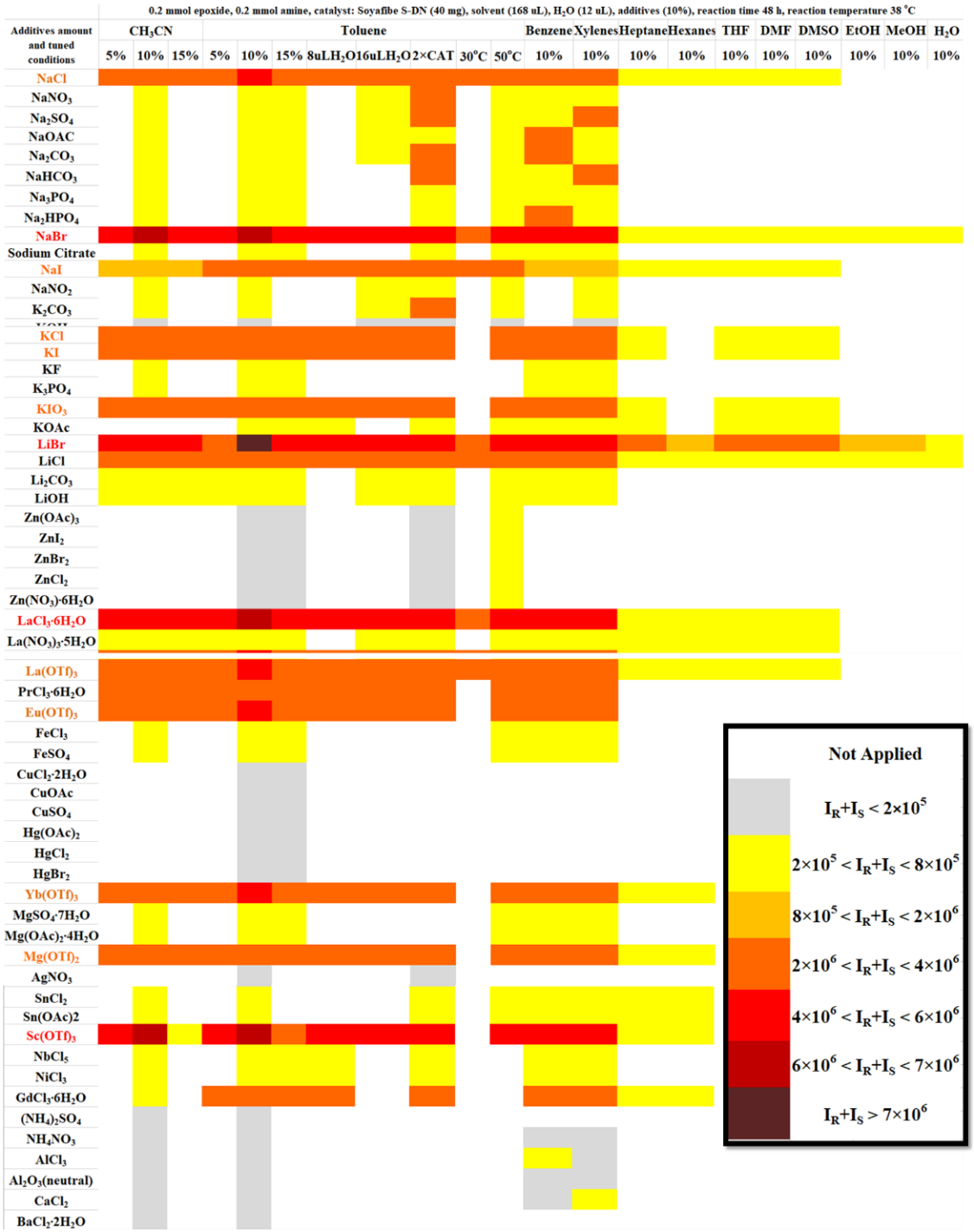

Standard reaction condition: 0.2 mmol epoxide, 0.2 mmol amine, catalyst: Soyafibe S-DN (40 mg), solvent (168 uL), H_2O (12 uL), additives (10%), reaction time 48 h, reaction temperature 38 °C. After reaction all the reaction vials were dried under vacuum for 2 h until no solvent could be observed before diluting the product mixture with Et_2O to the concentration of 10 mM if the yield was 100% as calculated. Then 80 uL of the Et_2O solution were taken to mix with the probe (*R*)-**2** and (*S*)-**2** in FC-72 (2×10^{-5} M).

Although both the concentration and the enantiomeric composition of the amino alcohol influence the fluorescence response of the probe, the use of (*R*)- and (*S*)-**2** sensor pair and their corresponding fluorescence response I_R+I_S and I_R-I_S we are able to evaluate the relative efficiency of a large number of reaction conditions very quickly in the Phase I study to indentify a few promising results.

2.2.3. Fluorescent Response of *Rac*-2 toward (*R, R*)- and (*S, S*)-3.

As described in Section 1 above, when (*R*)- or (*S*)-**2** was used to interact with the amino alcohol of various ee composition, there was a large nonlinear effect between the fluorescence enhancement and the ee of the substrate. That is, only when ee > 0 [(*R, R*)-**3** in excess], can (*R*)-**2** show fluorescence enhancement, and accordingly only when ee < 0 [(*S, S*)-**3** in excess], can (*S*)-**2** show fluorescence enhancement. Thus, the enantiomeric pair (*R*)- and (*S*)-**2** were used in our Phase I catalyst screening. The large nonlinear effect also suggests that it might be possible to use the racemic probe *Rac*-**2** to directly evaluate the enantiomeric excess of the substrate as we recently demonstrated in a polymer-based fluorescent probe.[18] In order to test this, we prepared the *Rac*-**2** starting from the racemic BINOL and studied its fluorescent response toward the amino alcohol **3** of various enantiomeric composition.

Solutions of various concentrations (62.5 mM – 250 mM) for both enantiomers of **3** were made in diethyl ether. Then the (*S, S*)-**3** and (*R, R*)-**3** solutions of the same concentration were mixed to form solutions with a variety of enantiomeric composition. 80 μL out of the diethyl ether solution was injected to the *Rac*-**2** perfluorohexanes (FC-

72) solution (2.5×10^{-5} M, 1.92 mL). After vigorous manually shaking for 30 seconds the samples were set at room temperature for another 2 hours followed by another vigorous manually shaking for 30 seconds right before the fluorescence measurement.

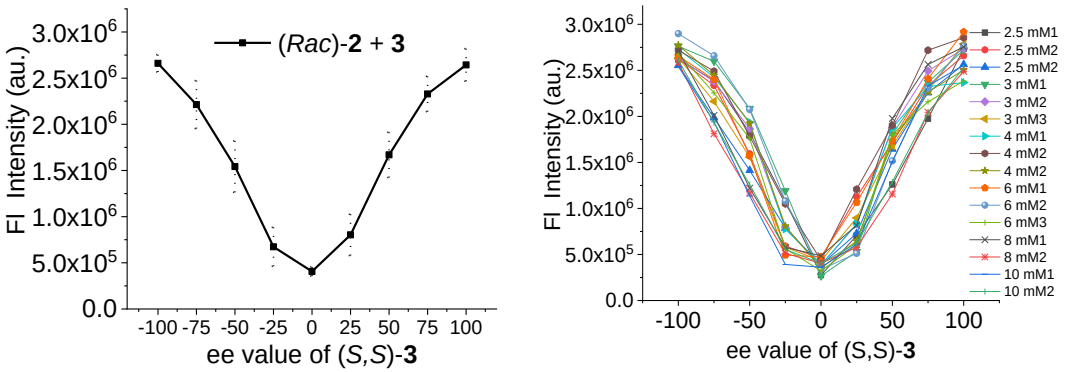

(a) (b)

Figure 2- 4. The averaged (a) and detailed (b) fluorescent intensities of (*Rac*)-**2** with **3** of various enantiomeric compositions and concentrations at 428 nm. ([**2**] = 2.5×10^{-5} M, [**3**] = 2.5 - 10 mM, in FC-72/Et_2O (96/4, v) slit: 3/3 nm, reaction time: 2 hours)

The small effect of the total concentration of the amino alcohol on the fluorescence response of *Rac*-**2** toward the enantiomeric composition makes it possible to directly use *Rac*-**2** to estimate the ee of an amino alcohol sample without the need to know the sample concentration.

2.2.4. Using the Racemic Probe *Rac*-2 to Evaluate the Asymmetric Reaction of 1,2-Epoxycyclohexane with $^{i}PrNH_2$.

In Phase I screening, we have identified several promising metal salt additives including LiBr, $LaCl_3 \cdot 6H_2O$, NaBr, $Yb(OTf)_3$, and $Sc(OTf)_3$, and solvents including toluene and acetonitrile for the asymmetric reaction of 1,2-epoxycyclohexane with iPr_2NH_2 catalyzed by Soyafibe S-DN. We thus used *Rac*-**2** to estimate the enantiomeric composition of these reactions in our Phase II study and the results are summarized in Table 2-3.

Table 2- 3. Phase II screening results with ee's determined by the fluorescent probe *Rac*-**2** in the fluorous phase

Additive / Solvent	$Yb(OTf)_3$	$LaCl_3 \cdot 6H_2O$	NaBr	LiBr	$Sc(OTf)_3$	None
CH_3CN (ee %)	48	50	44	52	20	43
CH_3CN (crude yield %)	70	71	77	64	85	50
Toluene (ee %)	50	**56**	47	**57**	50	45
Toluene (crude yield %)	61	62	70	69	74	53

The reactions were conducted in 4 mL vials by using 1,2-epoxycyclohexane (0.2 mmol), $^{i}PrNH_2$ (0.2 mmol), Soyafibe S-DN (40 mg), toluene or acetonitrile (168 µL), H_2O (12 µL), $Yb(OTf)_3$/ $LaCl_3 \cdot 6H_2O$/$Sc(OTf)_3$ (10% mol), or LiBr/NaBr (20% mol) at 38 ^{o}C for 60 h. All the vials were then dried under vacuum for 1 h and the product was extracted by Et_2O. The crude yields of the reactions were measured by weighing the sample after removal of the Et_2O extract. The crude product was dissolved in 0.8 mL Et_2O which gave a maximum concentration of 10 mM for the product. Then 80 µL of the Et_2O solution was drawn to mix with the probe *Rac*-**2** in FC-72 (2.5×10^{-5} M). On the basis of the fluorescence measurement by applying Figure 2-4 and Figure 2-5, the highest enantioselectivity was observed for the reactions with $LaCl_3 \cdot 6H_2O$ or LiBr as the

additive in toluene solution as shown in Table 2-3. Using these additives gave improved results over those without these additives.

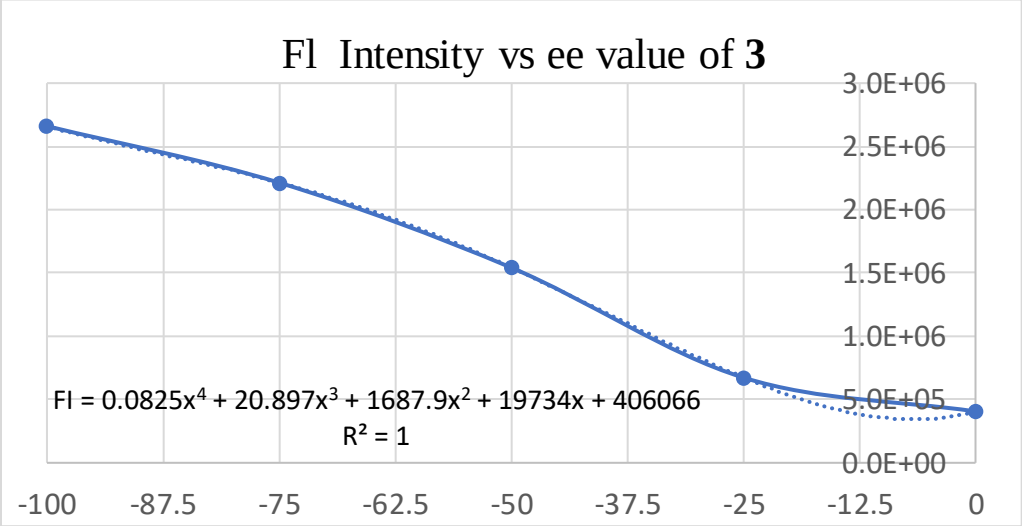

(a)

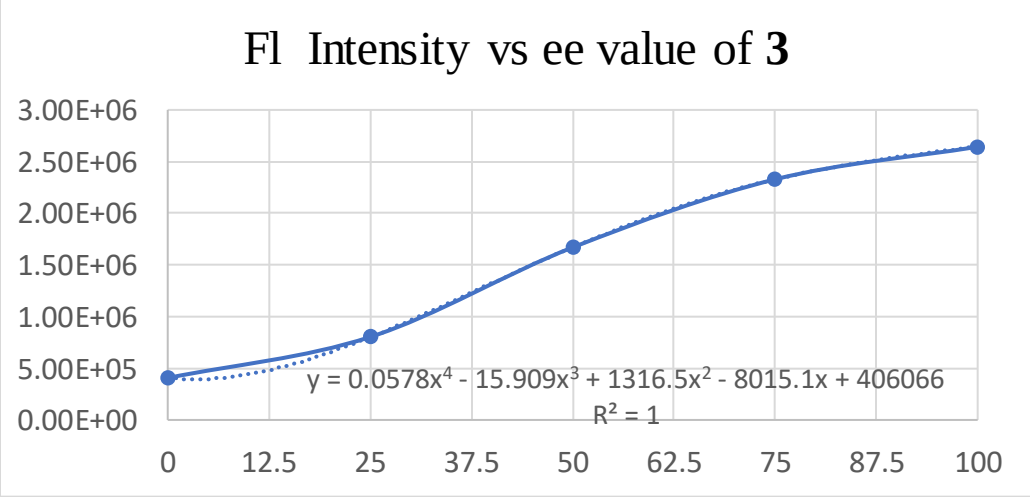

(b)

Figure 2- 5. Piecewise nonlinear curves (a) ee ≤ 0 and (b) ee ≥ 0 of Figure 2-4a with piecewise regression functions that were used to solve the ee values by the fluorescent intensities measured from the reaction product mixture with (*Rac*)-**2**.

We have thus undertaken a Phase III study to fine-tune the reaction conditions with the use of either LiBr or $LaCl_3 \cdot 6H_2O$ as the additive. The reaction conditions such as time, temperature, UV light exposure, amounts of water, catalyst and additive, and catalyst amount were explored to further refine the reaction conditions. In this study, we compared the ee's obtained by using *Rac*-**2**-based fluorescence measurement with those obtained by HPLC-chiral column analysis. The reactions were conducted in 4 mL vials by using 1,2-epoxycyclohexane (0.3 mmol), $^{i}PrNH_2$ (0.3 mmol), Soyafibe S-DN (50-80 mg), in toluene and H_2O with $LaCl_3 \cdot 6H_2O$ or LiBr / NaBr at certain temperature for 60 h. After reaction, all the vials were dried under vacuum for 1 h and Et_2O (1.2 mL) was added to extract the product to achieve a maximum product concentration of 10 mM.

According to the results of phase II study, a standard reaction condition for phase III study was confirmed as the following, 0.3 mmol epoxide, 0.3 mmol amine, Soyafibe S-DN (60 mg), Toluene (252 uL), H_2O (18 uL), $Yb(OTf)_3$ (10% mol) or LiBr (50% mol), reaction time 60 h, reaction temperature 38 ^{o}C. After reaction all the reaction vials were dried under vacuum for 2 h until no solvent could be observed before diluting the product mixture with 1.2 mL Et_2O to the concentration of 10 mM if the yield was 100% as calculated. Then 80 uL of the Et_2O solution were taken to mix with 1.92 mL of *Rac*-**2** in FC-72 (2.5×10^{-5} M) for fluorescence measurement.

We have conducted a total of 86 reactions in the Phase III study. When the fluorescence intensity of a product sample was lower than 30% of the maximum, it indicates less than 30% yield and the ee was not determined due to much lower accuracy at low concentration. The results of 30 reactions are listed in Table 2-4 and the remaining data are included in Table 2-5.

As shown in entries 1-11 in Table 2-4, the enantioselectivity of using $LaCl_3 \cdot 6H_2O$ as the additive could not be significantly improved by varying the reaction condictions. The highest enantioselectivity was found to be 59% ee by fluorescence measurement. In entries 13 – 30, the conditions for the use of LiBr as the additive were screened. It was found that when the amount of LiBr was increased to 50 mol %, the enantioselectivity was significantly improved from 54% ee to 72% ee as determined by the fluorescence measurement (entry 18). This enantioselectivity is also significantly higher than that described in a foreign patent.[8] When the catalyst was reused after extract of the product, the results were also close (entries 19, 20). Further increasing the amount of LiBr gave lower enantioselectivity (entries 21, 22). Increasing or decreasing the amount of Soyafibe S-DN gave lower ee's (entries 23, 24). Changing the amount of toluene or water reduced the enantioselectivity (entries 25-28). Pretreatment of Soyafibe S-DN with LiBr before the reaction gave greatly reduced ee (entry 29). Introduction of UV-vis LED light to the reaction did not improve the enantioselectivity (entry 30).

In the Phase III study, we have not only greatly improved the enantioselectivity for the Soyafibe S-DN-catalyzed asymmetric reaction of 1,2-epoxycyclohexane with $iPrNH_2$ by using LiBr as the additive. We have also demonstrated that the ee's determined by using the racemic fluorescent probe *Rac*-**2** were consistent with those determined by HPLC-chiral column analysis of the *m*-toluoyl derivatives of amino alcohols **3** products.[19]

Table 2- 4. Phase III Screening Selected Results by Fluorescence of (*Rac*)-**2** with the Product

Varieties / Entry	T (°C)	Additive (% mol)	Soyafibe S-DN (mg)	Toluene (µL)	Water (µL)	FL measured ee (%)	HPLC ee (%)
1	30	$LaCl_3 \cdot 6H_2O$, 10	60	252	18	33	34.5
2	38	$LaCl_3 \cdot 6H_2O$, 10	60	252	18	55	55
3	46	$LaCl_3 \cdot 6H_2O$, 10	60	252	18	36	34
4	38	$LaCl_3 \cdot 6H_2O$, 15	60	252	18	53	53
5	38	$LaCl_3 \cdot 6H_2O$, 30	60	252	18	49	52
6	38	$LaCl_3 \cdot 6H_2O$, 10	50	252	18	47	50.5
7	38	$LaCl_3 \cdot 6H_2O$, 10	80	252	18	43	46.5
8	38	$LaCl_3 \cdot 6H_2O$, 10	60	168	18	<30	31
9	38	$LaCl_3 \cdot 6H_2O$, 10	60	336	18	44	47.5
10	38	$LaCl_3 \cdot 6H_2O$, 10[a]	60	252	18	<30	19
11	38	$LaCl_3 \cdot 6H_2O$, 10[b]	60	252	18	59	57.5
12	38	$LaCl_3 \cdot 6H_2O$, 10	60	252	12	44	48
13	30	LiBr, 20	60	252	18	48	48
14	38	LiBr, 20	60	252	18	54	60
15	46	LiBr, 20	60	252	18	45	50.5
16	38	LiBr, 30	60	252	18	55	54.5
17	38	LiBr, 40	60	252	18	63.5	60
18	**38**	**LiBr, 50**	**60**	**252**	**18**	**72**	**70**
19	38	LiBr, 50[c]	60	252	18	69	67
20	38	LiBr, 50[d]	60	252	18	64	64.5
21	38	LiBr, 60	60	252	18	59	60
22	38	LiBr, 70	60	252	18	57	56.5
23	38	LiBr, 50	50	252	18	54	56
24	38	LiBr, 50	80	252	18	60	61.5
25	38	LiBr, 50	60	168	18	52	56
26	38	LiBr, 50	60	336	18	48	47.5
27	38	LiBr, 50	60	252	12	45	45
28	38	LiBr, 50	60	252	24	53	50.5
29	38	LiBr, 50[a]	60	252	18	<30	10
30	38	LiBr, 50[b]	60	252	18	66	60

(a) Catalyst (Soyafibe S-DN) pre-mixed with the additives in 100 uL H_2O, stirred overnight, then dried by vacuum before usage. (b) Under 365 nm UV-Vis LED irradiation during the entire reaction time. (c) Second-time use of the catalytic system after product extraction and dried. (d) Third-time use of the catalytic system after product extraction and dried.

Table 2- 5. Phase III Screening Remaining Results by Fluorescence of (*Rac*)-**2** with the Product [e]

Varieties / Entry	T (°C)	Additive (% mol)	Soyafibe S-DN (mg)	Toluene (µL)	Water (µL)	UV[d] (Y or N)	FL measured ee (%)	HPLC ee (%)
31	38	$LaCl_3 \cdot 6H_2O$, 5 [a]	60	252	18	N	34	40.5
32	38	$LaCl_3 \cdot 6H_2O$, 5	60	252	18	Y	40	46
33	41	$LaCl_3 \cdot 6H_2O$, 5	60	252	18	Y	33	39
34	41	$LaCl_3 \cdot 6H_2O$, 10 [a]	60	252	18	N	39	40.5
35	41	$LaCl_3 \cdot 6H_2O$, 10	60	252	18	N	44	51.5
36	38	$LaCl_3 \cdot 6H_2O$, 10	60	252	18	N	**40**	**67.5**
37	38	$LaCl_3 \cdot 6H_2O$, 10 [a]	60	252	18	N	45	51

38	38	$LaCl_3 \cdot 6H_2O$, 10	60	252	18	Y	43	50.5
39	41	$LaCl_3 \cdot 6H_2O$, 30	60	252	18	N	42	55
40	38	$LaCl_3 \cdot 6H_2O$, 30 [a]	60	252	18	N	**50**	**59**
41	38	$LaCl_3 \cdot 6H_2O$, 30	60	252	18	Y	**49**	**59.5**
42	41	$LaCl_3 \cdot 6H_2O$, 40	60	252	18	Y	**<30**	**36**
43	38	$LaCl_3 \cdot 6H_2O$, 40 [a]	60	252	18	N	50	57
44	38	$LaCl_3 \cdot 6H_2O$, 40	60	252	18	N	46	54
45	41	LiBr, 5	60	252	18	Y	44	43.5
46	38	LiBr, 5 [a]	60	252	18	N	43	40.5
47	38	LiBr, 5	60	252	18	N	53	56.5
48	41	LiBr, 10	60	252	18	N	54	57.5
49	38	LiBr, 10 [a]	60	252	18	N	49	43.5
50	38	LiBr, 10	60	252	18	Y	55	52
51	38	LiBr, 10	60	252	18	N	50	54.5
52	41	LiBr, 15	60	252	18	Y	50	33
53	38	LiBr, 15 [a]	60	252	18	N	53	58.5
54	41	LiBr, 15	60	252	18	N	54	57
55	38	LiBr, 15	60	252	18	Y	51	53.5
56	41	LiBr, 50	60	252	18	Y	54	58
57	38	LiBr, 50 [a]	60	252	18	N	50	48
58	38	LiBr, 50	60	252	18	Y	55	58
59	38	LiBr, 50	60	252	18	N	58	64.5
60	38	-	60	252	18	Y	44	39.5
61	38	NaBr, 5	60	252	18	Y	50	46.5
62	38	NaBr, 10	60	252	18	Y	35.5	42
63	38	NaBr, 20	60	252	18	N	65	61
64	41	NaBr, 20	60	252	18	N	**71**	**61**
65	41	NaBr, 30	60	252	18	N	62	56
66	38	NaBr, 30 [a]	60	252	18	N	59	60.5
67	41	NaBr, 50	60	252	18	N	**73**	**56**
68	38	NaBr, 50	60	252	18	N	**69**	**60.5**
69	41	LiBr, 50 [a]	60	252	18	N	56	51
70	41	LiBr, 50 [a]	60	252	18	Y	34	41.5
71	38	LiBr, 50 [a]	60	252	18	N	55	49
72	38	LiBr, 50 [c]	60	252	18	N	60	57.5
73	38	- [b]	60	252	18	N	48	51.5
74	38	LiBr, 50 [b]	60	252	18	N	70	65
75	38	LiBr, 50 [b]	60	252	18	N	68	63.5
76	38	LiBr, 50 [b]	60	252	18	N	68	64
77	38	LiBr, 50 [b]	60	252	18	N	66	60.5
78	38	LiBr, 50 [b]	60	252	18	N	67	62.5
79	38	LiBr, 50 [b]	60	252	18	N	67	63
80	38	-	60	252	18	N	36	42
81	38	LiBr, 50	60	252	18	N	68	61.5
82	38	LiBr, 50	60	252	18	N	70	67
83	38	LiBr, 50	60	252	18	N	69	67.5
84	38	LiBr, 50	60	252	18	N	75	67.5
85	38	LiBr, 50	60	252	18	N	**73**	**59.5**
86	38	LiBr, 50	60	252	18	N	70	62

(a) Additives pre-mixed with water to form clear solution at certain concentration before18.5 µL corresponding solution was added into the reaction (equivalent to 18 µL water and the solid additive were added in.) (b) reaction time t = 7 days. (c) forth-time use of the catalytic system after product extraction and dried. (d) Under 365 nm UV-Vis LED irradiation during the entire reaction time. (e) Some of the reactions with the same conditions were repeated multiple times to validate reproducibility.

2.3. Conclusion

We have discovered that the fluorophilic fluorescent probe (*R*)- or (*S*)-**2** exhibits highly enantioselective fluorescent response to a chiral amino alcohol containing a secondary amine group in the fluorous phase. It allows the use of both (*R*)- and (*S*)-**2** to facilitate the screening of the catalysts for the asymmetric reaction of 1,2-epoxycyclohexane with an alkyl amine. We further found that the fluorescent probe shows large nonlinear response toward the enantiomeric composition of the amino alcohol in the fluorous phase which was not observed previously in the interaction of the probe with primary amine-based amino alcohol.[13] This has allowed us to use the racemic probe *Rac*-**2** to conduct the catalyst screening. Thus, in this work, we have demonstrated that the enantiomerically pure probes as well as the racemic probe can all be used to facilitate the screening of the catalysts for the asymmetric reaction of a meso-epoxide with an alkyl amine. The fluorescence-based ee measurements have been confirmed by HPLC-chiral column analysis which has validated the fluorous phase-based enantioselective fluorescent sensing method.

In the catalyst screening study described in this work, all the experiments and fluorescence measurements were conducted manually. However, the entire procedure can also be automated and suitable for high throughput screening. Even with the manual screenings, we have already discovered a condition with significantly improved enantioselectivity for the polysaccharide-catalyzed asymmetric reaction of 1,2-epoxycyclohexane with an alkyl amine. This work demonstrates that the fluorous phase-

based enantioselective fluorescent sensor is practically useful for rapid screening of asymmetric reactions.

2.4. Experimental Section

2.4.1. General Data

The Soyafibe S-DN was provided by Creative Enzymes and FUJI OIL CO., LTD. Fluorous reagents were purchased from SynQuest Labs, Inc. All other chemicals were purchased from Sigma Aldrich Chemical Co., Alfa Aesar, TCI America and EnamineStore. The amino alcohol was recrystallized or distilled before using. Methylene chloride, diethyl ether and THF were dried by passing them through activated alumina columns under nitrogen. Toluene and THF was further dried by Na and distillation. All organic solvent involved in the catalytical reactions were stored with activated 4 A molecular sieves in well-sealed vials and used within one month. Other chemicals were used without further purification. UV-Vis LED light used: 2 meters of the ABI Double Density Blue Flexible LED Light Strip, 120 LED / Meter, Light Output: 2200 Lumens (440 Lm. / Meter), Voltage: 12V • Current: 520mA / meter. Optical rotations were measured on a Jasco P-2000 digital polarimeter. NMR spectra were recorded on a Varian-600 MHz spectrometer, a Bruker-600 MHz spectrometer and a Bruker-800 MHz spectrometer. Chemical shifts for ^{1}H NMR spectra were reported in parts per million relative to a singlet at 7.26 ppm for deuterated chloroform. Chemical shifts for ^{13}C NMR were reported relative to the centerline of a triplet at 77.16 ppm for deuterated chloroform. The ^{19}F NMR spectra were reported in units of part per million (ppm) relative to trifluoroacetic acid (δ -76.55 ppm) as an external reference. Steady-state fluorescence spectra were recorded on Horiba FluoroMax-4 spectrofluorometer. High-resolution mass

spectra were obtained by the University of Illinois at Urbana-Champaign (UIUC) Mass Spectrometry Facility. UV-Vis spectra were produced from a Shimadzu UV-2600 UV-Vis spectrophotometer. HPLC analysis was conducted in a Shimadzu LC-20AD series HPLC coupled with a photodiode array detector (SPD-M20A) via a chiral column (Chiralpak AD, 25 cm × 4.6 mm, Daicel).

2.4.2. Synthesis and Characterization

- **(*1R,2R*)-2-(isopropylamino)cyclohexan-1-ol, (*1R,2R*)-3.**

Under nitrogen, the primary amino alcohol (1R,2R)-2-aminocyclohexanol (10 mmol) was dissolved in toluene (25 mL), upon adding acetone (5 mL) the mixture was then refluxed for 6 hours. After removal of the solvent and vacuum dried, the product could be used without further purification. Next, the dried product was dissolved in methanol (20 mL) and $NaBH_4$ (1.5 eq, 0.6 g) was slowly added into the solution and stirred for 2 hours at room temperature. Then water (5 mL) was slowly added to quench the reaction. After removal of solvent finally the residue was sublimated to afford the desired pure product. 1.6 g of the crude residue was obtained. But for each sublimation only 100 mg residue was sublimated due to the apparatus size limitation. After sublimation, 63.7 mg pure product was isolated in an estimated yield of 65% if all 1.6 g crude residue was sublimated by 16 times of sublimation. Then the pure product was characterized by NMR, optical rotation, and hi-res mass spectroscopy as well as HPLC. ^{1}H NMR (600 MHz, Chloroform-*d*) δ 3.07 – 3.01 (m, 1H), 2.97 – 2.90 (m, 1H), 2.20 (ddd, *J* = 11.2, 9.2, 3.9 Hz, 1H), 2.04 (tddd, *J* = 10.3, 5.6, 3.1, 1.4 Hz, 2H), 1.73 – 1.65 (m, 2H), 1.31 – 1.16 (m, 3H), 1.04 (dd, *J* = 6.3, 1.4 Hz, 3H), 0.98 (dd, *J* = 6.1, 1.4 Hz, 3H), 0.90 – 0.82 (m, 1H). ^{13}C NMR (151 MHz, Chloroform-*d*) δ 74.1, 60.9, 45.4, 33.2, 31.5, 25.6,

24.9, 24.5, 22.9. $[\alpha]_D^{23}$ = -85.10 (c = 0.40, Et_2O) HRMS[ESI(TOF)] m/z: [M+H+] Calcd for C9H20NO 158.1545; found: 158.1547. The enantiomeric excess was determined to be 99.5% of (*1R,2R*)-**3** by HPLC in a Chiralpak AD, 25 cm × 4.6 mm, (Daicel) column, 28 °C, IPA/Hexanes = 88/12, 1 mL/min, t_{ss} = 8.6 min (minor), t_{rr} = 19.0 min (major). Wavelength: 210 nm; run time: 25 min, sample preparation: precolumn derivation with *m*-toluoyl chloride.

A reported characterization[6] of (*1R,2R*)-**3**. Yield: 90%; colorless oil; $[\alpha]_D^{20}$ = – 119.7 (c 1.0, CH_2Cl_2, 94% ee); ^{1}H NMR ($CDCl_3$, 300 MHz): δ 3.04-3.03 (m, 1 H), 2.94-2.89 (m, 1 H), 2.24-2.16 (m, 1 H), 2.05-1.93 (m, 2 H), 1.68-1.67 (m, 2 H), 1.23-1.16 (m, 3 H), 1.02 (d, J = 6.3 Hz, 3 H), 0.96 (d, J = 6.3 Hz, 3 H), 0.87-0.84 (m, 1 H) ppm. ^{13}C NMR ($CDCl_3$, 75 MHz); δ 73.85, 60.57, 45.02, 32.98, 31.18, 25.28, 24.67, 24.26, 22.69 ppm. FT-IR (KBr): ν = 3295, 2930, 2857, 1660, 1464, 1449, 1380, 1361, 1167, 1122, 1066, 858. The enantiomeric excess was determined by Chiral GC on a beta 120 column, 120°C, 0.7 mL/min, t_1 = 20.9 min (minor), t_2 = 21.5 min (major).

- **(*1S,2S*)-2-(isopropylamino)cyclohexan-1-ol, (*1S,2S*)-3.**

The same procedure was applied to synthesize the enantiomer (*1S,2S*)-**3** with an estimated yield of 60.4%. ^{1}H NMR (600 MHz, Chloroform-*d*) δ 3.04 (m, *J* = 9.3, 4.4, 2.0 Hz, 1H), 2.95 (p, *J* = 6.2 Hz, 1H), 2.21 (ddd, *J* = 11.3, 9.3, 3.9 Hz, 1H), 2.08 – 2.01 (m, 2H), 1.74 – 1.67 (m, 2H), 1.31 – 1.17 (m, 3H), 1.05 (dd, *J* = 6.4, 2.3 Hz, 3H), 0.99 (dd, *J* = 6.2, 2.4 Hz, 3H), 0.90 – 0.83 (m, 1H). ^{13}C NMR (151 MHz, Chloroform-*d*) δ 74.1, 60.9, 45.4, 33.2, 31.4, 25.6, 24.8, 24.5, 22.9. $[\alpha]_D^{23}$ = 87.20 (c = 0.40, Et_2O) HRMS[ESI(TOF)] m/z: [M+H+] Calcd for C9H20NO 158.1545; found: 158.1546. The

enantiomeric excess was determined to be 99.8% for (*1S,2S*)-**3** by chiral HPLC in a Chiralpak AD, 25 cm × 4.6 mm, (Daicel) column, 28 ^{o}C, IPA/Hexanes = 88/12, 1 mL/min, t_{ss} = 8.6 min (major), t_{rr} = 19.6 min (minor). Wavelength: 210 nm; run time: 25 min, sample preparation: precolumn derivation with *m*-toluoyl chloride.

- **Procedure for entry 18 of Table 5-4, the optimized asymmetric reaction catalyzed by Soyafibe S-DN**

All solid samples were measured with an analytical balance (200g × 0.1 mg) and liquid samples were transferred with pipets (5 - 50 µL, 20 - 200 µL, 0.1 - 1 mL).

- Synthesis

The catalyst (Soyafibe S-DN) (60 mg), lithium bromide (13 mg, 50% mol), and an 8 mm stir bar were added to a 4 mL dried vial before pipetting toluene (256 µL) and H_2O (18 µL) into the vial. Then the mixture was stirred for 5 mins before pipetting 1,2-epoxycyclohexane (30.1 µL, 0.3 mmol), and isopropyl amine (25.7 µL, 0.3 mmol) into the vial followed by tightly screwing the vial cap on to the vial and seal it with scotch black tape. The reaction mixture was stirred in the vial on a vial rack in an oil bath at 38 °C for 60 hours (The temperature was monitored and tuned until it went stable, over tenths of parallel reactions with vigorous stirring might cause temperature rising). Then the vial was taken out cooling down to room temperature before losing the screw cap and placed under vacuum for 2 hours to dry out all the solvent, especially water in the product mixture. Clear product crystals would usually form on the edges of the vials.

- Characterization

0.8 mL diethyl ether was used to dissolve the product and the solution was filtrated through a syringe filter (0.2 μm, PTFE). And another 0.4 mL diethyl ether was used to rinse the residue and filtration. Then 80 μL out of the combined product mixture in the diethyl ether (1.2 mL) would be evaluated with *Rac*-**2** by fluorescent measurement. After that the product mixture was dried with rotary evaporation and vacuum pump. Then a small portion (usually 4 mg) was measured to react with *m*-toluene acetyl chloride to form derivatives that would be used to confirm the ee value of the product by chiral HPLC. The rest crystal shape or cream like solid product was weighted out to be 26 mg. Combined with the used portions the product mixture was calculated to be 30 mg. Thus, the reaction had an isolated yield of 64%. If the crude product is analyzed by the ^{1}H NMR (600 MHz, Chloroform-*d*) δ 3.04 (td, *J* = 9.4, 4.5 Hz, 1H), 2.95 (hept, *J* = 6.2 Hz, 1H), 2.21 (ddd, *J* = 11.3, 9.3, 3.9 Hz, 1H), 2.08 – 2.02 (m, 2H), 1.70 (ddt, *J* = 9.5, 6.5, 3.1 Hz, 2H), 1.30 – 1.17 (m, 3H), 1.05 (d, *J* = 6.3 Hz, 3H), 0.99 (d, *J* = 6.1 Hz, 3H), 0.90 – 0.84 (m, 1H). ^{13}C NMR (201 MHz, $CDCl_3$) δ 74.1, 60.9, 45.4, 33.1, 31.5, 25.6, 24.9, 24.5, 23.0. HRMS[ESI(TOF)] m/z: [M+H+] Calcd for C9H20NO 158.1545; found: 158.1539.

- **Synthesis of optical pure sensor 2, (*S*)-2 and (*R*)-2**

(*S*)-1,1'-(2,2'-dihydroxy-[1,1'-binaphthalene]-3,3'-diyl)bis(2,2,3,3,4,4,5,5,6,6,7,7,8,8,8 -pentadecafluorooctan-1-one), (*S*)-**2** and (*R*)-1,1'-(2,2'-dihydroxy-[1,1'-binaphthalene]-3,3'-diyl)bis(2,2,3,3,4,4,5,5,6,6,7,7,8,8,8-pentadecafluorooctan-1-one), (*R*)-**2** were synthesized according to our previous report.[13] And the characterization data were well matched with the reported ones.

- **Synthesis of the racemic sensor-2, *Rac*-2, which was modified from the procedures for synthesis of (*S*)-2 and (*R*)-2**

○ (*Rac*)-2,2'-bis-methoxymethyl-1,1'-binaphthyl, (*Rac*)-**6**

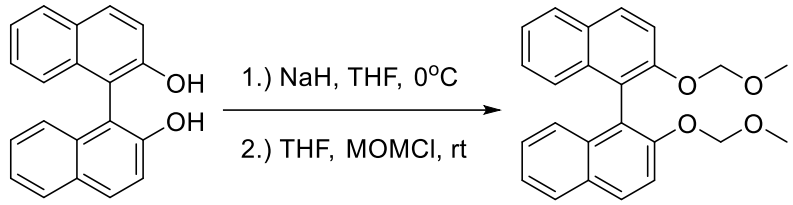

(*Rac*)-BINOL
(*Rac*)-**5**

(*Rac*)-**6**

(*Rac*)-1,1'-Binaphthol (2.86g, 10 mmol), (*Rac*)-**5** was added slowly to a suspension of NaH (60% in mineral oil, 1.6g, 40 mmol) in anhydrous THF (200 mL) at 0 °C under N_2 atmosphere with stirring. The resulting solution was stirred at 0 °C for 2 h. Then methoxymethyl chloride (3.9 mL, 30 mmol) was slowly added. The mixture was allowed to warm up to room temperature and stirred for another 6 h until TLC showed fully consumption of the starting material. After reaction complete, quenched by water (10 mL). The aqueous layer was extracted with ethyl acetate (3×100 mL). Combined organic layers were washed with brine (60 mL) and dried over anhydrous Na_2SO_4. Then the solvent was removed under reduced pressure; the resultant residue was recrystallized with EA/hexanes. Product (*Rac*)-**6** was obtained as a white powder in 85% yield. ^{1}H NMR (600 MHz, Chloroform-d) δ 7.96 (d, J = 9.1 Hz, 2H), 7.88 (d, J = 8.2 Hz, 2H), 7.58 (d, J = 9.1 Hz, 2H), 7.35 (t, J = 7.4 Hz, 2H), 7.23 (t, J = 7.6 Hz, 2H), 7.16 (d, J = 8.5 Hz, 2H), 5.09 (d, J = 6.9 Hz, 2H), 4.98 (d, J = 6.9 Hz, 2H), 3.15 (s, 6H).

○ (*Rac*)-1,1'-(2,2'-bis(methoxymethoxy)-[1,1'-binaphthalene]-3,3'-diyl)bis(2,2,3,3,4,4,5,5,6,6,7,7,8,8,8-pentadecafluorooctan-1-one), (*Rac*)-**7**

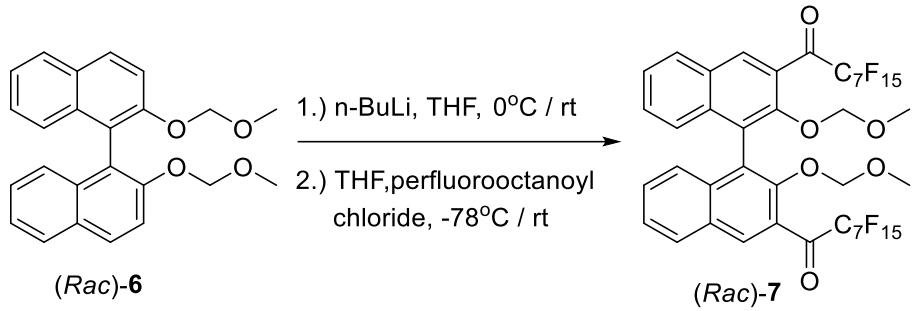

(*Rac*)-**6** (*Rac*)-**7**

Under nitrogen, 2,2'-bis-methoxymethyl-1,1'-binaphthyl, (*Rac*)-**6** (5 mmol, 1.87 g),1 was dissolved in THF (200 mL). The solution was cooled to 0 ºC, and n-BuLi (20 mmol, 2.5 M in hexane, 8 mL) was added dropwise. The reaction mixture was stirred at room temperature for 2 h and cooled to -78 ºC (dry ice/acetone), and then perfluorooctanoyl chloride (20 mmol, 5 mL) was added slowly. The reaction mixture was stirred at -78 °C for 2 h, and then warmed to 0 °C to react for 4 h to afford a yellow cream-like mixture. The mixture exhibited a bright green color under a UV-lamp, indicative of (*Rac*)-**7** formation. Saturated aqueous NH_4Cl solution (20 mL) was added to quench the reaction at 0 °C. The organic layer was separated, and the aqueous layer was extracted with dichloromethane (3*100 mL). The combined organic extracts were washed with brine, and dried over Na_2SO_4. TLC in Hexanes/EA (3/1) showed only one product spot was obtained. After evaporation of the solvent, the residue was further dried under vacuum pump to afford the crude product (*Rac*)-**7** (5.21g, 89% yield) as an orange sticky gel like mixture. Then it was used in the next step without further purification.

- (*Rac*)-1,1'-(2,2'-dihydroxy-[1,1'-binaphthalene]-3,3'-diyl)bis(2,2,3,3,4,4,5,5,6,6,7,7,8,8,8 - pentadecafluorooctan-1-one), (*Rac*)-**2**

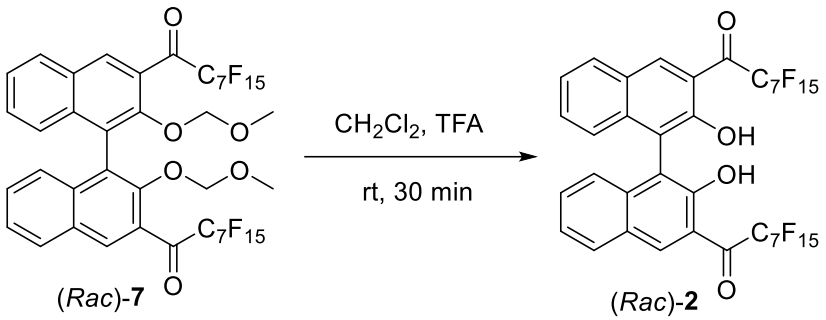

After compound (*Rac*)-**7** (2.34 g, 2.0 mmol) was dissolved in a minimum amount (10 mL) of CH_2Cl_2, trifluroacetic acid (6.0 mL) was added slowly at 0°C, and the mixture was stirred at room temperature for 30 min. Saturated aqueous $NaHCO_3$ solution was slowly added to quench the reaction at 0°C. The organic layer was separated, and the aqueous layer was extracted with CH_2Cl_2 (3 × 150 mL). The combined organic extracts were washed with brine, and dried over Na_2SO_4. After evaporation of the solvents, the residue was stirred in CH_2Cl_2/Hexanes (1/1, 50 mL) for 1 h before the solid was collected by filtration. Then this solid was purified another twice with the same procedure by CH_2Cl_2/Hexanes (1/1, 50 mL) to afford 1.36 grams of (*Rac*)-**2** as a red-orange powder with 63% yield. ^{1}H NMR (600 MHz, Chloroform-*d*) δ 10.57 (s, 2H), 8.78 (s, 2H), 8.04 – 7.99 (m, 2H), 7.46 (dddd, *J* = 25.4, 8.0, 6.8, 1.3 Hz, 4H), 7.16 (dd, *J* = 8.5, 1.1 Hz, 2H). ^{13}C NMR (201 MHz, $CDCl_3$) δ 187.6 (t, J = 25.7 Hz), 155.0, 138.5, 136.5, 132.3, 131.4, 127.2, 125.2, 124.7, 117.9, 116.7, 112.9-110.2 (m, 14C in the perfluro-chains). ^{19}F NMR (564 MHz, Chloroform-*d*) δ -81.16 (t, *J* = 10.0 Hz, 6F), -109.82 (m, 4F), -120.57 (m, 4F), -121.07(m, 4F), -122.25(m, 4F), -123.01(m, 4F), -126.50 (m, 4F), $[\alpha]_D^{23}$= 1.0 (c = 0.20, $CHCl_3$). HRMS[ESI(TOF)] m/z: [M+H+] Calcd for C36H13O4F30 1079.0335; Found: 1079.0376

- **Synthesis of racemic secondary amino alcohols from meso-epoxide**

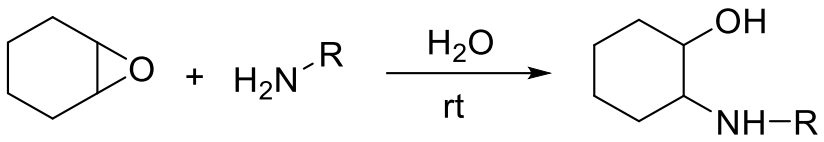

The meso-cyclohexene oxide (0.98 g, 10 mmol) was added into water (3 mL) and stirred at RT for 5 mins. Next the corresponding primary amine (1.5 eq.) was slowly added into the solution and the whole mixture stirred at RT overnight. After removal of solvent and vacuum dried the pure trans-form product could be obtained without further purification. The product was obtained as white porous powder of 1.50 g with a yield of 95.5% for (*Rac*)-**3**.

- (*Rac*)-2-(isopropylamino)cyclohexan-1-ol, (*Rac*)-**3**

^{1}H NMR (600 MHz, Chloroform-*d*) δ 3.04 (tdd, *J* = 9.4, 5.4, 2.1 Hz, 1H), 2.94 (pd, *J* = 6.2, 2.1 Hz, 1H), 2.21 (dddd, *J* = 11.3, 9.2, 4.0, 2.1 Hz, 1H), 2.04 (dddd, *J* = 14.2, 11.7, 5.4, 3.4 Hz, 2H), 1.70 (dtq, *J* = 9.4, 6.7, 2.9, 2.2 Hz, 2H), 1.31 – 1.15 (m, 3H), 1.04 (dd, *J* = 6.3, 2.1 Hz, 3H), 0.98 (dd, *J* = 6.1, 2.1 Hz, 3H), 0.91 – 0.83 (m, 1H). ^{13}C NMR (151 MHz, Chloroform-*d*) δ 74.1, 60.9, 45.3, 33.1, 31.5, 25.6, 24.9, 24.5, 23.0. The enantiomeric excess was determined to be 1.0 % of (*R*,*R*)-**3** by HPLC in a Chiralpak AD, 25 cm × 4.6 mm, (Daicel) column, 28 ^{o}C, IPA/Hexanes = 88/12, 1 mL/min, t_{ss} = 8.65 min (49.5%), t_{rr} = 19.76 min (50.5%). Wavelength: 210 nm; run time: 25 min, sample preparation: precolumn derivation with *m*-toluoyl chloride.

- **Catalytic amination of 1,2-epoxycyclohexane with isopropylamine at the 0.2 mL Scale**

A mixture of 1,2-epoxycyclohexane (20 μL, 0.2 mmol), isopropylamine (16 μL, 0.2 mmol), and the catalyst (Soyafibe S-DN) (40 mg) in toluene (0.168 mL) with the

required volume of water as well as the certain amount of additives was stirred at 37 ℃ for the specified time. After removal of the solvent under vacuum pump then it was re-dissolved in diethyl ether (1 mL × 2). After filtration the filtrate was used to characterization.

- **Synthesis of the m-toluoyl derivatives of amino alcohols 3 for HPLC analysis, *N*-(2-hydroxycyclohexyl)-N-isopropyl-3-methylbenzamide, 4**

The amino alcohol crude product was obtained by diethyl ether extraction from the reaction solid mixtures. Then the amino alcohol crude product (0.2 mmol) was dissolved in 1 mL anhydrous DCM or Et_2O followed by addition of 0.2 mmol triethylamine and 0.3 mmol *m*-toluoyl chloride via syringe slow addition. The reaction was stirred at rt for 12 hours. As the reaction went on white precipitates would form gradually. After removal of the solvent, diethyl ether (2×2 mL) was used to extract out the product. Then the product was obtained by rotary evaporation as a white solid and it was then directly dissolved in IPA/Hexane (1/9) before filtering by 0.2 μm syringe filter for the HPLC measurement. The enantiomers (*R*,*R*)-**4** and (*S*,*S*)-**4** were further crystalized from the IPA/Hexane (1/9) solution after 20 days and then confirmed by x-ray differentiation analysis of their single crystal structures.

The ^{1}H NMR spectra of (*Rac*)-**4**, ^{1}H NMR (600 MHz, Chloroform-*d*) δ 7.22 (d, *J* = 6.8 Hz, 1H), 7.12 (d, *J* = 16.0 Hz, 3H), 4.65 (s, 1H), 3.91 (s, 1H), 3.64 – 3.14 (m, 2H), 2.83 (m, 1H), 2.49 (m, 1H), 2.34 (s, 3H), 1.99 (m, 1H), 1.73 – 1.50 (m, 5H), 1.26 – 1.02 (m, 6H). ^{13}C NMR (151 MHz, Chloroform-*d*) δ 172.5, 138.9, 138.3, 129.5, 128.3, 126.7, 123.0, 69.5, 61.6, 35.4, 35.2, 23.0, 25.8, 24.6, 21.4, 21.3.

2.4.3. X-ray Crystal Analysis

A single crystal of (*S, S*)-**4** or (*R, R*)-**4** was coated with Paratone oil and mounted on a MiTeGen MicroLoop. The X-ray intensity data were measured on a Bruker Kappa APEXII Duo system equipped with an Incoatec Microfocus IμS (Cu K_α, λ = 1.54178 Å) and a multi-layer mirror monochromator.

The frames were integrated with the Bruker SAINT software package[20] using a narrow-frame algorithm. Data were corrected for absorption effects using the Multi-Scan method (SADABS).[20] The structure was solved and refined using the Bruker SHELXTL Software Package [21] within APEX3 [20] and OLEX2, [23] using the space group P $2_12_12_1$, with Z = 4 for the formula unit, $C_{17}H_{25}NO_2$. Non-hydrogen atoms were refined anisotropically. The OH hydrogen atoms were placed in sensible hydrogen bonding positions and refined isotropically with restraints on the O-H distances. All other hydrogen atoms were placed in geometrically calculated positions with $U_{iso} = 1.2U_{equiv}$ of the parent atom ($U_{iso} = 1.5U_{equiv}$ for methyl). A global RIGU restraint was used on the anisotropic displacement parameters of the atoms due to the extremely low resolution and redundancy of the diffraction from this crystal. During the refinement, some severely disordered solvent was located in the crystal lattice that could not be adequately modeled with or without restraints. Thus, the structure factors were modified using the PLATON SQUEEZE [23] technique, in order to produce a "solvate-free" structure factor set. PLATON reported a total electron density of 94 e^- and total solvent accessible volume of 258 Å [22].

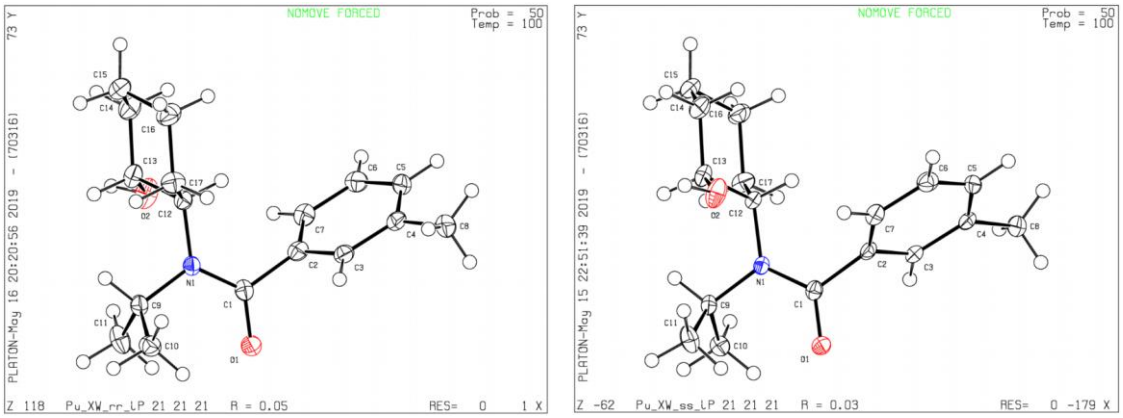

(a) (b)

Figure 2- 6. ORTEP diagram of the molecule (*R, R*)-**4** (a) and (*S, S*)-**4** (b) [ellipsoid contour probability: 50 %] by x-ray analysis of the single crystals.

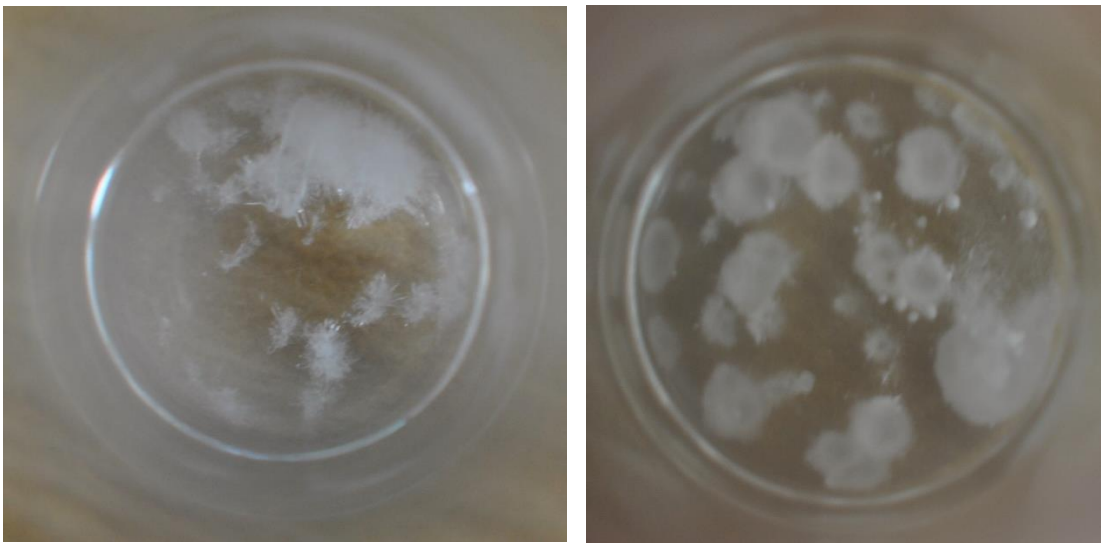

(a) (b)

Figure 2- 7. Photo images of the solid crystals of (*R, R*)-**4** (a) and (*S, S*)-**4** (b).

Table 2- 6. Sample and crystal data summary for (*S, S*)- and (*R, R*)-**4**

	(*S, S*)-**4**	(*R, R*)-**4**
CDCC #		
Chemical formula	C17H25NO2	C17H25NO2
FW (g/mol)	275.38	275.38
T (K)	100(2)	100(2)
λ (Å)	1.54178	1.54178
Crystal size (mm)	0.063 x 0.081 x 0.334	0.035 x 0.049 x 0.202
Crystal habit	colorless plate	colorless rod
Crystal system	orthorhombic	orthorhombic
Space group	P $2_12_12_1$	P $2_12_12_1$
a (Å)	6.4074(2)	6.4139(5)
b (Å)	11.8303(3)	11.8360(9)
c (Å)	20.8877(5)	20.8668(15)
α (°)	90	90
β (°)	90	90
γ (°)	90	90
Z	4	4
ρ_{calc} (g/cm$^{3)}$	1.155	1.155
μ (mm^{-1})	0.588	0.587
θ range (°)	4.23 to 68.25	4.24 to 68.30
Index ranges	$-7 \le h \le 7$, $-13 \le k \le 14$, $-24 \le l \le 25$	$-7 \le h \le 7$, $-14 \le k \le 13$, $-22 \le l \le 25$
Reflns coll.	14692	10972
Ind. reflns	2886 [R(int) = 0.0493]	2893 [R(int) = 0.0817]
Data / restraints / parameters	2886 / 0 / 188	2893 / 0 / 188
Goodness-of-fit on F^2	1.050	1.026
R_1 [I>2σ(I)]	0.0307	0.0491
wR_2 [all data]	0.0768	0.1172

2.5. References

1 Arai K., Lucarini S., Salter M. M., Ohta K., Yamashita Y., Kobayashi S., The Development of Scalemic Multidentate Niobium Complexes as Catalysts for the Highly Stereoselective Ring Opening of *meso*-Epoxides and *meso*-Aziridines. *J. Am. Chem. Soc*. **2007**, *129*, 8103.

2 Bao H., Zhou J., Wang Z., Guo Y., You T., Ding K., Insight into the Mechanism of the Asymmetric Ring-Opening Aminolysis of 4,4-Dimethyl-3,5,8-

trioxabicyclo[5.1.0]octane Catalyzed by Titanium/ BINOLate/ Water System: Evidence for the Ti(BINOLate)$_2$-Bearing Active Catalyst Entities and the Role of Water. *J. Am. Chem. Soc*. **2008**, *130*, 10116. 50.

3 (a) Sharma A., Agarwal J., Peddinti R. K., Direct access to the optically active VAChT inhibitor vesamicol and its analogues via the asymmetric aminolysis of meso-epoxides with secondary aliphatic amines. *Org. Biomol. Chem*. **2017**, *15*, 1913.

(b) Sun Z., Chen J., Liu Y., Tu T., Chiral Titanium Coordination Assemblies: Robust Cooperative Self-Supported Catalysts for Asymmetric Ring Opening of meso-Epoxides with Aliphatic Amines. *Adv. Synth. Catal*. **2017**, *359*, 494.

4 Meninno S., Lattanzi A., Organocatalytic Asymmetric Reactions of Epoxides: Recent Progress *Chem. Eur. J*. **2016**, *22*, 3632.

5 Roy S., Bhanja P., Islam Sk. S., Bhaumik A., Islam Sk. M., A new chiral Fe(III)–salen grafted mesoporous catalyst for enantioselective asymmetric ring opening of racemic epoxides at room temperature under solvent-free conditions *Chem. Commun*. **2016**, *52*, 1871.

6 Bao, H.; Wu, J.; Li, H.; Wang, Z.; You, T.; Ding, K. Enantioselective Ring Opening Reaction of *meso*-Epoxides with Aromatic and Aliphatic Amines Catalyzed by Magnesium Complexes of BINOL Derivatives. *Eur. J. Org. Chem.* **2010**, 6722–6726.

7 Yuki Takeuchi, Tatsuhiro Asano, Kazuya Tsuzaki, and Koichi Wada. Catalytic Asymmetric Amination of meso-Epoxide Using Soy Polysaccharide (Soyafibe S-DN). *Bull. Chem. Soc. Jpn*. **2018**, *91*, 678–683.

8 A Japanese patent: P2017-104044A, page 36-38.

9 Pu L., Fluorescence of Organic Molecules in Chiral Recognition. *Chem. Rev*. **2004**, 104, 1687–1716.

10 Leung D., Kang S. O., Anslyn E. V., Rapid Determination of Enantiomeric Excess: A Focus on Optical Approaches. *Chem. Soc. Rev*. **2012**, 41, 448–479.

11 (a) Accetta A., Corradini R., Marchelli R., Enantioselective Sensing by Luminescence. *Top. Curr. Chem.* **2010**, 300, 175–216.

(b) Zhang X., Yin J., Yoon J., Recent Advances in Development of Chiral Fluorescent and Colorimetric Sensors. *Chem. Rev*. **2014**, 114, 4918-4959.

12 Herrera B. T., Pilicer S. L., Anslyn E. V., Joyce L. A., Wolf C. Optical Analysis of Reaction Yield and Enantiomeric Excess: A New Paradigm Ready for Prime Time. *J. Am. Chem. Soc.* **2018**, *140*, 10385-10401.

13 Wang, C.; Wu, E.; Wu, X. D.; Xu, X. C.; Zhang, G. Q.; Pu, L. Enantioselective Fluorescent Recognition in the Fluorous Phase: Enhanced Reactivity and Expanded Chiral Recognition. *J. Am. Chem. Soc.* **2015**, *137*, 3747-3750.

14 Zhu Y.-Y., Wu X.-D., Abed M., Gu S.-X., Pu L. Biphasic Enantioselective Fluorescent Recognition of Amino Acids by a Fluorophilic Probe. *Chem: Eur. J.* **2019**, *25*, 7866 – 7873.

15 (a) Wang, C.; Wu, X. D.; Pu, L. A Highly Fluorinated Chiral Aldehyde for Enantioselective Fluorescent Recognition in a Biphasic System. *Chem. Eur. J.* **2017**, *23*, 10749-10752.

(b) Jiang L., Tian J., Zhao F., Yu S., Shi D., Wang X., Yu X., Pu L. Fluorescent Recognition of Functional Secondary Amines in the Fluorous Phase. *Eur. J. Org. Chem.* **2019**, 2533–2538.

16 Horváth, I. T.; Rábai, J. Facile Catalyst Separation Without Water: Fluorous Biphase Hydroformylation of Olefins. *Science* **1994**, 266, 72-75.

17 (a) Horváth, I. T. Fluorous Biphase Chemistry. *Acc. Chem. Res.* **1998**, *31*, 641–650.

(b) Handbook of Fluorous Chemistry; Gladysz, J. A., Curran, D. P., Horváth, I. T., Eds.; *Wiley-VCH: Weinheim, Germany*, 2004.

(c) O'Neal, K. L.; Zhang, H.; Yang, Y.; Hong, L.; Lu, D.; Weber, S. G. Fluorous Media for Extraction and Transport. *J. Chromatogr. A* **2010**, *1217*, 2287-2295.

18 Nian S., Pu L. Racemic Fluorescence Probe for Enantiomeric Excess Determination: Application of Cononsolvency of a Polymer in Sensing. *J. Org. Chem.* **2019**, *84*, 909−913.

19 Lu X., Xu Z., Tang G. Process Development on the Preparation of trans-(+)-2-Methylaminocyclohexanol: A Fascinating Resolution Example. *Org. Proc. Res. Dev.* **2001**, *5*, 184-185.

20 Bruker (2012). *Saint; SADABS; APEX3*. Bruker AXS Inc., Madison, Wisconsin, USA.

21 Sheldrick, G. M. (2015). *Acta Cryst*. A**71**, 3-8.

22 Dolomanov, O. V.; Bourhis, L. J.; Gildea, R. J.; Howard, J. A. K.; Puschmann, H. *J. Appl. Cryst.* (2009). **42**, 339-341.

23 Spek, A. L. *Acta Crystallogr. Sect C: Struct. Chem*. **2015**, C71, 9-18.

Chapter 3

Enantioselective Fluorescent Sensor for Secondary Amino Alcohols in the Fluorous Phase

3.1. Introduction

In the past two decades, significant progress has been made in the development of enantioselective fluorescent sensors for the recognition of chiral organic compounds.[1-3] These sensors are potentially useful for rapid real time assay of asymmetric reactions as well as monitoring chiral molecules in biological systems.[4] However, direct addition of a fluorescent sensor into the product mixture of a catalyst screening experiment could cause various degree of uncertainty in fluorescent analysis because of the possible interference from species other than the product. As a highly sensitive analysis tool, fluorescence measurement can be easily interfered by solvents, catalysts, by-products or even the air. If the product of a screening experiment could be conveniently separated from the reaction mixture, its analysis by using the enantioselective fluorescent sensor should be significantly simplified which should greatly facilitate the high throughput screening of chiral catalysts. The progress of the fluorous phase-based separation has prompted us to propose the use of fluorous phase for enantioselective recognition.[8] We envision that if the enantioselective fluorescent recognition of reaction products could be conducted in fluorous phase, it would be possible to use the fluorous-phase based separation to minimize the interference of other species in the screening experiments since most compounds without a highly fluorinated group are insoluble in fluorous

solvents.[9] The perfluoroalkyl-BINOL-based chiral diketones are found to show very different fluorescence responses toward the enantiomers of chiral amino alcohols in the fluorous phase.[5] Conducting the enantioselective fluorescent recognition in the fluorous phase can potentially minimize the interference of various reaction components in the measurement since most compounds cannot be dissolved in the hydrophobic and lipophobic fluorous solvents. A fluorous solution of an enantiomeric sensor pair can be used to extract the products, generated from the chiral catalyst screening experiments conducted in common organic solvents or aqueous solution, into the fluorous phase. Because only the sensors and their adducts with the chiral products could be dissolved in the fluorous phase, the interference of other species such as reagents, catalysts and starting materials is minimized.[6, 7] Through optical method like UV-vis, CD, and fluorescent measurement, both the yield and enantiomeric composition of the chiral products can be simultaneously determined. It's very likely to automate high throughput asymmetric reaction screenings in both academic and industrial research.

β-Amino alcohols are versatile intermediates in the synthesis of biologically active natural products, unnatural amino acids, *β*-blockers as well as insecticidal agent, and chiral auxiliaries. The asymmetric amination of meso-epoxides is an effective method to synthesize chiral *β*-aminoalcohols and their components as pharmaceuticals.[10] Unlike traditional optical resolution and kinetic resolution of racemic *β*-aminoalcohols with a yield less than 50%, the asymmetric amination of the meso-epoxides is possible to produce the desired trans-2-amino-1-cycloalkanols by a short process with a 100% maximum theoretical atom efficiency.[11] However, high enantioselectivity has been reported mainly with a combination of an organometallic catalyst and an amine with

aromatic substituents, such as aniline or benzylamine, and there are only a few reports using aliphatic amines, such as iso-propylamine, tert-butylamine, or piperidine.[12-15] Takeuchi etc. recently developed a bio-catalyzed asymmetric amination reaction of meso-epoxide using a water-soluble soy polysaccharide (Soyafibe S-DN) as a catalyst in hydrous toluene with very good yield and mild ee results.[16, 17] We anticipated our study in screening of the reaction conditions would be able to improve the enantioselectivity of the bio-catalyzed reaction by rapid fluorescence assay. The enantioselective fluorescent screening for the mentioned asymmetric catalytic reaction above has been thoroughly investigated by using both of the enantiopure sensors (*S*)-**1** and (*R*)-**1** as well as the racemic sensor (*Rac*)-**1** in Chapter 2 of this thesis. The fluorescence-based ee measurements have been confirmed by HPLC-chiral column analysis which has validated the fluorous phase-based enantioselective fluorescent sensing method. Even with the manual screenings, we have already discovered a condition with significantly improved enantioselectivity for the polysaccharide-catalyzed asymmetric reaction of 1,2-epoxycyclohexane with an alkyl amine. Works in Chapter 2 demonstrated that the fluorous phase-based enantioselective fluorescent sensor was practically useful for rapid screening of asymmetric reactions. In order to expand the analyte scope and to probe the concentrations of the analytes, a variety of chiral secondary *β*-amino alcohols were synthesized and tested for the enantioselectivity by using sensor (*S*)-**1** and (*R*)-**1**. Ten types of different chiral *β*-amino alcohols bearing a secondary amine group were investigated and demonstrated to have very good *ef* values (6.6– 65.0) with fluorescence enhancement differences at wavelengths from 420 to 435 nm. By using multiple techniques such as IR, NMR, and DLS, the mechanism of the enantioselectivity as well

as fluorescence enhancement were explored and rationalized. UV-vis spectroscopy was utilized to estimate the concentration of the amino alcohol with the same reaction mixtures as the fluorescence measurements in the fluorous phase.

3.2. Results and Discussion

3.2.1. Synthesis of the Sensor

The enantiopure (*S*)-**1** (1.4 g) and (*R*)-**1** (1.29 g) were prepared according to the reported procedures from (*S*)-BINOL and (*R*)-BINOL (2 mmol) in a total yield of 65% and 60%. (*Rac*)-**1** was synthesized by a similar protocol from (*Rac*)-BINOL but with much more solvent in all three steps of the reactions due to dramatically lower solubility of (*Rac*)-BINOL and its derivatives than their enantiopure ones With a much smaller solubility (≈ 10 mg / 5 mL CH_2Cl_2, while the enantiomers of **1** have an observed solubility in CH_2Cl_2 over 10 mg / 0.5 mL), (*Rac*)-**1** was also found to be still soluble in fluorous solvents. It can reach a concentration of 0.08 mM in FC-72 as a very clear yellow solution, which is also high enough for optic studies as the enantiopure (*S*)-**1** and (*R*)-**1** can make a 0.8 mM clear solution in FC-72.

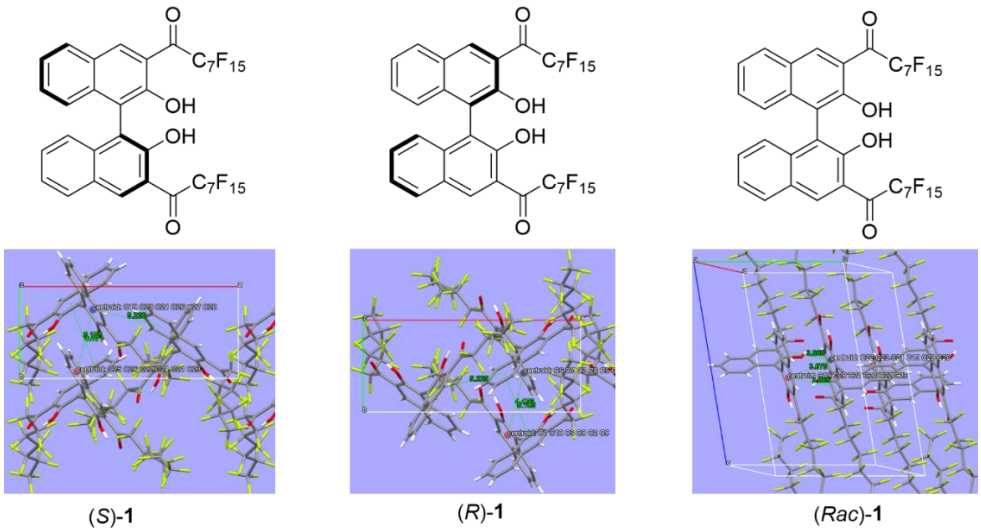

(*S*)-**1** (*R*)-**1** (*Rac*)-**1**

Figure 3- 1. The structures of (*S*)-**1**, (*R*)-**1** and (*Rac*)-**1** as well as their 2D stacking patterns revealed by x-ray analysis.

Through x-ray diffraction of the single crystals of (*S*)-**1,** (*R*)-**1** and (*Rac*)-**1**, the solubility difference among them could be partially explained indirectly. All their single crystals could be grown via very slow evaporation in the DCM solutions in air. From the crystal structures of the 3 compounds it was found that (*Rac*)-**1** maintained a totally different configuration from (*S*)-**1** and (*R*)-**1** (Figure 3-1 and more information in Appendix). The smallest separations of the ring centers intermolecularly is 4.471 or 4.476 Å, indicates very weak π-π interactions in the crystal (*S*)-**1** or (*R*)-**1**. While much shorter separations of the ring centers intermolecularly in (*Rac*)-**1** were measured out as 3.675, 3.865, and 3.865 Å. All of these distances are much more unified and in the range of π-π stackings that could give rise to a very rigid stacking pattern[18], which could contribute to the low solubility of the (*Rac*)-**1**. As perfluoro molecules their intermodular interaction strengths resulted from the intermolecular fluorine atoms could also be very crucial to their solubility. Surprisingly, a huge difference was found in this aspect. In either (*S*)-***1*** or (*R*)-***1*** crystal sample molecule only 7 pairs of effective interaction were found of fluorine atoms intermolecularly, and all of their distance are or over 2.85 Å, which implied a very weak intermolecular interactions produced by the fluorine atoms in the enantiomers, while in the crystal of (*Rac*)-**1**, 16 pairs of effective interactions, out of which 2 pairs are very strong, of fluorine atoms were found intermolecularly, and 7 pairs of them have a distance less than 2.85 Å, which suggested the racemic compound

demonstrate much stronger intermolecular interactions between the fluorine atoms than the ones of the enantiomers.

3.2.2. Synthesis of the Secondary Amino Alcohols

This work has expanded the excellent chiral recognition ability of the perfluoroalkyl-BINOL-based sensors in the fluorous phase to a variety of chiral secondary β-amino alcohols, most of which are not commercially available. Reductive amination of chiral primary amino alcohols with corresponding refluxing ethyl formate, aldehyde and ketone in toluene followed by adding $NaBH_4$ or $LiAlH_4$ were carried out to generate the chiral secondary β-amino alcohols in a total yield over 50% in most cases. The enantiopurity was later proved to be maintained after the reactions by the specific optical rotation, HPLC, and the fluorescent measurements. The detailed synthesis and characterization data are included in the experimental section.

3.2.3. The Interactions of Probe (*R*)-1, (*S*)-1 and Amino Alcohols in the Fluorous Solvent

Recently several perfluorous probes were developed and exhibited excellent enantioselectivities. Among these novel probes the perfluoroalkyl-BINOL-based chiral diketone **1** demonstrated great potential in rapid asymmetric reaction screening with its wide recognition substrate scope as well as the exclusive advantage of fluorous solvents in separation chemistry. To further expand the substrate scope, a variety of chiral secondary amino alcohols **5 – 14** were examined by using probe **1**.

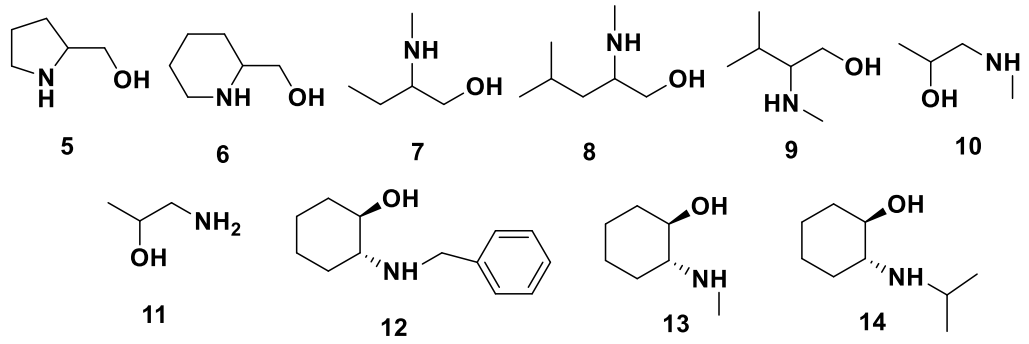

The interaction between **1** and **13** was first studied in the flourous phase. In FC-72, (*R*)-**1** showed almost no fluorescence. When (*R*)-**1** (1.0×10^{-5} M) was treated with (*S*, *S*)-**13** (2.0 mM) in FC-72 (containing 2% Et_2O to dissolve amino alcohol), large fluorescence enhancement (2500-3000 folds) at λ = 428 nm was observed as shown in Figure 3-1a. However, when (*R*)-**1** was treated with (*R*, *R*)-**13** in FC-72 under the same conditions, small fluorescence enhancement (50-200 folds) at λ = 428 nm was observed as shown in Figure 3-2a. Within 1 hour the fluorescence signal of **1** could become stable with amino alcohol **13.** The fluorinated sensor **1** was able to enantioselectively detect the pure chiral substance in a very quick fashion, which should be a very promising protocol for application in asymmetric reaction products analysis.

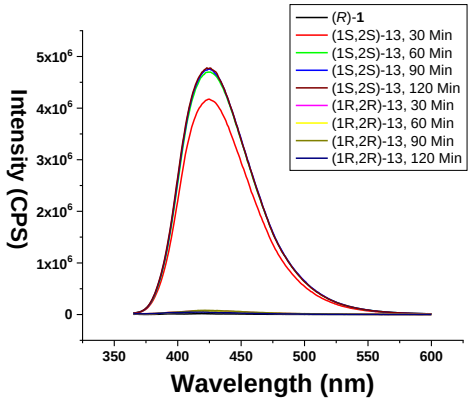

(a)

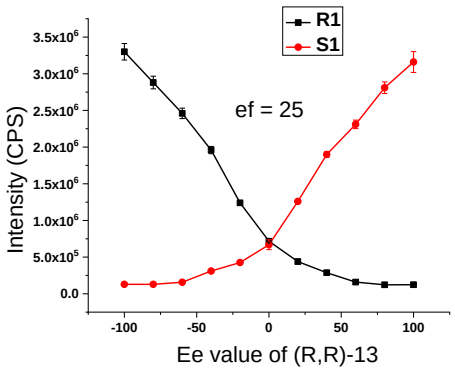

(b)

Figure 3- 2. Fluorescence spectra of (*R*)-**1** (1.0×10^{-5} M) with (*R, R*)-and (*S, S*)-**13** (2.0 mM) at different reaction time (a) and Fluorescent intensities of (*R*)-**1**, (*S*)-**1** with **13** (2.0 mM) at various enantiomeric excess (b). (in FC-72/Et_2O (98/2, v) λ_{exc} = 350 nm, slit: 3/3 nm, reaction time: 2 hours)

Both enantiomers of **1** were prepared and applied to study the response towards various enantiomeric composition of **13**. As shown in Figure 3-2b a mirror-image relationship was observed for the fluorescent response of (*S*)-**1** versus (*R*)-**1** toward the enantiomer mixtures of **13**. It confirms the observed enantioselective fluorescent recognition. A non-linear effect[19] was observed between the fluorescence response of the probe and the ee of the chiral substrate in the Figure 3-2b. That is, only when one enantiomer of the amino alcohols stays in excess the large fluorescence enhancement will appear otherwise the fluorescence enhancement would maintain small. With this effect, if the two enantiomeric sensors were used only one of their fluorescence intensities would increase by the excess enantiomer of the amino alcohols.

Ideally, the two enantiomers (*S*)-**1** and (*R*)-**1** could be applied to determine the enantiomeric composition (as well as absolute configuration), concentration of an amino alcohol sample by using the ratio *ef* of the fluorescent intensities (I_R/I_S or I_S/I_R), the sum of the fluorescent intensities (I_R+I_S) if there was no non-linear effect in the fluorescence response. One fluorescent intensity change could determine the enantiomeric composition (absolute configuration excluded) if the concentration of the amino alcohols had little influence on the fluorescence response at 428 nm. Enantiomeric excess versus fluorescent intensities of (*S*)-**1** and (*R*)-**1** at 428 nm were plotted at various concentrations

of **14**. All of them demonstrated huge non-linear effect between the fluorescence response of the probe and the ee of the amino alcohol **14**. That is the concentration of the amino alcohol would make a big difference in the fluorescent intensities at 428 nm (Figure 3-3). This is unique for these cyclohexyl amino alcohols especially **13** and **14**. Most of the fluorescence spectra of the probe (S)-**1**, (*R*)-**1** and (*Rac*)-**1** with **14** were presented in the chapter 2.

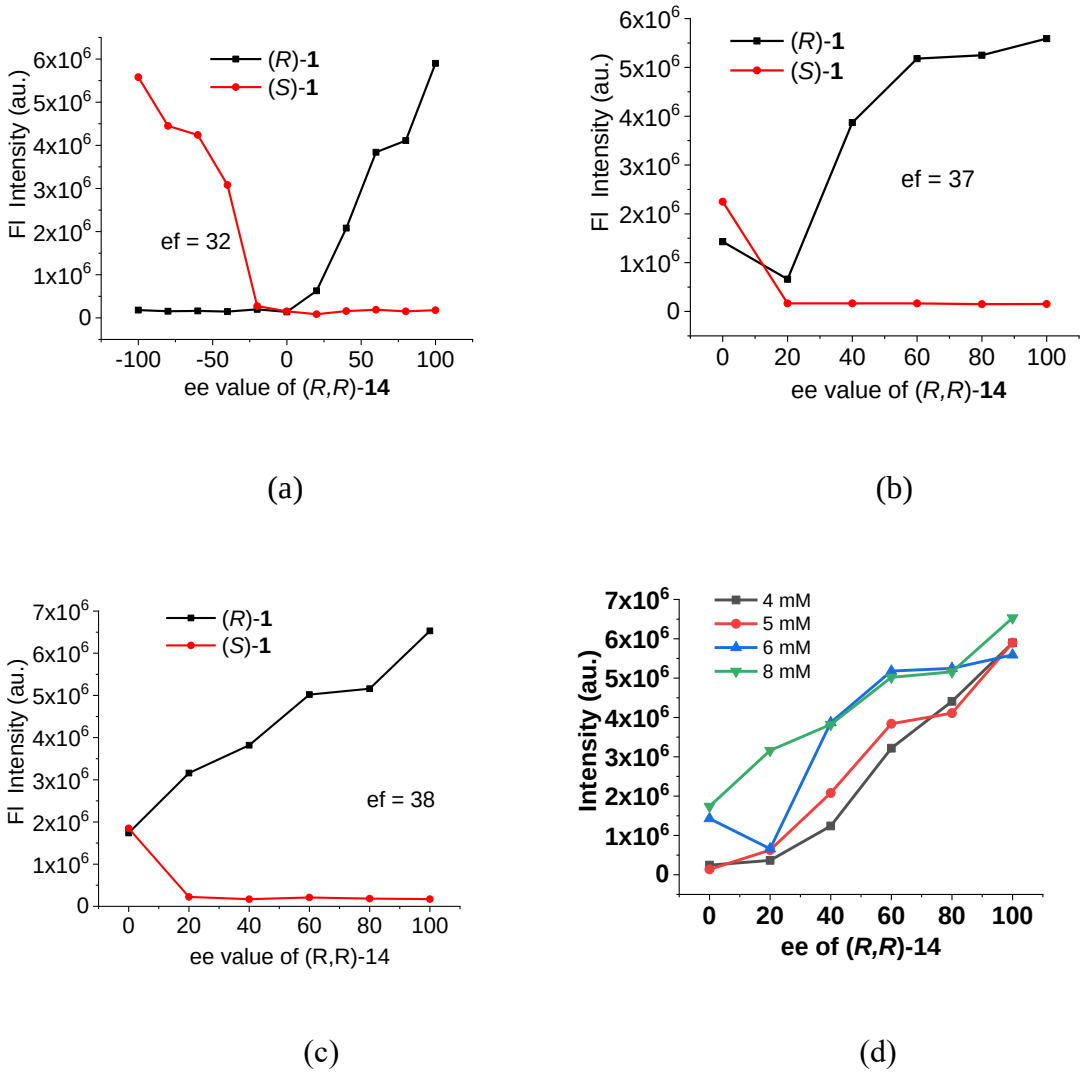

Figure 3- 3. Fluorescent intensities of (*R*)-**1**, (*S*)-**1** with **14** (5.0 mM) at various

enantiomeric excess (a), (*R*)-**1**, (*S*)-**1** with **14** (6.0 mM) at various enantiomeric excess (b), (*R*)-**1**, (*S*)-**1** with **14** (8.0 mM) at various enantiomeric excess (c) and the stacking curves of the fluorescent intensities of (*R*)-**1** with **14** at various enantiomeric excess under various concentrations at 428 nm (d). ([**1**] = 2.0×10^{-5} M in FC-72/Et_2O (96/4, v) λ_{exc} = 290 nm, slit: 3/3 nm, reaction time: 2 hours)

Other amino alcohols contain secondary amine groups (**5-10** and **12**) were also evaluated with the fluorescence response of probe **1**. It was exciting to find that the probe **1** demonstrated very high enantioselectivity to all of these amino alcohols and their fluorescent responses were all similar to that observed for the interaction of probe **1** with the amino alcohol **13**. It has been elaborated in the last chapter for this probe that in most cases excitation at both 290 nm and 350 nm in the fluorous phase could give enantioselective fluorescent enhancement at 428 nm. Either methylene chloride or diethyl ether could be used to dissolve the amino alcohols before they were mixed with Probe **1** in FC-72. The difference is that when methylene chloride was used there would be oil like thin layer or droplets generated in the sample mixtures with small fluorescent enhancement while when diethyl ether acted as the co-solvent the fluorous phase mixtures with low fluorescent intensities usually formed a clear one-phase solution of yellow color or colorless. All the sample mixtures with large fluorescent enhancement always showed a small amount of white precipitate which did not influence the fluorescence measurement.

Table 3- 1. The enantioselectivity of the investigated amino alcohols by using probe **1**

Amino Alcohol	**5**	**6**	**7**	**8**	**9**	**10**	**12**	**13**	**14**
ef. value	*65*	*16.5*	*60*	*18.5*	*18*	*6.6*	*50*	*25*	*35*

As shown in Table 3-1, Probe **1** exhibited highly enantioselective capability for amino alcohols containing a secondary amine group with *ef*. from 6.6 to 65.0 at certain concentration and conditions in the fluorous phase. And Probe **1** showed higher reactivity and sensitivity towards amino alcohols **5**-**10** and **13** due to less steric hinderance of the NH group while the probe was less reactive towards **12** and **14** that were bulkier around the NH group since a higher critical concentration was needed for **14** to enhance the fluorescence of the probe **1** and a longer reaction time was needed for **12** to reach a stable response.

When (*S*)-**1** was applied to react with amino alcohols **5** and **6**, we found the concentration of the probe had to be lowered less than 10 μM in order to achieve a good enantioselectivity while it also had to be more than 5 μM for good fluorescent signals. It was discovered that when the concentration of **5** remained smaller than 0.16 mM (in DCM) the enantioselectivity could stay very high while further increase the concentration of D-prolinol the fluorescent intensity of (*S*)-**1** at 425 nm would be enhanced to a comparable level to that of (*S*)-**1** with L-prolinol (Figure 3-4a,b and d) when excited at 350 nm. When follow the reaction by time, we found that in just 30 minutes the reaction of (*S*)-**1** with both D-and L-5 went stable in an equilibrium and the fluorescence could be recorded (Figure 3-4c). Interestingly, we used (*R*)-**1** (7.5×10^{-6} M in FC-72) to directly reactwith pure liquid **5** (3 mg) without adding any co-solvent the enantioselectivity could

be achieved with an *ef*. value ~ 2.5 and obvious fluorescence enhancement (Figure 3-4e). It might provide another sample preparation protocol of the enantioselective fluorescent recognition in the fluorous phase. When the reaction of (*S*)-**1** with D- and L-5 was carried out in DCM, the co-solvent that was used to dissolve the prolinol **5**, only very limited fluorescence enhancement and little enantioselectivity could be observed (Figure 3-4f). This demonstrated that the fluorous solvent played a very significant role in the enantioselective recognition of the amino alcohols by using the probe **1**. It not only enhanced the fluorescent intensity but also promoted the enantioselectivity.

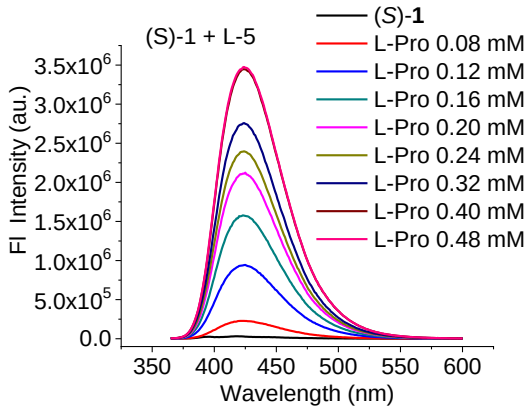

(a)

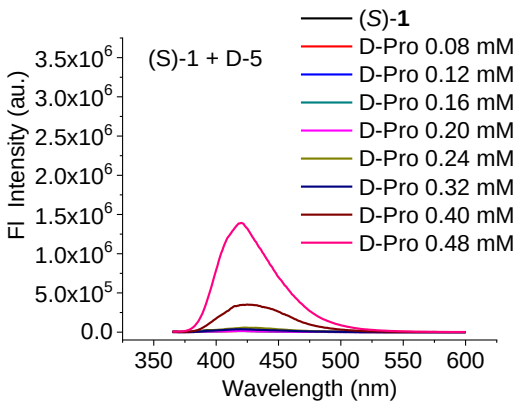

(b)

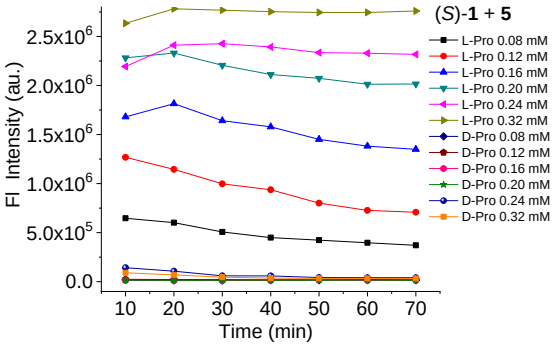

(c)

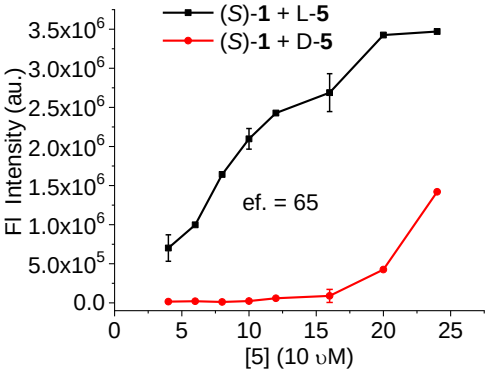

(d)

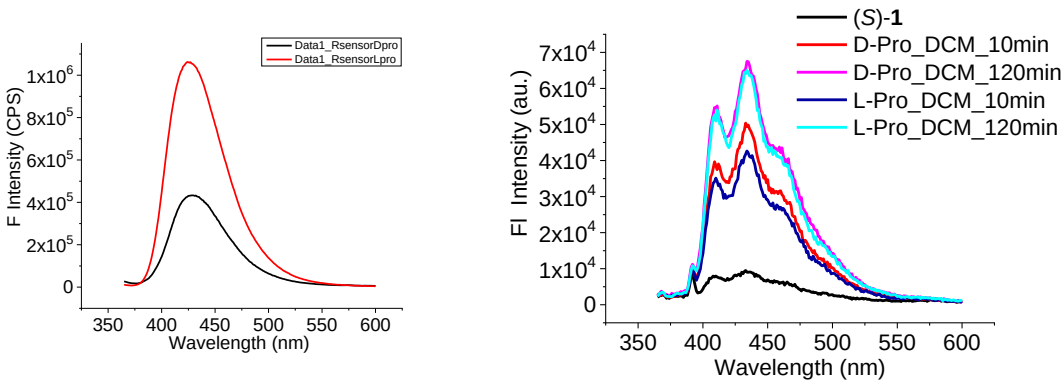

(e) (f)

Figure 3- 4. Fluorescence spectra of (*S*)-**1** (7.5×10^{-6} M) with (a) L-and (b) D-**5** (0.08 mM-0.48 mM) and Fluorescent intensities of (*S*)-**1** (7.5×10^{-6} M) with **5** (80 µM – 320 µM) at different reaction time (c) at 430 nm and Fluorescent intensities of (*S*)-**1** (7.5×10^{-6} M) with **5** (40-240 µM.) at 430 nm (d) and Fluorescence spectra of (*R*)-**1** (7.5×10^{-6} M in FC-72) with D-and L-**5 (**3 mg pure, no co-solvent was added) (e) and (*S*)-**1** (7.5×10^{-6} M in DCM) with D-and L-**5** (0.08 mM) in DCM (mostly in FC-72/DCM (98/2, v), λ_{exc} = 350 nm, slit: 3/3 nm, spectra recorded at 40 mins, unless otherwise noted).

With one more carbon compared with the prolinol **5**, the piperidinol **6** interacted with the probe **1** very similarly. When (*S*)-**1** with (*R*)-**6** or (*S*)-**6** in 2 mL FC-72/DCM, 98/2, (v) were measured by the fluorometer, a stable reading at 424 nm would be found in 120 minutes (Figure 3-5c). And mirror image like spectra of both (*S*)-**1** and (*R*)-**1** with both enantiomers of **6** were obtained under the same condition (Figure 3-5d, e). This validated the enantioselective process of probe **1** with **6**.

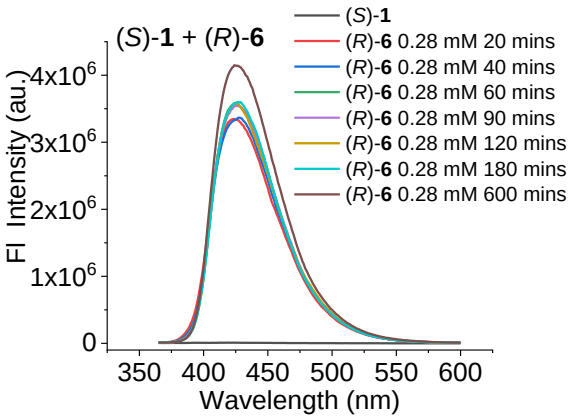
(S)-1 + (R)-6
(S)-1
(R)-6 0.28 mM 20 mins
(R)-6 0.28 mM 40 mins
(R)-6 0.28 mM 60 mins
(R)-6 0.28 mM 90 mins
(R)-6 0.28 mM 120 mins
(R)-6 0.28 mM 180 mins
(R)-6 0.28 mM 600 mins
FI Intensity (au.)
4x10^6
3x10^6
2x10^6
1x10^6
0
350 400 450 500 550 600
Wavelength (nm)

(a)

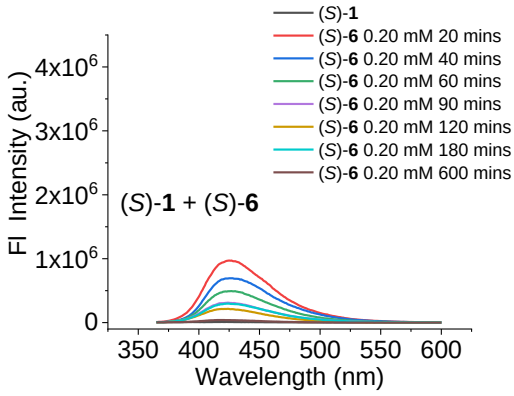
(S)-1
(S)-6 0.20 mM 20 mins
(S)-6 0.20 mM 40 mins
(S)-6 0.20 mM 60 mins
(S)-6 0.20 mM 90 mins
(S)-6 0.20 mM 120 mins
(S)-6 0.20 mM 180 mins
(S)-6 0.20 mM 600 mins
(S)-1 + (S)-6
FI Intensity (au.)
4x10^6
3x10^6
2x10^6
1x10^6
0
350 400 450 500 550 600
Wavelength (nm)

(b)

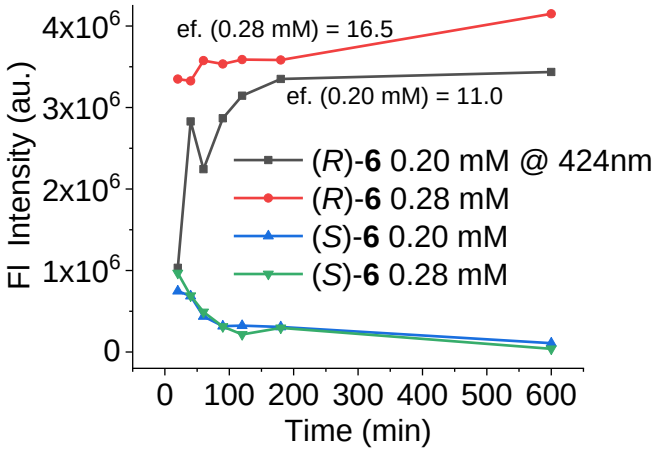
ef. (0.28 mM) = 16.5
ef. (0.20 mM) = 11.0
(R)-6 0.20 mM @ 424nm
(R)-6 0.28 mM
(S)-6 0.20 mM
(S)-6 0.28 mM
FI Intensity (au.)
4x10^6
3x10^6
2x10^6
1x10^6
0
0 100 200 300 400 500 600
Time (min)

(c)

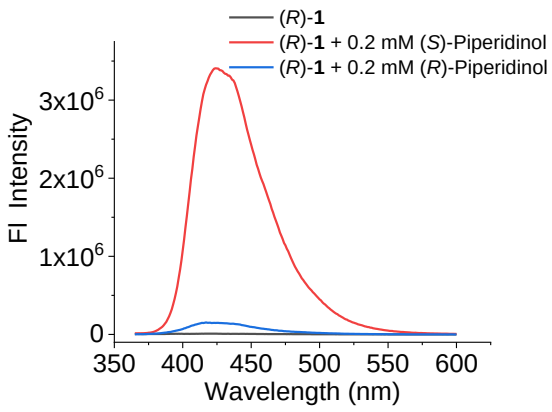
(R)-1
(R)-1 + 0.2 mM (S)-Piperidinol
(R)-1 + 0.2 mM (R)-Piperidinol
FI Intensity
3x10^6
2x10^6
1x10^6
0
350 400 450 500 550 600
Wavelength (nm)

(d)

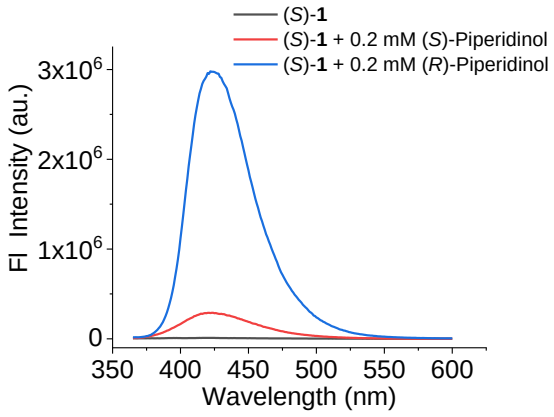
(S)-1
(S)-1 + 0.2 mM (S)-Piperidinol
(S)-1 + 0.2 mM (R)-Piperidinol
FI Intensity (au.)
3x10^6
2x10^6
1x10^6
0
350 400 450 500 550 600
Wavelength (nm)

(e)

Figure 3- 5. Fluorescence spectra of (*S*)-**1** (7.5×10^{-6} M) with (a) (*R*)-and (b) (*S*)-**6** (0.2 mM and 0.28 mM) at different reaction time and Fluorescent intensities of (*S*)-**1** (7.5×10^{-6} M) with both enantiomers of **6** (0.2 mM and 0.28 mM) at different reaction time at 424 nm (c) and Fluorescence spectra of (*R*)-**1** (7.5×10^{-6} M in FC-72) with (*R*)-and (*S*)-**6** (0.2 mM) (d) and (*S*)-**1** (7.5×10^{-6} M in FC-72) with (*R*)-and (*S*)-**6** (0.2 mM) (e) (in FC-72/DCM (98/2, v), λ_{exc} = 350 nm, slit: 3/3 nm, spectra recorded at 2 h, unless otherwise noted).

Bearing analogous structures, amino alcohols **7**, **8**, and **9** showed very similar fluorescence responses with (*S*)-**1** and (*R*)-**1** in FC-72/Et_2O, 96/4, (v). After the fluorescence responses were stabilized in 1-2 hours (Figure 3-6a), the spectra with emission around 425 nm and excitation at 290 nm were recorded. They all would reach a fluorescence saturation when the concentration of the amino alcohols reached1-2 mM. After that, the fluorescence changes of (*S*)-**1** and (*R*)-**1** with additional corresponding amino alcohols were small (Figure 3-6b, Figure 3-7c, and Figure 3-8c). By plotting the fluorescent intensities at the emission wavelengths (~425 nm) versus the enantiomeric composition of the amino alcohol, we found the enantiomeric pure probe **1** could probe the ees of the amino alcohol by the fluorescent intensity (Figure 3-6d, Figure 3-7e, and Figure 3-8d) with almost linear regressions. When DCM was used as a co-solvent to dissolve **8**, the enantioselectivity was even improved to an *ef*. value over 120. Therefore, both DCM and Et_2O could be used as the co-solvent for mixing in the fluorous phase. Mostly Et_2O was used since it's more miscible with perfluorohexanes.

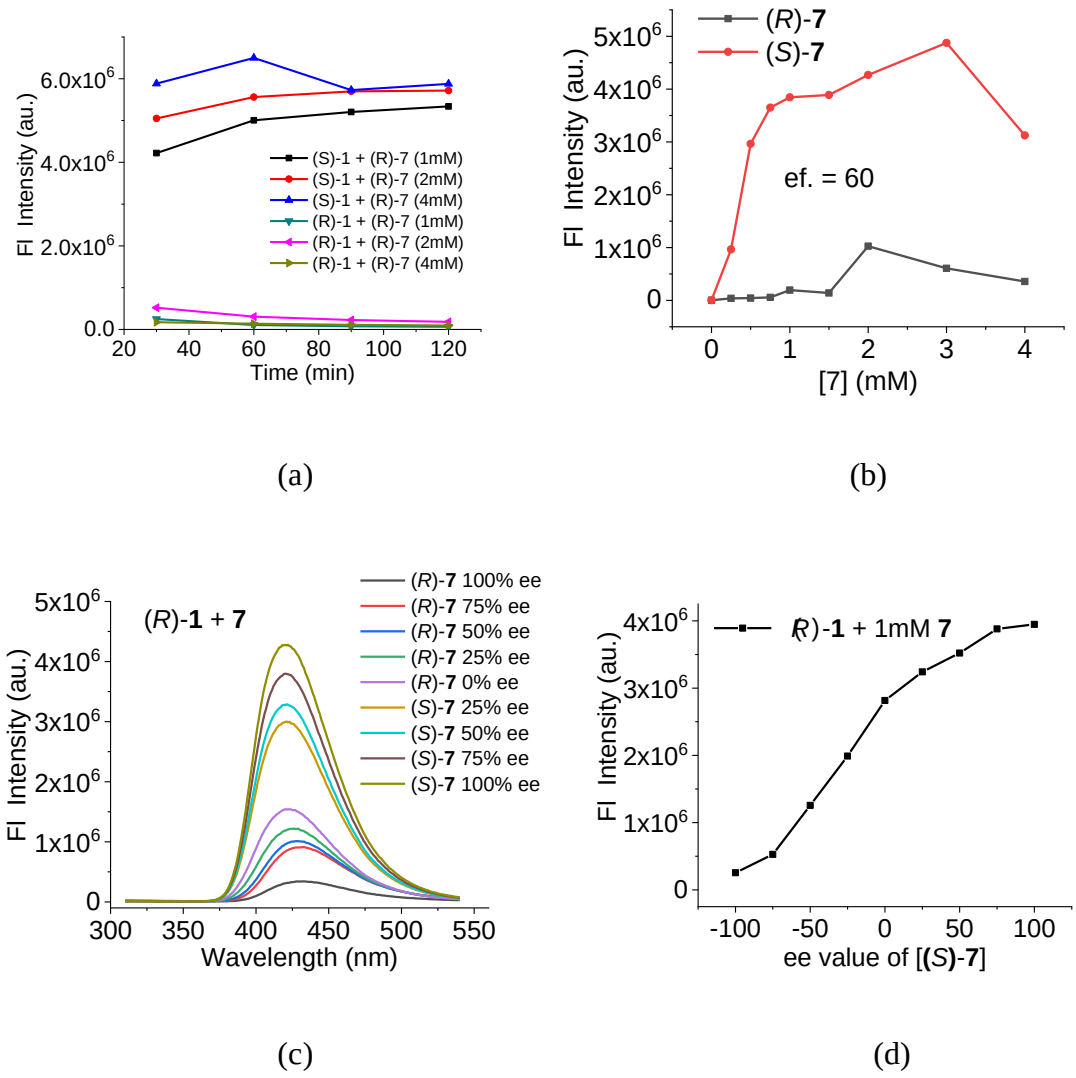

Figure 3- 6. Fluorescence spectra of (*S*)-and (*R*)-**1** (2×10^{-5} M) with (*R)*-**7** (1 - 4 mM) at different reaction time (a) and Fluorescent intensities of (*R*)-**1** (2×10^{-5} M) with both enantiomers of **7** (0 - 4 mM) at 422 nm (b) and Fluorescence spectra of (*R*)-**1** (2×10^{-5} M in FC-72) with **7** of various enantiomeric excess (1 mM) (c) and Fluorescent intensities of (*R*)-**1** (2×10^{-5} M in FC-72) with **7** of various enantiomeric excess (1 mM) at 422 nm (d) (in FC-72/Et_2O (96/4, v), λ_{exc} = 290 nm, slit: 3/3 nm, spectra recorded at 2 h, unless otherwise noted).

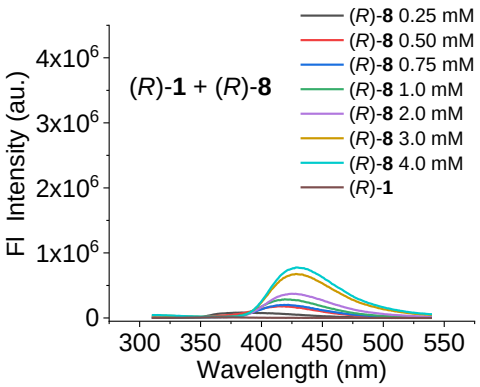
(R)-1 + (R)-8
(R)-8 0.25 mM
(R)-8 0.50 mM
(R)-8 0.75 mM
(R)-8 1.0 mM
(R)-8 2.0 mM
(R)-8 3.0 mM
(R)-8 4.0 mM
(R)-1
FI Intensity (au.)
Wavelength (nm)

(a)

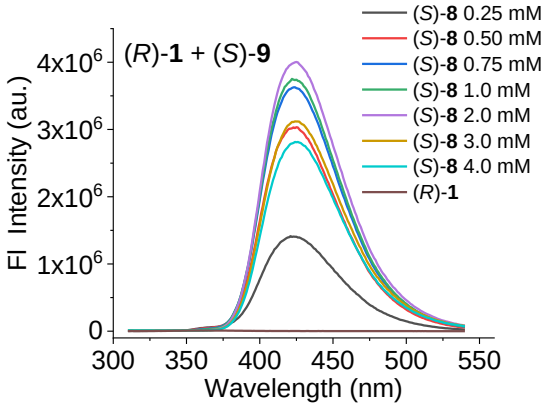
(R)-1 + (S)-9
(S)-8 0.25 mM
(S)-8 0.50 mM
(S)-8 0.75 mM
(S)-8 1.0 mM
(S)-8 2.0 mM
(S)-8 3.0 mM
(S)-8 4.0 mM
(R)-1
FI Intensity (au.)
Wavelength (nm)

(b)

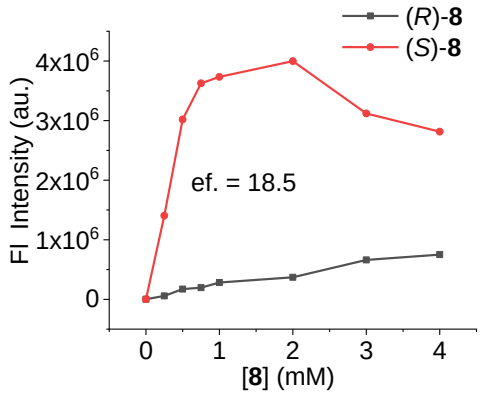
(R)-8
(S)-8
ef. = 18.5
FI Intensity (au.)
[8] (mM)

(c)

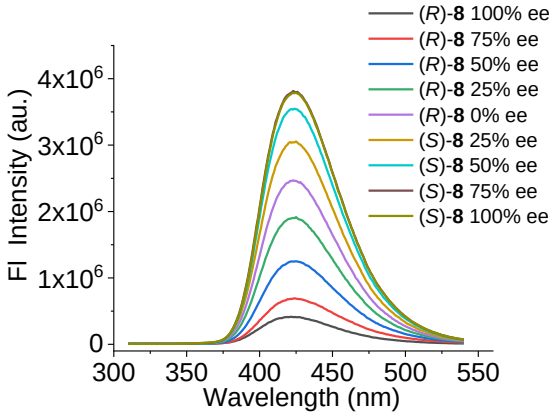
(R)-8 100% ee
(R)-8 75% ee
(R)-8 50% ee
(R)-8 25% ee
(R)-8 0% ee
(S)-8 25% ee
(S)-8 50% ee
(S)-8 75% ee
(S)-8 100% ee
FI Intensity (au.)
Wavelength (nm)

(d)

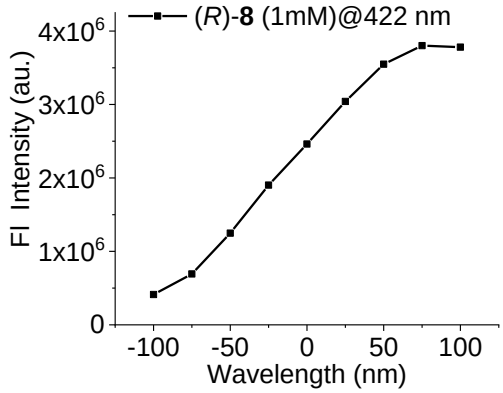
(R)-8 (1mM)@422 nm
FI Intensity (au.)
Wavelength (nm)

(e)

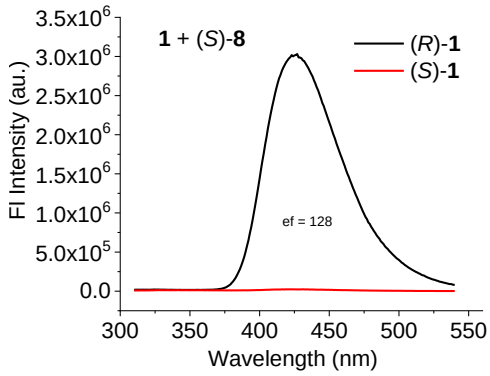
1 + (S)-8
(R)-1
(S)-1
ef = 128
FI Intensity (au.)
Wavelength (nm)

(f)

Figure 3- 7. Fluorescence spectra of (*R*)-**1** (2×10^{-5} M) with (a) (*R*)-**8** and (b) (*S*)-**8** (0 - 4 mM) and Fluorescent intensities of (*R*)-**1** (2×10^{-5} M) with both enantiomers of **8** (0 - 4 mM) at 422 nm (c) and Fluorescence spectra of (*R*)-**1** (2×10^{-5} M in FC-72) with **8** of various enantiomeric excess (1 mM) (d) and Fluorescent intensities of (*R*)-**1** (2×10^{-5} M in FC-72) with **8** of various enantiomeric excess (1 mM) at 422 nm (e) and Fluorescent spectra of (*S*)-and (*R*)-**1** (2×10^{-5} M in FC-72) with (*S*)-**8** (4 mM in DCM; FC-72/DCM, 96/4, v). (in FC-72/Et_2O (96/4, v), λ_{exc} = 290 nm, slit: 3/3 nm, spectra recorded at 2 h, unless otherwise noted)

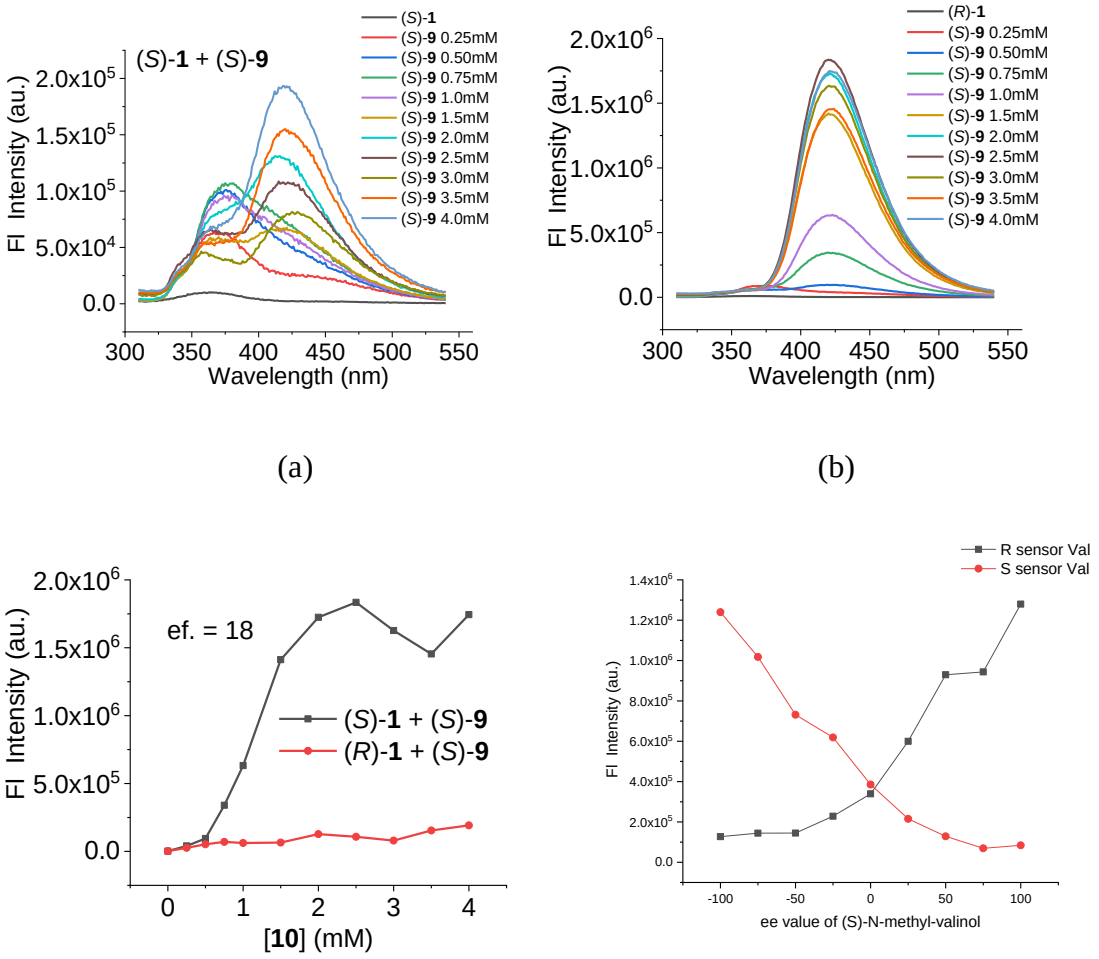

(c) (d)

Figure 3- 8. Fluorescence spectra of (a) (*S*)-**1** and (b) (*R*)-**1** (2×10^{-5} M) with (*S*)-**9** (0 - 4 mM) and Fluorescent intensities of (*R*)-**1** and (*S*)-**1** (2×10^{-5} M) with (*S*)-**9** (0 - 4 mM) at 426 nm (c) and Fluorescent intensities of (*R*)-**1** and (*S*)-**1** (2×10^{-5} M in FC-72) with **9** of various enantiomeric excess (2 mM) at 426 nm (d). (in FC-72/Et_2O (96/4, v), λ_{exc} = 290 nm, slit: 3/3 nm, spectra recorded at 2 h, unless otherwise noted)

Amino alcohol **10** was derived from the primary amino alcohol **11** that has its amine group connected with a primary carbon, which made them different from other amino alcohols investigated before. (*R*)-**1** was employed to investigate its fluorescence response of (*S*)-**10** and (*R*)-**10**, and the fluorescence spectra were recorded at various time with an excitation wavelength at 350 nm and emission at 428 nm. It was found that stable fluorescent intensities usually obtained in 2 hours. At this time, a variety of concentrations of **10** (1 mM – 8mM) could give good enantioselectivity. And when [**10**] ≥ 2 mM, the fluorescent intensity remained at a relatively stable level regardless of the concentrations.

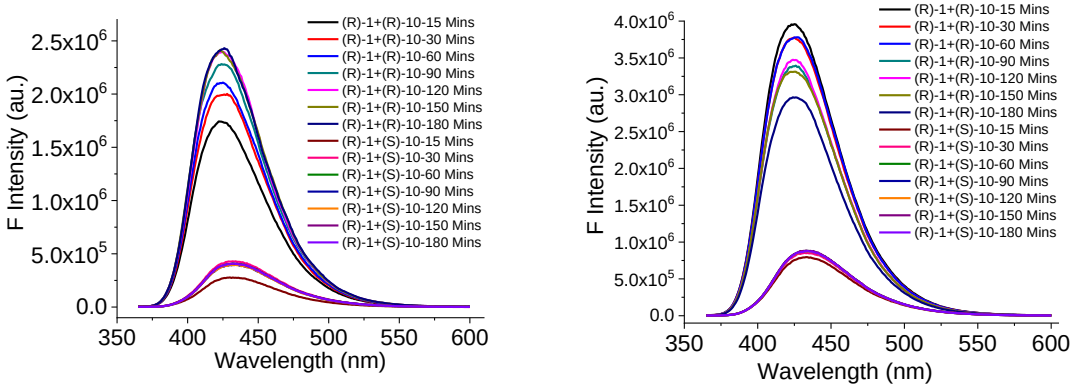

(a) (b)

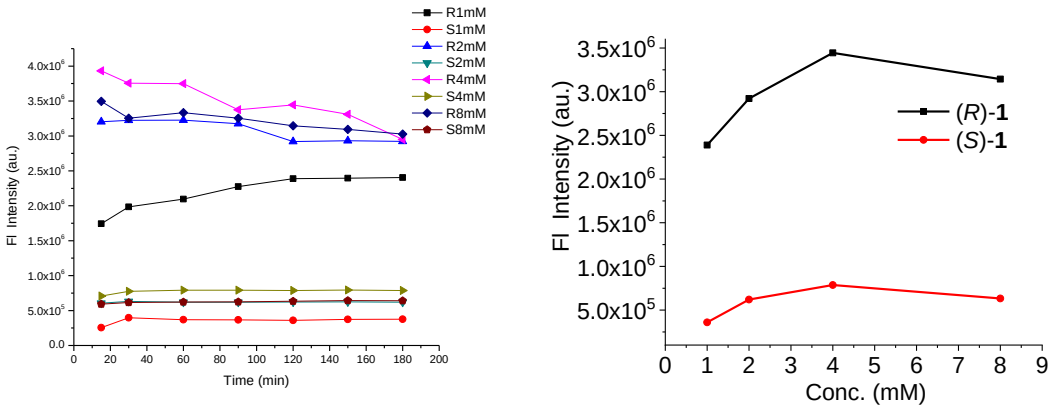

(c) (d)

Figure 3- 9. Fluorescence spectra of (*R*)-**1** (2×10^{-5} M) with (*R*)-**10** and (*S*)-**10** of different concentrations(a, 1 mM, b, 4 mM) and Fluorescent intensities of (*R*)-**1** and (*S*)-**1** (2×10^{-5} M) with (*R*)-**10** (1 - 8 mM) at 428 nm (c) and Fluorescent intensities of (*R*)-**1** and (*S*)-**1** (2×10^{-5} M in FC-72) with (*R*)-**10** of various concentrations (1 - 8 mM) at 428 nm (d). (in FC-72/Et_2O (96/4, v), λ_{exc} = 350 nm, slit: 3/3 nm, spectra recorded at 2 h, unless otherwise noted)

With a benzyl group attached to the amine group, amino alcohol **12** might have a relatively slower reaction with the probe **1** and an equilibrium was difficult to achieve. The fluorescent intensity was low and its increase continued even in 3 hours. The fluorescence enhancement was also observed at ~ 430 nm, which indicates that the reactions of (*R*)-**1** and (*S*)-**1** with (*S, S*)-**12** were similar to those with other amino alcohols especially with both **13** and **14** that contained the cyclohexyl ring as the aliphatic backbone of the amino alcohols. In the mixed solvent of FC-72/Et_2O/DCM, 96/2/2, (v),

the enantioselectivity was high with the *ef*. value up to 50.0. The excitation spectra for the emission at 434 nm also reflected the enantioselectivity with distinct intensity difference at 350 nm.

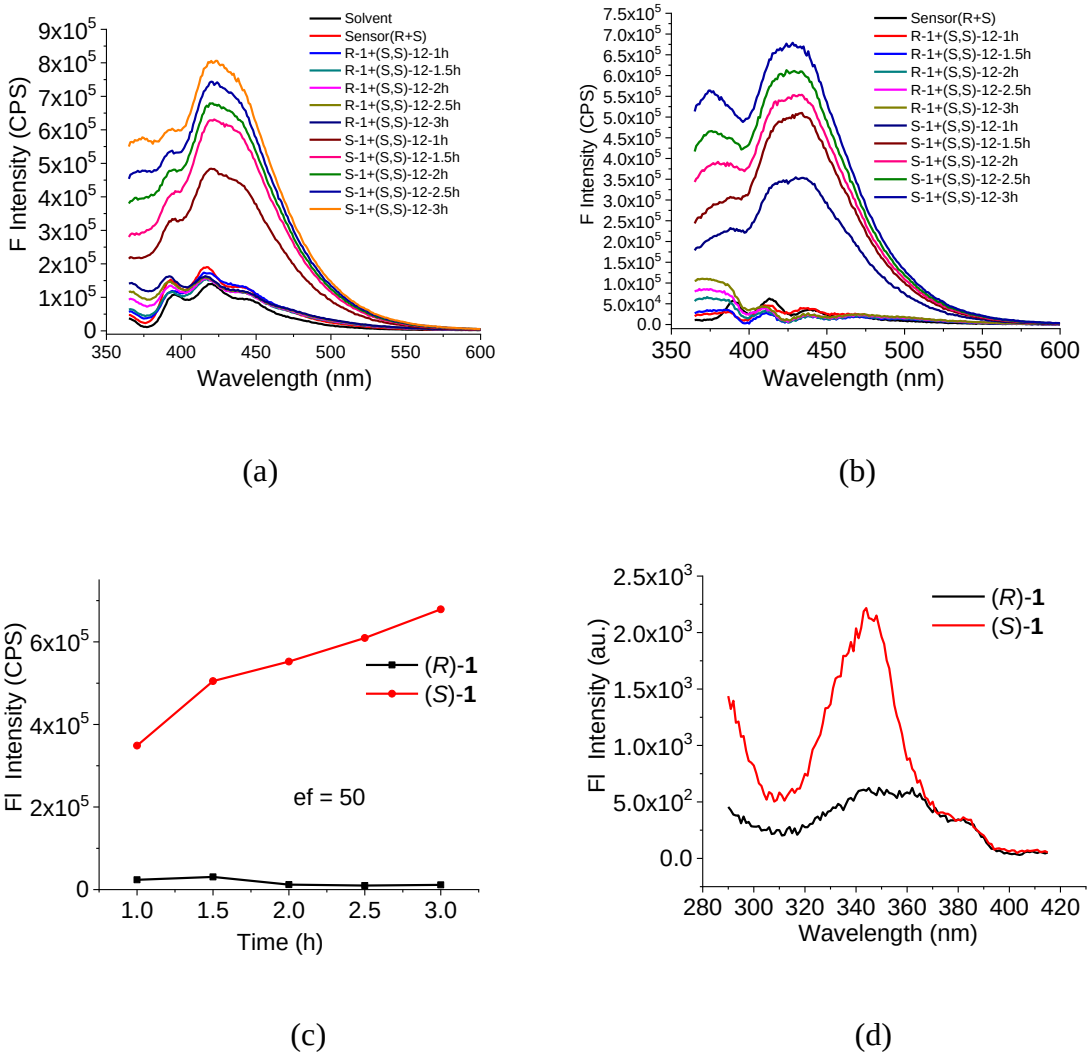

Figure 3- 10. Fluorescence spectra of (*R*)-**1** and (*S*)-**1** (1.5×10^{-5} M) with (*S, S*)-**12** (1 mM) at different reaction time (a) solvent background subtracted (b) and Fluorescent intensities of (*R*)-**1** and (*S*)-**1** (1.5×10^{-5} M) with (*S, S*)-**12** (1 mM) at different reaction time at 434 nm (c) and excitation spectra of (*R*)-**1** and (*S*)-**1** (1.5×10^{-5} M in FC-72) with (*S, S*)-**12** (1 mM) for emission at 434 nm. (in FC-72/Et_2O/DCM (96/2/2, v), λ_{exc} = 350 nm, slit: 3/3

nm, excitation spectra recorded at 2 h)

Unlike other secondary amino alcohols, the primary amino alcohol **11** enhanced the fluorescence of the probe at 502 nm without any enantioselectivity. Thus, this probe couldn't distinguish the enantiomers of the amino alcohols whose NH_2 group is connected to a primary carbon. This was different from our previous report that probe **1** had showed highly enantioselective fluorescent response toward primary amino alcohols in which the NH_2 group was connected to a chiral secondary carbon.

When compound **11** was converted to the secondary amino alcohol **10**, highly enantioselective fluorescence response with the probe **1** was observed as described in a previous paragraph.

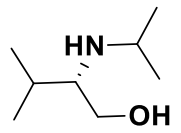

16

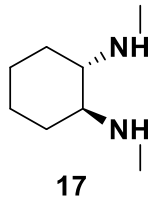

17

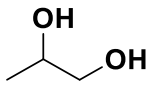

18

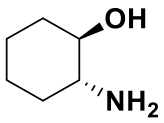

19

Another amino alcohol **16** was synthesized in the same procedures. But under the same condition upon treated with 8 mM (*S*)-**16**, only small enhancement obtained and little enantioselectivity was observed by using both (*S*)-**1** and (*R*)-**1**. The two isopropyl group might have blocked the nucleophilic addition. Compound **17** and **18** were also examined with probe **1**. It was found that the diamine **17** would strongly enhance the fluorescent intensity at 415 nm while no fluorescent enhancement could be generated by the diol **18**. Thus, the carbonyl groups in probe **1** preferred to react with the nucleophilic

N on the secondary amino alcohols. Probe **1** didn't show very reliable fluorescence response when treated with 2-aminocyclohexan-1- ol, **19**.

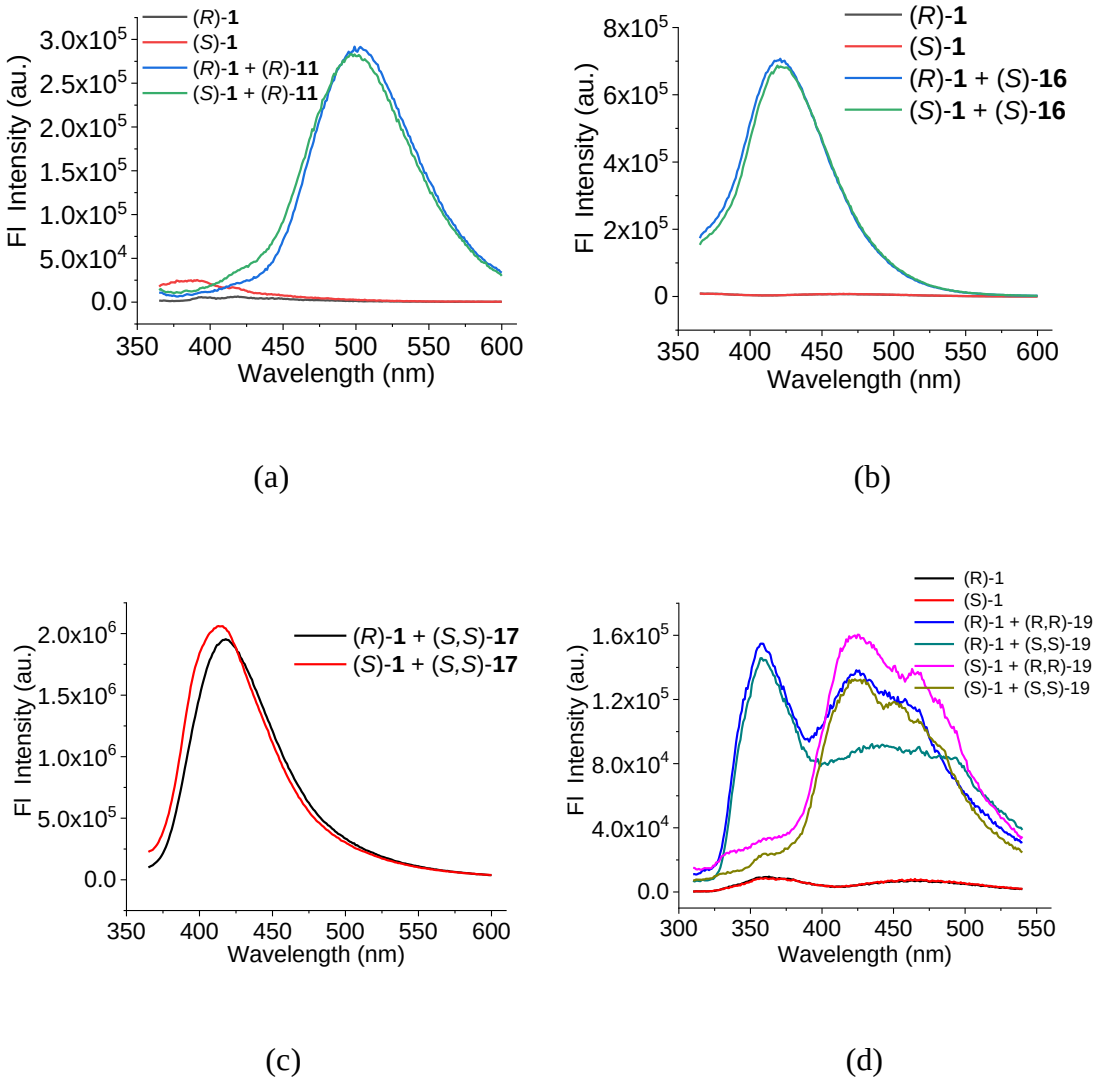

Figure 3- 11. Fluorescence spectra of (*R*)- and (*S*)-**1** (2×10^{-5} M) with (*R*)-and (S)-**11** (4 mM) (a) and with (*R*)-and (S)-**16** (8 mM) (b) and with (*S, S*)-**17** (6 mM) (c) and with (*S, S*)-**19** and (*R, R*)-**19** (8 mM) (d). (in FC-72/Et_2O (96/4, v) for a-c, λ_{exc} = 350 nm, and for d, λ_{exc} = 290 nm, all slit: 3/3 nm, reaction time: 2 hours)

3.2.4. Mechanism Investigation

NMR, IR spectroscopic, and DLS techniques were used to investigate the reaction process of the secondary amino alcohols with probe **1**. In the NMR titration experiments, a solution of (*S, S*)-**14** in Et_2O was added to (*S*)-**1** (0.8 mM) in FC-72 with an external standard of acetone-d6 in a capillary tube. Figure 3-12a and Figure 3-12b compare the ^{1}H NMR responses of (*R*)- and (*S*)-**1** when treated with (*S, S*)-**14**. Both figures show that as the amount of (*S, S*)-**14** increased, the intensity of the signals of the probes decreased. This indicates that the products of these reactions might have aggregated in the fluorous phase. As shown in Figure 3-12b, when >35 μL (*S, S*)-**14** was added, all the ^{1}H NMR signal disappeared with the continuous formation of white precipitate. This suggests the formation of large aggregates from the reaction of (*S*)-**1** with (*S, S*)-**14**, giving the observed large fluorescence enhancement. However, for the reaction of (*R*)-**1** with (*S, S*)-**14**, the reaction mixture remained a clear yellow solution even though the ^{1}H NMR signals also disappeared when (*R*)-**1** was treated with 50 μL (*S, S*)-**14**. This suggests that the product aggregates from the reaction of (*R*)-**1** with (*S, S*)-**14** should be much smaller than that from the reaction of (*S*)-**1** with (*S, S*)-**14**. Little fluorescence enhancement from the reaction of (*R*)-**1** with (*S, S*)-**14** could be attributed to its very different aggregate structure in comparison with those generated from the reaction of (*S*)-**1** with (*S, S*)-**14**.

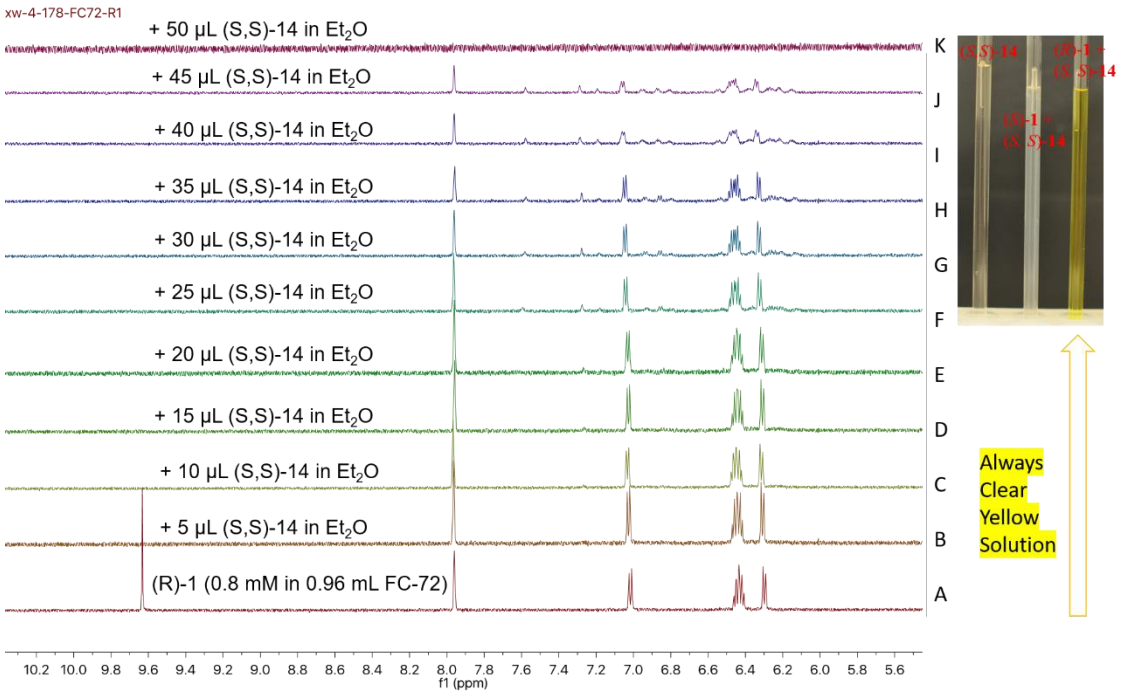
xw-4-178-FC72-R1
+ 50 µL (S,S)-14 in Et2O
+ 45 µL (S,S)-14 in Et2O
+ 40 µL (S,S)-14 in Et2O
+ 35 µL (S,S)-14 in Et2O
+ 30 µL (S,S)-14 in Et2O
+ 25 µL (S,S)-14 in Et2O
+ 20 µL (S,S)-14 in Et2O
+ 15 µL (S,S)-14 in Et2O
+ 10 µL (S,S)-14 in Et2O
+ 5 µL (S,S)-14 in Et2O
(R)-1 (0.8 mM in 0.96 mL FC-72)
K
J
I
H
G
F
E
D
C
B
A
10.2 10.0 9.8 9.6 9.4 9.2 9.0 8.8 8.6 8.4 8.2 8.0 7.8 7.6 7.4 7.2 7.0 6.8 6.6 6.4 6.2 6.0 5.8 5.6
f1 (ppm)
(S,S)-14
(R)-1 + (S, S)-14
(S)-1 + (S, S)-14
Always Clear Yellow Solution

(a)

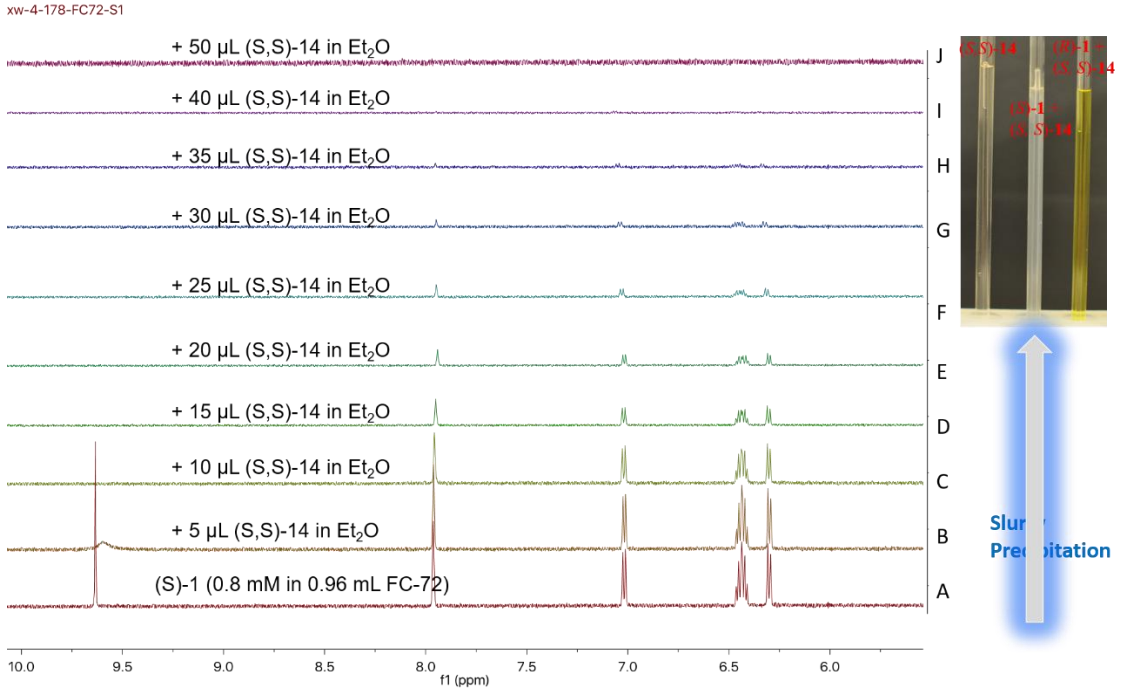
xw-4-178-FC72-S1
+ 50 µL (S,S)-14 in Et2O
+ 40 µL (S,S)-14 in Et2O
+ 35 µL (S,S)-14 in Et2O
+ 30 µL (S,S)-14 in Et2O
+ 25 µL (S,S)-14 in Et2O
+ 20 µL (S,S)-14 in Et2O
+ 15 µL (S,S)-14 in Et2O
+ 10 µL (S,S)-14 in Et2O
+ 5 µL (S,S)-14 in Et2O
(S)-1 (0.8 mM in 0.96 mL FC-72)
J
I
H
G
F
E
D
C
B
A
10.0 9.5 9.0 8.5 8.0 7.5 7.0 6.5 6.0
f1 (ppm)
(S,S)-14
(R)-1 + (S, S)-14
(S)-1 + (S, S)-14
Slur
Prec itation

(b)

Figure 3- 12. ^{1}H NMR titration study of (*S, S*)-**14** (100 mM in 5-50 μL Et_2O) with (a) (*R*)-**1** and (b) (*S*)-**1** (0.8 mM in 0.96 mL FC-72) and a capillary tube filled with [D_6]acetone was put added in the NMR tube as an external standard. (See full spectra and photo images of the samples in the Appendix for chapter 3)

The reactions were also investigated by dynamic light scattering (DLS) technique in order to characterize the difference between the adducts formed by one enantiomer of the probe **1** and the two enantiomers of the amino alcohols. DLS study was conducted on the slury solution from the reaction of (*S*)-**1** (8.0×10^{-5} M) with (*S, S*)-**14** (4 mM) in FC- 72 (4% Et_2O) which gave large fluorescence enhancement observable under a UV lamp. It showed a lognormal distribution of the particle sizes of 1000-2000 nm. The almost clear solution formed from the reaction of (*S*)-**1** with (*R, R*)-**14** under the same conditions showed a bad distribution of the particle sizes less than 300 nm (Table 3-2) with very little fluorescence enhancement under a UV lamp. Similarly, when (*R*)-**1** (8.0×10^{-5} M) was treated with (*S, S*)- and (*R, R*)-**14** (4 mM) in FC- 72 (4% Et_2O), the one with much stronger fluorescence enhancement would demonstrate a bigger particle size [1-1.8 μm for (*R*)-**1** with (*R, R*)-**14**, 0.2 μm for (*R*)-**1** with (*S, S*)-**14**].

Table 3- 2. DLS data for (*R*)-**1** and (*S*)-**1** with (*S, S*)-**14** and (*R, R*)-**14**

[Sensor]=80 uM, [14]=4mM							
Sample Name	**Z-Ave**	**PdI**	**Pk 1 Mean Int**	**Pk 2 Mean Int**	**Time**	**Pk 1 Area Int**	**Pk 2 Area Int**
	d.nm		d.nm	d.nm		Percent	Percent
(S)-**1** BLANK	0	0	0	0	01, 21, 2020 12:14:07 PM	0	0
Results of the measurement above: No particles found and instrument stopped.							
(R)-**1** BLANK	0	0.089	0	0	01, 21, 2020 12:23:31 PM	0	0
Results of the measurement above: No particles found and instrument stopped.							
(R)-1 + (S, S)-14	1280	1	192.5	0	01, 21, 2020 5:02:50 PM	100	0
(R)-1 + (S, S)-14	1930	1	144.4	0	01, 21, 2020 5:05:15 PM	100	0
(R)-1 + (S, S)-14	1925	1	123.5	0	01, 21, 2020 5:07:39 PM	100	0
Results of the 3 parallel measurements above: some 0.2 µm particles formed with a very bad size distribution.							
(S)-1 + (R, R)-14	1075	0.783	246.9	0	01, 21, 2020 5:14:13 PM	100	0
(S)-1 + (R, R)-14	1346	0.841	229.7	0	01, 21, 2020 5:17:08 PM	100	0
(S)-1 + (R, R)-14	1190	0.76	220.2	0	01, 21, 2020 5:20:04 PM	100	0
Results of the 3 parallel measurements above: some 0.3 µm particles formed with a bad size distribution.							
(S)-1 + (S, S)-14	1646	0.427	1075	0	01, 21, 2020 5:27:04 PM	100	0
(S)-1 + (S, S)-14	2121	0.461	1329	0	01, 21, 2020 5:29:08 PM	100	0
(S)-1 + (S, S)-14	2385	0.564	1060	0	01, 21, 2020 5:31:12 PM	100	0
Results of the 3 parallel measurements above: 1-2 µm particles formed with a good size distribution.							
(R)-1 + (R, R)-14	1746	0.507	1820	609.2	01, 21, 2020 5:37:00 PM	69.9	30.1
(R)-1 + (R, R)-14	1328	0.245	1041	0	01, 21, 2020 5:39:04 PM	100	0
(R)-1 + (R, R)-14	1837	0.454	1142	0	01, 21, 2020 5:41:08 PM	100	0
Results of the 3 parallel measurements above: 1-1.8 µm particles formed with a good size distribution.							

These DLS observations support the hypothesis described in the above ^{1}H NMR experiments. That is, the observed highly enantioselective fluorescence enhancement could be attributed to the greater aggregation of the product formed from the chirality matched probe and substrate. The same tests were also done with another amino alcohol (*S*)- and (*R*)-**7** by using (*R*)-**1**, and the expected results were observed: the fluorescence enhanced probe and amino alcohol pair would give a lognormal distribution of the particle sizes of 800 nm while the clear solution of the counter pair cannot send good signal to the instrument (Table 3-3). These observed intermolecular aggregations are very similar to those previously reported from our lab for the reaction of the probe **1** with primary amino alcohols in FC-72. [5]

Table 3- 3. DLS data for (*R*)-**1** with (*R*)-**7** and (*S*)-**7**

[Sensor]=40 uM, [7]=2mM							
Sample Name	**Z-Ave**	**PdI**	**Pk 1 Mean Int**	**Pk 2 Mean Int**	**Time**	**Pk 1 Area Int**	**Pk 2 Area Int**
	d.nm		d.nm	d.nm		Percent	Percent
(R)-1 + (R)-7	3.82E+04	1	0	0	01, 21, 2020 11:04:53 AM	0	0
(R)-1 + (R)-7	8342	1	0	0	01, 21, 2020 11:07:17 AM	0	0
(R)-1 + (R)-7	4.77E+04	0.253	0	0	01, 21, 2020 11:09:41 AM	0	0
Results of the 3 parallel measurements above: very little particles formed with a bad size distribution.							
(R)-1 + (S)-7	740.3	0.31	642.8	0	01, 21, 2020 11:18:20 AM	100	0
(R)-1 + (S)-7	783.7	0.272	713.3	5560	01, 21, 2020 11:21:05 AM	98.9	1.1
(R)-1 + (S)-7	877.6	0.23	739.2	0	01, 21, 2020 11:23:50 AM	100	0
Results of the 3 parallel measurements above: 0.8 µm particles formed with very good size distribution.							

The IR spectra of (*R*)-**1** and the precipitate products from the reaction of (*R*)-**1** with (*R, R*)-**14** show that the two intense signals at 1660.5 cm^{-1} and 1623.3 cm^{-1} for the carbonyl groups of (*R*)-**1** disappeared upon reaction with (*R, R*)-**14**, indicating a nucleophilic addition of the amino alcohol to the carbonyl groups. Two weak signals appeared at 1617.7 cm^{-1} and 1587.8 cm^{-1} would represent the partial formation of the amide adducts in the solid state (Figure 3-13, for full spectra see Appendix for chapter 3).

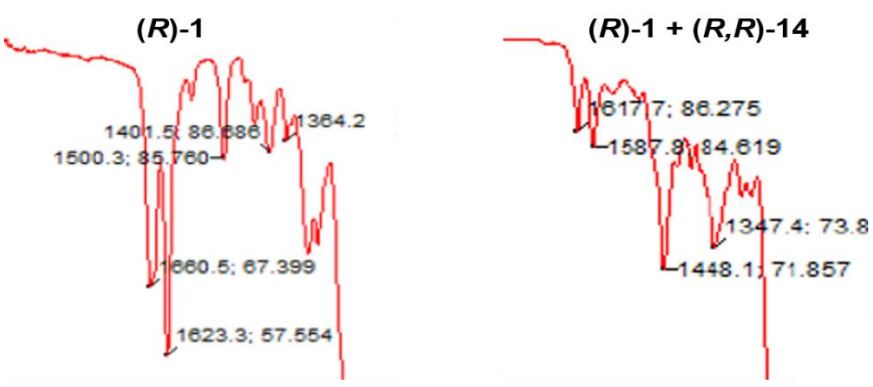

(a) (b)

Figure 3- 13. Partial IR spectra of (a) the solid powder of (*R*)-**1** as well as (b) the precipitate formed from the reaction of (*R*)-**1** and (*R, R*)-**14**.

3.2.5. Concentration determination by using UV-Vis spectroscopy

Although for rapid asymmetric reaction screening it's less important to determine the reaction yield by measuring the concentration of the product, the reaction yield would still be a necessary parameter if good conditions for high enantioselectivity were found. Thus, we developed an independent protocol by utilizing the UV-vis spectroscopy and probe **1** to determine the concentration of the product. The differences in fluorescence spectra were also reflected in the corresponding UV-vis spectra as shown in Figure 3-14. (*R*)-**1** alone shows three major absorption peaks at 258, 317 and 439 nm respectively. When (*R, R*)-**14** was added, all the peaks became broad or diminished, while two new peaks emerged at ~250 nm 350 nm and broad weak absorptions were observed from 300 nm to 500 nm. When (*S, S*)-**14** was added, the original peaks of (*R*)-**1** decreased, with no obvious appearance of new peaks though there's a trend in formation of new broad weak absorptions over 340 nm. This means that the fluorescence enhancement was mostly originated from the ground-state reactions between the probe and the amino alcohol. While there's only very limited ground-state reactions between the probe and the amino alcohol in the chiral mismatched cases [(*R*)-**1** with (*S, S*)-**14** and (*S*)-**1** with (*R, R*)-**14**] where the fluorescence enhancement was very small.

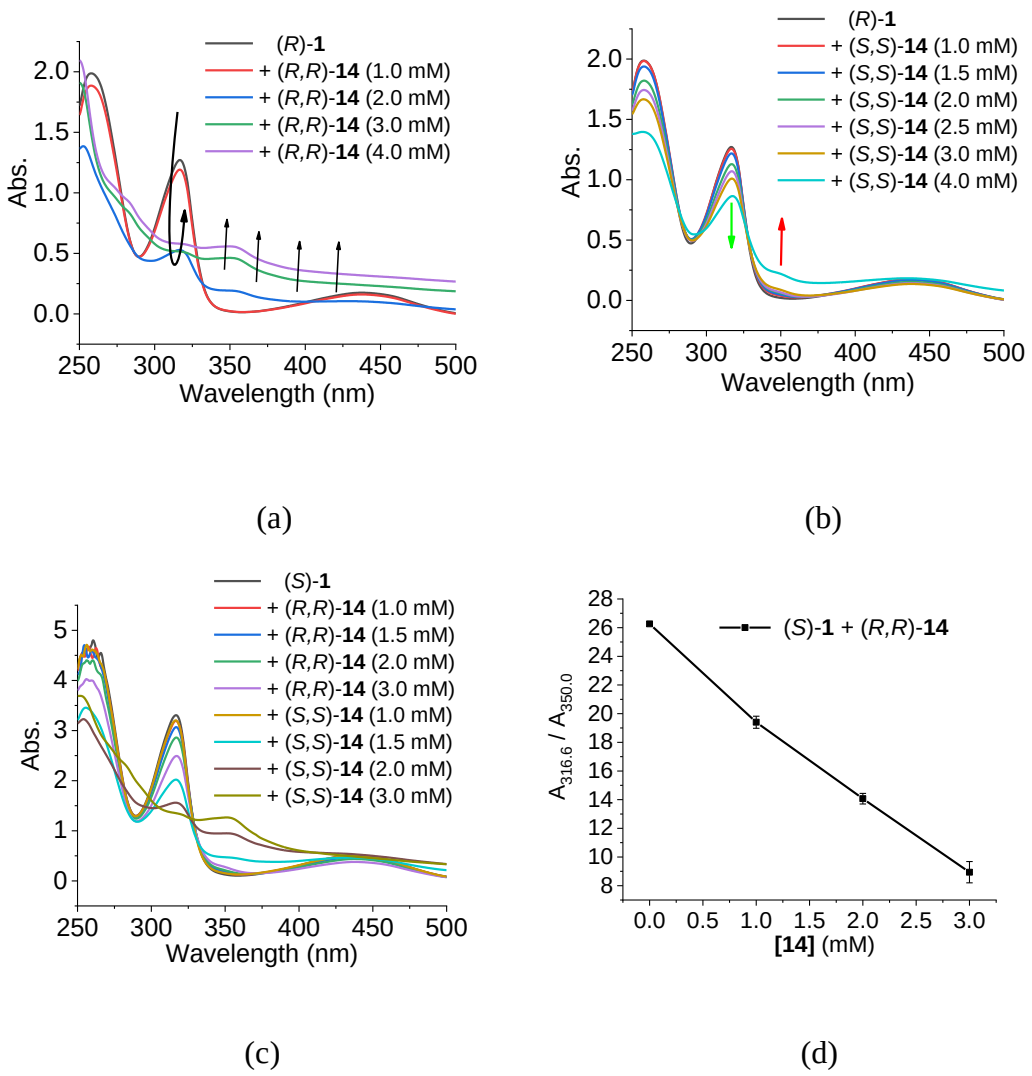

Figure 3- 14. UV-vis spectra of (*R*)- **1** (4×10^{-5} M) with (*R, R*)-**14** (0 – 4mM) (a) and with (*S, S*)-**14** (0 – 4mM) (b) and UV-vis spectra of (*S*)- **1** (6×10^{-5} M) with (*R, R*)-**14** and (*S, S*)-**14** (0 – 3mM) (c) and the plots of the ratio of $A_{316.6\ nm}$ and $A_{350\ nm}$ versus. [(*R, R*)-**14**] (d) (in FC-72/Et_2O (96/4, v) (reaction time: 2 hours).

As we discussed earlier when a pair of the enantiomeric probes was applied to test one enantiomer of **14**, at least the perfluoro solution of one probe would emit weak

fluorescence. We found all these fluorous sample solutions with weak emission at 428 nm were all clear solutions where no precipitate formed. Then we measured the UV-Vis spectra of the samples of (*S*)-**1** and (*R, R*)-**14** at various concentrations we found the ratio of $A_{316.6\ nm}$ and $A_{350\ nm}$ was linear related to the concentration of (*R, R*)-**14** (Figure 3-14d). Therefore, UV-vis could probably be applied to probe the concentration of **14** in the fluorous solution mixture by using only one enantiomer of the probe **1**.

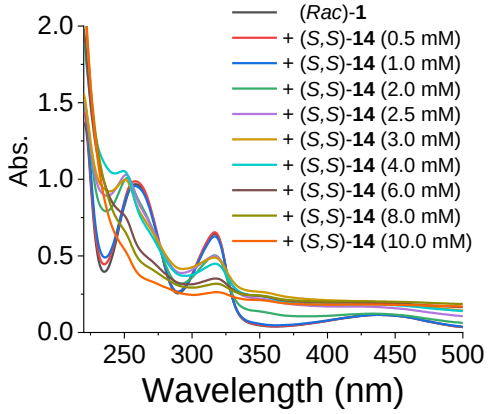

(a)

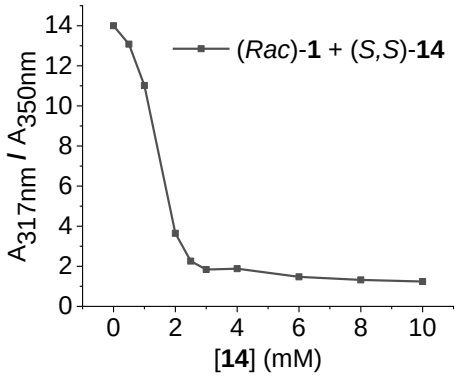

(b)

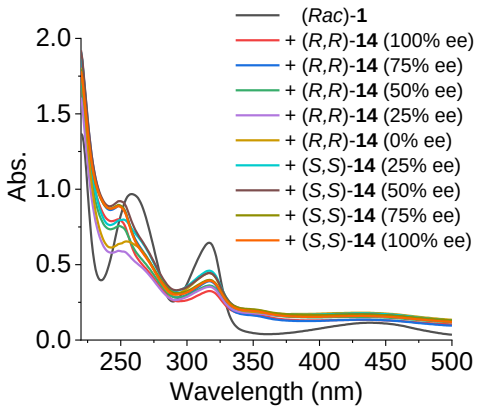

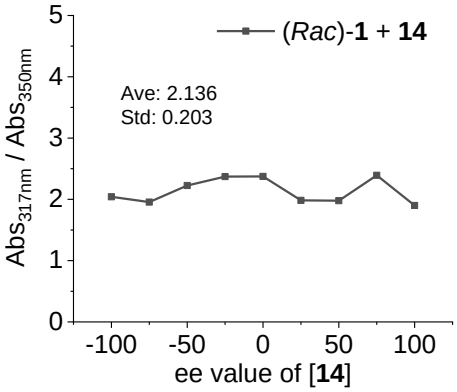

(c) (d)

Figure 3- 15. UV-vis spectra of (*Rac*)- **1** (2×10^{-5} M) with (*R, R*)-**14** (0-10 mM) (a) and the plots of the ratio of $A_{317\ nm}$ and $A_{350\ nm}$ versus. [(*S, S*)-**14**] (b) and UV-vis spectra of (*Rac*)- **1** (2×10^{-5} M) with **14** (4 mM) of various ee (c) and the plots of the ratio of $A_{317\ nm}$ and $A_{350\ nm}$ versus. ee of **14** (d). (in FC-72/Et_2O (96/4, v) (reaction time: 2 hours)

As we also mentioned in chapter 2, due to the strong non-linear effect between the fluorescence response of the probe (*R*)-**1** or (*S*)-**1** with the ee of the chiral substrate **14**, the racemic probe (*Rac*)-**1** could be used to accurately measure the enantiomeric composition of **14** regardless of the absolute configuration of **14**. We measured the UV-Vis spectra as shown in Figure 3-15. (*Rac*)-**1** alone also shows three major absorption peaks at 258, 317 and 438 nm respectively almost the same as those of (*R*)-**1** and (*S*)-**1**. When (*S, S*)-**14** was added, all the peaks became diminished, while only one new peak emerged at 250 nm and broad weak absorptions were observed from 300 nm to 500 nm (Figure 3-15a). When (*R, R*)-**14** was added, very similar peaks changes with the ones of (*S, S*)-**14** were also observed (Figure 3-15c). However, these absorption changes of (*Rac*)-**1** demonstrated moderate degree of reaction of the probe and amino alcohol **14**, which should be very reasonable due to the fact that only less than half of the probe **1** in the perfluoro solutions were undergoing the ground-state reactions.

We further found (*Rac*)-**1** would be able to probe the concentration range of substrate **14** as shown in Figure 3-15b. When the concentration of the amino alcohol in the fluorous phase went over 4 mM the ratio of $A_{317\ nm}$ and $A_{350\ nm}$ would drop below 2.

And when the concentration of **14** maintained at 4 mM regardless of the enantiomeric composition of **14**, the ratio of $A_{317\ nm}$ and $A_{350\ nm}$ stayed at an average number of 2.136 with a small variation less than 10%, which could be good enough to estimate the concentration of a crude product **14** from a reaction mixture. In this way it would be possible to confirm the yield range of the reaction screened by just using one racemic probe rapidly.

3.3. Conclusion

In conclusion, this study expanded the excellent chiral recognition ability of the BINOL-perfluoro-diketone sensors to a variety of chiral amino alcohols contain secondary amine groups in the fluorous phase ($ef = (I_S-I_0)/(I_R-I_0)$ value up to 66.0). The racemic probe **1** was also synthesized in a reformed protocol and it has been succeeded in reporting the ee and concentration of amino alcohols bearing secondary amine groups with fluorescent and UV-vis measurement. It's very possible we can develop a protocol of monitoring the reaction enantioselectivity and estimating the reaction yield with fluorescence and UV-vis spectroscopy in a combination fashion. In the future, the probe **1** could be applied in high-throughput screening facilities to monitor the reactions producing chiral secondary β-amino alcohols.

3.4. Experimental Section

3.4.1. General Data

Fluorous reagents were purchased from SynQuest Labs, Inc. All other chemicals were purchased from Sigma Aldrich Chemical Co., Alfa Aesar, TCI America and EnamineStore. The amino alcohols were recrystallized or distilled before use. Methylene

chloride, diethyl ether and THF were dried by passing them through activated alumina columns under nitrogen. Toluene and THF were further dried by Na and distillation. All organic solvents involved in the catalytical reactions were stored with activated 4 Å molecular sieves in well-sealed vials and used within one month. Other chemicals were used without further purification. Optical rotations were measured on a Jasco P-2000 digital polarimeter. NMR spectra were recorded on a Varian-600 MHz spectrometer, a Bruker-600 MHz spectrometer and a Bruker-800 MHz spectrometer. Chemical shifts for ^{1}H NMR spectra were reported in parts per million relative to a singlet at 7.26 ppm for deuterated chloroform. Chemical shifts for ^{13}C NMR were reported relative to the centerline of a triplet at 77.16 ppm for deuterated chloroform. The ^{19}F NMR spectra were reported in units of part per million (ppm) relative to trifluoroacetic acid (δ -76.55 ppm) as an external reference. Steady-state fluorescence spectra were recorded on Horiba FluoroMax-4 spectrofluorometer. High-resolution mass spectra were obtained by the University of Illinois at Urbana-Champaign (UIUC) Mass Spectrometry Facility. DLS were measured with a Malvern Zetasizer Nano ZS instrument at the Virginia Tech National Center for Earth and Environmental Nanotechnology Infrastructure (NanoEarth), samples in 3.5 mL Hellma® fluorescence quartz cuvettes with PTFE stoppers. UV-Vis spectra were produced from a Shimadzu UV-2600 UV-Vis spectrophotometer. HPLC analysis was conducted in a Shimadzu LC-20AD series HPLC coupled with a photodiode array detector (SPD-M20A) via a chiral column (Chiralpak AD, 25 cm × 4.6 mm, Daicel).

3.4.2. Synthesis and Characterization of Compounds

(*S*)-1,1'-(2,2'-dihydroxy-[1,1'-binaphthalene]-3,3'-diyl)bis(2,2,3,3,4,4,5,5,6,6,7,7,8,8,8 -pentadecafluorooctan-1-one), **(*S*)-1** and (*R*)-1,1'-(2,2'-dihydroxy-[1,1'-binaphthalene]-

3,3'-diyl)bis(2,2,3,3,4,4,5,5,6,6,7,7,8,8,8 - pentadecafluorooctan-1-one), **(*R*)-1** and (*Rac*)-1,1'-(2,2'-dihydroxy-[1,1'-binaphthalene]-3,3'-diyl)bis(2,2,3,3,4,4,5,5,6,6,7,7,8,8,8 - pentadecafluorooctan-1-one), **(*Rac*)-1,** (*1S,2S*)-2-(isopropylamino)cyclohexan-1-ol, **(*1S,2S*)-14,** (*1R,2R*)-2-(isopropylamino)cyclohexan-1-ol, **(*1R,2R*)-14**, were all synthesized and characterized in the chapter 2 of this thesis.

- **General Method 1 for synthesizing other optical pure secondary amino alcohols from optical pure primary amino alcohols**

Under nitrogen, the primary amino alcohol (10 mmol) was dissolved in ethyl formate (5 mL) , then the mixture was refluxed for 3 hours. After removal of the solvent and vacuum dried, product purity usually above 95% by H^1NMR, which could be applied in the following reaction. Otherwise the residue was distilled under reduced pressure to afford pure N-formyl product. Next, a solution of the N-formyl amino alcohol (10 mmol) in THF (4 mL) was added dropwise to a stirred suspension of $LiAlH_4$ (0.57 g, 15 mmol) in THF (16 mL) , and the mixture was stirred overnight at RT. Then a saturated Na_2SO_4 solution (2 mL) was added into the mixture for another 3 hours stirring at RT. The solid was filtered off, and the filtrate was concentrated and the solvent was also removed under vacuum. Finally, the residue was distilled or sublimated under reduced pressure to afford pure product as the corresponding secondary amino alcohol.

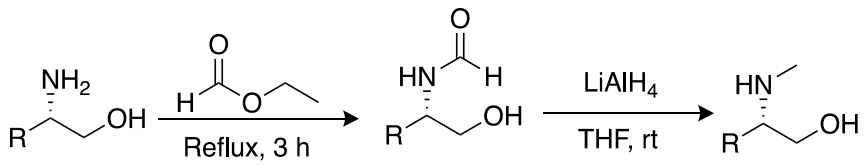

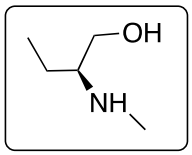

(*S*)-2-(methylamino)butan-1-ol, (*S*)-7

^{1}H NMR (600 MHz, Chloroform-*d*) δ 3.61 (dd, *J* = 10.8, 3.9 Hz, 1H), 3.31 (dd, *J* = 10.8, 6.5 Hz, 1H), 2.42 (tdd, *J* = 5.9, 4.4, 2.9 Hz, 1H), 2.39 (s, br, 2H), 2.37 – 2.32 (m, 2H), 1.49 (dqd, *J* = 15.1, 7.6, 5.7 Hz, 1H), 1.41 – 1.33 (m, 1H), 0.89 (t, *J* = 7.5 Hz, 3H). ^{13}C NMR (151 MHz, Chloroform-*d*) δ 62.35, 62.10, 33.46, 23.66, 10.46. HRMS Calcd for C5H14NO(MH+): 104.1075, found: 104.1074

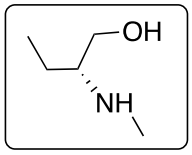

(*R*)-2-(methylamino)butan-1-ol, (*R*)-7

^{1}H NMR (600 MHz, Chloroform-*d*) δ 3.62 (dd, *J* = 10.7, 3.9 Hz, 1H), 3.31 (dd, *J* = 10.8, 6.5 Hz, 1H), 2.45 – 2.41 (m, 1H), 2.40 (s, 3H), 2.19 (s, br, 2H), 1.54 – 1.46 (m, 1H), 1.38 (dp, *J* = 13.8, 7.4 Hz, 1H), 0.90 (t, *J* = 7.5 Hz, 3H). ^{13}C NMR (151 MHz, Chloroform-*d*) δ 62.34, 62.06, 33.44, 23.73, 10.49. HRMS Calcd for C5H14NO(MH+): 104.1075, found: 104.1065

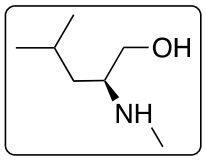

(*S*)-4-methyl-2-(methylamino)pentan-1-ol, (*S*)-N-methyl-leucinol, (*S*)-8

^{1}H NMR (600 MHz, Chloroform-*d*) δ 3.63 (ddd, *J* = 10.8, 3.9, 0.8 Hz, 1H), 3.28 (ddd, *J* = 10.8, 6.3, 0.8 Hz, 1H), 2.60 – 2.55 (m, 1H), 2.40 (s, 3H), 2.35 (s, br, 2H), 1.65 – 1.58

(m, 1H), 1.36 – 1.31 (m, 1H), 1.23 – 1.18 (m, 1H), 0.91 (d, *J* = 0.9 Hz, 3H), 0.90 (d, *J* = 0.9 Hz, 3H). ^{13}C NMR (151 MHz, Chloroform-*d*) δ 62.81, 58.54, 40.48, 33.28, 25.09, 23.19, 22.78. HRMS Calcd for C7H18NO(MH+): 132.1388, found: 132.1381

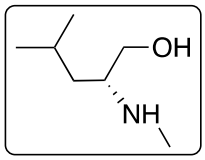

(*R*)-4-methyl-2-(methylamino)pentan-1-ol, (*R*)-N-methyl-leucinol, (*R*)-8

^{1}H NMR (600 MHz, Chloroform-*d*) δ 3.62 (dd, *J* = 10.8, 3.8 Hz, 1H), 3.27 (dd, *J* = 10.8, 6.3 Hz, 1H), 2.56 (dtd, *J* = 7.3, 6.3, 3.8 Hz, 1H), 2.39 (s, 3H), 2.34 (s, br, 2H), 1.61 (dh, *J* = 7.7, 6.6 Hz, 1H), 1.33 (ddd, *J* = 13.9, 7.7, 6.3 Hz, 1H), 1.21 – 1.16 (m, 1H), 0.90 (d, *J* = 2.3 Hz, 3H), 0.89 (d, *J* = 2.6 Hz, 3H). ^{13}C NMR (151 MHz, Chloroform-*d*) δ 62.86, 58.53, 40.54, 33.35, 25.08, 23.18, 22.79. HRMS Calcd for C7H18NO(MH+): 132.1388, found: 132.1381

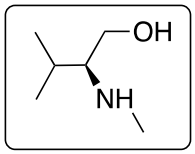

(S)-3-methyl-2-(methylamino)butan-1-ol, (S)-N-methyl-valinol, (S)-9

^{1}H NMR (600 MHz, Chloroform-*d*) δ 3.61 (ddd, *J* = 10.7, 4.3, 0.6 Hz, 1H), 3.33 (ddd, *J* = 10.6, 7.2, 0.6 Hz, 1H), 2.40 (d, *J* = 0.7 Hz, 3H), 2.26 (td, *J* = 6.8, 4.2 Hz, 1H), 2.15 (s, br, 2H), 1.80 (dp, *J* = 13.5, 6.8 Hz, 1H), 0.95 (dd, *J* = 6.9, 0.6 Hz, 3H), 0.88 (dd, *J* = 6.9, 0.6 Hz, 3H). ^{13}C NMR (151 MHz, Chloroform-*d*) δ 66.09, 60.27, 33.78, 28.43, 19.68, 18.53. HRMS Calcd for C6H16NO(MH+): 118.1232, found: 118.1226

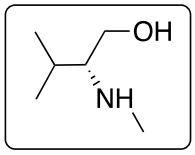

(*R*)-3-methyl-2-(methylamino)butan-1-ol, (*R*)-N-methyl-valinol, (*R*)-9

^{1}H NMR (600 MHz, Chloroform-*d*) δ 3.62 (dd, *J* = 10.6, 4.2 Hz, 1H), 3.33 (dd, *J* = 10.6, 7.2 Hz, 1H), 2.41 (s, 3H), 2.29 – 2.24 (m, 1H), 2.12 (s, br, 2H), 1.81 (dp, *J* = 13.6, 6.8 Hz, 1H), 0.95 (d, *J* = 6.9 Hz, 3H), 0.88 (d, *J* = 6.8 Hz, 3H). ^{13}C NMR (151 MHz, Chloroform-*d*) δ 66.08, 60.26, 33.77, 28.43, 19.69, 18.54. HRMS Calcd for C6H16NO(MH+): 118.1232, found: 118.1222

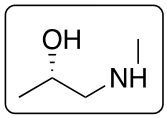

(S)-1-(methylamino)propan-2-ol, (S)-10

^{1}H NMR (600 MHz, Chloroform-*d*) δ 3.80 (dtd, *J* = 12.5, 6.2, 3.0 Hz, 1H), 3.07 – 3.01 (m, 2H), 2.58 (dd, *J* = 12.1, 3.1 Hz, 1H), 2.45 – 2.41 (m, 1H), 2.40 (d, *J* = 0.8 Hz, 3H), 1.12 (dd, *J* = 6.2, 0.9 Hz, 3H). ^{13}C NMR (151 MHz, Chloroform-*d*) δ 65.38, 59.10, 36.12, 20.83.

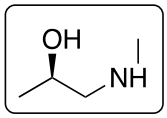

(R)-1-(methylamino)propan-2-ol, (R)-10

^{1}H NMR (600 MHz, Chloroform-*d*) δ 3.80 (dqd, *J* = 9.3, 6.2, 3.0 Hz, 1H), 2.62 (dd, *J* = 12.0, 3.1 Hz, 1H), 2.44 (s, 3H), 2.42 – 2.39 (m, 1H), 2.37 – 2.33 (m, 2H), 1.15 (d, *J* = 6.2 Hz, 3H). ^{13}C NMR (151 MHz, Chloroform-*d*) δ 65.35, 59.11, 36.26, 20.66. HRMS Calcd for C4H12NO(MH+): 90.0919, found: 90.0915

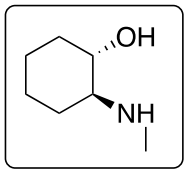

(1S,2S)-2-(methylamino)cyclohexan-1-ol, (1S,2S)-13

^{1}H NMR (600 MHz, Chloroform-*d*) δ 3.17 (ddd, *J* = 10.8, 9.0, 4.6 Hz, 1H), 2.42 (s, 3H), 2.14 – 2.05 (m, 2H), 2.01 (m, 1H), 1.75 – 1.67 (m, 2H), 1.32 – 1.14 (m, 3H), 0.95 – 0.85 (m, 1H). ^{13}C NMR (151 MHz, Chloroform-*d*) δ 73.67, 65.17, 33.78, 33.32, 29.71, 25.09, 24.57. $[\alpha]_D$ = 92.30 (c = 0.40, Et_2O) HRMS Calcd for C7H16NO(MH+): 130.1232, found: 130.1220

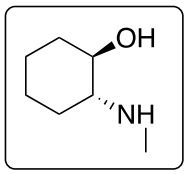

(1R,2R)-2-(methylamino)cyclohexan-1-ol, (1R,2R)-13

^{1}H NMR (600 MHz, Chloroform-*d*) δ 3.17 (dddd, *J* = 9.1, 6.1, 4.6, 2.6 Hz, 1H), 2.42 (d, *J* = 0.7 Hz, 3H), 2.14 – 2.06 (m, 2H), 2.04 – 1.97 (m, 1H), 1.72 (dt, *J* = 9.6, 2.5 Hz, 2H), 1.31 – 1.17 (m, 3H), 0.95 – 0.87 (m, 1H). ^{13}C NMR (151 MHz, Chloroform-*d*) δ 73.72, 65.19, 33.71, 33.31, 29.74, 25.14, 24.56. $[\alpha]_D$ = -80.10 (c = 0.40, Et_2O) HRMS Calcd for C7H16NO(MH+): 130.1232, found: 130.1226

The following enantio-pure secondary amino alcohols are commercially available:

D-Prolinol, D-**5**; L-Prolinol, L-**5**; D-2-Piperidinol, D-**6**; L-2-Piperidinol, L-**6**; (*1S,2S*)-2-(benzylamino)cyclohexan-1-ol, (*1S,2S*)-**12**

3.4.3. X-ray Crystal Analysis

A single crystal of (*S*)-**1** or (*R*)-**1**, or (*Rac*)-**1** was coated with Paratone oil and mounted on a MiTeGen MicroLoop. The X-ray intensity data were measured on a Bruker Kappa APEXII Duo system equipped with an Incoatec Microfocus IμS (Cu K_α, λ = 1.54178 Å) and a multi-layer mirror monochromator.

The frames were integrated with the Bruker SAINT software package[20] using a narrow-frame algorithm. Data were corrected for absorption effects using the Multi-Scan method (SADABS).[20] The structure was solved and refined using the Bruker SHELXTL Software Package [21] within APEX3 [20] and OLEX2, [23] using the space group P 2_1 or P -1, with Z = 2 for the formula unit, $C_{36}H_{12}F_{30}O_4$. Non-hydrogen atoms were refined anisotropically. The OH hydrogen atoms were placed in sensible hydrogen bonding positions and refined isotropically with restraints on the O-H distances. All other hydrogen atoms were placed in geometrically calculated positions with $U_{iso} = 1.2U_{equiv}$ of the parent atom ($U_{iso} = 1.5U_{equiv}$ for methyl). A global RIGU restraint was used on the anisotropic displacement parameters of the atoms due to the extremely low resolution and redundancy of the diffraction from this crystal. During the refinement, some severely disordered solvent was located in the crystal lattice that could not be adequately modeled with or without restraints. Thus, the structure factors were modified using the PLATON SQUEEZE [23] technique, in order to produce a "solvate-free" structure factor set. PLATON reported a total electron density of 94 e^- and total solvent accessible volume of 258 Å [22].

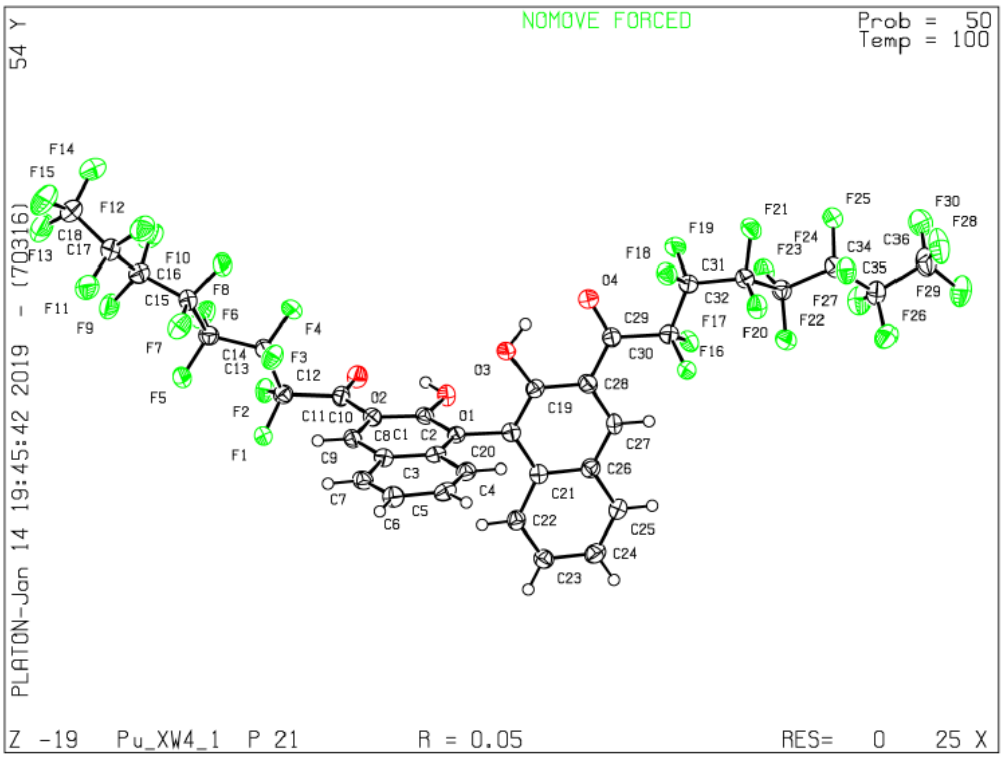

Figure 3- 16. ORTEP diagram of the molecule (*S*)-**1** [ellipsoid contour probability: 50 %] by x-ray analysis of the single crystals.

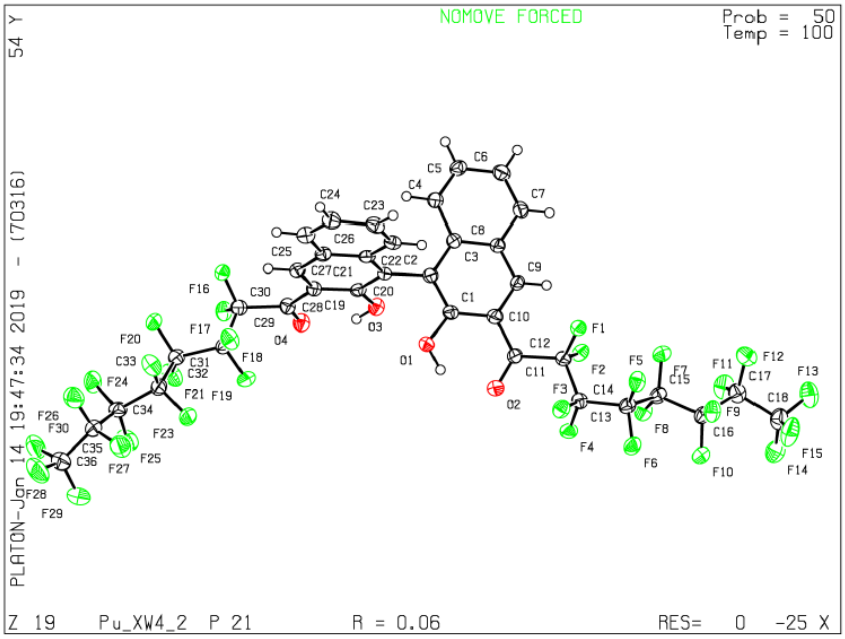

Figure 3- 17. ORTEP diagram of the molecule (*R*)-**1** [ellipsoid contour probability: 50 %] by x-ray analysis of the single crystals.

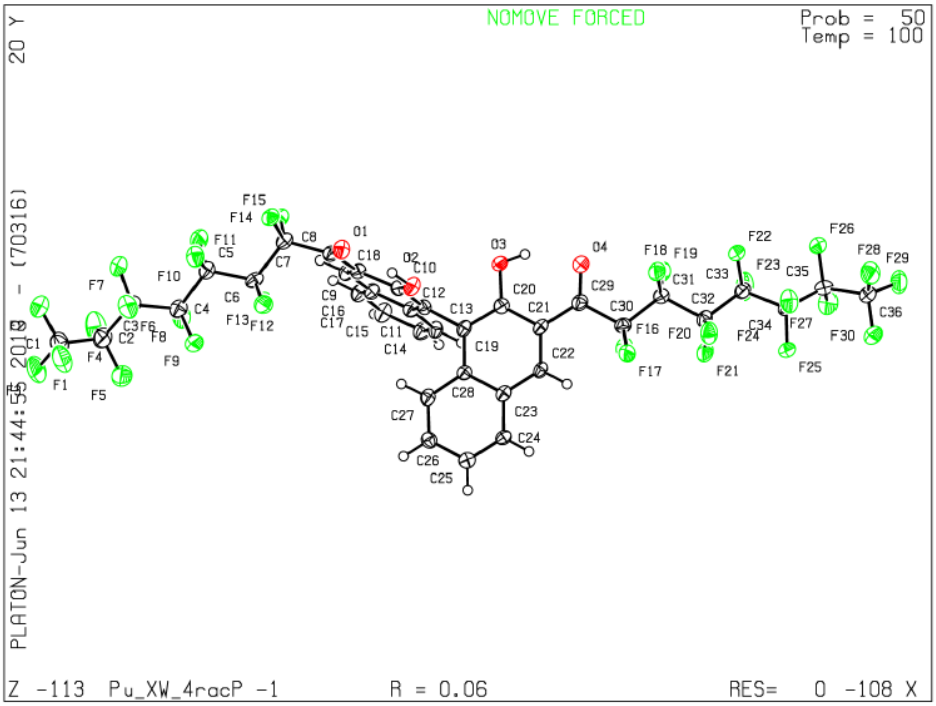

Figure 3- 18. ORTEP diagram of the molecule (*Rac*)-**1** [ellipsoid contour probability: 50 %] by x-ray analysis of the single crystals.

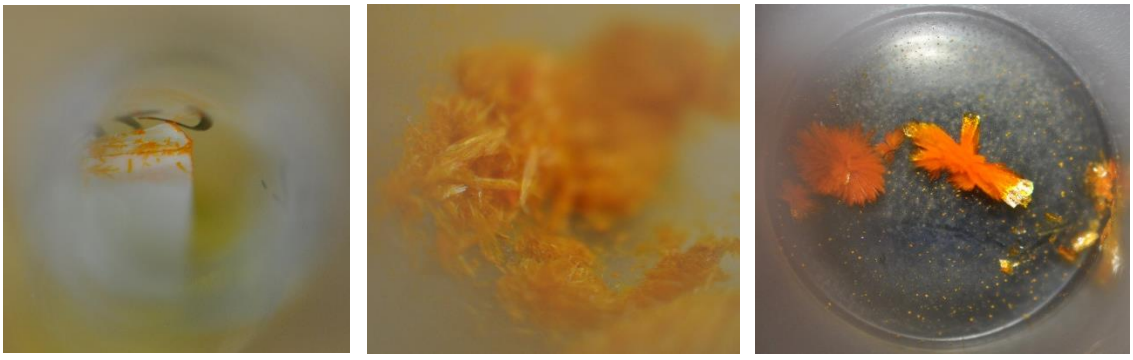

(a) (b) (c)

Figure 3- 19. Photo images of the solid crystals of (*S*)-**1** (a), (*R*)-**1** (b) and (*Rac*)-**1** (c).

Table 3- 4. Sample and crystal data summary for (*S*)-, (*R*)- and (*Rac*)-**1**.

	(*S*)-**1**	(*R*)-**1**	(*Rac*)-**1**
CDCC #			
Chemical formula	$C_{36}H_{12}F_{30}O_4$	$C_{36}H_{12}F_{30}O_4$	$C_{36}H_{12}F_{30}O_4$
FW (g/mol)	1078.46	1078.46	1078.46
T (K)	100(2)	100(2)	100(2)
λ (Å)	1.54178	1.54178	1.54178
Crystal size (mm)	0.084 x 0.090 x 0.215 mm	0.060 x 0.148 x 0.560 mm	0.086 x 0.171 x 0.465 mm
Crystal habit	orange block	orange plate	orange plate
Crystal system	monoclinic	monoclinic	triclinic
Space group	P 2_1	P 2_1	P -1
a (Å)	15.0562(6)	15.0326(7)	11.0172(11)
b (Å)	6.2943(3)	6.3026(3)	11.6711(11)
c (Å)	20.2591(9)	20.2772(10)	16.1008(15)
α (°)	90	90	80.852(3)
β (°)	96.271(3)	96.218(3)	82.349(3)
γ (°)	90	90	69.610(3)
Z	2	2	2
ρ_{calc} (g/cm$^{3)}$	1.877	1.875	1.876
μ (mm^{-1})	2.033	2.032	0.220 mm
θ range (°)	2.19 to 68.32	2.19 to 68.47	1.88 to 25.77
Index ranges	$-18 \le h \le 18$, $-7 \le k \le 7$, $-24 \le l \le 24$	$-18 \le h \le 17$, $-7 \le k \le 7$, $-24 \le l \le 24$	$-13 \le h \le 8$, $-14 \le k \le 13$, $-19 \le l \le 19$
Reflns coll.	25334	58594	29117
Ind. reflns	7009 [R(int) = 0.0702]	7020 [R(int) = 0.1044]	7288 [R(int) = 0.0768]
Data / restraints / parameters	7009 / 1 / 639	7020 / 1 / 640	7288 / 0 / 639
Goodness-of-fit on F^2	1.038	1.003	1.017
R_1 [I>2σ(I)]	0.0457	0.0567	0.0603
wR_2 [all data]	0.1179	0.1510	0.1901

3.5. References

1 Pu L., Fluorescence of Organic Molecules in Chiral Recognition. *Chem. Rev*. **2004**, 104, 1687–1716.

2 Leung D., Kang S. O., Anslyn E. V., Rapid Determination of Enantiomeric Excess: A Focus on Optical Approaches. *Chem. Soc. Rev.* **2012**, 41, 448–479.

3 (a) Accetta A., Corradini R., Marchelli R., Enantioselective Sensing by Luminescence.

Top. Curr. Chem. **2010**, 300, 175–216.

(b) Zhang X., Yin J., Yoon J., Recent Advances in Development of Chiral Fluorescent and Colorimetric Sensors. *Chem. Rev.* **2014**, 114, 4918-4959.

4 Herrera B. T., Pilicer S. L., Anslyn E. V., Joyce L. A., Wolf C. Optical Analysis of Reaction Yield and Enantiomeric Excess: A New Paradigm Ready for Prime Time. *J. Am. Chem. Soc.* **2018**, 140, 10385-10401.

5 Wang, C.; Wu, E.; Wu, X. D.; Xu, X. C.; Zhang, G. Q.; Pu, L. Enantioselective Fluorescent Recognition in the Fluorous Phase: Enhanced Reactivity and Expanded Chiral Recognition. *J. Am. Chem. Soc.* **2015**, *137*, 3747-3750.

6 Zhu Y.-Y., Wu X.-D., Abed M., Gu S.-X., Pu L. Biphasic Enantioselective Fluorescent Recognition of Amino Acids by a Fluorophilic Probe. *Chem: Eur. J.* **2019**, *25*, 7866 – 7873.

7 (a) Wang, C.; Wu, X. D.; Pu, L. A Highly Fluorinated Chiral Aldehyde for Enantioselective Fluorescent Recognition in a Biphasic System. *Chem. Eur. J.* **2017**, *23*, 10749-10752.

(b) Jiang L., Tian J., Zhao F., Yu S., Shi D., Wang X., Yu X., Pu L. Fluorescent Recognition of Functional Secondary Amines in the Fluorous Phase. *Eur. J. Org. Chem.* **2019**, 2533–2538.

8 Horváth, I. T.; Rábai, J. Facile Catalyst Separation Without Water: Fluorous Biphase Hydroformylation of Olefins. *Science* **1994**, 266, 72-75.

9 (a) Horváth, I. T. Fluorous Biphase Chemistry. *Acc. Chem. Res.* **1998**, *31*, 641–650.

(b) Handbook of Fluorous Chemistry; Gladysz, J. A., Curran, D. P., Horváth, I. T., Eds.; *Wiley-VCH: Weinheim, Germany*, 2004.

(c) O'Neal, K. L.; Zhang, H.; Yang, Y.; Hong, L.; Lu, D.; Weber, S. G. Fluorous Media for Extraction and Transport. *J. Chromatogr. A* **2010**, *1217*, 2287-2295.

10 Arai K., Lucarini S., Salter M. M., Ohta K., Yamashita Y., Kobayashi S., The Development of Scalemic Multidentate Niobium Complexes as Catalysts for the Highly Stereoselective Ring Opening of *meso*-Epoxides and *meso*-Aziridines. *J. Am. Chem. Soc*. **2007**, *129*, 8103.

11 Bao H., Zhou J., Wang Z., Guo Y., You T., Ding K., Insight into the Mechanism of the Asymmetric Ring-Opening Aminolysis of 4,4-Dimethyl-3,5,8-trioxabicyclo[5.1.0]octane Catalyzed by Titanium/ BINOLate/ Water System: Evidence for the Ti(BINOLate)$_2$-Bearing Active Catalyst Entities and the Role of Water. *J. Am. Chem. Soc*. **2008**, *130*, 10116. 50.

12 (a) Sharma A., Agarwal J., Peddinti R. K., Direct access to the optically active VAChT inhibitor vesamicol and its analogues via the asymmetric aminolysis of meso-epoxides with secondary aliphatic amines. *Org. Biomol. Chem*. **2017**, *15*, 1913.

(b) Sun Z., Chen J., Liu Y., Tu T., Chiral Titanium Coordination Assemblies: Robust Cooperative Self-Supported Catalysts for Asymmetric Ring Opening of meso-Epoxides with Aliphatic Amines. *Adv. Synth. Catal*. **2017**, *359*, 494.

13 Meninno S., Lattanzi A., Organocatalytic Asymmetric Reactions of Epoxides: Recent Progress *Chem. Eur. J*. **2016**, *22*, 3632.

14 Roy S., Bhanja P., Islam Sk. S., Bhaumik A., Islam Sk. M., A new chiral Fe(III)–salen grafted mesoporous catalyst for enantioselective asymmetric ring opening of racemic epoxides at room temperature under solvent-free conditions *Chem. Commun*. **2016**, *52*, 1871.

15 Bao, H.; Wu, J.; Li, H.; Wang, Z.; You, T.; Ding, K. Enantioselective Ring Opening Reaction of *meso*-Epoxides with Aromatic and Aliphatic Amines Catalyzed by Magnesium Complexes of BINOL Derivatives. *Eur. J. Org. Chem.* **2010**, 6722–6726.

16 Yuki Takeuchi, Tatsuhiro Asano, Kazuya Tsuzaki, and Koichi Wada. Catalytic Asymmetric Amination of meso-Epoxide Using Soy Polysaccharide (Soyafibe S-DN). *Bull. Chem. Soc. Jpn*. **2018**, *91*, 678–683.

17 A Japanese patent: P2017-104044A, page 36-38.

18 (a) Kruszynski R., Sieranski T., *Cryst. Growth Des.* **2016**, *16*, 587−595.

(b) Sinnokrot M.O., Valeev E. F., Sherrill C. D, , *J. Am. Chem. Soc*. **2002**, *124*, 36, 10887-10893.

19 Nian S., Pu L. Racemic Fluorescence Probe for Enantiomeric Excess Determination: Application of Cononsolvency of a Polymer in Sensing. *J. Org. Chem*. **2019**, *84*, 909−913.

20 Lu X., Xu Z., Tang G. Process Development on the Preparation of trans-(+)-2-Methylaminocyclohexanol: A Fascinating Resolution Example. *Org. Proc. Res. Dev.* **2001**, *5*, 184-185.

21 Bruker (2012). *Saint; SADABS; APEX3*. Bruker AXS Inc., Madison, Wisconsin, USA.

22 Sheldrick, G. M. (2015). *Acta Cryst*. A**71**, 3-8.

23 Dolomanov, O. V.; Bourhis, L. J.; Gildea, R. J.; Howard, J. A. K.; Puschmann, H. *J. Appl. Cryst.* (2009). **42**, 339-341.

24 Spek, A. L. *Acta Crystallogr. Sect C: Struct. Chem*. **2015**, C71, 9-18.

Chapter 4

Recent Advances in Chiral Analysis for Amino Acids

4.1. Introduction of Amino Acids

Amino acids known as the organic molecules contain amine ($-NH_2$), carboxyl (-COOH) functional groups, and a side chain (R group) that is unique for every amino acid. Over 500 naturally occurring amino acids are found and studied (while only 22 types of amino acids appear in the genetic code) to have very diverse biofunctions in the living organisms and they can be classified in a variety of ways according to different standards.[1] The carbon atom next to the carboxyl is the α carbon. The α amino acids are the most common form found in nature. All α amino acids but glycine (Gly) have the chiral α carbon and exist in either of two enantiomers, namely, L- or D- amino acid. There are 22 genetically encoded (proteinogenic) amino acids, of which 20 (often referred as common amino acids) are in the standard genetic code and an additional 2, selenocysteine and pyrrolysine, can be incorporated by special translation mechanisms. Proteinogenic amino acids are a small fraction of all amino acids while they are the most important part of the amino acids. And all my research has been focusing on the 20 common amino acids.[2, 3]

(Proteinogenic or natural) L-amino acids serve the building blocks of proteins. Besides the starring role as residues in proteins, amino acids participate in a number of

processes such as neurotransmitter transport and biosynthesis serving as precursors to compounds that play many critical roles in our body such as hormones, nucleotides, and neurotransmitters.[4]

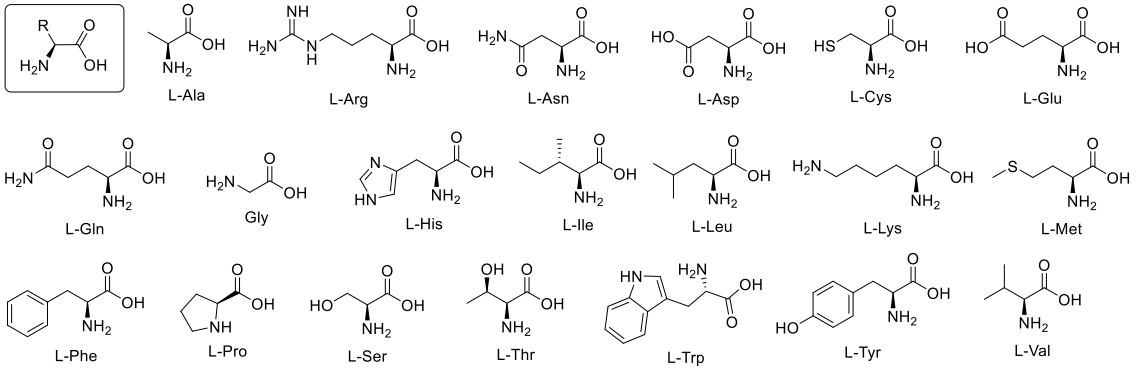

Figure 4- 1. The general structure of an α-L-amino acid and the 20 common L-amino acids.

Amino acids also serve as versatile synthetic precursors to diverse functional organic compounds including many pharmaceutical products,[5] food additives, nutritional supplements,[6] fertilizers,[7] livestock feed,[8] biodegradable plastics,[9, 10] and chirality sources for asymmetric synthesis and catalysis.[11] In an everyday chemistry example, glutamic acid is used as a flavor enhancer,[12] and L-aspartame (N-(L-α-Aspartyl)-L-phenylalanine,1-methyl ester) as a low-calorie artificial sweetener whereas D-aspartame is tasteless.[13, 14] A new, interdisciplinary research area has emerged known as bioorganometallic chemistry. α-Amino acid and peptide ligands have proven particularly versatile and provide access to compounds (organometallic fragments) that display interesting stereochemistry.[15]

Although in the living organisms, a high excess of the L-amino acids is observed, their antipodes, D-amino acids, had long been believed to have no biological functions especially in the higher animals. However, along with the progress of analytical technologies, especially by the advances of the highly sensitive and chiral separation methods, various D-amino acids are found in mammals including human beings.[16, 17] While D-Amino acids are rare in nature and L-amino acids represent all of the amino acids found in proteins during translation in the ribosome, more and more research have shown that D-amino acids not only displayed crucial biological functions but also could be associated with dysfunctions such as Alzheimer's disease and schizophrenia. The distribution and physiological functions of D-enantiomers have been gradually clarified mostly in the past two decades.[18, 19] D-amino acids are found in some proteins produced by enzyme posttranslational modifications after translation and translocation to the endoplasmic reticulum, as in exotic sea-dwelling organisms such as cone snails.[20] They are also abundant components of the peptidoglycan cell walls of bacteria,[21] while there are also compounds containing D-amino acids such as tyrocidine and valinomycin that are the chemicals disrupt bacterial cell walls, particularly in Gram-positive bacteria.[22] Gramicidin is a polypeptide made up from mixture of D- and L-amino acids.[23] A most studied and validated example is that D-serine acts as a neurotransmitter in the brain.[24] Moreover, a recent study by employing 2D-HPLC-fluorecence technique has successfully validated that D-glutamate was metabolized in the heart mitochondria and for the first time a significant amount of D-glutamate was detected in mammalian tissue. Further analysis of D-glutamate metabolism indicated that 9030617O03Rik was the protein identified as the enzyme responsible for mammalian D-glutamate metabolism.[25]

D-amino acids were also used in racemic crystallography to create centrosymmetric crystals, which allowed for easier and more robust protein structure determination.[26] In industry and pharmaceutical, the majority of applications of d-amino acids are related to antimicrobial activities because of a the large number of natural antibiotics containing d-amino acids isolated mainly from bacteria.[5]

The commercial production of amino acids usually relies on mutant bacteria that overproduce individual amino acids using glucose as a carbon source. Some amino acids are produced by enzymatic conversions of synthetic intermediates. 2-Aminothiazoline-4-carboxylic acid is an intermediate in one industrial synthesis of L-cysteine for example. Aspartic acid is produced by the addition of ammonia to fumarate using a lyase.[27] More detailed knowledge of the D-amino acids could be systematically learned in a recent review article by *Genchi*.[28] The high demand of the massive production of amino acids especially D-amino acids that are not actually naturally occurring makes a great need for the separation and determination of the enantiomers of amino acids after their chemical synthesis. A number of applicable chromatography techniques (GC, HPLC, CE, and SFC)[29, 30] have been developed to enantioselectively separate and analyze the enantiomers of amino acids in a very high proficiency over the decades. The boom of these enantioselective techniques could also somehow be modified and transferred to fit other chiral substrates such as amines, amino alcohols, and carboxylic acids.

4.2. Related Enantioselective Techniques for Amino Acids

Some of the D-amino acids are playing crucial roles in the regulation of neuronal and hormonal systems.[31] The relationships between these D-amino acids and various diseases are also being increasingly clarified.[32] However, the amounts of D-amino acids

in the mammals are trace in most cases, for instance, as of an analysis conducted in the year of 2011, only 837 D-amino acids (D-alanine, the most frequently occurring, was found to be 6-fold more frequent than the 2nd most, D-serine. See Table 4-1) were found in the Swiss-Prot database out of a total of 187 million amino acids.[33] and the precise determination of these D-enantiomers is difficult due to the presence of uncountable intrinsic molecules. Therefore, the development/utilization of highly sensitive and selective methods is critical for D-amino acid analysis and separations.

Table 4- 1. Statistics of experimentally validated D-isomers. Adapted with permission from ref 33. *Copyright © 2011, Springer Nature.*

PTM Type #	Experimental Sites
D-alanine	664
D-serine	114
D-methionine	19
D-phenylalanine	15
D-valine	8
D-tryptophan	7
D-leucine	6
D-asparagine	2
D-threonine	2
Total	837

4.2.1 Chromatography

- **HPLC**

In the area of chiral analysis and separation for amino acids, chromatographic techniques such as GC, HPLC, CE, and SFC are the applicable ones widely used in industry. Among them, multi-dimensional high-performance liquid chromatography (HPLC) is the most straightforward approaches. Two-dimensional (2D) and three-

dimensional (3D) HPLC methods used mainly for the separation of proteinogenic amino acids are demonstrated applications in various real-world matrices including clinical/biological/extraterrestrial samples.[29, 34]

In a very recent study by *Furusho et al.*, a selective 3D-HPLC system equipped with reversed-phase, anion-exchange, enantioselective columns and fluorescence detectors has been designed and developed for the determination of the D-enantiomers of asparagine, serine, alanine and proline that have been reported to significantly increase in the plasma of patients with chronic kidney disease (CKD).[29] The amino acids were precolumn derivatized with 4-fluoro-7-nitro-2,1,3-benzoxadiazole (NBD) to gain a high sensitivity by detecting their fluorescence. The system was validated by using human plasma in addition to the standard amino acids, and results with a sufficient linearity, precision, and accuracy were obtained (Figure 4-2). The amounts of these D-amino acids are low (around 1% of the L-form or lower), and their analyses were complicated by various interfering compounds in many clinical samples.[35] In this study, the 3D-HPLC system was applied to the plasma of patients with different stages of CKD and all of the target D-amino acids were clearly observed without interferences for all 25 tested patients. Good correlations were shown between the kidney function of the patients and the %D values of the target analytes, especially D-Asn and D-Ser, indicating that the present 3D-HPLC method is useful for the sensitive diagnosis of CKD.

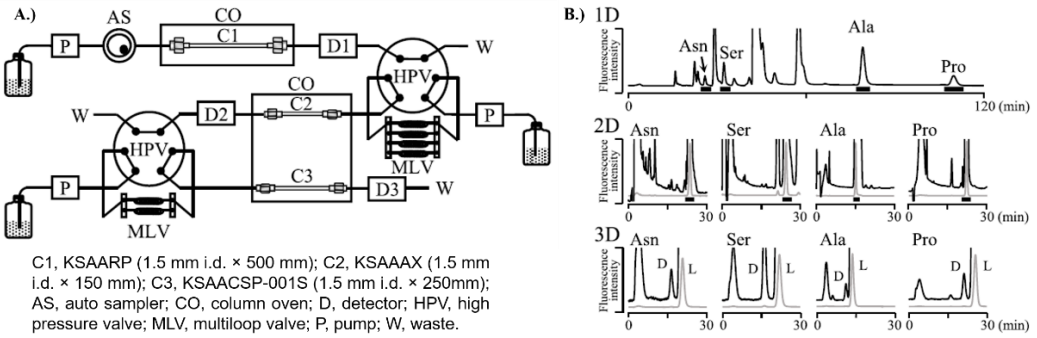

Figure 4- 2. A.) The flow diagram of the 3D-HPLC system for the determination of the amino acid enantiomers as their NBD derivatives. B.) 3D-HPLC separations of NBD-Asn, Ser, Ala, and Pro in the plasma of the patient with high eGFR. (In the second and third dimensions, solid lines represent 100× magnification of the gray lines, high eGFR patients contain low amount of d-amino acids) Adapted with permission from ref 29. *Copyright [2019] American Chemical Society.*

In another recent case of HPLC-MS technique, *Nakano et al*. developed a highly sensitive analytical method for the enantio-separation of chiral amino acids without any derivatization by liquid chromatography-tandem mass spectrometry (LC-MS/MS).[36] Via optimizing MS/MS parameters, a quantification method that allowed the simultaneous analysis of 18 D-amino acids with high sensitivity and reproducibility was established (Table 4-1). Practically, the protocol was also applied to food sample (vinegar) for the validation, and successfully quantified trace levels of D-amino acids in samples. However, besides expensive instrumentation, most of these chiral HPLC systems are not readily available for non-experts and not solvent and chemical saving choices due to the fact that in most cases precolumn purification was still demanded. Though recently some minimized instrumentation called nano liquid chromatography appeared to reduce the

mobile phase consumption while to increase the column efficiency in tended to overcome some drawbacks of the conventional HPLC.[37]

Table 4- 2. Evaluation results of the LC-MS/MS method. Reprinted with permission from ref 36. *Copyright © 2016, The Society for Biotechnology, Japan. All rights reserved.*

	Range (nmol/mL)	R^2 value	RSD (%)	LOD (nmol/mL)
D-Ala	0.5–100	0.9958	15.9	0.5
D-Arg	0.005–50	0.9994	4.7	0.005
D-Asn	0.01–50	0.9967	0.7	0.01
D-Asp	0.01–100	0.9869	18.2	0.01
D-Cys	0.01–100	0.9965	7.1	0.01
D-Gln	0.005–50	0.9996	10.3	0.005
D-Glu	0.005–50	1.0000	7.3	0.005
D-His	0.005–50	0.9995	9.0	0.005
D-Ile	0.01–50	0.9997	5.8	0.01
D-Leu	0.01–50	0.9993	11.5	0.01
D-Lys	0.01–100	0.9988	5.8	0.01
D-Met	0.005–100	0.9951	6.6	0.005
D-Phe	0.05–50	0.9993	18.7	0.05
D-Ser	0.05–100	0.9905	12.5	0.05
D-Thr	0.05–100	0.9940	11.7	0.05
D-Trp	0.005–50	0.9986	2.9	0.005
D-Tyr	0.005–50	0.9974	4.3	0.005
D-Val	0.01–50	0.9999	2.1	0.01

- **GC**

As early as in 1966, the first example of direct enantio-separation of a derivatized α-amino acid on a chiral stationary phase (CSP) comprising an involatile α-amino acid derivative by gas chromatography (GC) was reported. Over half a century, systematic derivatization strategies and multiple kinds of CSPs including 4 types of hydrogen-bonding CSPs and 3 types of cyclodextrin-derived CSPs for the GC enantio-separation of derivatized α-amino acids.[38] In terms of the derivatization strategy, it's usually required to increase volatility, speed of analysis and good peak shapes, as well as to provide suitable functions for detection, hyphenation and improved chirality recognition.

The derivatization strategy should also assist the simultaneous enantio-separation of α-amino acids without extensive peak overlapping. As for the CSPs of GC, being similar with other CSP based chromatography techniques, it is governed by the enthalpy term of the Gibbs–Helmholtz equation. The high resolution power of capillary GC enables the quantitative enantio-separation even for racemates with enantio-separation factors of less than $\alpha = 1.02$, corresponding to $\Delta_{l,d}(\Delta G)$ as small as -0.015 kcal/mol at 100 ^{o}C (See a state-of-the-art example of GC with the powerful enantioselective separation capability for derivatized α-amino acid as shown in Figure 4-3 [39]). While usually efforts to rationalize chirality recognition by molecular modeling studies are discouraged if $\alpha \leq 1.5$. Such a powerful technique has been widely used in the investigating of absolute configuration of α-amino acid enantiomers in peptides, biological fluids, extraterrestrial material, sediments and soil. Another significant application of enantioselective GC must be the determination of enantiomeric excesses (ee) in asymmetric synthesis and asymmetric catalysis like an early example for chiral rhodium(I)-complex-catalyzed homogeneous hydrogenation of the corresponding dehydro-α-amino acids to optically active *N*-acetyl-alanine and *N*-acetyl-phenylalanine.[40] Even though GC demonstrated even much more powerful resolution capability under certain conditions it's still not even as accessible as HPLC no matter in terms of the price of the instrumentation and maintenance or the time and chemicals consumed in the process of derivatizations.

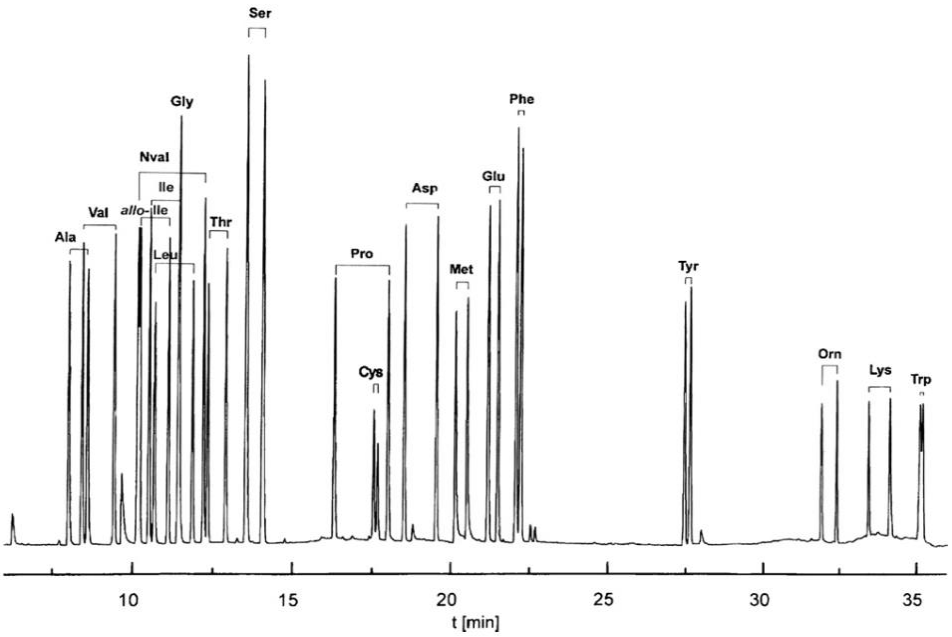

Figure 4- 3. Enantio-separation of *N*-TFA α-amino acid *O*-ethyl esters by HRC-GC. Reprinted with permission from ref 38 and 39. *Copyright © 2011 Elsevier B.V. All rights reserved.*

- **Novel Material Based Chiral Separation**

Hou et al. have developed a class of artificial chiral selective transmembrane amino acid channels from peptide-appended pillar[n]arenes (n=5, 6). The whole molecules are induced to form a tubular architecture by the intramolecular hydrogen bonding of the peptide chains.[41] This unique shape enables efficient transport of amino acids across membranes in a single molecule manner. In several cases, chiral selectivity was realized, which is one of the key functions of natural amino acid channels.

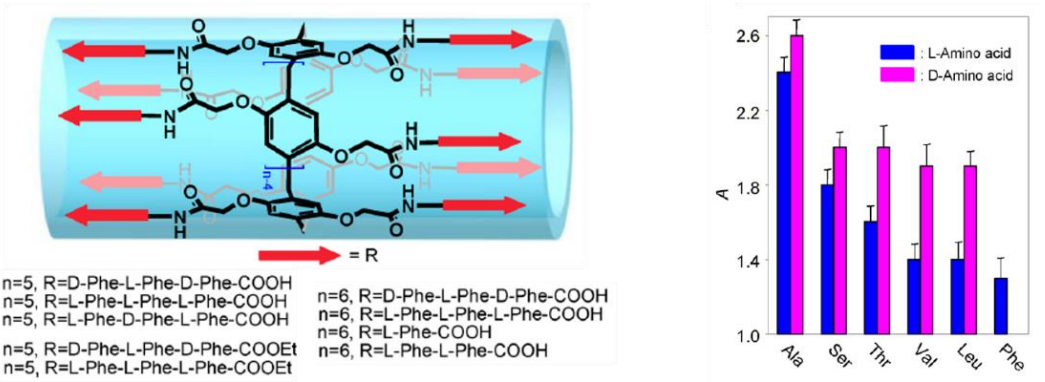

Figure 4- 4. Structures and transport activities of the membrane (n=6, R=L-Phe-L-Phe-L-Phe-COOH) for L- and D-amino acids. Adapted with permission from ref 41. *Copyright [2013] American Chemical Society.*

Similarly, in order to mimic cellular transport mechanisms, *Cui et al*. has made some solid-state smart nanochannels by using COFs to overcome the critical synthetic challenge.[42] As very porous crystalline materials with tailor-made nanochannels COFs inherently hold great potential for ion and molecule transport. By imine condensations of a trialdehyde and a mixture of diamines with and without divinyl groups, two vinylfunctionalized 2D COFs were hydrothermally crystallized. The one-dimensional mesoporous channels were formed by either AA or AB stacking of layered hexagonal networks confirmed by PXRD experiments and calculations. After further modification with chiral *β*-cyclodextrin (*β*-CD) by thiol−ene click reactions, the COFs were lastly fabricated into mixed matrix membranes (MMMs) that can selectively transport amino acids (Scheme 4-1). To evaluate the change, the current change ratio ($R= (I-I_0)/I_0$, where I_0 and I are the current measured at -1 V before and after treating with His) was calculated. The separation factors R_L-His (0.34) and R_D-His (0.01) are 34.0 for the CD-COF-**1** MMM and 1.7 for the CD-COF-**2** MMM (R_L-His =0.31 and R_D-His =0.18). The bar graph in

Scheme 4-1 illustrates the ionic current change ratios before and after *β*-CD modification of the COF channels in the presence of L- or D-His. The chiral selectivity of the CD-COF could be given by an electronic signal as long as the ionic went through the COF MMM. And the CD-COF-**1** MMM displayed higher chiral selectivity to L-His though a drawback of this work was it couldn't validate the enantioselectivity by tuning the COFs with the enantiomer of *β*-CD.

Scheme 4- 1. Synthesis and operation principle of the chiral CD-COF-MMM System with high enantioselectivity to amino acids. Adapted with permission from ref 42. *Copyright [2019] American Chemical Society.*

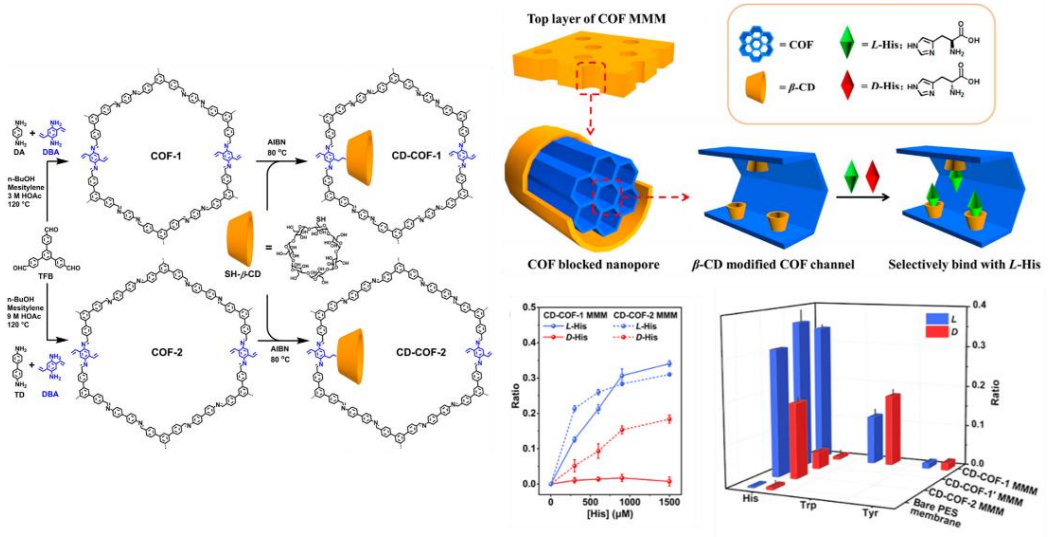

4.2.2 Chiral Probes and Analysis

Excepting some examples of the enantioselective probes and analysis methods for amino acids mentioned previously in the first chapter and the enantioselective chromatography techniques discussed above, several important recent progress should also be included and discussed to give a better understanding of this area of chiral

recognition of amino acids.[43, 44, 45, 46, 47] Particularly, it's noteworthy to repeat and to advertise a couple of chiral selective fluorescence protocols that are one step away from the real enantioselective high throughput screening (HTS) via determination of both ee and concentration (yield) of sample products in asymmetric synthesis and asymmetric catalysis. [48, 49]

Lately, *Zhu et al*. have then introduced a perfluoroalkyl chain to the bisBINOL-based aldehyde to make the fluorinated probe (*R, R*)-**3**.[49] This compound was soluble in a fluorous solvent 1H,1H,2H,2H-perfluoro-1-octanol (PFOH). When a solution of (*R, R*)-**3** (4.0×10^{-5} M, 2.0 mL) in PFOH was mixed with an aqueous solution (2.0 mL) of amino acids and Zn (1 equiv) in the presence of TBAOH, measuring the fluorescence of the fluorous phase in the biphasic system showed good enantioselective enhancement. The observed *ef*'s $[(I_D-I_0)/(I_L-I_0)]$ were distinctively high with a number of 14 for phenylalanine, 45.2 for histidine.

Because the fluorous solvent allows the amino acids to be separated from the original aqueous phase for fluorescence measurement, this biphasic fluorescent sensing was very reliable and applicable to analyze the enantiomeric composition of the crude amino acid products generated from an enzyme-catalyzed asymmetric hydrolysis of a racemic amino acid ester.

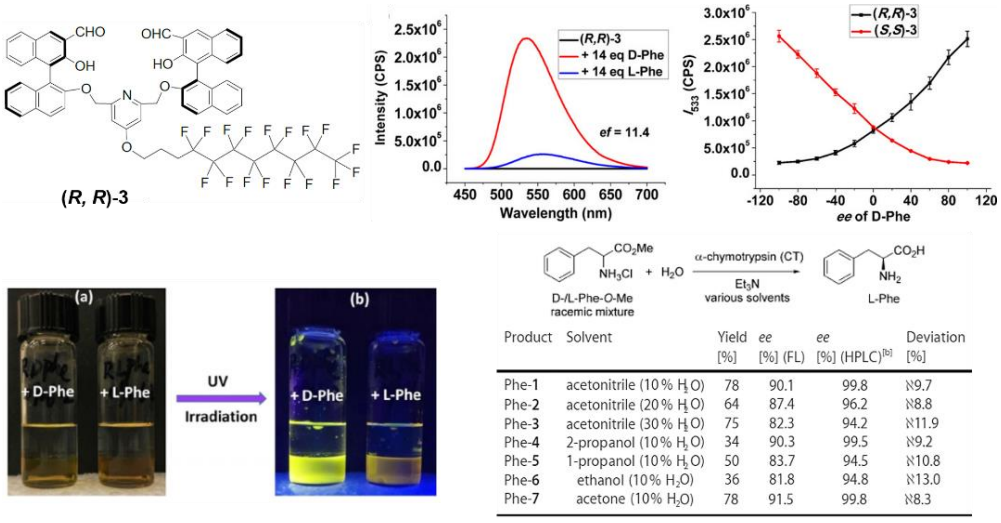

Product	Solvent	Yield [%]	*ee* [%] (FL)	*ee* [%] (HPLC)[b]	Deviation [%]
Phe-1	acetonitrile (10% H_2O)	78	90.1	99.8	ℵ9.7
Phe-2	acetonitrile (20% H_2O)	64	87.4	96.2	ℵ8.8
Phe-3	acetonitrile (30% H_2O)	75	82.3	94.2	ℵ11.9
Phe-4	2-propanol (10% H_2O)	34	90.3	99.5	ℵ9.2
Phe-5	1-propanol (10% H_2O)	50	83.7	94.5	ℵ10.8
Phe-6	ethanol (10% H_2O)	36	81.8	94.8	ℵ13.0
Phe-7	acetone (10% H_2O)	78	91.5	99.8	ℵ8.3

Figure 4- 5. The biphasic enantioselective fluorescent recognition of amino acids by a fluorophilic probe **3** and its application in analyzing ee of the crude amino acid products via an enzyme-catalyzed asymmetric hydrolysis. Adapted with permission from ref 49. *Copyright © 2019 Wiley-VCH Verlag GmbH & Co. KGaA, Weinheim.*

This work has accelerated the investigation of the usage of the fluorinated probes in rapid fluorescent screening of reactions that producing chiral substrates. Chiral recognition in the fluorous phase offers the advantage of minimizing the interference of other species in a screening protocol, potentially giving rise to the rapid screening of crude reaction mixtures. Overall, it minimizes the workup needed prior to optical determination of ee values, and is a major advance in conducting optical ee assays.

4.3. Enantioselective Probes for Amino Acids with Bio-imaging Potential and Ability

The *Pu* group has been long aimed at developing fluorescent sensors that could visualizing and mapping the bioactive chiral molecules by noninvasive real time imaging.

Among all the imaging techniques, fluorescence could be one of the best candidates owing to its easily available instruments, high sensitivity, diverse sensing signals, as well as intensive researches in enantioselective recognition. Recently, *Zeng et al*. synthesized a pair of enantioselective sensors, the SPINOL-based chiral aldehydes (*R*)-**3** and (*S*)-**3**, which have been found together with Zn^{2+} highly enantioselective for structurally diverse chiral amino acids by fluorescent difference.[50] When this enantiomeric sensor pair was incubated in *HeLa* cells containing a free amino acid it shows consistent fluorescence difference as it was observed in the solution conditions outside of the cells. This might allow a quick determination of the chiral configuration of the free amino acid in the cells. For the first time, enantioselective imaging of free amino acids in living cells has been made by this fluorescent sensor pair. One drawback of this method might lay on the solubility of **4** as it's not water soluble and to better gather the probe and the amino acids additional Bu_4NOH was needed in both solution and cellular imaging study, which is unfavored in other living cell imaging study.

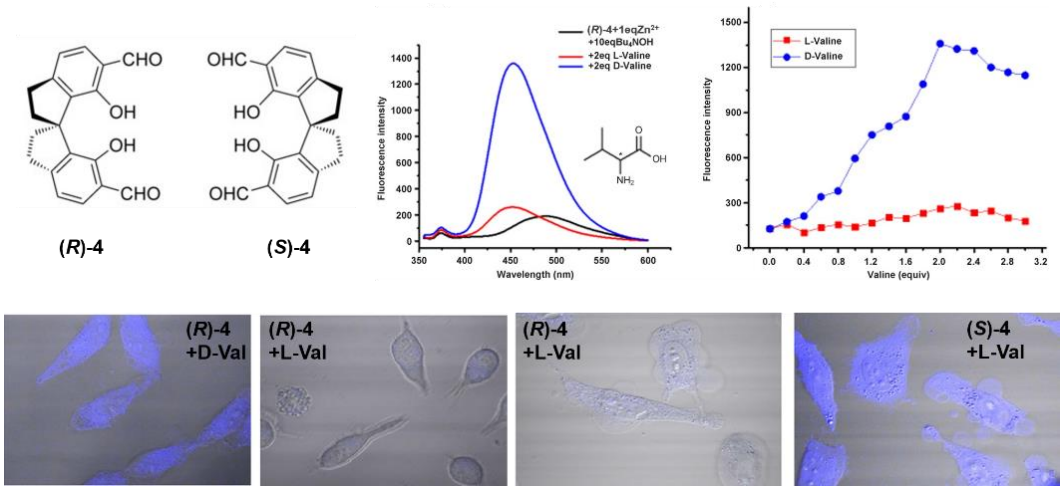

Figure 4- 6. The SPINOL-based chiral aldehydes probe **4** and its application in enantioselective fluorescent imaging of free amino acids in living cells. Adapted with

permission from ref 50. *Copyright © 2017 Wiley-VCH Verlag GmbH & Co. KGaA, Weinheim.*

To achieve a better hydrophilicity of the probes, several works have been accomplished and reported recently. Chemical synthetic strategies including introduction of hydrophilic oligo-ethylene-glycol[51] or sulfonate functional groups[52] and amphiphilic poly(isopropylacrylamide) [poly(NIPAM)] chains[46]. Moreover, a di-block copolymer-based micelle encapsulation protocol[53] was lately reported emerging as another direction of realizing chemoselective as well as enantioselective fluorescent imaging in vivo. However, no more report in the enantioselective of chiral molecules in living cells as well as tissues has been seen so far.

4.4. Conclusion

Besides conventional enantioselective techniques that are still developing rapidly and becoming more and more powerful. New materials are joining the field of enantioselective sensing for amino acids. Most importantly, several fluorescent probes have also demonstrated great potentials for practical applications due to their high enantioselectivity and sensitivity in either organic media or aqueous solution with various amino acids. However, there would be still obviously problematic and challenging if these probes were directly applied to high throughput chiral assay or biological imaging. For example, the starting materials, reagents, metal catalysts, various additives and side products in an asymmetric production of chiral amino acids would interfere the reactions between the fluorescent probe and amino acid products without separation. In the field

of fluorescent real time imaging of amino acids in life, progress is advancing by further modification of the currently developed enantioselective fluorescent probes. However, there would be still a long way in increasing the compatibility (linking bio-compatible functional groups to the probes) and reducing the toxicity (extending the excitation and emission wavelengths to red or near infrared region) of the probes to cells and animals without diminishing the enantioselectivity and sensitivity. The rest of this thesis will transmit the subject to develop enantioselective fluorescent probes for amino acids with potential capability in both high throughput screening as well as real time bioimaging in vivo.

4.5. References

1 Wagner I, Musso H, *Angew. Chem. Int. Ed.,* **1983**, *22* (11), 816–828.

2 Wang Q, Parrish AR, Wang L, *Chemistry & Biology*, **2009**, *16* (3), 323–336.

3 Hertweck C, *Angew. Chem. Int. Ed.*, **2011**, *50* (41): 9540–9541.

4 *The Structures of Life*. National Institute of General Medical Sciences. Reprinted July **2007**.

5 Martínez-Rodríguez S, Martínez-Gómez AI, Rodríguez-Vico F, Clemente-Jiménez JM, Las Heras-Vázquez FJ, *Chem Biodivers*. **2010**, *7*(6),1531-1548.

6 Ashmead HD, The Role of Amino Acid Chelates in Animal Nutrition. *Westwood: Noyes Publications*, **1993**.

7 Ashmead HD, Foliar Feeding of Plants with Amino Acid Chelates. *Park Ridge: Noyes Publications*, **1986**.

8 Leuchtenberger W, Huthmacher K, Drauz K, *Applied Microbiology and Biotechnology* **2005**, *69* (1), 1–8.

9 Sanda F, Endo T, *Macromolecular Chemistry and Physics*, **1999**, *200* (12), 2651–2661.

10 Gross RA, Kalra B, *Science*, **2002**, *297* (5582), 803–807.

11 Shi BF, Maugel N, Zhang YH, Yu JQ, *Angew. Chem. Int. Ed*. **2008**, *47*, 4882 – 4886.

12 Garattini S, *The Journal of Nutrition.* **1999**, *130* (4S Suppl): 901S–909S.

13 Stegink LD, *The American Journal of Clinical Nutrition*, **1987**, 46 (1 Suppl): 204–215.

14 Joseph Gal, *Chirality*, **2012**, *24* (12), 959–976.

15 Severin, K.; Bergs, R.; Beck, W., *Angew. Chem. Int. Ed*. **1998**, *37* (12), 1635–1654.

16 Maeda, H.; Takata, T.; Fujii, N.; Sakaue, H.; Nirasawa, S.; Takahashi, S.; Sasaki, H.; Fujii, N. *Anal. Chem*. **2015**, *87*, 561−568.

17 Woiwode, U.; Reischl, R. J.; Buckenmaier, S.; Lindner, W.; Lämmerhofer, M. *Anal. Chem*. **2018**, *90*, 7963−7971.

18 Henneberger, C.; Papouin, T.; Oliet, S. H. R.; Rusakov, D. A. *Nature*, **2010**, *463*, 232−236.

19 Miyoshi, Y.; Koga, R.; Oyama, T.; Han, H.; Ueno, K.; Masuyama, K.; Itoh, Y.; Hamase, K. *J. Pharm. Biomed. Anal*. **2012**, *69*, 42−49.

20 Pisarewicz K, Mora D, Pflueger FC, Fields GB, Marí F, *Journal of the American Chemical Society*, **2005**, *127* (17), 6207–15.

21 Van Heijenoort J, *Glycobiology*, **2001**, *11* (3), 25R–36R.

22 Michal G, Schomburg D, eds. Biochemical Pathways: An Atlas of Biochemistry and Molecular Biology (2nd ed.), *Oxford: Wiley-Blackwell*, **2012**.

23 Ketchem RR, Hu W, Cross TA, *Science*, **1993**, *261* (5127), 1457–1460.

24 Wolosker H, Dumin E, Balan L, Foltyn VN, *The FEBS Journal*. **2008**, *275* (14), 3514–3526.

25 Ariyoshi, M., Katane, M., Hamase, K. et al., *Sci Rep*., **2017**, *7*, 43911.

26 Matthews BW, *Protein Science*, **2009**, *18* (6), 1135–1138.

27 Drauz K, Grayson I, Kleemann A, Krimmer H, Leuchtenberger W, Weckbecker C, *Ullmann's Encyclopedia of Industrial Chemistry*. **2006**.

28 Genchi G., An overview on d-amino acids, *Amino Acids*, **2017**, *49*, 1521–1533.

29 Furusho A, Koga R, Akita T, Mita M, Kimura T, Hamase K, *Anal. Chem*. **2019**, *91*, 11569−11575.

30 Liu Y., Berthod A., Mitchell C.R., Xiao T.L., Zhang B., Armstrong D.W., *J. Chromatogr., A* **2002**, *978*, 185.

31 Katane, M.; Homma, H. *J. Chromatogr. B* **2011**, *879*, 3108-3121.

32 Labrie V, Wong AHC, Roder JC, *Neuropharmacology*, **2012**, *62*, 1484–1503.

33 Khoury GA, Baliban RC, Floudas CA, *Scientific Reports*, **2011**, *1* (90), 1-5.

34 Ishii C, Furusho A, Hsien CL, Hamase K, *Chromatography*, **2020**, 10.15583/jpchrom.2020.004.

35 Kimura, T.; Hamase, K.; Miyoshi, Y.; Yamamoto, R.; Yasuda, K.; Mita, M.; Rakugi, H.; Hayashi, T.; Isaka, Y. *Sci. Rep*. **2016**, *6*, 26137.

36 Nakano Y, Konya Y, Taniguchi M, Fukusaki E, *Journal of Bioscience and Bioengineering*, **2017**, *123* (1), 134-138.

37 D'Orazio G., *Trends in Analytical Chemistry*, **2020**, *125*, 115832.

38 V. Schurig, *J. Chromatogr. B*, **2011**, *879*, 3122-3140.

39 Schurig, V., Juza, M., Preschel, M., Nicholson, G.J., Bayer, E., *Enantiomer*, **1999**, *4*, 297-303.

40 Schurig V. In: J.D. Morrison (Ed.), Asymmetric Synthesis, Analytical Methods, Vol. 1, *Academic Press, London*, **1983**, p. 59 (Chapter 5).

41 Chen L, Si W, Zhang L, Tang G, Li ZT, Hou JL, *J. Am. Chem. Soc*. **2013**, *135*, 2152−2155.

42 Yuan C, Wu X, Gao R, Han X, Liu Y, Long Y, Cui Y, *J. Am. Chem. Soc*. **2019**, *141*, 20187−20197.

43 Corradini, R.; Paganuzzi, C.; Marchelli, R.; Pagliari, S.; Sforza, S.; Dossena, A.; Galavernaa, G.; Duchateau, A. *J. Mater. Chem*. **2005**, *15*, 2741–2746.

44 Leung D, Anslyn EV., *J. Am. Chem. Soc*. **2008**, *130*, 37, 12328-12333.

45 Song, L.; Wang, S.; Kotov, N. A.; Xia, Y. *Anal. Chem*. **2012**, *84*, 7330−7335.

46 Nian, S.; Pu, L. *Chem. Eur. J*. **2017**, *23*, 18066-18073.

47 Iqbal, S.; Yu, S.; Jiang, L.; Wang, X.; Chen, Y.; Wang, Y.; Yu, X.; Pu, L. *Chem. Eur. J*. **2019**, *25*, 9967 – 9972.

48 Wen, K.; Yu, S.; Huang, Z.; Chen, L.; Xiao, M.; Yu, X.; Pu, L. *J. Am. Chem. Soc*. **2015**, *137*, 4517−4524.

49 Zhu, Y.-Y.; Wu, X.-D.; Abed, M.; Gu, S.-X.; Pu, L. *Chem: Eur. J*. **2019**, *25*, 7866 – 7873.

50 Zeng C, Zhang X, Pu L, C*hemistry–A European Journal*, **2017**, *23* (10), 2432-2438.

51 Zhao, F.; Du, Y.; Tian, J.; Shi, D.; Wang, Y.; Hu, L.; Yu, S.; Yu, X.; Pu, L. *Eur. J. Org. Chem.* **2018**, 1891–1895.

52 Zhao F, Wang Y, Wu X, Yu S, Yu X, Pu L, *Chem. Eur. J*. **2020**, *26, just accepted*, *https://doi.org/10.1002/chem.202000423.*

53 Du, G.; Pu, L. *Org. Lett.* **2019**, *21*, 4777-4781.

Chapter 5

A BINOL-Coumarin-Based Probe for Enantioselective Fluorescent Recognition of Amino Acids in Aqueous Phase

5.1 Introduction

In recent years, enantioselective fluorescent recognition of chiral amino acids by using molecular probes has been actively investigated.[1-3] These probes are potentially useful for rapid and on-line analysis of the enantiomeric composition of amino acids generated from either asymmetric reactions or biological processes. Unlike the analysis of an achiral substrate with a fluorescent probe which often aims at obtaining only one parameter, that is, the quantity (concentration) of the substrate, analysis of a chiral amino acid requires the determination of two parameters including the concentration and enantiomeric composition. This presents a significant challenge if only one fluorescent probe is used without separating the amino acid enantiomers since both concentration and enantiomeric composition can influence the fluorescence response, and one often needs to have two independent methods in order to determine the two parameters. Previously, we reported that one fluorescent probe can be used to determine both the concentration and enantiomeric composition of a substrate if the probe shows two emission wavelengths that respond differently to the concentration and enantiomeric composition of a chiral compound.[11] Previously, Feuster and Glass reported the use of an achiral coumarin compound **1** for fluorescent detection of amino acids.[4] It was found that amino acids can enhance the fluorescence of **1** in the absence of a metal ion additive such as Zn^{2+}. This is

different from the 1,1'-bi-2-naphthol (BINOL)-based aldehydes, such as (*S*)-**2**, developed previously in our laboratory which requires the addition of Zn^{2+} in order to observe the enantioselective fluorescent enhancement in the presence of amino acids.[5] We have recently linked the chiral BINOL unit with the coumarin aldehyde to make a fluorescent probe for the enantioselective recognition of amino acids in the absence of Zn^{2+}.[6,7] Then we discovered this new strategy to determine the concentration and enantiomeric composition of chiral amino acids by exciting one fluorescent probe at two different wavelengths. Excitation of the probe at one wavelength shows large and similar fluorescent enhancement with both enantiomers of an amino acid, while excitation at another wavelength shows highly enantioselective fluorescent enhancement with the amino acid. This work further demonstrates the advantage of using fluorescent probes in molecular recognition because of their diverse sensing modes.

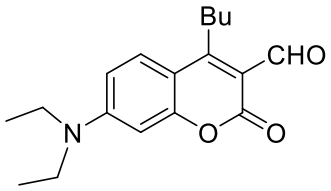

1

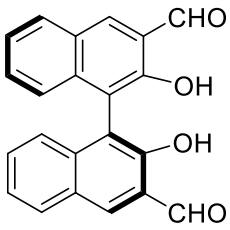

(*S*)-**2**

This probe not only shows highly enantioselective fluorescent response toward a number of amino acids, but can also allow the determination of both concentration and enantiomeric composition. It was the first fluorescent probe that can be excited at two different wavelengths to report the two parameters of a chiral substrate. In order to understand the unique fluorescence response of this amino acid probe, we have also

conducted a detailed study on its reaction with amino acids which has revealed its intriguing reactivity. Herein, these works and results that have been completed in collaboration with Dr. Qin Wang in our laboratory are reported in this chapter.

5.2 Results and Discussion

5.2.1 Study of the BINOL-Coumarin Conjugates (*S*)- and (*R*)-6.

Based on our previous study on the enantioselective sensing for amino acids by (*S*)-**2** and the achiral coumarin-based aldehyde probe **1** for amino acids detection. We have thus designed compound **6** by combining the chiral structure of BINOL with the coumarin aldehyde structure[7a−c] for the enantioselective fluorescent recognition of chiral amino acids in the absence of Zn^{2+}. Compound **6** contains two electrophilic sites that could undergo both 1,2-[4] and 1,4-additions[10] with the nucleophilic amines of amino acids. These two reaction pathways may lead to different fluorescence responses since they should generate different intermediates or products with different optical properties. The chiral binaphthyl structure could provide stereo-control for the nucleophilic addition, and the pyridine group linked with the binaphthyl could provide an additional binding site for an amino acid to enhance the chiral bias.

Scheme 5- 1. Synthesis of the BINOL-Pyridine-Coumarin Conjugate (*S*)-**6**.

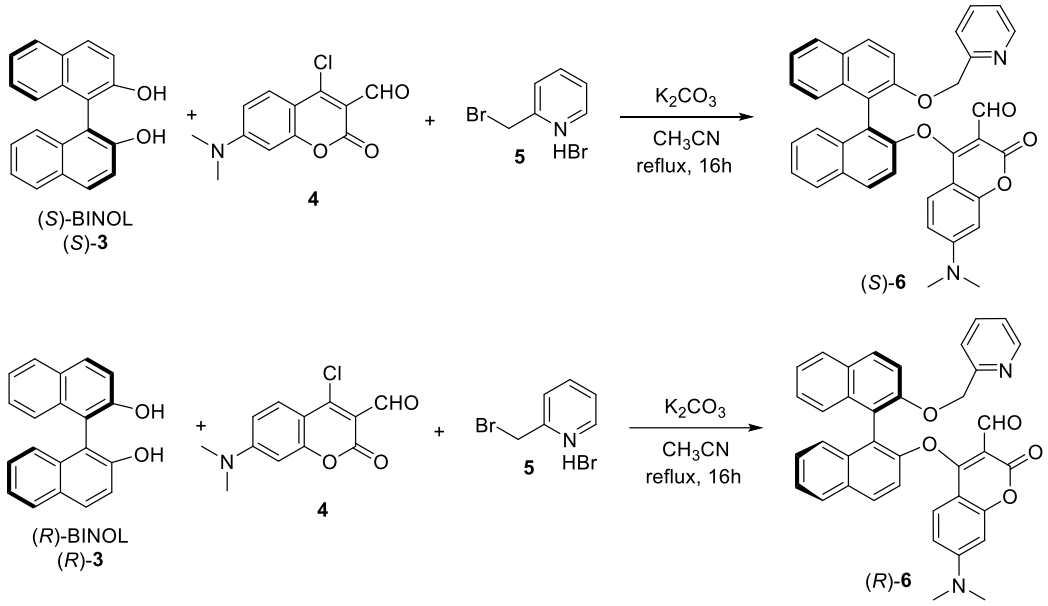

From a one-pot reaction of (*S*)-BINOL, a coumarin chloride **4**[8] and a 2-bromomethylpyridine salt **5** in the presence of K_2CO_3 in refluxing acetonitrile, the BINOL-coumarin conjugate (*S*)-**6** was obtained as a yellow solid in 35% yield (Scheme 1). X-ray analysis on a single crystal of (*S*)-**6** formed via slow evaporation of its solution in CH_2Cl_2/hexanes (v, 1/15) was conducted and it shows that the pyridine ring and the coumarin plane were almost parallel with an angle of 4.5^o (Figure 5-1). A water molecule was found to form hydrogen bonding interaction to link the pyridine nitrogen of one (*S*)-**6** molecule with the aldehyde oxygen of another (*S*)-**6** molecule. We also prepared compound (*R*)-**6**, the enantiomer of (*S*)-**6**, from (*R*)-BINOL. Compound (*S*)-**7** was also obtained from the reaction of (*S*)- BINOL with **4**.

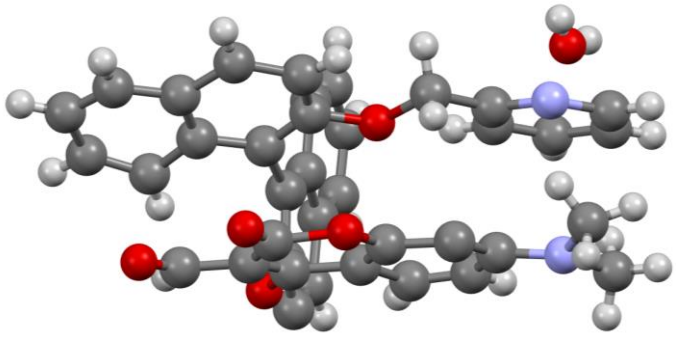

Figure 5- 1. X-ray structure of (*S*)-**6**.

Figure 5-2a compares the UV spectrum of (S)-6 in DMSO with those of (S)-BINOL, 3 and (S)-**7**. It shows that (S)-6 has two absorption bands at λ(ε) = 333 nm (1.35×10^4) and 429 nm (3.24×10^4). When excited at λ = 333 nm, (S)-6 gave two emission bands at λ = 372 and 488 nm (Figure 5-2b). The absorption and emission bands of (S)-6 at the short wavelength can be attributed to those of the naphthol unit, and the long wavelength absorption and emission bands should be generated by the conjugation of a naphthol unit with the coumarin ring. That is, linking BINOL with coumarin has led to long-wavelength absorption and emission.

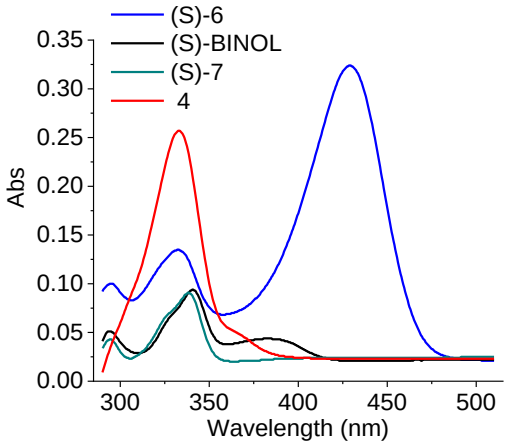

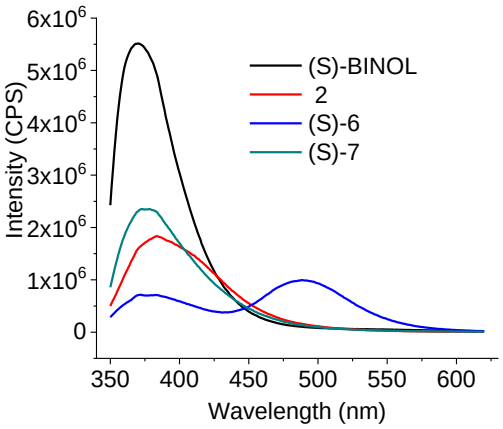

(a) (b)

Figure 5- 2. UV-vis (a) and fluorescence (b) spectra of (*S*)-**6**, (*S*)-BINOL, (*S*)-**7**, and **4** (All 10 μM in DMSO. λ_{exc} = 333 nm, slits: 3/3 nm).

5.2.2 Fluorescence Study (*S*)- and (*R*)-6 with Valine.

The fluorescence response of both (*R*)-**6** and (*S*)-**6** toward D- and L-Val was investigated. Figure 5-3a shows the fluorescence response of (*R*)-**6** toward D-/L-Val in aqueous buffer solution (HEPES, pH = 7.4). In this aqueous solution, (*R*)-**6** showed one broad emission at λ = 554 nm upon excitation at λ_1 = 365 nm, indicating an efficient energy transfer from the naphthyl unit to the naphthol−coumarin conjugate since the emission of the naphthyl rings at λ < 500 nm diminished. When treated with valine (100.0 equiv), large fluorescence enhancement at λ = 465 nm was observed upon excitation at 365 nm. It was found that both D- and L-valine caused similar fluorescence enhancement at this excitation. The reduced emission at the long wavelength (λ = 554 nm) accompanied by the greatly enhanced emission at the short wavelength (λ = 465 nm) suggested a possible 1,4- addition to disrupt the conjugation of the naphthol unit with the coumarin ring.[10]

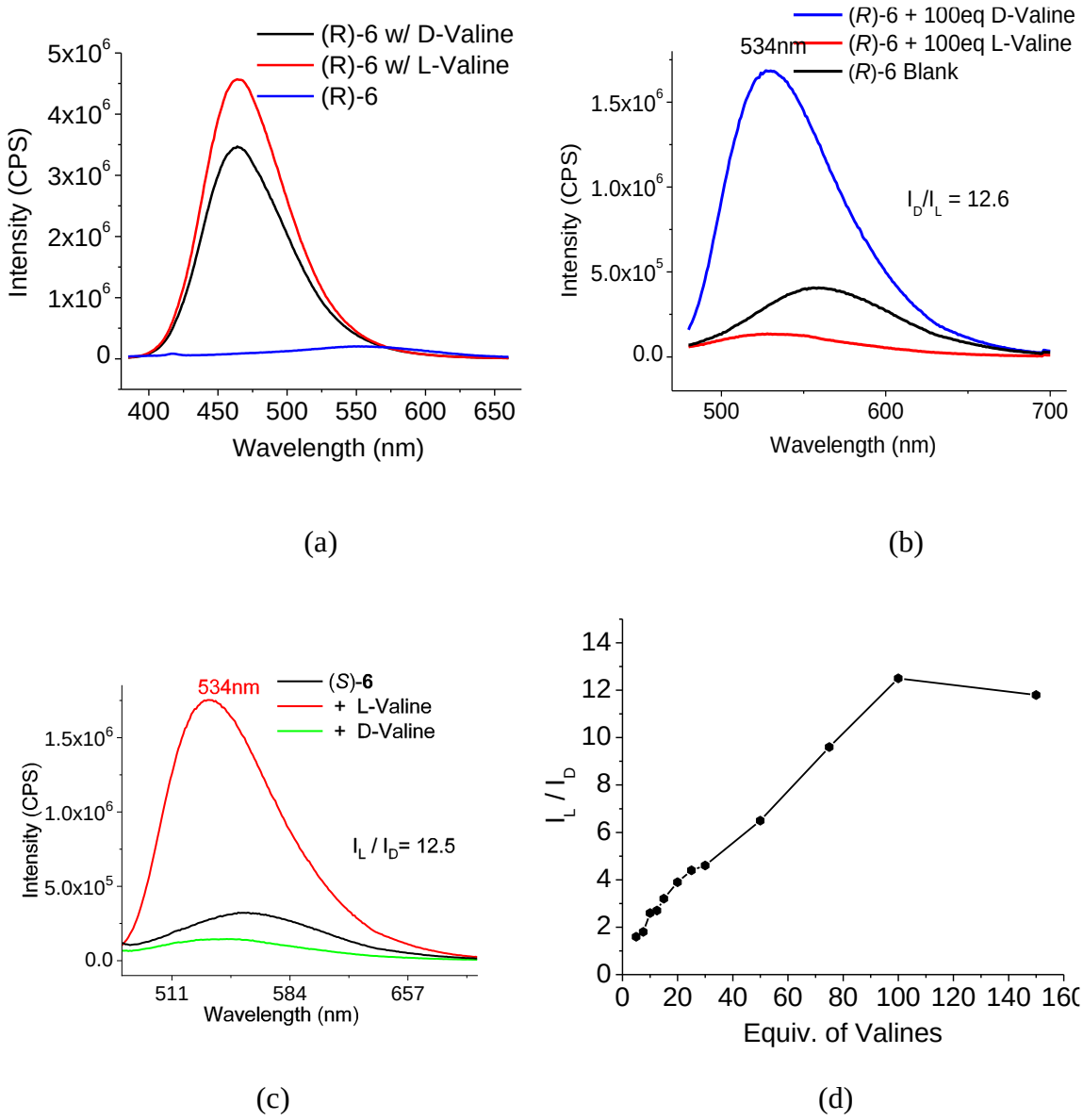

Figure 5- 3. Fluorescence spectra of (*R*)-**6** (1.0 x 10^{-5} M in HEPES/1% DMSO, pH = 7.4) with L- and D-Val (100 equiv) while excited at (a) λ_{exc} = 365 nm, and (b) λ_{exc} = 467 nm. (c) Fluorescence spectra of (*S*)-**6** (1.0 x 10^{-5} M in HEPES/1% DMSO) with L- and D-Val (100 equiv) λ_{exc} = 467 nm and (d) Fluorescence intensity ratio I_L/I_D at 534 nm versus valine concentration. (0 – 150 equiv) (slits: 3/3 nm)

When the HEPES buffer solution of (*R*)-6 was excited at λ_2 = 467 nm, a broad emission at λ = 558 nm was observed. It was found that this emission band exhibits highly enantioselective response upon reaction with valine. As shown in Figure 5-3b, while D-Val greatly enhanced the fluorescence of (*R*)-6, L-Val slightly quenched this fluorescence. In the presence of the amino acid, there was also a slight blue shift of the emission maximum. Figure 5-3c compares the fluorescence spectra of (*S*)- **6** with D- and L-Val at 100 equiv which gave a fluorescence ratio I_L/I_D of 12.5 at λ = 534 nm. Figure 5-3d shows that the enantioselectivity represented by I_L/I_D increases as the concentration of the amino acid increases which reached maximum at 100 equiv of the amino acid. In these experiments, (*S*)-6 (1.0 mM in DMSO, 1.0 equiv) was reacted with L- and D-Val (5.0−100.0 equiv) in HEPES buffer for 2 h and then diluted to 1.0×10^{-5} M with HEPES. After the resulting solution was set for 1 h, a relatively stable fluorescence response was observed and recorded (Figure 5-4a, b). These experiments demonstrate that the BINOL-coumarinbased fluorescent probes (*R*)-**6** and (*S*)-**6** are highly enantioselective when excited at 467 nm. The enhanced long-wavelength emission [λ = 467 (exc)/534 (em) nm] suggests that this fluorescence response should be due to a different reaction of (*S*)-**6** with the amino acid in comparison with the fluorescence response at the short wavelength [λ = 365 (exc)/465 (em) nm]. That is, a 1,2- addition of the amino acid to the probe to form an imine might occur with the retention of the conjugation between the naphthol unit and the coumarin ring.[4]

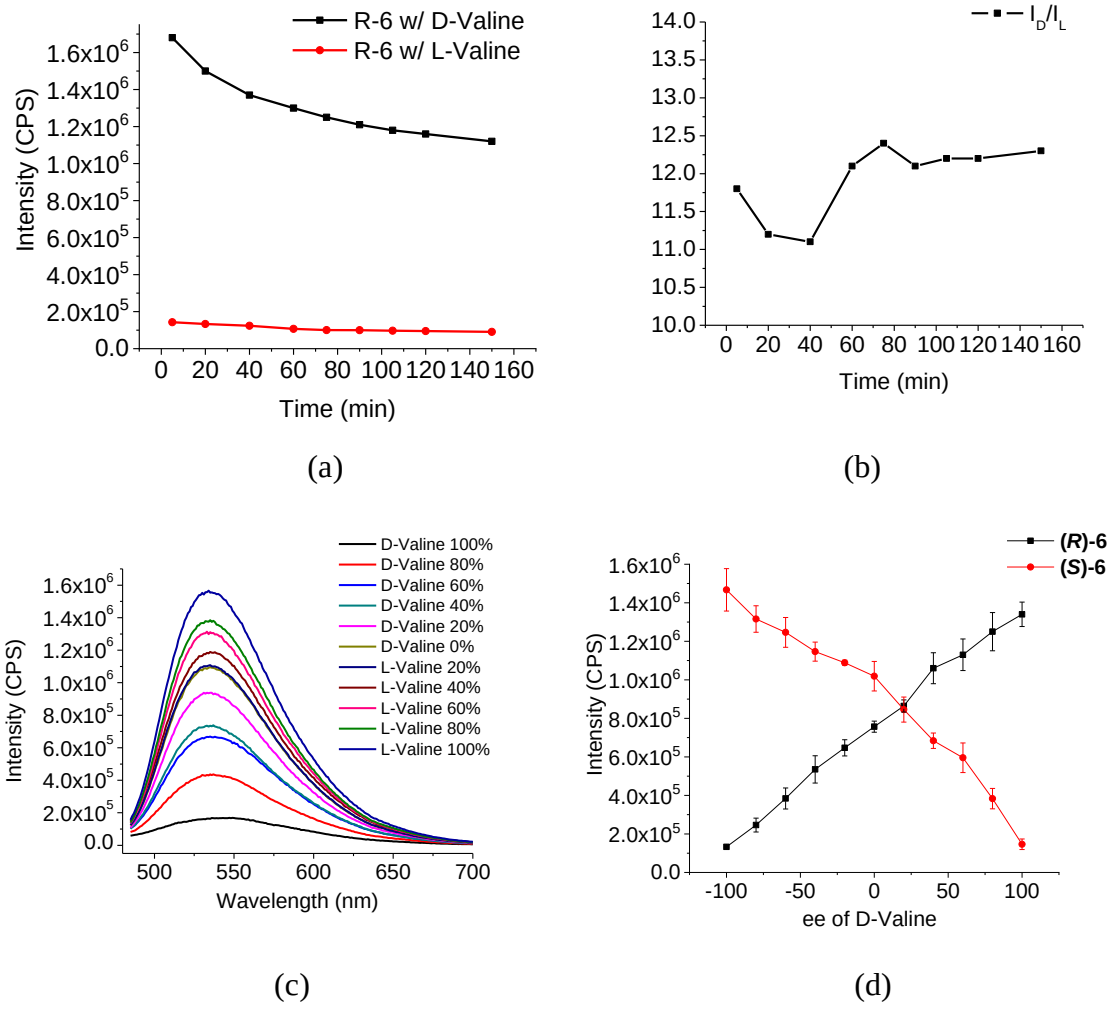

Figure 5- 4. (a) Fluorescence intensity of (*R*)-**6** at 534 nm with L- and D-Val (100 eq in HEPES) versus the time after dilution. (b) Fluorescence intensity ratio versus the time after dilution. [After (*R*)-**6** (1.0 mM in DMSO) was mixed with the amino acid for 2 h and diluted with HEPES, the fluorescence spectrum was measured. λ_{exc} = 467 nm, slits: 3/3 nm] (c) Fluorescence spectra for the reaction of (*S*)-**6** with different enantio-composition of valine (100 equiv in HEPES) (d)Fluorescence intensity of (*R*)-**6** (black) and (*S*)-**6** (red) at 534 nm versus the enantiomeric composition of valine (100 equiv). ([**6**]= 1.0 x 10^{-5} M in HEPES/1% DMSO, λ_{exc} = 467 nm, slits: 3/3 nm. The error bars were obtained from three independent experiments)

The fluorescence response of both (*S*)- and (*R*)-**6** toward valine at various enantiomeric compositions was investigated. Figure 5-4d plots the fluorescence intensity of each enantiomeric probe at 534 nm versus the enantiomeric excess [ee = ([L] − [D])/([L] + [D])] of valine upon excitation at λ_2. A mirror image relation was observed between the fluorescence responses of (*R*)-**6** and (*S*)-**6** toward the enantiomers of valine which confirms the inherent chiral recognition process. These plots can be used to determine the enantiomeric composition of the amino acid.

As described above, when excited at 365 nm (Figure 5-3a), the two enantiomers of the amino acid produced similar fluorescence enhancement on the probe; however, when excited at 467 nm (Figure 5-3b,c), one enantiomer of the amino acid greatly enhanced the fluorescence of the probe, while the other enantiomer did not. On the basis of this discovery, it is proposed that the excitation at 365 nm should allow us to determine the concentration of the amino acid, and the excitation at 467 nm should allow the determination of the enantiomeric composition.

We thus studied the effects of the concentration as well as the enantiomeric composition of the amino acid on the fluorescence responses of (*R*)-**6** at λ_1 = 365 nm (emission at λ = 465 nm) as well as at λ_2 = 467 nm (emission at λ = 534 nm). Figure 5-5a plots the fluorescence intensity I_{465} of (*R*)-**6** excited at λ_1 with varying enantiomeric composition and concentration (1.0×10^{-4} to 9.0×10^{-4} M). It shows that at this excitation/emission wavelength the fluorescence intensity of (*R*)-**6** is mostly influenced by the concentration of valine (at <90 equiv) with only a small effect by the enantiomeric composition. Figure 5-5b plots the fluorescence intensity I_{534} of (*R*)-**6** excited at λ_2 with varying enantiomeric composition and concentration (1.0×10^{-4} to 9.0×10^{-4} M). It shows

that at this excitation/emission wavelength the fluorescence intensity of (*R*)-**6** is strongly influenced by the enantiomeric composition of valine but less by the concentration. The same results were obtained for the reaction of the enantiomeric probe (*S*)-**6** with valine (Figure 5-6).

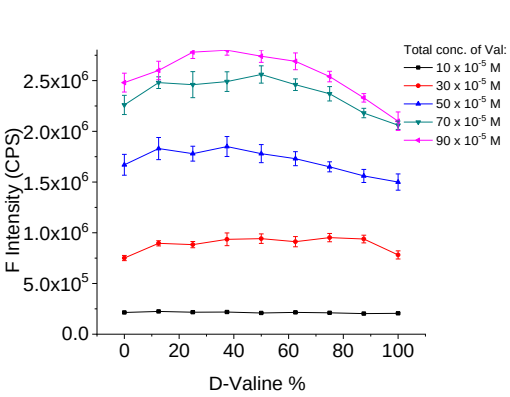

(a)

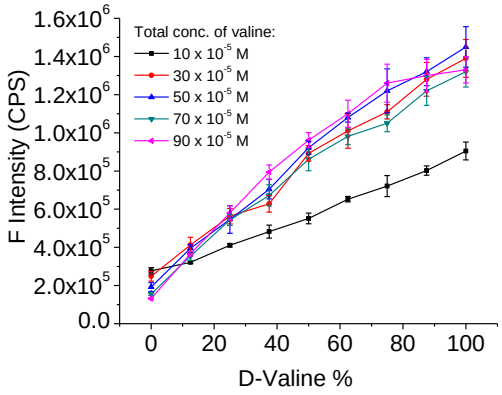

(b)

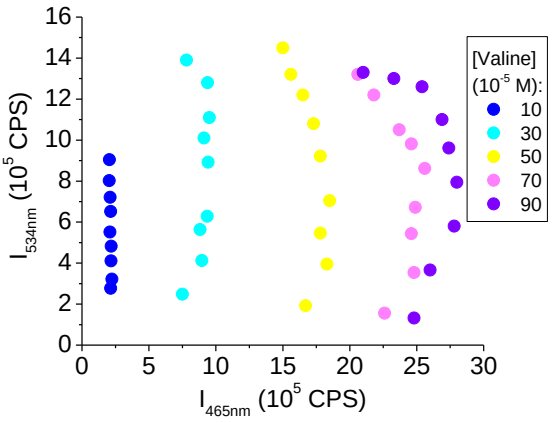

(c)

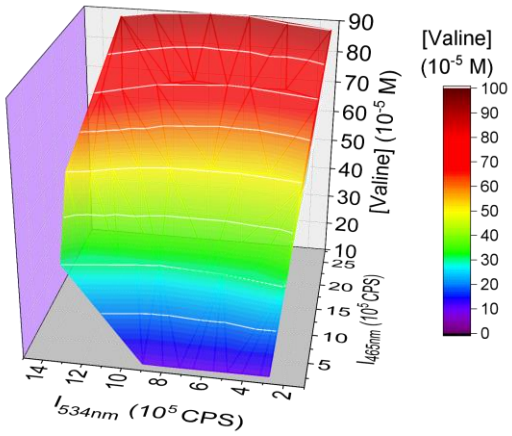

(d)

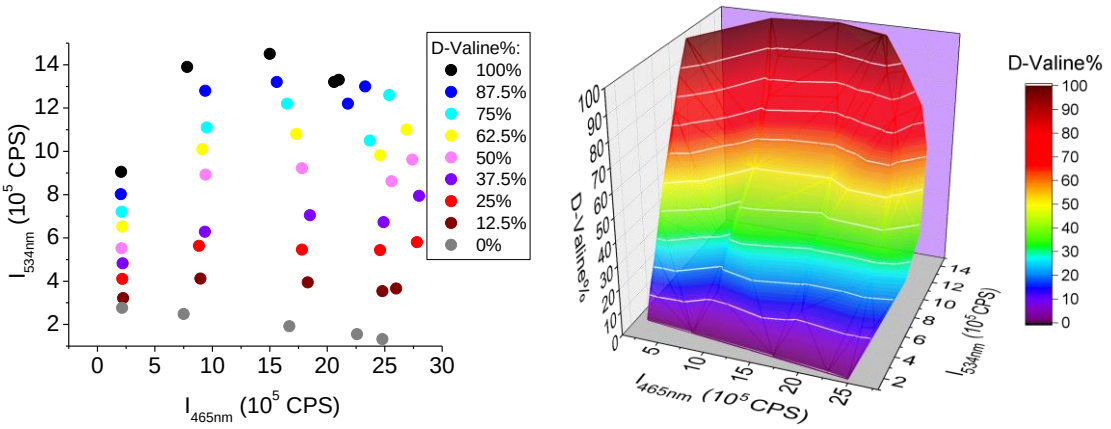

(e) (f)

Figure 5- 5. Fluorescent response of (*R*)-**6** (1.0 x 10^{-5} M in HEPES/1% DMSO) toward valine (0 – 100 equiv). (a) I_{465} (λ_{exc} = 365 nm) versus D-Val% at varying concentration. (b) I_{534} (λ_{exc} = 467 nm) versus D-Val% at varying concentration. (c) and (d) I_{465} versus I_{534} at varying concentration. (e) and (f) I_{465} versus I_{534} at varying D-Val%. (All slits: 3/3 nm and all the data were obtained from three independent experiments)

In Figure 5-5c, the fluorescence intensities of (*R*)-**6** at both I_{465} and I_{534} are plotted with varying concentration of valine. Figure 5-5d is the 3D plot of Figure 5-5c. Thus, Figure 5d allows the determination of the concentration of the amino acid mainly by I465 with the consideration of the small effect of the enantiomeric composition by incorporating I_{534}. In Figure 5-5e, the fluorescence intensities of (*R*)-**6** at both I_{465} and I_{534} are plotted with varying enantiomeric composition of valine. Figure 5-5f is the 3D plot of Figure 5-5e. This 3D figure allows the determination of the enantiomeric composition of the amino acid mainly by I_{534} with the consideration of the small effect of the concentration by incorporating I_{465}. Therefore, using one fluorescent probe (*R*)-**6**, both the concentration

and enantiomeric composition of the amino acid can be determined by excitation at two different wavelengths.

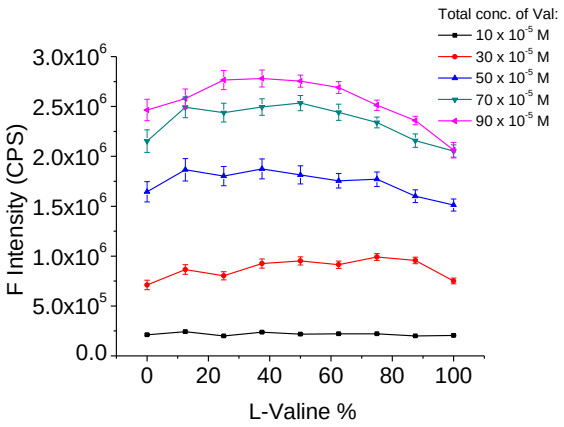

(a)

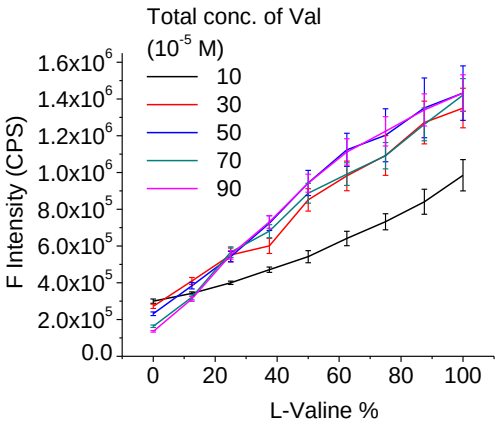

(b)

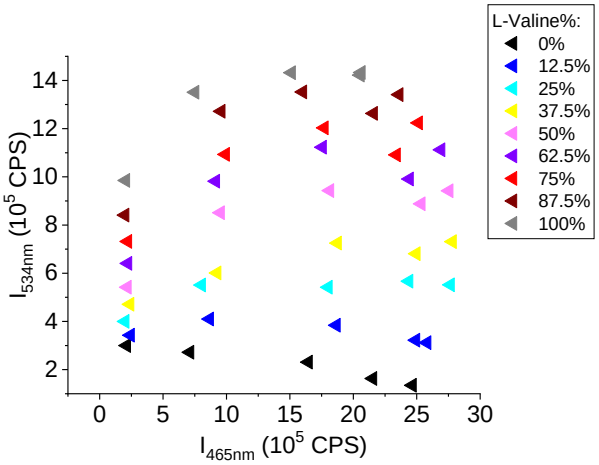

(c)

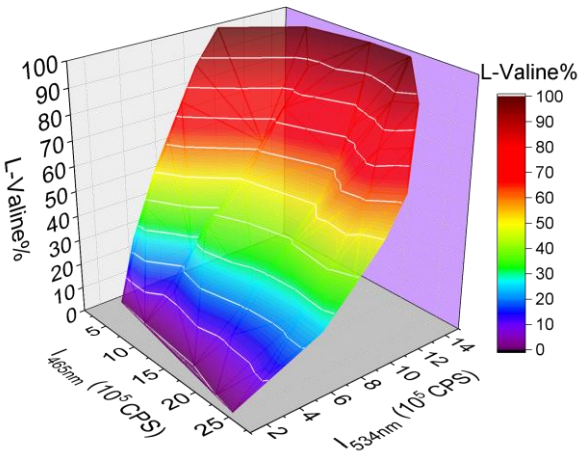

(d)

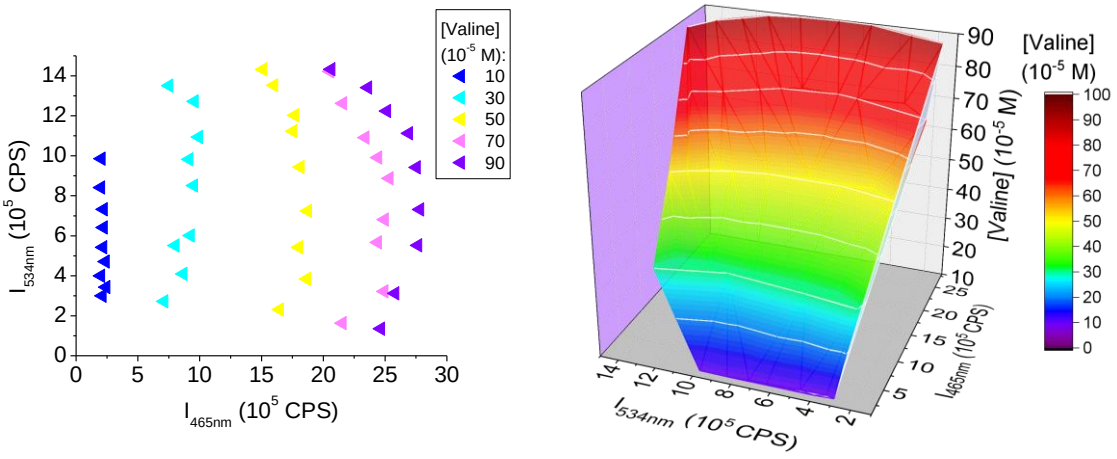

(e) (f)

Figure 5- 6. Fluorescent response of (*S*)-**6** (1.0 x 10^{-5} M in HEPES/1% DMSO) with valine (0 – 100 equiv). (a) I_{465} (λ_{exc} = 365 nm) versus L-Val% at varying concentration. (b) I_{534} (λ_{exc} = 467 nm) versus L-Val% at varying concentration. (c) and (d) I_{465} versus I_{534} at varying L-Val%. (e) and (f) I_{465} versus I_{534} at varying concentration. (All slits: 3/3 nm and all the data were obtained from three independent experiments)

We have applied the 3D plots Figure 5-5d, f to analyze the concentration and enantiomeric composition of several valine samples. As the results summarized in Table 5-1 show, the values of D-Val % and valine concentrations obtained from the fluorescent measurements had good agreement with the actual data.

Table 5- 1. Measuring both concentration and enantiomeric compositions of the valine samples with (*R*)-**2** by fluorescence[a]

Entry	Actual D-Val%	Found D-Val%	Actual [Val] (10^{-5} M)	Found [Val] (10^{-5} M)
1	85	86 ± 2.4	25	16 ± 3.7
2	50	55 ± 2.7	40	37 ± 6.0
3	35	36 ± 9.5	65	60 ± 1.3
4	20	23 ± 2.3	80	80 ± 6.3
5	30	33 ± 4.2	95	94 ± 8.5

a) λ_{ex} = 365 nm, λ_{em} = 465 nm; λ_{ex} = 467 nm, λ_{em} = 534 nm, slits: 3/3 nm. All the data were obtained from three independent experiments.

We also studied the fluorescence responses of (*S*)-**6** toward 19 common amino acids (including valine) (Figure 5-7).

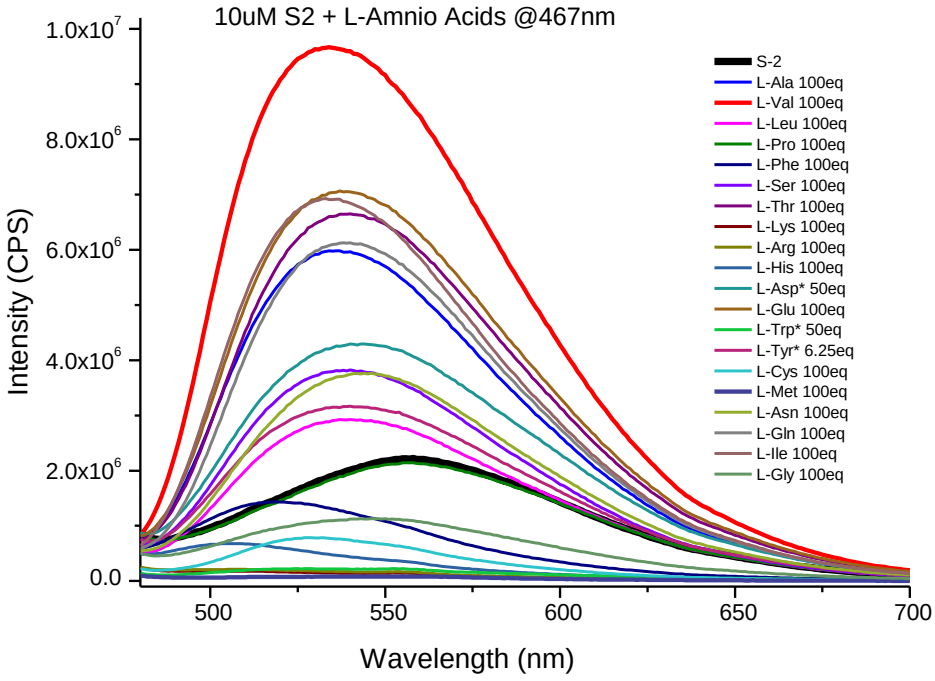

(a)

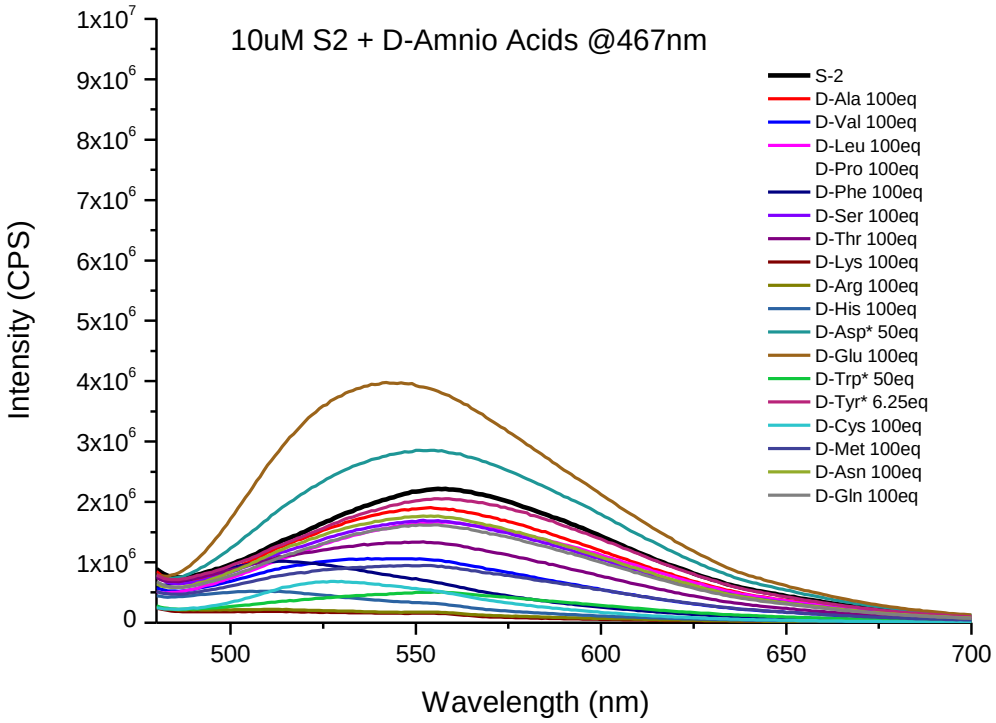

(b)

Figure 5- 7. Fluorescence spectra for the reaction of (*S*)-**6** (1.0 mM in DMSO) with (a) L- and (b) D-amino acids (100 equiv) in HEPES. (reaction time: 2 h, then diluted to 1.0 x 10^{-5} M probe with HEPES. λ_{exc} = 467 nm, slits: 5/5 nm)

Under the same conditions, enantioselective fluorescence enhancements were observed (Figure 5-8, Table 5-2) for the following 11 amino acids: valine, threonine, isoleucine, methionine, glutamine, leucine, alanine, asparagine, serine, aspartic acid, and glutamic acid when excited at the long wavelength λ_2.

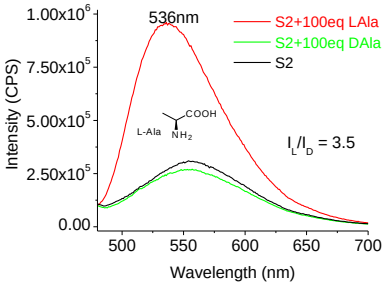
536nm
S2+100eq LAla
S2+100eq DAla
S2
L-Ala
I_L/I_D = 3.5
Intensity (CPS)
Wavelength (nm)

(a)

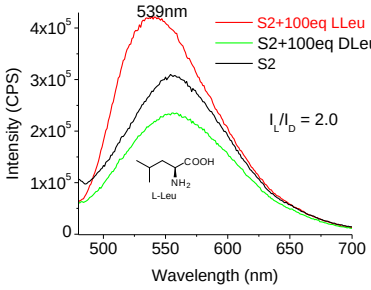
539nm
S2+100eq LLeu
S2+100eq DLeu
S2
L-Leu
I_L/I_D = 2.0
Intensity (CPS)
Wavelength (nm)

(b)

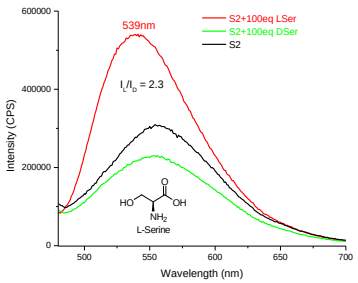
539nm
S2+100eq LSer
S2+100eq DSer
S2
I_L/I_D = 2.3
L-Serine
Intensity (CPS)
Wavelength (nm)

(c)

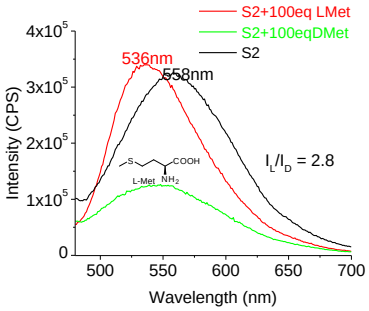
S2+100eq LMet
S2+100eqDMet
S2
536nm
558nm
L-Met
I_L/I_D = 2.8
Intensity (CPS)
Wavelength (nm)

(d)

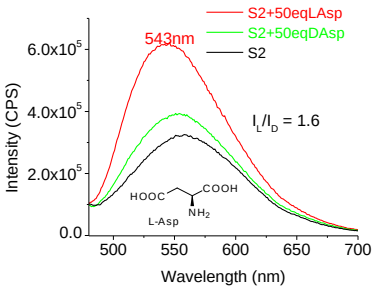
S2+50eqLAsp
S2+50eqDAsp
S2
543nm
L-Asp
I_L/I_D = 1.6
Intensity (CPS)
Wavelength (nm)

(e)

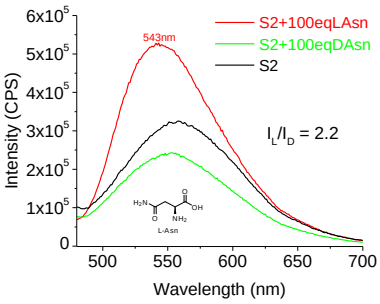
S2+100eqLAsn
S2+100eqDAsn
S2
543nm
L-Asn
I_L/I_D = 2.2
Intensity (CPS)
Wavelength (nm)

(f)

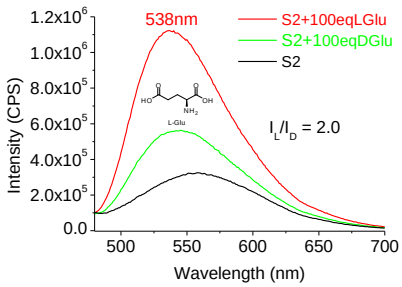
538nm
S2+100eqLGlu
S2+100eqDGlu
S2
L-Glu
I_L/I_D = 2.0
Intensity (CPS)
Wavelength (nm)

(g)

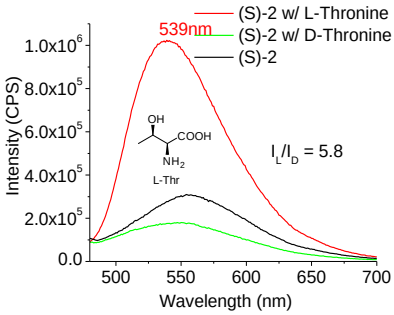
539nm
(S)-2 w/ L-Thronine
(S)-2 w/ D-Thronine
(S)-2
L-Thr
I_L/I_D = 5.8
Intensity (CPS)
Wavelength (nm)

(h)

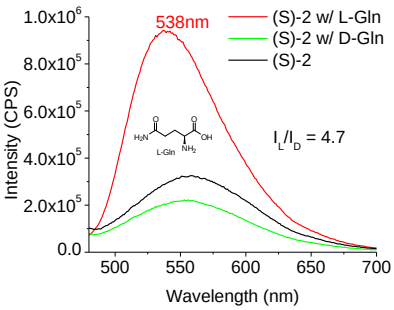
538nm
(S)-2 w/ L-Gln
(S)-2 w/ D-Gln
(S)-2
L-Gln
I_L/I_D = 4.7
Intensity (CPS)
Wavelength (nm)

(i)

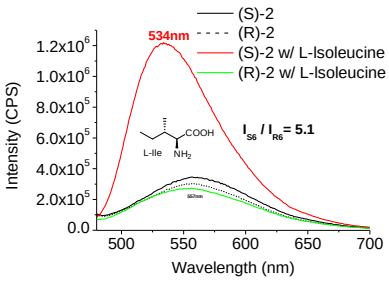
534nm
(S)-2
(R)-2
(S)-2 w/ L-Isoleucine
(R)-2 w/ L-Isoleucine
L-Ile
I_{S6} / I_{R6} = 5.1
Intensity (CPS)
Wavelength (nm)

(j)

Figure 5- 8. Fluorescence spectra for the reaction of (*S*)-**6** (1.0 mM in DMSO) with both enantiomers of (a) Ala, (b) Leu, (c) Ser, (d) Met, (e) Asp, (f) Asn, (g) Glu, (h) Thr, (i) Gln (100 equiv) in HEPES and Fluorescence spectra for the reaction of (*S*)-**6** and (*R*)-**6** (1.0 mM in DMSO) with L-Isoleucine (100 equiv) in HEPES. (reaction time: 2 h, then diluted to 1.0 x 10^{-5} M probe with HEPES. λ_{exc} = 467 nm, slits: 3/3 nm)

Table 5- 2. Amino acids showed good enantioselectivity and the fluorescence intensity ratio I_L/I_D

Amino Acid	Ala	Val	Leu	Ser	Thr	Met	Asp	Asn	Glu	Gln
I_L / I_D	3.5	12.5	2.0	2.3	5.8	2.8	1.6	2.2	2.0	4.7

Figures 5-9 and 5-10 give two examples for the fluorescent response of (*R*)-**6** toward amino acids threonine and glutamine at varying concentrations and enantiomeric compositions while excited at λ_1 and λ_2, which are very similar to Figure 5-5.

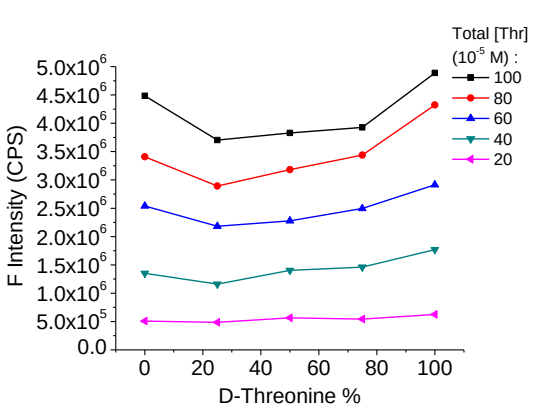

(a)

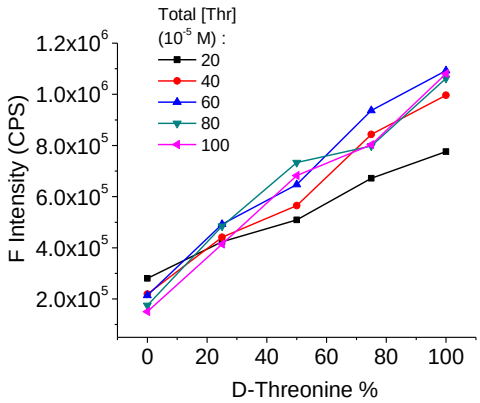

(b)

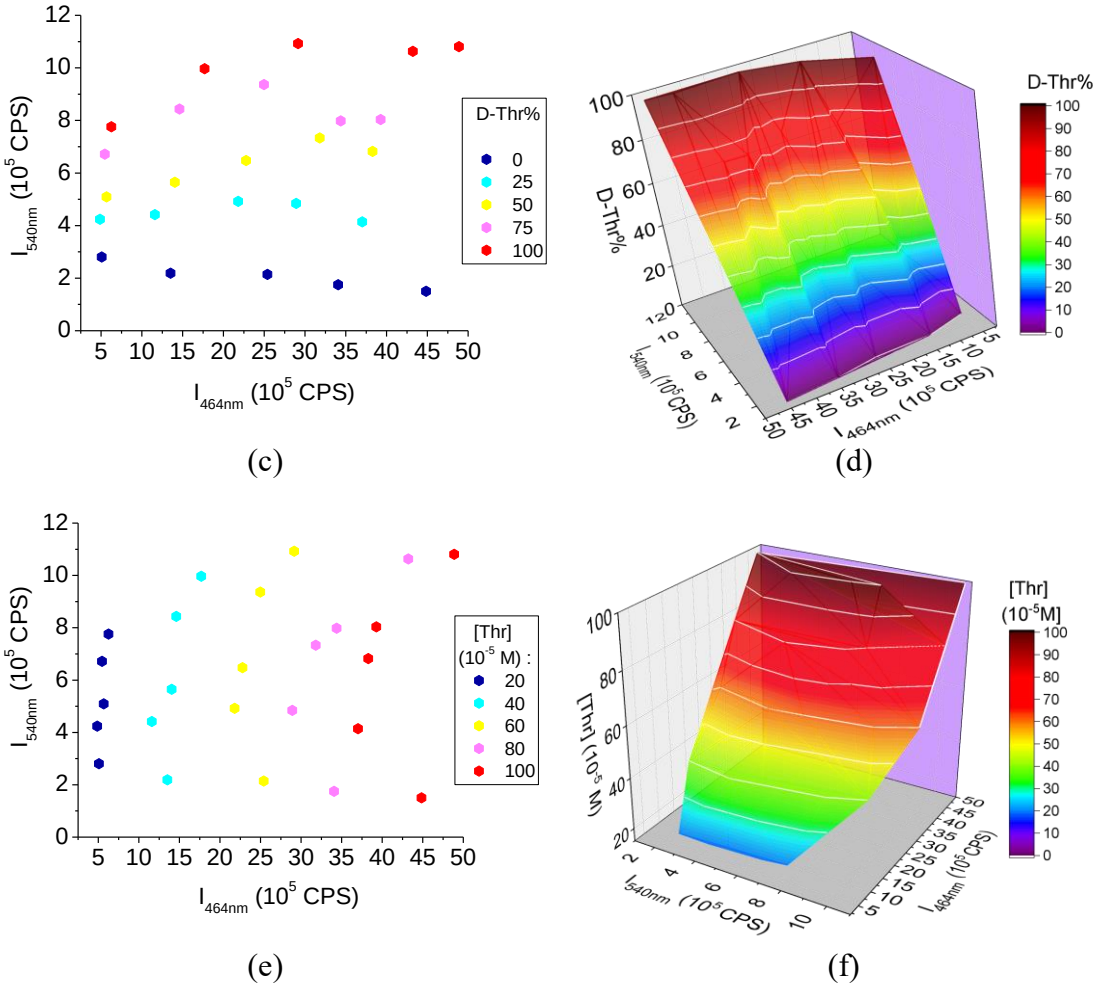

Figure 5- 9. Fluorescent response of (*R*)-**6** (1.0 x 10^{-5} M in HEPES/1% DMSO) toward threonine (0 – 100 equiv). (a) I_{464} (λ_{exc} = 365 nm, slits: 3/3 nm) versus D-Thr% at varying concentration of threonine. (b) I_{540} (λ_{exc} = 467 nm, slits: 3/3 nm) versus D-Thr% at varying concentration of threonine. (c) and (d) I_{464} versus I_{540} at varying D-Thr%. (e) and (f) I_{464} versus I_{540} at varying concentration of threonine.

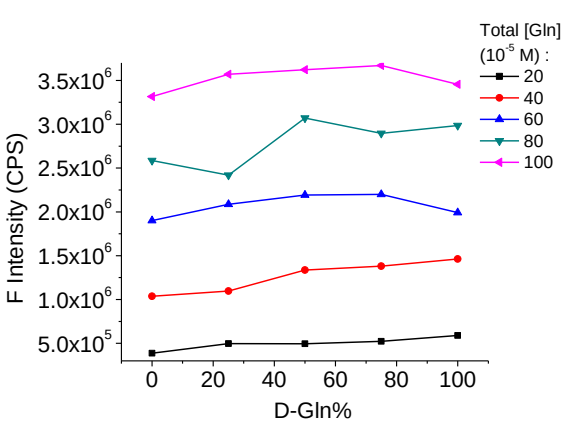
F Intensity (CPS)
D-Gln%
Total [Gln]
(10-5 M) :
20
40
60
80
100

(a)

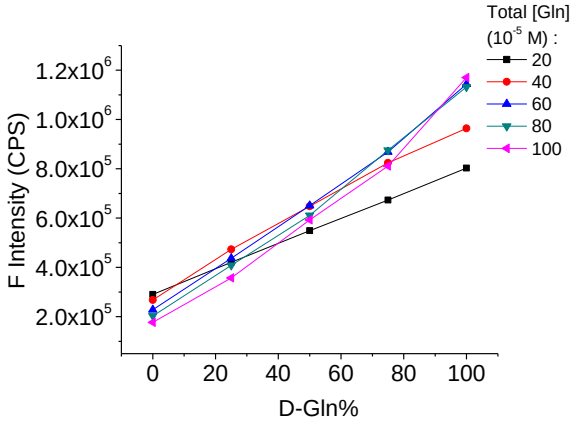
F Intensity (CPS)
D-Gln%
Total [Gln]
(10-5 M) :
20
40
60
80
100

(b)

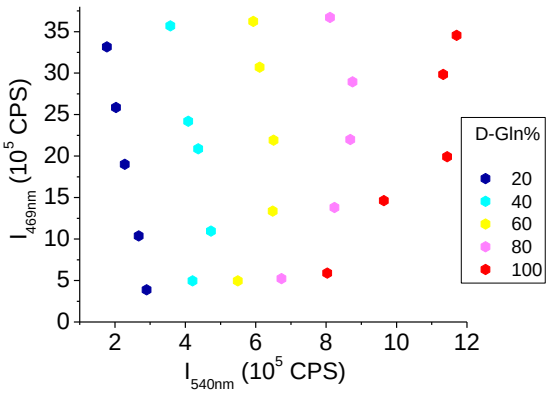
I469nm (10^5 CPS)
I540nm (10^5 CPS)
D-Gln%
20
40
60
80
100

(c)

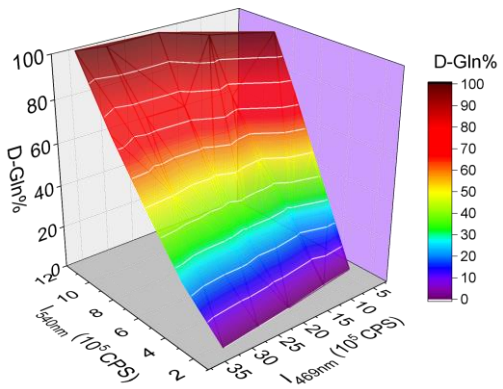
D-Gln%
I540nm (10^5 CPS)
I469nm (10^5 CPS)
D-Gln%

(d)

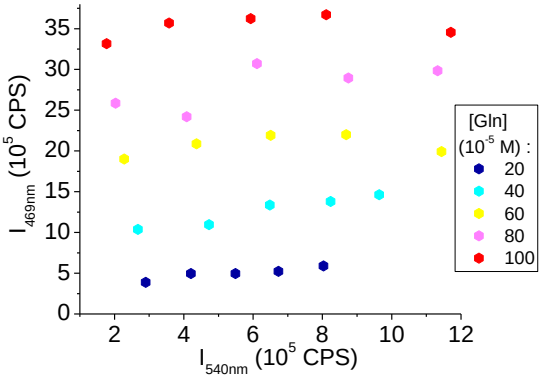
I469nm (10^5 CPS)
I540nm (10^5 CPS)
[Gln]
(10-5 M) :
20
40
60
80
100

(e)

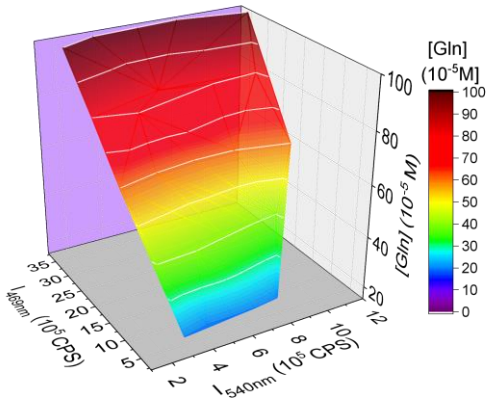
I469nm (10^5 CPS)
I540nm (10^5 CPS)
[Gln] (10-5 M)
[Gln]
(10-5M)

(f)

Figure 5- 10. Fluorescent response of (*R*)-**6** (1.0 x 10^{-5} M in HEPES/1% DMSO) toward glutamine (0 – 100 equiv). (a) I_{469} (λ_{exc} = 365 nm, slits: 3/3 nm) versus D-Gln% at varying concentration of glutamine. (b) I_{540} (λ_{exc} = 467 nm, slits: 3/3 nm) versus D-Gln% at varying concentration of glutamine. (c) I_{469} versus I_{540} at varying D-Gln%. (d) I_{469} versus I_{540} at varying concentration of glutamine.

5.2.3 Mechanism Study of Probe 6 with Valine.

In order to understand how the probe reacts with the amino acids to give the observed fluorescence responses, we conducted a mass spectroscopic analysis on the reaction of (*S*)-**6** with valine. Because the large amount of HEPES in the reaction mixture interfered with the mass analysis, we acquired the mass spectra for the reaction of (*S*)-**6** (1 mM) in DMSO with D- and L-Val (1 mM) in HEPES (25 mM, pH = 7.4, 120 mM NaCl) by direct diluting it with water instead of HEPES and used the flow injection method to obtain the spectra of the reaction mixture. In the mass spectrum of the product mixture of (*S*)-**6** with L-Val (Figure S5-18a in Appendix), we have identified peaks at m/z = 378.1486 for **7** (calcd for **7**+H^+: 378.1494), 333.1453 for compound **8** (calcd for **8**+H^+: 333.1450), 432.2123 for compound **9** (calcd for **9**+H^+: 432.2135), and 692.2758 for intermediate **10** (calcd for **10**+H^+: 692.2761) respectively. Similar mass signals are also found in the product mixture of (*S*)-**6** with D-Val (Figure S5-18b in Appendix), but the peak intensity at 692.2748 for intermediate **10** was much weaker than that in the reaction of L-Val.

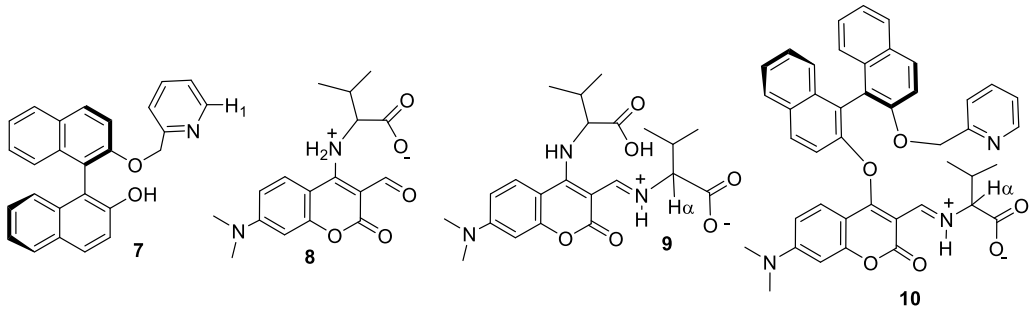

Figure 5- 11. Product and intermediate structures formed from the reaction of (*R*)-**6** with valine.

We further studied the reaction of (*R*)-**6** with valine by ^{1}H NMR spectroscopic analysis. As shown in Figure 4, when (*R*)-**6** was treated with D-Val for 2 – 4 h, there was only a small degree of reaction (Figure 5-12d-f). This suggests that during the fluorescence measurement (2 h reaction time), the extent of the reaction between (*R*)-**6** and the amino acid should be very small. After 36 h, there was about 40% conversion of (*R*)-**6** to the corresponding products (Figure 5-12i). In Figure 5-12i, the signals at 5.17, 6.88, 7.00 and 8.42 can be attributed to the product **7** by comparing with the ^{1}H NMR spectrum of **7**, prepared from the reaction of **3** with **5**,[9] under the same conditions. The singlet at 9.81 is assigned to the aldehyde proton signal of the product **8** and the two signals at 4.24 and 4.44 can be assigned to the H signals of **9** and **10**.

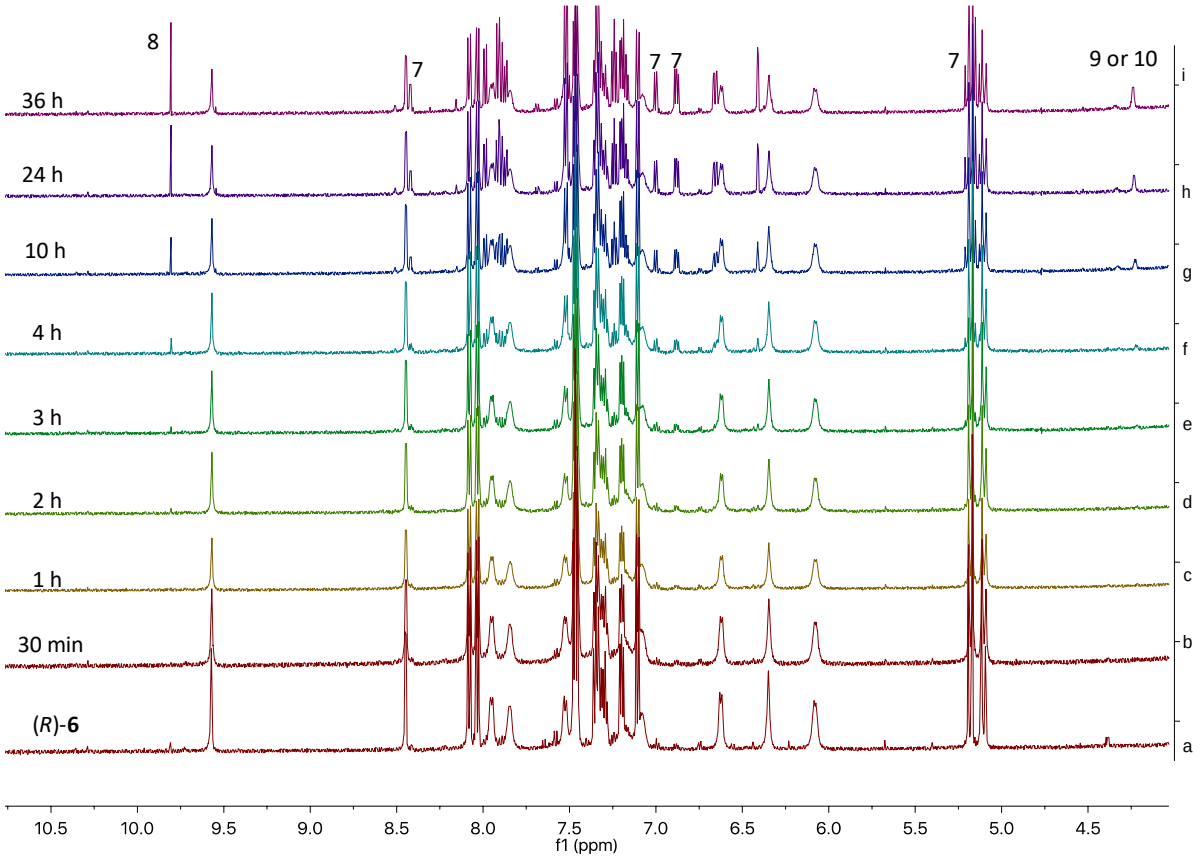

Figure 5- 12. ^{1}H NMR spectra of (*R*)-**6** (1.0 mM in DMSO-d_6) (a) with D-Val (40 equiv) in HEPES (D_2O, 25 mM HEPES, 120 mM NaCl, pD=7.4) for 30 min to 36 h (b-i). [DMSO-d_6: HEPES-D_2O = 9:1 (v). The full spectra are given in Figure S5-10 in Appendix]

In order to provide additional characterization for compounds **8** and **9**, we studied the reaction of **4** with L-Val (1.0 equiv) in DMSO-d_6 (Scheme 5-2). After 55 h at rt, the ^{1}H NMR spectrum of the reaction mixture showed complete consumption of **4** with the formation of compound **8** as the major product (Figure S12 in SI, compound **8** could not be separated from the other minor products).[10b] The aldehyde proton signal of **8** was observed at δ 9.74 (in 9:1 DMSO-d_6/D_2O) or 9.72 (in pure DMSO-d_6) very close to that in Figure 4i. When additional amount of L-Val (40 equiv) was added to the solution of **8**, the aldehyde signal of **8** disappeared with the

appearance of an imine proton signal at 8.32 and the H signal at 4.35 for the product **9** (Figure S5-14 in Appendix). The mass spectra of the reaction mixtures confirmed the formation of compounds **8** and **9** as the major products (Figures S5-13 and S5-15 in Appendix). In the ^{1}H NMR spectrum of the product mixtures of **8** and L-valine, the signals are found to be similar to those in Figure 5-12i but not identical (Figure S5-11d in Appendix). This discrepancy could be attributed to various intermolecular interactions of these highly polar molecules in the HEPES buffer solution of the reaction mixture of (*R*)-**6** with valine.

Scheme 5- 2. Reaction of **4** with L-Val.

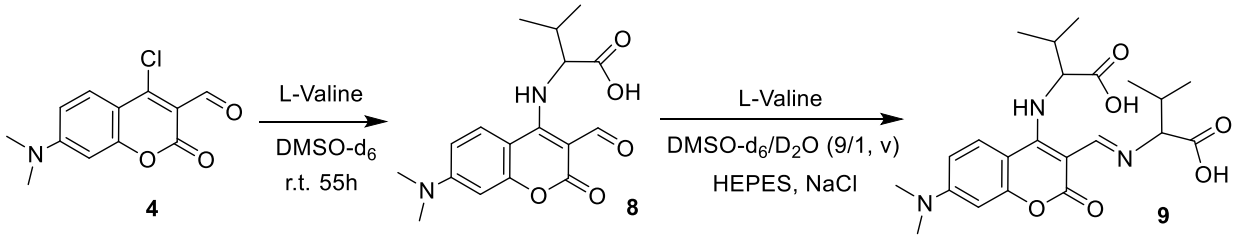

We measured the fluorescence spectra of the above product mixtures of **8** and **9** after they were diluted with HEPES buffer to ~5 μM. As shown in Figure 5-13a, both of them show similar fluorescence when excited at 365 nm with emission maxima at 476 and 468 nm for **8** and **9** respectively. When excited at 467 nm, the emissions of **8** and **9** were very weak (Figure 5-14). Figure 5-13b gives the fluorescence spectra of **7** in HEPES buffer solution and pure DMSO which show very weak or no emission when excited at 365 nm. These spectra indicate that the observed enantioselective fluorescence enhancement at 534 nm in the reaction of (*R*)-**6** with D-Val is not contributed by the three products **7**, **8** and **9**.

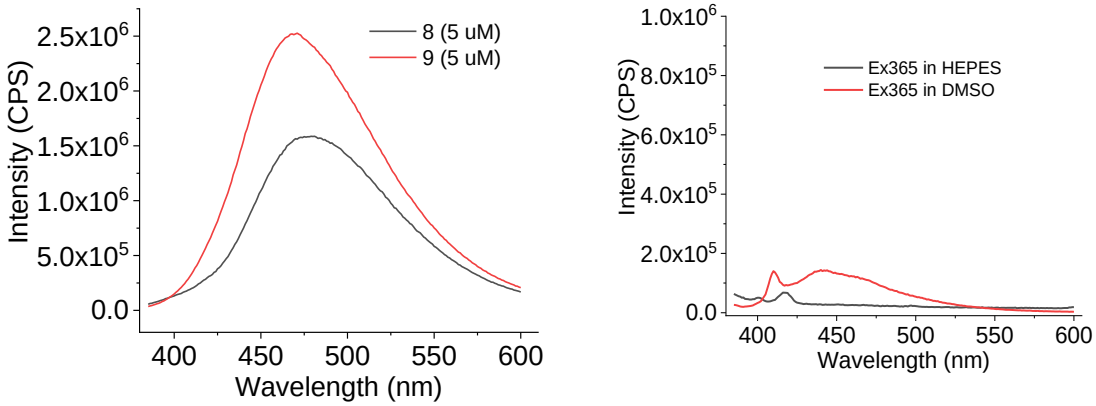

(a) (b)

Figure 5- 13. Fluorescence spectra of (a) the product mixtures of **8** and **9** from the reaction of **4** with valine (diluted with HEPES buffer in H_2O to ~5 µM, λ_{exc} = 365 nm, slits: 3/3 nm). (b) Compound **7** (1.0×10^{-5} M) in HEPES/1%DMSO (pH = 7.4) and DMSO. (λ_{exc} = 365 nm, slits: 3/3 nm)

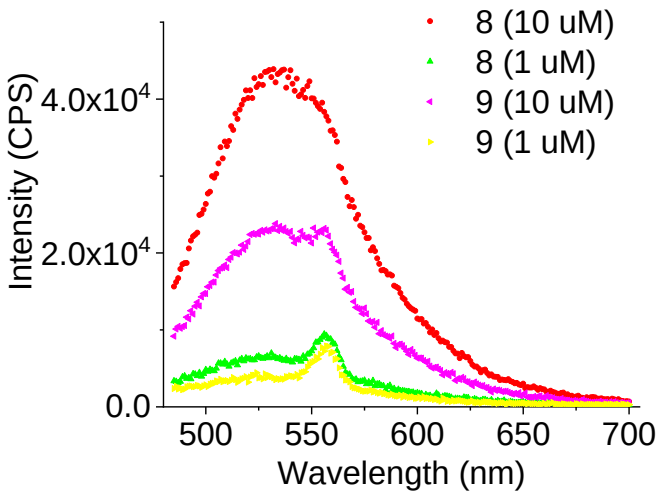

Figure 5- 14. Fluorescence spectra of the crude product mixtures of **8** and **9**. [in DMSO-d_6 (90%) and HEPES in D_2O (10%) and diluted with HEPES buffer in H_2O to 1 - 10 µM, λ_{exc} = 467 nm, slits: 3/3 nm]

Although no significantly new ^{1}H NMR signal appeared from the reaction of (*R*)-**6** with D-Val in 2 h as shown in Figure 5-12d, the UV spectrum for the reaction of (*R*)-**6** with D-Val in 2 h gave a new signal at = 467 nm which was missing in the reaction with L-Val (Figure 5-15a). A close to mirror image relation was observed in the UV spectra of the enantiomeric probe (*S*)-**6** with L- and D-Val (Figure 5-15b). The new absorption at 467 nm is correlated with the observed large fluoresce enhancement at 534 nm (λ_{exc} = 467 nm) for the reaction of (*R*)-**6** with D-Val during the same period of reaction time (See the excitation spectra in (Figure 5-16).

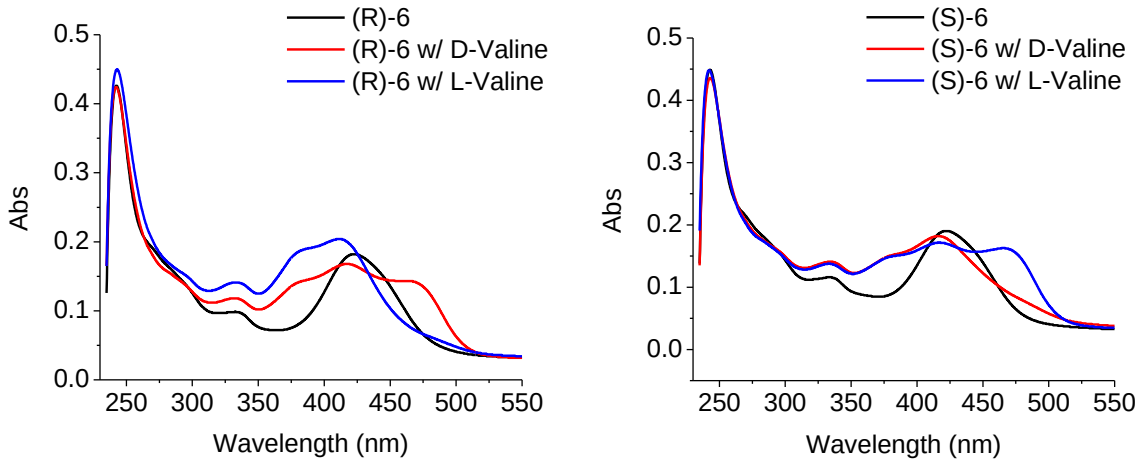

(a) (b)

Figure 5- 15. UV-vis absorption spectra of (*R*)-**6** (a) or (*S*)-**6** (b) and its reaction with D- and L-Val [**6** (1.0 mM, DMSO) was mixed with D- or L-Val (100 equiv in HEPES, pH = 7.4) for 2 hours before it was diluted with HEPES to 1.0 x 10^{-5} M and measured in 30 min]

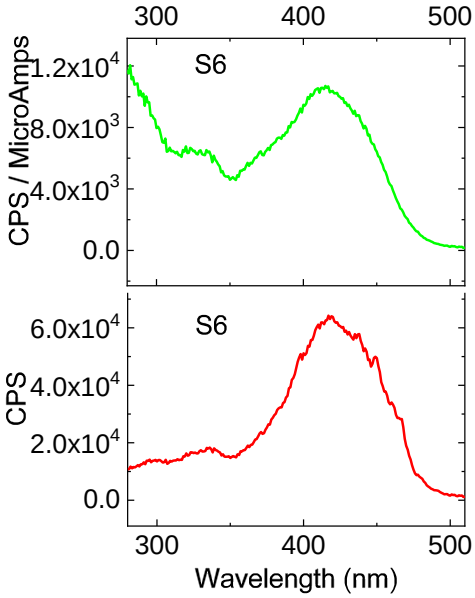
S6
CPS / MicroAmps
CPS
Wavelength (nm)

(a)

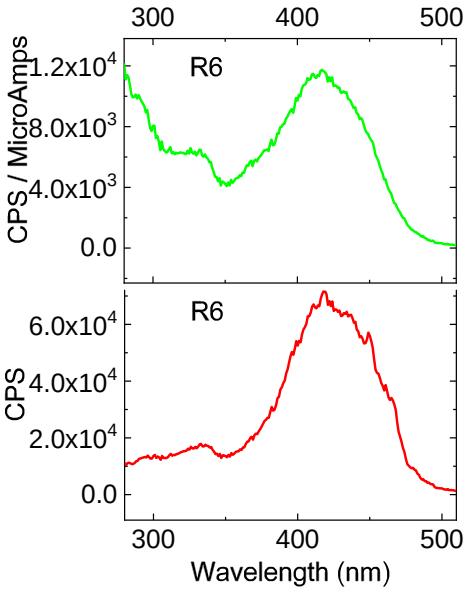
R6
CPS / MicroAmps
CPS
Wavelength (nm)

(b)

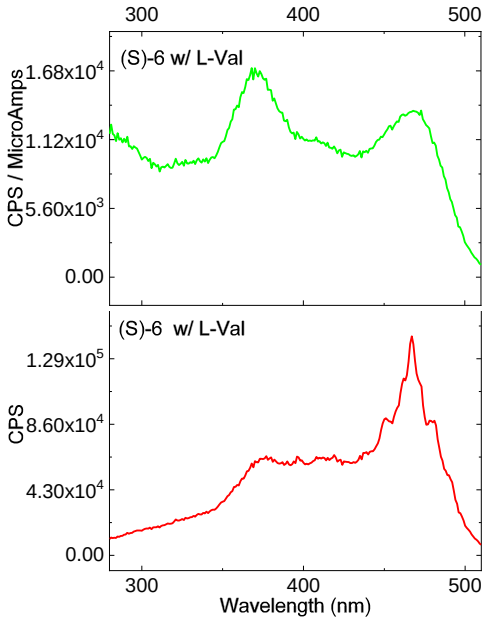
(S)-6 w/ L-Val
CPS / MicroAmps
CPS
Wavelength (nm)

(c)

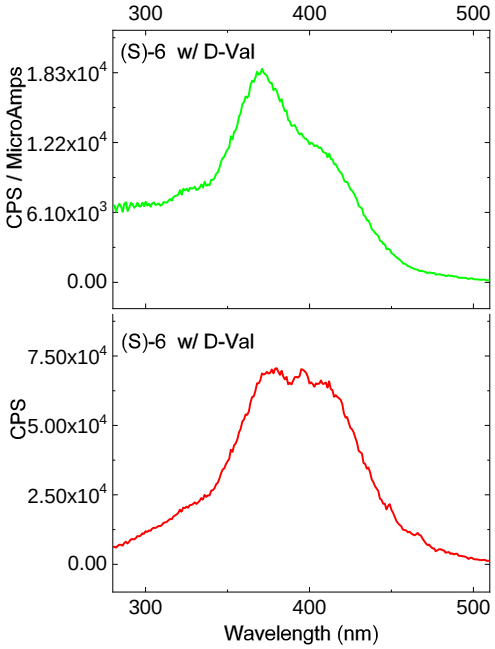
(S)-6 w/ D-Val
CPS / MicroAmps
CPS
Wavelength (nm)

(d)

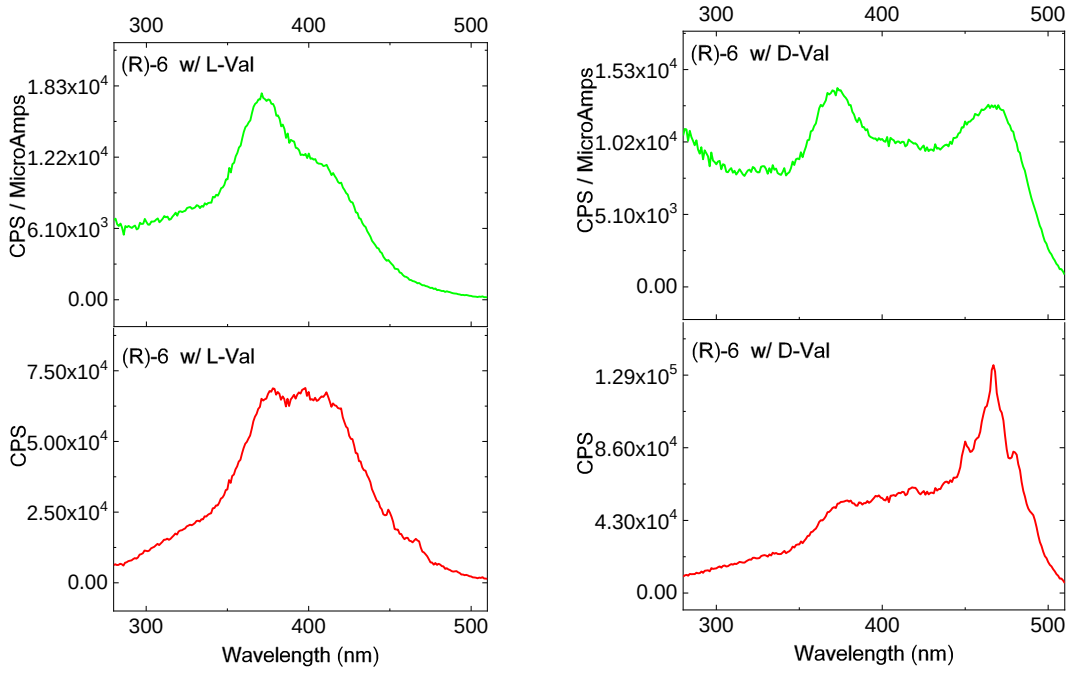

(e) (f)

Figure 5- 16. Fluorescence excitation spectra for the reaction of (a) (*S*)-**6**, (b) (*R*)-**6** (1.0 mM in DMSO) with L-Val (c) and (e) as well as D-Val (d) and (f) (100 eq in HEPES). (reaction time: 2 h, then diluted to 1.0×10^{-5} M probe with HEPES. The spectra were acquired in 1 h after dilution. λ_{em} = 534 nm, slits: 3/3 nm)

Both **7** and the product mixtures of **8** and **9** from the reaction of **4** with Val do not show this long wavelength absorption at 10 μM (Figure 5-17). Therefore, we attribute the observed enantioselective fluorescence enhancement at 534 nm in Figure 5-3b,c to the proposed intermediate **10** formed at the beginning of the reaction of (*R*)-**6** with valine, but not the final products **7**, **8** and **9**.

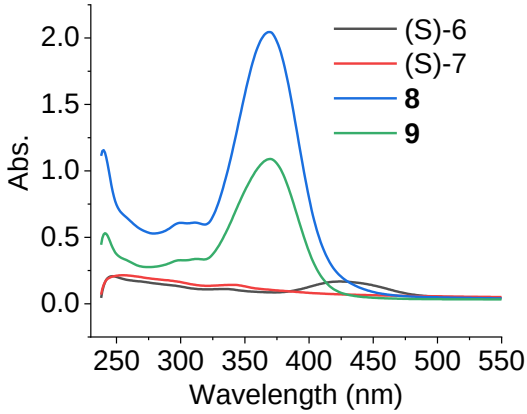

Figure 5- 17. UV-Vis spectra of (*S*)-**6**, (*S*)-**7**, **8** and **9**. (All 10 μM in 99% HEPES and 1% DMSO)

On the basis of the above spectroscopic analyses, a mechanism for the reaction of the probe **6** with valine can be proposed. As shown in Scheme 5-3, valine can react with (*R*)-**6** in two different pathways. In one reaction pathway, the 1,2-addition intermediate **10** can be generated,[4] which is supported by the mass spectroscopic analysis of the reaction mixture. This intermediate should give the long wavelength emission at 534 nm due to the conjugation between the coumarin-iminium and the naphthalene ring. The subsequent 1,4-addition of **10** with valine followed by elimination should give the products **7** and **9**. In another reaction pathway, the 1,4-addition[10a] intermediate **11** could be generated which can then undergo elimination to give the products **7** and **8**. The short wavelength emission at 467 nm could be attributed to the disrupted conjugation between the naphthalene and coumarin units, giving rise to the formation of the products **8** and even **9**. Evidence for the formation of the intermediate **11** was obtained when we conducted another high-resolution mass spectroscopic study on the reaction of (*R*)-**6** with the tetrabutylammonium (TBA) salts of D- and L-Val in DMSO. In the mass spectrum of the product mixture for the reaction of (*R*)-**6** with D- and L-Val-TBA (20 equiv) in DMSO (Figure S5-19 in

Appendix), besides the peaks for **7**, **8**, and **9**, a signal at m/z = 710.2852 could be assigned to **11**-L and that at m/z = 710.2853 to **11**-D (calcd for **11**+H^+: 710.2866).

Scheme 5- 3. Proposed reaction of **6** with Val.

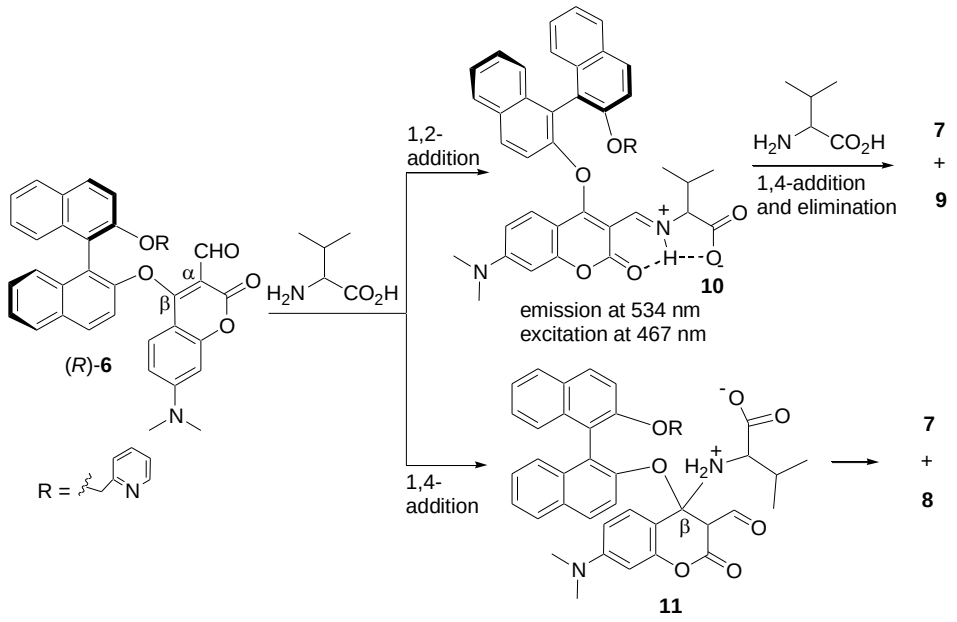

In order to understand the different enantioselective fluorescent responses at the short and long wavelength emissions, we conducted a density functional calculation by using the SPARTAN'18 program (B97X-D, 6-31G*). Figure 5-18 shows the energy minimized structures for the two diastereomeric intermediates **10** formed from the condensation of (*R*)-**6** with D-Val (**10**-D) and L-Val (**10**-L). In these structures, the coumarin ring is parallel with the naphthyl pyridinylmethyl ether unit similar to that observed in the crystal structure of (*R*)-**6**. The hydrogen bonding interactions of the iminium proton with the carbonyl group of the coumarin lactone group and with the carboxylate oxygen are present. In **10**-D, the isopropyl group is pointing away from the upper naphthalene ring with little steric interaction. It makes **10**-D more stable than **10**-L in which the isopropyl group is pointing toward the upper naphthalene ring with increased steric

interaction. The calculated energy difference of these two diastereomers in water is 7.25 kcal/mole. This stability difference might lead to the observed large difference in the fluorescence response when (*R*)-**6** was treated with D-Val versus L-Val. We also calculated the energy difference between the two diastereomers of the intermediate **11** formed from the reaction of (*R*)-**6** with L- and D-Val (Figure 5-19). It was found that the energy difference of these two diastereomers (**11**-D and **11**-L) is much smaller than that of **10**-D and **10**-L, consistent with the much lower enantioselective fluorescent response at the short wavelength emission.

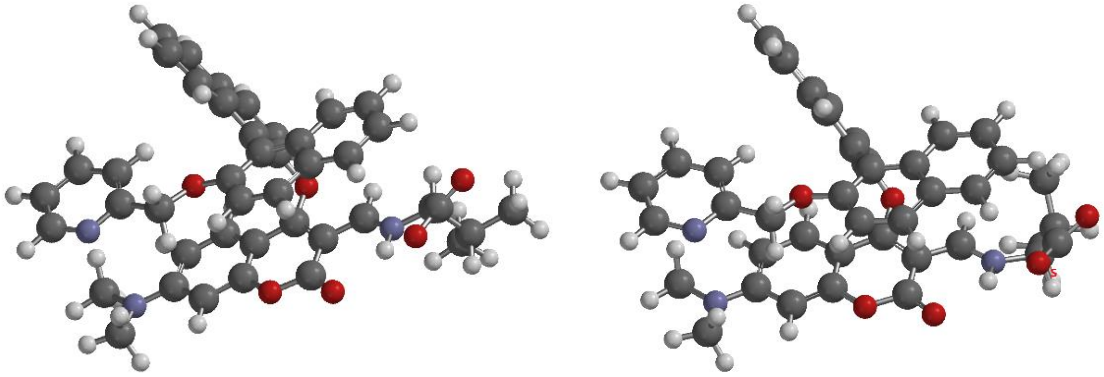

10-D **10**-L

Figure 5- 18. Molecular modeling structures of the proposed intermediates **10**-D and **10**-L.

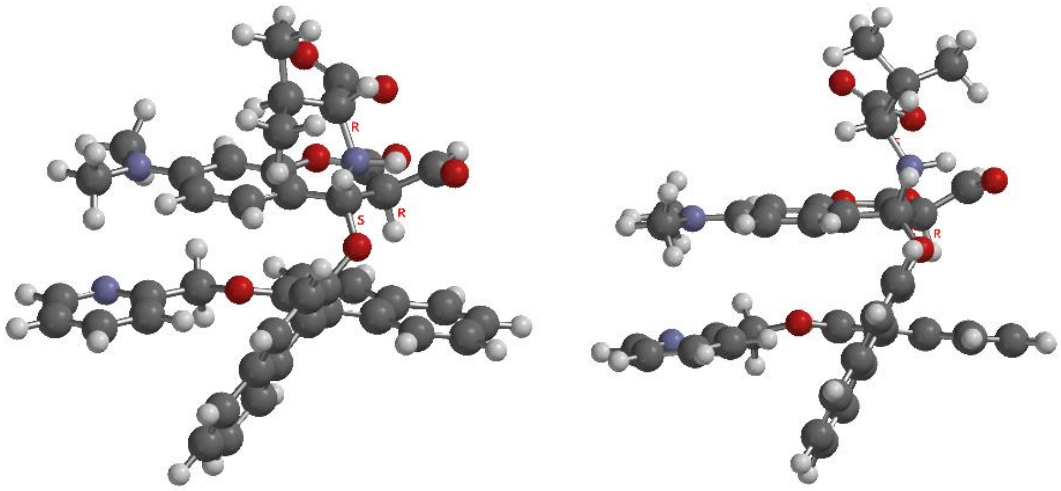

11-D **11**-L

Figure 5- 19. Molecular modeling structures of the proposed intermediates **11**-D and **11**-L.

We also prepared the BINOL-coumarin conjugate (*S*)-**12** from the reaction of **4** with (*S*)-BINOL (**3**) in the presence of K_2CO_3 (Scheme 5-4). The fluorescence response of (*S*)-**12** toward amino acids in aqueous solution (HEPES buffer, pH = 7.4) was studied. In these experiments, (*S*)-**12** (1.0 mM) was used to react with an amino acid for 2 h and then diluted with HEPES to 1.0 x 10^{-5} M before fluorescence measurement.

Scheme 5- 4. Synthesis of the BINOL-Coumarin Conjugate (*S*)-**12**.

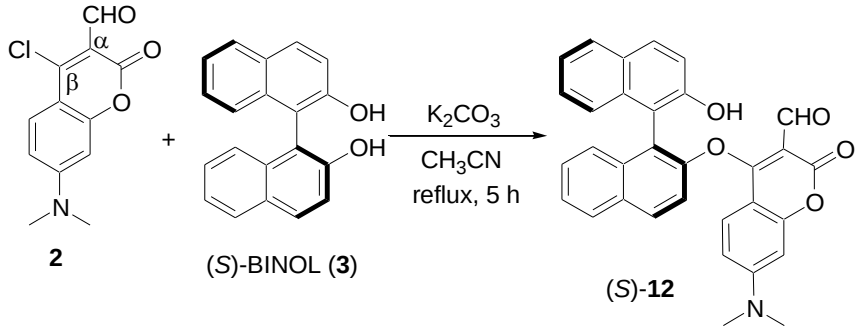

When (*S*)-**12** was excited at = 365 nm in the presence of valine (100 equiv), large fluorescence enhancement at the short wavelength (467 nm) was observed with small enantioselectivity (Figure 5-20a). When (*S*)-**12** was excited at = 467 nm, it gave an emission signal at 555 nm which was greatly reduced upon reaction with the amino acid and little enantioselectivity was observed (Figure 5-20b). Study of (*S*)-**12** demonstrates that the pyridine group of (*S*)- or (*R*)-**6** is necessary for the observed enantioselective fluorescent response when excited at 467 nm. ^{1}H NMR spectroscopic study was conducted for the reaction of (*S*)-**12** (1.0 mM) with D- and L-Val (20 equiv) in DMSO/HEPES (9:1) solution which showed similar reaction pattern as those observed for (*R*)-**6** (Figure S5-11a, b, and d in Appendix).

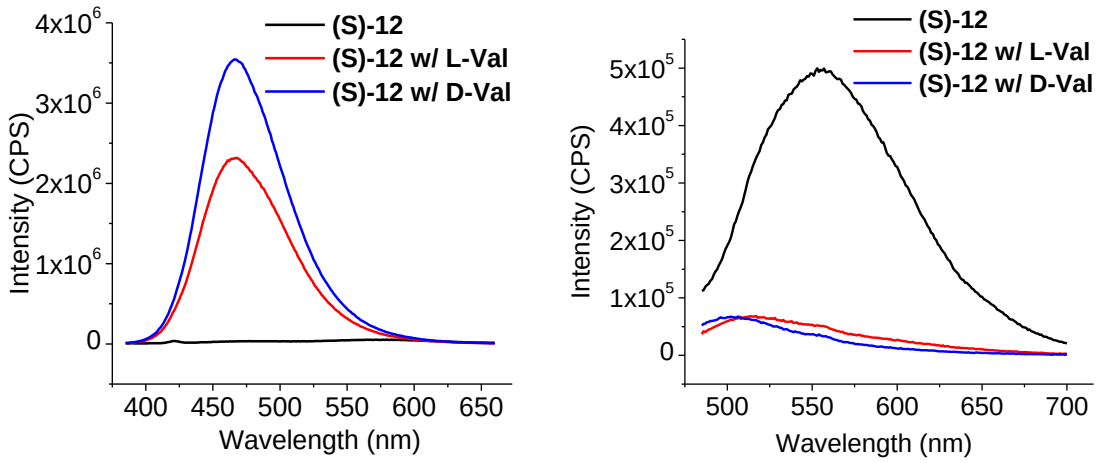

(a) (b)

Figure 5- 20. Fluorescence spectra of (*S*)-**12** (1.0 x 10^{-5} M in HEPES/ 1% DMSO, pH = 7.4) with (a) L- and D-Val (100 equiv) (λ_{exc} = 365 nm, slits: 3/3 nm); (b) L- and D-Val (100 equiv). (λ_{exc} = 467 nm, slits: 3/3 nm)

5.3 Conclusion

A new method to determine both the concentration and enantiomeric composition of a chiral substrate with a single fluorescent probe has been developed. The BINOL-coumarin-based compound **6** was found to show very different fluorescent response toward the enantiomers of amino acids when excited at two different wavelengths. This is the first example to utilize two different excitation wavelengths of a fluorescent probe to determine the two important parameters of a chiral substrate. In comparison with the previously reported BINOL-based fluorescent probes for amino acids which require the addition of Zn^{2+} in order to observe enantioselective fluorescent enhancement,[5] the new probe described in this work has exhibited another advantage since no addition of a metal cation is needed. This makes it more convenient for practical application.

On the basis of a series of spectroscopic studies, we have identified two different pathways for the reaction of the probe with an amino acid. That is, the unsaturated aldehyde unit of **6** can undergo 1,4- and 1,2-addition to give different intermediates and products which contribute to the observed very different fluorescent responses. The 1,2-addition of **6** with an amino acid can generate an iminium ion intermediate with extended conjugation which probably gives the highly enantioselective long wavelength emission. The 1,4-addition of **6** with the amino acid disrupts the conjugation between the naphthalene ring and the coumarin unit contributing to the short wavelength emission. The very different fluorescence responses at the two wavelengths allow the use of this probe to determine both the concentration and enantiomeric composition of amino acids. This is remarkable since normally two independent probes are needed in order to determine both concentration and enantiomeric composition of a chiral substrate except in rare cases.[11] Our study of **6** demonstrates that when two different reactive sites are incorporated into

a fluorescent probe, they may be used to report more information about the substrates in comparison with the conventional probes that normally have only one type of binding or reactive site. This represents a new strategy to design enantioselective fluorescent probes for chiral recognition.

5.4 Experimental Section

5.4.1 General Data

Nitrogen atmosphere was applied to all the synthetic reactions unless otherwise noted and the commercially available compounds were from Sigma Aldrich Chemical Co. or Alfa Aesar. All solvents used in the fluorescence measurement were HPLC or spectroscopic grades. NMR spectra were recorded on a Varian-600 MHz spectrometer, a Bruker-600 MHz spectrometer, and a Bruker-800 MHz spectrometer. Optical rotation measurements were conducted on a Jasco P-2000 digital polarimeter. Chemical shifts for ^{1}H NMR spectra were recorded in parts per million relative to solvent signals at 7.26 ppm for $CDCl_3$, and 2.50 ppm for DMSO-d_6. Chemical shifts for ^{13}C NMR were recorded relative to the centerline of a triplet at 77.16 ppm for $CDCl_3$. Mass spectroscopic analyses were conducted by the University of Illinois at Urbana-Champaign Mass Spectrometry Facility and the Agilent LC-Q-TOF Mass Spectrometer in the Department of Chemistry of University of Virginia. Steady-state fluorescence spectra were recorded with a Horiba FluoroMax-4 spectrofluorometer. UV-Vis spectra were measured by Shimadzu UV-2600 UV-Vis spectrometer. Single crystal X-ray diffraction data were collected on a Bruker Kappa APEXII Duo diffractometer running the APEX3 software suite using the Mo Kα fine-focus sealed tube (λ = 0.71073 Å) for (*S*)-**6**. The structures were solved and refined using the Bruker SHELXTL Software Package within OLEX2. Non-hydrogen atoms were refined anisotropically.

Hydrogen atoms were placed in geometrically calculated positions with Uiso = 1.2Uequiv of the parent atom (Uiso = 1.5Uequiv for methyl).

5.4.2 Sample Preparations

- **UV-vis and fluorescence measurement**

All HEPES buffers used were prepared with 25 mM HEPES and 120 mM NaCl in water (HPLC grade) (pH = 7.4). stock solutions of (*S*)-**6** or (*R*)-**6** (1 mM in DMSO), and 1 – 100 mM amino acids (in HEPES buffer) were all freshly prepared for each measurement. The reaction mixtures (typically 25 μL stock solution of **6** in DMSO and 25 μL amino acid solution in HEPES buffer) were all allowed to stand at rt for 2 h (unless otherwise noted) without nitrogen protection. Then, they were diluted to 1.0×10^{-5} M with the HEPES buffer. UV-Vis or fluorescence measurements were conducted after 1 h, and finished within 30 min.

- **Enantiomeric excess (ee) and concentration correlations**

All HEPES buffers used were prepared with 25 mM HEPES and 120 mM NaCl in water (HPLC grade) (pH = 7.4). stock solutions of (*S*)-**6** or (*R*)-**6** (1 mM in DMSO), and 1 – 100 mM amino acids (in HEPES buffer) were all freshly prepared for each measurement. The *ee* was defined as follows: *ee* = (R - *S*) / (*R* + *S*). Solutions containing each amino acid in HEPES were prepared in 4 mL vial with a certain total concentration for a series of *ee* values. This was performed by mixing two enantiomers of the same concentration in varying ratios and a total volume of 25 μL. The reaction mixtures (typically 25 μL stock solution of **6** in DMSO and 25 μL amino acid solution in HEPES buffer) were all allowed to stand at rt for 2 h (unless otherwise noted) without nitrogen protection. Then, they were diluted to 1.0×10^{-5} M with the HEPES buffer. Fluorescence measurements were conducted after 1 h, and finished within 30 min.

5.4.3 Synthesis and Characterization

- **Synthesis of compound 4**

Scheme 5- 5. Synthesis of compound **4**.

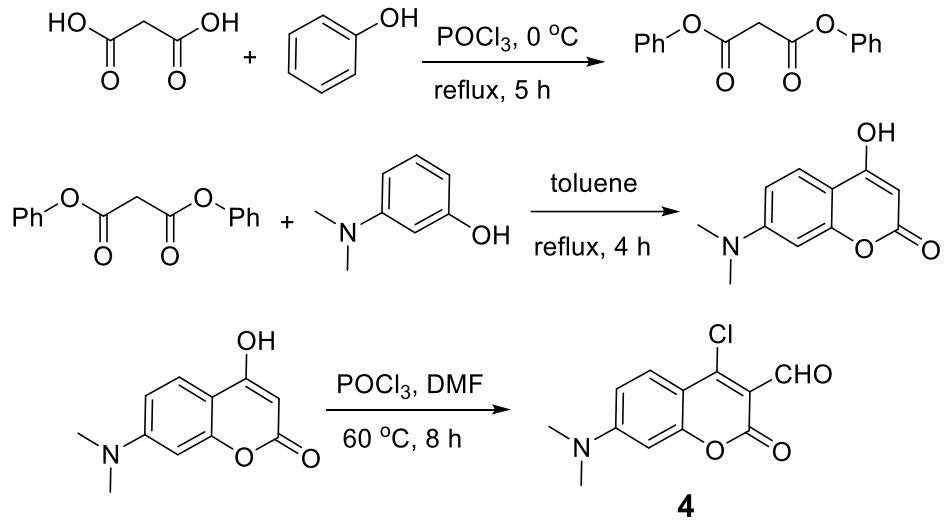

According to the previously reported procedures, compound 4 [4-chloro-7-dimethylaminocoumarin-3-aldehyde], was synthesized in three-step as shown above with a total yield of 50% (8 g), as an orange to red solid powder.

- **Synthesis and characterization of (*S*)-6**

Under nitrogen, (*S*)-BINOL (1.99 mmol, 569 mg), compound **4** (500 mg, 1.99 mmol), compound **5** (503 mg, 1.99 mmol), and K_2CO_3 (4.39 g, 15.98 mmol, 16 equiv) in CH_3CN (20 mL) were bubbled with N_2 for 15 minutes which was then heated at reflux with stirring for 16 h. After filtration to remove the remaining K_2CO_3 and rotary-evaporation to remove the solvent, the residue was purified by column chromatography on silica gel, gradient eluted with hexanes/ethyl acetate (1/1, v) to pure ethyl acetate. Then, recrystallization was carried out with CH_2Cl_2 and hexanes to give (*R*)-**6** as a yellow powder (green to yellow emission under 365 nm UV-Vis lamp)

in 35 % yield (415 mg). ^{1}H NMR (600 MHz, $CDCl_3$) δ 9.72 (s, 1 H), 8.47 (d, J = 6.0 Hz, 1 H), 8.01 (d, J = 12.0 Hz, 1 H), 7.95 (d, J = 6.0 Hz, 1 H), 7.80 (d, J = 6.0 Hz, 1 H), 7.74 (s, 1 H), 7.50 (d, J = 6.0 Hz, 1 H), 7.44 (m, 1 H), 7.35-7.28 (m, 6 H), 7.24 (d, J = 6.0 Hz, 3 H), 7.06 (t, J = 12.0 Hz, 1 H), 6.58 (t, J = 6.0 Hz, 1 H), 6.19 (s, 1 H), 5.90 (d, J = 12.0 Hz, 1 H), 5.15 (t, J = 24.0 Hz, 1 H), 2.93 (s, 6 H). ^{13}C NMR (151 MHz, $CDCl_3$) δ 185.33, 168.29, 157.20, 156.91, 154.64, 153.73, 153.58, 148.67(2), 136.69(2), 134.02, 133.86, 130.93, 130.71, 129.94, 128.98, 128.15(2), 128.07, 127.22, 126.98, 125.85, 125.24, 125.00, 124.16, 122.28(2), 120.65, 120.02, 117.24, 113.31, 109.00, 104.17, 96.77, 70.66, 40.04(2). HRMS: m/z calcd. for $C_{38}H_{28}N_2O_5$ $[M + H]^+$: 593.2076, found 593.2081. $[\alpha]_D^{23}$ = –13.04 (c = 0.059, DMSO).

- **Synthesis and characterization of (*R*)-6**

Under nitrogen, (*R*)-BINOL (0.1479 g, 0.52 mmol) and compound **4** (0.1236 g, 0.49 mmol) with compound **5** (0.1246 g, 0.49 mmol) were stirred in refluxing CH_3CN (10 mL) in the presence of K_2CO_3 (1.0541 g, 7.62 mmol, 15 equiv) for 16 h. After filtration to remove the remaining K_2CO_3 and rotary-evaporation to remove the solvent, the residue was separated and purified by column chromatography on silica gel (loaded by %1 triethylamine in hexanes, gradient elution with hexanes/ethylacetate from 6/1 to 1/1) to give the product (*R*)-**6** as a yellow powder (green to yellow emission under 365 nm UV lamp) in 33% yield. ^{1}H NMR (600 MHz, $CDCl_3$) δ 9.73 (s, 1 H), 8.47 (d, *J* = 6.0 Hz, 1 H), 8.01 (d, *J* = 6.0 Hz, 1 H), 7.95 (d, *J* = 12.0 Hz, 1 H), 7.80 (d, *J* = 12.0 Hz, 1 H), 7.74 (s, 1 H), 7.50 (d, *J* = 6.0 Hz, 1 H), 7.45-7.42 (m, 1 H), 7.36-7.27 (m, 6 H), 7.24 (d, *J* = 6.0 Hz, 3 H), 7.08 (t, *J* = 12.0 Hz, 1 H), 6.60 (t, *J* = 6.0 Hz, 1 H), 6.20 (s, 1 H), 5.93 (d, *J* = 6.0 Hz, 1 H), 5.17 (t, *J* = 24.0 Hz, 1 H), 2.95 (s, 6 H). ^{13}C NMR (151 MHz, $CDCl_3$) δ 185.39, 168.35, 157.19, 154.74, 153.80, 153.66, 148.56, 145.88, 136.94, 134.10, 133.95, 131.01, 130.78, 130.03, 129.08, 128.23, 128.15, 127.30, 127.07, 126.81, 125.92, 125.32, 125.09, 124.26,

122.42, 120.82, 120.09, 117.36, 113.44, 109.11, 104.25, 96.85, 70.66, 69.62, 40.12. HRMS: *m/z* calcd for $C_{38}H_{28}N_2O_5$ [M + H]+: 593.2076, found 593.2075. $[\alpha]_D^{23}$ = +13.76 (*c* = 0.059, DMSO).

- **Synthesis and characterization of (*S*)-7**

(*S*)-**7** were synthesized from (*S*)-BINOL (284 mg, 1 mmol) and 2-bromomethylpyridine HBr salt (254 mg, 1 mmol) and characterized according to the reported method in a yield of 90% (340 mg). ^{1}H NMR spectrum matches with the reported. ^{1}H NMR (600 MHz, $CDCl_3$) δ 8.41 (ddd, J = 4.9, 1.8, 0.9 Hz, 1H), 7.94 – 7.82 (m, 5H), 7.55 (td, J = 7.7, 1.8 Hz, 1H), 7.40 (d, J = 8.8 Hz, 1H), 7.35 (ddd, J = 8.1, 6.7, 1.2 Hz, 1H), 7.34 – 7.24 (m, 3H), 7.25 – 7.17 (m, 2H), 7.14 – 7.10 (m, 1H), 7.07 (dq, J = 8.5, 0.8 Hz, 1H), 7.02 (dt, J = 7.9, 1.0 Hz, 1H), 5.41 (d, J = 14.8 Hz, 1H), 5.30 (d, J = 14.9 Hz, 1H).

- **Synthesis and characterization of (*S*)-12**

(*S*)-BINOL (0.8576 g, 3.0 mmol) and **4** (0.7512 g, 3.0 mmol) were stirred in refluxing CH_3CN (20 mL) in the presence of K_2CO_3 (2.0732 g, 15 mmol) for 5 h. After filtration to remove the remaining K_2CO_3 and roto-evaporation to remove the solvent, the residue was purified by column chromatography on silica gel (gradient elution with hexanes/ethyl acetate from 1:5 to 1:1) to give the product (*S*)-**12** as a yellow powder in 66% yield (0.9916 g). ^{1}H NMR (600 MHz, $CDCl_3$) *δ* 9.90 (s, 1 H), 7.86 (m, 4 H), 7.57 (s, 1 H), 7.43 (t, *J* = 18.0 Hz, 1 H), 7.33 (m, 3 H), 7.27 (m, 3 H), 7.13 (m, 2 H), 6.37 (m, 1 H), 6.35 (s, 1 H), 3.03 (s, 6 H). ^{13}C NMR (151 MHz, $CDCl_3$) *δ* 187.37, 166.11, 157.56, 157.55, 155.65, 152.81, 152.60, 134.29, 133.92, 130.65, 130.64, 130.23, 130.22, 128.93, 128.17, 128.16, 127.56, 127.47, 126.41, 125.77, 125.76, 125.36, 125.35, 124.43, 123.06, 119.19, 113.89, 110.27, 105.10, 97.10, 40.21, 40.20. HRMS: *m/z* calcd for $C_{32}H_{24}NO_5$: 502.1654, found 502.1657. $[\alpha]_D^{23}$ = –230.50 (*c* = 0.05, DMSO).

5.4.4 X-Ray Analysis Data of (*S*)-6 (Pu_XW4_SW2)

- **Crystal preparation**

100 mg of (*S*)-**6** was fully dissolved with 10 mL of CH_2Cl_2 (ACS grade) in a round bottom flask and then 150 mL hexanes (ACS grade) was slowly added into the flask and a clear yellow solution was generated in the rubber septum sealed flask. After 4 hours very tiny crystal started forming in the solution. And in 3 days a good amount of crystals clusters was generated before a needle like crystal was picked to be analyzed by the X-ray differentiator.

- **Crystal structure determination**

A single crystal of (*S*)-**6** was coated with Paratone oil and mounted on a MiTeGen MicroLoop. The X-ray intensity data were measured on a Bruker Kappa APEXII Duo system equipped with an Incoatec Microfocus IμS (Cu K_α, λ = 1.54178 Å) and a multi-layer mirror monochromator.

The frames were integrated with the Bruker SAINT software package[12] using a narrow-frame algorithm. Data were corrected for absorption effects using the Multi-Scan method (SADABS).[12] The structure was solved and refined using the Bruker SHELXTL Software Package[13] within APEX3[12] and OLEX2,[14] using the space group P 2_1, with Z = 2 for the formula unit, $C_{38}H_{28}N_2O_6$. Non-hydrogen atoms were refined anisotropically. The OH hydrogen atoms were placed in sensible hydrogen bonding positions and refined isotropically with restraints on the O-H distances. All other hydrogen atoms were placed in geometrically calculated positions with $U_{iso} = 1.2U_{equiv}$ of the parent atom ($U_{iso} = 1.5U_{equiv}$ for methyl). A global RIGU restraint was used on the anisotropic displacement parameters of the atoms due to the extremely low resolution and redundancy of the diffraction from this crystals. During the refinement, some severely

disordered solvent was located in the crystal lattice that could not be adequately modeled with or without restraints. Thus, the structure factors were modified using the PLATON SQUEEZE[15] technique, in order to produce a "solvate-free" structure factor set. PLATON reported a total electron density of 94 e^- and total solvent accessible volume of 258 Å[14].

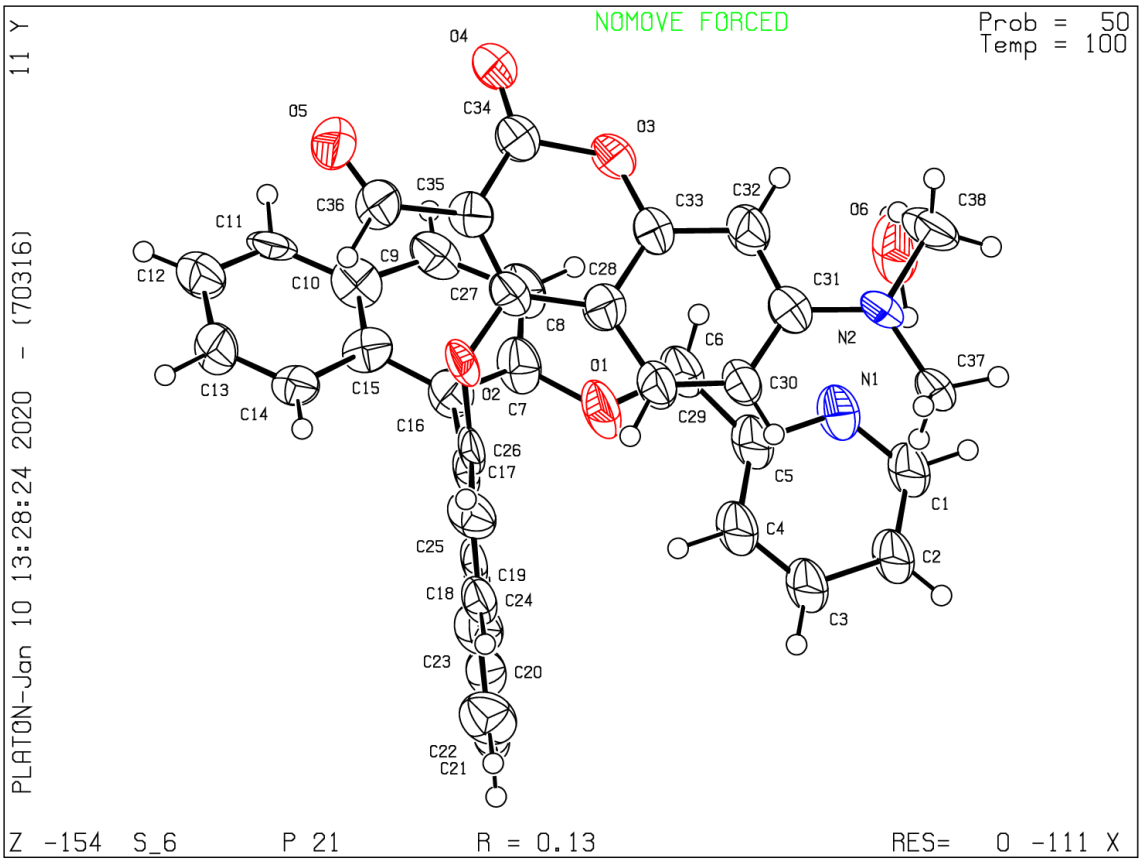

Figure 5- 21. The ORTEP view (thermal ellipsoid plot) of the molecules of (*S*)-**6** (CDCC: 1976654), showing ellipsoids at 50% ellipsoid contour probability level.

Table 5- 3. Sample and crystal data summary for (*S*)-**6**.

	(*S*)-**6**
CCDC	1976654
Chemical formula	$C_{38}H_{30}N_2O_6$
FW (g/mol)	610.64
T (K)	100(2)
λ (Å)	1.54178
Crystal size (mm)	0.017 x 0.030 x 0.171
Crystal habit	yellow needle
Crystal system	monoclinic
Space group	P 2_1
a (Å)	13.329(10)
b (Å)	7.430(3)
c (Å)	16.909(8)
α (°)	90
β (°)	93.69(4)
γ (°)	90
Z	2
ρ_{calc} (g/cm^3)	1.214
μ (mm^{-1})	0.671
θ range (°)	2.62 to 44.48
Index ranges	$-11 \leq h \leq 12$ $-6 \leq k \leq 6$ $-14 \leq l \leq 15$
Reflns coll.	4191
Ind. reflns	2530 [R(int) = 0.3411]
Data / restraints / parameters	2530 / 375 / 367
Goodness-of-fit on F^2	0.875
R_1 [I>2σ(I)]	0.1310
wR_2 [all data]	0.4721

5.5 References

1 Selected reports on enantioselective fluorescent recognition of free amino acids:

(a) Pagliari, S.; Corradini, R.; Galaverna, G.; Sforza, S.; Dossena, A.; Montalti, M.; Prodi, L.; Zaccheroni, N.; Marchelli, R. Enantioselective fluorescence sensing of amino acids by

modified cyclodextrins: role of the cavity and sensing mechanism. *Chem. Eur. J*. **2004**, *10*, 2749–2758.

(b) Corradini, R.; Paganuzzi, C.; Marchelli, R.; Pagliari, S.; Sforza, S.; Dossena, A.; Galaverna, G.; Duchateau, A. Fast parallel enantiomeric analysis of unmodified amino acids by sensing with fluorescent β-cyclodextrins. *J. Mater. Chem*. **2005**, *15*, 2741–2746.

(c) Wang, H.; Chan, W. H.; Lee, A. W. M. Cholic acid-based fluorescent probes for enantioselective recognition of trifunctional amino acids. *Org. Biomol. Chem*. **2008**, *6*, 929–934. (d) Kwong, H. L.; Wonga, W. L; Lee, C. S.; Yeung, C. T.; Teng, P. F. Zinc(II) complex of terpyridine-crown macrocycle: A new motif in fluorescence sensing of zwitterionic amino acids. *Inorg. Chem. Commun.* **2009**, *12*, 815–818.

(e) Yang, L.; Qin, S.; Su, X.; Yang, F.; You, J.; Hu, C.; Xie, R.; Lan, J. 1,1′-Binaphthyl-based imidazolium chemosensors for highly selective recognition of tryptophan in aqueous solutions. *Org. Biomol. Chem*. **2010**, *8*, 339–348.

(f) Tang, L.; Wei, G.; Nandhakumar, R.; Guo, Z. Facile synthesis of the uryl Pendant Binaphthol Aldehyde and Its Selective Fluorescent recognition of tryptophan. *Bull. Korean Chem. Soc*. **2011**, *32*, 3367–3371.

(g) X. Yang, X. Liu, K. Shen, C. Zhu, Y. Cheng. A chiral perazamacrocyclic fluorescent sensor for cascade recognition of Cu(II) and the Unmodified α-Amino Acids in Protic Solutions. *Org. Lett*. **2011**, *13*, 3510-3513.

(h) L. Song, S. Wang, N. A. Kotov, Y. Xia. Nonexclusive fluorescent sensing for l/d enantiomers enabled by dynamic nanoparticle-nanorod assemblies. *Anal. Chem*. **2012**, *84*, 7330−7335.

(i) Li, F.; Li, L.; Yang, W.; Zheng, L.-S.; Zheng, Z.-J.; Jiang, K.; Lu, Y.; Xu, L.-W. Chiral Ar-BINMOL-derived salan as fluorescent sensor for recognition of CuCl and cascade discrimination of α-amino acids. *Tetrahedron Lett*. **2013**, *54*, 1584–1588.

(j) B. Aswathy, G. Sony. Fluorescence turn-on recognition of chiral amino acids using dye incorporated *β*-CD functionalized AuNPs assembly. *J. Luminescence* **2014**, *154*, 541–548.

(k) Feng, H.-T.; Zhang, X.; Zheng, Y.-S. Fluorescence turn-on enantioselective recognition of both chiral acidic compounds and α-amino acids by a chiral tetraphenylethylene macrocycle amine. *J. Org. Chem.* **2015,** *80*, 8096–8101.

(l) Wang, C.; Zeng, C.; Zhang, X.; Pu, L. Enantioselective fluorescent recognition of amino acids by amide formation: an unusual concentration effect. *J. Org. Chem.* **2017,** *82*, 12669–12673.

(m) Zeng, C.; Zhang, X.; Pu, L. Enantioselective fluorescent imaging of free amino acids in living cells. *Chem. Eur. J.* **2017,** *23*, 2432–2438.

2 Reviews on fluorescent detection of amino acids:

(a) Zhou, Y.; Yoon, J. Recent progress in fluorescent and colorimetric chemosensors for detection of amino acids. *Chem. Soc. Rev*. **2012**, *41*, 52–67.

(b) Wang, J.; Liu, H. –B.; Tong, Z.; Ha, C. –S. Fluorescent/luminescent detection of natural amino acids by organometallic systems. *Coord. Chem. Rev*. **2015**, *303*, 139–184.

3 Reviews on enantioselective fluorescent recognition:

(a) Pu, L. Fluorescence of organic molecules in chiral recognition. *Chem. Rev*. **2004**, *104*, 1687–1716.

(b) Leung, D.; Kang, S. O.; Anslyn, E. V. Rapid determination of enantiomeric excess: a focus on optical approaches. *Chem. Soc. Rev*. **2012**, *41*, 448–479.

(c) Accetta, A.; Corradini, R.; Marchelli, R. Enantioselective sensing by luminescence. *Top. Curr. Chem*. **2011**, *300*, 175–216.

(d) Zhang, X.; Yin, J.; Yoon, J. Fluorescence and colorimetric chemosensors for fluoride-ion detection. *Chem. Rev*. **2014**, *114*, 4918-4959.

(e) B.T. Herrera, S. L. Pilicer, E. V. Anslyn, L. A. Joyce, C. Wolf. Optical analysis of reaction yield and enantiomeric excess: a new paradigm ready for prime time. *J. Am. Chem. Soc*. **2018**, *140*, 33, 10385-10401.

4 Feuster, E. K.; Glass, T. E. Detection of amines and unprotected amino acids in aqueous conditions by formation of highly fluorescent iminium ions. *J. Am. Chem. Soc*. **2003,** *125* (52), 16174-16175

5 (a) Z. Huang, S. S. Yu, K. L. Wen, X. Q. Yu, L. Pu. Zn(ii) promoted dramatic enhancement in the enantioselective fluorescent recognition of functional chiral amines by a chiral aldehyde. *Chem. Sci*. **2014**, *5*, 3457– 3462.

(b) Zhu, Y.-Y.; Wu, X.-D.; Gu S.-X.; Pu, L. Free amino acid recognition: a bisbinaphthyl-based fluorescent probe with high enantioselectivity. *J. Am. Chem. Soc*. **2019**, *141*, 175-181.

6 Wang, Q.; Wu, X.; Pu, L. Excitation of one fluorescent probe at two different wavelengths to determine the concentration and enantiomeric composition of amino acids. *Org. Lett*. **2019**, *21*, 9036-9039.

7 (a) A BINOL-coumarin-based compound showed enantioselective fluorescent response to an amino alcohol in THF: J. Jiao, X. Liu, X. Mao, J. Li, Y. Cheng, C. Zhu. A coumarin-based chiral fluorescence sensor for the highly enantioselective recognition of phenylalaninol. *New J. Chem.* **2013**, *37*, 317—322.

(b) A representative example of coumarin-based fluorescent probes: Yue, Y.; Huo, F.; Ning, P.; Zhang, Y.; Chao, J.; Meng, X.; Yin, C. Dual-site fluorescent probe for visualizing the metabolism of Cys in living cells. *J. Am. Chem. Soc.* **2017**, *139*, 3181−3185.

(c) A recent review of coumarin-based small-molecule fluorescent chemosensors: Cao, D.; Liu, Z.; Verwilst, P.; Verwilst, P.; Koo, S.; Jangjili, P.; Kim, J. S.; W. Lin, W. Coumarin-based small-molecule fluorescent chemosensors. *Chem. Rev*. **2019**, *119*, 10403-10519.

8 (a) Liu, J.; Sun, Y.-Q.; Huo, Y.; Zhang, H.; Wang, L.; Zhang, P.; Song, D.; Shi, Y.; Guo, W. Simultaneous fluorescence sensing of Cys and GSH from different emission channels. *J. Am. Chem. Soc*. **2014**, *136*, 574-577.

(b) Zhang, P.; Liu, W.; Niu, G.; Xiao, H.; Wang, M.; Ge, J.; Wu, J.; Zhang, H.; Li, Y.; Wang, P. Coumarin-based boron complexes with aggregation-induced emission. *J. Org. Chem*. **2017**, *82*, 3456-3462.

9 (a) Fernández-Mateos, E.; Maciá, B.; Yus, M. Catalytic enantioselective addition of alkyl Grignard reagents to aliphatic aldehydes. *Adv. Syn. Cat.* **2013**, *355*, 1249-1254.

(b) Dong, C.; Song, T.; Bai, X.-F.; Cui, Y.-M.; Xu, Z.; Xu, L.-W. Enantioselective conjugate addition of cyanide to chalcones catalyzed by a magnesium-Py-BINMOL complex. *Cat. Sci. Tech*. **2015**, *5*, 4755-4759.

10 (a) Kuo, P.-Y.; Yang, D.-Y. Design of a coumarin-based triketone as a fluorescent protecting group for primary amines. *J. Org. Chem*. **2008**, *73*, 6455-6458.

(b) Kim, Y.; Mulay, S. V.; Choi, M.; Yu, S. B.; Jon, S.; Churchill, D. G. Exceptional time response, stability and selectivity in doubly-activated phenyl selenium-based glutathione-selective platform. *Chem. Sci*. **2015**, *6*, 5435-5439.

11 (a) Yu, S.; Plunkett, W.; Kim, M.; Pu, L. Simultaneous determination of both the enantiomeric composition and concentration of a chiral substrate with one fluorescent sensor. *J. Am. Chem. Soc*. **2012**, *134*, 20282–20285.

(b) Wen, K. –L.; Yu, S. –S.; Huang, Z.; Chen, L. –M.; Xiao, M.; Yu, X. –Q.; Pu, L. Rational design of a fluorescent sensor to simultaneously determine both the enantiomeric composition and the concentration of chiral functional amines. *J. Am. Chem. Soc*. **2015**, *137*, 4517-4524.

12 Bruker (2012). *Saint; SADABS; APEX3*. Bruker AXS Inc., Madison, Wisconsin, USA.

13 Sheldrick, G. M. (2015). *Acta Cryst*. A**71**, 3-8.

14 Dolomanov, O. V.; Bourhis, L. J.; Gildea, R. J.; Howard, J. A. K.; Puschmann, H. *J. Appl. Cryst.* (2009). **42**, 339-341.

15 Spek, A. L. *Acta Crystallogr. Sect C: Struct. Chem*. **2015**, C71, 9-18.

Chapter 6

Highly Selective Fluorescent Recognition of Cysteine by a BINOL-Coumarin-Based Probe in the Aqueous Phase

6.1 Introduction

Biothiols such as cysteine (Cys), homocysteine (Hcy), and glutathione (GSH) are associated with innumerable bioprocesses.[1, 2, 3, 4] These intracellular thiols play crucial roles in maintaining biological redox homeostasis[5] as well as monitoring unusual cellular activities, abnormal bioreactions, and various diseases.[6, 7] Even though these thiol molecules have similar structures, they play different roles in biological systems. So far, myriad studies have been reported in detecting these molecules that are still difficult to be distinguished. Therefore, specific detection of one thiol molecule has gained increasing attention over the decades. Fluorescent molecular probes have come out as an ideal and practical tool for selective biological molecular sensing and imaging. Compared to other probing techniques,[8, 9, 10, 11, 12, 13, 14, 15] fluorescent spectroscopy is more readily available owing to its advantages[16, 17] such as easily accessible instrumentation, low detection limit, high selectivity, real-time imaging ability and potential for further in vivo mapping of substrates in living cells as well as in organisms. A number of fluorescent probes are found to be able to discriminate Cys, Hcy, and GSH in vitro or in vivo.[18, 19, 20, 21, 22] Designing and synthesis of new fluorescent probes with higher selectivity and lower detection limit for these biothiols still remained great challenge due to their similar structures including the thiol, amine, and carboxylic acid functional groups. Coumarin-based fluorescent sensors[23, 24, 25, 26, 27, 28, 29, 30, 31] with aldehyde functionality like **1a**[32] and **lb**[33, 34] have

achieved some selectivity for either Cys and Hcy or GSH via different reaction pathways that resulted in various fluorescence signal change of the sensors. However, the coumarin aldehyde-based fluorescent probes like **1a** and **1b** cannot distinguish Cys from Hcy.

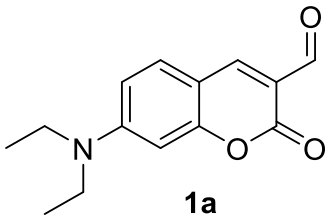

1a

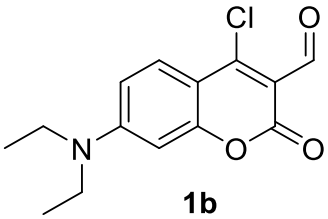

1b

We have recently linked the chiral BINOL unit with the coumarin aldehyde to make a fluorescent probe **2** that not only shows highly enantioselective fluorescent response toward a number of amino acids, but can also allow the determination of both concentration and enantiomeric composition in the absence of Zn^{2+}. The reactions of the probe with the amino acids were conductedat a concentrated condition (0.5 mM of the probe) initially in the DMSO and aqueous HEPES buffer solution which were then diluted with the buffer solution to 10 μM of **2** for fluorescence measurement.[35, 36] We also examined the treatment of the probe **2** with various amino acids directly at the diluted aqueous solutions (10 μM of **2**, 1% DMSO), which showed selective fluorescence enhancement with Cys but not with other thiols and amino acids at 461 nm. We have conducted a mechanistic investigation which has revealed the chemistry behind the high selectivity and sensitivity of this unique BINOL-pyridine-coumarin conjugated probe for cysteine. Herein, we report the results of this research.

6.2. Results and Discussion

6.2.1. Synthesis and Background of the Probe

A one-pot reaction of (*S*)-BINOL, a coumarin chloride **4**[37] and a 2-bromomethylpyridine salt **5** in the presence of K_2CO_3 in acetonitrile was refluxed for 16 h, and the BINOL-coumarin

conjugate (*S*)-**2** was obtained as a yellow solid in 35% yield after a flash silica column (Scheme 1).[34] The fluorescent probe (*S*)-**2** was found to be enantioselective for a number of amino acids over 530 nm when excited at 467 nm and sensitive to the amino acids at 465 nm when excited at 365 nm under an aqueous condition (DMSO/HEPES buffer= 1/99, v, pH=7.4, 10 μM). But in the reaction of (*S*)-**2** with the amino acids needs to be conducted at a concentrated solution (DMSO/HEPES buffer= 1/99, v, 0.5 mM of the probe and 25 mM of the amino acids) for 2 hours before it was diluted to 10 μM with the HEPES buffer for fluorescence measurement. When the probe (*S*)-**2** was applied to react with all the amino acids under dilute conditions (10 μM of **2**), it showed selective discrimination of thiols.

Scheme 6- 1. Synthesis of the BINOL-Pyridine-Coumarin Conjugate (*S*)-**2**.

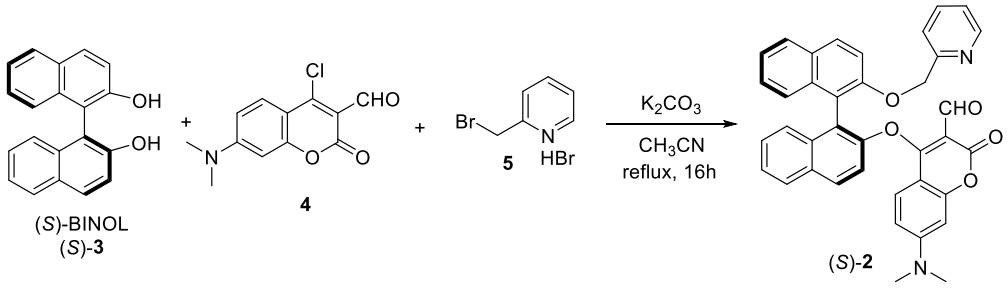

6.2.2. Fluorescent Selectivity for Thiols at Room Temperature

Under the dilute condition, the probe (*S*)-**2** (10 μM, DMSO/HEPES buffer = 1/99 v, pH=7.4) was reacted with 22 amino acids (0.3 mM, including the thiols) at room temperature for 8 hours. Then the fluorescence responses of (*S*)-**2** towards the substrates such as glutathione (GSH), L-homocysteine (Hcy) and L-cysteine (Cys), and those without the mercapto groups such as L-alanine (Ala), L-arginine (Arg), L-asparagine (Asp), L-glutamine (Gln), L-glutamic acid(Glu), L-glycine (Gly), L-histidine (His), L-leucine (Leu), L-lysine (Lys), L-methionine

(Met), L-phenylalanine (Phe), L-proline (Pro), L-serine (Ser), L-threonine (Thr), L-tryptophan (Trp), L-tyrosine (Tyr), L-valine (Val), and cystine (Cst, the oxidized form of L-cysteine), as well as the N-ethylmaleimide (NEM, an irreversible inhibitor of the thiols at the neutral pH) were examined. In absence of the thiols, as shown in Figure 6-1a, (*S*)-**2** shows emission at 570 nm upon excitation at 362 nm indicating good conjugation of the binaphthol unit and the coumarin unit. Figure 6-1b shows that only in the presence of thiols (30 equiv.) was there fluorescence enhancement. Among these thiols, Cys produced the most significant enhancement at 461 nm for (*S*)-**2**. No noticeable increase of the fluorescent signal with other amino acids bearing no mercapto groups was observed. When an equivalent amount of the thiol inhibitor NEM was added into the reaction mixture, the fluorescent signals at 461 nm were depressed for the thiols. This demonstrates that the mercpto groups played a key role in the selective fluorescent response of (*S*)-**2** for cysteines. The excitation spectra for the reaction of (*S*)-**2** with L-Cys (Figure 6-1d) show that for the emission at 461 nm an excitation peak at 362 nm was observed and for the emission at 570 nm a broad excitation signal from 400 nm to 460 nm was observed with a highest intensity at 415 nm. Therefore, the emissions over 500 nm were also studied for the reaction of (*S*)-**2** with all the analytes with excitation at 362 nm or 415 nm which however showed little change in fluorescence (Figure 6-1a and c). We also examined the fluorescence response of (*S*)-**2** toward the enantiomeric amino acids D-Cys and D-Lys but the same fluorescence changes as their L-enantiomers were observed at 461 nm and 570 nm, and no obvious enantioselectivity could be detected when (*S*)-**2** was used under the same diluting condition.

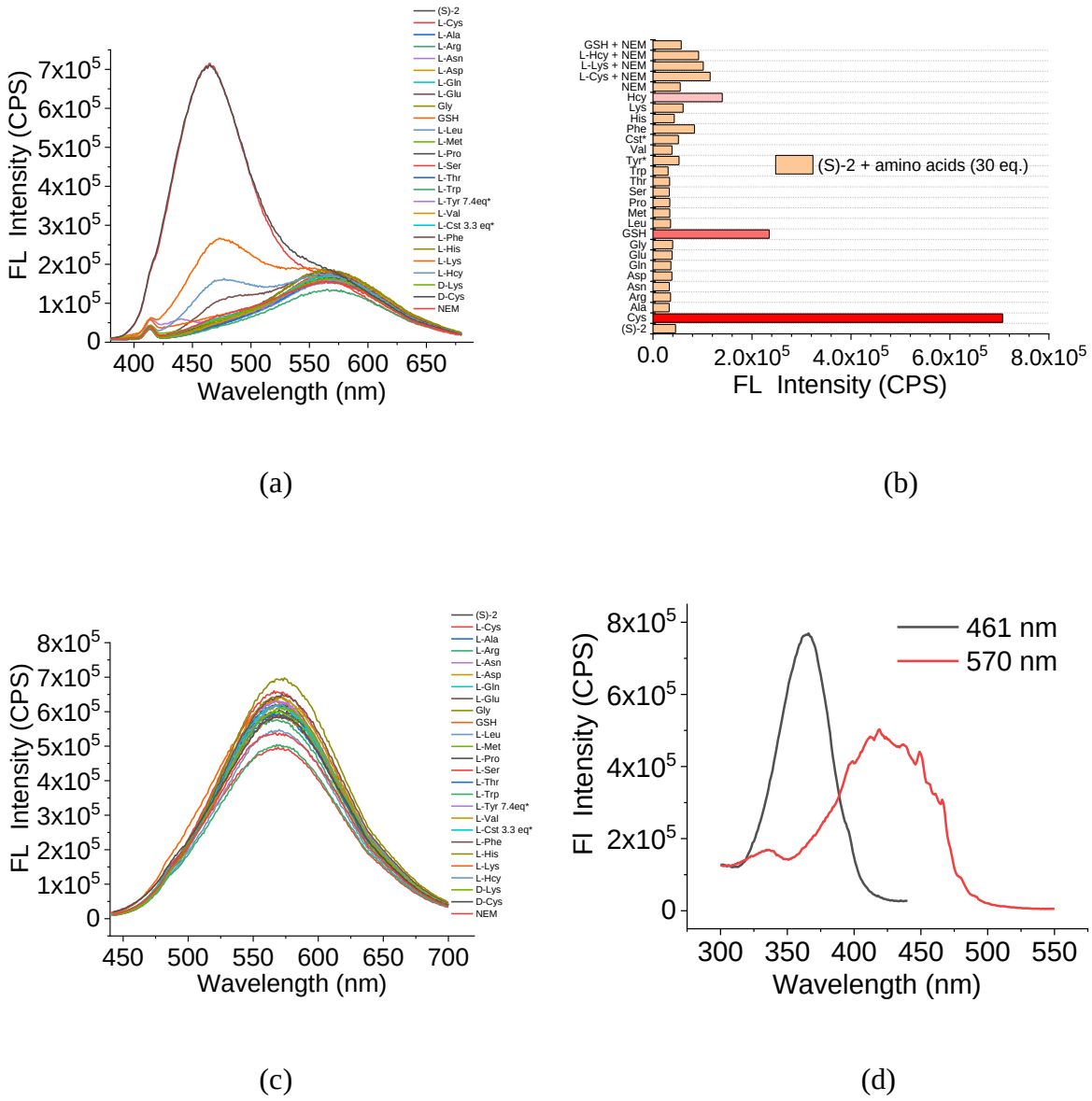

Figure 6- 1. The fluorescence spectra of (*S*)-**2** (1.0×10^{-5} M in HEPES/ 1% DMSO, pH = 7.4) with various substrates (30 equiv) at the excitation wavelength of 362 nm (a) and 415 nm (c) as well as the bar graph of the fluorescence intensities at 461 nm (b) from graph a, and the fluorescence excitation spectra of (*S*)-**2** (1.0×10^{-5} M in HEPES/ 1% DMSO, pH = 7.4) with L-Cys (30 equiv) (d) (reaction time: 8h, at room temperature, $\lambda_{em1} = 461$ nm, $\lambda_{em2} = 570$ nm, slits: 3/3 nm, and the saturated concentrations were applied to calculate the reacted concentrations for Tyr and Cst since both tyrosine and cystine had very low solubilities)

6.2.3. Fluorescent Selectivity for Thiols by Controlling the Temperature

In order to reduce the reaction time for the interaction of (*S*)-**2** with the amino acids under the dilute conditions, we studied the reactions at 37 °C. As shown in Figure 6-2a, when (*S*)-**2** was heated at 37 °C for 1.5 h to 4 h, there was continuous increase of the fluorescence at 461 nm and no equilibrium was reached during this time. In order to obtain a stable fluorescence measurement, we have chosen to let the reaction of (*S*)-**2** with L-Cys to proceed at 37 °C for 3 h and then quench the reaction in ice bath for fluorescence measurement. As shown in Figure 6-2b, the chilled solution for the reaction of (*S*)-**2** with L-Cys gave stable fluorescence response at either 461 nm or 570 nm. This procedure was also applied for the reactions of (*S*)-**2** with L-Hcy, L-His, and L-Lys and stable fluorescence responses were also observed (See Figure S6-4 in Appendix).

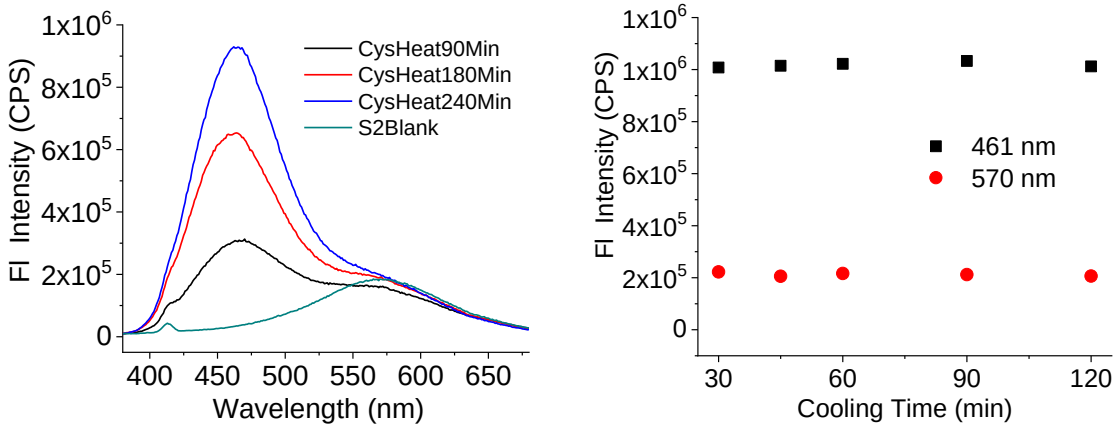

(a) (b)

Figure 6- 2. The fluorescence spectra of (*S*)-**2** (1.0×10^{-5} M in HEPES/ 1% DMSO, pH = 7.4) with L-Cys (30 equiv) (a) as well as the fluorescence intensities versus cooling time of the same sample in graph a after it was cooled in an ice bath (b). (reaction time: 3h, at 37 °C, λ_{exc} = 362 nm, slits: 3/3 nm)

The fluorescence response of (*S*)-**2** towards various amount of L-Cys was studied by heating at 37 °C for 3 h and quenching in ice bath as described above. The fluorescence intensity at 461nm increased as the concentration of L-Cys increased. A good linear relationship was found between the fluorescence intensity (at 461 nm) versus the concentration of L-Cys in the HEPES buffer (Figure 6-3b).

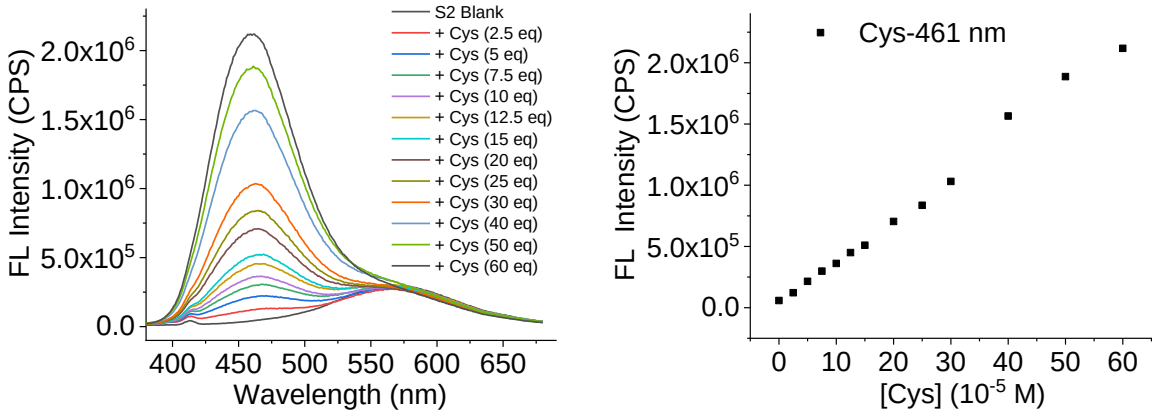

(a) (b)

Figure 6- 3. The fluorescence spectra of (*S*)-**2** (1.0×10^{-5} M in HEPES/ 1% DMSO, pH = 7.4) with L-Cys (0-60 equiv) (a) as well as the fluorescence intensities at 461 nm versus the L-Cys concentrations (b). (reaction time: 3h, at 37 °C, fluorescence spectra were measured after the reactions were quenched at 0 °C for at least 3 mins, λ_{exc} = 362 nm, slits: 3/3 nm)

From three independent fluorescence titrations for the reaction of (*S*)-**2** with L-Cys, the detection limit was determined to be 1.60 µM (See Figure S5 in the Appendix) which is much lower than the normal cellular Cys concentration level (30–200 µM).[38, 39] The probe could also possibly be used to quantify the cysteine concentration over 200 µM to implicate the abnormal level of Cys cellularly. Figure 6-4a shows the fluorescence responses of (*S*)-**2** (10 µM) at 461

nm toward all the analytes (100 μM) under the same conditions as describe above. At this relative lower concentration, a high chemoselectivity for cysteine (the selectivity $s=(F_{Cys}-F_0)/(F_a-F_0)$ was calculated to be ranged from 4.2 to 252.0 according to Figure 6-4a) was achieved among all competitive amino acids and thiols. The fluorescence response of (*S*)-**2** toward Cys (10 equiv.) in the presence of additional analytes (2-30 equiv.) was investigated in order to determine the specificity of (*S*)-**2** towards Cys. It was found that GSH would greatly influence the fluorescence signal at 462 nm when there's over 20 μM glutathione in presence of 100 μM cysteine; Hcy and Phe started to interrupt the chemo-selectivity at the concentration of 150 μM; and over 200 μM of additional Lys, His, Trp, and Arg would also impact the results. However, the other amino acids at even 300 μM couldn't affect the fluorescent signal generated by (*S*)-**2** and Cys (100 μM).

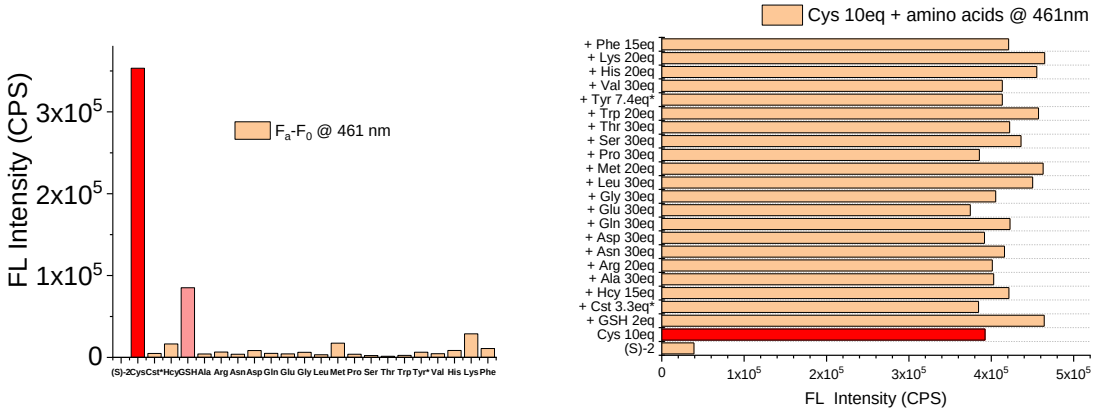

(a) (b)

Figure 6- 4. The fluorescence enhancement (bar graphs) of (*S*)-**2** (1.0×10^{-5} M in HEPES/ 1% DMSO, pH = 7.4) with various amino acids (10 equiv) (a) as well as the changes of the fluorescence intensities of (*S*)-**2** (1.0×10^{-5} M) towards Cys (10 equiv) in the presence of the competing analytes (b). (reaction time: 3h, at 37 °C, fluorescence spectra were measured after the reactions were quenched at 0 °C for at least 3 mins, λ_{exc} = 362 nm, slits: 3/3 nm, and any

concentrations of the competing analytes under 30 equiv could be taken as the tolerance limitation of the substrate, and the saturated concentrations were applied to calculate the reacted concentrations for Tyr and Cst since both tyrosine and cystine had very low solubilities)

Since glutathione played a very competitive role with cysteine, its concentration versus the fluorescent intensity was further investigated and the selectivity for Cys over GSH at different concentrations was also examined. When the concentration of GSH increased to 100 μM and more, (S)-2 showed enhanced emission at 471 nm when excited at 362 nm (Figure 6-5a). When taking the fluorescence enhancement ratio $[(F_{Cys}-F_0)461nm/(F_{GSH}-F_0)471nm]$ as the chemo-selectivity, in the normal cellular Cys concentration range (30–200 μM) high chemo-selectivity from 2.3 to 7.0 was observed (Figure 6-5b). When the concentration of the thiols was over 250 μM, the chemoselectivity was reduced to 1.7 (Figure 6-5b.). This demonstrates that probe **2** could be useful to selectively detect Cys among various analytes including amino acids and thiols especially with a relatively low GSH concentration (e.g. 200 μM or less).

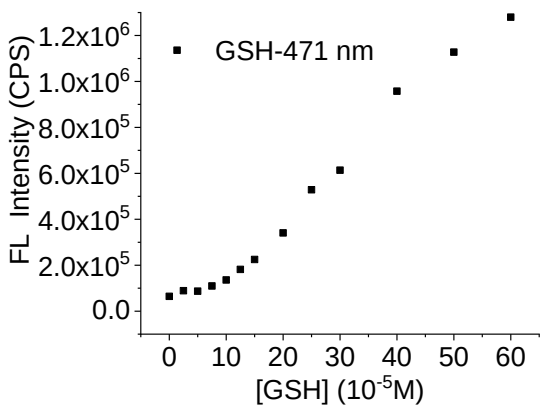

(a)

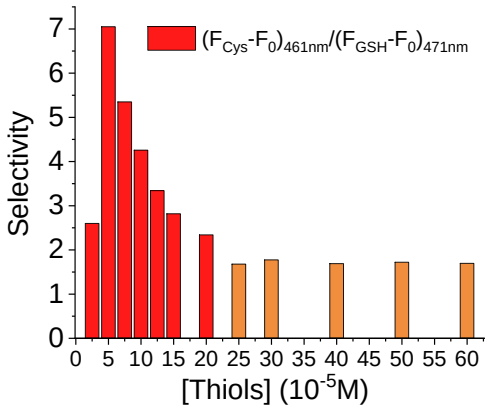

(b)

Figure 6- 5. The fluorescence response of (*S*)-**2** (1.0×10^{-5} M in HEPES/ 1% DMSO, pH = 7.4) with GSH (0-60 equiv) (a) as well as the fluorescence intensities ratios of L-Cys to GSH at various concentrations (b). (reaction time: 3h, at 37 ^{o}C, λ_{exc} = 362 nm, slits: 3/3 nm)

6.2.4 Mechanism Investigation

It was reported that the coumarin-based fluorescent sensor **1a** was selective for Cys and Hcy over other thiols by favorably forming a 6- or 5-membered ring thiazolidine or thiazinane to give quenched fluorescence at 488 nm (λ_{ex}=448 nm, in EtOH).[32] Another sensor analog **1b** could possibly generate the amino-coumarin products with Cys and Hcy via a thiol-halogen S_NAr reaction pathway while with GSH it might undergo an intramolecular aldimine condensation to form a cyclic iminium cation.[33] However, very limited solid evidence (eg. ^{1}H NMR, ^{13}C NMR and high-resolution mass spectroscopy) has been ever reported to confirm the reaction mechanism proposal of the coumarin-based fluorescent sensors like **1b** even though a similar mechanism was explored in a BODIPY-based fluorescent sensor with ^{1}H NMR.[19] A better understanding of the mechanism for the reaction of these coumarin-based fluorescent sensors with thiols should help further development of these probes. We have used various spectroscopic methods such as UV-Vis spectroscopy, high-resolution mass spectroscopy, and ^{1}H NMR to investigate the reaction pathways of (*S*)-**2** with the thiols.

We first studied the UV-vis spectroscopic responses (Figure 6-6a.) of (*S*)-**2** toward the thiols under the same reaction conditions as the fluorescence study (See Figure 6-1a.) and the reactions were conducted at room temperature for 8 hours. As the concentration of L-Cys increased, (*S*)-**2** showed decreased absorption at 420 nm accompanied with increased absorption at 370 nm. This is consistent with the fluorescence excitation spectra, indicating a disrupted

conjugation of the BINOL with coumarin and the formation of new coumarin units with the absorption at 370 nm. When (*S*)-**2** and various amino acids were heated at 37 °C for 3 h, only cysteine would largely enhance the absorption at 370 nm while greatly reduce the absorption at 420 nm (Figure 6-6b). GSH, Hcy, Lys, and Val had less influence on the absorptions at both 420 nm and 370 nm than Cys, which could explain the high selectivity of (*S*)-**2** for cysteine.

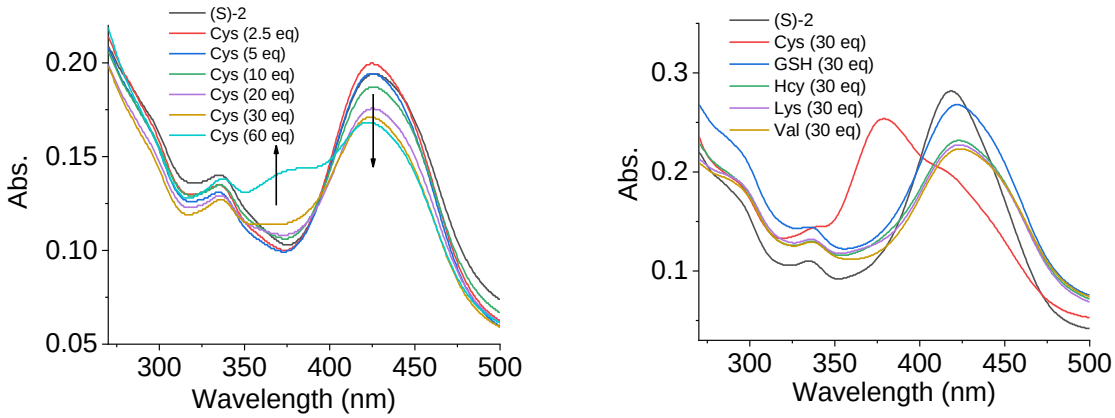

(a) (b)

Figure 6- 6. The UV-Vis spectra of (*S*)-**2** (1.0×10^{-5} M in HEPES/ 1% DMSO, pH = 7.4) with L-Cys (0-60 equiv, reaction time: 8h, at room temperature) (a) as well as with Cys, GSH, Hcy, and Lys (all 30 equiv, reaction time: 3h, 37 °C) (b).

In order to understand how the probe reacts with the thiols to give the observed fluorescence responses, we then conducted a high resolution ESI-mass spectroscopic analysis on the reaction of (*S*)-**2** with cysteine. Because the excess amount of HEPES in the reaction mixture interfered with the mass analysis, we acquired the mass spectra for the reaction of (*S*)-**2** (1.9 mM) in DMSO with L-Cys (5 mM) in HEPES (25 mM, pH = 7.4, 120 mM NaCl) by direct diluting it with water instead of HEPES. In the mass spectrum of the product mixture of (*S*)-**2** with L-Cys

(Figure S6-20 in the Appendix), we have identified peaks at m/z = 378.1486 for **6** (calcd for **6**+H^+: 378.1494), 337.0867 for intermediate **7** or **7'** (calcd for **7**+H^+ or **7'**+H^+: 337.0858), 440.0904 for compound **8** or **8'** (calcd for **8**+H^+ or **8'**+H^+: 440.0950), and 696.2162 for product **9** (calcd for **9**+H^+: 696.2168) respectively.

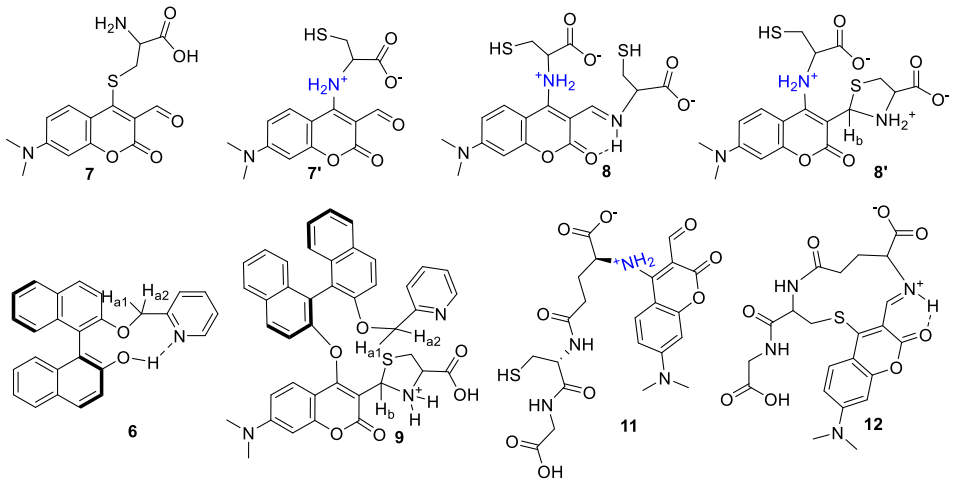

Figure 6- 7. Product and intermediate structures formed from the reaction of (*S*)-**6** with L-Cys and GSH.

We further studied the reaction of (*S*)-**2** with cysteine by ^{1}H NMR spectroscopic analysis. As shown in Figure 6-8, when (*S*)-**2** (1 mM) was treated with L-Cys (3 mM), the probe was continuously consumed from 10 mins to 4 hours and almost no probe left by 4 hours (Figure 6-8b-f). In these spectra, the signals at δ 11.83 can be attributed to the protonated amine group of the product **7'** or **8** (**8'**), and the two singlets at δ 9.81 and 9.83 are assigned to the aldehyde proton signal of the product **7** and **7'**. After 20 h, there was about 90% conversion of **7 or 7'** to the corresponding products **8** or **8'** (Figure 6-8g). In Figure 6-8g, the signals at δ 5.17, 6.88, 7.00, 7.88, 8.42, and 9.60 can be attributed to the product **6** by comparing with the ^{1}H NMR spectrum

of **6**, prepared from the reaction of **3** with **5**.[39] The multiplet signals at δ 5.30 is assigned to the methylene protons of the product **9** which might exist as a diastereomeric mixture because of the newly formed chiral carbon center (See Figure S6-10c in Appendix). The singlet at δ 10.33 is the ammonium proton signal of L-cysteine.

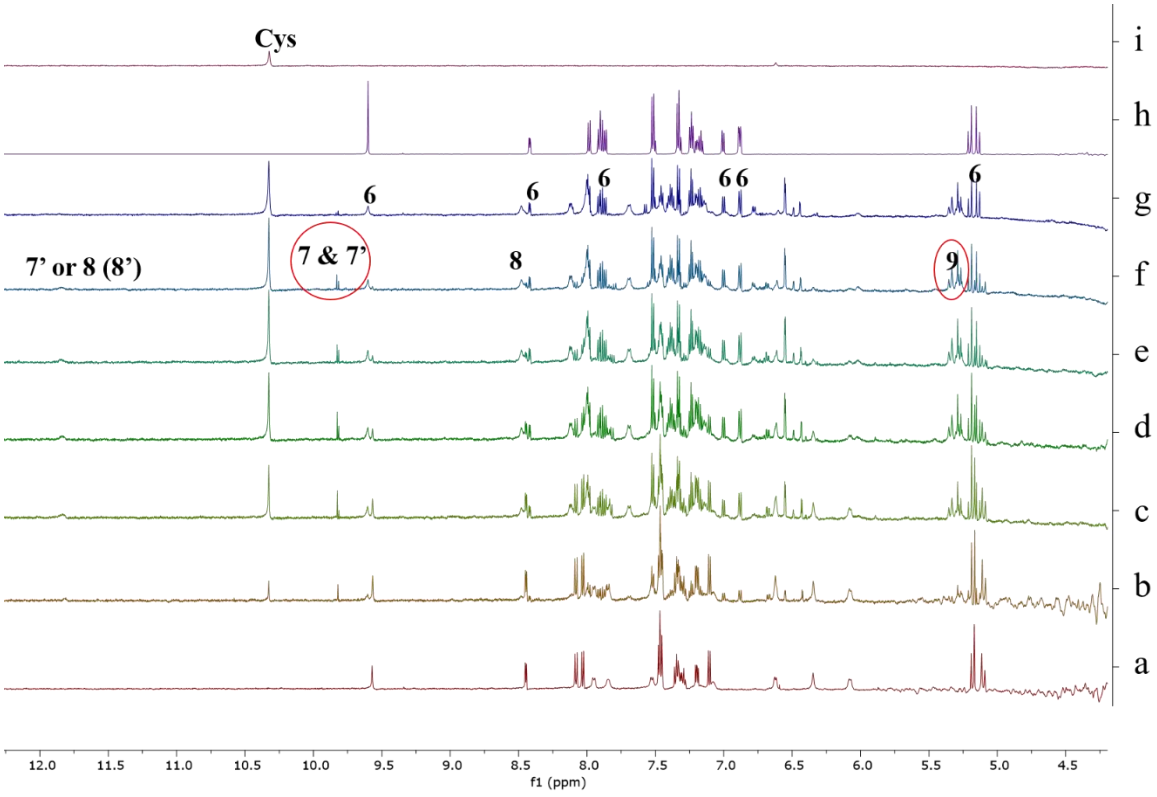

Figure 6- 8. ^{1}H NMR spectra of (*S*)-**2** (1.0 mM in DMSO-d_6) (a) with L-Cys (3 equiv) in H_2O for 0 min (a), 10 min (b), 1 h (c), 2 h (d), 3 h (e), 4 h (f), 20 h (g), (*S*)-**6** (h) and L-Cys (i). [DMSO-d_6: H_2O = 9: 1 (v). The full spectra are given in Figure S6-10a in the Appendix for chapter 6]

In order to provide additional characterization for compounds **7'** and **8'**, we studied the reaction of **4** with L-Cys (0.9 equiv) in DMSO-d_6 (Scheme 6-2). After 50 h at rt, the ^{1}H NMR spectrum of the reaction mixture showed complete consumption of **4** with the formation of

compound **7'** as the major product (Figure S6-15 in Appendix, other byproducts could not be separated from the mixture).[40] The protonated amine group of the product **7'** was found to give broad peaks at δ 11.75-11.90 very close to that in Figure 6-8b-f. The aldehyde proton signal of **7'** was observed at δ 9.70 (in 9:1 DMSO-d_6/D_2O) or 9.72 (in pure DMSO-d_6) very close to that in Figure S6-12 in the Appendix. When more L-Cys (3 equiv) was added to the solution of **7'**, the aldehyde signal of **7'** almost disappeared with the appearance of a signal at δ 5.27 that could be assigned to the Hb of the thiazolidine product **8'** (Figure S6-16 in the Appendix).[32]

Scheme 6- 2. Reaction of **4** and L-Cys.

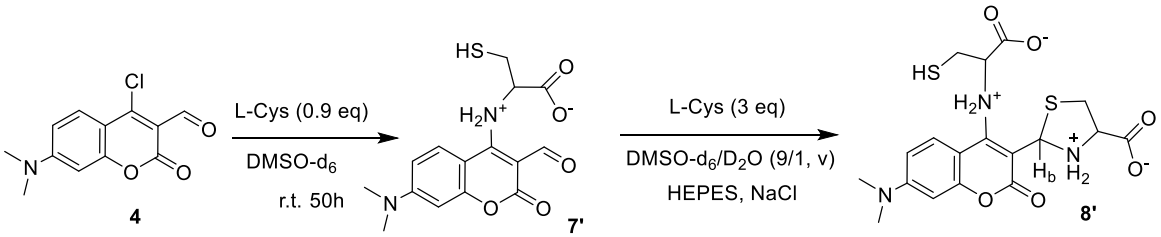

To reduce the byproduct amount and further confirm the formation of **8'** a direct reaction of **4** with 3 equiv of L-Cys was carried out in DMSO-d6. After 20 h and 22 h, the ^{1}H NMR spectrum shows an almost complete consumption of **4** and formation of **8** and **8'** with the minimized existence of the aldehyde proton signals. While the strong signals of the protonated amine groups observed at 11.85-11.95 (Figure S6-16,17 in the Appendix, 20 h, in pure DMSO-d6), and the imine proton of intermediate **8** also seen at δ 8.36-8.49. The signals at 5.34 and 5.27 (20 h, in pure DMSO-d6) and the signals 5.31 and 5.25 (22 h, in DMSO-d6/D_2O) could be attribute to the proton Hb on the newly formed thiazolidine ring of **8'** (Figure S6-16,17 in the Appendix for chapter 6). Therefore, in Figure 8c-g the overlapped multiplet signals at 5.30 could be assigned to **9** as well as **8'**.

Another ^{1}H NMR study of (*S*)-**2** (1 mM) with cysteine (3 mM) in DMSO-d6 and D_2O was carried out to confirm assignment of the active protons. In the spectra (Figure S6-12 in the Appendix) very similar signals could be found as those in Figure 6-8 except the acidic protons (the protonated amine groups of **7'**, **8**, **8'** and Cys). After 3 hours 1 equiv of the reaction product **7'** (in DMSO-d6/D_2O, 9/1) was added into the ^{1}H NMR analysis sample and studied after 30 mins. It was found even though there's a minor difference of the aldehyde protons between the new mixtures (δ 9.80) and the previous mixtures (δ 9.83, while the δ 9.83 signal still maintained in the new mixtures) no other obvious new signal was observed in spectrum e and f compared to spectrum d (in Figure 6-9), which confirmed the formation of **7'** in the reaction process. To continue monitor the reaction another spectrum was taken overnight. The disappearance of almost all the aldehyde protons around δ 9.80 was observed while a new signal appeared at 5.34, which validated the cyclic thiazolidine formation.

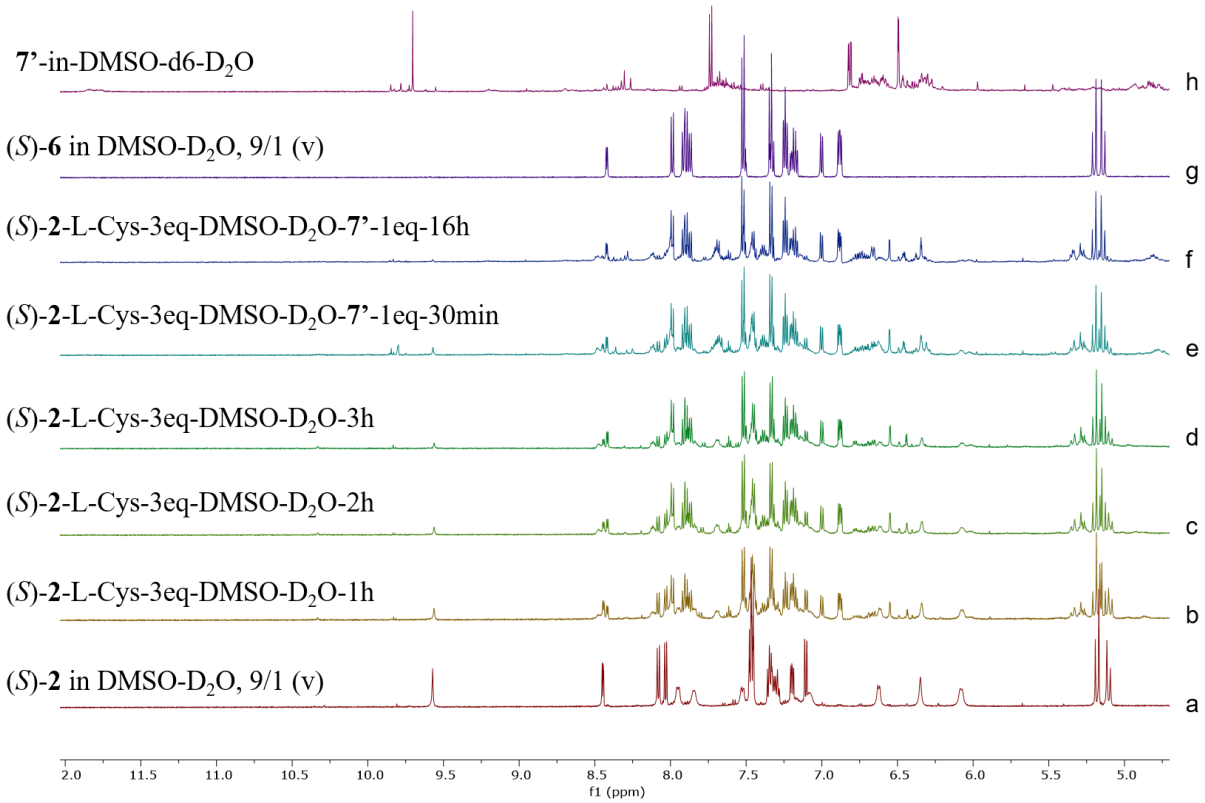

Figure 6- 9. ^{1}H NMR spectra of (*S*)-**2** (1.0 mM in DMSO-d_6) with L-Cys (3 equiv) in HEPES (D_2O, 25 mM HEPES, 120 mM NaCl, pD=7.4). [reaction time: 0 – 3 h. DMSO: HEPES = 9:1 (v)] (a)-(d), **7'** (1 equiv.) added in to the mixture (e)-(f), **6** (g), and **7'** (h) (1.0 mM in DMSO-d6 and HEPES) The full spectra are given in Figure S6-12 in the Appendix for chapter 6]

To explore the selectivity among thiols, on one hand, similar NMR studies (Figure S6-11e-h and Figure S6-13 in Appendix) were also carried out for the reaction of (*S*)-**2** (1 mM) with GSH (2-3 mM), and within hours (*S*)-**2** was all consumed via 1,4 addition and transformed into **6**, **11** and **12** which were detected by the mass spectroscopy (Figure S6-21 in the Appendix). But almost no 1, 2 addition products were observed. Product **11** probably has a similar emission property with **7'** while **12** only emits fluorescence at 550 nm[33]. This explains why when the probe

was treated with GSH, the absorbance decreased the least at 420 nm and some increased absorbance was seen over 450 nm while the emission at 570 nm changed almost the least among all the analytes. The optical property of **12** made up the part lost caused by the disruption of (*S*)-**2**. On the basis of a 1H NMR experiment, we found that the reaction of (*S*)-**2** with Hcy (1 equiv) was much less favorable than it with Cys (1 equiv) (Figure S6-11i-n in the Appendix) under the same condition. After 20 h, there was still a large amount of S-2 remained for the reaction with Hcy. Unlike that observed for the reaction with Cys, (*S*)-**2** was completely consumed in less than 4 h (Figure 6-8f). This could lead to the much greater fluorescence enhancement of (*S*)-**2** with Cys than with Hcy. This is very different from the previously reported probe 1a which gave similar fluorescence enhancement for the reaction with Cys and Hcy.

Scheme 6- 3. A proposed reaction pathway of **2** and Cys.

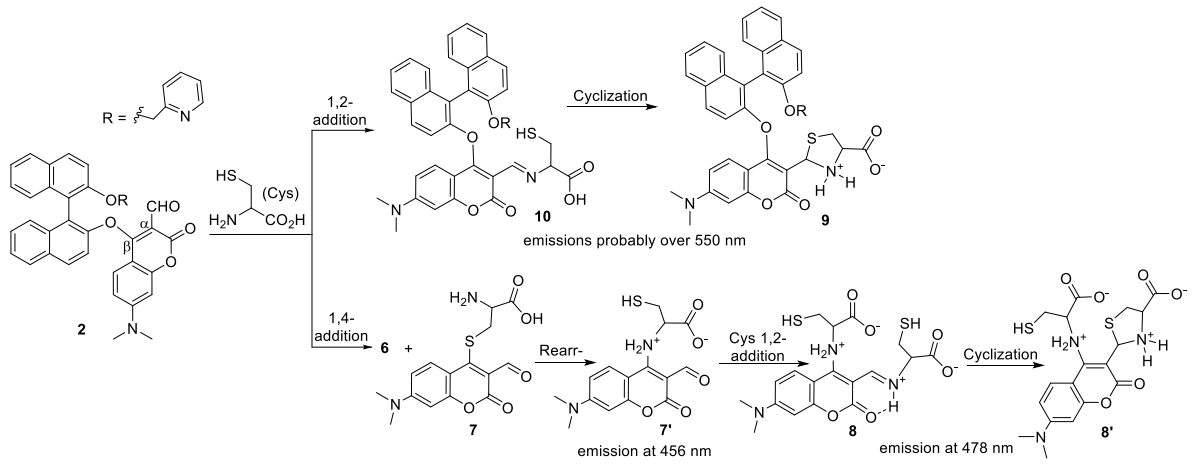

At last, the ^{1}H NMR spectra of (*S*)-**2** (in DMSO-d6) and L-Cys (in H_2O) were stacked together to probe the reaction process. The 1, 4 addition occurred at the beginning (10 minutes, 1.0 equiv cysteine) with the formation of **6**, **7'** (or **7**) when new aldehyde proton peaks appeared at δ 9.82 and 9.83 and the peaks of **6** started to rise in the spectra (Figure S6-14 in Appendix).

With continuous titration more intensive 1,4 addition reaction was seen as well as 1,2 addition could also be observed at some extent (quartets at δ 5.30). Almost a full consumption of (*S*)-**2**, at least two type of aldehyde protons formation (δ 9.82 and 9.83), and appearance of Hb (δ 5.26, 5.28 mixed with the quartets at δ 5.30) were observed 4 hours after 3 equiv of cysteine was all titrated into the reaction mixture. Therefore, a reaction pathway is proposed based on all the mechanism exploration (Scheme 6-3). After treated with cysteine probe **2** would prefer a 1,4 addition to produce product **6** and **7'** that might further undergo another 1, 2 addition to generate **8** and **8'**. Compounds **7'**, **8** and **8'** show emissions around 465 nm which could account for the enhanced emission for the reaction of S-2 with L-Cys when excited at 362 nm (Figure S6-10).

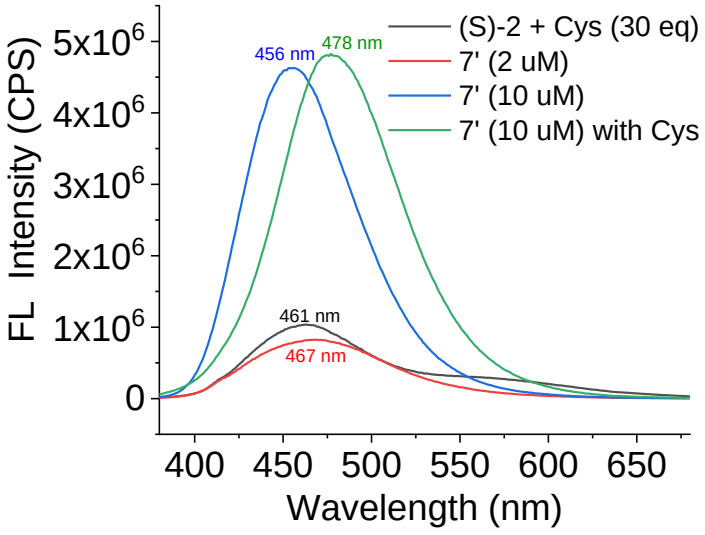

Figure 6- 10. Fluorescence spectra of the crude product mixtures of **7'** and **7'** with Cys (3 equiv). [in DMSO-d_6 (90%) and HEPES in D_2O (10%) and diluted with HEPES buffer in H_2O to 2 - 10 μM, λ_{exc} = 362 nm, slits: 3/3 nm]

Reaction of S-2 with L-Cys via 1,2 addition could produce the imine intermediate **10** before cyclization to form product **9** if enough cysteine was added. Both **9** and **10** maintained the conjugation of the BINOL and coumarin units, which would make up the long wavelength emission loss caused by the 1, 4 addition reaction since very intensive peaks of **9** or **10** were observed in the high resolution ESI-mass spectrum of the reaction between (S)-2 and L-Cys (Figure S6-20 in the Appendix). We also proposed reasonable reaction pathways (Scheme 6-4 and Figure S6-22 in the Appendix) for (*S*)-**2** with Hcy or GSH according to the mechanism investigation above.

Scheme 6- 4. A proposed reaction pathway of **2** and GSH.

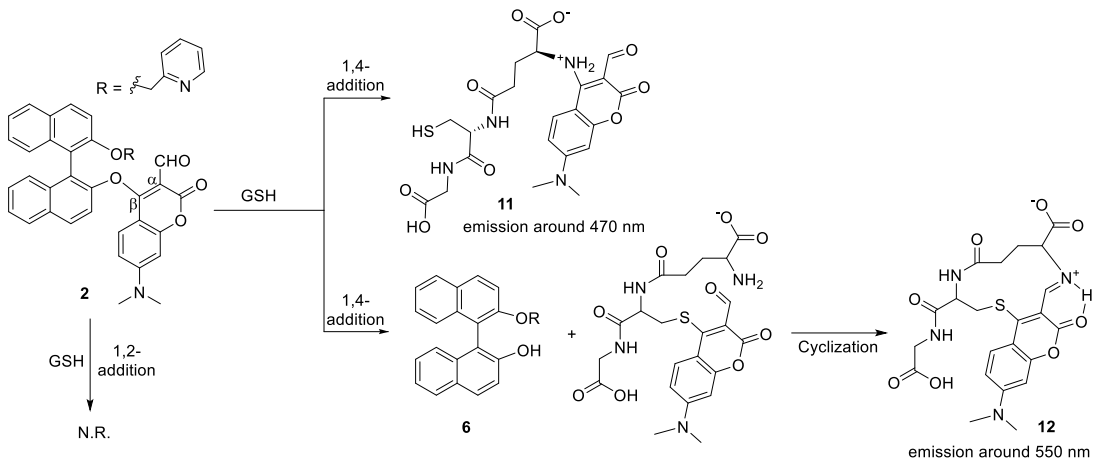

6.3 Conclusion

The BINOL-coumarin probe (*S*)-**2** was found to show highly selective fluorescence enhancement at 461 nm with cysteine when its 10 μM solution in neutral buffer solution was directly interacted with various amino acid substrates. This is very different from the previous observation that when a more concentrated solution of (*S*)-**2** (0.5 mM) was first reacted with the amino acid substrates and then diluted to 10 μM, it showed highly enantioselective fluorescent

responses at >520 nm toward a variety of amino acids. When 10 μM solution of (*S*)-**2** was used, the reaction of the amino acids with the probe was much slower and only cysteine was able to generate large fluorescence enhancement at 461 nm. Among all the competing analytes cysteine was selectively detectable at both normal and abnormal cellular cysteine concentrations of mammals. The observed high selectivity of the coumarin-based dual-site sensor for cysteine was investigated by techniques such as UV-vis, high-resolution mass, and ^{1}H NMR spectroscopy.[32, 33] Probes derived from coumarin[41, 42] has been validated to be useful for selective detection of cysteine in living cells with enhanced near-infrared (NIR) fluorescence. The related biological research for thiols is undergoing to apply various new probes including **2** to multiple types of living cells.

6.4 Experimental Section

6.4.1 General Data

Nitrogen atmosphere was applied to all the synthetic reactions unless otherwise noted and the commercially available compounds were from Sigma Aldrich Chemical Co. and Alfa Aesar. All solvents used in the fluorescence measurement were HPLC or spectroscopic grades. NMR spectra were recorded on a Bruker-600 MHz spectrometer. Chemical shifts for ^{1}H NMR spectra were recorded in parts per million relative to solvent signals at 7.26 ppm for $CDCl_3$, and 2.50 ppm for DMSO-d_6. Chemical shifts for ^{13}C NMR were recorded relative to the centerline of a septet at 39.52ppm for DMSO-d_6, and a triplet at 77.16 ppm for $CDCl_3$. Mass spectroscopic analyses were conducted by the University of Illinois at Urbana-Champaign Mass Spectrometry. UV-Vis spectra were measured by Shimadzu UV-2600 UV-Vis spectrometer. Steady-state fluorescence spectra were recorded with a Horiba FluoroMax-4 spectrofluorometer with a chamber at room temperature. All HEPES buffers used were freshly prepared with 25 mM

HEPES (pH = 7.4) and 120 mM NaCl in water (HPLC grade) every time. For all fluorescence measurements, the excitations were at 362 nm and 415 nm, the slit widths were 3 nm.

6.4.2 Methods for Fluorescent Measurements at Different Temperatures

Stock solutions of (*S*)-**2** (1 mM in DMSO), and 10 mM amino acids (in HEPES buffer) were all freshly prepared for each measurement. The reaction mixtures (typically 20 μL stock solution (*S*)-**2** in DMSO, 1.96 mL HEPES buffer, and 20 μL the amino acids in HEPES buffer for 10 equivalences of the amino acids to the sensor amount.) were sequentially added into a 4 mL vial in a total volume of 2 mL. The reaction samples were allowed to be at room temperature for 8 h without nitrogen protection before conducting fluorescent measurement at room temperature.

If needed the reaction samples were allowed to be heated at 37 ^{o}C for 3 h without nitrogen protection. Then, they were placed into an ice bath to for 30 minutes before transferring into quartz cuvettes. The cuvettes with samples were put into ice bath for at least 3 minutes before fluorescence measurements. A single measurement should be finished within 1 minute after the cuvette had been taken out of the ice bath, otherwise re-put the cuvette into the ice bath for at least 3 minutes before conducting another fluorescence measurement.

6.4.3 Detection Limit

The detection limit was evaluated based on the fluorescence titration. Under the heating-cooling conditions, a good linear relationship between the fluorescence intensity and the Cys concentration could be obtained from 0 to 200 μmol/L (R^2 = 0.99979). The detection limit was then calculated with the equation (IUPAC): detection limit=3δ/m, where δ is the standard deviation of blank measurements; m is the averaged slope between intensity versus sample concentrations (n=3).

6.4.4 Synthesis and Characterization

- **Synthesis of compound 4 and (*S*)-2**

According to the same procedures as described for compound **4** and (*S*)-**6** in chapter 5 of this thesis, compound **4** and (*S*)-**2** was synthesized and characterized.

6.5 References

1 A. Pastore, A. Alisi, G. di Giovamberardino, A. Crudele, S. Ceccarelli, N. Panera, C. Dionisi-Vici, V. Nobili, *Int. J. Mol. Sci.* **2014**, *15*, 21202.

2 N.M. Giles, A.B. Watts, G.I. Giles, F.H. Fry, J.A. Littlechild, C. Jacob, *Chem. Biol.* **2003**, *10*, 677–693.

3 L. B. Poole, *Free Radical Biol. Med.* **2015**, *80*, 148-157.

4 L. Turell, D. A. Vitturi, E. L. Coitino, L. Lebrato, M. N. Moller, C. Sagasti, S. R. Salvatore, S. R. Woodcock, B. Alvarez and F. J. Schopfer, *J. Biol. Chem.* **2017**, *292*, 1145-1159.

5 N. Brandes, S. Schmitt and U. Jakob, *Antioxid. Redox Signaling* **2009**, *11*, 997-1014.

6 S. Jung, X. Chen, J.S. Kim, J. Yoon, *Chem. Soc. Rev.* **2013**, *42*, 6019–6031.

7 L. Zhai, Y. Tu, Z. Shi, S. Pu, *Spectrochim. Acta. Part. A* **2019**, *218*, 171-177.

8 D.R. Jenke, D.S. Brown, *Anal. Chem.* **1987**, *59*, 1509-1512.

9 A. Waseem, M. Yaqoob, A. Nabi. *Curr. Pharmaceut, Anal.* **2013**, *9*, 363-395.

10 A. Nezamzadeh-Ejhieh, H.S. Hashemi, *Talanta* **2012**, *88*, 201-208.

11 J.S. Stamler, J. Loscalzo. *Anal, Chem.* **1992**, *64*, 779-785.

12 I.M. Moodie, R.D. George, *J. Chromatogr. A* **1976**, *124*, 315-319.

13 M.L. Polan, W.J. McMurray, S.R. Lipsky, S. Lande, *Biochem. Biophys. Res. Commun.* **1970**, *38*, 1127-1133.

14 M.R. Hormozi-Nezhad, E. Seyedhosseini, H. Robatjazi, *Sci. Iran.* **2012**, *19*, 958-963.

15 S.C. Liang, H. Wang, Z.M. Zhang, X. Zhang, H.S. Zhang, *Spectrochim. Acta A Mol. Biomol. Spectrosc.* **2002**, *58*, 2605-2611.

16 L. Pu, *Accounts of chemical research* **2012**, *45*, 150-163.

17 W. Chen, X. Wu, L. Pu, *Tetrahedron Letters* **2017**, *58*, 1781–1783.

18 X. F. Yang, Y. X. Guo, R. M. Strongin, *Angew. Chem. Int. Ed.* **2011**, *50*, 10690 –10693.

19 L.Y. Niu, Y.S. Guan, Y.Z. Chen, L.Z. Wu, C.H. Tung, Q.Z. Yang, *J. Am. Chem. Soc.* **2012**, *134*, 18928-18931.

20 Z. Guo, S.W. Nam, S. Park, J. Yoon, *Chem. Sci.* **2012**, *3*, 2760-2765.

21 S.Y. Lim, K.H. Hong, D.I. Kim, H. Kwon, H.J. Kim, *J. Am. Chem. Soc.* **2014**, *136*, 7018−7025.

22 Y. Kim, M. Choi, S.V. Mulay, M. Jang, J.Y. Kim, W.H. Lee, S. D.G. Churchill, *Chem. Eur. J.* **2018**, *24*, 5623 –5629.

23 X. Dai, Q.H. Wu, P.C. Wang, J. Tian, Y. Xu, S.Q. Wang, J.Y. Miao, B.X. Zhao, *Biosensors and Bioelectronics* **2014**, *59*, 35–39.

24 L. He, Q. Xu, Y. Liu, H. Wei, Y. Tang, W. Lin, *ACS Appl. Mater. Interfaces* **2015**, *7*, 23, 12809-12813.

25 H.S. Jung, T. Pradhan, J.H. Han, K.J. Heo, J.H. Lee, C. Kang, J.S. Kim, *Biomaterials* **2012**, *33*, 8495-8502.

26 Y.C. Liao, P. Venkatesan, L.F. Wei, S.P. Wu, *Sensors and Actuators B* **2016**, *232*, 732–737.

27 Y. Liu, X. Lv, J. Liu, Y.Q. Sun, W. Guo, *Chem. Eur. J.* **2015**, *21*, 4747 – 4754.

28 K.P. Wang, S. Xu, Y. Lei, W.J. Zheng, Q. Zhang, S. Chen, H.Y. Hu, Z.Q. Hu, *Talanta* **2019**, *196*, 243–248.

29 M.J. Chang, J.H. Joo, M.H. Lee, *Bull. Korean Chem. Soc.* **2019**, *40*, 539–543.

30 Y. Yue, F. Huo, P. Ning, Y. Zhang, J. Chao, X. Meng, C. Yin, *J. Am. Chem. Soc.* **2017**, *139*, 3181−3185.

31 D. Cao, Z. Liu, P. Verwilst, S. Koo, P. Jangjili, J. S. Kim, W. Lin, *Chem. Rev*. **2019**, *119*, 10403-10519.

32 T.K. Kim, D.N. Lee, H.J. Kim, *Tetrahedron Letters* **2008**, *49*, 4879–4881.

33 C. Xu, H.D. Li, B.Z. Yin, *Biosensors and Bioelectronics* **2015**, *72*, 275–281.

34 X Dai, ZY Wang, ZF Du, J Cui, JY Miao, BX Zhao, *Analytica chimica acta*, **2015**, *900*, 103-110.

35 Q. Wang, X. Wu, L. Pu, *Org. Lett*. **2019**, *21*, 9036-9039

36 X Wu, Q Wang, DA. Dickie, L Pu, *J. Org. Chem*. **2020**, *85*, *ASAP*.

37 P. Zhang, W. Liu, G. Niu, H. Xiao, M. Wang, J. Ge, J. Wu, H. Zhang, Y. Li, P. Wang, *J. Org. Chem*. **2017**, *82*, 3456-3462.

38 M. Tian, F. Guo, Y. Sun, W. Zhang, F. Miao, Y. Liu, G. Song, C.L. Ho, X. Yu, J.Z. Sun, W.Y. Wong, *Org. Biomol. Chem.* **2014,** *12*, 6128-6133.

39 C. Dong, T. Song, X.F. Bai, Y.M. Cui, Z. Xu, L.W. Xu, *Catal. Sci. Technol*. **2015**, *5*, 4755-4759

40 Y. Kim, S.V. Mulay, M. Choi, S.B. Yu, S. Jon, D.G. Churchill, *Chem. Sci.* **2015**, *6*, 5435-5439.

41 S. Feng, Y. Fang, W. Feng, Q. Xia, G. Feng, *Dyes and Pigments* **2017**, *146*, 103-111.

42 X. Yang, W. Liu, J. Tang, P. Li, H. Weng, Y. Ye, M. Xian, B. Tang, Y. Zhao, *Chem. Commun.* **2018**, *54*, 11387-11390.

Appendix for Chapter 2.

^{1}H NMR spectrum of (*Rac*)-**2**

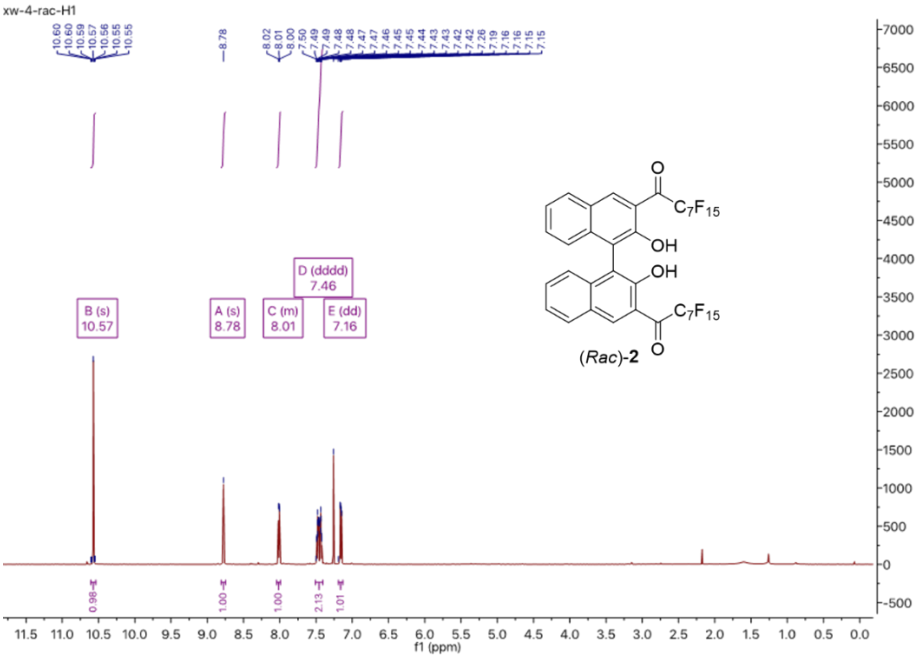

^{13}C{^{1}H} NMR spectrum of (*Rac*)-**2**

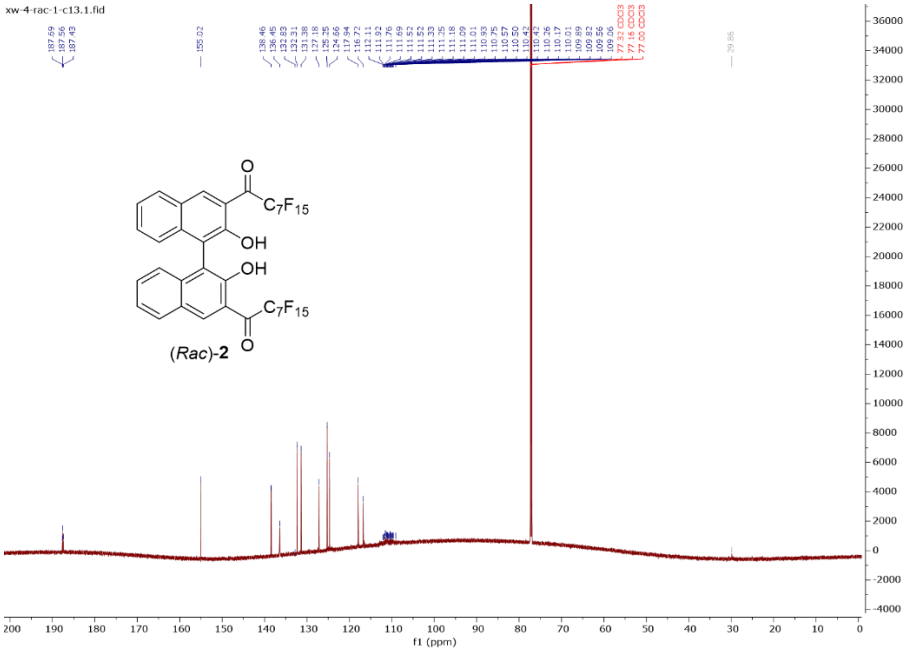

^{19}F NMR spectrum of (*Rac*)-**2**

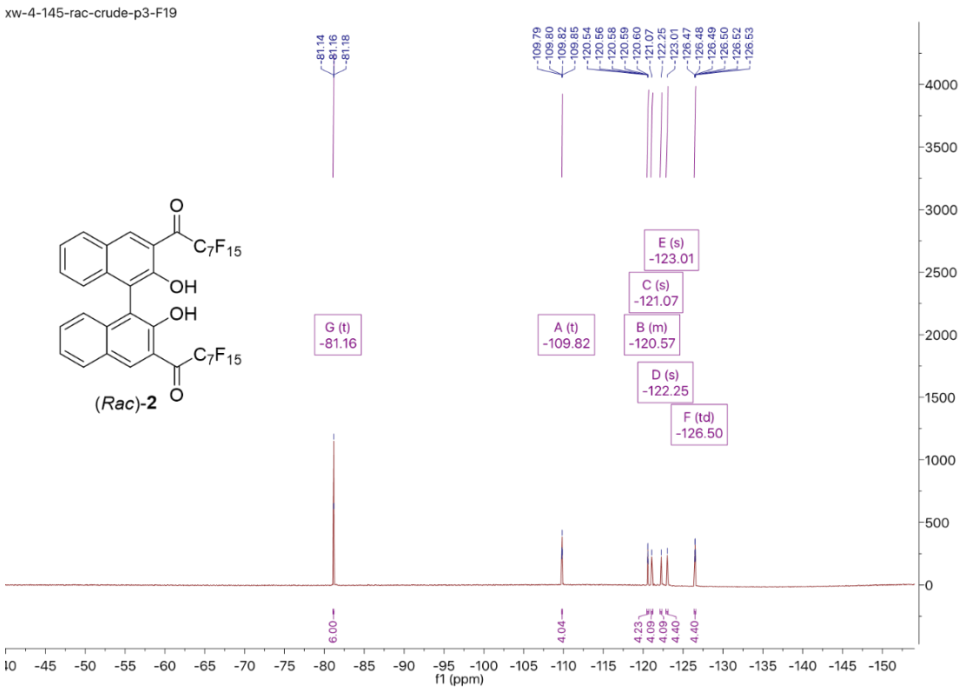

HRMS Spectrum of (*Rac*)-**2**

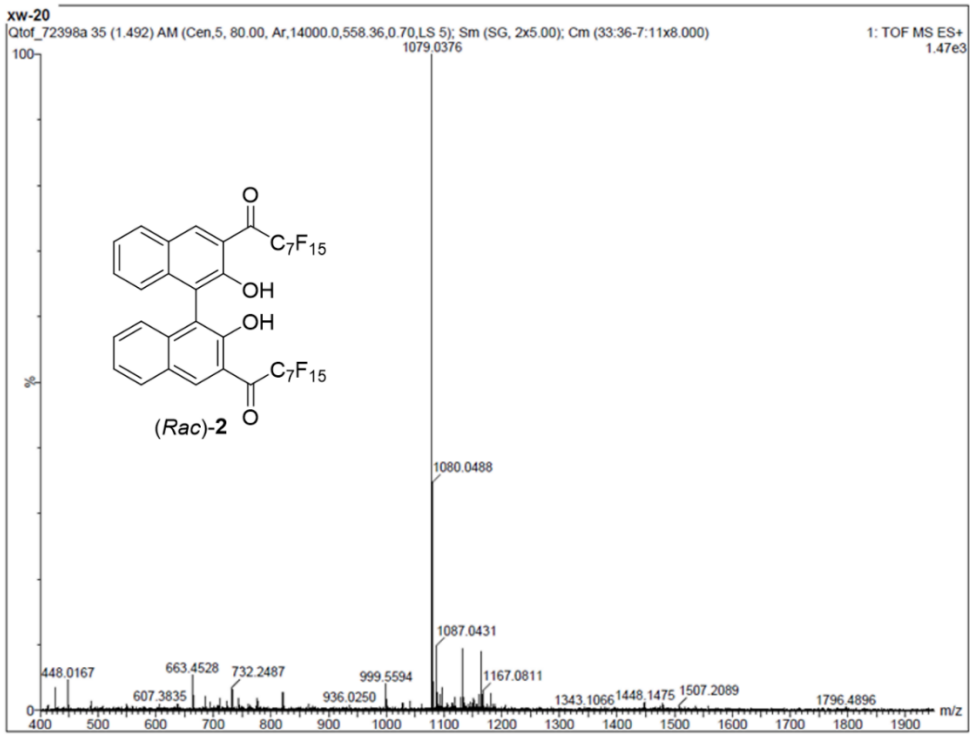

^{1}H NMR spectrum of (*R*)-**2**

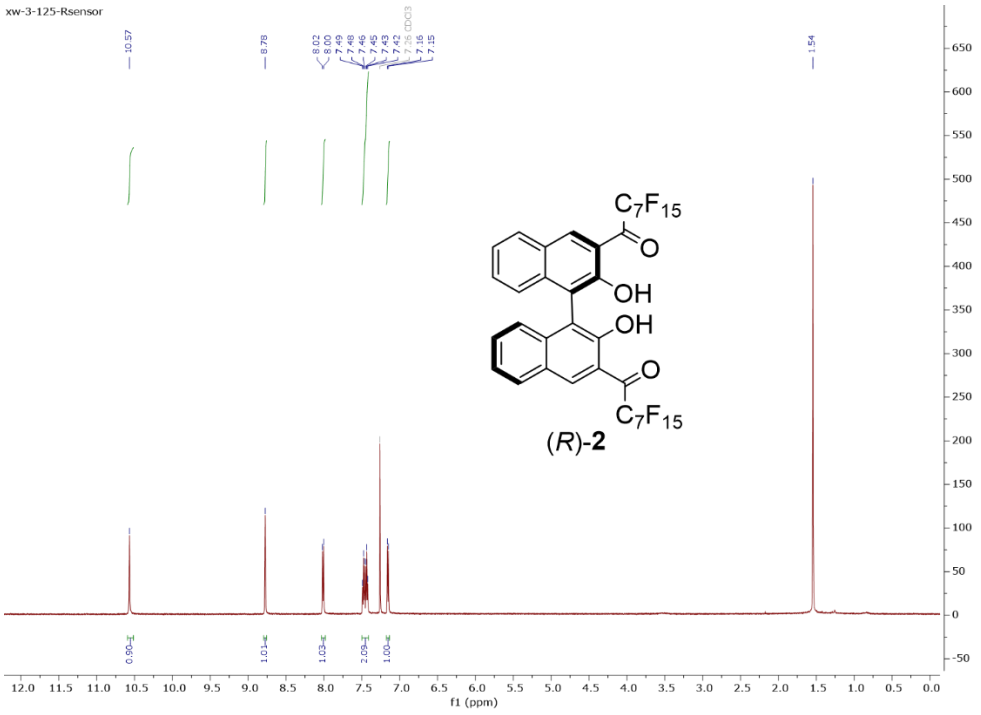

^{13}C{^{1}H} NMR spectrum of (*R*)-**2**

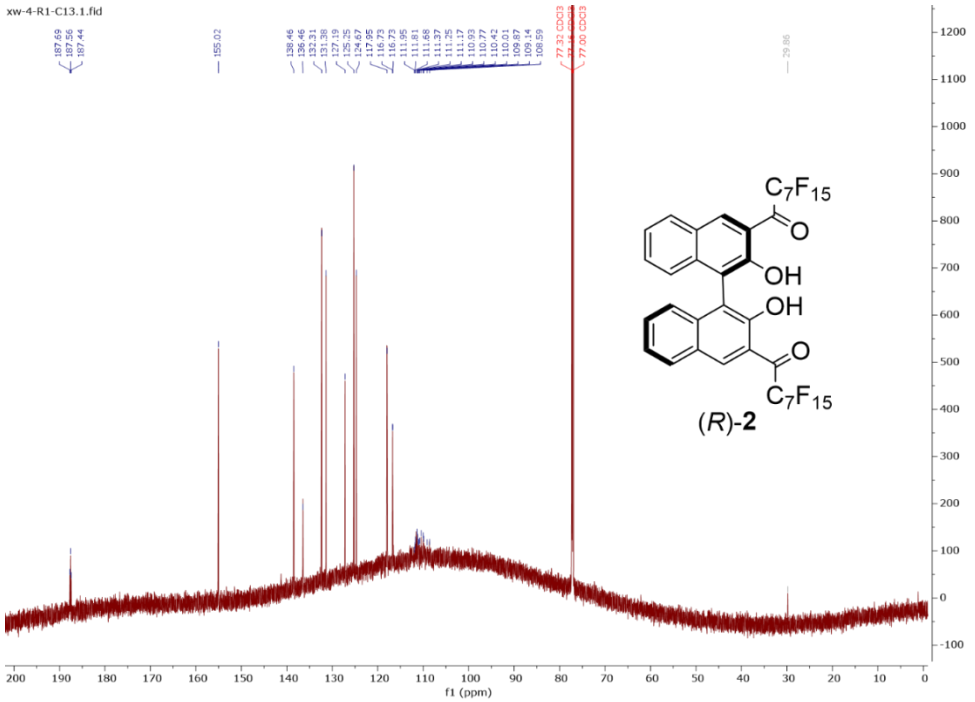

^{19}F NMR spectrum of (*R*)-**2**

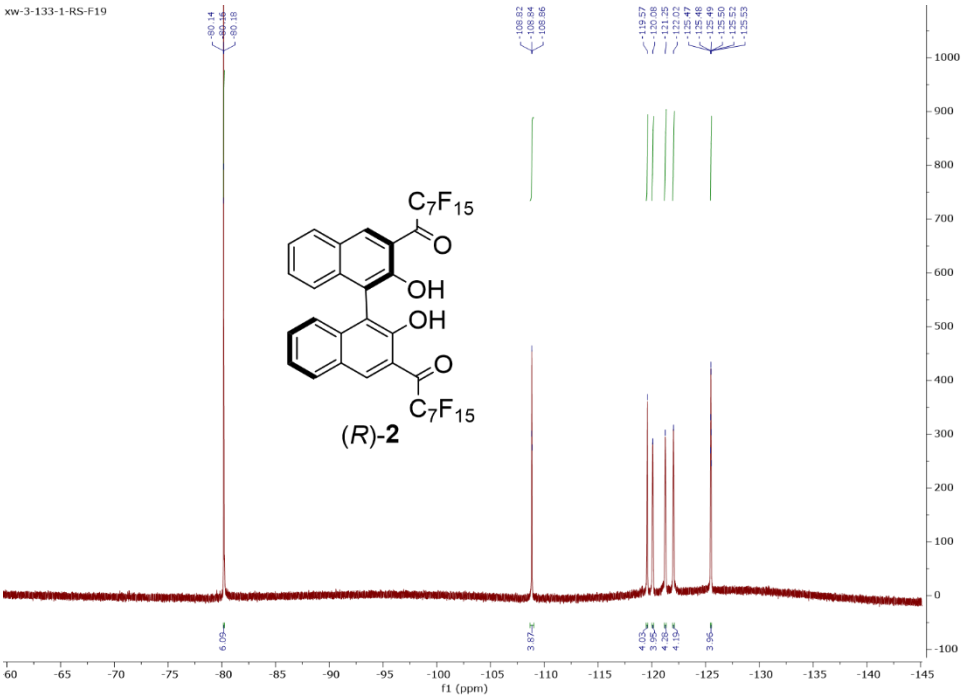

HRMS Spectrum of (*R*)-**2**

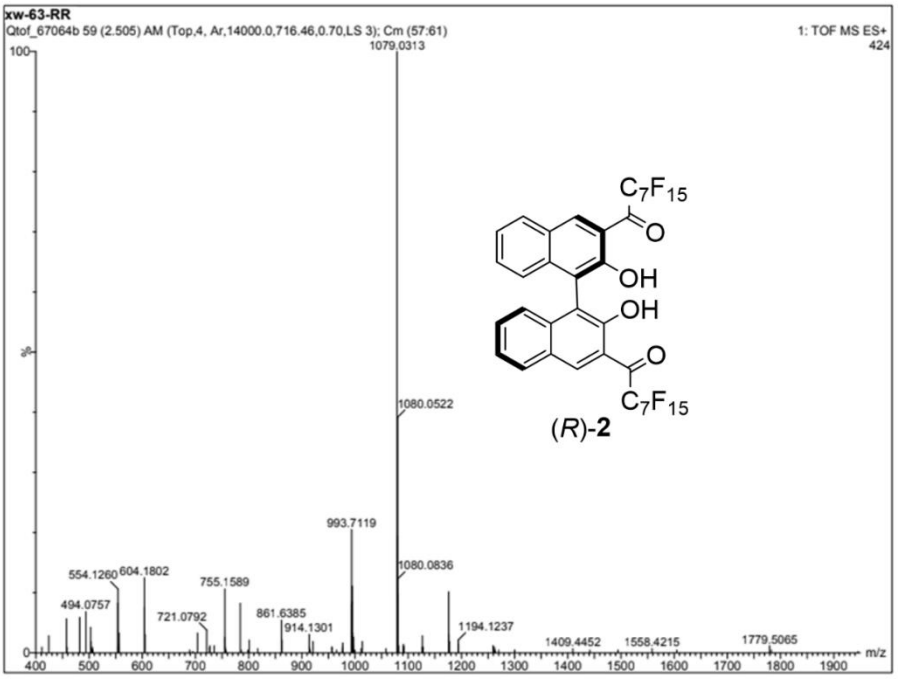

^{1}H NMR spectrum of (*S*)-**2**

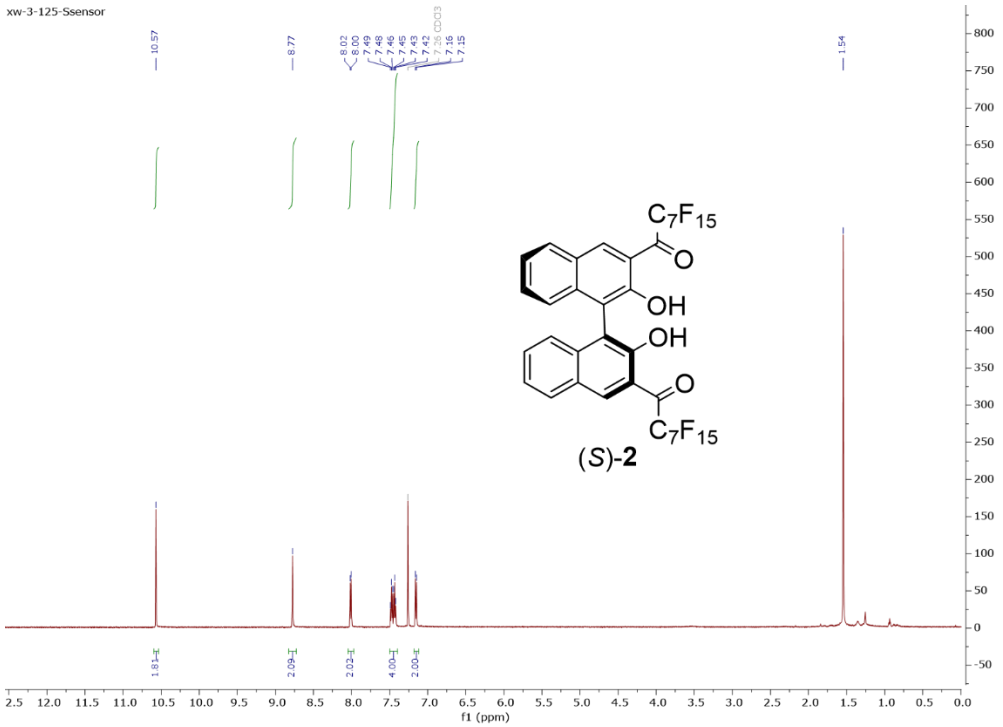

^{13}C{^{1}H} NMR spectrum of (*S*)-**2**

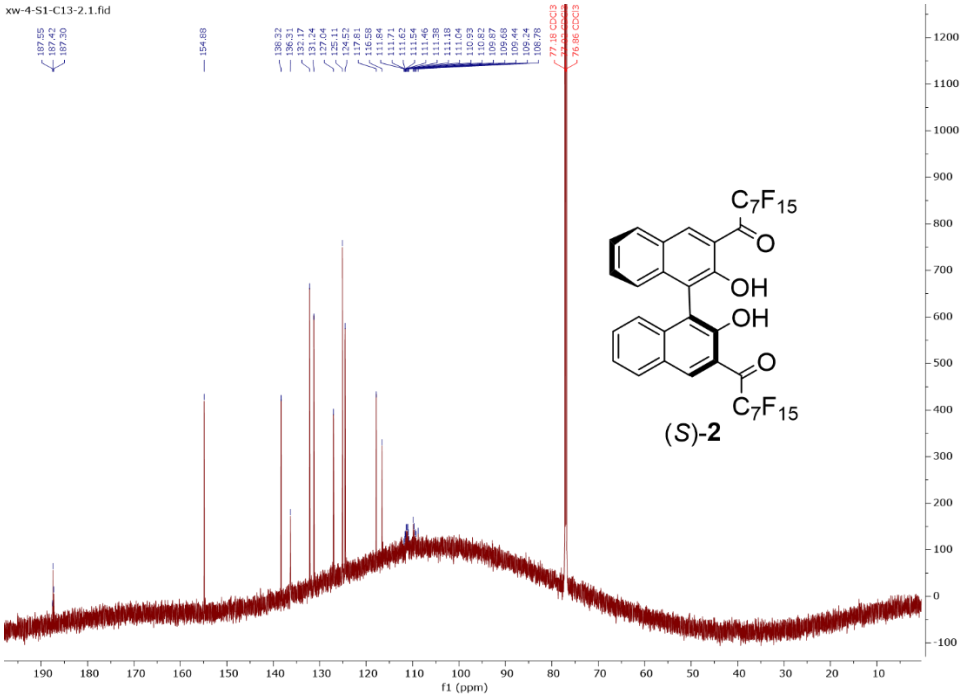

^{19}F NMR spectrum of (*S*)-**2**

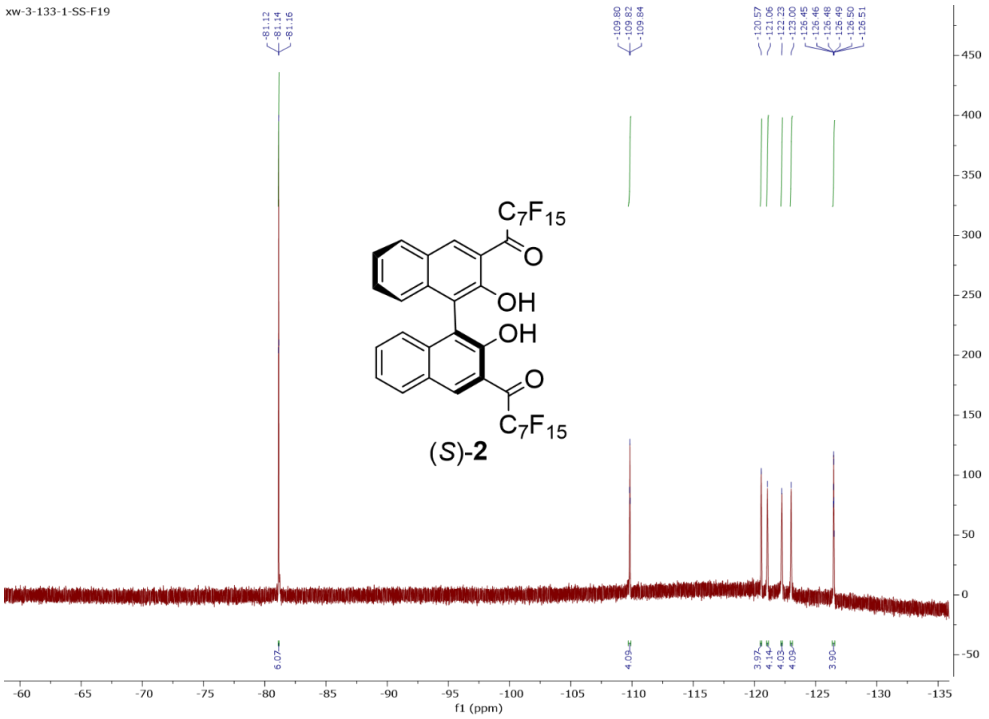

HRMS Spectrum of (*S*)-**2**

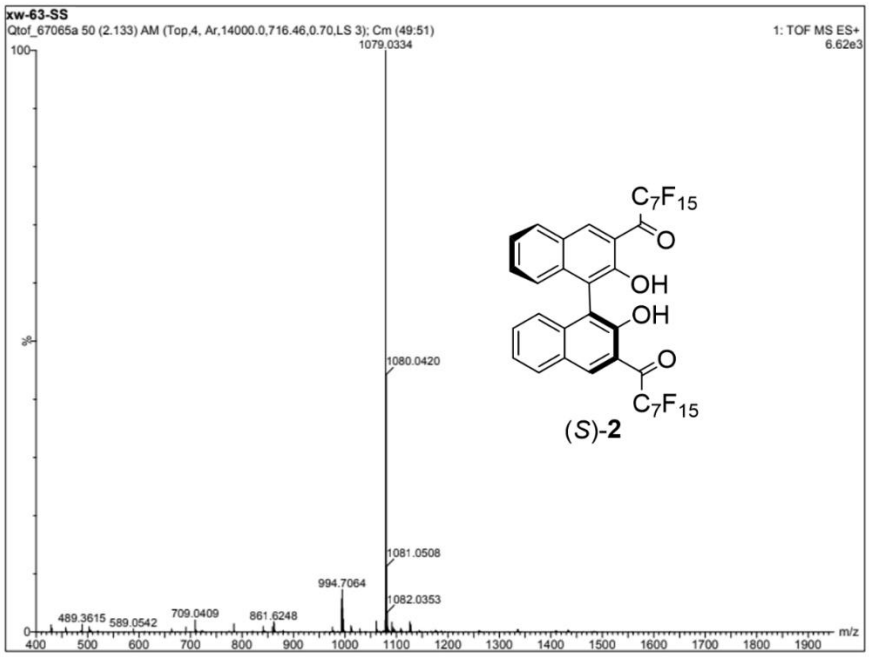

^{1}H NMR spectra of (*S*, *S*)-**3**

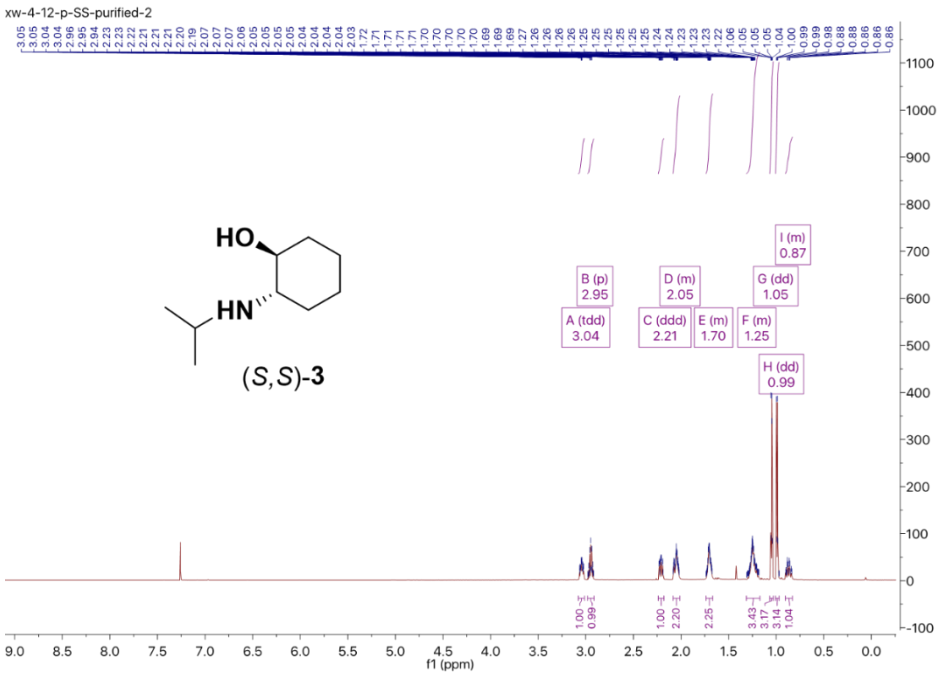

^{13}C{^{1}H} NMR spectrum of (*S*, *S*)-**3**

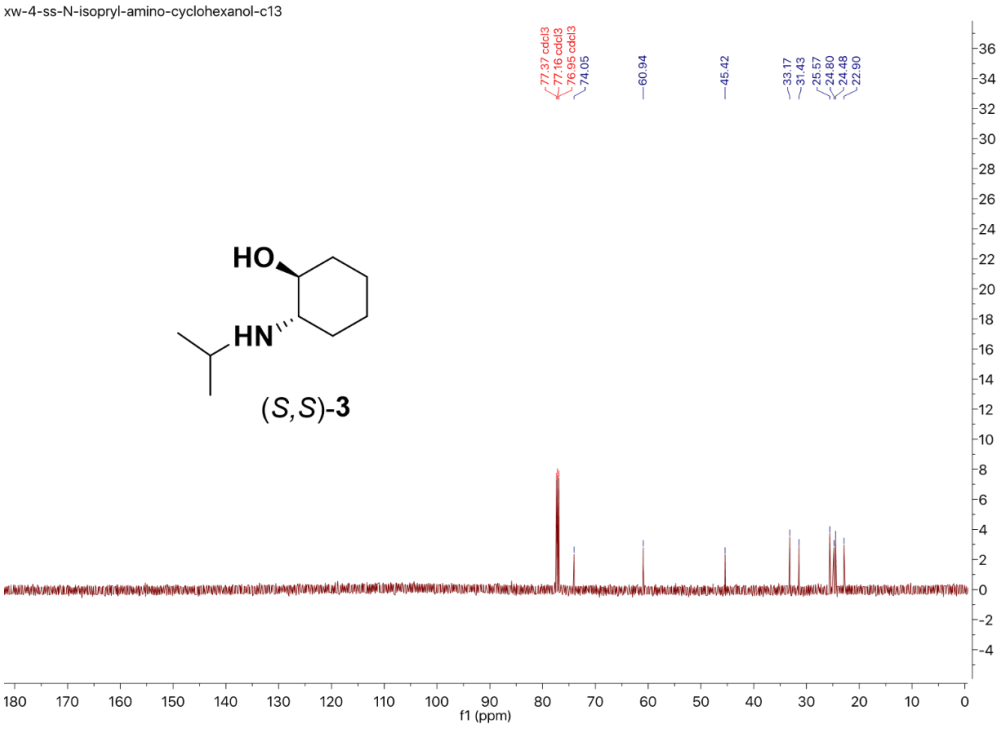

HRMS Spectrum of (*S*, *S*)-**3**

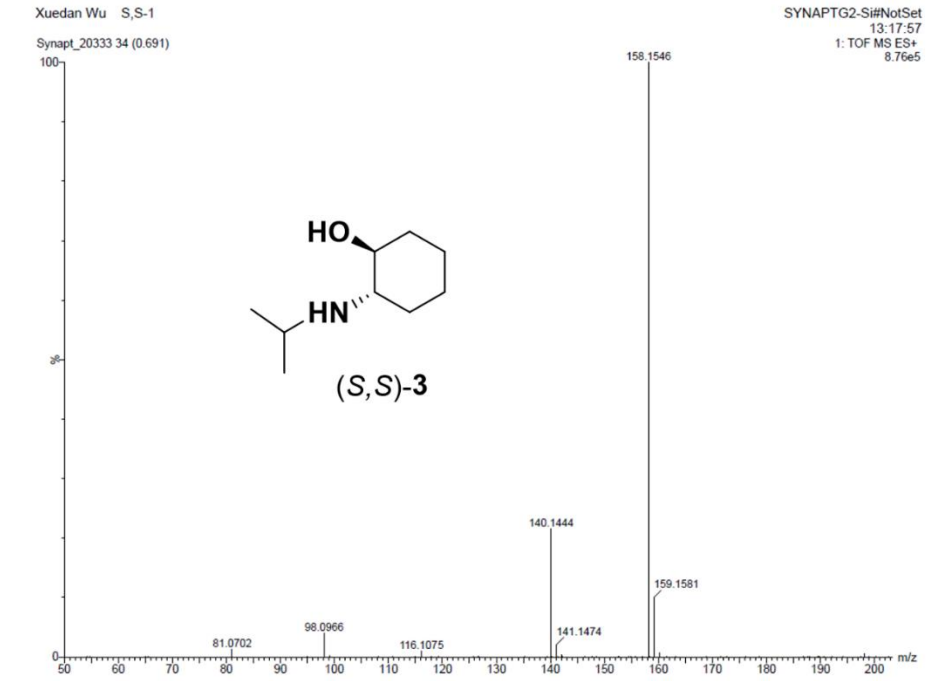

^{1}H NMR spectra of (*R*, *R*)-**3**

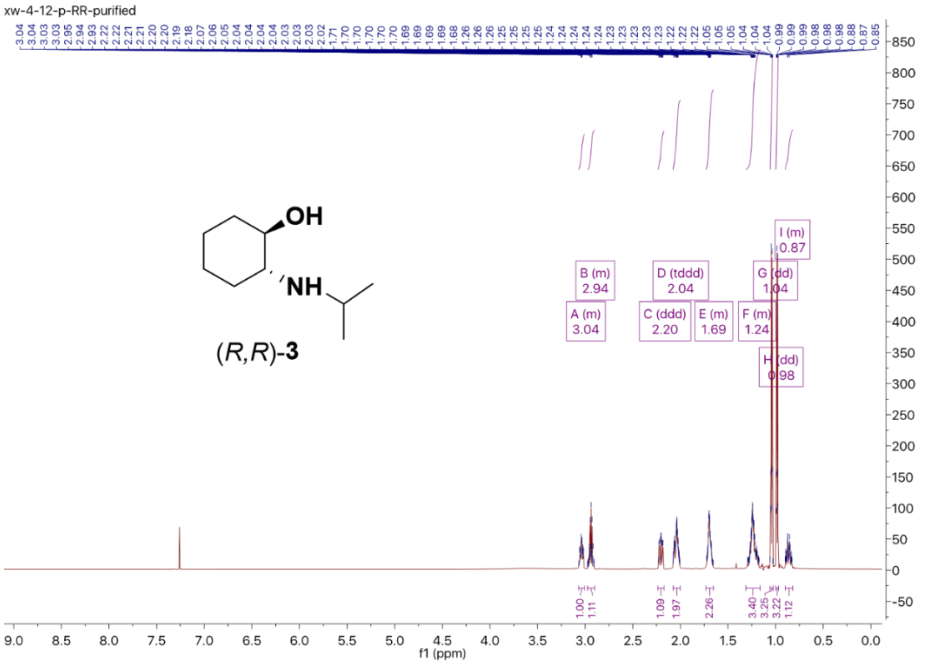

$^{13}C\{^{1}H\}$ NMR spectrum of (*R*, *R*)-**3**

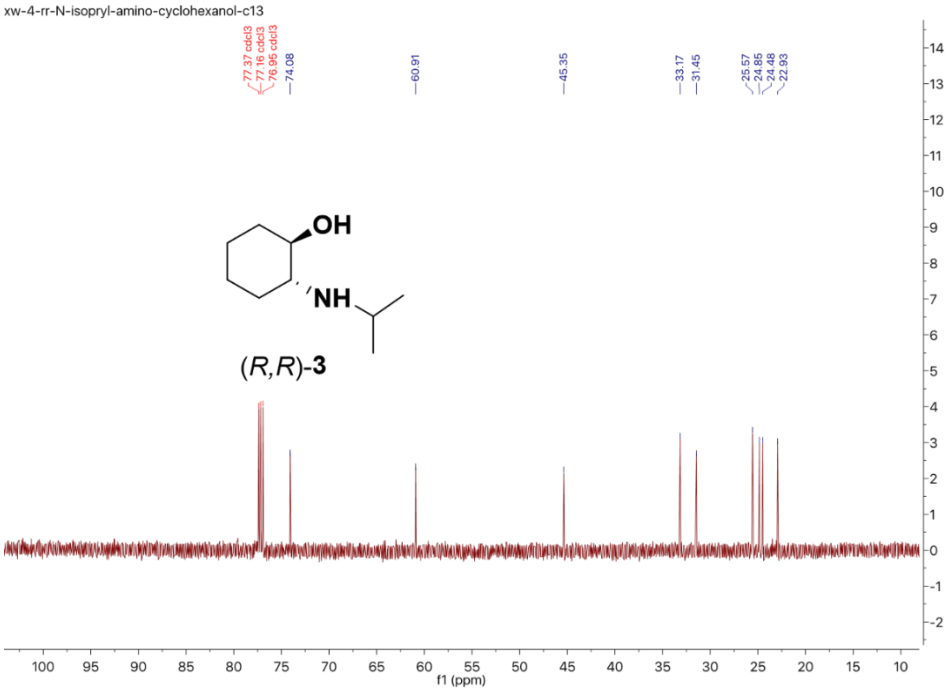

HRMS Spectrum of (*R*, *R*)-**3**

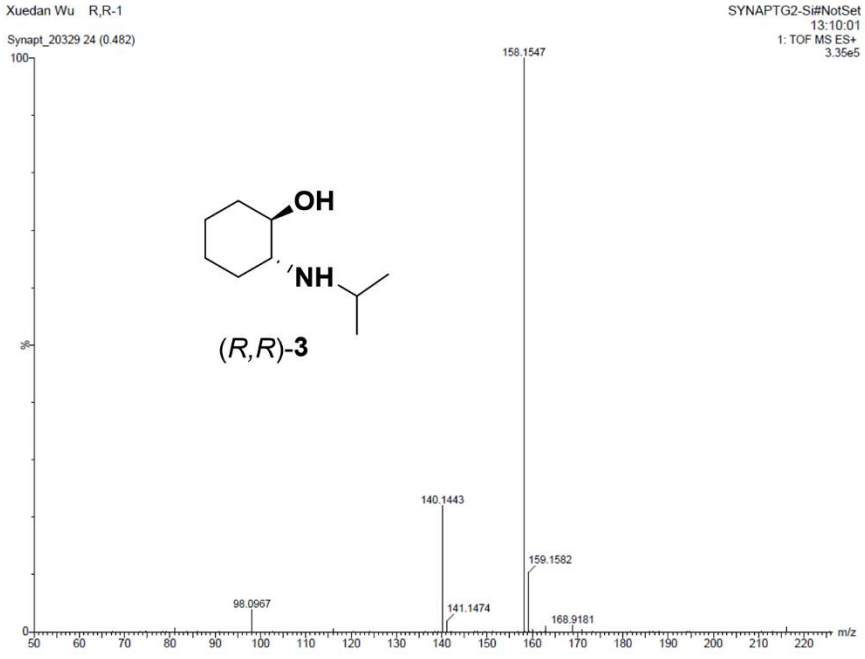

^{1}H NMR spectrum of (*Rac*)-**3**

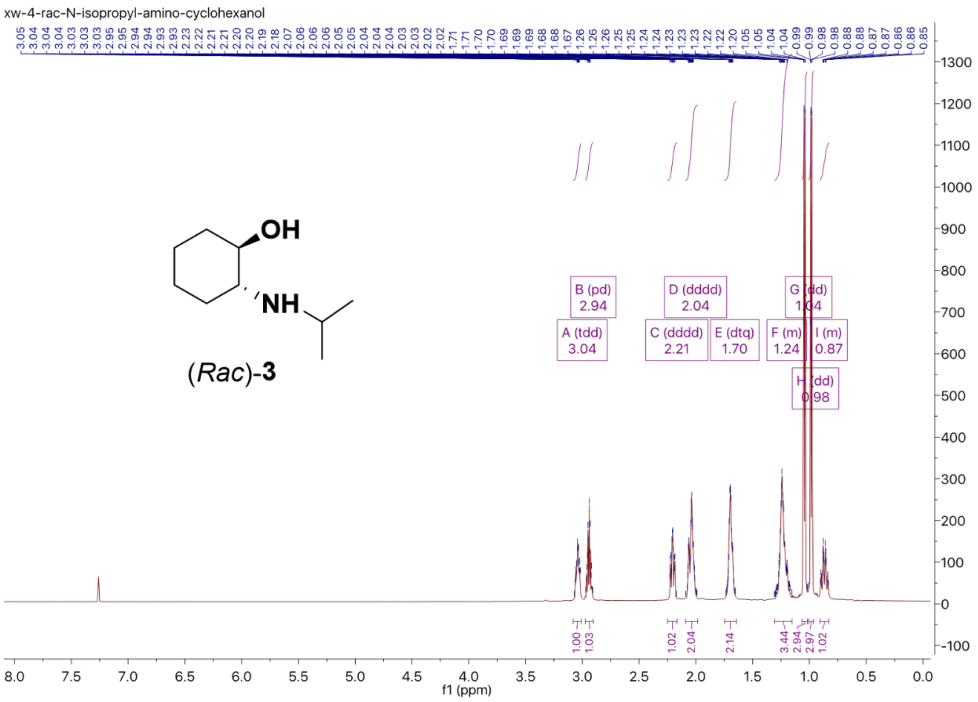

^{13}C{^{1}H} NMR spectrum of (*Rac*)-**3**

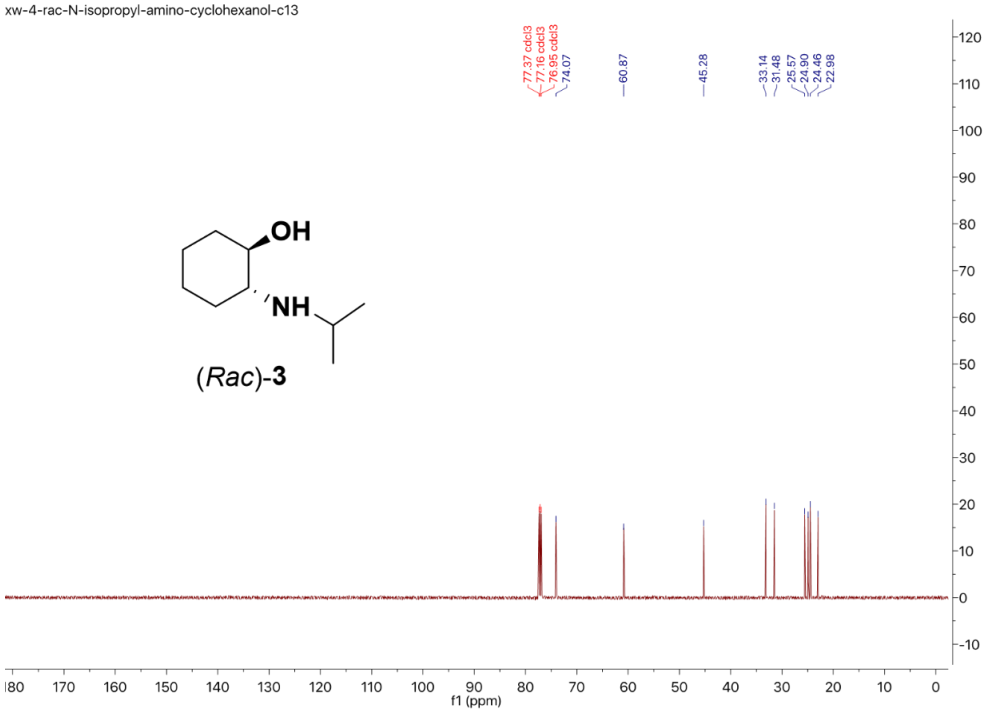

^{1}H NMR spectrum of a crude product of **3** by the asymmetric reaction

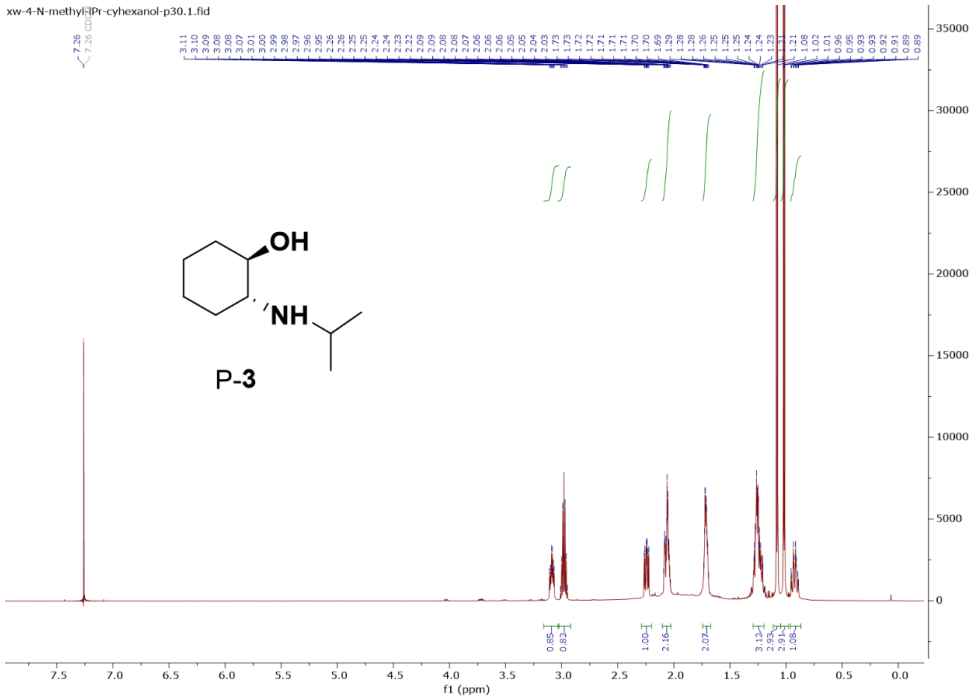

^{1}H NMR spectrum of a crude product of **3** by the asymmetric reaction

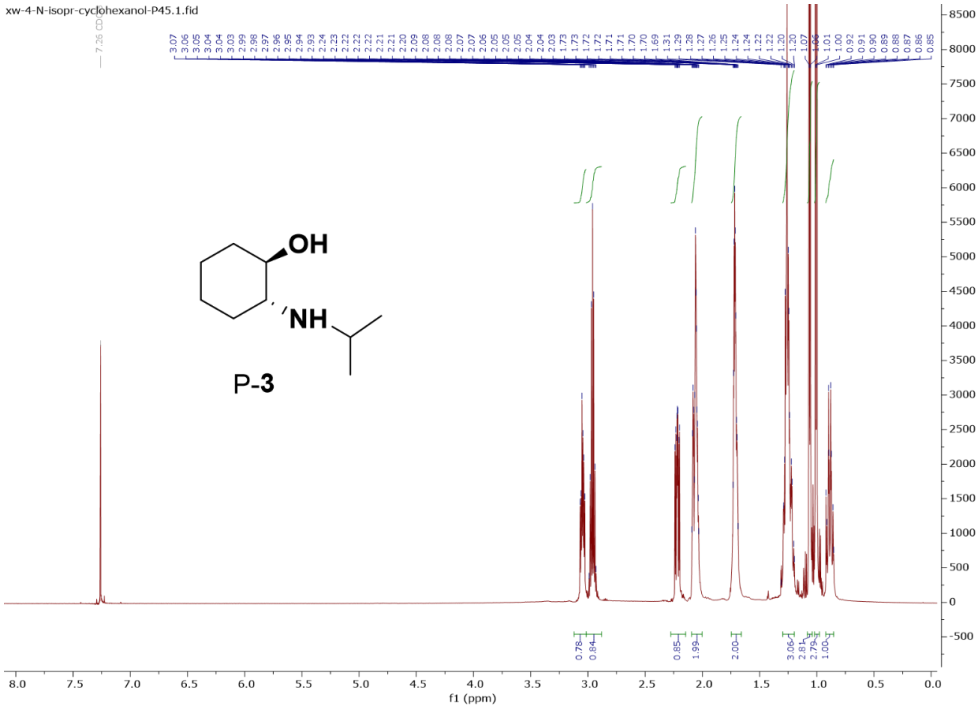

^{1}H NMR spectrum of a crude product of **3** by the asymmetric reaction

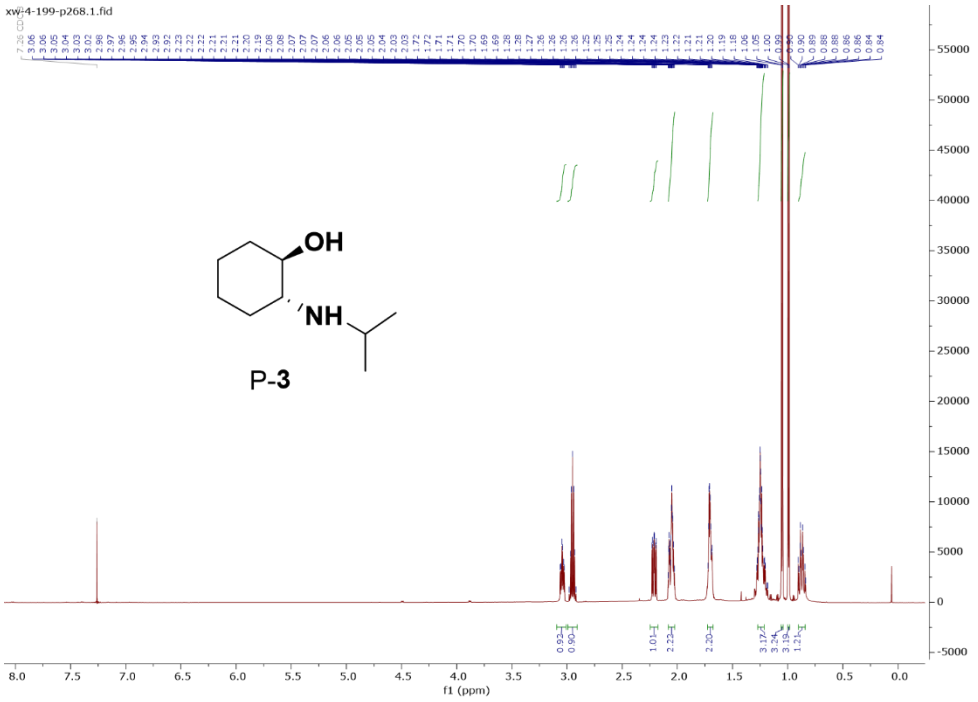

^{13}C{^{1}H} NMR spectrum of a crude product of **3** by the asymmetric reaction

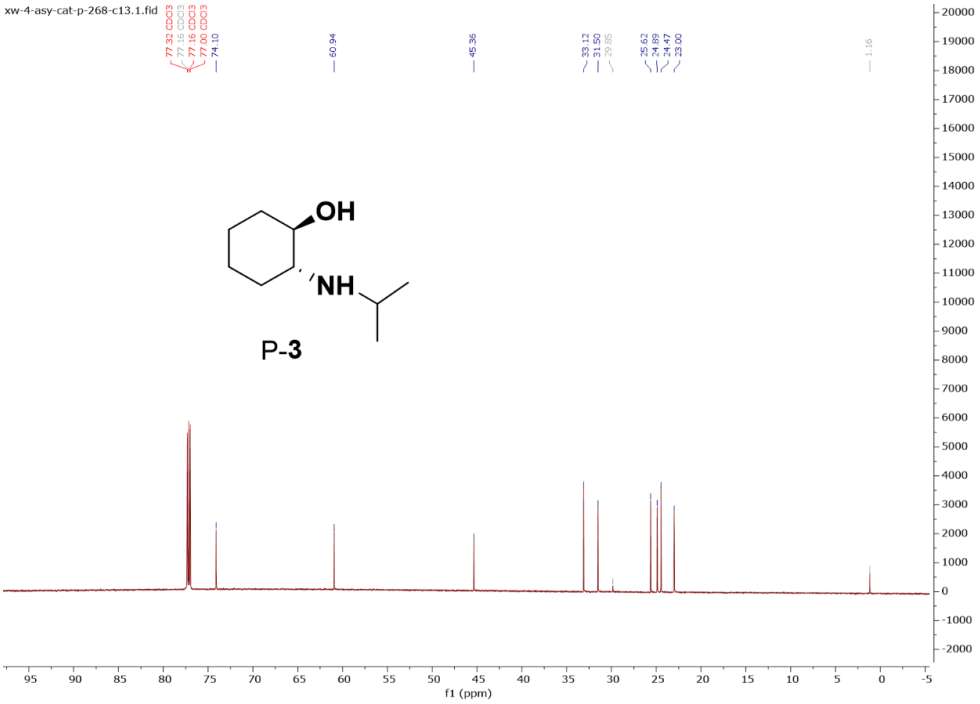

HRMS Spectrum of a crude product of **3** by the asymmetric reaction

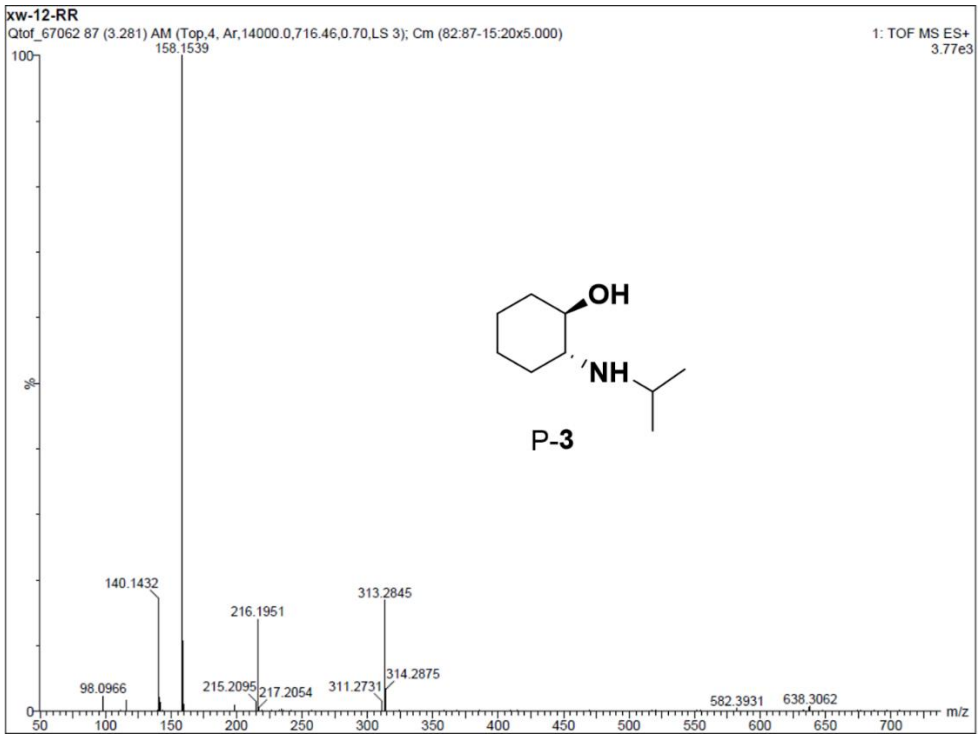

^{1}H NMR spectrum of (*Rac*)-**4**

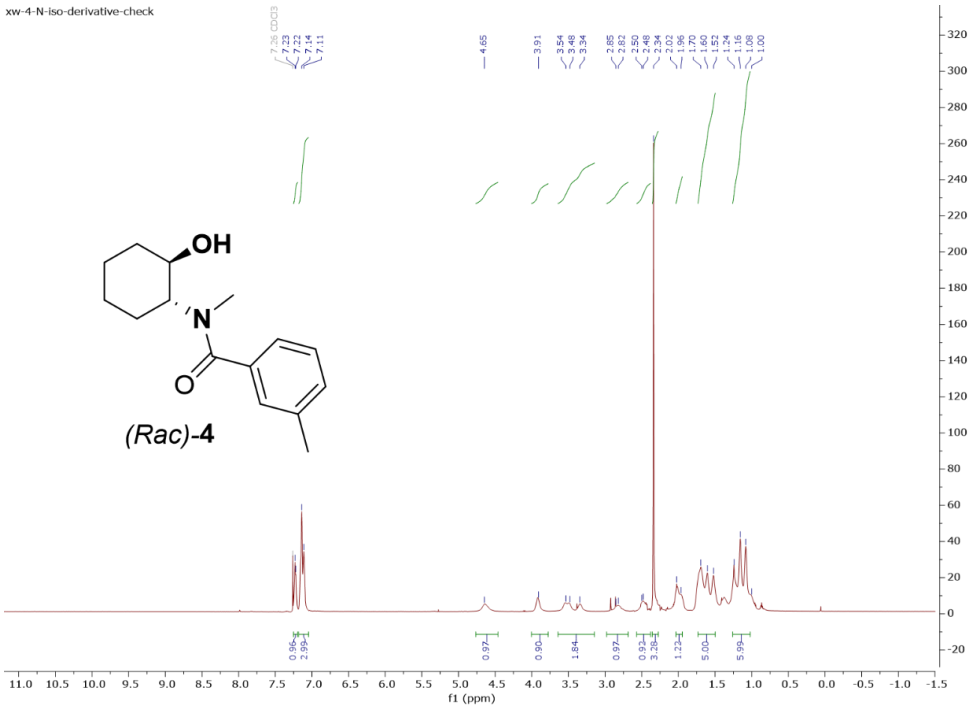

^{13}C{^{1}H} NMR spectrum of (*Rac*)-**4**

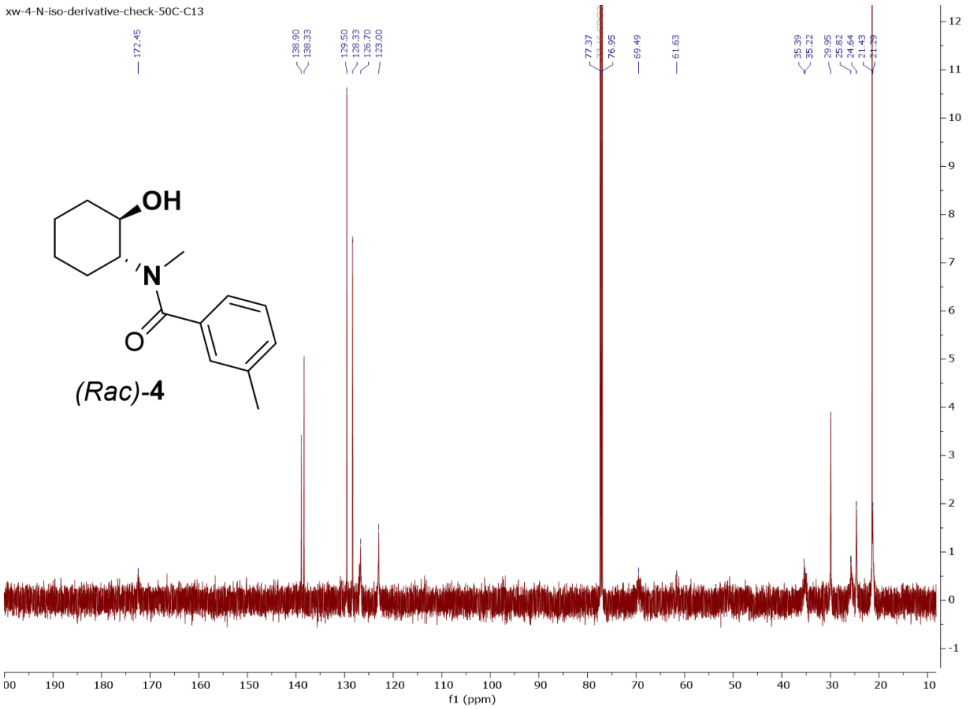

^{1}H NMR spectrum of (*Rac*)-**6**

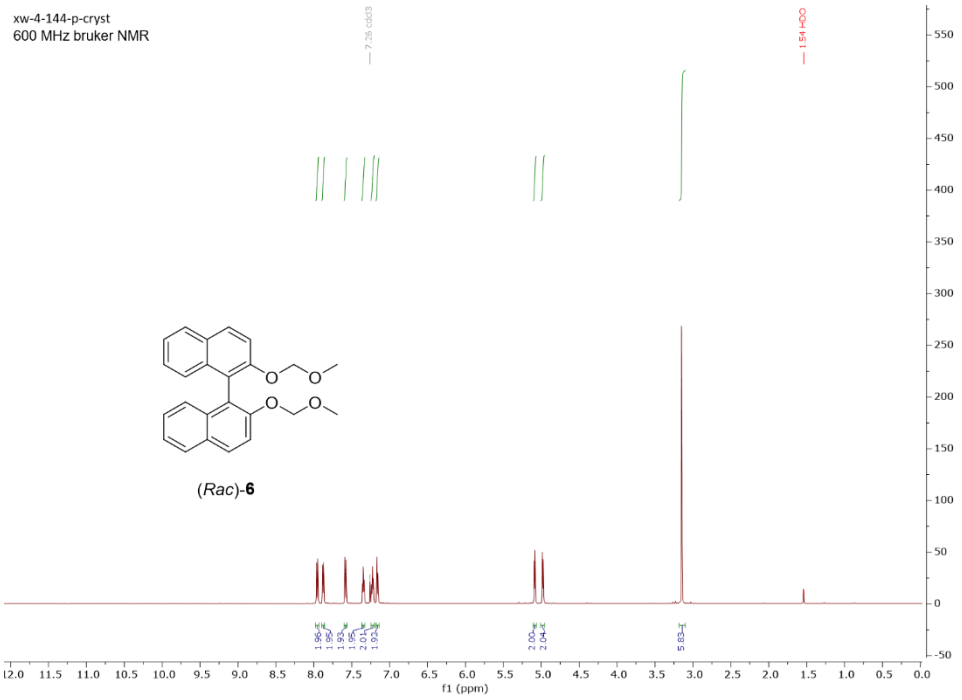

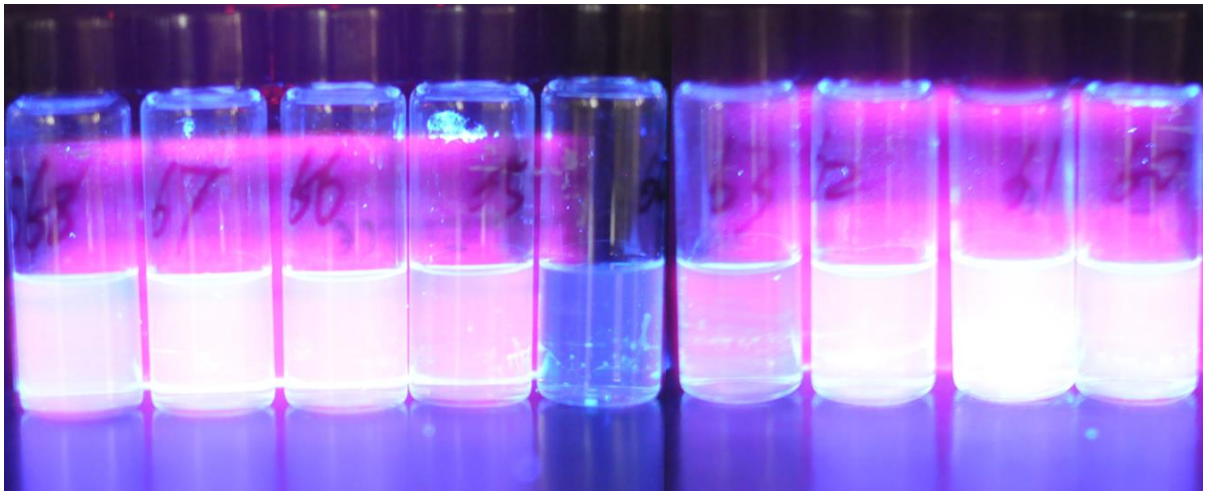

Figure S2- 1. Photo images observed under a 365 nm UV lamp of the reactions of (*Rac*)-**2** with **3** at various enantiomeric compositions. ([**2**] = 2.5×10^{-5} M, [**3**] = 6 mM, in FC-72/Et_2O (96/4, v) reaction time: 2 hours)

(*Rac*)-**4** derived from (*Rac*)-**3**: HPLC: 1.0% ee

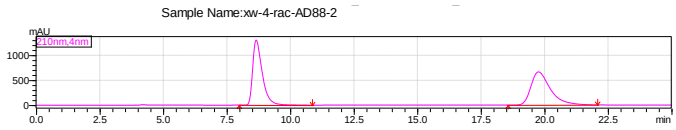

Peak #	Ret. Time	Area	Height	Area%
1	8.657	34343700	130218	49.431
2	19.765	35134045	663463	50.569
Total		69477745	1965643	100

(*S*,*S*)-**4** derived from (*S*,*S*)-**3**: HPLC: -99.8% ee

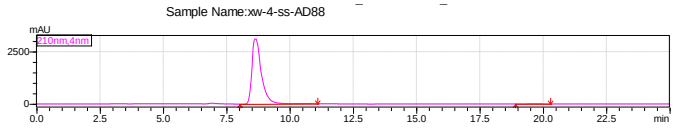

Peak#	Ret. Time	Area	Height	Area%
1	8.639	81328128	3118899	99.937
2	19.6	51630	1258	0.063
Total		81379758	3120157	100

(*R*,*R*)-**4** derived from (*R*,*R*)-**3**: HPLC: 99.5% ee

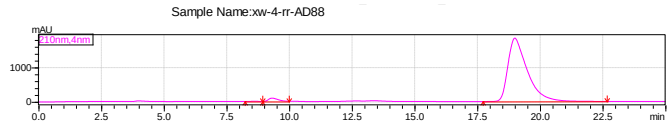

Peak#	Ret. Time	Area	Height	Area%
1	8.592	226654	8383	0.229
2	18.993	98736458	1845764	99.771
Total		98963112	1854147	100

HPLC data of Phase II screening

Yb(OTf)$_3$-ACN (HPLC 50% ee, Fl 48% ee)

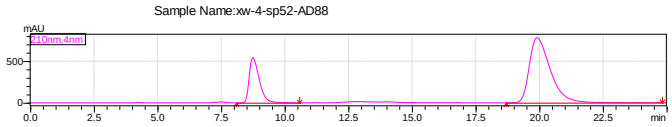

Peak#	Ret. Time	Area	Height	Area%
1	8.742	14967579	542937	25.04
2	19.911	44808201	780349	74.96
Total		59775780	1323286	100

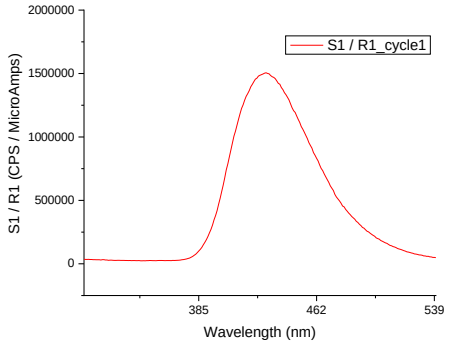

Yb(OTf)$_3$-Toluene (HPLC 49% ee, Fl 50% ee)

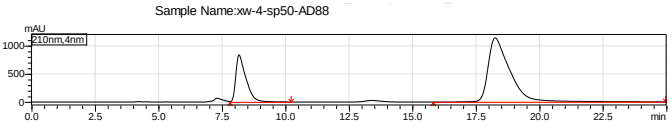

Peak#	Ret. Time	Area	Height	Area%
1	8.171	23276410	837623	25.534
2	18.257	67883241	1140791	74.466
Total		91159651	1978414	100

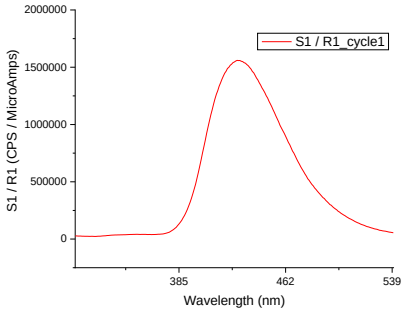

$LaCl_3 \cdot 6H_2O$-ACN (HPLC 57% ee, Fl 50% ee)

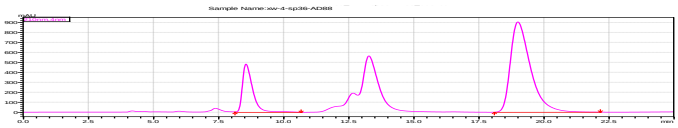

Peak#	Ret. Time	Area	Height	Area%
1	8.559	13107154	482544	21.372
2	19.005	48221649	903744	78.628
Total		61328803	1386288	

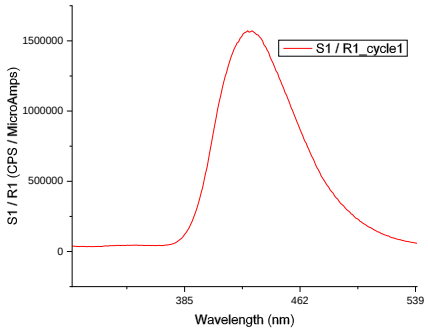

$LaCl_3 \cdot 6H_2O$-Toluene (HPLC 54% ee, Fl 56% ee)

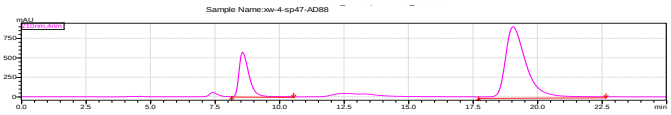

Peak#	Ret. Time	Area	Height	Area%
1	8.573	15582700	572709	22.907
2	19.055	52443489	912872	77.093
Total		68026189	1485580	100

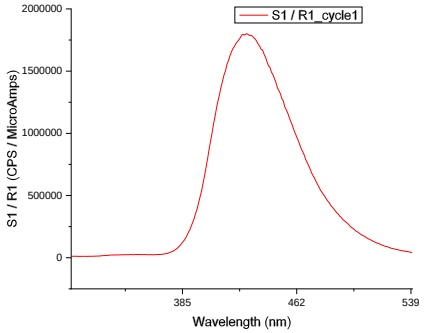

NaBr-ACN (HPLC 43% ee, Fl 44% ee)

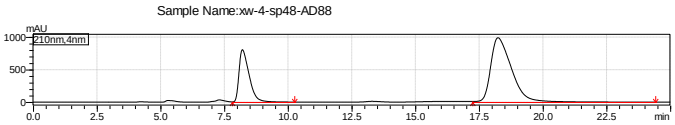

Peak#	Ret. Time	Area	Height	Area%
1	8.212	22254925	807075	28.336
2	18.244	56284976	990532	71.664
Total		78539901	1797607	100

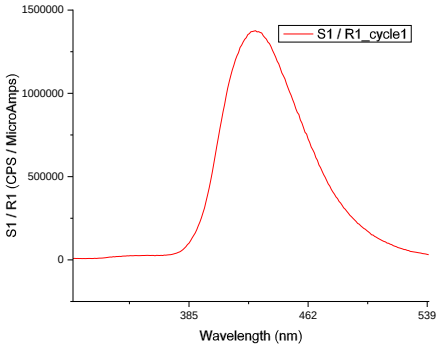

NaBr-Toluene (HPLC 45.5% ee, Fl 47% ee)

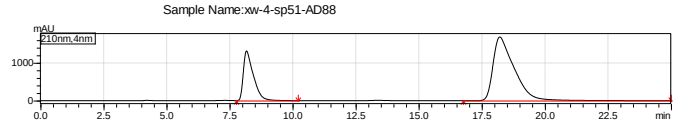

Peak#	Ret. Time	Area	Height	Area%
1	8.169	36730988	1319620	27.135
2	18.212	98631021	1690958	72.865
Total		135362009	3010577	100

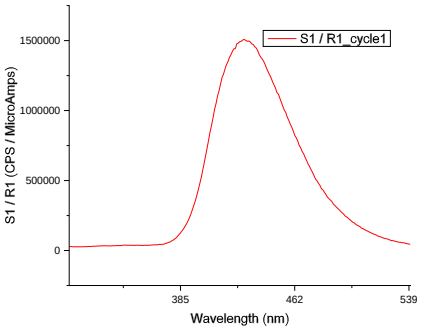

LiBr-ACN (HPLC 51% ee, Fl 52% ee)

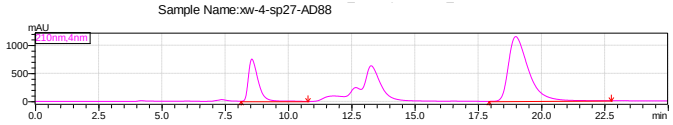

Peak#	Ret. Time	Area	Height	Area%
1	8.56	20276609	755357	24.455
2	18.988	62637297	1151072	75.545
Total		82913905	1906429	100

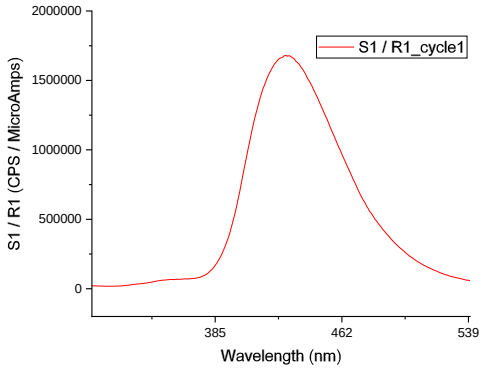

LiBr-Toluene (HPLC 58.5% ee, Fl 57% ee)

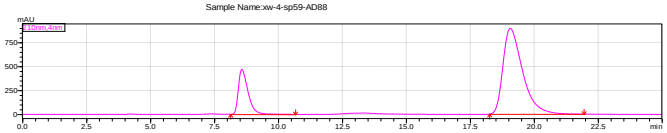

Peak#	Ret. Time	Area	Height	Area%
1	8.575	12460435	471456	20.736
2	19.069	47630424	896431	79.264
Total		60090859	1367887	100

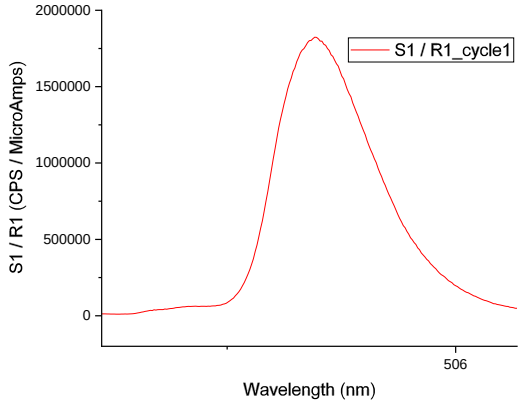

Sc(OTf)$_3$-ACN (HPLC 20% ee, Fl 20% ee)

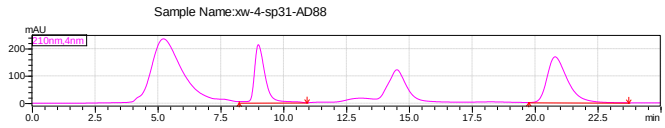

Peak#	Ret. Time	Area	Height	Area%
1	9	6243524	213208	39.934
2	20.806	9391052	167923	60.066
Total		15634576	381131	100

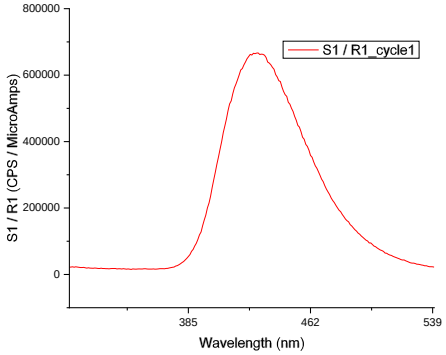

Sc(OTf)$_3$-Toluene (HPLC 51.5% ee, Fl 50% ee

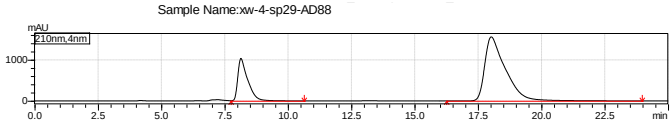

Peak#	Ret. Time	Area	Height	Area%
1	8.141	28292079	1033999	24.258
2	18.024	88335643	1556832	75.742
Total		116627722	2590831	100

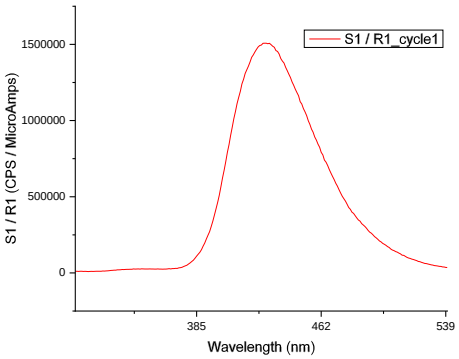

HPLC data of Phase III screening

1. HPLC 34.5% ee

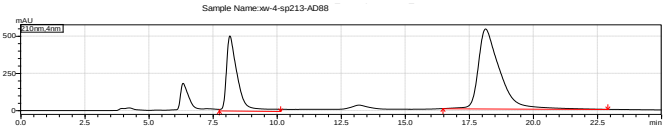

Peak#	Ret. Time	Area	Height	Area%
1	8.163	15064646	502178	32.741
2	18.14	30946682	535275	67.259
Total		46011328	1037453	100

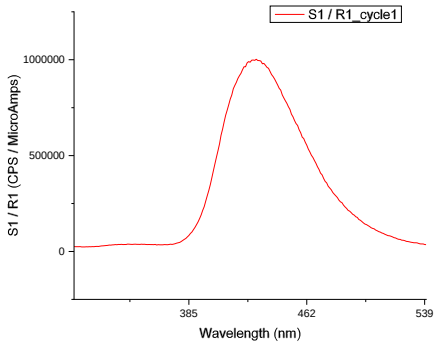

2. HPLC 55% ee

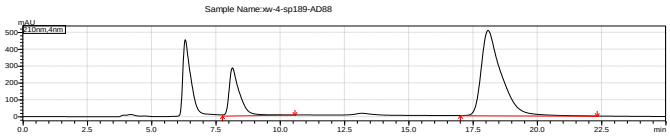

Peak#	Ret. Time	Area	Height	Area%
1	8.148	7924322	284222	22.494
2	18.089	27303899	505052	77.506
Total		35228222	789274	100

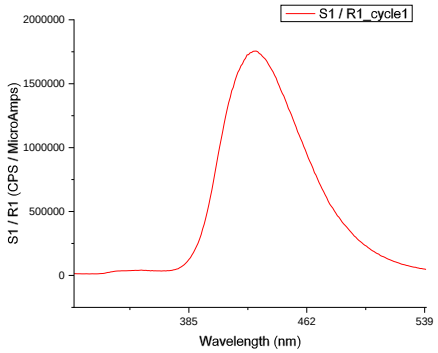

3. HPLC 34% ee

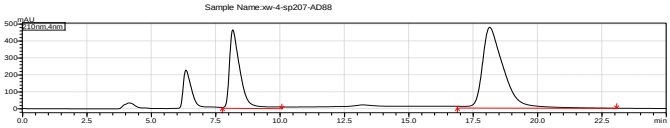

Peak#	Ret. Time	Area	Height	Area%
1	8.172	13265479	461587	32.94
2	18.15	27006584	475699	67.06
Total		40272064	937286	100

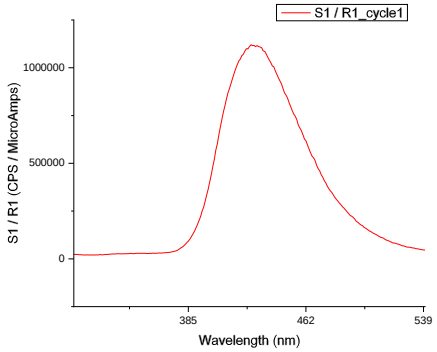

4. HPLC 53% ee

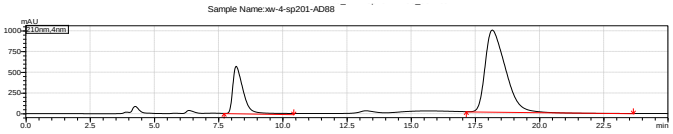

Peak#	Ret. Time	Area	Height	Area%
1	8.19	16429774	570424	23.56
2	18.165	53306794	987810	76.44
Total		69736568	1558234	100

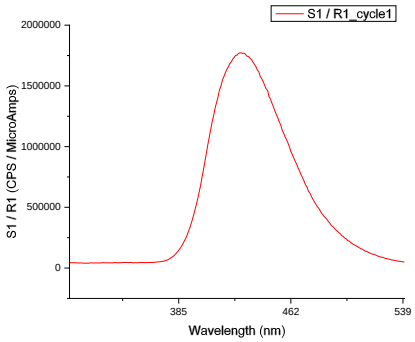

5. HPLC 52% ee

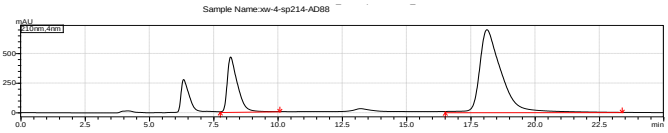

Peak#	Ret. Time	Area	Height	Area%
1	8.164	12910169	465574	23.982
2	18.132	40923686	699180	76.018
Total		53833855	1164754	100

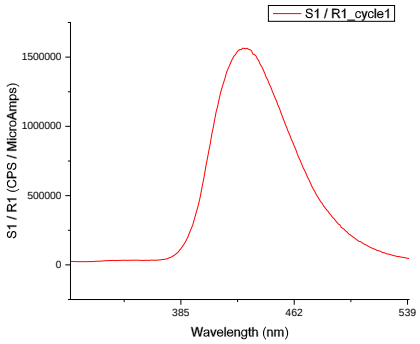

6. HPLC 50.5% ee

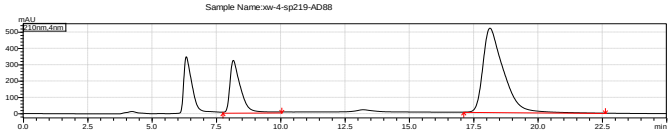

Peak#	Ret. Time	Area	Height	Area%
1	8.163	9319146	322039	24.722
2	18.137	28376448	515727	75.278
Total		37695594	837765	100

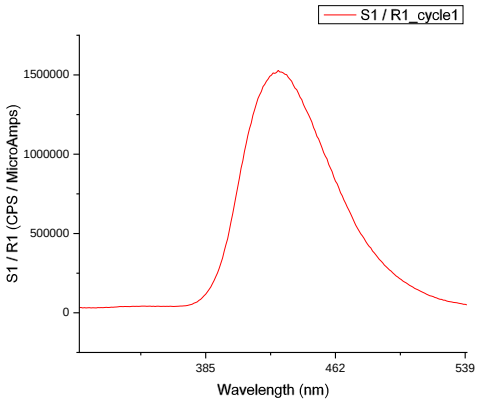

7. HPLC 46.5% ee

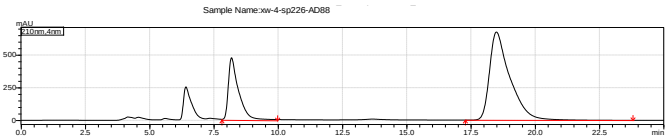

Peak#	Ret. Time	Area	Height	Area%
1	8.189	13551916	478417	26.765
2	18.494	37081527	674674	73.235
Total		50633442	1153091	100

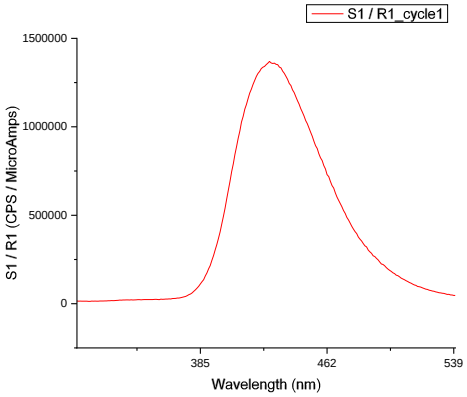

8. HPLC 31% ee

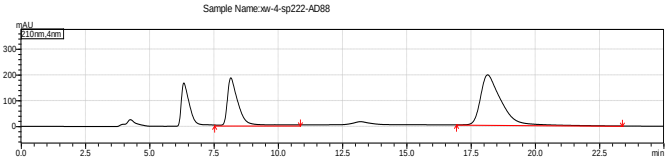

Peak#	Ret. Time	Area	Height	Area%
1	8.16	5629866	186170	34.401
2	18.15	10735363	195001	65.599
Total		16365229	381171	100

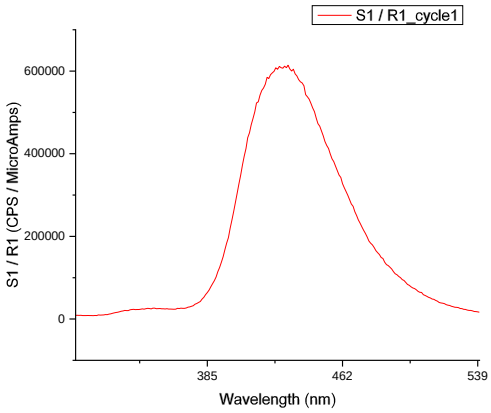

9. HPLC 47.5% ee

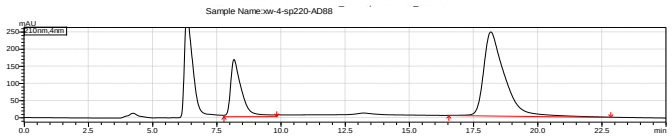

Peak#	Ret. Time	Area	Height	Area%
1	8.178	4904172	166050	26.252
2	18.181	13776905	244663	73.748
Total		18681077	410713	100

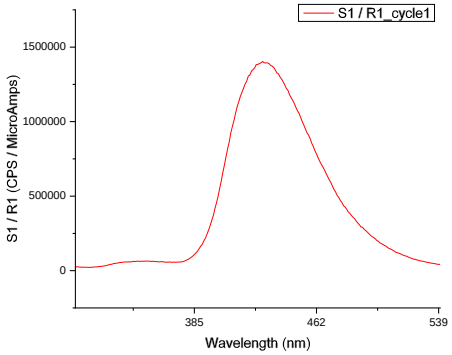

10. HPLC 19% ee

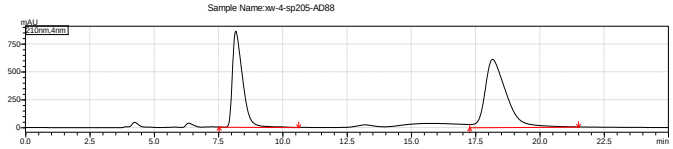

Peak#	Ret. Time	Area	Height	Area%
1	8.176	23522931	859913	40.381
2	18.166	34729382	609967	59.619
Total		58252313	1469879	100

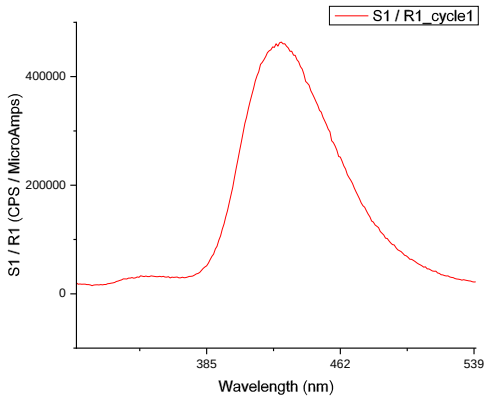

11. HPLC 57.5% ee

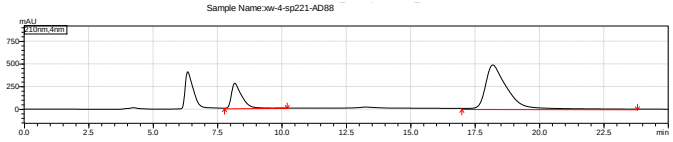

Peak#	Ret. Time	Area	Height	Area%
1	8.174	7872392	279488	21.183
2	18.192	29290841	488981	78.817
Total		37163233	768469	100

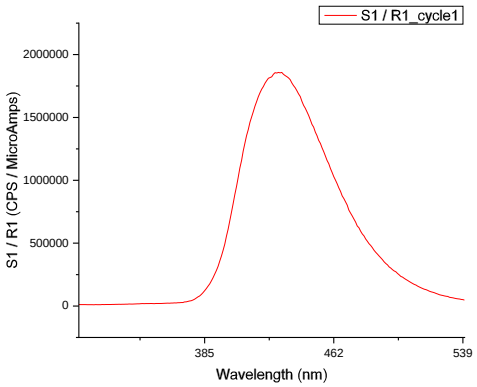

12. HPLC 48% ee

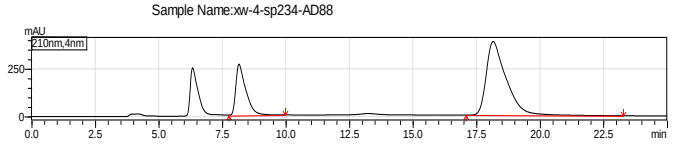

Peak#	Ret. Time	Area	Height	Area%
1	8.16	7429157	269608	26.063
2	18.158	21075939	386461	73.937
Total		28505096	656069	100

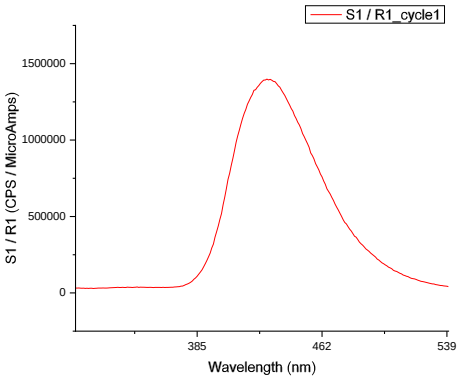

13. HPLC 48% ee

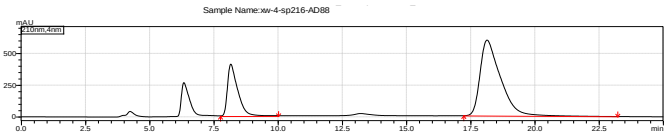

Peak#	Ret. Time	Area	Height	Area%
1	8.162	11625105	411408	26.034
2	18.14	33027854	597164	73.966
Total		44652959	1008572	100

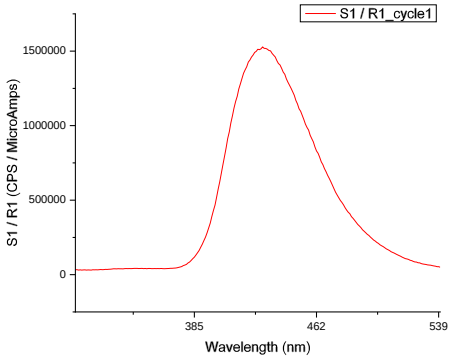

14. HPLC 60% ee

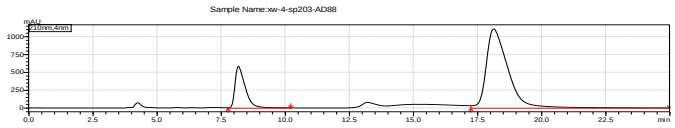

Peak#	Ret. Time	Area	Height	Area%
1	8.179	16068427	583479	19.911
2	18.135	64634213	1108269	80.089
Total		80702641	1691748	100

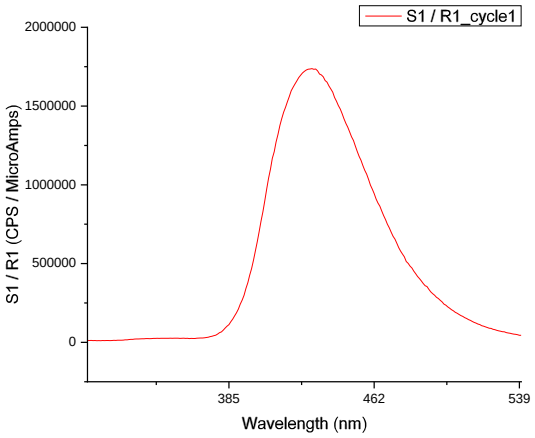

15. HPLC 50.5% ee

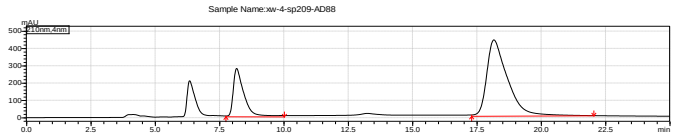

Peak#	Ret. Time	Area	Height	Area%
1	8.168	8088365	277932	24.786
2	18.164	24544368	439349	75.214
Total		32632733	717281	100

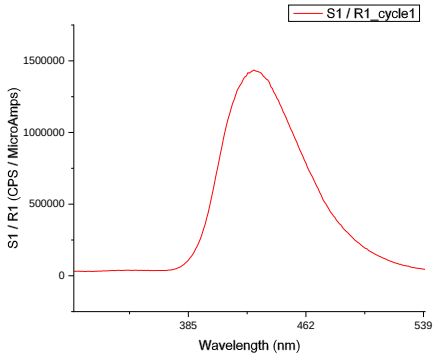

16. HPLC 54.5% ee

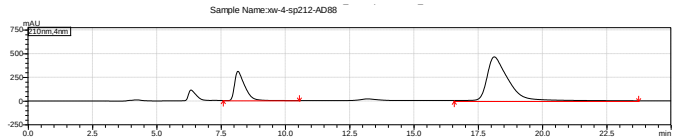

Peak#	Ret. Time	Area	Height	Area%
1	8.16	8350694	308379	22.693
2	18.129	28448319	468181	77.307
Total		36799013	776560	100

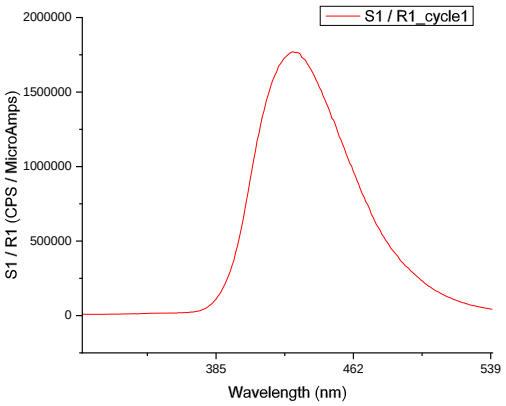

17. HPLC 60% ee

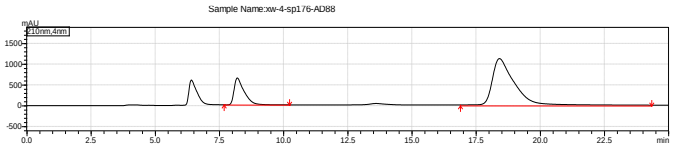

Peak#	Ret. Time	Area	Height	Area%
1	8.203	17802127	647519	19.963
2	18.417	71373804	1131953	80.037
Total		89175931	1779472	100

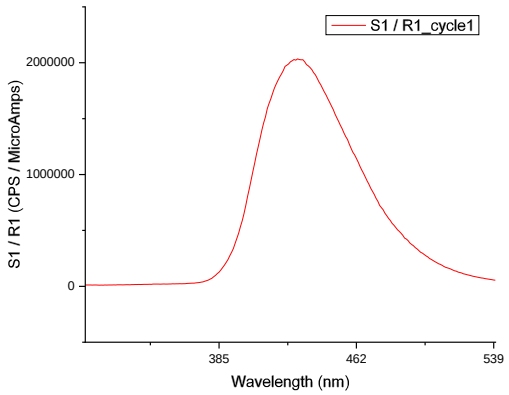

18. HPLC 70% ee

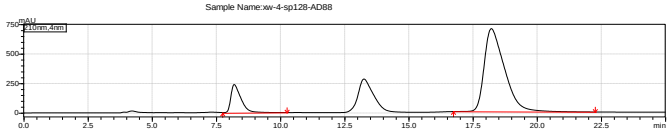

Peak#	Ret. Time	Area	Height	Area%
1	8.2	6810879	241523	14.965
2	18.217	38700198	703946	85.035
Total		45511076	945468	100

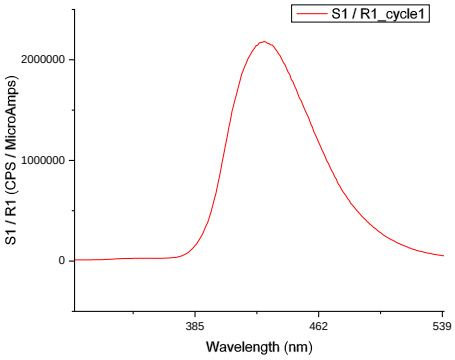

19. HPLC 67% ee

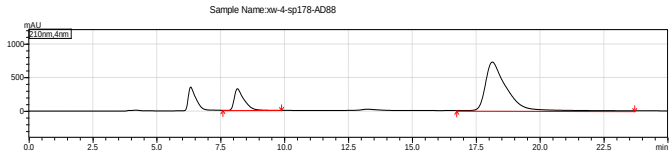

Peak#	Ret. Time	Area	Height	Area%
1	8.16	8483269	321460	16.439
2	18.135	43120491	728923	83.561
Total		51603760	1050383	100

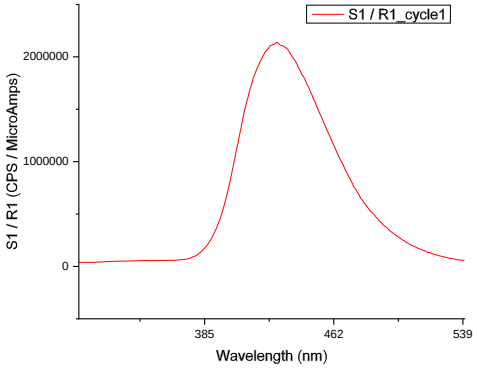

20. HPLC 64.5% ee

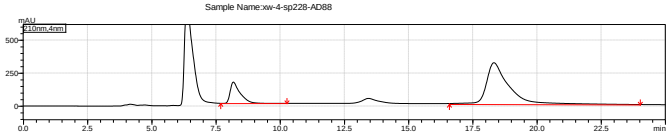

Peak#	Ret. Time	Area	Height	Area%
1	8.182	4287381	161197	17.724
2	18.329	19902142	315681	82.276
Total		24189523	476878	100

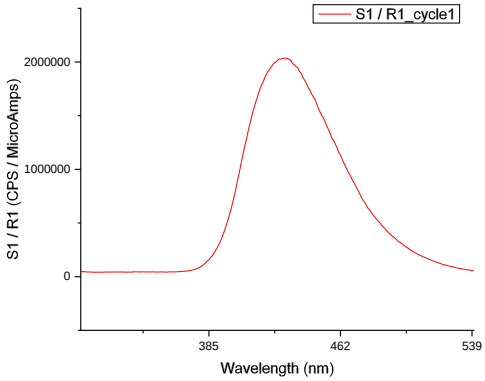

21. HPLC 60% ee

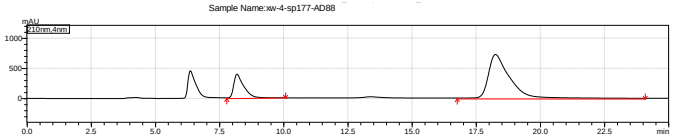

Peak#	Ret. Time	Area	Height	Area%
1	8.183	11112012	399580	19.989
2	18.257	44479823	732535	80.011
Total		55591835	1132115	100

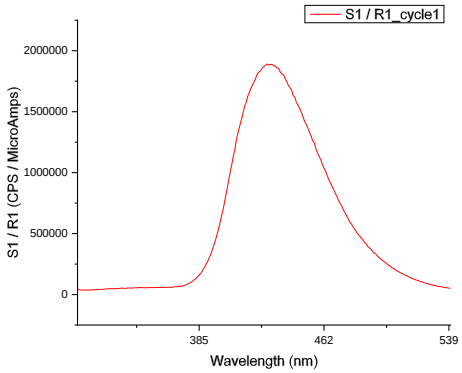

22. HPLC 56.5% ee

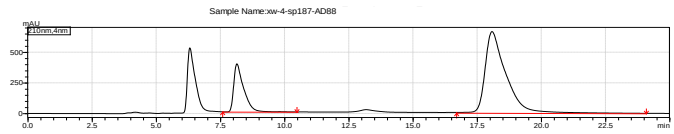

Peak#	Ret. Time	Area	Height	Area%
1	8.146	10488571	392254	21.698
2	18.083	37851214	665108	78.302
Total		48339785	1057361	100

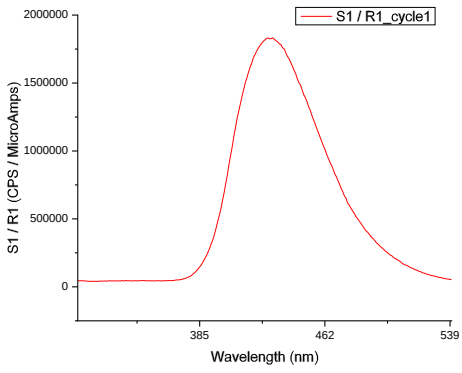

23. HPLC 56% ee

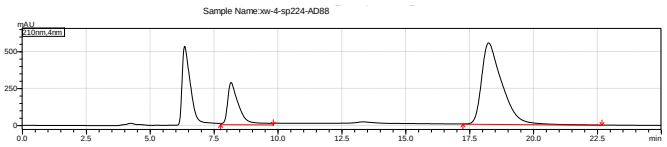

Peak#	Ret. Time	Area	Height	Area%
1	8.172	8586887	284401	22.098
2	18.248	30270682	549881	77.902
Total		38857568	834283	100

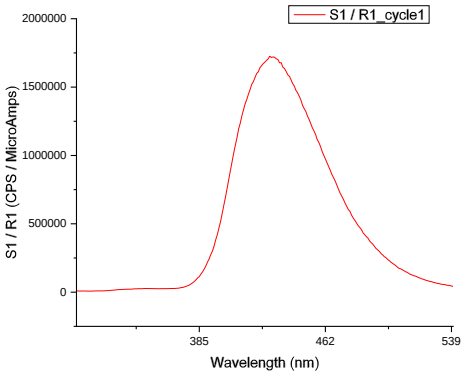

24. HPLC 61.5% ee

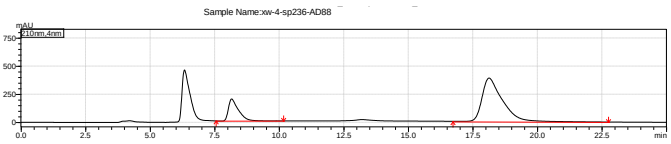

Peak#	Ret. Time	Area	Height	Area%
1	8.161	5208270	195252	19.18
2	18.131	21946699	389118	80.82
Total		27154970	584369	100

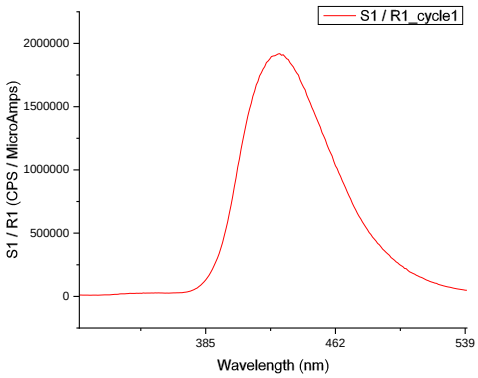

25. HPLC 56% ee

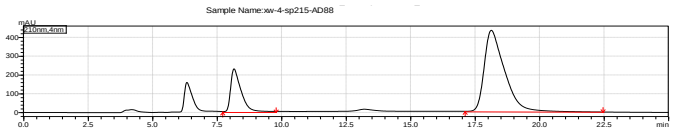

Peak#	Ret. Time	Area	Height	Area%
1	8.159	6689325	231017	21.921
2	18.132	23826471	433208	78.079
Total		30515796	664225	100

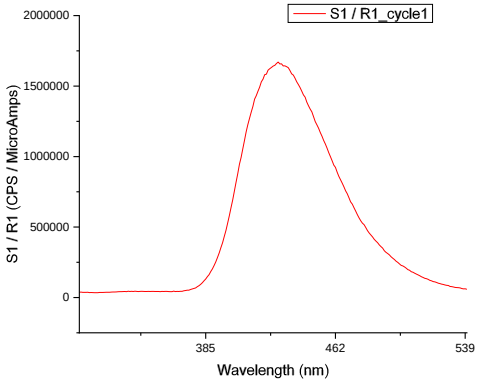

26. HPLC 47.5% ee

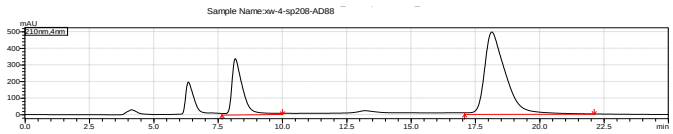

Peak#	Ret. Time	Area	Height	Area%
1	8.176	9912129	337711	26.222
2	18.144	27888513	495160	73.778
Total		37800642	832871	100

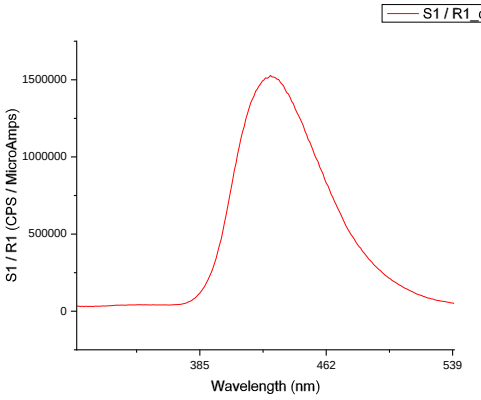

27. HPLC 45% ee

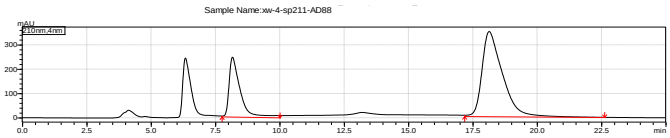

Peak#	Ret. Time	Area	Height	Area%
1	8.164	7288400	244864	27.47
2	18.137	19243550	349150	72.53
Total		26531950	594014	100

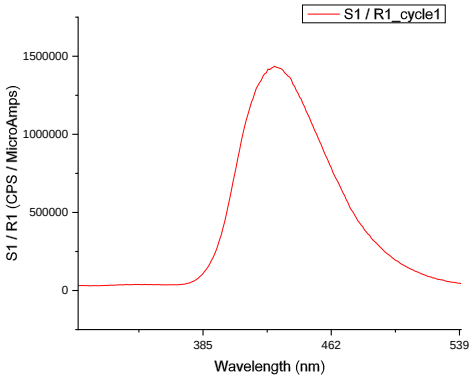

28. HPLC 50.5% ee

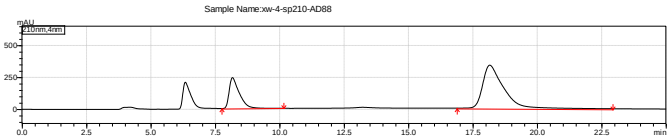

Peak#	Ret. Time	Area	Height	Area%
1	8.168	6728497	243185	24.671
2	18.157	20544814	342195	75.329
Total		27273311	585380	100

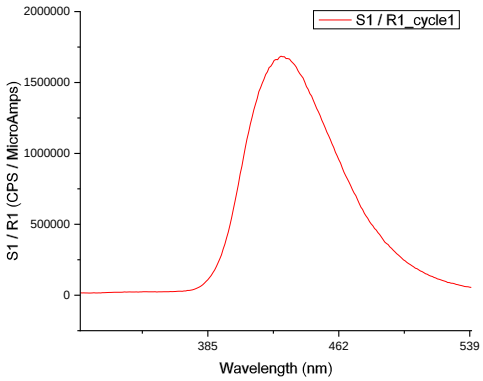

29. HPLC 10% ee

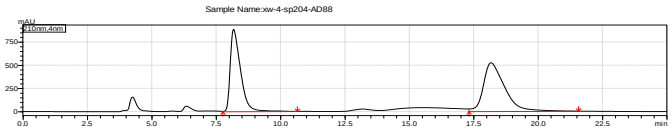

Peak#	Ret. Time	Area	Height	Area%
1	8.181	24488556	885763	44.986
2	18.176	29946984	523937	55.014
Total		54435541	1409700	100

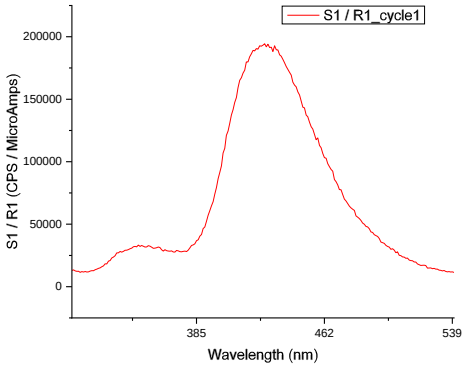

30. HPLC 60% ee

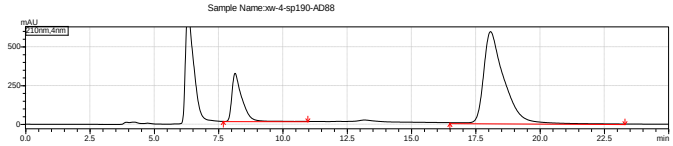

Peak#	Ret. Time	Area	Height	Area%
1	8.147	8261249	309802	20.065
2	18.08	32911068	592871	79.935
Total		41172316	902673	100

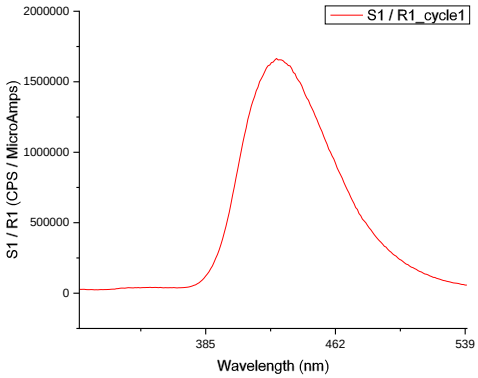

31. HPLC 40.5% ee

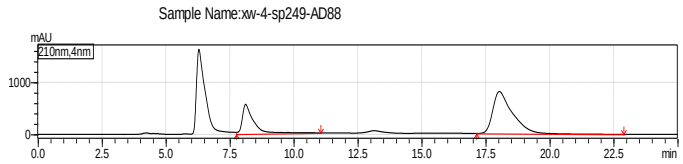

Peak#	Ret. Time	Area	Height	Area%
1	8.121	17609136	569918	29.252
2	18.038	42589542	806398	70.748
Total		60198678	1376316	100

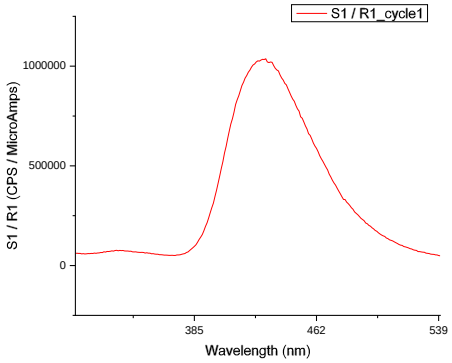

32 HPLC 46% ee

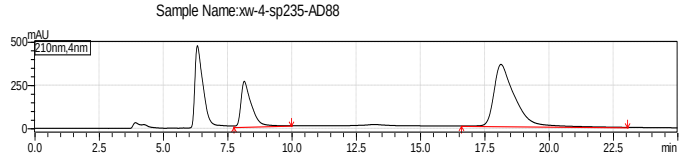

Peak#	Ret. Time	Area	Height	Area%
1	8.154	7386766	262661	27.008
2	18.138	19963842	357949	72.992
Total		27350608	620610	100

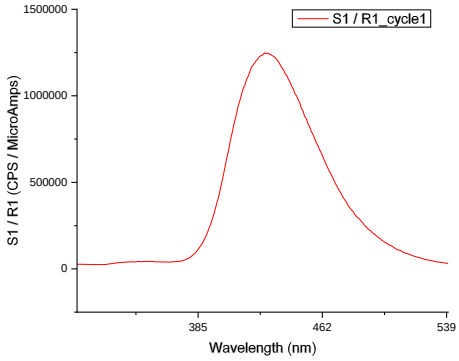

33 HPLC 39% ee

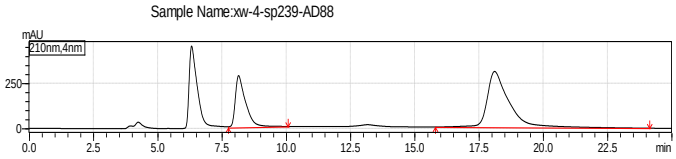

Peak#	Ret. Time	Area	Height	Area%
1	8.153	8053640	288280	30.43
2	18.115	18412794	309777	69.57
Total		26466434	598057	100

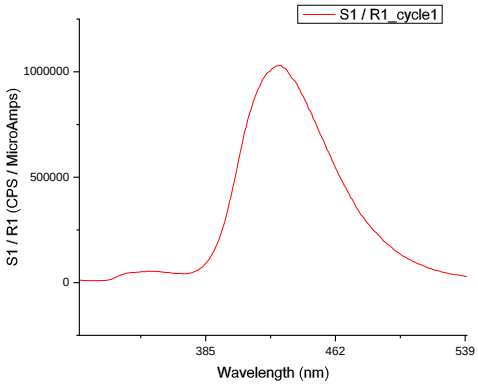

34 HPLC 40.5% ee

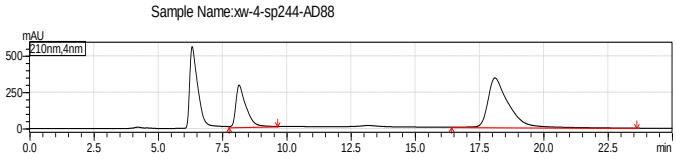

Peak#	Ret. Time	Area	Height	Area%
1	8.152	7936029	290314	29.635
2	18.109	18843446	340760	70.365
Total		26779475	631074	100

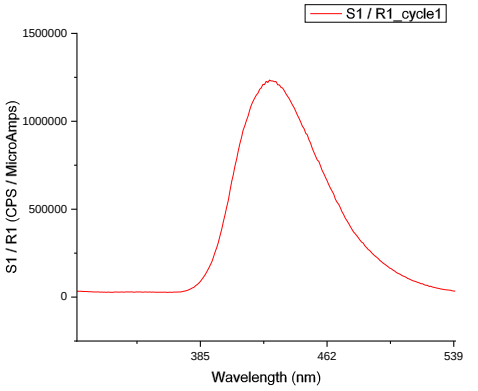

35 HPLC 51.5% ee

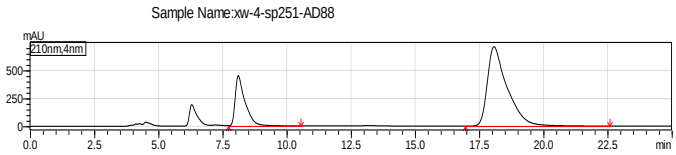

Peak#	Ret. Time	Area	Height	Area%
1	8.111	12144316	451617	24.14
2	18.076	38164371	710594	75.86
Total		50308687	1162212	100

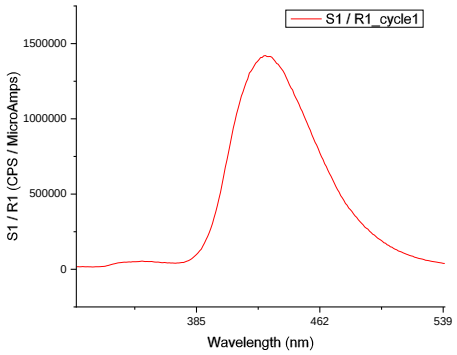

36 HPLC: 67.5% ee

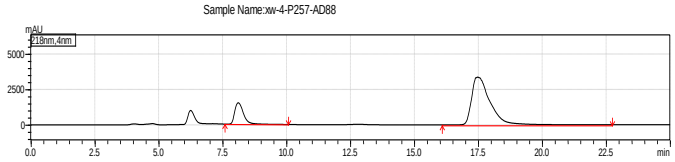

Peak#	Ret. Time	Area	Height	Area%
1	8.111	35993759	1505276	16.109
2	17.481	187439377	3414882	83.891
Total		223433137	4920158	100

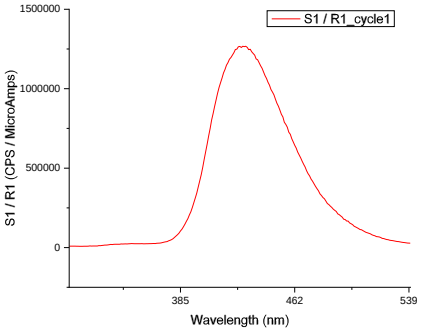

37 HPLC 51% ee

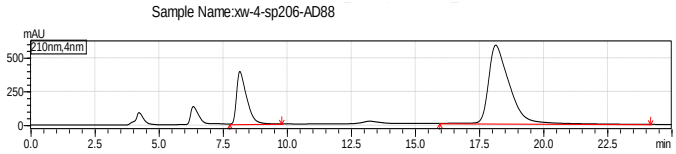

Peak#	Ret. Time	Area	Height	Area%
1	8.161	10692455	392401	24.569
2	18.144	32827316	583499	75.431
Total		43519770	975900	100

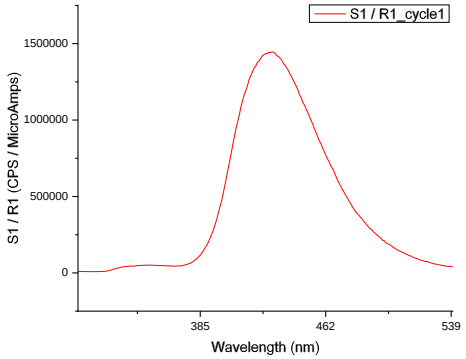

38 HPLC 50.5% ee

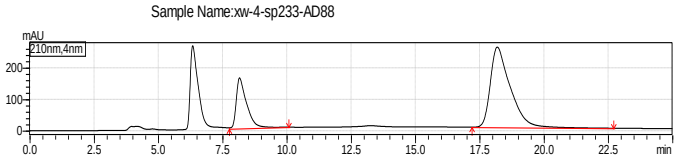

Peak#	Ret. Time	Area	Height	Area%
1	8.166	4493832	160336	24.722
2	18.192	13683800	254332	75.278
Total		18177632	414668	100

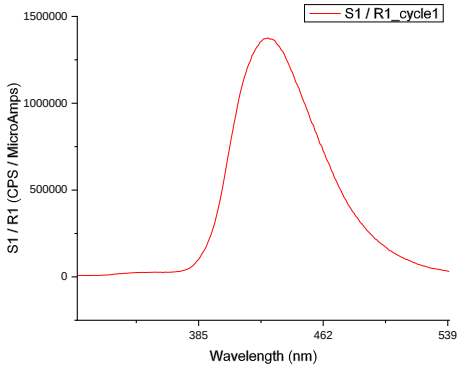

39 HPLC 55% ee

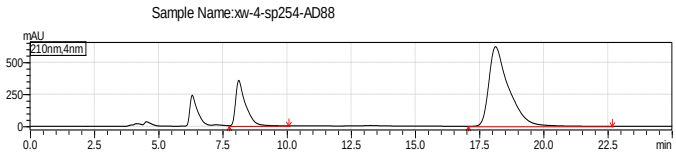

Peak#	Ret. Time	Area	Height	Area%
1	8.126	9596481	356096	22.421
2	18.131	33204433	619588	77.579
Total		42800913	975685	100

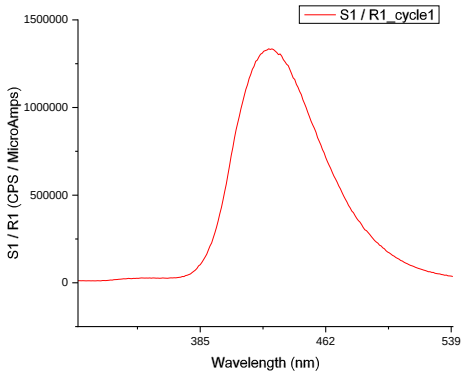

40 HPLC: 59% ee

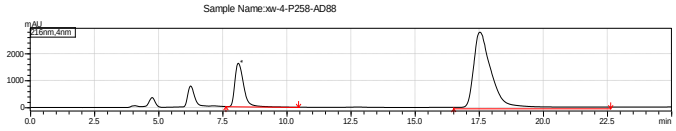

Peak#	Ret. Time	Area	Height	Area%
1	8.111	37733695	1604607	20.556
2	17.542	145829582	2826525	79.444
Total		183563277	4431131	100

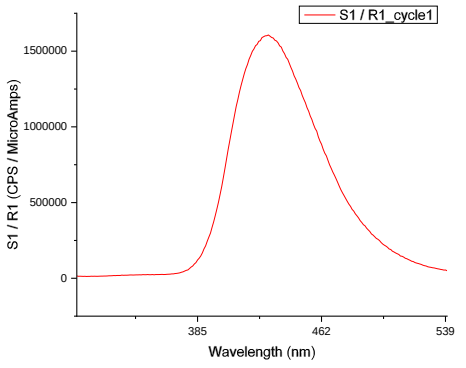

41 HPLC: 59.5% ee

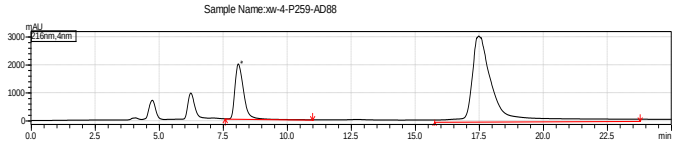

Peak#	Ret. Time	Area	Height	Area%
1	8.096	45280886	1966943	19.739
2	17.489	184114240	3073379	80.261
Total		229395127	5040322	100

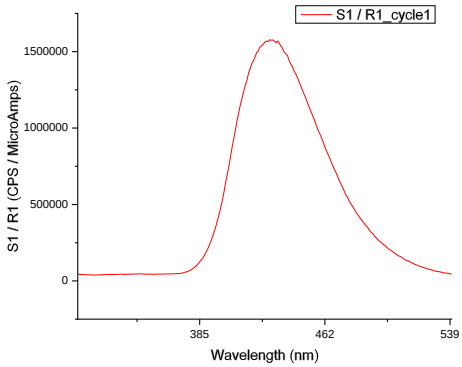

42 HPLC 36% ee

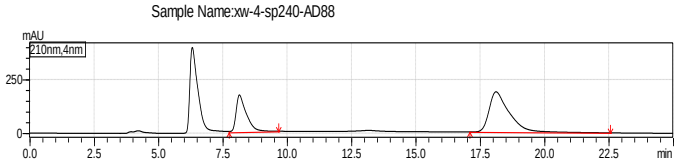

Peak#	Ret. Time	Area	Height	Area%
1	8.151	4789855	173471	31.811
2	18.124	10267569	188200	68.189
Total		15057424	361672	100

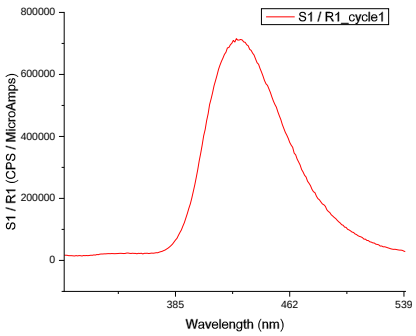

43 HPLC 57% ee

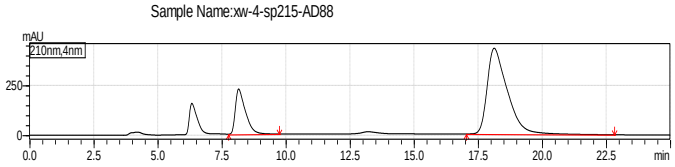

Peak#	Ret. Time	Area	Height	Area%
1	8.159	6273735	228619	21.024
2	18.132	23567740	431783	78.976
Total		29841475	660402	100

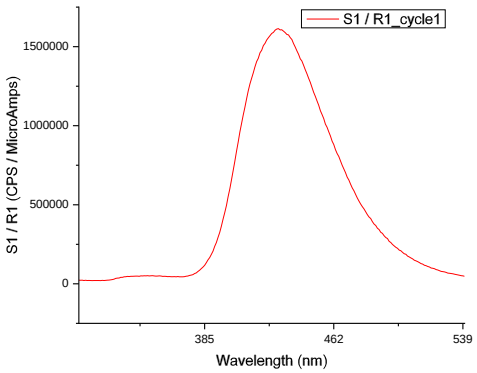

44 HPLC: 54% ee

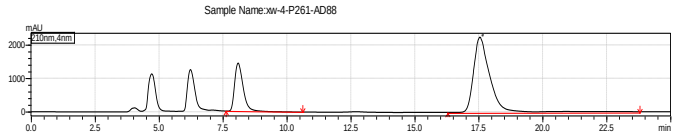

Peak#	Ret. Time	Area	Height	Area%
1	8.094	32974540	1438955	23.071
2	17.537	109950400	2269544	76.929
Total		142924939	3708499	100

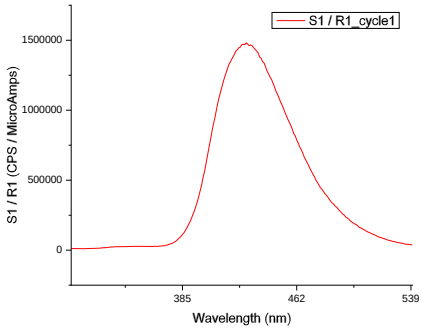

45 HPLC 43.5% ee

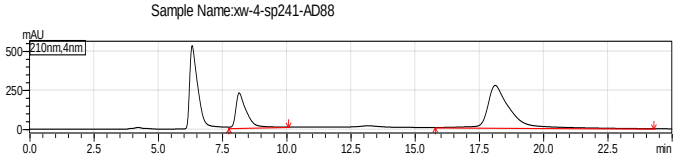

Peak#	Ret. Time	Area	Height	Area%
1	8.158	6346641	224862	28.284
2	18.125	16092288	271850	71.716
Total		22438928	496712	100

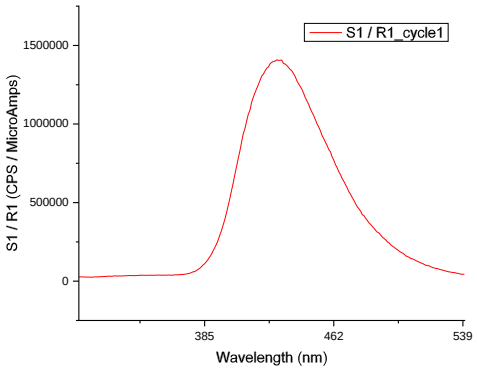

46 HPLC 40.5% ee

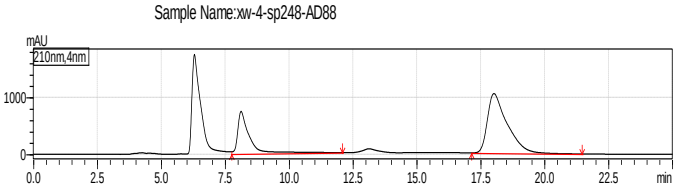

Peak#	Ret. Time	Area	Height	Area%
1	8.127	23770228	745705	29.742
2	18.023	56151206	1045839	70.258
Total		79921434	1791544	100

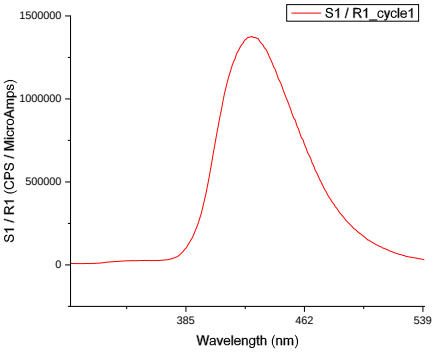

47 HPLC: 56.5% ee

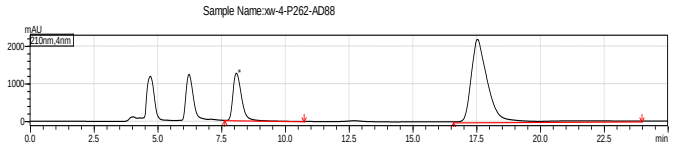

Peak#	Ret. Time	Area	Height	Area%
1	8.086	28855752	1257671	21.669
2	17.529	104310975	2207980	78.331
Total		133166727	3465652	100

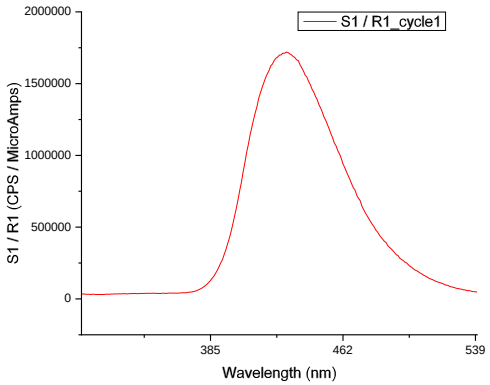

48 HPLC 57.5% ee

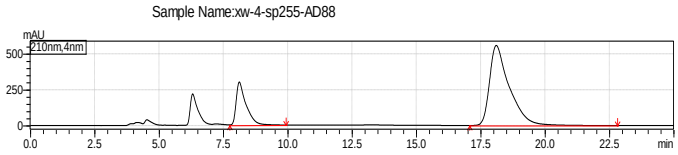

Peak#	Ret. Time	Area	Height	Area%
1	8.124	8069050	301722	21.35
2	18.111	29724993	557656	78.65
Total		37794043	859377	100

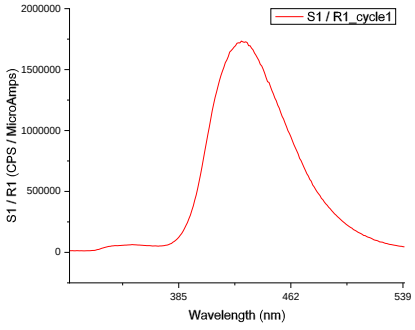

49 HPLC 43.5% ee

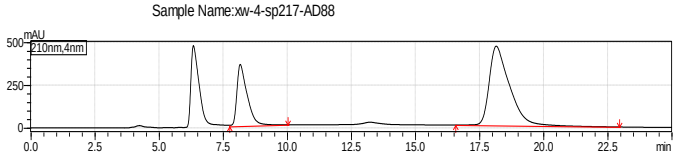

Peak#	Ret. Time	Area	Height	Area%
1	8.173	10116289	361174	28.164
2	18.158	25802998	464929	71.836
Total		35919288	826102	100

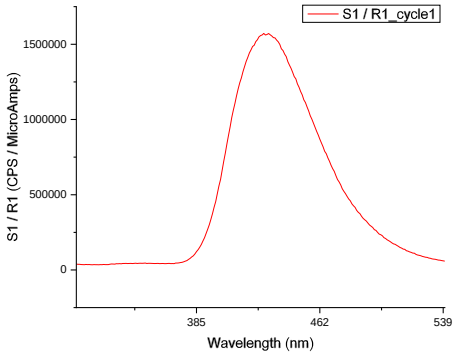

50 HPLC 52% ee

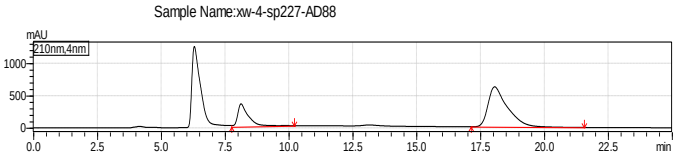

Peak#	Ret. Time	Area	Height	Area%
1	8.131	10400137	353937	24.093
2	18.061	32767138	619020	75.907
Total		43167276	972957	100

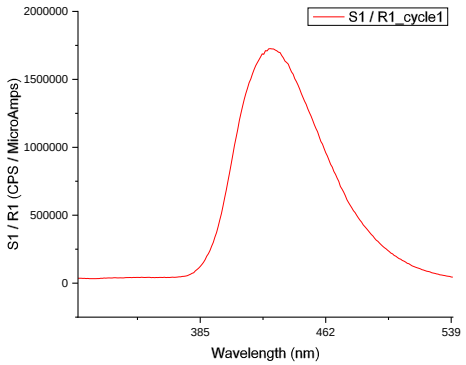

51 HPLC: 54.5% ee

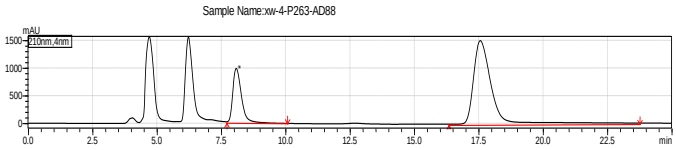

Peak#	Ret. Time	Area	Height	Area%
1	8.086	23259025	986075	22.799
2	17.57	78760240	1523966	77.201
Total		102019264	2510041	100

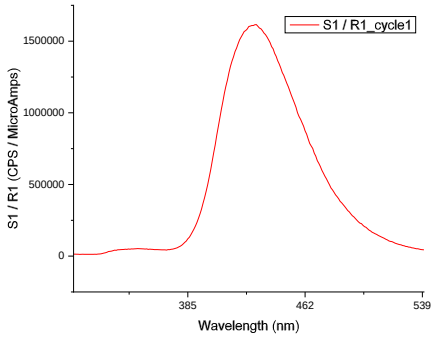

52 HPLC 33% ee

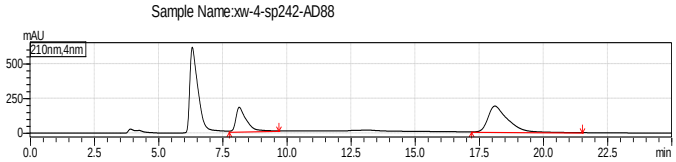

Peak#	Ret. Time	Area	Height	Area%
1	8.151	4965180	176368	33.476
2	18.118	9867032	186925	66.524
Total		14832213	363293	100

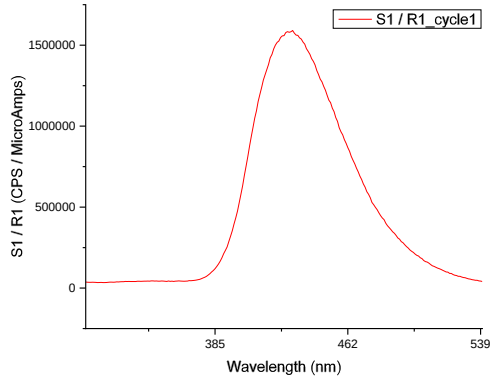

53 HPLC 58.5% ee

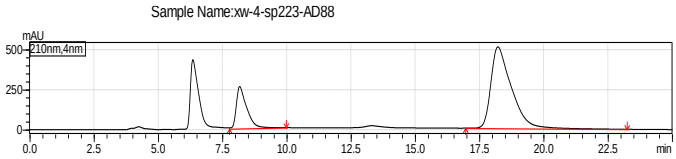

Peak#	Ret. Time	Area	Height	Area%
1	8.173	7356596	262645	20.647
2	18.223	28274278	508957	79.353
Total		35630874	771601	100

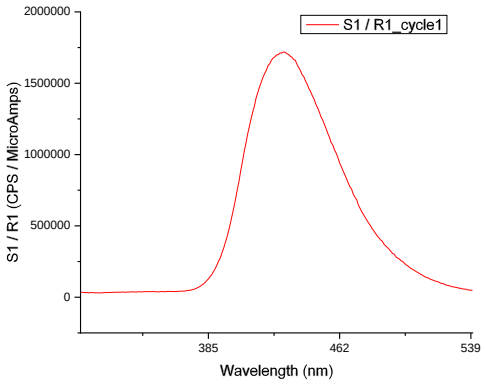

54 HPLC 57% ee

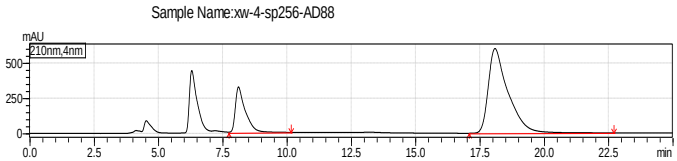

Peak#	Ret. Time	Area	Height	Area%
1	8.121	8842680	325951	21.598
2	18.095	32099224	600900	78.402
Total		40941904	926850	100

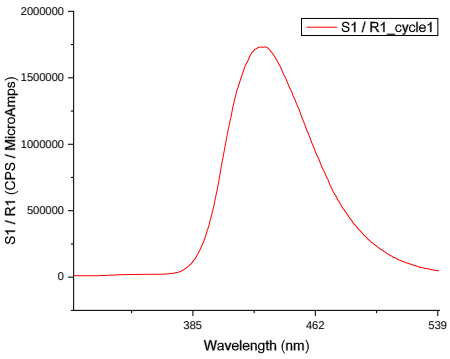

55 HPLC 56.5% ee

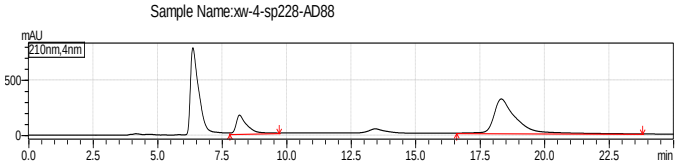

Peak#	Ret. Time	Area	Height	Area%
1	8.182	5005278	169784	21.612
2	18.329	18154769	310801	78.388
Total		23160047	480585	100

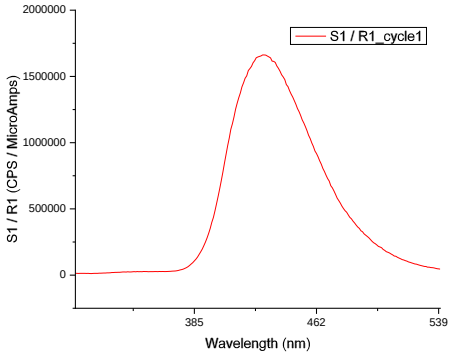

HPLC 50% ee (Second independent measurement)

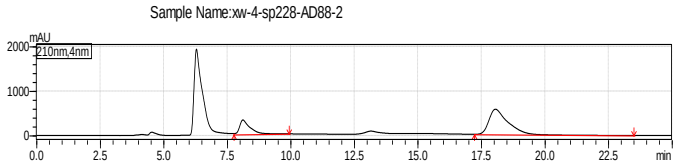

Peak#	Ret. Time	Area	Height	Area%
1	8.125	9547579	325993	25.033
2	18.063	28591974	565941	74.967
Total		38139553	891934	100

56 HPLC 60.5% ee

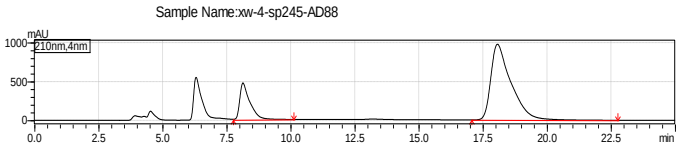

Peak#	Ret. Time	Area	Height	Area%
1	8.138	13117309	474896	19.753
2	18.072	53287806	975148	80.247
Total		66405115	1450044	100

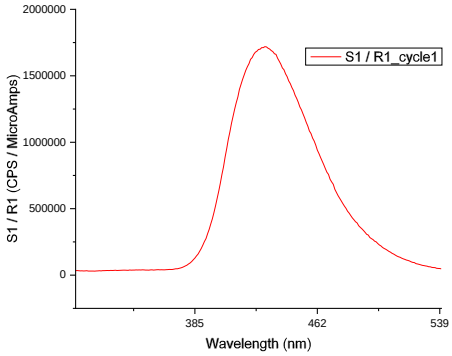

HPLC 55.5% ee (Second independent measurement)

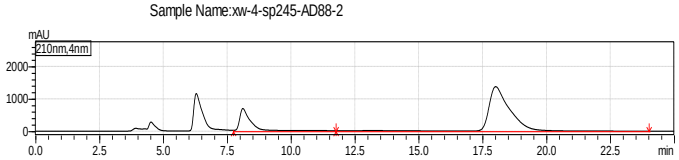

Peak#	Ret. Time	Area	Height	Area%
1	8.121	22998095	701809	22.233
2	18.017	80442465	1376882	77.767
Total		103440560	2078691	100

57 HPLC 50.5% ee

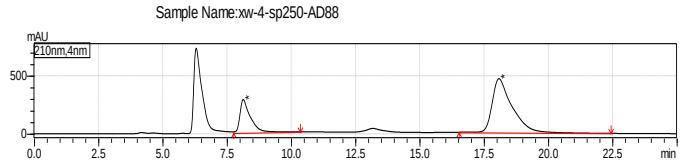

Peak#	Ret. Time	Area	Height	Area%
1	8.137	8175251	287372	24.702
2	18.087	24919808	464260	75.298
Total		33095058	751632	100

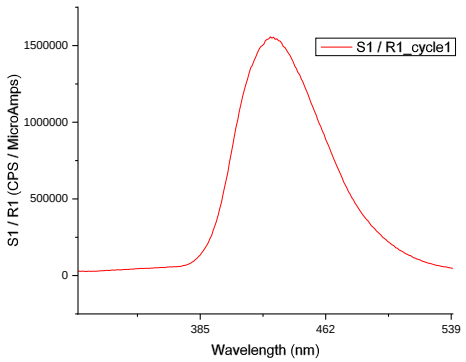

HPLC 44% ee (Second independent measurement)

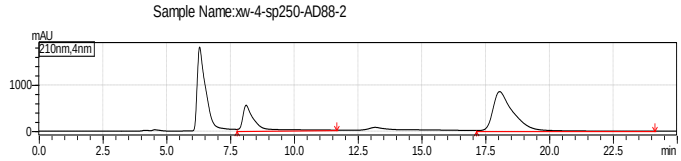

Peak#	Ret. Time	Area	Height	Area%
1	8.12	18516183	558968	28.047
2	18.055	47501168	853688	71.953
Total		66017351	1412656	100

58 HPLC 58% ee

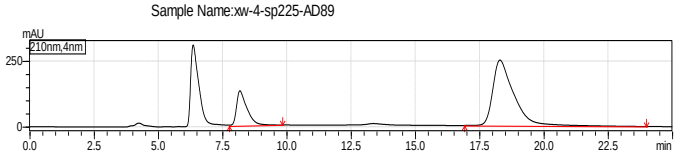

Peak#	Ret. Time	Area	Height	Area%
1	8.182	3780992	133628	21.048
2	18.299	14182697	249746	78.952
Total		17963689	383374	100

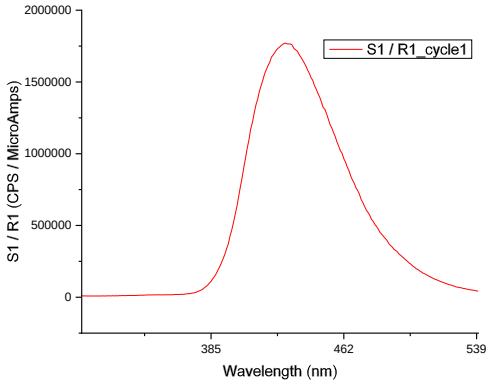

59 HPLC 64.5% ee

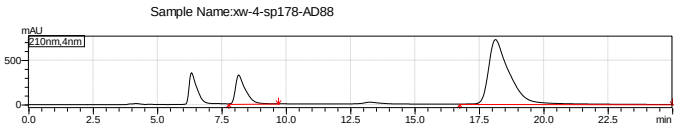

Peak#	Ret. Time	Area	Height	Area%
1	8.16	8749320	324951	17.822
2	18.135	40342712	722947	82.178
Total		49092032	1047899	100

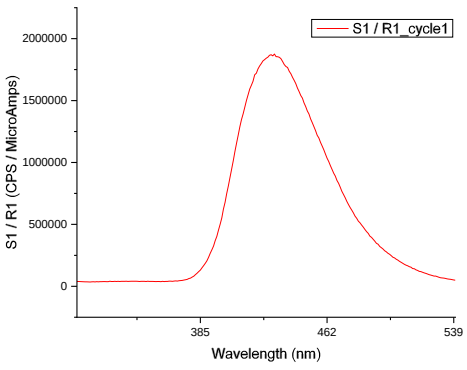

60 HPLC 39.5% ee

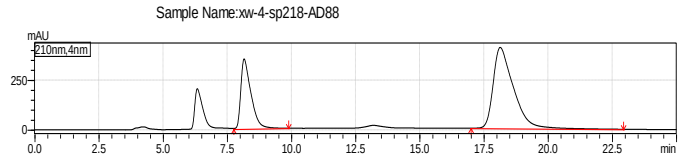

Peak#	Ret. Time	Area	Height	Area%
1	8.164	9613085	350739	30.17
2	18.143	22249519	406402	69.83
Total		31862604	757141	100

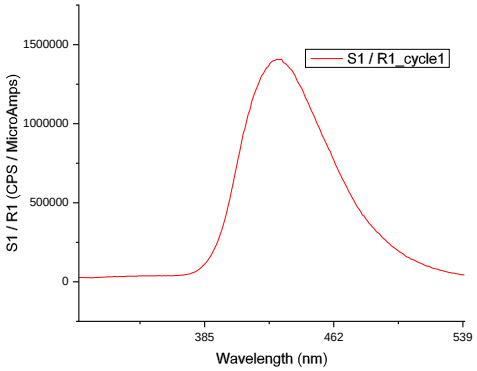

61 HPLC 46.5% ee

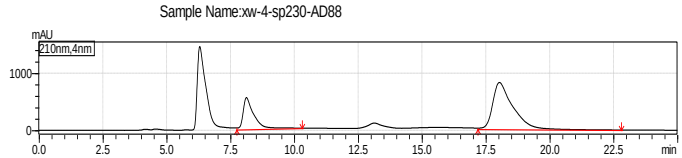

Peak#	Ret. Time	Area	Height	Area%
1	8.128	16320486	556607	26.661
2	18.036	44894654	816173	73.339
Total		61215141	1372780	100

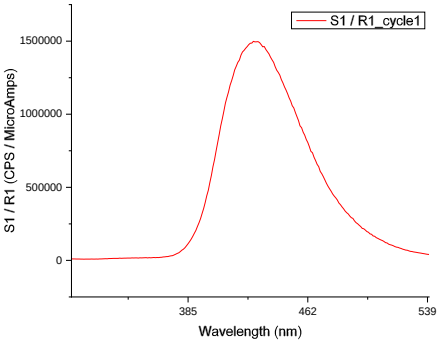

62 HPLC 42% ee

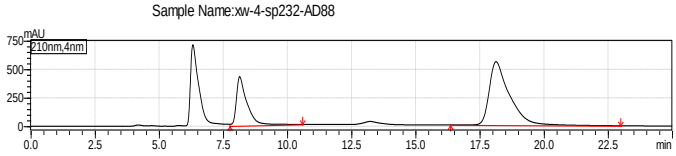

Peak#	Ret. Time	Area	Height	Area%
1	8.145	12411686	430853	28.813
2	18.136	30664480	557480	71.187
Total		43076167	988333	100

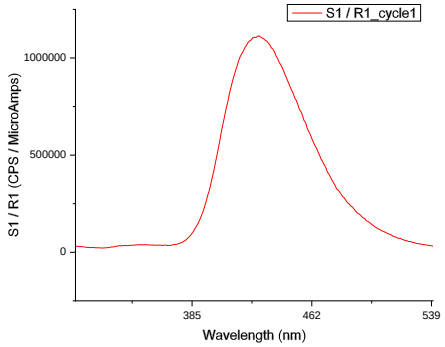

63 HPLC: 61% ee

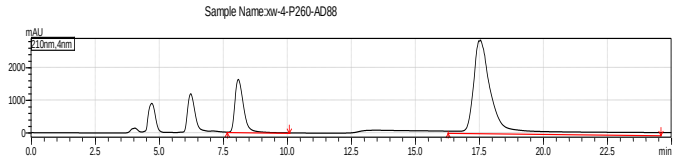

Peak#	Ret. Time	Area	Height	Area%
1	8.093	37416208	1617479	19.494
2	17.534	154516520	2835143	80.506
Total		191932728	4452622	100

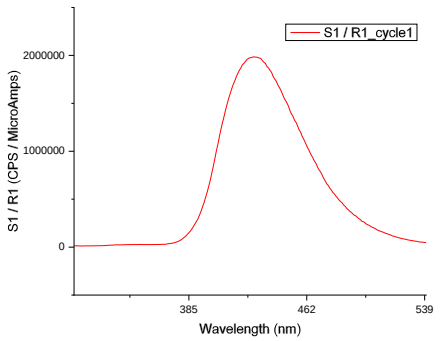

64 HPLC 61% ee

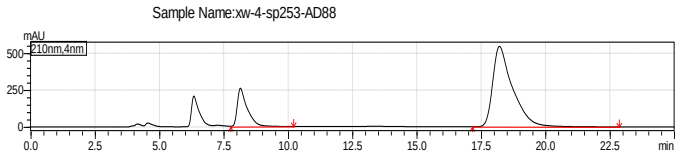

Peak#	Ret. Time	Area	Height	Area%
1	8.149	7085769	261374	19.503
2	18.214	29245568	545328	80.497
Total		36331337	806702	100

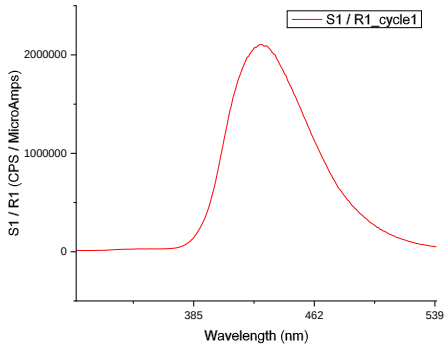

65 HPLC 56% ee

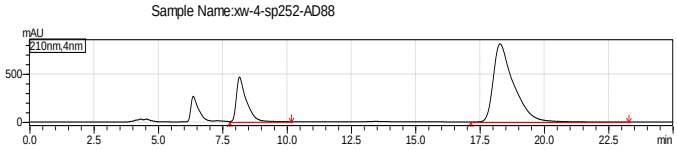

Peak#	Ret. Time	Area	Height	Area%
1	8.161	12595063	465288	22.076
2	18.289	44456963	811955	77.924
Total		57052026	1277243	100

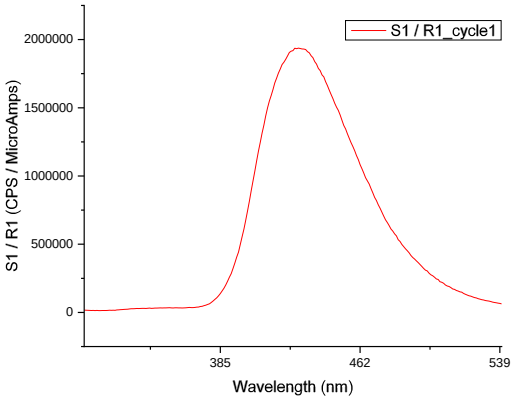

66 HPLC 60.5% ee

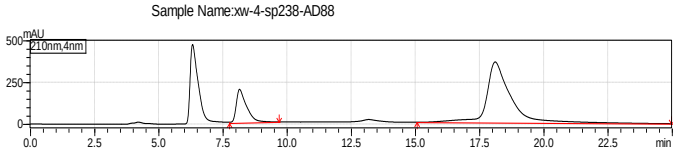

Peak#	Ret. Time	Area	Height	Area%
1	8.158	5590498	200635	19.123
2	18.116	23644610	363401	80.877
Total		29235107	564036	100

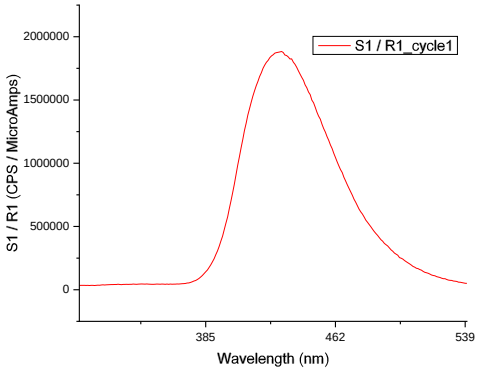

67 HPLC 56% ee

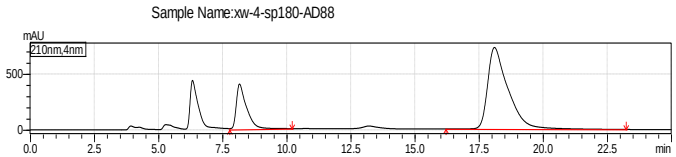

Peak#	Ret. Time	Area	Height	Area%
1	8.166	11385868	406960	21.91
2	18.109	40579860	731276	78.09
Total		51965729	1138236	100

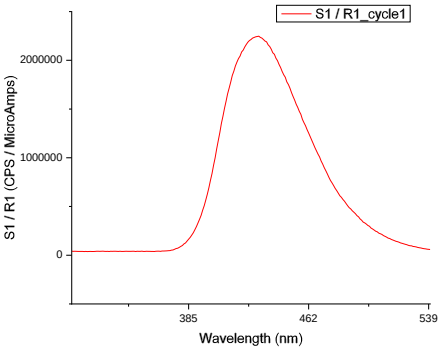

68 HPLC 60.5% ee

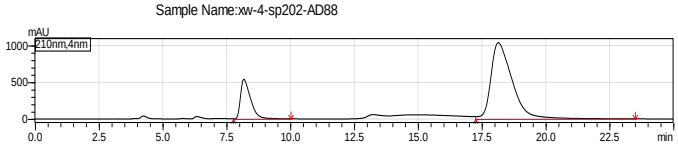

Peak#	Ret. Time	Area	Height	Area%
1	8.178	14705842	539217	19.67
2	18.143	60058297	1037436	80.33
Total		74764139	1576653	100

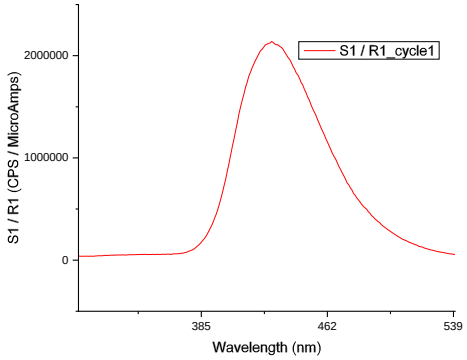

69 HPLC 51% ee

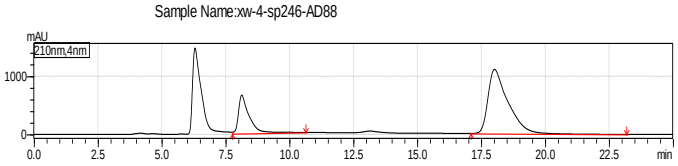

Peak#	Ret. Time	Area	Height	Area%
1	8.13	19395495	661496	24.578
2	18.022	59519619	1101300	75.422
Total		78915113	1762796	100

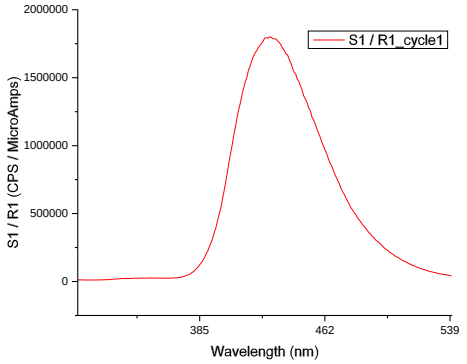

70 HPLC 41.5% ee

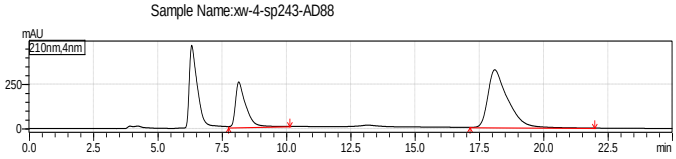

Peak#	Ret. Time	Area	Height	Area%
1	8.152	7162310	256368	29.269
2	18.107	17308059	325500	70.731
Total		24470368	581868	100

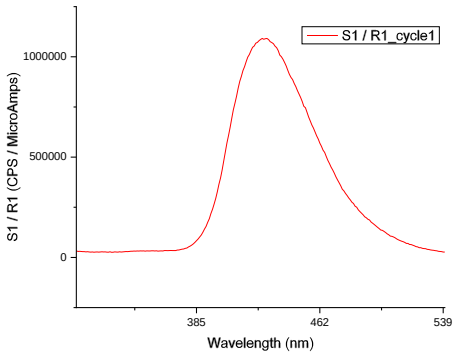

71 HPLC 49% ee

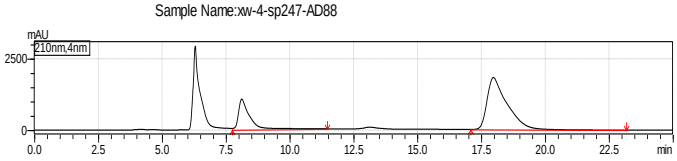

Peak#	Ret. Time	Area	Height	Area%
1	8.121	33673478	1072763	25.449
2	17.973	98642278	1821533	74.551
Total		132315755	2894296	100

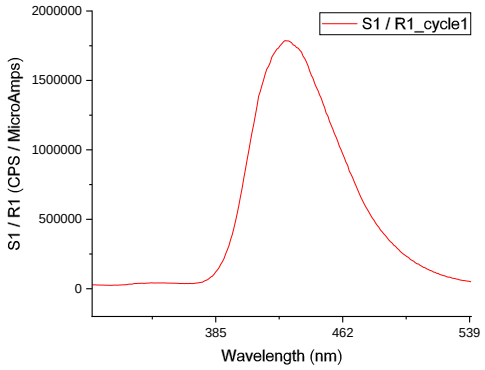

72 HPLC 57.5% ee

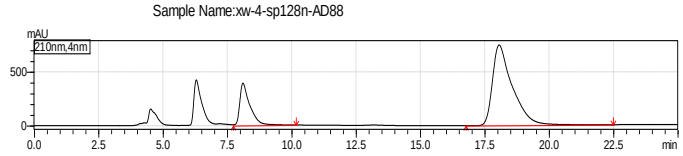

Peak#	Ret. Time	Area	Height	Area%
1	8.113	10748665	394279	21.145
2	18.063	40085216	748967	78.855
Total		50833881	1143246	100

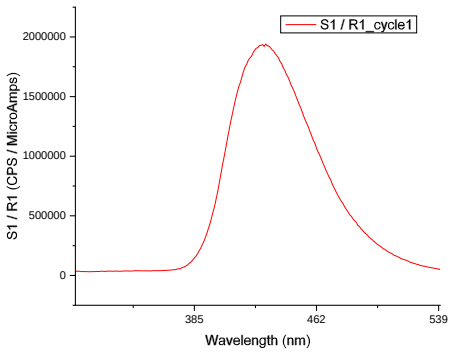

73 HPLC: 51.5% ee

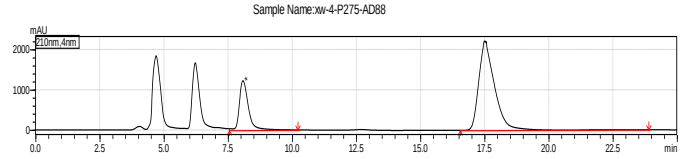

Peak#	Ret. Time	Area	Height	Area%
1	8.085	30279670	1232806	24.288
2	17.495	94389594	2220935	75.712
Total		124669264	3453742	100

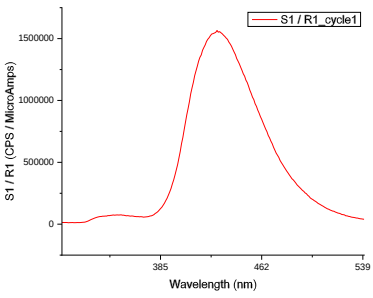

74 HPLC: 65% ee

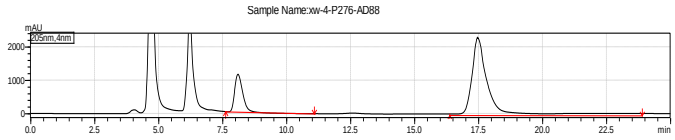

Peak#	Ret. Time	Area	Height	Area%
1	8.108	23089622	1127923	17.408
2	17.462	109552041	2340420	82.592
Total		132641663	3468343	100

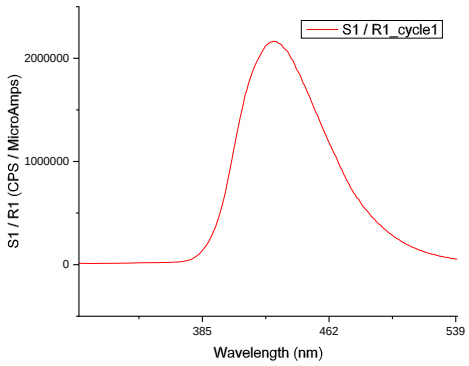

75 HPLC: 63.5% ee

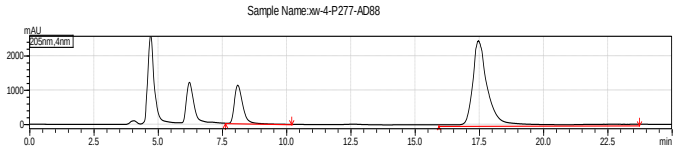

Peak#	Ret. Time	Area	Height	Area%
1	8.104	24535463	1115202	18.158
2	17.451	110584797	2477394	81.842
Total		135120260	3592596	100

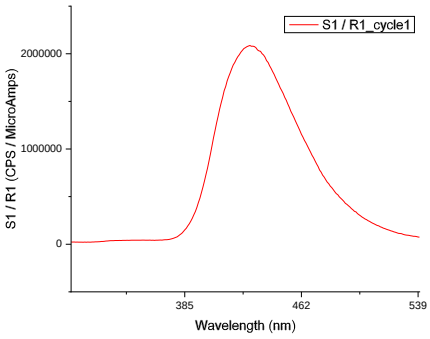

76 HPLC: 64% ee

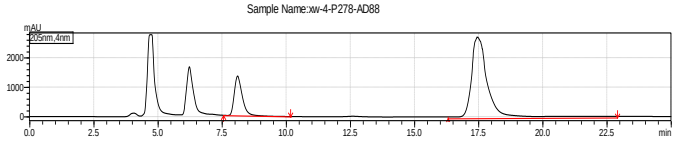

Peak#	Ret. Time	Area	Height	Area%
1	8.107	28632143	1343034	18.064
2	17.444	129874269	2762704	81.936
Total		158506412	4105739	100

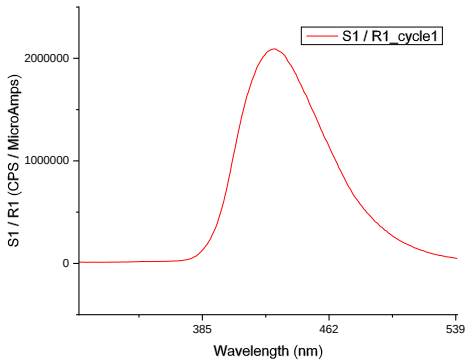

77 HPLC: 60.5% ee

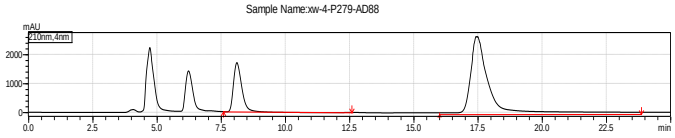

Peak#	Ret. Time	Area	Height	Area%
1	8.118	35094928	1696005	19.658
2	17.431	143432219	2687004	80.342
Total		178527147	4383009	100

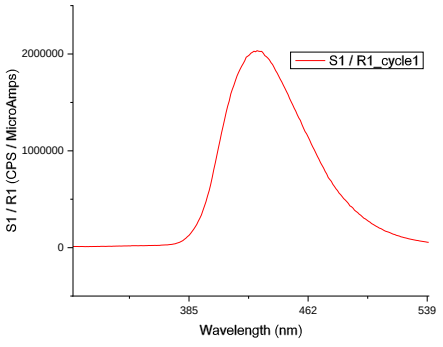

78 HPLC: 62.5% ee

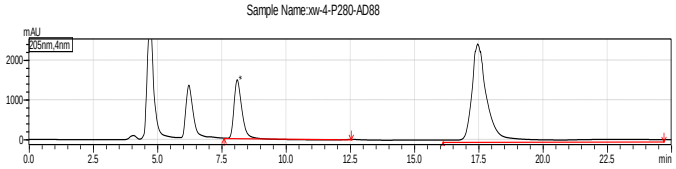

Peak#	Ret. Time	Area	Height	Area%
1	8.105	27195117	1471046	18.756
2	17.465	117797516	2465459	81.244
Total		144992634	3936505	100

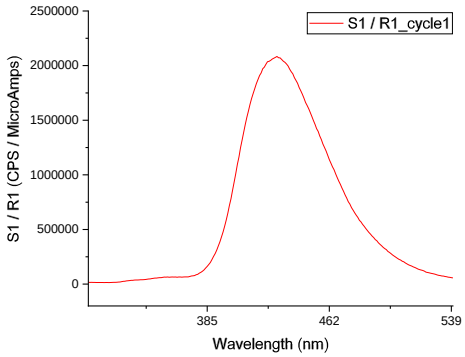

79 HPLC: 63% ee

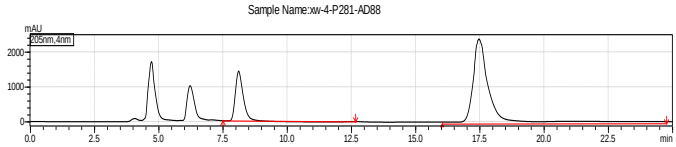

Peak#	Ret. Time	Area	Height	Area%
1	8.117	26962349	1427730	18.498
2	17.471	118797597	2426360	81.502
Total		145759946	3854090	100

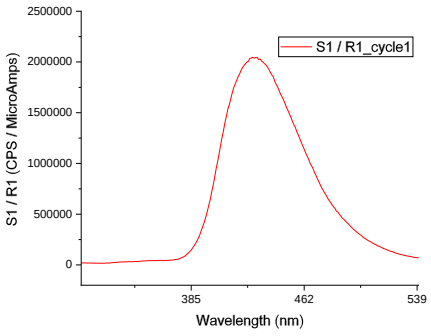

80 HPLC: 42% ee

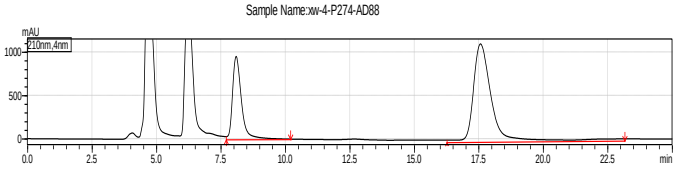

Peak#	Ret. Time	Area	Height	Area%
1	8.094	23163016	955494	28.918
2	17.574	56935801	1128338	71.082
Total		80098816	2083832	100

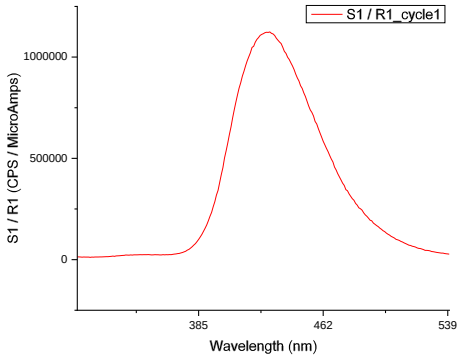

81 HPLC: 61.5% ee

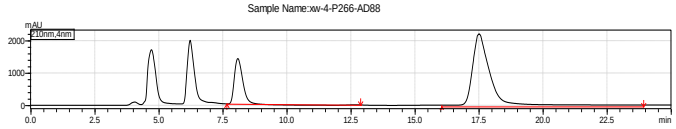

Peak#	Ret. Time	Area	Height	Area%
1	8.086	28343771	1402932	19.172
2	17.504	119493745	2249670	80.828
Total		147837515	3652602	100

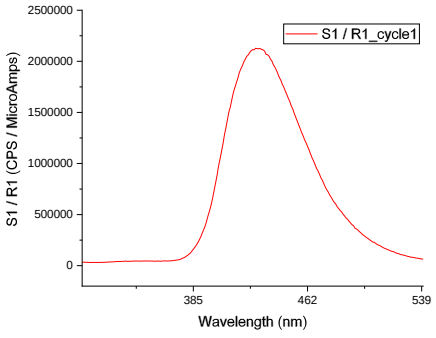

82 HPLC: 67% ee

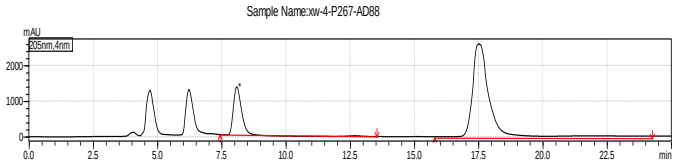

Peak#	Ret. Time	Area	Height	Area%
1	8.086	26603337	1347929	16.535
2	17.524	134284217	2638697	83.465
Total		160887554	3986627	100

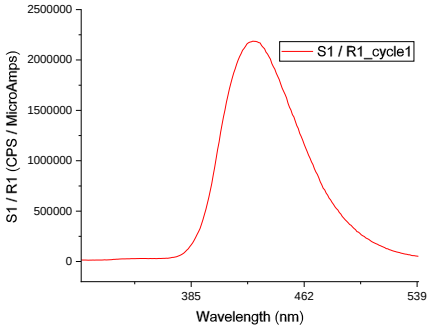

83 HPLC: 67.5% ee

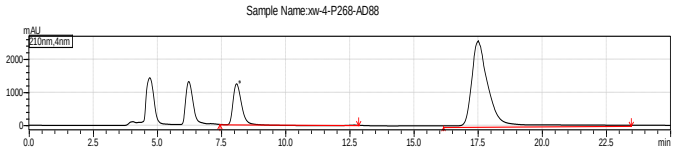

Peak#	Ret. Time	Area	Height	Area%
1	8.09	23972565	1229128	16.174
2	17.487	124243118	2572108	83.826
Total		148215683	3801235	100

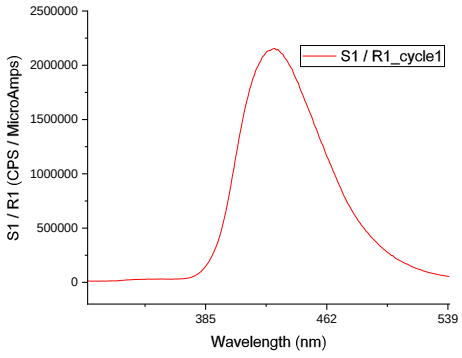

84 HPLC: 67.5% ee

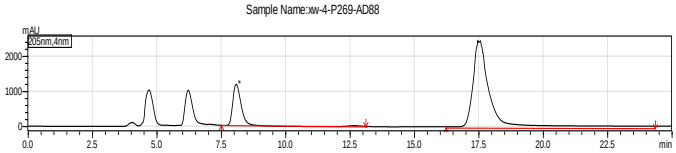

Peak#	Ret. Time	Area	Height	Area%
1	8.087	24035011	1174684	16.228
2	17.473	124070799	2489346	83.772
Total		148105810	3664030	100

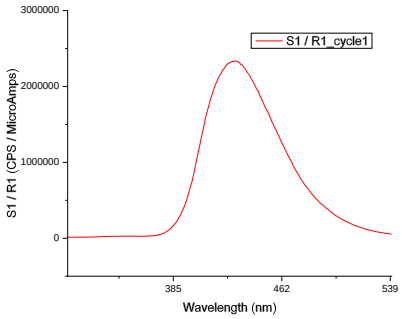

85 HPLC: 59.5% ee

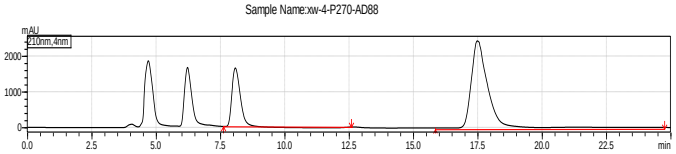

Peak#	Ret. Time	Area	Height	Area%
1	8.083	32500993	1640863	20.258
2	17.487	127930801	2477539	79.742
Total		160431795	4118402	100

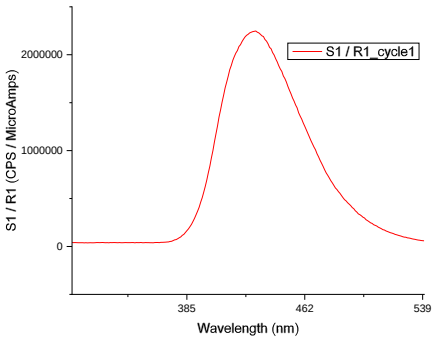

86 HPLC: 62% ee

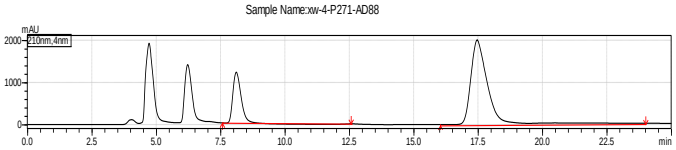

Peak#	Ret. Time	Area	Height	Area%
1	8.113	23604653	1204191	19.052
2	17.464	100292682	2026682	80.948
Total		123897335	3230872	100

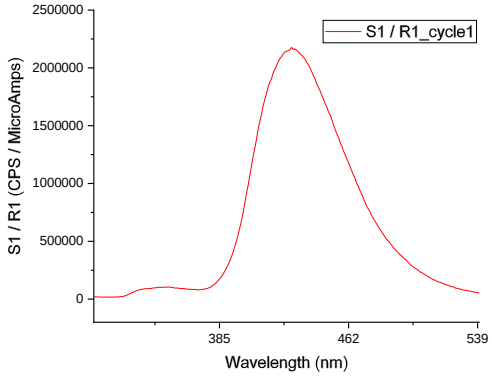

Crystal Structure Report for Pu_XW_ss_ipr_cy_dev

A colorless plate-like specimen of $C_{17}H_{25}NO_2$, approximate dimensions 0.063 mm x 0.081 mm x 0.334 mm, was coated with Paratone oil and mounted on a MiTeGen MicroLoop. The X-ray intensity data were measured on a Bruker Kappa APEXII Duo system equipped with a Incoatec Microfocus IμS (Cu K_α, λ = 1.54178 Å) and a multilayer mirror monochromator.

The total exposure time was 11.88 hours. The frames were integrated with the Bruker SAINT software package[1] using a narrow-frame algorithm. The integration of the data using an orthorhombic unit cell yielded a total of 14692 reflections to a maximum θ angle of 68.25° (0.83 Å resolution), of which 2886 were independent (average redundancy 5.091, completeness = 99.8%, R_{int} = 4.93%, R_{sig} = 3.53%) and 2743 (95.05%) were greater than $2\sigma(F^2)$. The final cell constants of a = 6.4074(2) Å, b = 11.8303(3) Å, c = 20.8877(5) Å, volume = 1583.32(7) $Å^3$, are based upon the refinement of the XYZ-centroids of 7079 reflections above 20 σ(I) with 8.466° < 2θ < 136.4°. Data were corrected for absorption effects using the Multi-Scan method (SADABS).[1] The ratio of minimum to maximum apparent transmission was 0.902. The calculated minimum and maximum transmission coefficients (based on crystal size) are 0.8280 and 0.9640. The structure was solved and refined using the Bruker SHELXTL Software Package[2] within APEX3 [1] and OLEX2,[3] using the space group P $2_12_12_1$, with Z = 4 for the formula unit, $C_{17}H_{25}NO_2$. Non-hydrogen atoms were refined anisotropically. The O-H hydrogen atom was located in the diffraction map and refined isotropically. All other hydrogen atoms were placed in geometrically calculated positions with U_{iso} = 1.2U_{equiv} of the parent atom (U_{iso} = 1.5U_{equiv} for

1 Bruker (2012). *Saint; SADABS; APEX3*. Bruker AXS Inc., Madison, Wisconsin, USA.
2 Sheldrick, G. M. (2015). *Acta Cryst.* A**71**, 3-8.
3 Dolomanov, O. V.; Bourhis, L. J.; Gildea, R. J.; Howard, J. A. K.; Puschmann, H. *J. Appl. Cryst.* (2009). **42**, 339-341.

methyl). The final anisotropic full-matrix least-squares refinement on F^2 with 188 variables converged at R1 = 3.07%, for the observed data and wR2 = 7.68% for all data. The goodness-of-fit was 1.050. The largest peak in the final difference electron density synthesis was 0.136 $e^-/Å^3$ and the largest hole was -0.224 $e^-/Å^3$ with an RMS deviation of 0.035 $e^-/Å^3$. On the basis of the final model, the calculated density was 1.155 g/cm^3 and F(000), 600 e^-.

Table S2-1. Sample and crystal data for Pu_XW_ss_ipr_cy_dev.

Identification code	Pu_XW_ss_ipr_cy_dev	
Chemical formula	$C_{17}H_{25}NO_2$	
Formula weight	275.38 g/mol	
Temperature	100(2) K	
Wavelength	1.54178 Å	
Crystal size	0.063 x 0.081 x 0.334 mm	
Crystal habit	colorless plate	
Crystal system	orthorhombic	
Space group	P $2_12_12_1$	
Unit cell dimensions	a = 6.4074(2) Å	α = 90°
	b = 11.8303(3) Å	β = 90°
	c = 20.8877(5) Å	γ = 90°
Volume	1583.32(7) $Å^3$	
Z	4	
Density (calculated)	1.155 g/cm^3	
Absorption coefficient	0.588 mm^{-1}	
F(000)	600	

Table S2-2. Data collection and structure refinement for Pu_XW_ss_ipr_cy_dev.

Diffractometer	Bruker Kappa APEXII Duo	
Radiation source	Incoatec Microfocus IμS (Cu K_α, λ = 1.54178 Å)	
Theta range for data collection	4.23 to 68.25°	
Index ranges	-7<=h<=7, -13<=k<=14, -24<=l<=25	
Reflections collected	14692	
Independent reflections	2886 [R(int) = 0.0493]	
Coverage of independent reflections	99.8%	
Absorption correction	Multi-Scan	
Max. and min. transmission	0.9640 and 0.8280	
Structure solution technique	direct methods	
Structure solution program	SHELXT 2014/5 (Sheldrick, 2014)	
Refinement method	Full-matrix least-squares on F^2	
Refinement program	SHELXL-2018/3 (Sheldrick, 2018)	
Function minimized	$\Sigma\, w(F_o^2 - F_c^2)^2$	
Data / restraints / parameters	2886 / 0 / 188	
Goodness-of-fit on F^2	1.050	
Final R indices	2743 data; I>2σ(I)	R1 = 0.0307, wR2 = 0.0752
	all data	R1 = 0.0330, wR2 = 0.0768
Weighting scheme	$w=1/[\sigma^2(F_o^2)+(0.0383P)^2+0.2292P]$ where $P=(F_o^2+2F_c^2)/3$	

Absolute structure parameter -0.22(12)

Largest diff. peak and hole 0.136 and -0.224 eÅ^{-3}

R.M.S. deviation from mean 0.035 eÅ^{-3}

Table S2-3. Atomic coordinates and equivalent isotropic atomic displacement parameters (Å^2) for Pu_XW_ss_ipr_cy_dev.

U(eq) is defined as one third of the trace of the orthogonalized U_{ij} tensor.

	x/a	y/b	z/c	U(eq)
O1	0.2337(2)	0.73460(11)	0.24035(6)	0.0230(3)
O2	0.5584(2)	0.42356(12)	0.30291(7)	0.0289(3)
N1	0.2068(2)	0.56340(12)	0.28885(7)	0.0166(3)
C1	0.2631(3)	0.67274(14)	0.28780(8)	0.0170(4)
C2	0.3556(3)	0.72581(14)	0.34687(8)	0.0169(4)
C3	0.2334(3)	0.80437(14)	0.37947(8)	0.0179(4)
C4	0.3100(3)	0.86143(15)	0.43309(8)	0.0202(4)
C5	0.5124(3)	0.83767(15)	0.45313(8)	0.0216(4)
C6	0.6361(3)	0.76090(16)	0.42020(9)	0.0224(4)
C7	0.5593(3)	0.70431(15)	0.36697(9)	0.0206(4)
C8	0.1756(4)	0.94733(17)	0.46685(9)	0.0282(5)
C9	0.1069(3)	0.51280(15)	0.23131(8)	0.0192(4)
C10	0.8971(3)	0.56773(16)	0.21663(9)	0.0220(4)
C11	0.2554(3)	0.51223(17)	0.17408(9)	0.0282(4)
C12	0.2377(3)	0.49036(14)	0.34552(8)	0.0168(4)
C13	0.3689(3)	0.38590(15)	0.33044(9)	0.0210(4)

	x/a	y/b	z/c	U(eq)
C14	0.4049(4)	0.31825(17)	0.39166(10)	0.0299(5)
C15	0.2003(4)	0.28472(16)	0.42387(9)	0.0305(5)
C16	0.0669(3)	0.38841(16)	0.43757(9)	0.0266(4)
C17	0.0302(3)	0.45757(16)	0.37661(9)	0.0232(4)

Table S2-4. Bond lengths (Å) for Pu_XW_ss_ipr_cy_dev.

O1-C1	1.246(2)	O2-C13	1.416(2)
O2-H2	0.90(3)	N1-C1	1.343(2)
N1-C12	1.479(2)	N1-C9	1.488(2)
C1-C2	1.506(2)	C2-C3	1.393(3)
C2-C7	1.394(3)	C3-C4	1.397(2)
C3-H3	0.95	C4-C5	1.391(3)
C4-C8	1.507(3)	C5-C6	1.388(3)
C5-H5	0.95	C6-C7	1.388(3)
C6-H6	0.95	C7-H7	0.95
C8-H8A	0.98	C8-H8B	0.98
C8-H8C	0.98	C9-C10	1.524(3)
C9-C11	1.528(3)	C9-H9	1.0
C10-H10A	0.98	C10-H10B	0.98
C10-H10C	0.98	C11-H11A	0.98
C11-H11B	0.98	C11-H11C	0.98
C12-C13	1.528(2)	C12-C17	1.529(3)
C12-H12	1.0	C13-C14	1.526(3)

C13-H13	1.0	C14-C15	1.526(3)
C14-H14A	0.99	C14-H14B	0.99
C15-C16	1.522(3)	C15-H15A	0.99
C15-H15B	0.99	C16-C17	1.531(2)
C16-H16A	0.99	C16-H16B	0.99
C17-H17A	0.99	C17-H17B	0.99

Table S2-5. Bond angles (°) for Pu_XW_ss_ipr_cy_dev.

C13-O2-H2	110.3(19)	C1-N1-C12	122.68(14)
C1-N1-C9	119.33(14)	C12-N1-C9	117.98(14)
O1-C1-N1	122.54(16)	O1-C1-C2	117.79(15)
N1-C1-C2	119.59(14)	C3-C2-C7	120.04(16)
C3-C2-C1	117.23(16)	C7-C2-C1	122.61(16)
C2-C3-C4	121.12(17)	C2-C3-H3	119.4
C4-C3-H3	119.4	C5-C4-C3	118.12(17)
C5-C4-C8	121.87(17)	C3-C4-C8	120.01(17)
C6-C5-C4	121.02(17)	C6-C5-H5	119.5
C4-C5-H5	119.5	C5-C6-C7	120.67(17)
C5-C6-H6	119.7	C7-C6-H6	119.7
C6-C7-C2	119.02(17)	C6-C7-H7	120.5
C2-C7-H7	120.5	C4-C8-H8A	109.5
C4-C8-H8B	109.5	H8A-C8-H8B	109.5
C4-C8-H8C	109.5	H8A-C8-H8C	109.5
H8B-C8-H8C	109.5	N1-C9-C10	111.75(14)
N1-C9-C11	111.47(15)	C10-C9-C11	113.19(15)

N1-C9-H9	106.7	C10-C9-H9	106.7
C11-C9-H9	106.7	C9-C10-H10A	109.5
C9-C10-H10B	109.5	H10A-C10-H10B	109.5
C9-C10-H10C	109.5	H10A-C10-H10C	109.5
H10B-C10-H10C	109.5	C9-C11-H11A	109.5
C9-C11-H11B	109.5	H11A-C11-H11B	109.5
C9-C11-H11C	109.5	H11A-C11-H11C	109.5
H11B-C11-H11C	109.5	N1-C12-C13	112.41(14)
N1-C12-C17	111.84(14)	C13-C12-C17	111.14(15)
N1-C12-H12	107.0	C13-C12-H12	107.0
C17-C12-H12	107.0	O2-C13-C14	112.06(16)
O2-C13-C12	107.54(14)	C14-C13-C12	109.56(15)
O2-C13-H13	109.2	C14-C13-H13	109.2
C12-C13-H13	109.2	C15-C14-C13	112.07(17)
C15-C14-H14A	109.2	C13-C14-H14A	109.2
C15-C14-H14B	109.2	C13-C14-H14B	109.2
H14A-C14-H14B	107.9	C16-C15-C14	110.85(16)
C16-C15-H15A	109.5	C14-C15-H15A	109.5
C16-C15-H15B	109.5	C14-C15-H15B	109.5
H15A-C15-H15B	108.1	C15-C16-C17	111.12(16)
C15-C16-H16A	109.4	C17-C16-H16A	109.4
C15-C16-H16B	109.4	C17-C16-H16B	109.4
H16A-C16-H16B	108.0	C12-C17-C16	110.82(16)
C12-C17-H17A	109.5	C16-C17-H17A	109.5
C12-C17-H17B	109.5	C16-C17-H17B	109.5

H17A-C17-H17B 108.1

Table S2-6. Torsion angles (°) for Pu_XW_ss_ipr_cy_dev.

C12-N1-C1-O1	-178.74(17)	C9-N1-C1-O1	0.5(3)
C12-N1-C1-C2	-2.0(2)	C9-N1-C1-C2	177.30(15)
O1-C1-C2-C3	67.5(2)	N1-C1-C2-C3	-109.47(19)
O1-C1-C2-C7	-108.5(2)	N1-C1-C2-C7	74.5(2)
C7-C2-C3-C4	-1.1(3)	C1-C2-C3-C4	-177.17(15)
C2-C3-C4-C5	0.0(2)	C2-C3-C4-C8	179.06(17)
C3-C4-C5-C6	1.1(3)	C8-C4-C5-C6	-177.93(18)
C4-C5-C6-C7	-1.2(3)	C5-C6-C7-C2	0.1(3)
C3-C2-C7-C6	1.0(2)	C1-C2-C7-C6	176.87(16)
C1-N1-C9-C10	-63.7(2)	C12-N1-C9-C10	115.58(17)
C1-N1-C9-C11	64.0(2)	C12-N1-C9-C11	-116.66(17)
C1-N1-C12-C13	-122.85(18)	C9-N1-C12-C13	57.9(2)
C1-N1-C12-C17	111.30(18)	C9-N1-C12-C17	-67.97(19)
N1-C12-C13-O2	54.71(19)	C17-C12-C13-O2	-179.06(14)
N1-C12-C13-C14	176.73(15)	C17-C12-C13-C14	-57.0(2)
O2-C13-C14-C15	175.99(15)	C12-C13-C14-C15	56.7(2)
C13-C14-C15-C16	-56.0(2)	C14-C15-C16-C17	54.8(2)
N1-C12-C17-C16	-176.34(14)	C13-C12-C17-C16	57.1(2)
C15-C16-C17-C12	-55.7(2)		

Table S2-7. Anisotropic atomic displacement parameters (Å^2) for Pu_XW_ss_ipr_cy_dev.

The anisotropic atomic displacement factor exponent takes the form: $-2\pi^2[h^2 a^{*2} U_{11} + ... + 2 h k a^* b^* U_{12}]$

	U_{11}	U_{22}	U_{33}	U_{23}	U_{13}	U_{12}
O1	0.0343(7)	0.0167(6)	0.0180(6)	0.0030(5)	-0.0003(6)	-0.0058(5)
O2	0.0207(7)	0.0197(7)	0.0462(8)	-0.0055(6)	0.0067(6)	0.0026(6)
N1	0.0208(7)	0.0123(7)	0.0167(7)	-0.0010(5)	0.0005(6)	0.0000(6)
C1	0.0171(8)	0.0147(8)	0.0191(8)	-0.0010(6)	0.0026(7)	-0.0015(7)
C2	0.0214(9)	0.0107(8)	0.0187(8)	0.0020(6)	0.0019(7)	-0.0025(7)
C3	0.0221(9)	0.0123(8)	0.0193(8)	0.0024(6)	-0.0007(7)	0.0003(7)
C4	0.0306(10)	0.0114(8)	0.0185(8)	0.0026(7)	0.0006(7)	-0.0004(7)
C5	0.0301(10)	0.0162(9)	0.0185(9)	0.0003(7)	-0.0044(8)	-0.0063(7)
C6	0.0210(9)	0.0213(9)	0.0249(9)	0.0043(7)	-0.0023(7)	-0.0037(7)
C7	0.0219(9)	0.0163(9)	0.0236(9)	0.0001(7)	0.0028(7)	-0.0001(7)
C8	0.0422(12)	0.0191(10)	0.0234(9)	-0.0039(7)	-0.0051(8)	0.0071(9)
C9	0.0246(9)	0.0137(9)	0.0192(8)	-0.0028(6)	-0.0002(7)	-0.0020(7)
C10	0.0237(9)	0.0219(9)	0.0203(8)	-0.0009(7)	-0.0023(7)	-0.0015(8)
C11	0.0299(11)	0.0305(11)	0.0242(9)	-0.0119(8)	0.0046(9)	-0.0033(9)
C12	0.0205(9)	0.0117(8)	0.0183(8)	0.0004(6)	-0.0014(7)	0.0006(7)
C13	0.0214(9)	0.0130(9)	0.0286(9)	-0.0018(7)	-0.0009(8)	0.0002(7)
C14	0.0383(12)	0.0185(10)	0.0328(10)	-0.0016(8)	-0.0060(9)	0.0107(8)
C15	0.0522(13)	0.0153(10)	0.0240(9)	0.0033(7)	0.0002(9)	0.0036(9)
C16	0.0367(11)	0.0201(10)	0.0229(9)	0.0046(7)	0.0047(8)	0.0014(8)
C17	0.0243(9)	0.0221(10)	0.0233(9)	0.0049(7)	0.0027(8)	0.0028(7)

Table S2-8. Hydrogen atomic coordinates and isotropic atomic displacement parameters (Å^2) for Pu_XW_ss_ipr_cy_dev.

	x/a	y/b	z/c	U(eq)
H2	0.631(5)	0.365(2)	0.2871(14)	0.047(8)
H3	0.0956	0.8194	0.3650	0.021
H5	0.5667	0.8746	0.4899	0.026
H6	0.7747	0.7470	0.4342	0.027
H7	0.6442	0.6517	0.3446	0.025
H8A	0.1824	1.0195	0.4439	0.042
H8B	0.2262	0.9577	0.5107	0.042
H8C	0.0309	0.9206	0.4679	0.042
H9	0.0775	0.4319	0.2419	0.023
H10A	-0.1940	0.5617	0.2542	0.033
H10B	-0.1681	0.5292	0.1802	0.033
H10C	-0.0816	0.6476	0.2061	0.033
H11A	0.2811	0.5901	0.1601	0.042
H11B	0.1926	0.4693	0.1389	0.042
H11C	0.3877	0.4770	0.1865	0.042
H12	0.3171	0.5357	0.3777	0.02
H13	0.2928	0.3377	0.2988	0.025
H14A	0.4854	0.2492	0.3813	0.036
H14B	0.4890	0.3640	0.4218	0.036
H15A	0.1225	0.2323	0.3957	0.037
H15B	0.2306	0.2448	0.4645	0.037

	x/a	y/b	z/c	U(eq)
H16A	0.1373	0.4362	0.4699	0.032
H16B	-0.0691	0.3642	0.4554	0.032
H17A	-0.0536	0.4127	0.3460	0.028
H17B	-0.0493	0.5268	0.3873	0.028

Table S2-9. Hydrogen bond distances (Å) and angles (°) for Pu_XW_ss_ipr_cy_dev.

	Donor-H	Acceptor-H	Donor-Acceptor	Angle
O2-H2···O1	0.90(3)	1.86(3)	2.7547(19)	175.(3)

Crystal Structure Report for Pu_XW_rr_ipr_cy_dev

A colorless rod-like specimen of $C_{17}H_{25}NO_2$, approximate dimensions 0.035 mm x 0.049 mm x 0.202 mm, was coated with Paratone oil and mounted on a MiTeGen MicroLoop. The X-ray intensity data were measured on a Bruker Kappa APEXII Duo system equipped with a Incoatec Microfocus IμS (Cu K_α, λ = 1.54178 Å) and a multilayer mirror monochromator.

The total exposure time was 11.71 hours. The frames were integrated with the Bruker SAINT software package[4] using a narrow-frame algorithm. The integration of the data using an orthorhombic unit cell yielded a total of 10972 reflections to a maximum θ angle of 68.30° (0.83 Å resolution), of which 2893 were independent (average redundancy 3.793, completeness = 99.9%, R_{int} = 8.17%, R_{sig} = 6.79%) and 2399 (82.92%) were greater than 2σ(F^2). The final cell constants of a = 6.4139(5) Å, b = 11.8360(9) Å, c = 20.8668(15) Å, volume = 1584.1(2) $Å^3$, are based upon the refinement of the XYZ-centroids of 2126 reflections above 20 σ(I) with 8.474° < 2θ < 136.2°. Data were corrected for absorption effects using the Multi-Scan method (SADABS).[1] The ratio of minimum to maximum apparent transmission was 0.849. The calculated minimum and maximum transmission coefficients (based on crystal size) are 0.8910 and 0.9800.

The structure was solved and refined using the Bruker SHELXTL Software Package[5] within APEX3 [1] and OLEX2,[6]using the space group $P\,2_12_12_1$, with Z = 4 for the formula unit, $C_{17}H_{25}NO_2$. Non-hydrogen atoms were refined anisotropically. The O-H hydrogen atom was located in the diffraction map and refined isotropically. All other hydrogen atoms were placed in geometrically calculated positions with U_{iso} = 1.2U_{equiv} of the parent atom (U_{iso} = 1.5U_{equiv} for methyl). The final anisotropic full-matrix least-squares refinement on F^2 with 188 variables converged at R1 = 4.91%, for the observed data and wR2 =

[4] Bruker (2012). *Saint; SADABS; APEX3*. Bruker AXS Inc., Madison, Wisconsin, USA.
[5] Sheldrick, G. M. (2015). *Acta Cryst.* A**71**, 3-8.
[6] Dolomanov, O. V.; Bourhis, L. J.; Gildea, R. J.; Howard, J. A. K.; Puschmann, H. *J. Appl. Cryst.* (2009). **42**, 339-341.

11.72% for all data. The goodness-of-fit was 1.026. The largest peak in the final difference electron density synthesis was 0.156 $e^-/Å^3$ and the largest hole was -0.231 $e^-/Å^3$ with an RMS deviation of 0.046 $e^-/Å^3$. On the basis of the final model, the calculated density was 1.155 g/cm^3 and F(000), 600 e^-.

Table S2-10. Sample and crystal data for Pu_XW_rr_ipr_cy_dev.

Identification code	Pu_XW_rr_ipr_cy_dev	
Chemical formula	$C_{17}H_{25}NO_2$	
Formula weight	275.38 g/mol	
Temperature	100(2) K	
Wavelength	1.54178 Å	
Crystal size	0.035 x 0.049 x 0.202 mm	
Crystal habit	colorless rod	
Crystal system	orthorhombic	
Space group	P $2_12_12_1$	
Unit cell dimensions	a = 6.4139(5) Å	α = 90°
	b = 11.8360(9) Å	β = 90°
	c = 20.8668(15) Å	γ = 90°
Volume	1584.1(2) $Å^3$	
Z	4	
Density (calculated)	1.155 g/cm^3	
Absorption coefficient	0.587 mm^{-1}	
F(000)	600	

Table S2-11. Data collection and structure refinement for Pu_XW_rr_ipr_cy_dev.

Diffractometer	Bruker Kappa APEXII Duo	
Radiation source	Incoatec Microfocus IμS (Cu K_α, λ = 1.54178 Å)	
Theta range for data collection	4.24 to 68.30°	
Index ranges	-7<=h<=7, -14<=k<=13, -22<=l<=25	
Reflections collected	10972	
Independent reflections	2893 [R(int) = 0.0817]	
Coverage of independent reflections	99.9%	
Absorption correction	Multi-Scan	
Max. and min. transmission	0.9800 and 0.8910	
Structure solution technique	direct methods	
Structure solution program	SHELXT 2014/5 (Sheldrick, 2014)	
Refinement method	Full-matrix least-squares on F^2	
Refinement program	SHELXL-2018/3 (Sheldrick, 2018)	
Function minimized	$\Sigma\ w(F_o^2 - F_c^2)^2$	
Data / restraints / parameters	2893 / 0 / 188	
Goodness-of-fit on F^2	1.026	
Final R indices	2399 data; I>2σ(I)	R1 = 0.0491, wR2 = 0.1106
	all data	R1 = 0.0630, wR2 = 0.1172
Weighting scheme	$w=1/[\sigma^2(F_o^2)+(0.0588P)^2]$ where $P=(F_o^2+2F_c^2)/3$	
Absolute structure parameter	0.1(3)	
Largest diff. peak and hole	0.156 and -0.231 $eÅ^{-3}$	
R.M.S. deviation from mean	0.046 $eÅ^{-3}$	

Table S2-12. Atomic coordinates and equivalent isotropic atomic displacement parameters (Å^2) for Pu_XW_rr_ipr_cy_dev.

U(eq) is defined as one third of the trace of the orthogonalized U_{ij} tensor.

	x/a	y/b	z/c	U(eq)
O1	0.7663(4)	0.73470(19)	0.24036(10)	0.0261(5)
O2	0.4405(4)	0.4238(2)	0.30289(13)	0.0316(6)
N1	0.7924(4)	0.5637(2)	0.28881(12)	0.0180(5)
C1	0.7356(5)	0.6727(3)	0.28791(14)	0.0193(7)
C2	0.6447(5)	0.7264(3)	0.34682(15)	0.0197(7)
C3	0.7653(5)	0.8047(3)	0.37955(14)	0.0199(7)
C4	0.6896(5)	0.8614(3)	0.43321(15)	0.0221(7)
C5	0.4874(6)	0.8376(3)	0.45314(16)	0.0251(8)
C6	0.3644(5)	0.7605(3)	0.42019(15)	0.0241(7)
C7	0.4416(5)	0.7045(3)	0.36680(16)	0.0229(7)
C8	0.8231(6)	0.9476(3)	0.46687(16)	0.0310(8)
C9	0.8926(5)	0.5128(3)	0.23127(15)	0.0211(7)
C10	0.1026(5)	0.5673(3)	0.21666(16)	0.0244(7)
C11	0.7444(6)	0.5125(3)	0.17392(16)	0.0299(8)
C12	0.7621(5)	0.4904(3)	0.34556(14)	0.0188(7)
C13	0.6313(5)	0.3857(3)	0.33038(17)	0.0229(7)
C14	0.5953(6)	0.3184(3)	0.39190(18)	0.0323(9)
C15	0.7989(6)	0.2845(3)	0.42391(17)	0.0340(9)
C16	0.9331(6)	0.3885(3)	0.43730(17)	0.0298(8)
C17	0.9694(5)	0.4577(3)	0.37645(16)	0.0258(8)

Table S2-13. Bond lengths (Å) for Pu_XW_rr_ipr_cy_dev.

O1-C1	1.250(4)	O2-C13	1.425(4)
O2-H2	0.96(5)	N1-C1	1.341(4)
N1-C12	1.481(4)	N1-C9	1.489(4)
C1-C2	1.501(4)	C2-C3	1.387(5)
C2-C7	1.392(4)	C3-C4	1.393(4)
C3-H3	0.95	C4-C5	1.391(5)
C4-C8	1.506(5)	C5-C6	1.389(5)
C5-H5	0.95	C6-C7	1.388(5)
C6-H6	0.95	C7-H7	0.95
C8-H8A	0.98	C8-H8B	0.98
C8-H8C	0.98	C9-C10	1.524(5)
C9-C11	1.528(4)	C9-H9	1.0
C10-H10A	0.98	C10-H10B	0.98
C10-H10C	0.98	C11-H11A	0.98
C11-H11B	0.98	C11-H11C	0.98
C12-C17	1.528(5)	C12-C13	1.530(4)
C12-H12	1.0	C13-C14	1.528(5)
C13-H13	1.0	C14-C15	1.521(5)
C14-H14A	0.99	C14-H14B	0.99
C15-C16	1.528(5)	C15-H15A	0.99
C15-H15B	0.99	C16-C17	1.528(5)
C16-H16A	0.99	C16-H16B	0.99
C17-H17A	0.99	C17-H17B	0.99

Table S2-14. Bond angles (°) for Pu_XW_rr_ipr_cy_dev.

C13-O2-H2	108.(3)	C1-N1-C12	122.6(3)
C1-N1-C9	119.7(3)	C12-N1-C9	117.7(2)
O1-C1-N1	122.2(3)	O1-C1-C2	117.6(3)
N1-C1-C2	120.1(3)	C3-C2-C7	119.9(3)
C3-C2-C1	118.0(3)	C7-C2-C1	122.0(3)
C2-C3-C4	121.6(3)	C2-C3-H3	119.2
C4-C3-H3	119.2	C5-C4-C3	117.9(3)
C5-C4-C8	121.9(3)	C3-C4-C8	120.2(3)
C6-C5-C4	121.0(3)	C6-C5-H5	119.5
C4-C5-H5	119.5	C7-C6-C5	120.6(3)
C7-C6-H6	119.7	C5-C6-H6	119.7
C6-C7-C2	119.1(3)	C6-C7-H7	120.5
C2-C7-H7	120.5	C4-C8-H8A	109.5
C4-C8-H8B	109.5	H8A-C8-H8B	109.5
C4-C8-H8C	109.5	H8A-C8-H8C	109.5
H8B-C8-H8C	109.5	N1-C9-C10	111.8(3)
N1-C9-C11	111.3(3)	C10-C9-C11	113.2(3)
N1-C9-H9	106.7	C10-C9-H9	106.7
C11-C9-H9	106.7	C9-C10-H10A	109.5
C9-C10-H10B	109.5	H10A-C10-H10B	109.5
C9-C10-H10C	109.5	H10A-C10-H10C	109.5
H10B-C10-H10C	109.5	C9-C11-H11A	109.5
C9-C11-H11B	109.5	H11A-C11-H11B	109.5

C9-C11-H11C	109.5	H11A-C11-H11C	109.5
H11B-C11-H11C	109.5	N1-C12-C17	111.8(3)
N1-C12-C13	112.4(2)	C17-C12-C13	111.0(3)
N1-C12-H12	107.1	C17-C12-H12	107.1
C13-C12-H12	107.1	O2-C13-C14	111.9(3)
O2-C13-C12	107.4(3)	C14-C13-C12	109.3(3)
O2-C13-H13	109.4	C14-C13-H13	109.4
C12-C13-H13	109.4	C15-C14-C13	112.1(3)
C15-C14-H14A	109.2	C13-C14-H14A	109.2
C15-C14-H14B	109.2	C13-C14-H14B	109.2
H14A-C14-H14B	107.9	C14-C15-C16	110.6(3)
C14-C15-H15A	109.5	C16-C15-H15A	109.5
C14-C15-H15B	109.5	C16-C15-H15B	109.5
H15A-C15-H15B	108.1	C15-C16-C17	111.4(3)
C15-C16-H16A	109.3	C17-C16-H16A	109.3
C15-C16-H16B	109.3	C17-C16-H16B	109.3
H16A-C16-H16B	108.0	C12-C17-C16	110.7(3)
C12-C17-H17A	109.5	C16-C17-H17A	109.5
C12-C17-H17B	109.5	C16-C17-H17B	109.5
H17A-C17-H17B	108.1		

Table S2-15. Torsion angles (°) for Pu_XW_rr_ipr_cy_dev.

C12-N1-C1-O1	178.3(3)	C9-N1-C1-O1	-1.0(5)
C12-N1-C1-C2	2.4(4)	C9-N1-C1-C2	-176.8(3)

O1-C1-C2-C3	-67.0(4)	N1-C1-C2-C3	109.1(4)
O1-C1-C2-C7	109.3(4)	N1-C1-C2-C7	-74.6(4)
C7-C2-C3-C4	1.2(5)	C1-C2-C3-C4	177.6(3)
C2-C3-C4-C5	-0.4(5)	C2-C3-C4-C8	-178.8(3)
C3-C4-C5-C6	-0.6(5)	C8-C4-C5-C6	177.9(3)
C4-C5-C6-C7	0.6(5)	C5-C6-C7-C2	0.2(5)
C3-C2-C7-C6	-1.1(5)	C1-C2-C7-C6	-177.3(3)
C1-N1-C9-C10	64.0(4)	C12-N1-C9-C10	-115.3(3)
C1-N1-C9-C11	-63.8(4)	C12-N1-C9-C11	117.0(3)
C1-N1-C12-C17	-111.5(3)	C9-N1-C12-C17	67.8(3)
C1-N1-C12-C13	122.8(3)	C9-N1-C12-C13	-57.9(4)
N1-C12-C13-O2	-54.8(3)	C17-C12-C13-O2	179.0(3)
N1-C12-C13-C14	-176.5(3)	C17-C12-C13-C14	57.4(4)
O2-C13-C14-C15	-176.0(3)	C12-C13-C14-C15	-57.2(4)
C13-C14-C15-C16	56.1(4)	C14-C15-C16-C17	-54.7(4)
N1-C12-C17-C16	176.3(3)	C13-C12-C17-C16	-57.2(4)
C15-C16-C17-C12	55.6(4)		

Table S2-16. Anisotropic atomic displacement parameters (Å^2) for Pu_XW_rr_ipr_cy_dev.

The anisotropic atomic displacement factor exponent takes the form: $-2\pi^2[h^2 a^{*2} U_{11} + ... + 2 h k a^* b^* U_{12}]$

	U_{11}	U_{22}	U_{33}	U_{23}	U_{13}	U_{12}
O1	0.0371(14)	0.0216(12)	0.0197(11)	0.0018(10)	0.0004(10)	0.0071(11)
O2	0.0190(12)	0.0259(13)	0.0498(15)	-0.0048(12)	-0.0063(11)	-0.0026(11)

	U_{11}	U_{22}	U_{33}	U_{23}	U_{13}	U_{12}
N1	0.0193(12)	0.0163(12)	0.0184(12)	-0.0016(11)	0.0006(10)	0.0015(11)
C1	0.0188(16)	0.0203(16)	0.0187(15)	-0.0024(13)	-0.0029(14)	0.0028(13)
C2	0.0192(16)	0.0189(16)	0.0209(15)	0.0040(13)	-0.0044(12)	0.0043(13)
C3	0.0199(16)	0.0182(15)	0.0214(15)	0.0033(13)	0.0023(13)	0.0013(13)
C4	0.0295(18)	0.0159(15)	0.0210(15)	0.0029(13)	-0.0015(13)	0.0019(13)
C5	0.033(2)	0.0199(17)	0.0221(17)	0.0005(14)	0.0045(15)	0.0079(14)
C6	0.0215(16)	0.0257(17)	0.0250(16)	0.0040(15)	0.0020(13)	0.0045(14)
C7	0.0214(17)	0.0221(17)	0.0253(16)	0.0002(15)	-0.0037(13)	0.0011(14)
C8	0.043(2)	0.0245(18)	0.0253(17)	-0.0056(15)	0.0055(15)	-0.0063(16)
C9	0.0250(17)	0.0181(16)	0.0202(15)	-0.0024(13)	0.0010(13)	0.0035(14)
C10	0.0247(17)	0.0261(17)	0.0224(15)	0.0010(15)	0.0025(13)	0.0029(15)
C11	0.0290(18)	0.0347(19)	0.0260(16)	-0.0124(15)	-0.0047(15)	0.0037(16)
C12	0.0199(16)	0.0172(15)	0.0194(14)	-0.0010(12)	0.0009(12)	-0.0022(13)
C13	0.0202(16)	0.0173(16)	0.0312(17)	-0.0022(14)	0.0009(14)	-0.0003(13)
C14	0.038(2)	0.0231(18)	0.036(2)	-0.0028(16)	0.0057(17)	-0.0116(16)
C15	0.055(2)	0.0205(17)	0.0263(17)	0.0030(16)	0.0002(17)	-0.0039(17)
C16	0.037(2)	0.0256(18)	0.0271(17)	0.0047(15)	-0.0069(16)	-0.0028(16)
C17	0.0241(18)	0.0284(19)	0.0250(17)	0.0031(15)	-0.0021(14)	-0.0025(14)

Table S2-17. Hydrogen atomic coordinates and isotropic atomic displacement parameters ($Å^2$) for Pu_XW_rr_ipr_cy_dev.

	x/a	y/b	z/c	U(eq)
H2	0.371(8)	0.359(4)	0.285(2)	0.068(16)
H3	0.9028	0.8201	0.3650	0.024
H5	0.4326	0.8747	0.4898	0.03
H6	0.2261	0.7459	0.4343	0.029
H7	0.3571	0.6520	0.3442	0.028
H8A	0.9679	0.9212	0.4679	0.046
H8B	0.7726	0.9580	0.5108	0.046
H8C	0.8158	1.0196	0.4438	0.046
H9	0.9213	0.4319	0.2420	0.025
H10A	1.0813	0.6465	0.2046	0.037
H10B	1.1698	0.5269	0.1813	0.037
H10C	1.1916	0.5635	0.2548	0.037
H11A	0.6135	0.4753	0.1859	0.045
H11B	0.8088	0.4714	0.1383	0.045
H11C	0.7158	0.5904	0.1608	0.045
H12	0.6828	0.5356	0.3779	0.023
H13	0.7072	0.3375	0.2987	0.027
H14A	0.5121	0.3645	0.4221	0.039
H14B	0.5141	0.2495	0.3817	0.039
H15A	0.8761	0.2318	0.3957	0.041
H15B	0.7687	0.2449	0.4647	0.041
H16A	1.0691	0.3643	0.4550	0.036
H16B	0.8632	0.4364	0.4698	0.036
H17A	1.0489	0.5268	0.3872	0.031
H17B	1.0530	0.4128	0.3457	0.031

Table S2-18. Hydrogen bond distances (Å) and angles (°) for Pu_XW_rr_ipr_cy_dev.

	Donor-H	Acceptor-H	Donor-Acceptor	Angle
O2-H2···O1	0.96(5)	1.80(5)	2.753(3)	174.(5)

Appendix for Chapter 3

(1S,2S)-2-(isopropylamino)cyclohexan-1-ol, (1S,2S)-14

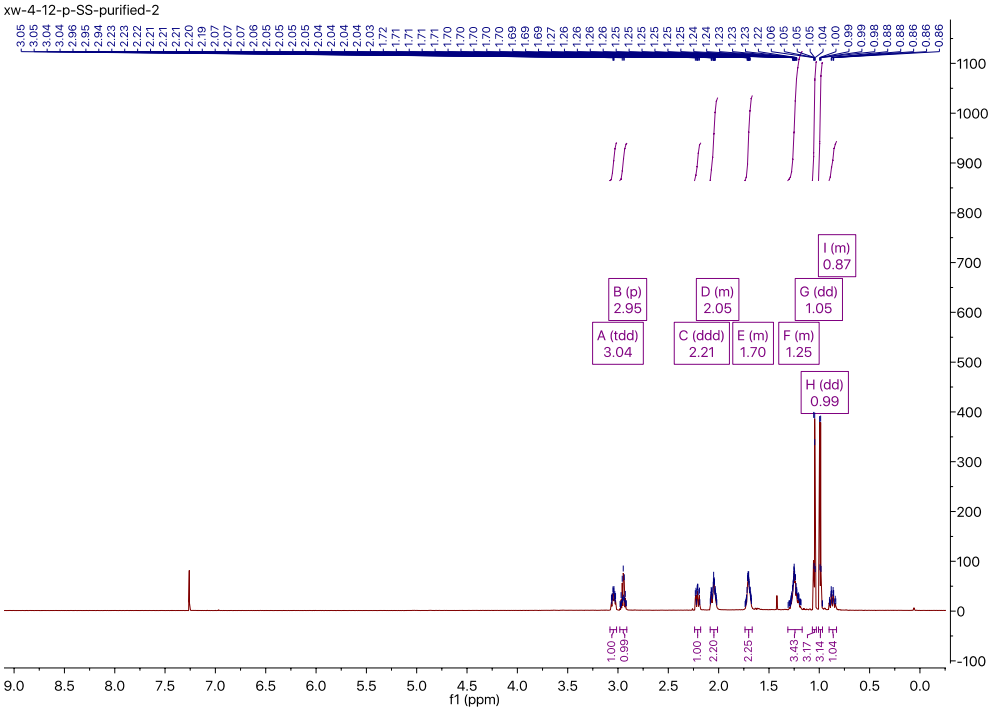

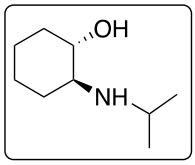

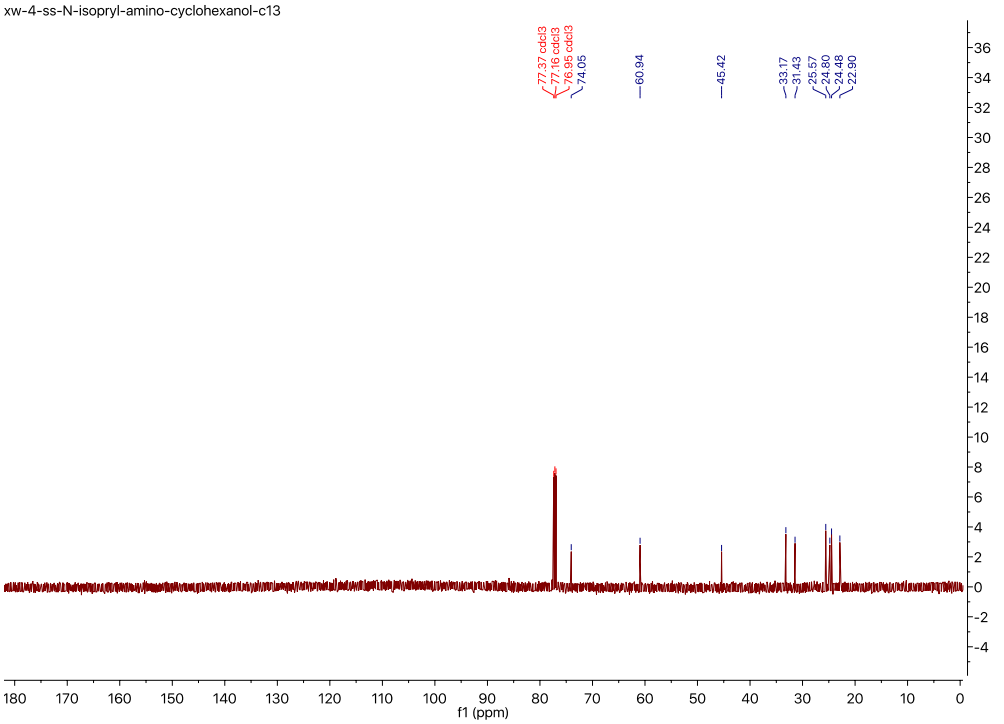

(1R,2R)-2-(isopropylamino)cyclohexan-1-ol, (1R,2R)-14

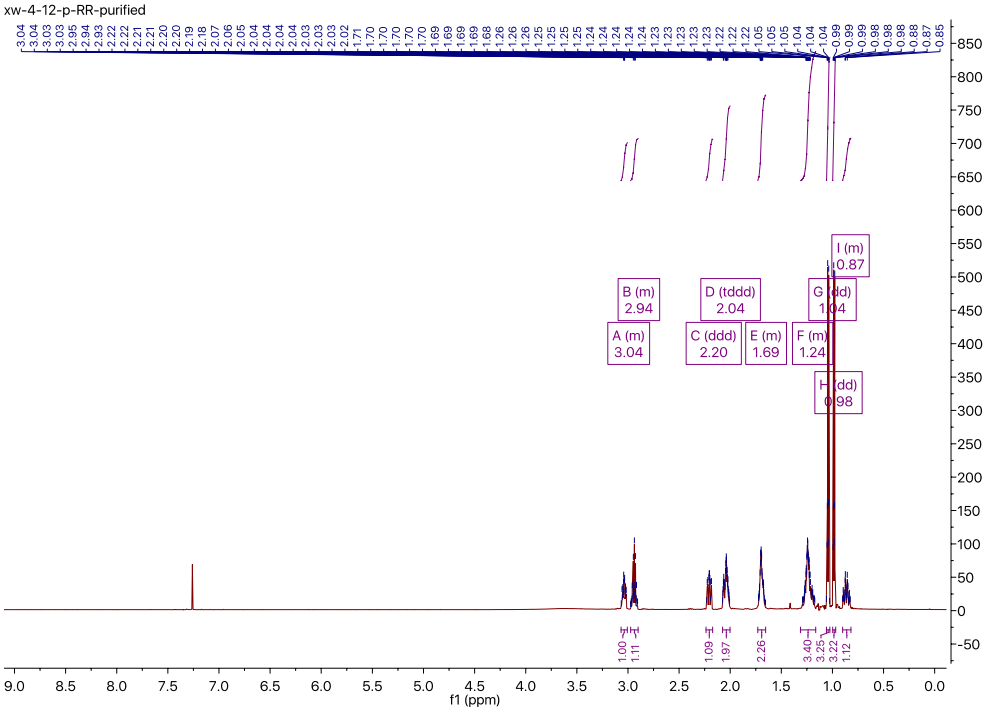

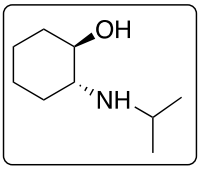

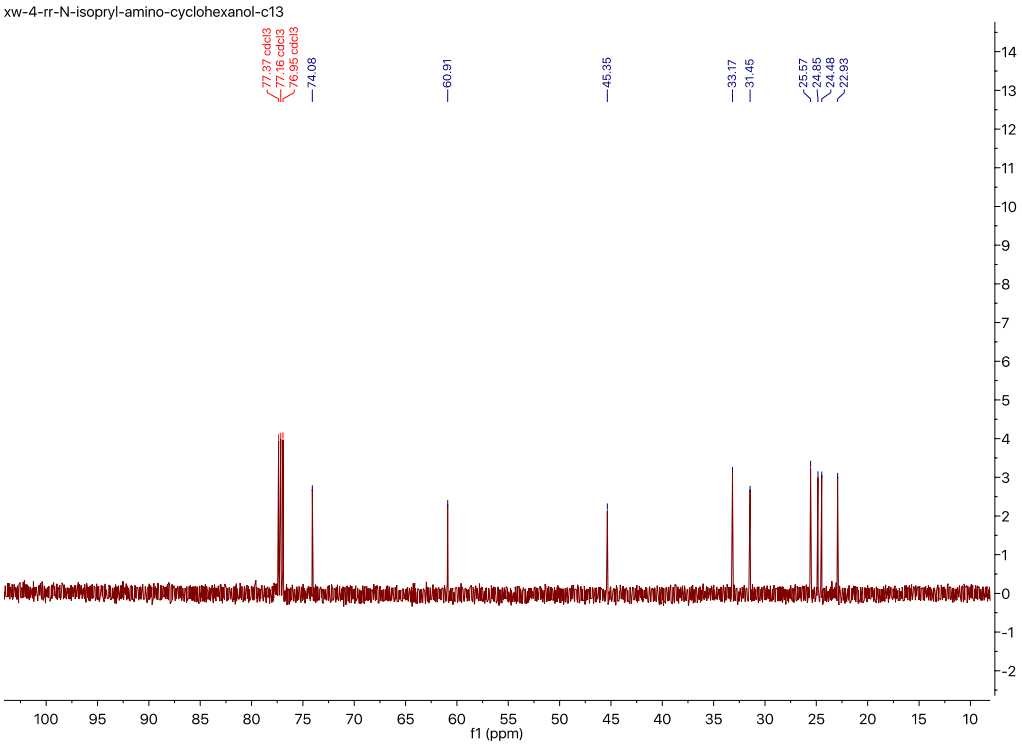

(1S,2S)-2-(methylamino)cyclohexan-1-ol, (1S,2S)-13

xw-3-SS-N-methyl-aminocyclohexanol

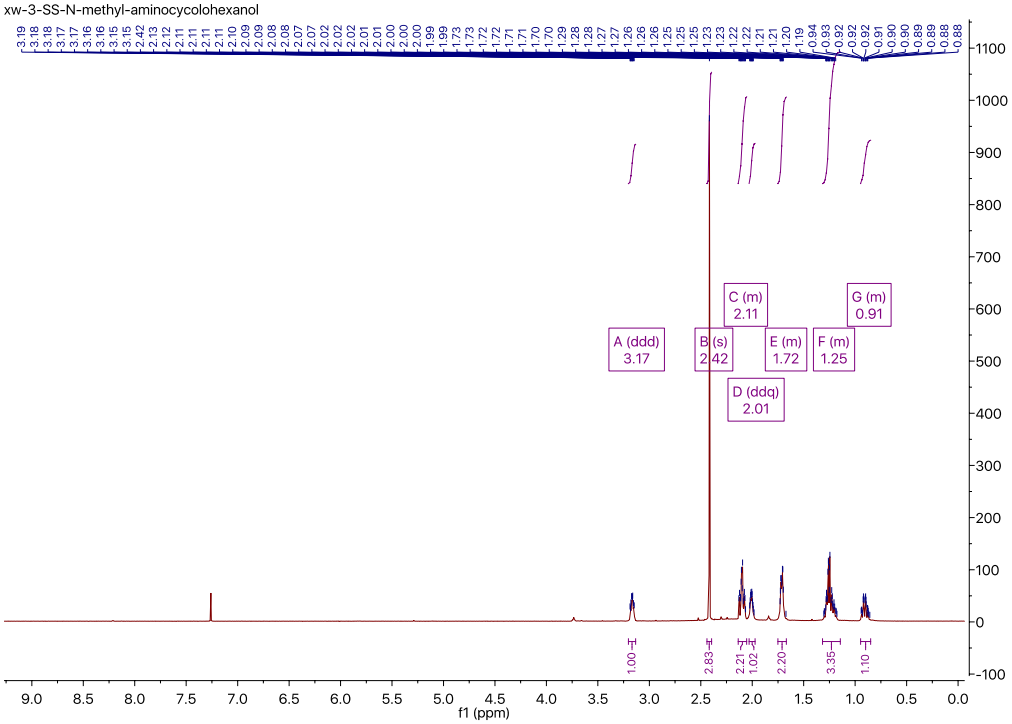

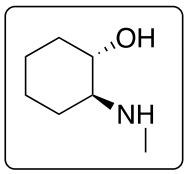

xw-4-ss-N-methyl-amino-cyclohexanol-c13

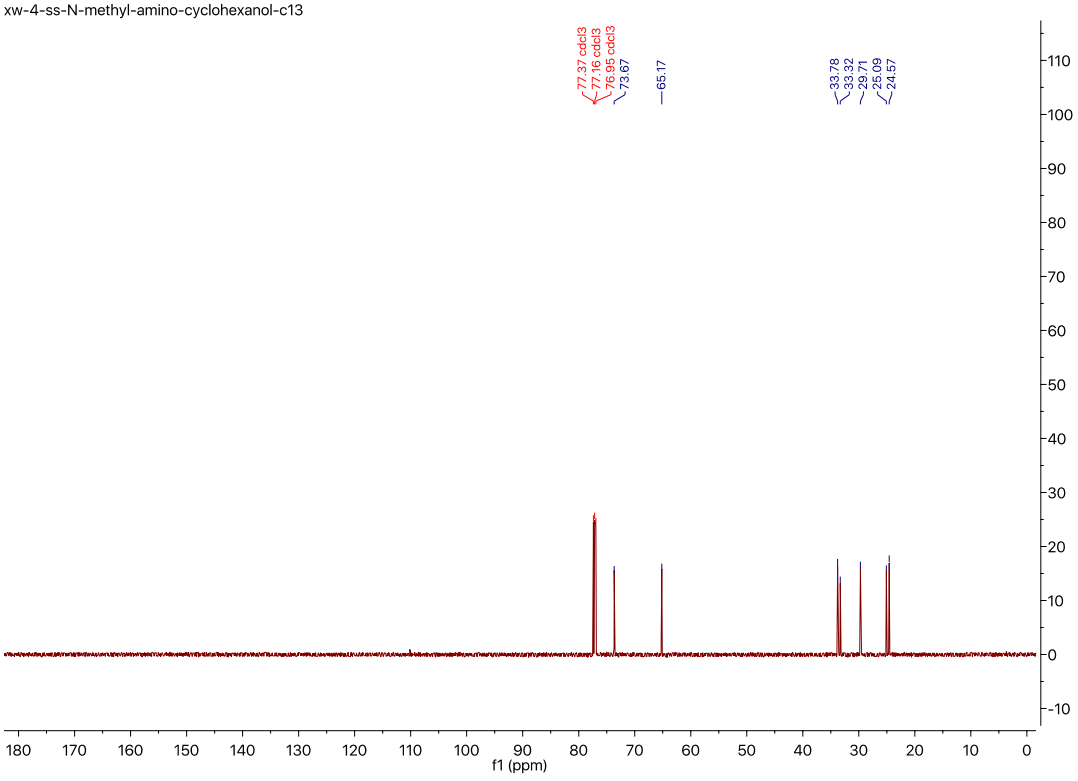

(1R,2R)-2-(methylamino)cyclohexan-1-ol, (1R,2R)-13

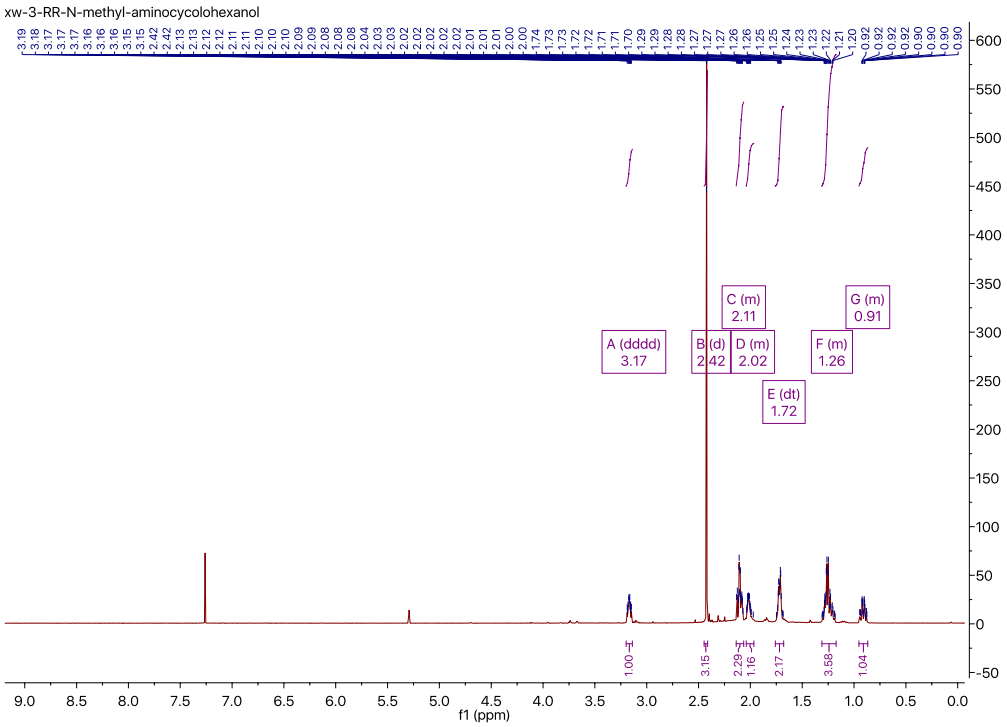

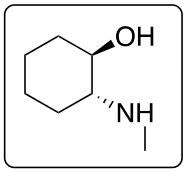

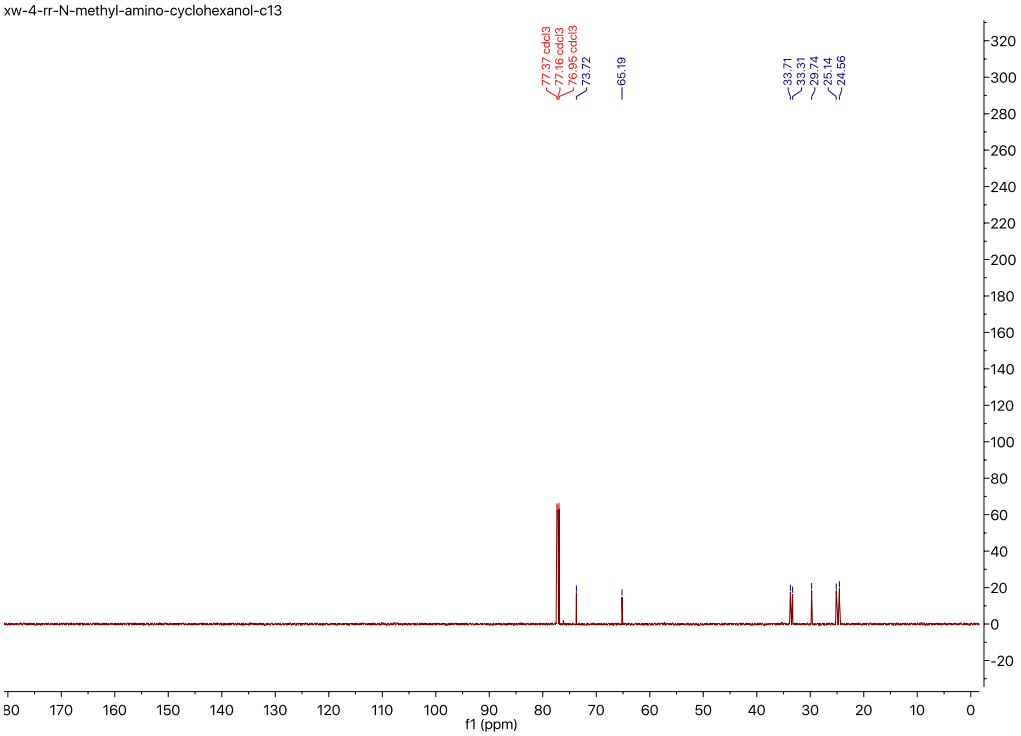

(S)-1-(methylamino)propan-2-ol, (S)-10

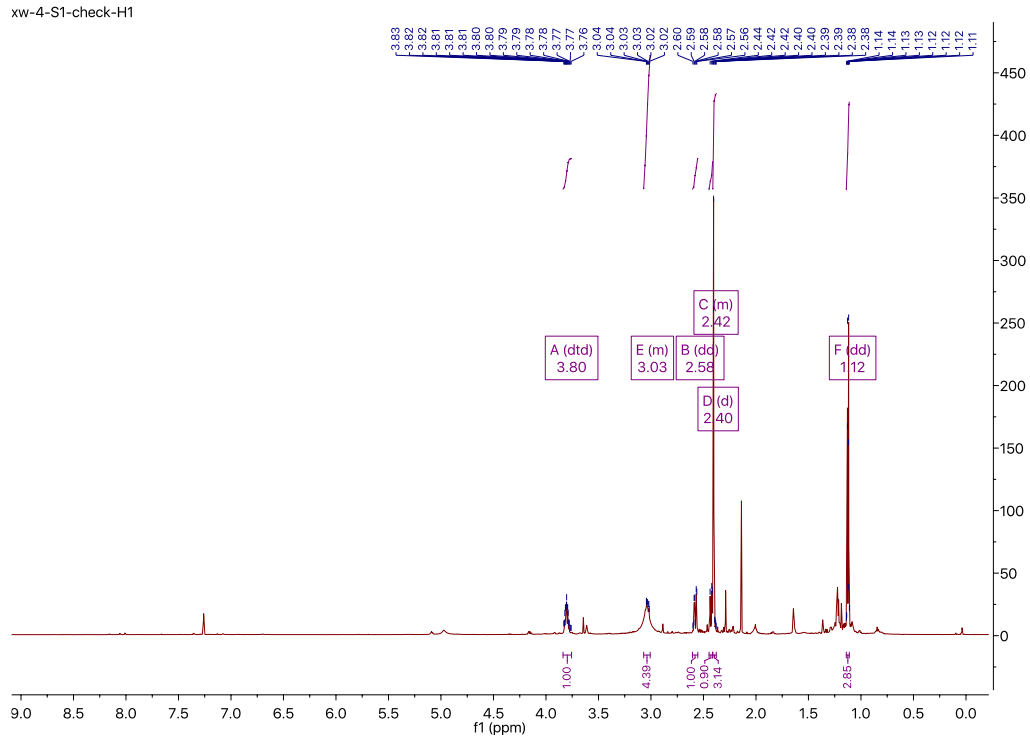

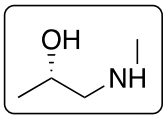

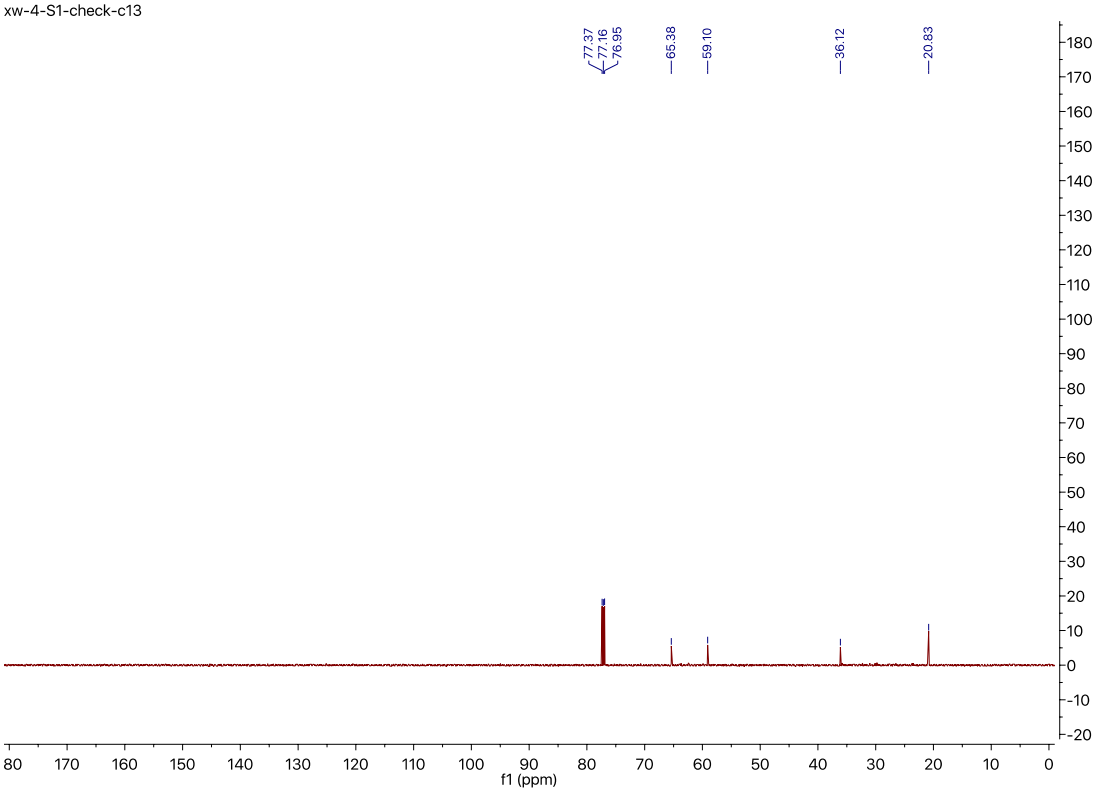

(R)-1-(methylamino)propan-2-ol, (R)-10

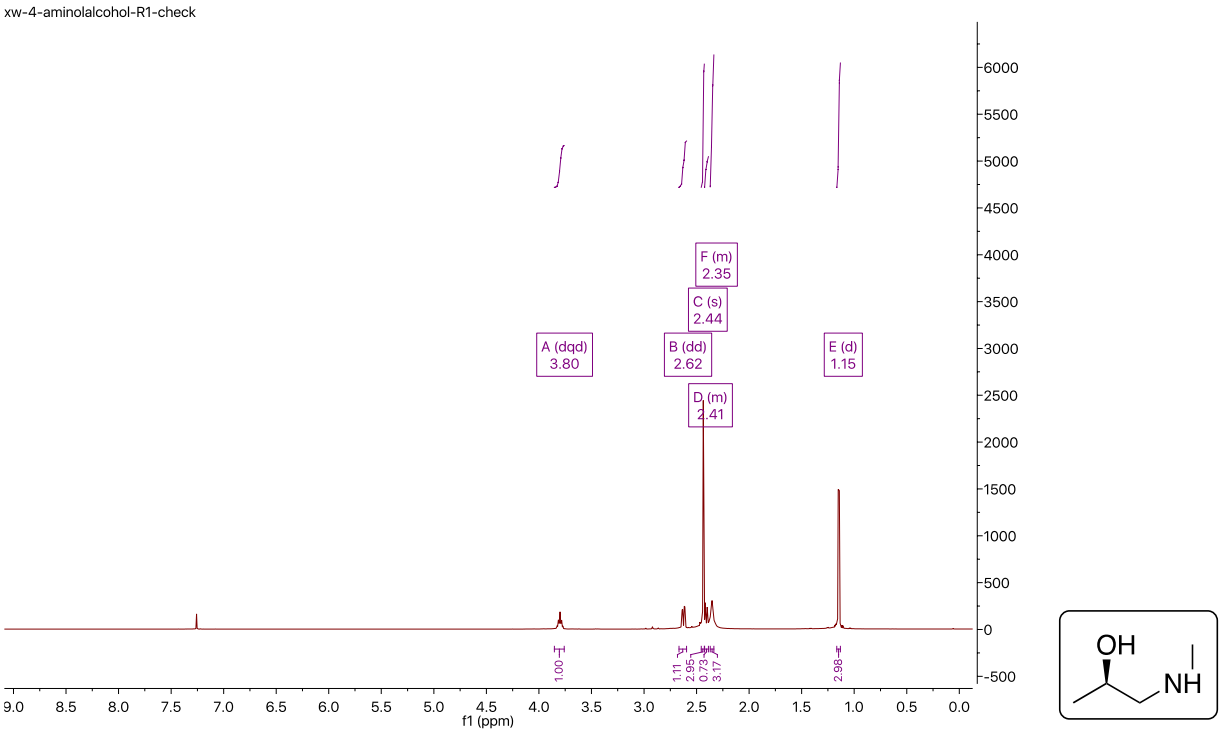

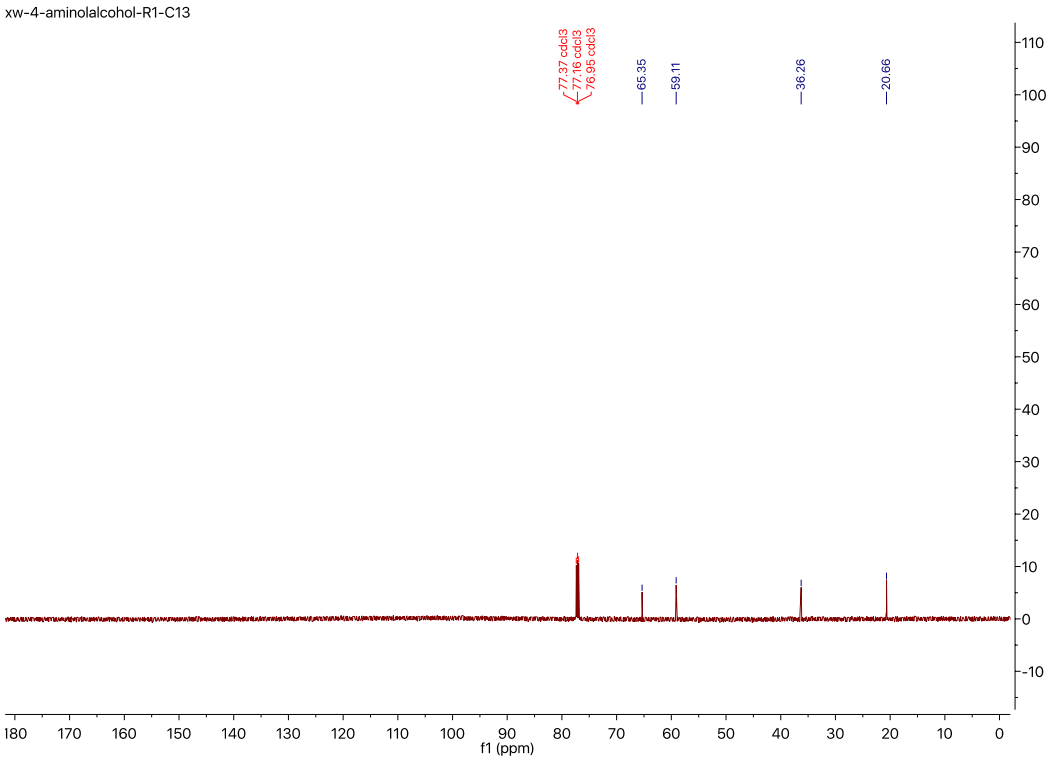

(S)-3-methyl-2-(methylamino)butan-1-ol, (S)-N-methyl-valinol, (S)-9

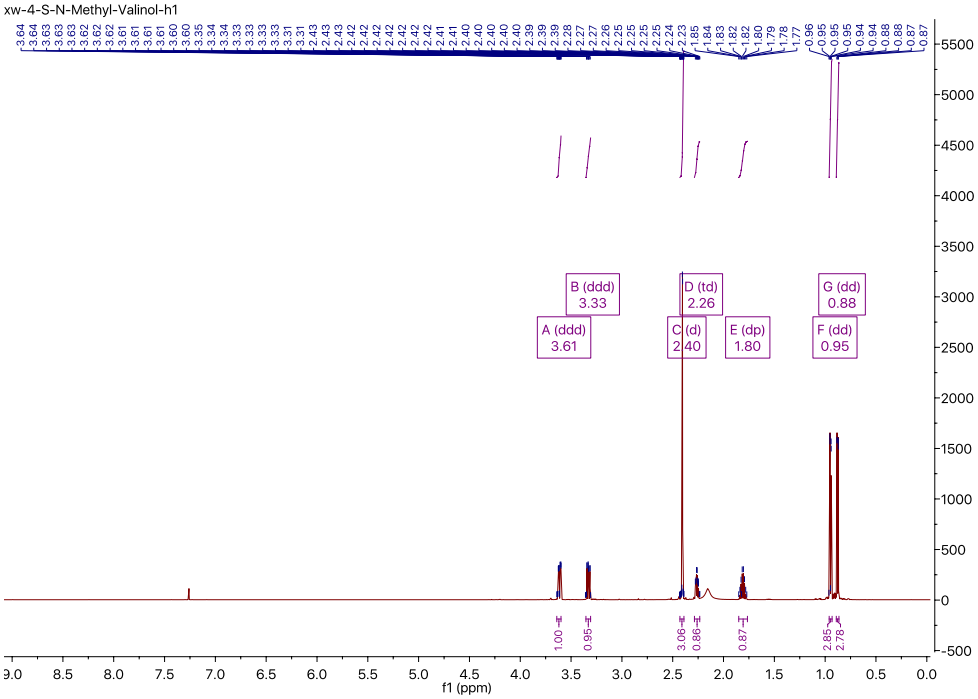

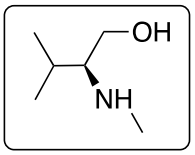

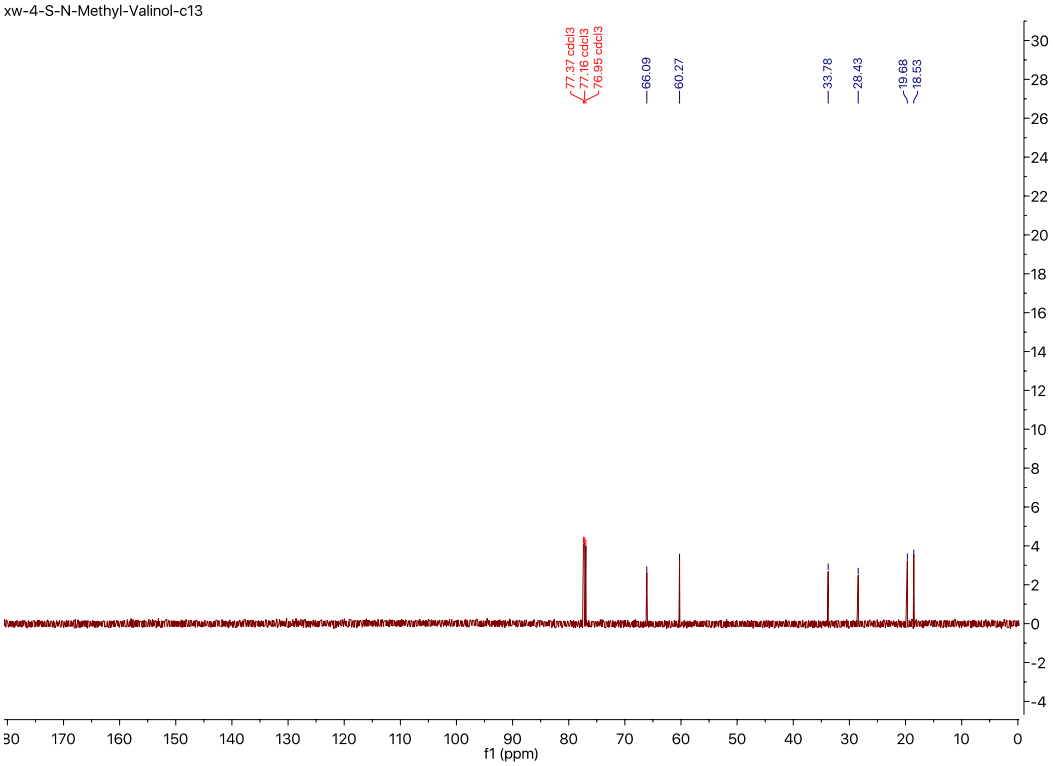

(*R*)-3-methyl-2-(methylamino)butan-1-ol, (*R*)-N-methyl-valinol, (*R*)-9

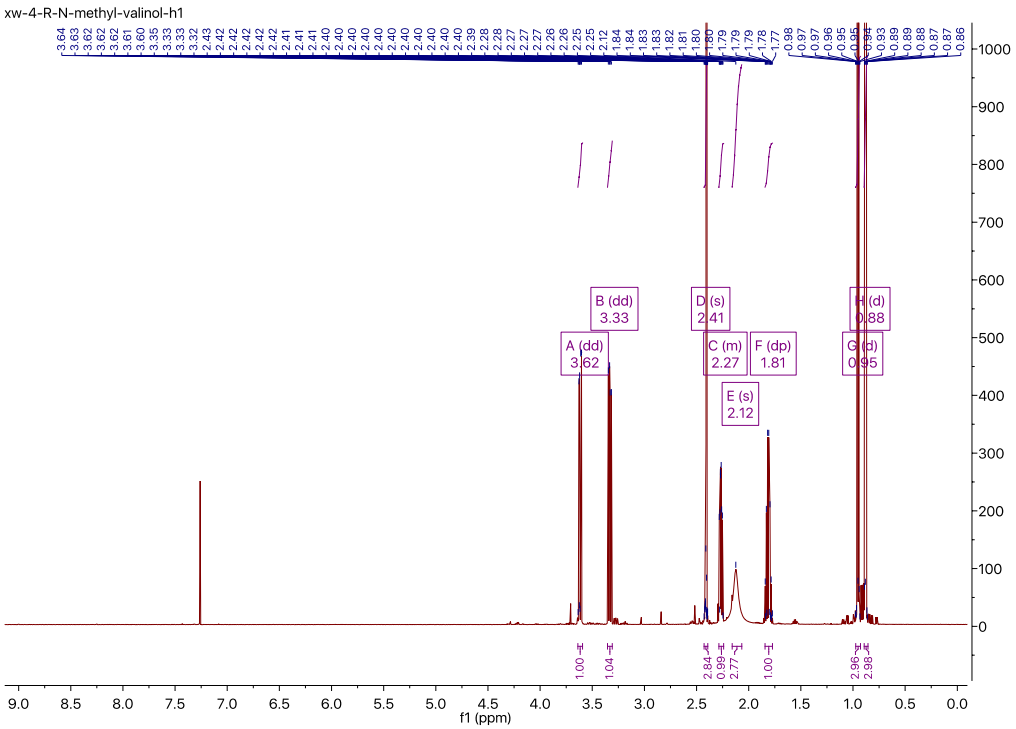

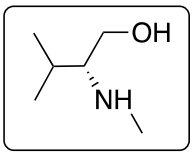

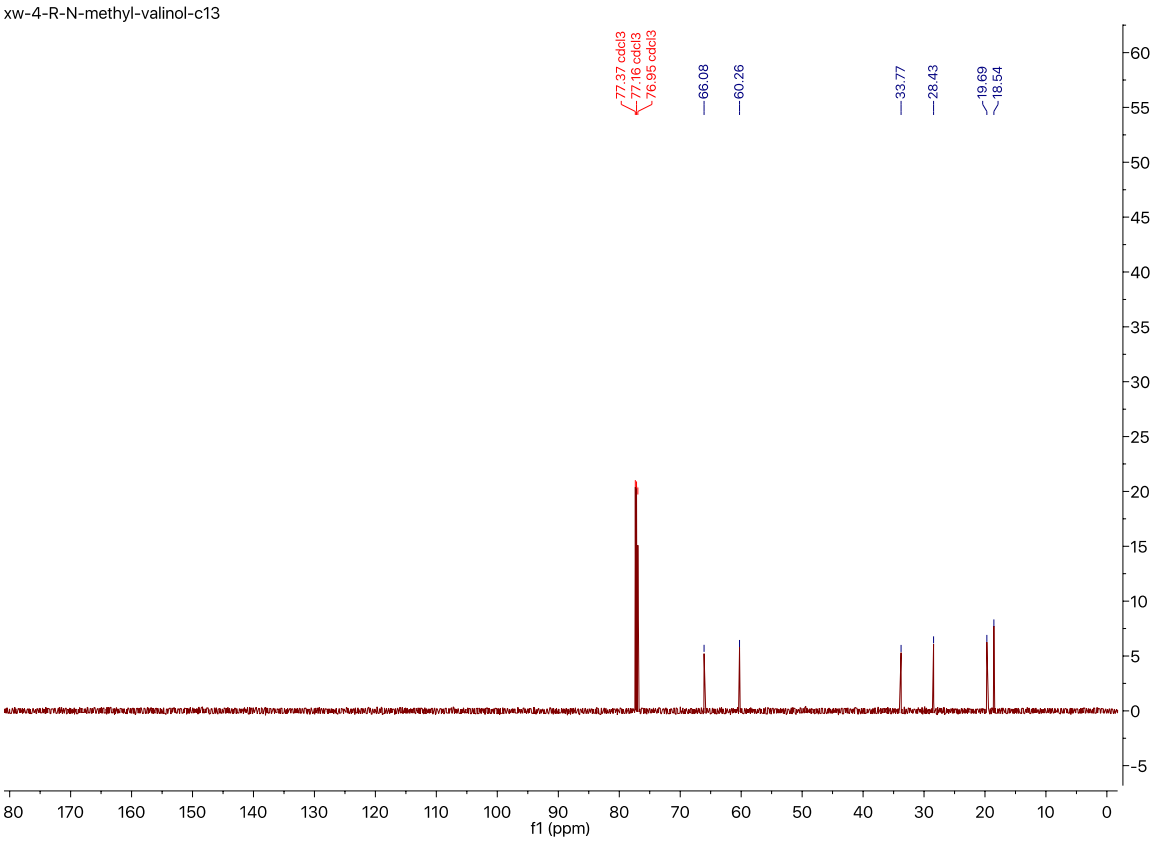

(*S*)-2-(methylamino)butan-1-ol, (*S*)-7

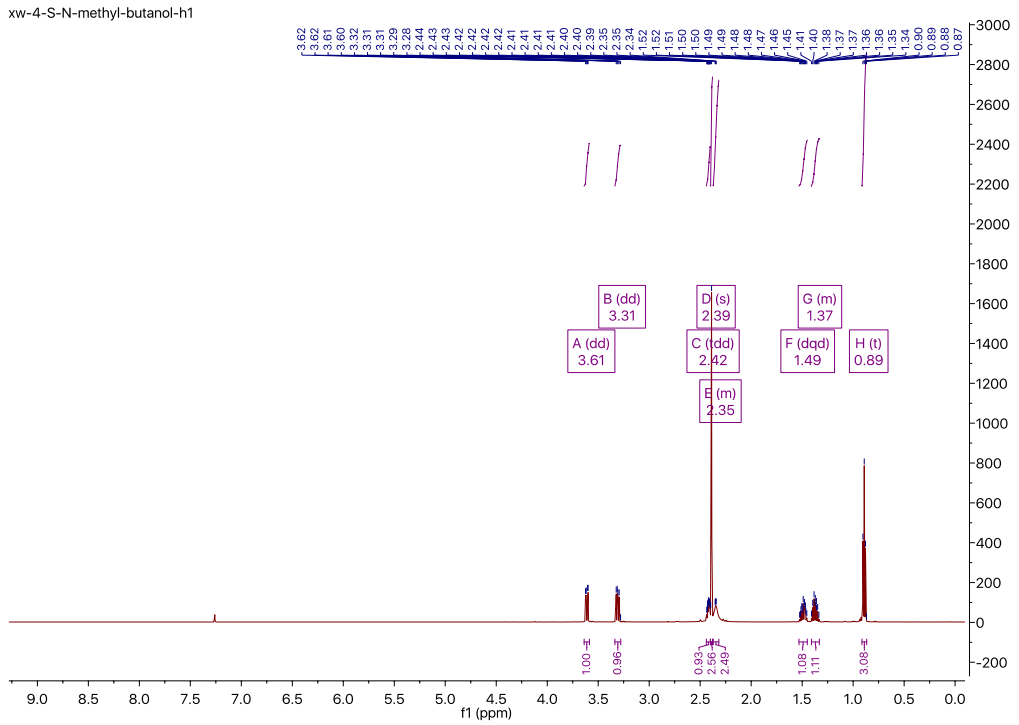

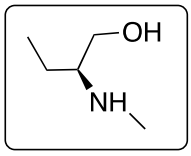

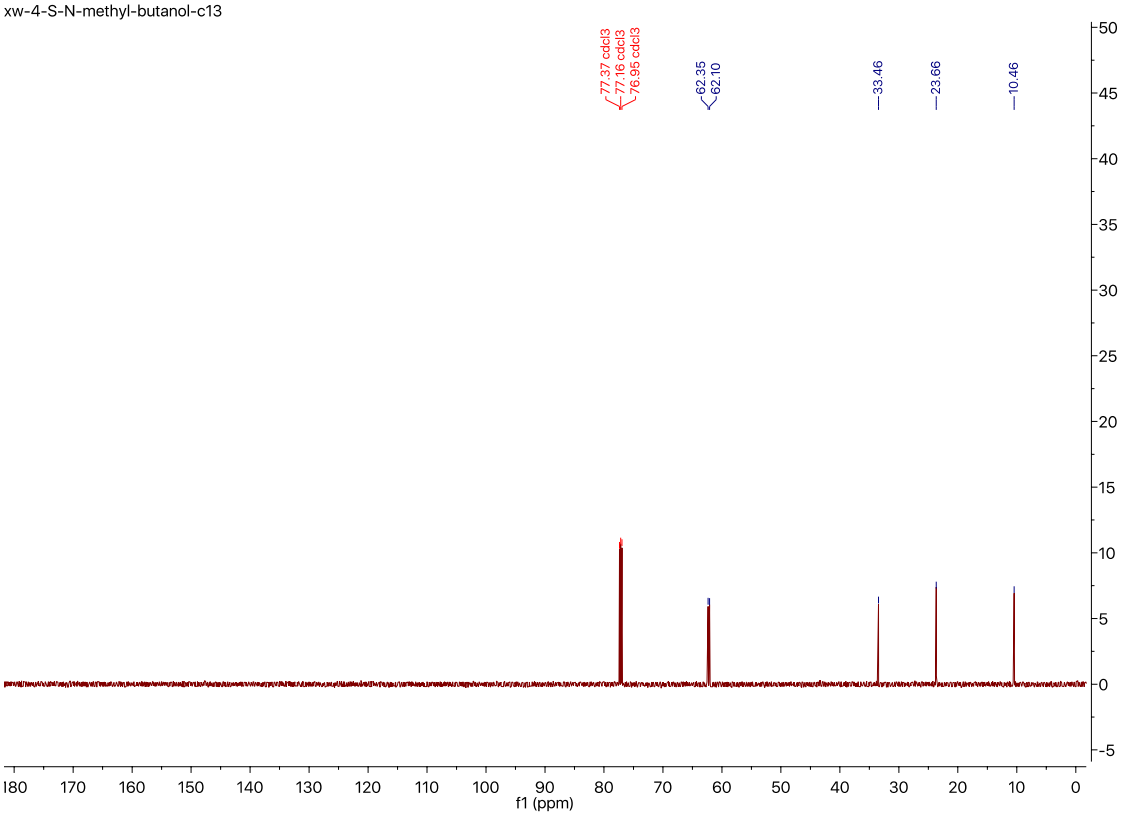

(*R*)-2-(methylamino)butan-1-ol, (*R*)-7

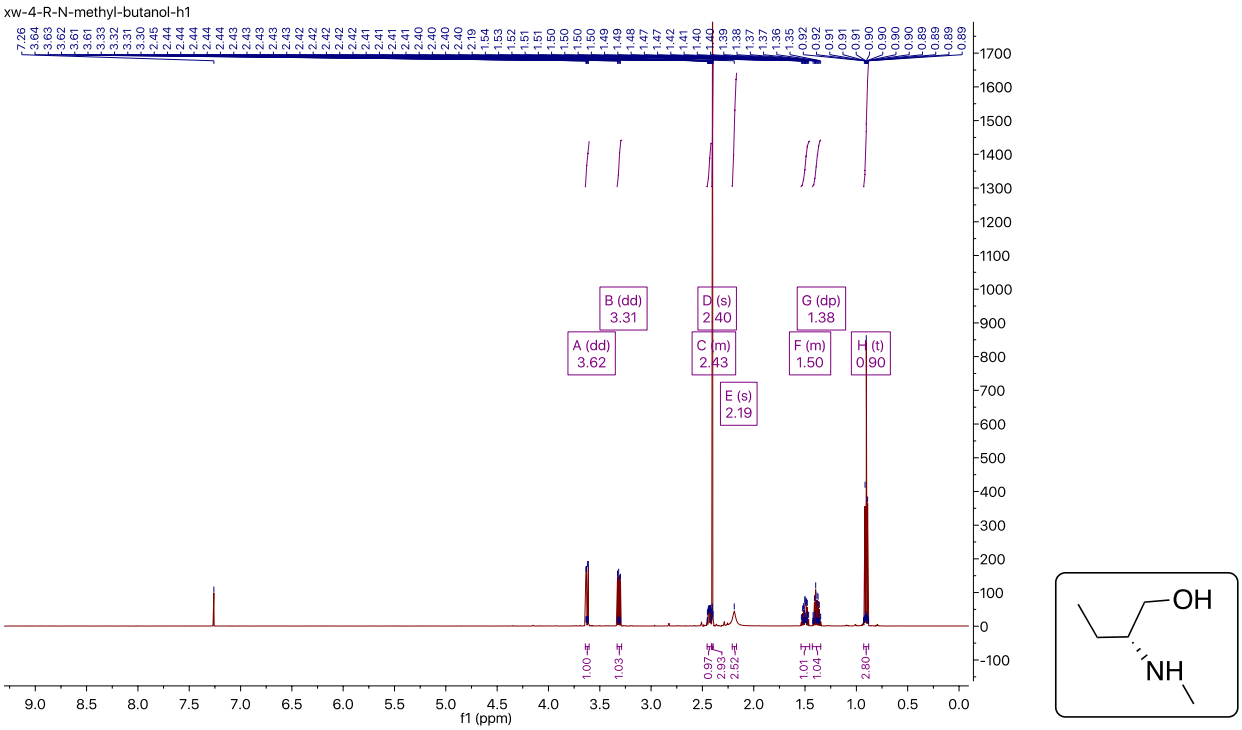

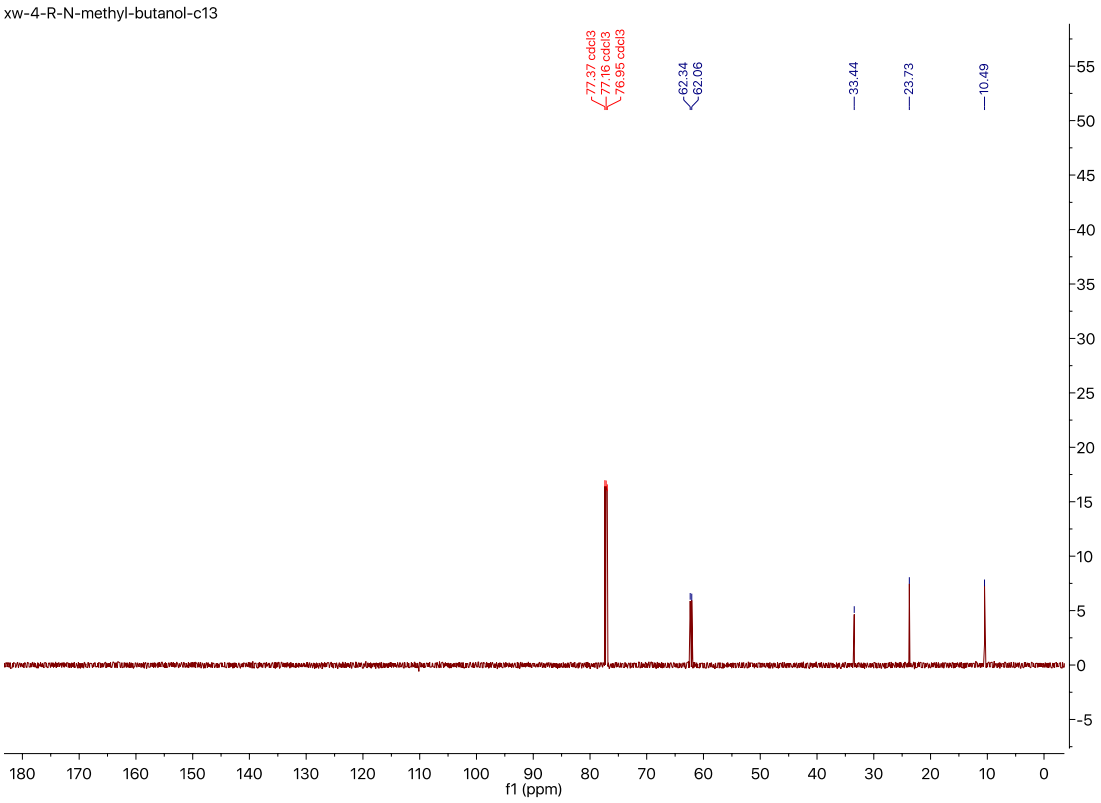

(*S*)-4-methyl-2-(methylamino)pentan-1-ol, (*S*)-N-methyl-leucinol, (*S*)-8

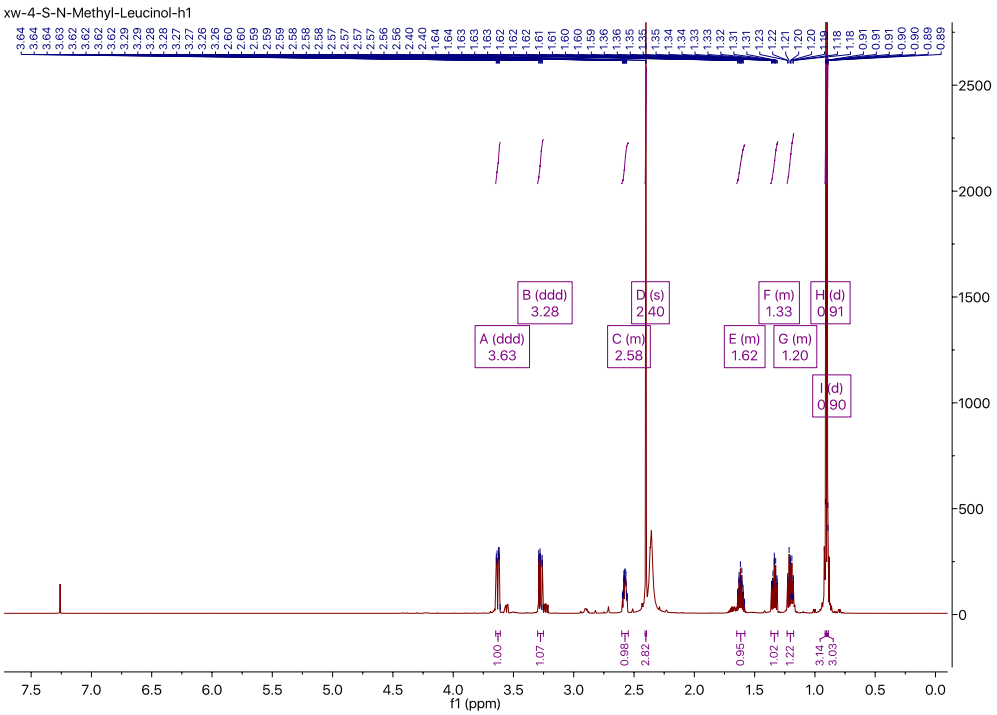

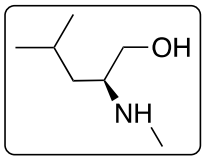

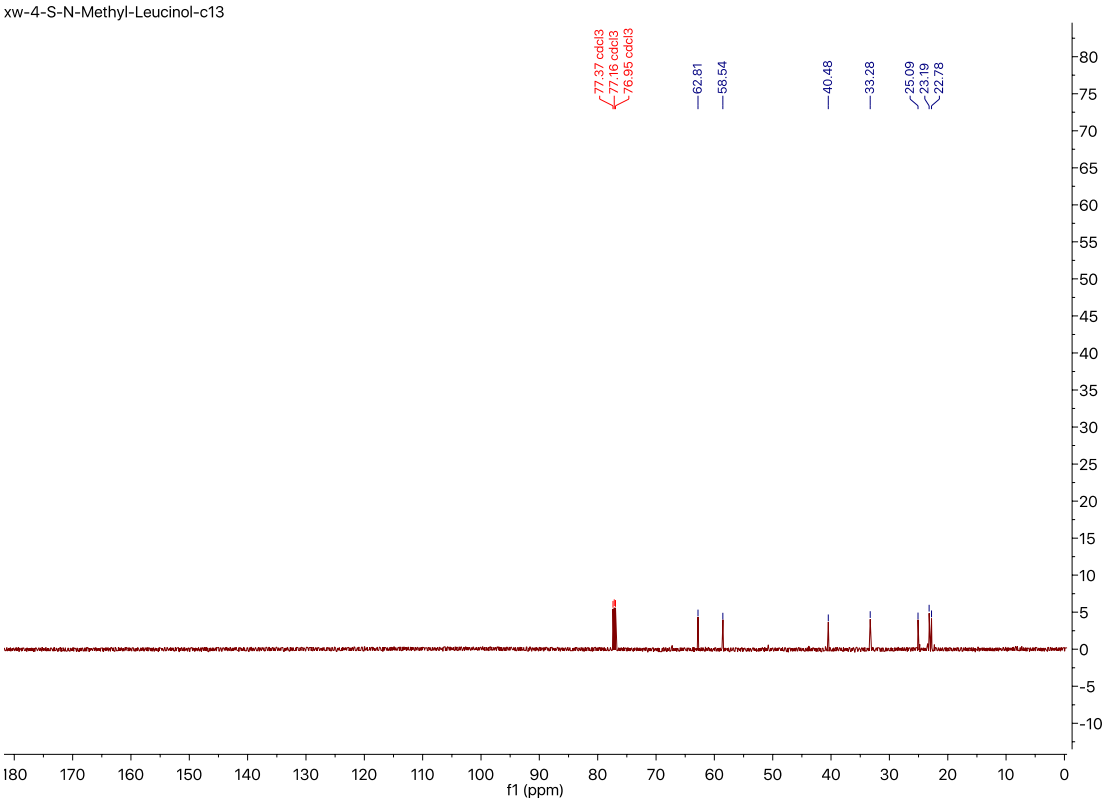

(*R*)-4-methyl-2-(methylamino)pentan-1-ol, (*R*)-N-methyl-leucinol, (*R*)-8

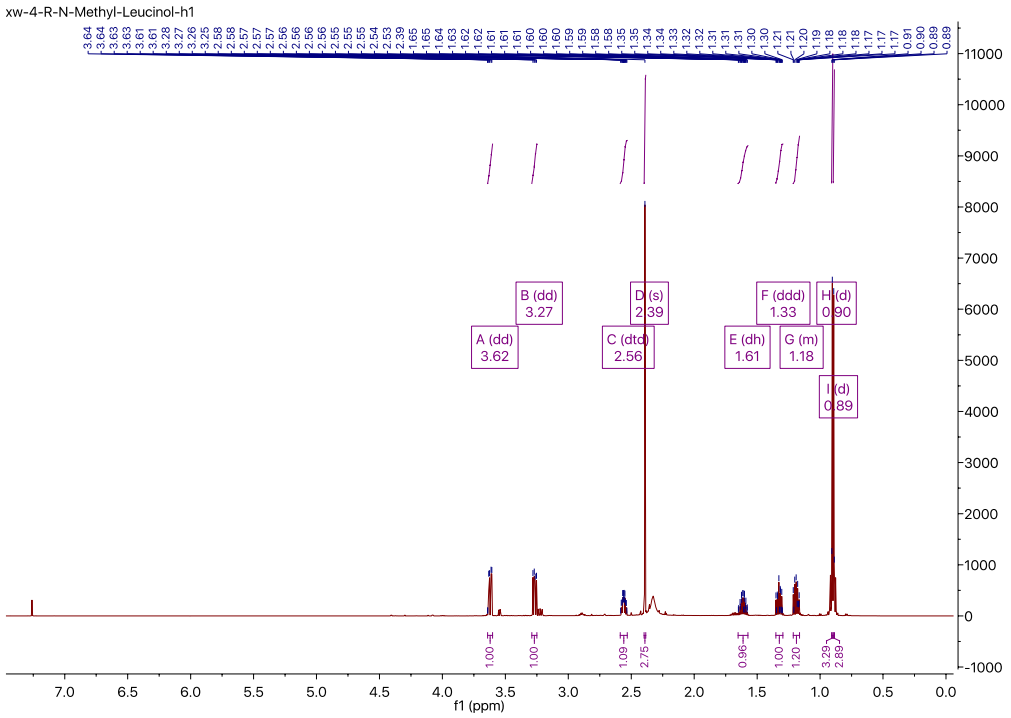

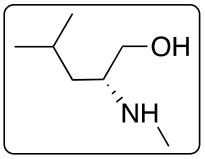

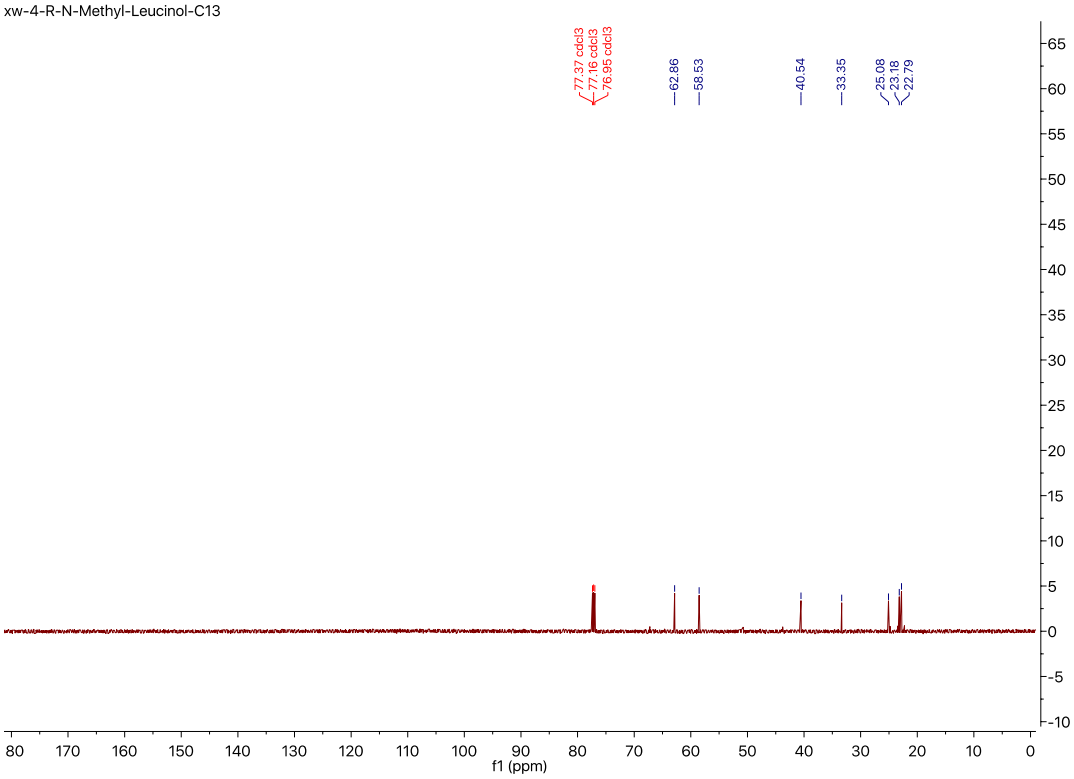

(*Rac*)-2-(isopropylamino)cyclohexan-1-ol, (*Rac*)-14

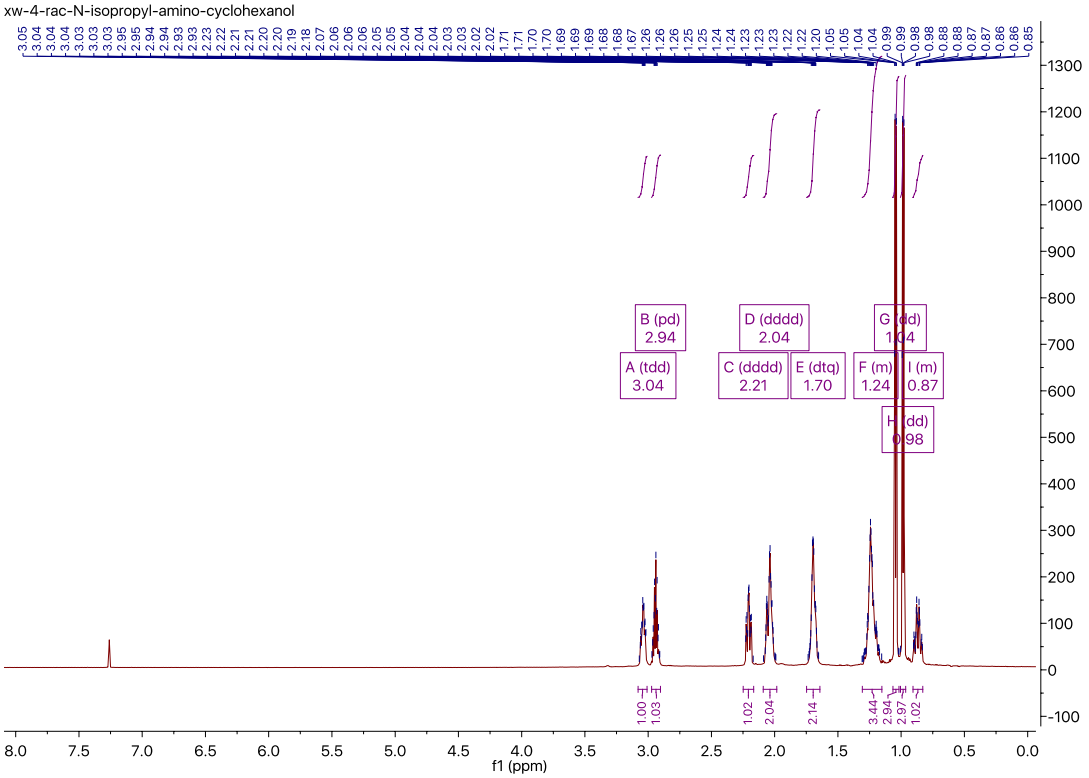

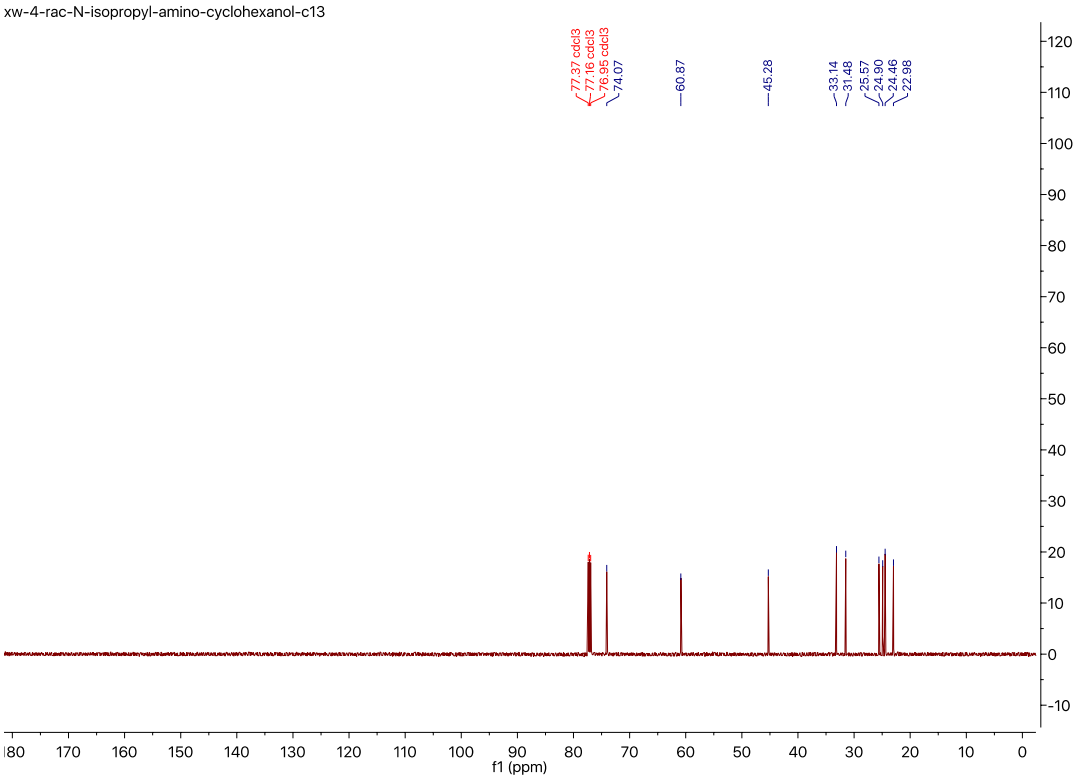

(*Rac*)-2-(methylamino)cyclohexan-1-ol, (*Rac*)-13

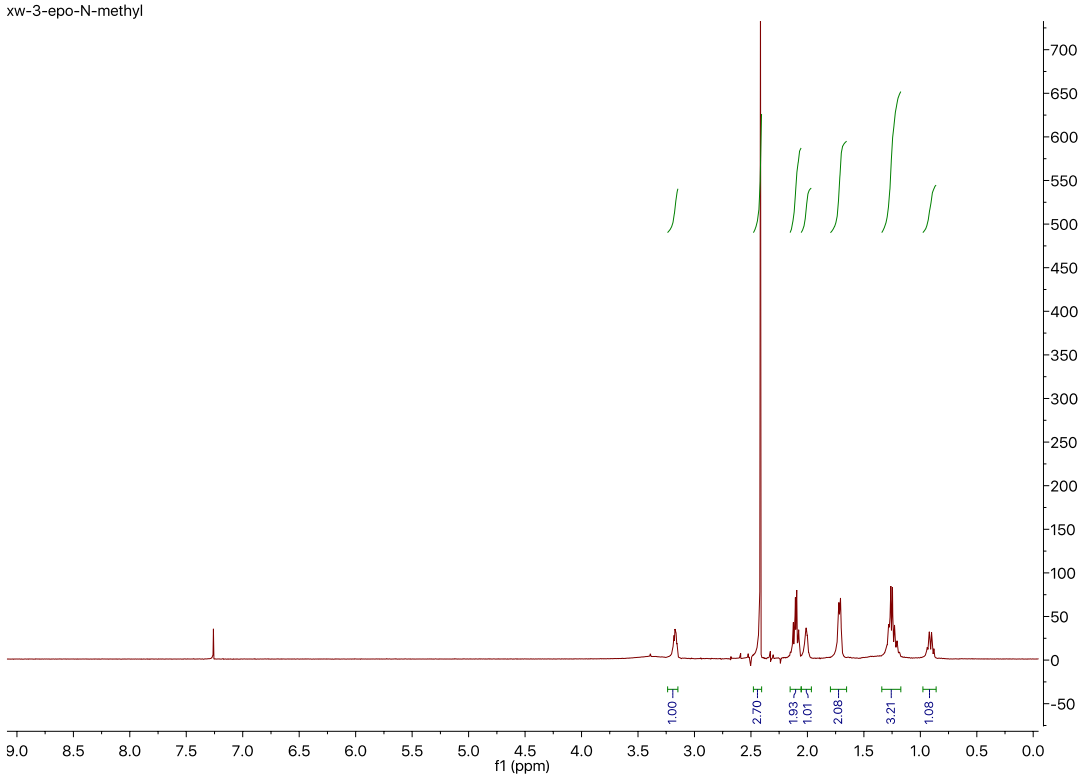

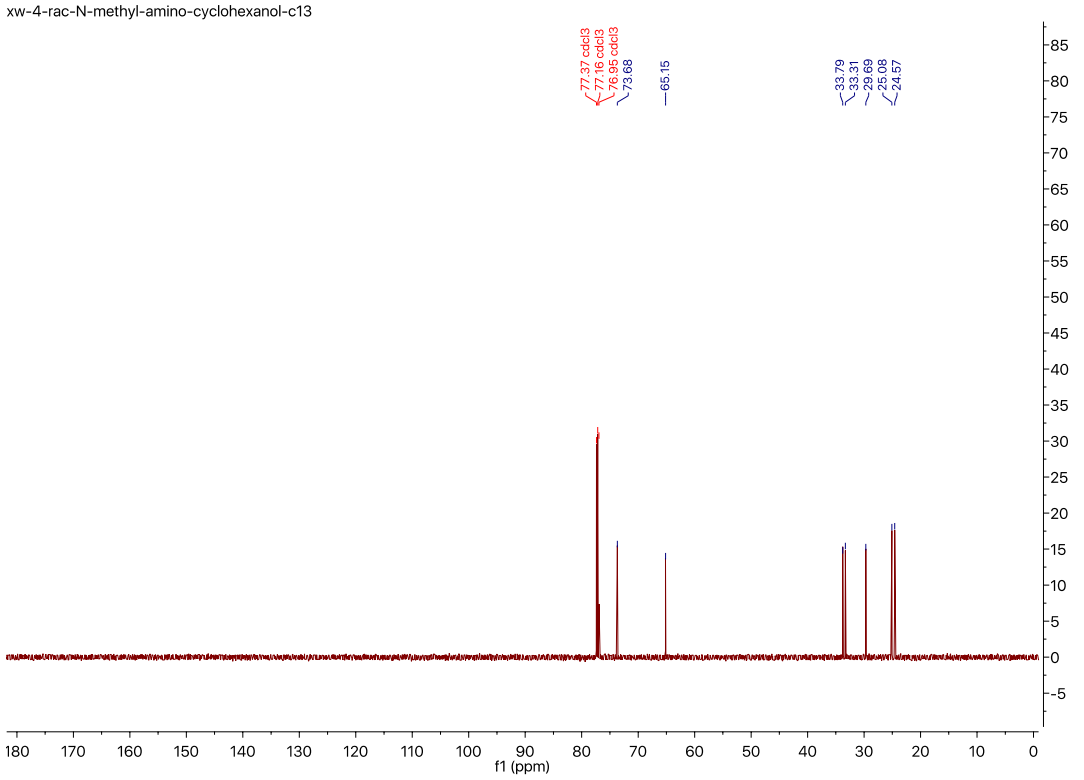

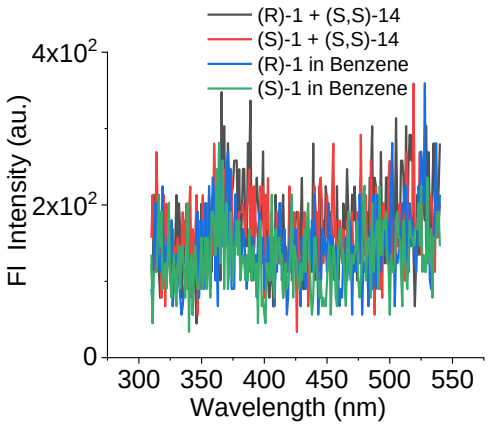
(R)-1 + (S,S)-14
(S)-1 + (S,S)-14
(R)-1 in Benzene
(S)-1 in Benzene
Fl Intensity (au.)
Wavelength (nm)

(a)

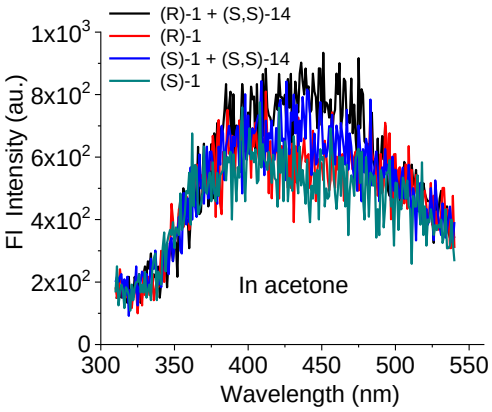
(R)-1 + (S,S)-14
(R)-1
(S)-1 + (S,S)-14
(S)-1
In acetone
Fl Intensity (au.)
Wavelength (nm)

(b)

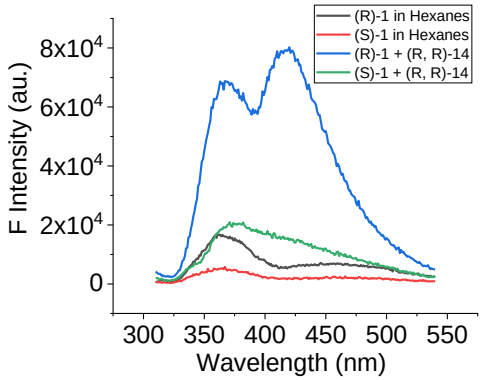
(R)-1 in Hexanes
(S)-1 in Hexanes
(R)-1 + (R, R)-14
(S)-1 + (R, R)-14
F Intensity (au.)
Wavelength (nm)

(c)

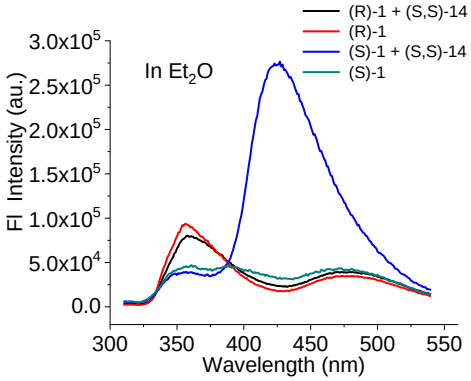
(R)-1 + (S,S)-14
(R)-1
(S)-1 + (S,S)-14
(S)-1
In Et2O
Fl Intensity (au.)
Wavelength (nm)

(d)

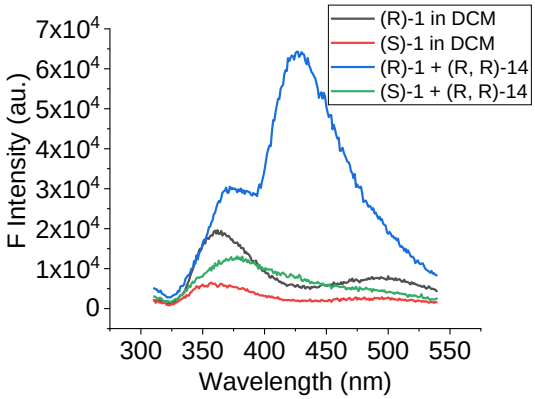
(R)-1 in DCM
(S)-1 in DCM
(R)-1 + (R, R)-14
(S)-1 + (R, R)-14
F Intensity (au.)
Wavelength (nm)

(e)

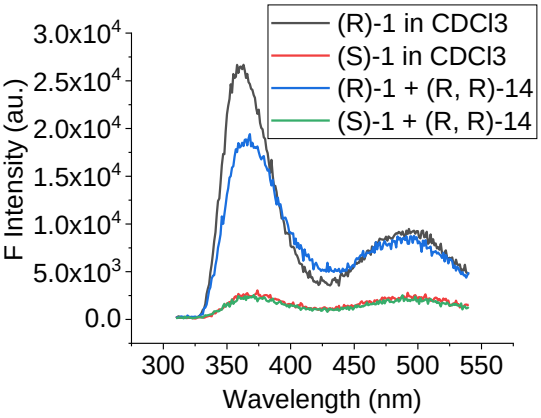
(R)-1 in CDCl3
(S)-1 in CDCl3
(R)-1 + (R, R)-14
(S)-1 + (R, R)-14
F Intensity (au.)
Wavelength (nm)

(f)

Figure S3-1. Fluorescent spectra of (*R*)- and (*S*)-**1** (2×10^{-5} M) with (*S*, *S*)- or (*R*, *R*)-**14** (3 mM) in various organic solvents: benzene (a), acetone (b), hexanes (c), Et_2O (d), DCM (e), $CDCl_3$ (f) (λ_{exc} = 290 nm, slit: 3/3 nm, reaction time: 2 hours).

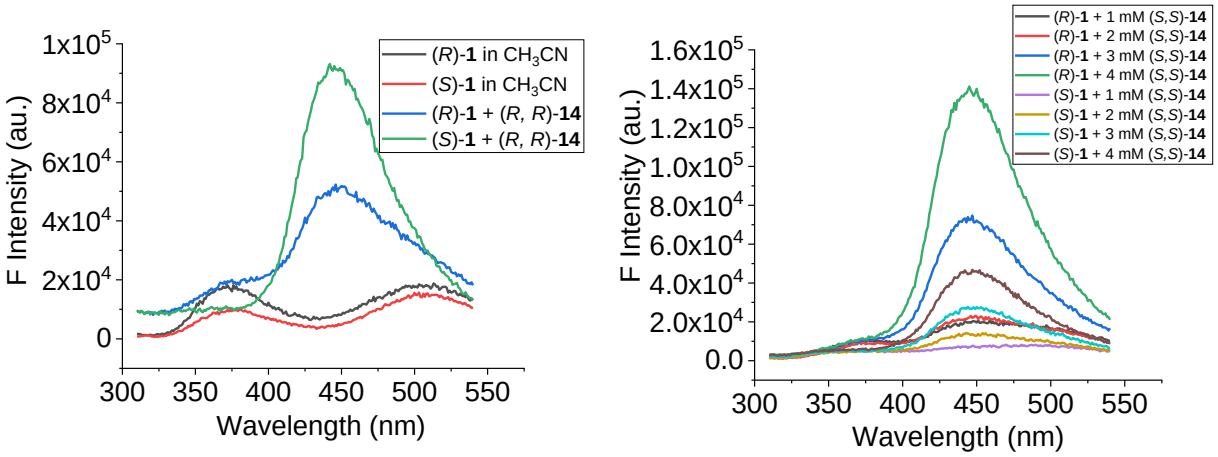

(a) (b)

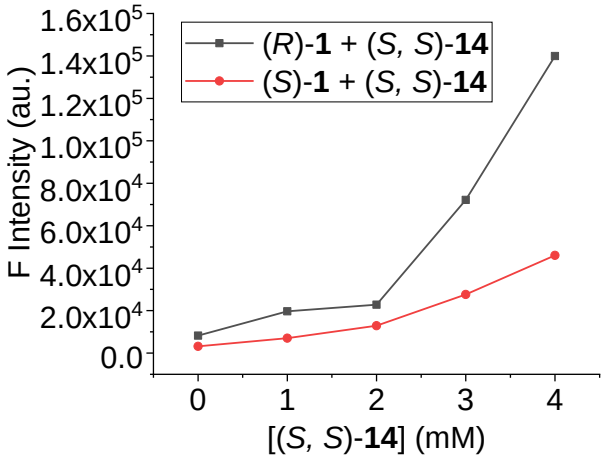

(c)

Figure S3-2. Fluorescent spectra of (*R*)- and (*S*)-**1** (2×10^{-5} M) with (*R*, *R*)-**14** (3 mM) (a). (*R*)- and (*S*)-**1** (2×10^{-5} M) with (*S*, *S*)-**14** at various concentrations (1-4 mM) (b). Plots of the fluorescent intensities of

(*R*)- and (*S*)-**1** (2×10^{-5} M) with (*S, S*)-**14** at 450 nm versus concentrations (1-4 mM) of (*S, S*)-**14**. (all in CH_3CN, λ_{exc} = 290 nm, slit: 3/3 nm, reaction time: 2 hours)

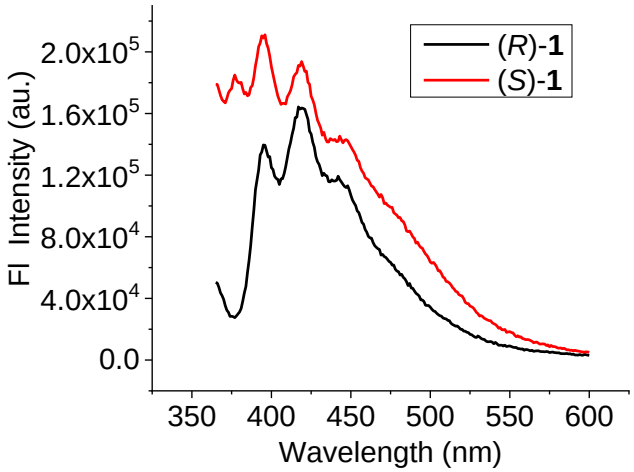

Figure S3-3. Fluorescent spectra of (*R*)- and (*S*)-**1** (2×10^{-5} M) with (*R, R*)-**19** (8 mM) (in FC-72/Et_2O (96/4, v). (λexc = 350 nm, slit: 3/3 nm, reaction time: 2 hours).

Figure S3-4a. ^{1}H NMR titration study of (*S*, *S*)-**14** (100 mM in 5-50 μL Et_2O) with (a) (*R*)-**1** and a capillary tube filled with [D_6]acetone was put added in the NMR tube as an external standard.

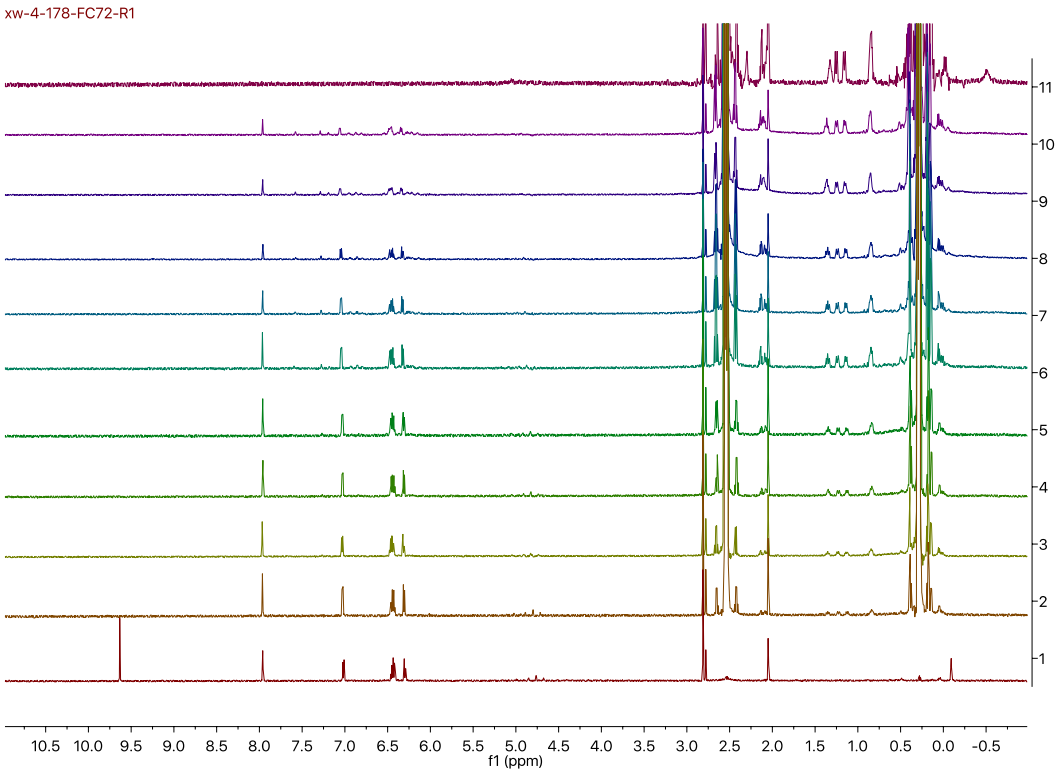

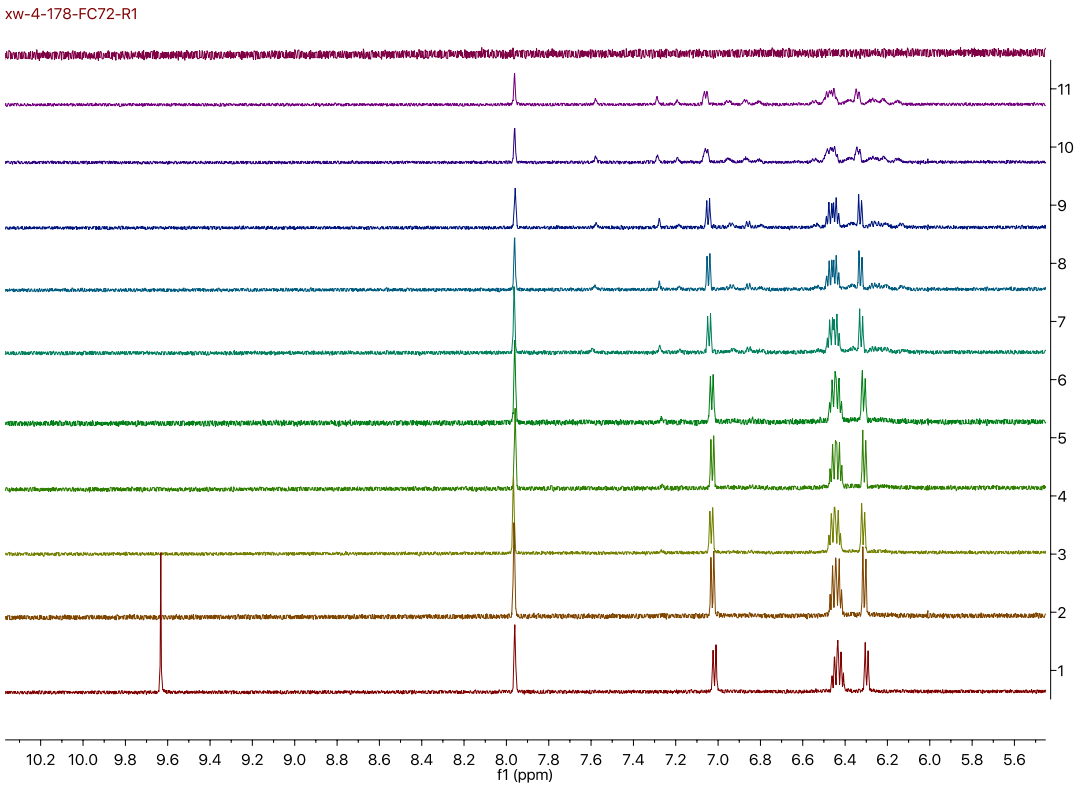
xw-4-178-FC72-R1
11
10
9
8
7
6
5
4
3
2
1
10.2 10.0 9.8 9.6 9.4 9.2 9.0 8.8 8.6 8.4 8.2 8.0 7.8 7.6 7.4 7.2 7.0 6.8 6.6 6.4 6.2 6.0 5.8 5.6
f1 (ppm)

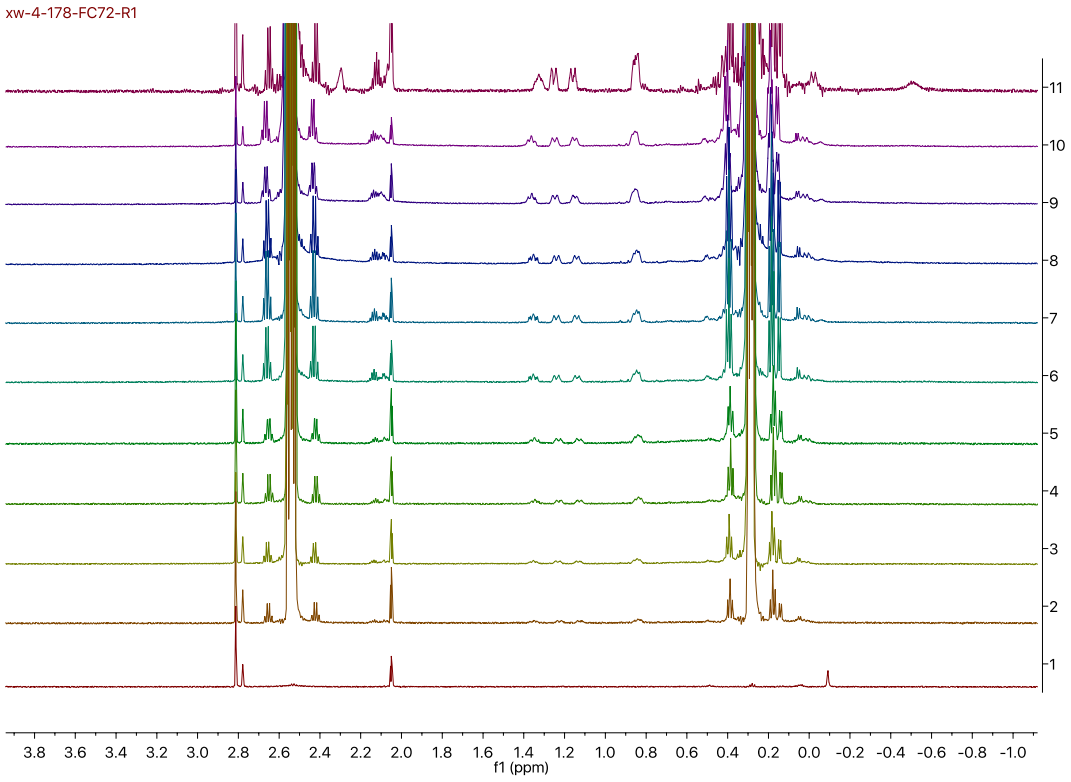
xw-4-178-FC72-R1
11
10
9
8
7
6
5
4
3
2
1
3.8 3.6 3.4 3.2 3.0 2.8 2.6 2.4 2.2 2.0 1.8 1.6 1.4 1.2 1.0 0.8 0.6 0.4 0.2 0.0 -0.2 -0.4 -0.6 -0.8 -1.0
f1 (ppm)

Figure S3-4b. ^{1}H NMR titration study of (*S*, *S*)-**14** (100 mM in 5-50 μL Et_2O) with (*S*)-**1** and a capillary tube filled with [D_6]acetone was put added in the NMR tube as an external standard.

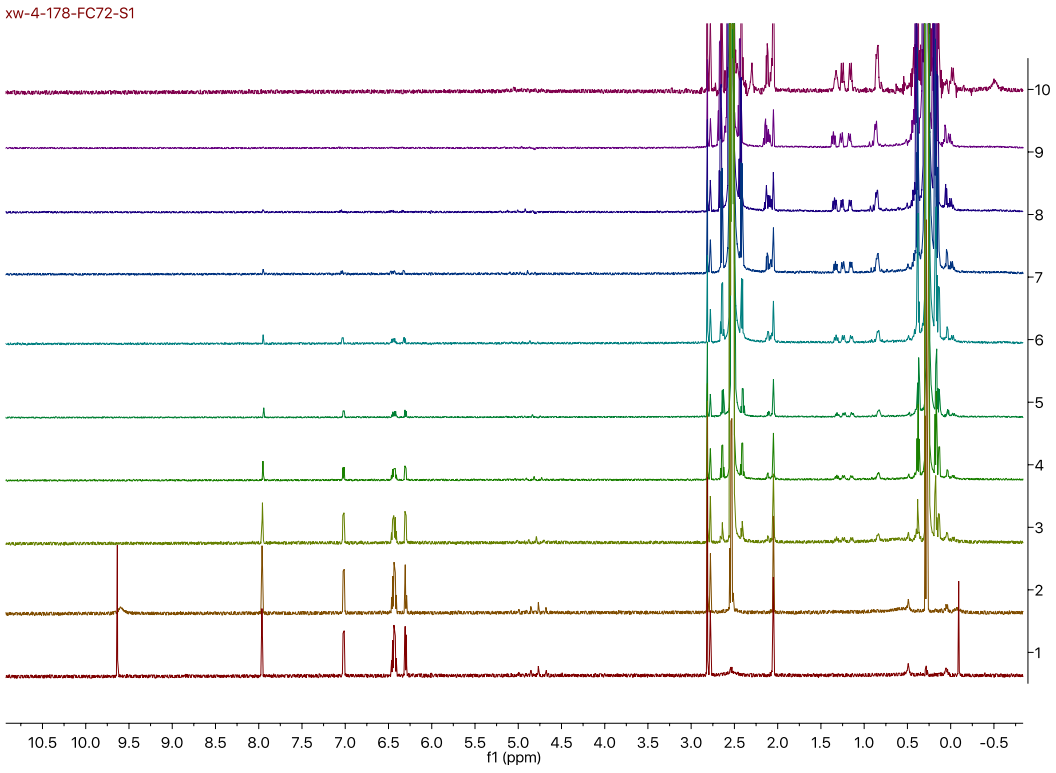

xw-4-178-FC72-S1

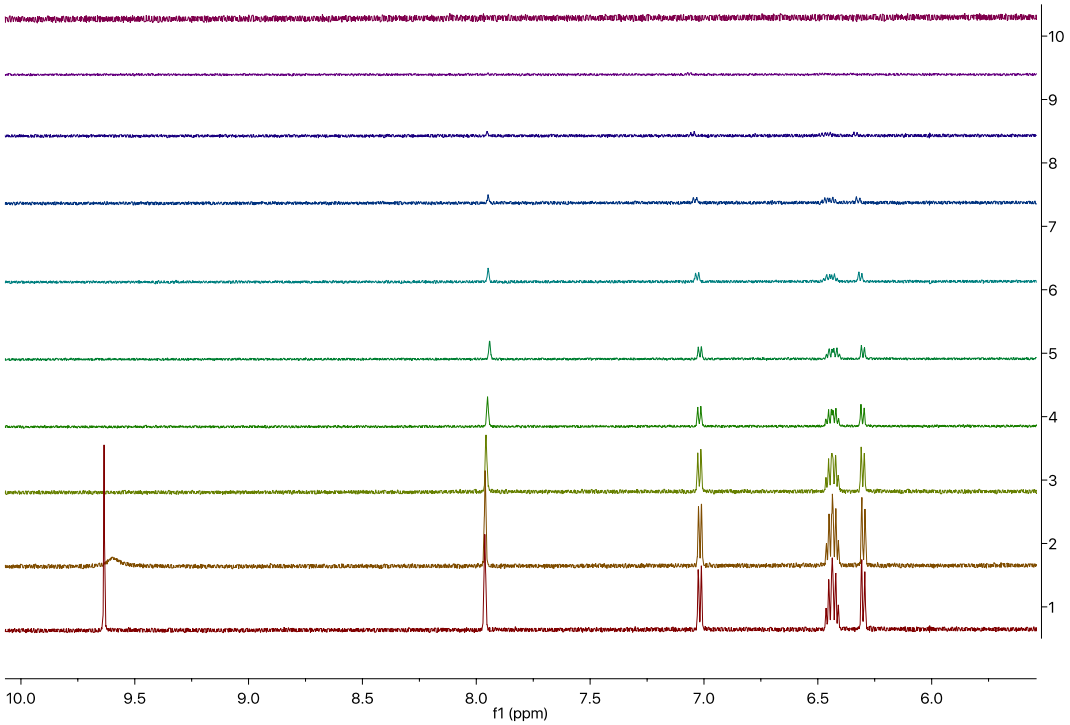

xw-4-178-FC72-S1

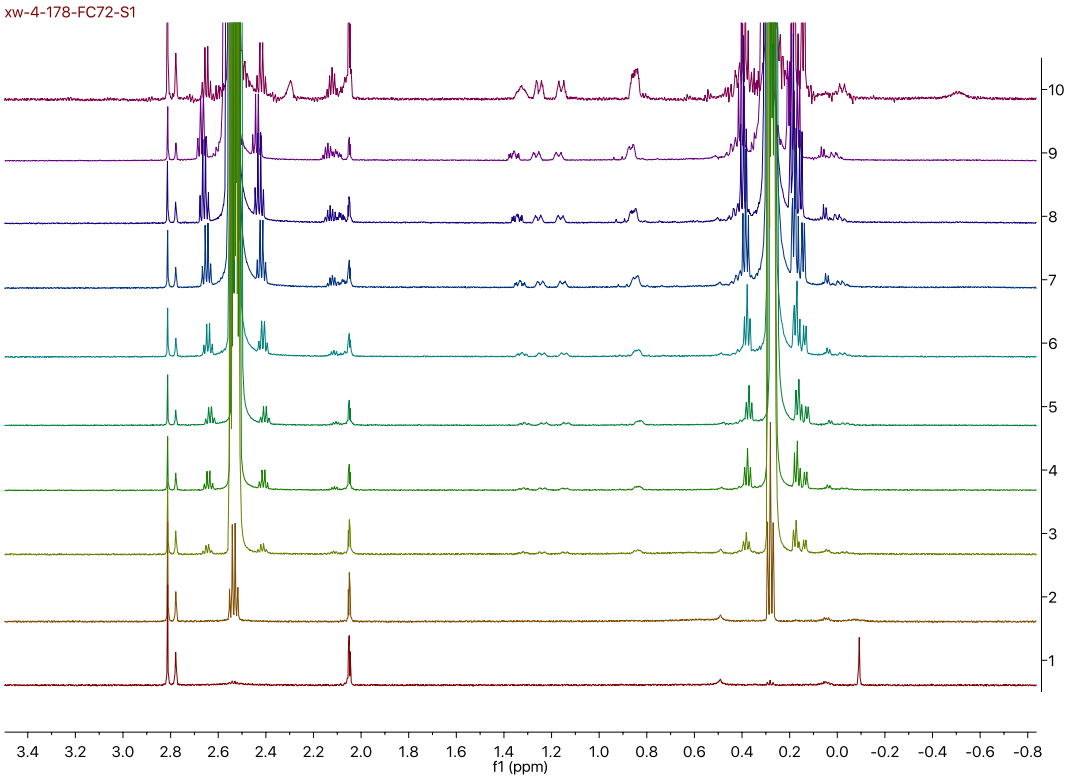

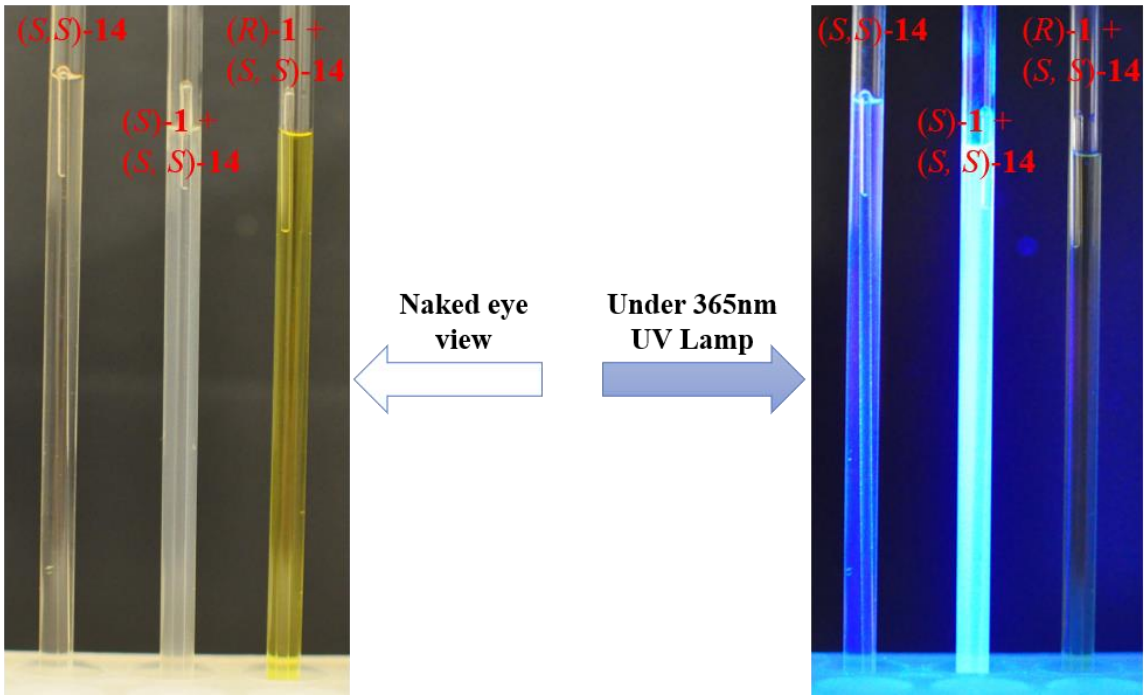

(a) (b)

Figure S3-5. Photo images of the samples of the ^{1}H NMR titration study above. Naked eye view (a) and observation under a 365 nm UV lamp. [(*S, S*)-**14** (100 mM in 5-50 µL Et_2O) with (*S*)-**1** and a capillary tube filled with [D_6]acetone was put added in the NMR tube as an external standard]

IR spectra of the solid sample of (*R*)-1 (5 mg):

Agilent Technologies

Sample ID:R-1
Sample Scans:8
Background Scans:8
Resolution:4
System Status:Good
Method Name:Wilson Method
User:admin
Date/Time:03/08/2019 1:36:22 PM
Range:4000 - 650
Apodization:Happ-Genzel
File Location:C:\Users\Public\Documents\Agilent\MicroLab\Results\\R-1_2019-03-08T13-36-22.a2r

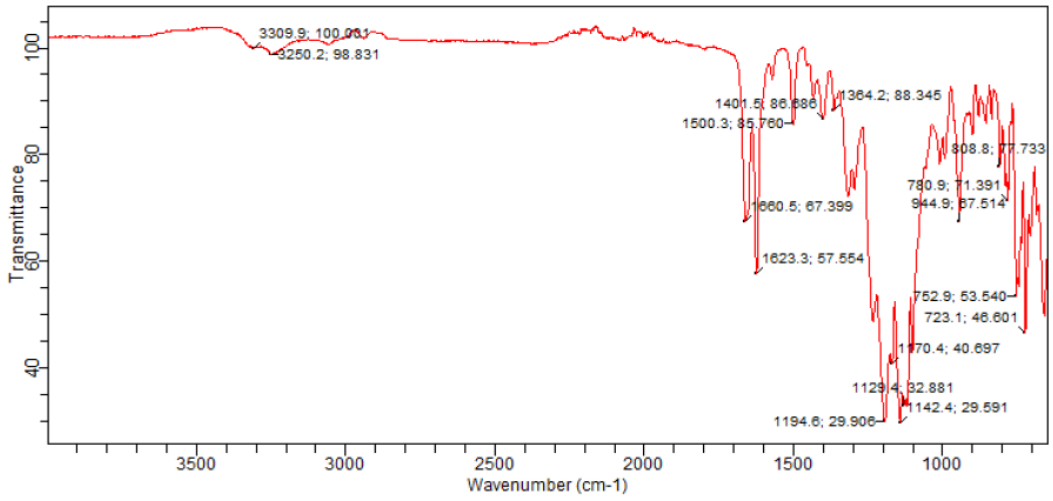

IR spectra of the solid product (reacted in FC-72/Et_2O = 96/4) of (*R*)-1 (0.8 mM, 5.68 mL in FC-72) and (*R, R*)-14 (200 mM, 0.32 mL in Et_2O) for 4 hours then filtrated and dried by rotary evaporation and vacuum pump:

Agilent Technologies

Sample ID:2019-03-08T13-32-42
Sample Scans:8
Background Scans:8
Resolution:4
System Status:Good
Method Name:Wilson Method
User:admin
Date/Time:03/08/2019 1:32:42 PM
Range:4000 - 650
Apodization:Happ-Genzel
File Location:C:\Users\Public\Documents\Agilent\MicroLab\Results\\2019-03-08T13-32-42.a2r

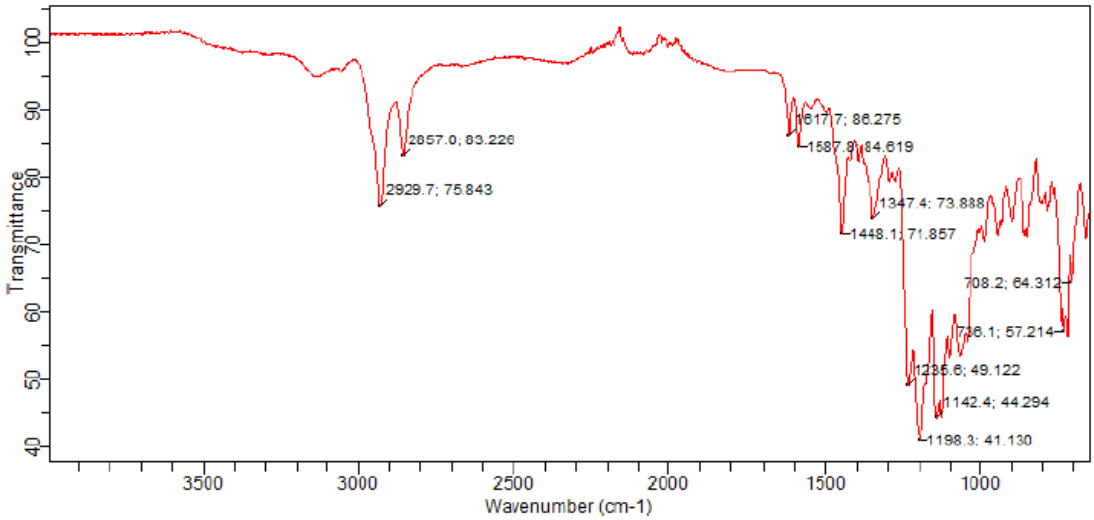

The IR spectrum of the precipitate [(*R*)-**1** + (*R, R*)-**14**] shows that the two intense signals at 1660.5 cm^{-1} and 1623.3 cm^{-1} for the carbonyl groups of (*R*)-**1** disappeared, indicating a nucleophilic addition of the amino alcohol to the carbonyl groups.

(*R*)-**1** + (*S, S*)-**14** didn't generate any solid, therefore, IR couldn't run with the evaporated products. Liquid phase IR was also attempted but it failed with very low signal with high background noise at this concentration (0.8 mM, the saturated concentration in FC-72).

SEM study of the solid product (reacted in FC-72/Et_2O = 96/4) of (*S*)-1 (0.8 mM, 5.68 mL in FC-72) and (*S, S*)-14 (200 mM, 0.32 mL in Et_2O) for 4 hours then filtrated and dried by rotary evaporation and vacuum pump:

Sample name: Sss

Phenom ProX desktop scanning electron microscope with a BSD detector

User name: PHENOM-WORLD-PC\Phenom-World

Contains 1 image with a total of 2 analyses

01. Image 1

2 analyses: 1x spot, 1x region

Image 1

1. spot

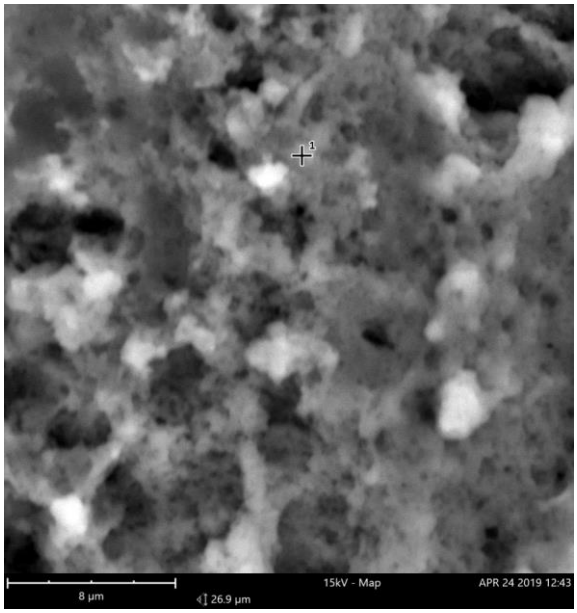

Element Number	Element Symbol	Element Name	Atomic Conc.	Weight Conc.
6	C	Carbon	45.18	36.08
9	F	Fluorine	30.04	37.95
8	O	Oxygen	21.77	23.16
7	N	Nitrogen	3.01	2.81

FOV: 26.9 µm, Mode: 15kV - Map, Detector: BSD Full, Time: APR 24 2019 12:43

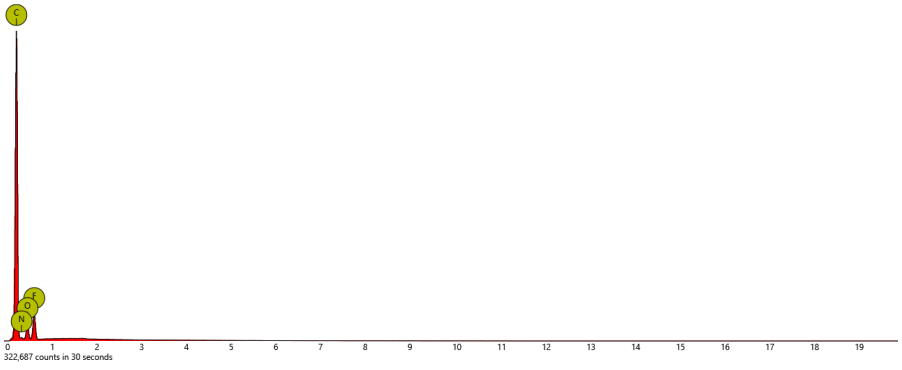

Disabled elements: B

2. region

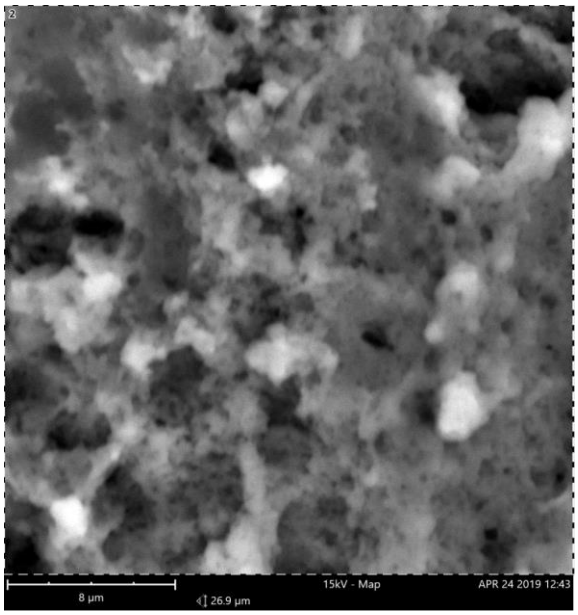

Element Number	Element Symbol	Element Name	Atomic Conc.	Weight Conc.
6	C	Carbon	40.28	31.40
9	F	Fluorine	36.05	44.46
8	O	Oxygen	20.32	21.10
7	N	Nitrogen	3.35	3.04

FOV: 26.9 µm, Mode: 15kV - Map, Detector: BSD Full, Time: APR 24 2019 12:43

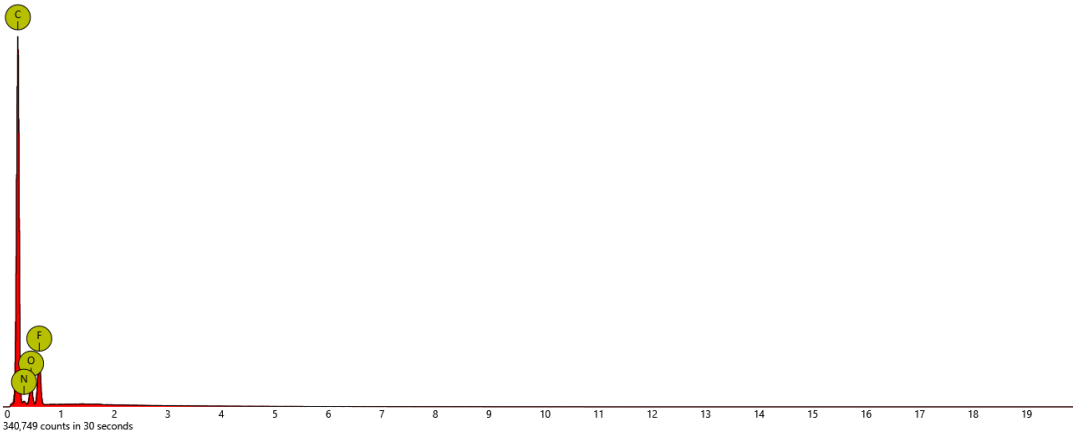

Disabled elements: B

The maintained high composition of the fluorine element indicated the perfluoro chain still on the reaction products that gave high fluorescence emission enhancement. But the MALDI mass spectrum also indicated there's still much of the probe remained unreacted.

(*R*)-**1** + (*S, S*)-**14** didn't generate any solid but a transparent gel like product, therefore, under SEM there's no image captured.

The fluorescence spectra of **1** and **14**. In FC-72/Et_2O 0.8 mM **1**, 4 mM **14**. Then the solvent was filtrated, and the filtrates evaporated to solid or gel like samples to measure IR and SEM.

Table S3-1. Sample and crystal data for Pu_XW4_1. [(*S*)-1]

Identification code	Pu_XW4_1	
Chemical formula	$C_{36}H_{12}F_{30}O_4$	
Formula weight	1078.46 g/mol	
Temperature	100(2) K	
Wavelength	1.54178 Å	
Crystal size	0.084 x 0.090 x 0.215 mm	
Crystal habit	orange block	
Crystal system	monoclinic	
Space group	P 2_1	
Unit cell dimensions	a = 15.0562(6) Å	α = 90°
	b = 6.2943(3) Å	β = 96.271(3)°
	c = 20.2591(9) Å	γ = 90°
Volume	1908.43(15) $Å^3$	
Z	2	
Density (calculated)	1.877 g/cm^3	
Absorption coefficient	2.033 mm^{-1}	
F(000)	1060	

Table S3-2. Data collection and structure refinement for Pu_XW4_1.

Diffractometer	Bruker Kappa APEXII Duo
Radiation source	Incoatec Microfocus IμS (Cu K_α, λ = 1.54178 Å)
Theta range for data collection	2.19 to 68.32°

Index ranges	-18<=h<=18, -7<=k<=7, -24<=l<=24	
Reflections collected	25334	
Independent reflections	7009 [R(int) = 0.0702]	
Coverage of independent reflections	99.9%	
Absorption correction	Multi-Scan	
Max. and min. transmission	0.8480 and 0.6690	
Structure solution technique	direct methods	
Structure solution program	SHELXT 2014/5 (Sheldrick, 2014)	
Refinement method	Full-matrix least-squares on F^2	
Refinement program	SHELXL-2017/1 (Sheldrick, 2017)	
Function minimized	$\Sigma\ w(F_o^2 - F_c^2)^2$	
Data / restraints / parameters	7009 / 1 / 639	
Goodness-of-fit on F^2	1.038	
Final R indices	6030 data; I>2σ(I)	R1 = 0.0457, wR2 = 0.1107
	all data	R1 = 0.0545, wR2 = 0.1179
Weighting scheme	$w=1/[\sigma^2(F_o^2)+(0.0616P)^2]$ where $P=(F_o^2+2F_c^2)/3$	
Absolute structure parameter	0.10(10)	
Largest diff. peak and hole	0.233 and -0.304 $eÅ^{-3}$	
R.M.S. deviation from mean	0.060 $eÅ^{-3}$	

Table S3-3. Atomic coordinates and equivalent isotropic atomic displacement parameters ($Å^2$) for Pu_XW4_1.

U(eq) is defined as one third of the trace of the orthogonalized U_{ij} tensor.

	x/a	y/b	z/c	U(eq)
F1	0.03188(19)	0.2164(4)	0.63232(14)	0.0292(6)
F2	0.94757(18)	0.4755(5)	0.59251(14)	0.0319(6)
F3	0.16004(19)	0.4832(5)	0.68094(15)	0.0364(7)
F4	0.0964(2)	0.7493(5)	0.62481(15)	0.0409(7)
F5	0.9916(2)	0.4457(5)	0.73785(15)	0.0364(7)
F6	0.9623(2)	0.7579(6)	0.69488(15)	0.0421(8)
F7	0.1330(2)	0.5737(6)	0.80939(15)	0.0400(7)
F8	0.1427(2)	0.8653(6)	0.75251(16)	0.0447(8)
F9	0.9591(2)	0.7308(6)	0.83466(17)	0.0442(8)
F10	0.0043(3)	0.0323(6)	0.79737(18)	0.0531(9)
F11	0.0879(3)	0.7115(6)	0.92885(16)	0.0479(8)
F12	0.1677(2)	0.9487(7)	0.88529(18)	0.0509(9)
F13	0.9578(3)	0.0250(7)	0.9386(2)	0.0628(11)
F14	0.0539(3)	0.2532(6)	0.9094(2)	0.0651(12)
F15	0.0854(4)	0.0625(8)	0.9961(2)	0.0706(13)
F16	0.55312(19)	0.4422(4)	0.24231(14)	0.0297(6)
F17	0.44841(19)	0.6433(5)	0.19150(14)	0.0310(6)
F18	0.62452(19)	0.8032(5)	0.30924(14)	0.0322(6)
F19	0.52294(19)	0.9924(4)	0.25009(15)	0.0315(6)
F20	0.69591(19)	0.6723(5)	0.20610(15)	0.0350(6)
F21	0.67875(19)	0.0176(5)	0.20973(14)	0.0334(6)
F22	0.5754(2)	0.6300(5)	0.10495(15)	0.0363(7)
F23	0.52129(19)	0.9502(5)	0.11592(15)	0.0359(6)

	x/a	y/b	z/c	U(eq)
F24	0.74509(19)	0.8574(5)	0.09624(14)	0.0363(7)
F25	0.6589(2)	0.1357(5)	0.07864(16)	0.0386(7)
F26	0.6646(3)	0.6517(6)	0.99637(16)	0.0471(8)
F27	0.5513(2)	0.8688(7)	0.98505(16)	0.0471(8)
F28	0.7734(3)	0.0065(8)	0.97295(18)	0.0603(11)
F29	0.6793(3)	0.8921(7)	0.89443(16)	0.0568(10)
F30	0.6517(3)	0.1786(6)	0.94534(18)	0.0573(10)
O1	0.1527(2)	0.4389(6)	0.41541(16)	0.0265(6)
O2	0.0383(2)	0.5370(6)	0.49689(17)	0.0311(7)
O3	0.3686(2)	0.5288(6)	0.42801(16)	0.0294(7)
O4	0.4607(2)	0.7510(6)	0.34960(18)	0.0340(8)
C1	0.1901(3)	0.3092(7)	0.4641(2)	0.0238(9)
C2	0.2648(3)	0.1958(7)	0.4515(2)	0.0244(9)
C3	0.3090(3)	0.0643(7)	0.5018(2)	0.0240(9)
C4	0.3895(3)	0.9557(8)	0.4930(2)	0.0272(9)
C5	0.4290(3)	0.8253(8)	0.5418(3)	0.0301(10)
C6	0.3912(3)	0.7930(8)	0.6019(3)	0.0320(10)
C7	0.3141(3)	0.8982(8)	0.6124(2)	0.0292(10)
C8	0.2731(3)	0.0392(7)	0.5633(2)	0.0254(9)
C9	0.1960(3)	0.1539(8)	0.5745(2)	0.0250(9)
C10	0.1545(3)	0.2913(8)	0.5268(2)	0.0256(9)
C11	0.0763(3)	0.4148(8)	0.5377(2)	0.0262(9)
C12	0.0335(3)	0.4131(8)	0.6051(2)	0.0261(9)

	x/a	y/b	z/c	U(eq)
C13	0.0810(3)	0.5672(8)	0.6570(2)	0.0286(10)
C14	0.0281(3)	0.6250(8)	0.7166(2)	0.0285(10)
C15	0.0857(3)	0.7264(9)	0.7758(2)	0.0310(10)
C16	0.0310(4)	0.8464(8)	0.8248(3)	0.0342(11)
C17	0.0837(4)	0.8920(9)	0.8932(3)	0.0369(12)
C18	0.0423(5)	0.0634(11)	0.9348(3)	0.0492(15)
C19	0.3534(3)	0.3931(7)	0.3764(2)	0.0253(9)
C20	0.3008(3)	0.2193(8)	0.3858(2)	0.0246(9)
C21	0.2808(3)	0.0694(7)	0.3335(2)	0.0244(9)
C22	0.2298(3)	0.8835(8)	0.3412(2)	0.0263(9)
C23	0.2096(3)	0.7468(8)	0.2893(2)	0.0299(10)
C24	0.2401(3)	0.7864(8)	0.2264(3)	0.0321(10)
C25	0.2907(3)	0.9609(8)	0.2177(2)	0.0300(10)
C26	0.3136(3)	0.1075(7)	0.2710(2)	0.0256(9)
C27	0.3702(3)	0.2804(8)	0.2637(2)	0.0259(9)
C28	0.3913(3)	0.4239(8)	0.3149(2)	0.0272(9)
C29	0.4508(3)	0.6055(8)	0.3089(2)	0.0285(10)
C30	0.5055(3)	0.6213(8)	0.2481(2)	0.0282(10)
C31	0.5707(3)	0.8111(8)	0.2515(2)	0.0278(9)
C32	0.6361(3)	0.8299(8)	0.1973(2)	0.0281(10)
C33	0.5965(3)	0.8305(8)	0.1231(2)	0.0287(10)
C34	0.6618(3)	0.9218(8)	0.0759(3)	0.0311(10)
C35	0.6404(4)	0.8534(10)	0.0018(3)	0.0364(11)

	x/a	y/b	z/c	U(eq)
C36	0.6880(4)	0.9876(11)	0.9524(3)	0.0443(13)

Table S3-4. Bond lengths (Å) for Pu_XW4_1.

F1-C12	1.356(6)	F2-C12	1.350(6)
F3-C13	1.343(6)	F4-C13	1.351(6)
F5-C14	1.347(6)	F6-C14	1.333(6)
F7-C15	1.338(6)	F8-C15	1.346(6)
F9-C16	1.338(7)	F10-C16	1.338(6)
F11-C17	1.344(7)	F12-C17	1.341(7)
F13-C18	1.307(8)	F14-C18	1.320(8)
F15-C18	1.336(8)	F16-C30	1.348(6)
F17-C30	1.363(6)	F18-C31	1.350(6)
F19-C31	1.347(6)	F20-C32	1.338(6)
F21-C32	1.355(6)	F22-C33	1.343(6)
F23-C33	1.355(6)	F24-C34	1.339(6)
F25-C34	1.349(6)	F26-C35	1.329(7)
F27-C35	1.350(7)	F28-C36	1.312(7)
F29-C36	1.314(7)	F30-C36	1.322(8)
O1-C1	1.354(6)	O1-H1	0.82(8)
O2-C11	1.224(6)	O3-C19	1.351(6)
O3-H3	0.88(9)	O4-C29	1.230(6)
C1-C2	1.378(7)	C1-C10	1.438(6)
C2-C3	1.420(7)	C2-C20	1.498(6)

C3-C4	1.419(7)	C3-C8	1.420(7)
C4-C5	1.369(7)	C4-H4	0.95
C5-C6	1.415(7)	C5-H5	0.95
C6-C7	1.373(7)	C6-H6	0.95
C7-C8	1.422(7)	C7-H7	0.95
C8-C9	1.407(7)	C9-C10	1.393(7)
C9-H9	0.95	C10-C11	1.448(6)
C11-C12	1.572(6)	C12-C13	1.547(7)
C13-C14	1.560(6)	C14-C15	1.540(7)
C15-C16	1.553(7)	C16-C17	1.547(7)
C17-C18	1.542(8)	C19-C20	1.376(7)
C19-C28	1.439(6)	C20-C21	1.426(6)
C21-C22	1.417(7)	C21-C26	1.429(6)
C22-C23	1.367(7)	C22-H22	0.95
C23-C24	1.423(7)	C23-H23	0.95
C24-C25	1.359(7)	C24-H24	0.95
C25-C26	1.433(7)	C25-H25	0.95
C26-C27	1.400(7)	C27-C28	1.386(7)
C27-H27	0.95	C28-C29	1.465(7)
C29-C30	1.559(6)	C30-C31	1.543(7)
C31-C32	1.557(6)	C32-C33	1.557(6)
C33-C34	1.553(6)	C34-C35	1.561(7)
C35-C36	1.544(8)		

Table S3-5. Bond angles (°) for Pu_XW4_1.

C1-O1-H1	111.(5)	C19-O3-H3	107.(5)
O1-C1-C2	117.4(4)	O1-C1-C10	121.7(4)
C2-C1-C10	120.9(4)	C1-C2-C3	119.8(4)
C1-C2-C20	119.6(4)	C3-C2-C20	120.5(4)
C4-C3-C8	117.9(4)	C4-C3-C2	122.0(4)
C8-C3-C2	120.0(4)	C5-C4-C3	120.5(4)
C5-C4-H4	119.7	C3-C4-H4	119.7
C4-C5-C6	121.6(5)	C4-C5-H5	119.2
C6-C5-H5	119.2	C7-C6-C5	119.3(5)
C7-C6-H6	120.3	C5-C6-H6	120.3
C6-C7-C8	120.2(5)	C6-C7-H7	119.9
C8-C7-H7	119.9	C9-C8-C3	119.0(4)
C9-C8-C7	120.6(4)	C3-C8-C7	120.3(4)
C10-C9-C8	121.4(4)	C10-C9-H9	119.3
C8-C9-H9	119.3	C9-C10-C1	118.7(4)
C9-C10-C11	122.5(4)	C1-C10-C11	118.8(4)
O2-C11-C10	124.1(4)	O2-C11-C12	112.7(4)
C10-C11-C12	123.1(4)	F2-C12-F1	106.5(4)
F2-C12-C13	108.0(4)	F1-C12-C13	108.9(4)
F2-C12-C11	108.0(4)	F1-C12-C11	112.7(4)
C13-C12-C11	112.5(4)	F3-C13-F4	108.4(4)
F3-C13-C12	108.9(4)	F4-C13-C12	107.1(4)
F3-C13-C14	108.7(4)	F4-C13-C14	107.7(4)

C12-C13-C14	115.7(4)	F6-C14-F5	108.5(4)
F6-C14-C15	109.3(4)	F5-C14-C15	108.2(4)
F6-C14-C13	108.4(4)	F5-C14-C13	108.2(4)
C15-C14-C13	114.1(4)	F7-C15-F8	108.7(4)
F7-C15-C14	108.8(4)	F8-C15-C14	108.8(4)
F7-C15-C16	108.3(4)	F8-C15-C16	108.1(4)
C14-C15-C16	114.0(4)	F10-C16-F9	109.0(5)
F10-C16-C17	108.1(4)	F9-C16-C17	108.1(4)
F10-C16-C15	108.4(4)	F9-C16-C15	109.0(4)
C17-C16-C15	114.1(5)	F12-C17-F11	107.5(5)
F12-C17-C18	108.8(5)	F11-C17-C18	107.2(5)
F12-C17-C16	109.9(4)	F11-C17-C16	108.3(4)
C18-C17-C16	114.9(5)	F13-C18-F14	111.1(7)
F13-C18-F15	108.8(6)	F14-C18-F15	107.2(6)
F13-C18-C17	110.9(5)	F14-C18-C17	110.0(5)
F15-C18-C17	108.7(6)	O3-C19-C20	116.5(4)
O3-C19-C28	122.4(4)	C20-C19-C28	121.1(4)
C19-C20-C21	120.0(4)	C19-C20-C2	118.2(4)
C21-C20-C2	121.8(4)	C22-C21-C20	122.5(4)
C22-C21-C26	118.7(4)	C20-C21-C26	118.8(4)
C23-C22-C21	120.9(4)	C23-C22-H22	119.6
C21-C22-H22	119.6	C22-C23-C24	120.8(5)
C22-C23-H23	119.6	C24-C23-H23	119.6
C25-C24-C23	119.8(5)	C25-C24-H24	120.1
C23-C24-H24	120.1	C24-C25-C26	121.0(4)

C24-C25-H25	119.5	C26-C25-H25	119.5
C27-C26-C21	119.9(4)	C27-C26-C25	121.3(4)
C21-C26-C25	118.8(4)	C28-C27-C26	121.3(4)
C28-C27-H27	119.4	C26-C27-H27	119.4
C27-C28-C19	118.7(4)	C27-C28-C29	122.6(4)
C19-C28-C29	118.7(4)	O4-C29-C28	123.8(4)
O4-C29-C30	116.5(4)	C28-C29-C30	119.7(4)
F16-C30-F17	107.8(4)	F16-C30-C31	108.1(4)
F17-C30-C31	107.4(4)	F16-C30-C29	110.3(4)
F17-C30-C29	109.4(4)	C31-C30-C29	113.7(4)
F19-C31-F18	108.6(4)	F19-C31-C30	108.7(4)
F18-C31-C30	109.2(4)	F19-C31-C32	107.3(4)
F18-C31-C32	104.3(4)	C30-C31-C32	118.4(4)
F20-C32-F21	108.9(4)	F20-C32-C33	108.1(4)
F21-C32-C33	107.5(4)	F20-C32-C31	108.6(4)
F21-C32-C31	105.0(4)	C33-C32-C31	118.4(4)
F22-C33-F23	108.8(4)	F22-C33-C34	109.0(4)
F23-C33-C34	107.8(4)	F22-C33-C32	108.4(4)
F23-C33-C32	109.4(4)	C34-C33-C32	113.2(4)
F24-C34-F25	108.8(4)	F24-C34-C33	109.4(4)
F25-C34-C33	108.6(4)	F24-C34-C35	107.5(4)
F25-C34-C35	108.1(4)	C33-C34-C35	114.3(4)
F26-C35-F27	108.8(5)	F26-C35-C36	108.5(5)
F27-C35-C36	108.5(5)	F26-C35-C34	108.2(4)
F27-C35-C34	108.5(4)	C36-C35-C34	114.2(5)

F28-C36-F29	108.8(5)	F28-C36-F30	109.4(6)
F29-C36-F30	108.6(5)	F28-C36-C35	110.7(5)
F29-C36-C35	108.7(5)	F30-C36-C35	110.6(5)

Table S3-6. Torsion angles (°) for Pu_XW4_1.

O1-C1-C2-C3	177.3(4)	C10-C1-C2-C3	-2.0(7)
O1-C1-C2-C20	-0.2(6)	C10-C1-C2-C20	-179.4(4)
C1-C2-C3-C4	-175.6(4)	C20-C2-C3-C4	1.8(7)
C1-C2-C3-C8	4.0(7)	C20-C2-C3-C8	-178.5(4)
C8-C3-C4-C5	2.3(7)	C2-C3-C4-C5	-178.1(4)
C3-C4-C5-C6	0.4(7)	C4-C5-C6-C7	-1.4(8)
C5-C6-C7-C8	-0.4(7)	C4-C3-C8-C9	176.7(4)
C2-C3-C8-C9	-3.0(7)	C4-C3-C8-C7	-4.0(6)
C2-C3-C8-C7	176.3(4)	C6-C7-C8-C9	-177.6(5)
C6-C7-C8-C3	3.1(7)	C3-C8-C9-C10	-0.1(7)
C7-C8-C9-C10	-179.4(4)	C8-C9-C10-C1	2.2(7)
C8-C9-C10-C11	-178.6(4)	O1-C1-C10-C9	179.6(4)
C2-C1-C10-C9	-1.1(7)	O1-C1-C10-C11	0.3(6)
C2-C1-C10-C11	179.6(4)	C9-C10-C11-O2	179.9(5)
C1-C10-C11-O2	-0.8(7)	C9-C10-C11-C12	2.7(7)
C1-C10-C11-C12	-178.0(4)	O2-C11-C12-F2	24.7(6)
C10-C11-C12-F2	-157.8(4)	O2-C11-C12-F1	142.0(4)
C10-C11-C12-F1	-40.5(6)	O2-C11-C12-C13	-94.3(5)
C10-C11-C12-C13	83.2(6)	F2-C12-C13-F3	166.8(4)

F1-C12-C13-F3	51.6(5)	C11-C12-C13-F3	-74.2(5)
F2-C12-C13-F4	-76.1(5)	F1-C12-C13-F4	168.6(4)
C11-C12-C13-F4	42.9(5)	F2-C12-C13-C14	44.0(5)
F1-C12-C13-C14	-71.2(5)	C11-C12-C13-C14	163.1(4)
F3-C13-C14-F6	163.4(4)	F4-C13-C14-F6	46.1(5)
C12-C13-C14-F6	-73.7(5)	F3-C13-C14-F5	-79.1(5)
F4-C13-C14-F5	163.6(4)	C12-C13-C14-F5	43.7(5)
F3-C13-C14-C15	41.3(6)	F4-C13-C14-C15	-75.9(5)
C12-C13-C14-C15	164.2(4)	F6-C14-C15-F7	161.5(4)
F5-C14-C15-F7	43.5(5)	C13-C14-C15-F7	-77.0(5)
F6-C14-C15-F8	-80.3(5)	F5-C14-C15-F8	161.7(4)
C13-C14-C15-F8	41.2(6)	F6-C14-C15-C16	40.5(6)
F5-C14-C15-C16	-77.5(5)	C13-C14-C15-C16	162.0(4)
F7-C15-C16-F10	162.6(4)	F8-C15-C16-F10	45.0(6)
C14-C15-C16-F10	-76.1(6)	F7-C15-C16-F9	-78.8(5)
F8-C15-C16-F9	163.6(4)	C14-C15-C16-F9	42.4(6)
F7-C15-C16-C17	42.1(6)	F8-C15-C16-C17	-75.5(6)
C14-C15-C16-C17	163.3(4)	F10-C16-C17-F12	-80.8(6)
F9-C16-C17-F12	161.3(5)	C15-C16-C17-F12	39.9(6)
F10-C16-C17-F11	162.1(5)	F9-C16-C17-F11	44.2(6)
C15-C16-C17-F11	-77.2(6)	F10-C16-C17-C18	42.3(7)
F9-C16-C17-C18	-75.6(6)	C15-C16-C17-C18	163.0(5)
F12-C17-C18-F13	174.0(5)	F11-C17-C18-F13	-70.0(7)
C16-C17-C18-F13	50.4(7)	F12-C17-C18-F14	50.7(7)
F11-C17-C18-F14	166.6(6)	C16-C17-C18-F14	-73.0(7)

F12-C17-C18-F15	-66.4(7)	F11-C17-C18-F15	49.6(7)
C16-C17-C18-F15	170.0(5)	O3-C19-C20-C21	179.4(4)
C28-C19-C20-C21	-1.9(7)	O3-C19-C20-C2	0.3(6)
C28-C19-C20-C2	179.1(4)	C1-C2-C20-C19	80.5(6)
C3-C2-C20-C19	-96.9(5)	C1-C2-C20-C21	-98.5(5)
C3-C2-C20-C21	84.1(6)	C19-C20-C21-C22	177.6(4)
C2-C20-C21-C22	-3.4(7)	C19-C20-C21-C26	-2.2(7)
C2-C20-C21-C26	176.8(4)	C20-C21-C22-C23	177.9(4)
C26-C21-C22-C23	-2.3(7)	C21-C22-C23-C24	0.7(7)
C22-C23-C24-C25	0.7(8)	C23-C24-C25-C26	-0.5(8)
C22-C21-C26-C27	-174.8(4)	C20-C21-C26-C27	5.0(7)
C22-C21-C26-C25	2.5(6)	C20-C21-C26-C25	-177.7(4)
C24-C25-C26-C27	176.1(5)	C24-C25-C26-C21	-1.1(7)
C21-C26-C27-C28	-3.8(7)	C25-C26-C27-C28	179.0(5)
C26-C27-C28-C19	-0.3(7)	C26-C27-C28-C29	179.6(4)
O3-C19-C28-C27	-178.1(4)	C20-C19-C28-C27	3.2(7)
O3-C19-C28-C29	2.0(7)	C20-C19-C28-C29	-176.7(4)
C27-C28-C29-O4	169.4(5)	C19-C28-C29-O4	-10.8(8)
C27-C28-C29-C30	-10.4(7)	C19-C28-C29-C30	169.5(4)
O4-C29-C30-F16	126.5(5)	C28-C29-C30-F16	-53.7(6)
O4-C29-C30-F17	-115.2(5)	C28-C29-C30-F17	64.6(6)
O4-C29-C30-C31	4.9(6)	C28-C29-C30-C31	-175.3(4)
F16-C30-C31-F19	173.5(4)	F17-C30-C31-F19	57.5(5)
C29-C30-C31-F19	-63.6(5)	F16-C30-C31-F18	-68.2(5)
F17-C30-C31-F18	175.8(4)	C29-C30-C31-F18	54.6(5)

F16-C30-C31-C32	50.8(5)	F17-C30-C31-C32	-65.2(5)
C29-C30-C31-C32	173.7(4)	F19-C31-C32-F20	168.1(4)
F18-C31-C32-F20	53.0(5)	C30-C31-C32-F20	-68.6(5)
F19-C31-C32-F21	51.7(5)	F18-C31-C32-F21	-63.3(5)
C30-C31-C32-F21	175.1(4)	F19-C31-C32-C33	-68.2(5)
F18-C31-C32-C33	176.7(4)	C30-C31-C32-C33	55.1(6)
F20-C32-C33-F22	46.3(5)	F21-C32-C33-F22	163.7(4)
C31-C32-C33-F22	-77.7(5)	F20-C32-C33-F23	164.9(4)
F21-C32-C33-F23	-77.7(5)	C31-C32-C33-F23	40.9(6)
F20-C32-C33-C34	-74.8(5)	F21-C32-C33-C34	42.6(5)
C31-C32-C33-C34	161.2(4)	F22-C33-C34-F24	-82.1(5)
F23-C33-C34-F24	159.9(4)	C32-C33-C34-F24	38.7(6)
F22-C33-C34-F25	159.3(4)	F23-C33-C34-F25	41.3(5)
C32-C33-C34-F25	-79.9(5)	F22-C33-C34-C35	38.5(6)
F23-C33-C34-C35	-79.5(5)	C32-C33-C34-C35	159.3(4)
F24-C34-C35-F26	47.3(6)	F25-C34-C35-F26	164.6(4)
C33-C34-C35-F26	-74.4(6)	F24-C34-C35-F27	165.2(4)
F25-C34-C35-F27	-77.5(5)	C33-C34-C35-F27	43.5(6)
F24-C34-C35-C36	-73.7(6)	F25-C34-C35-C36	43.6(6)
C33-C34-C35-C36	164.6(5)	F26-C35-C36-F28	-72.4(7)
F27-C35-C36-F28	169.6(5)	C34-C35-C36-F28	48.4(7)
F26-C35-C36-F29	47.1(7)	F27-C35-C36-F29	-71.0(6)
C34-C35-C36-F29	167.9(5)	F26-C35-C36-F30	166.2(5)
F27-C35-C36-F30	48.2(7)	C34-C35-C36-F30	-72.9(6)

Table S3-7. Anisotropic atomic displacement parameters (Å^2) for Pu_XW4_1.

The anisotropic atomic displacement factor exponent takes the form: $-2\pi^2[h^2 a^{*2} U_{11} + ... + 2 h k a^* b^* U_{12}]$

	U_{11}	U_{22}	U_{33}	U_{23}	U_{13}	U_{12}
F1	0.0341(14)	0.0268(13)	0.0279(13)	0.0007(11)	0.0088(11)	-0.0020(11)
F2	0.0231(12)	0.0420(16)	0.0316(14)	-0.0011(12)	0.0066(11)	0.0032(12)
F3	0.0276(14)	0.0472(18)	0.0343(14)	-0.0098(13)	0.0022(11)	0.0041(13)
F4	0.062(2)	0.0300(15)	0.0331(15)	0.0013(13)	0.0154(15)	-0.0123(15)
F5	0.0420(16)	0.0380(15)	0.0310(14)	-0.0032(13)	0.0115(12)	-0.0116(14)
F6	0.0453(18)	0.0488(19)	0.0313(14)	-0.0034(14)	0.0002(13)	0.0211(16)
F7	0.0399(16)	0.0461(18)	0.0324(15)	-0.0040(13)	-0.0032(13)	0.0092(14)
F8	0.0516(19)	0.0477(19)	0.0383(16)	-0.0119(15)	0.0201(15)	-0.0218(16)
F9	0.0382(17)	0.055(2)	0.0417(17)	-0.0141(16)	0.0162(14)	-0.0070(15)
F10	0.083(3)	0.0367(17)	0.0402(17)	0.0024(15)	0.0081(18)	0.0227(18)
F11	0.070(2)	0.0434(18)	0.0302(15)	0.0006(14)	0.0031(15)	0.0006(17)
F12	0.0452(18)	0.060(2)	0.0486(19)	-0.0198(18)	0.0088(15)	-0.0135(18)
F13	0.066(2)	0.067(2)	0.061(2)	-0.024(2)	0.029(2)	-0.007(2)
F14	0.100(3)	0.038(2)	0.062(2)	-0.0130(18)	0.028(2)	-0.005(2)
F15	0.098(4)	0.075(3)	0.0390(19)	-0.026(2)	0.010(2)	-0.005(3)
F16	0.0340(14)	0.0252(13)	0.0314(13)	-0.0003(11)	0.0100(11)	-0.0007(12)
F17	0.0304(14)	0.0347(14)	0.0280(13)	0.0047(12)	0.0037(11)	-0.0049(12)
F18	0.0327(14)	0.0362(15)	0.0276(13)	0.0016(12)	0.0022(11)	-0.0047(12)
F19	0.0338(14)	0.0249(14)	0.0368(14)	0.0021(11)	0.0084(12)	0.0022(11)
F20	0.0316(15)	0.0395(16)	0.0346(14)	0.0056(13)	0.0072(12)	0.0089(12)
F21	0.0306(14)	0.0375(16)	0.0328(14)	0.0019(13)	0.0059(12)	-0.0099(13)

	U_{11}	U_{22}	U_{33}	U_{23}	U_{13}	U_{12}
F22	0.0415(16)	0.0340(15)	0.0338(15)	-0.0006(13)	0.0058(13)	-0.0084(14)
F23	0.0304(14)	0.0431(16)	0.0345(14)	0.0054(14)	0.0049(12)	0.0037(13)
F24	0.0281(14)	0.0513(18)	0.0295(14)	0.0017(13)	0.0035(11)	-0.0011(13)
F25	0.0494(18)	0.0335(15)	0.0350(15)	-0.0006(13)	0.0140(14)	-0.0072(14)
F26	0.064(2)	0.0423(17)	0.0365(17)	-0.0056(15)	0.0113(16)	0.0017(17)
F27	0.0405(17)	0.066(2)	0.0336(15)	0.0003(16)	-0.0033(13)	-0.0012(16)
F28	0.047(2)	0.099(3)	0.0359(17)	0.006(2)	0.0109(15)	-0.016(2)
F29	0.070(2)	0.076(3)	0.0250(15)	-0.0012(17)	0.0081(16)	0.001(2)
F30	0.085(3)	0.050(2)	0.0391(18)	0.0093(16)	0.0130(19)	-0.001(2)
O1	0.0250(15)	0.0309(16)	0.0239(14)	0.0031(14)	0.0045(12)	0.0029(14)
O2	0.0320(17)	0.0343(18)	0.0269(16)	0.0040(15)	0.0030(14)	0.0071(15)
O3	0.0369(18)	0.0268(16)	0.0252(16)	-0.0025(14)	0.0066(13)	-0.0071(14)
O4	0.0408(19)	0.0298(18)	0.0329(17)	-0.0044(15)	0.0108(15)	-0.0063(15)
C1	0.025(2)	0.024(2)	0.023(2)	0.0001(17)	0.0009(17)	-0.0052(18)
C2	0.027(2)	0.023(2)	0.022(2)	-0.0025(17)	0.0020(17)	-0.0043(17)
C3	0.024(2)	0.020(2)	0.028(2)	-0.0041(17)	0.0005(17)	0.0002(17)
C4	0.027(2)	0.026(2)	0.029(2)	-0.0039(19)	0.0023(18)	-0.0021(19)
C5	0.030(2)	0.027(2)	0.034(2)	-0.006(2)	0.002(2)	0.0038(19)
C6	0.034(2)	0.032(2)	0.029(2)	0.003(2)	-0.002(2)	0.002(2)
C7	0.035(2)	0.026(2)	0.025(2)	0.0033(19)	-0.0002(19)	-0.002(2)
C8	0.026(2)	0.023(2)	0.028(2)	0.0006(18)	0.0022(18)	-0.0004(18)
C9	0.026(2)	0.027(2)	0.0219(19)	0.0009(18)	0.0029(17)	-0.0034(19)
C10	0.026(2)	0.026(2)	0.025(2)	0.0011(18)	0.0021(18)	-0.0021(18)

	U_{11}	U_{22}	U_{33}	U_{23}	U_{13}	U_{12}
C11	0.025(2)	0.031(2)	0.023(2)	-0.0027(19)	0.0040(17)	-0.0020(19)
C12	0.025(2)	0.026(2)	0.028(2)	-0.0015(19)	0.0038(18)	-0.0011(18)
C13	0.029(2)	0.029(2)	0.029(2)	0.0025(19)	0.0067(19)	-0.0005(19)
C14	0.028(2)	0.027(2)	0.031(2)	0.000(2)	0.0044(19)	0.000(2)
C15	0.034(2)	0.032(2)	0.028(2)	0.002(2)	0.008(2)	-0.001(2)
C16	0.043(3)	0.027(2)	0.034(2)	-0.002(2)	0.009(2)	0.002(2)
C17	0.046(3)	0.036(3)	0.031(2)	-0.004(2)	0.011(2)	-0.005(2)
C18	0.065(4)	0.042(3)	0.042(3)	-0.013(3)	0.017(3)	-0.009(3)
C19	0.026(2)	0.025(2)	0.025(2)	-0.0019(18)	0.0022(17)	-0.0005(17)
C20	0.022(2)	0.027(2)	0.024(2)	0.0005(19)	0.0013(17)	-0.0006(18)
C21	0.021(2)	0.027(2)	0.024(2)	0.0025(18)	0.0006(17)	0.0035(17)
C22	0.022(2)	0.029(2)	0.028(2)	0.0000(19)	0.0062(17)	0.0028(18)
C23	0.029(2)	0.028(2)	0.033(2)	0.000(2)	0.0052(19)	-0.002(2)
C24	0.033(2)	0.032(2)	0.031(2)	-0.007(2)	0.0032(19)	-0.001(2)
C25	0.032(2)	0.032(2)	0.026(2)	-0.0027(19)	0.0058(19)	0.001(2)
C26	0.027(2)	0.026(2)	0.024(2)	-0.0007(18)	0.0018(17)	0.0011(18)
C27	0.025(2)	0.031(2)	0.022(2)	0.0034(18)	0.0069(17)	0.0025(18)
C28	0.029(2)	0.027(2)	0.026(2)	0.0024(18)	0.0041(17)	-0.0020(19)
C29	0.031(2)	0.027(2)	0.028(2)	0.0013(19)	0.0066(19)	0.0013(19)
C30	0.032(2)	0.026(2)	0.027(2)	0.0000(19)	0.0055(19)	0.000(2)
C31	0.030(2)	0.025(2)	0.028(2)	0.0007(18)	0.0043(19)	0.0007(19)
C32	0.028(2)	0.029(2)	0.029(2)	0.000(2)	0.0068(19)	-0.0026(19)
C33	0.025(2)	0.032(2)	0.030(2)	0.0000(19)	0.0036(19)	-0.0020(19)

	U_{11}	U_{22}	U_{33}	U_{23}	U_{13}	U_{12}
C34	0.034(2)	0.030(2)	0.030(2)	0.003(2)	0.007(2)	-0.004(2)
C35	0.038(3)	0.042(3)	0.030(2)	0.001(2)	0.008(2)	0.003(2)
C36	0.049(3)	0.056(4)	0.029(2)	0.004(3)	0.006(2)	-0.004(3)

Table S3-8. Hydrogen atomic coordinates and isotropic atomic displacement parameters (Å²) for Pu_XW4_1.

	x/a	y/b	z/c	U(eq)
H1	0.112(5)	0.509(13)	0.428(4)	0.06(2)
H3	0.397(5)	0.640(14)	0.414(4)	0.06(2)
H4	0.4162	-0.0263	0.4530	0.033
H5	0.4830	-0.2452	0.5350	0.036
H6	0.4189	-0.3005	0.6347	0.038
H7	0.2880	-0.1232	0.6525	0.035
H9	0.1717	0.1373	0.6156	0.03
H22	0.2094	-0.1464	0.3830	0.032
H23	0.1747	-0.3761	0.2953	0.036
H24	0.2250	-0.3088	0.1905	0.039
H25	0.3113	-0.0140	0.1757	0.036
H27	0.3947	0.2997	0.2228	0.031

Table S3-9. Hydrogen bond distances (Å) and angles (°) for Pu_XW4_1.

	Donor-H	Acceptor-H	Donor-Acceptor	Angle
O1-H1···O2	0.82(8)	1.88(8)	2.587(5)	144.(8)
O3-H3···O4	0.88(9)	1.84(8)	2.624(5)	147.(8)

Table S3-10. Sample and crystal data for Pu_XW4_2 [(*R*)-1].

Identification code	Pu_XW4_2	
Chemical formula	$C_{36}H_{12}F_{30}O_4$	
Formula weight	1078.46 g/mol	
Temperature	100(2) K	
Wavelength	1.54178 Å	
Crystal size	0.060 x 0.148 x 0.560 mm	
Crystal habit	orange plate	
Crystal system	monoclinic	
Space group	P 2_1	
Unit cell dimensions	a = 15.0326(7) Å	α = 90°
	b = 6.3026(3) Å	β = 96.218(3)°
	c = 20.2772(10) Å	γ = 90°
Volume	1909.85(16) $Å^3$	
Z	2	
Density (calculated)	1.875 g/cm^3	
Absorption coefficient	2.032 mm^{-1}	
F(000)	1060	

Table S3-11. Data collection and structure refinement for Pu_XW4_2.

Diffractometer	Bruker Kappa APEXII Duo
Radiation source	Incoatec Microfocus IμS (Cu K_α, λ = 1.54178 Å)
Theta range for data collection	2.19 to 68.47°
Index ranges	-18<=h<=17, -7<=k<=7, -24<=l<=24

Reflections collected	58594	
Independent reflections	7020 [R(int) = 0.1044]	
Coverage of independent reflections	99.6%	
Absorption correction	Multi-Scan	
Max. and min. transmission	0.8880 and 0.3960	
Structure solution technique	direct methods	
Structure solution program	SHELXT 2014/5 (Sheldrick, 2014)	
Refinement method	Full-matrix least-squares on F^2	
Refinement program	SHELXL-2017/1 (Sheldrick, 2017)	
Function minimized	$\Sigma\ w(F_o^2 - F_c^2)^2$	
Data / restraints / parameters	7020 / 1 / 640	
Goodness-of-fit on F^2	1.003	
Final R indices	6198 data; $I>2\sigma(I)$	R1 = 0.0567, wR2 = 0.1439
	all data	R1 = 0.0633, wR2 = 0.1510
Weighting scheme	$w=1/[\sigma^2(F_o^2)+(0.1170P)^2]$ where $P=(F_o^2+2F_c^2)/3$	
Absolute structure parameter	-0.05(17)	
Extinction coefficient	0.0034(6)	
Largest diff. peak and hole	0.336 and -0.379 $eÅ^{-3}$	
R.M.S. deviation from mean	0.089 $eÅ^{-3}$	

Table S3-12. Atomic coordinates and equivalent isotropic atomic displacement parameters ($Å^2$) for Pu_XW4_2.

U(eq) is defined as one third of the trace of the orthogonalized U_{ij} tensor.

	x/a	y/b	z/c	U(eq)
F1	0.55332(19)	0.5593(5)	0.24225(15)	0.0289(7)
F2	0.44871(19)	0.3579(5)	0.19144(15)	0.0302(7)
F3	0.62450(19)	0.1988(5)	0.30931(15)	0.0310(7)
F4	0.5228(2)	0.0086(5)	0.25005(17)	0.0297(7)
F5	0.6962(2)	0.3290(6)	0.20630(17)	0.0341(7)
F6	0.6789(2)	0.9847(5)	0.20941(16)	0.0327(7)
F7	0.5757(2)	0.3712(5)	0.10490(17)	0.0355(7)
F8	0.52147(19)	0.0520(6)	0.11580(16)	0.0337(7)
F9	0.74519(19)	0.1453(6)	0.09629(16)	0.0360(8)
F10	0.6593(2)	0.8662(6)	0.07880(18)	0.0378(8)
F11	0.5514(2)	0.1322(7)	0.98473(19)	0.0454(9)
F12	0.6649(3)	0.3510(6)	0.99617(18)	0.0449(9)
F13	0.6797(3)	0.1096(8)	0.89440(19)	0.0550(11)
F14	0.6515(3)	0.8226(7)	0.9450(2)	0.0546(10)
F15	0.7735(3)	0.9943(9)	0.9735(2)	0.0608(13)
F16	0.03179(19)	0.7852(5)	0.63216(16)	0.0285(6)
F17	0.94779(18)	0.5250(5)	0.59259(16)	0.0311(7)
F18	0.15984(19)	0.5176(6)	0.68094(17)	0.0362(8)
F19	0.0965(2)	0.2518(6)	0.62477(17)	0.0401(8)
F20	0.9916(2)	0.5551(6)	0.73802(17)	0.0352(7)
F21	0.9623(2)	0.2427(6)	0.69480(17)	0.0415(9)
F22	0.1333(2)	0.4265(6)	0.80963(17)	0.0394(8)
F23	0.1431(2)	0.1362(6)	0.75247(19)	0.0442(9)
F24	0.9586(2)	0.2700(7)	0.83444(19)	0.0439(9)

F25	0.0043(3)	0.9684(6)	0.7974(2)	0.0511(10)
F26	0.0879(3)	0.2900(7)	0.92900(18)	0.0478(9)
F27	0.1678(2)	0.0515(7)	0.8853(2)	0.0515(10)
F28	0.0858(4)	0.9381(9)	0.9960(2)	0.0700(14)
F29	0.0536(3)	0.7474(7)	0.9094(3)	0.0637(12)
F30	0.9576(3)	0.9760(8)	0.9386(2)	0.0626(12)
O1	0.3689(2)	0.4731(6)	0.42779(18)	0.0281(8)
O2	0.4610(3)	0.2497(6)	0.3497(2)	0.0330(9)
O3	0.1526(2)	0.5622(6)	0.41554(18)	0.0271(8)
O4	0.0384(2)	0.4630(7)	0.49713(19)	0.0298(8)
C1	0.3529(3)	0.6084(8)	0.3763(3)	0.0229(10)
C2	0.3008(3)	0.7825(8)	0.3861(3)	0.0235(10)
C3	0.2807(3)	0.9313(8)	0.3335(3)	0.0231(10)
C4	0.2301(3)	0.1177(8)	0.3412(3)	0.0245(10)
C5	0.2100(3)	0.2547(9)	0.2897(3)	0.0283(11)
C6	0.2401(3)	0.2145(9)	0.2265(3)	0.0309(11)
C7	0.2909(3)	0.0400(9)	0.2179(3)	0.0289(11)
C8	0.3140(3)	0.8937(8)	0.2711(2)	0.0229(10)
C9	0.3699(3)	0.7212(8)	0.2637(3)	0.0243(10)
C10	0.3912(3)	0.5771(8)	0.3151(3)	0.0258(10)
C11	0.4503(3)	0.3955(8)	0.3091(3)	0.0265(11)
C12	0.5055(3)	0.3799(8)	0.2481(3)	0.0247(10)
C13	0.5701(3)	0.1899(9)	0.2514(3)	0.0261(10)
C14	0.6363(3)	0.1704(9)	0.1968(3)	0.0267(11)
C15	0.5966(3)	0.1711(9)	0.1232(3)	0.0273(11)

C16	0.6616(3)	0.0776(9)	0.0758(3)	0.0293(11)
C17	0.6403(4)	0.1486(10)	0.0023(3)	0.0333(12)
C18	0.6875(4)	0.0128(12)	0.9531(3)	0.0417(14)
C19	0.1905(3)	0.6914(8)	0.4642(3)	0.0236(10)
C20	0.2648(3)	0.8058(8)	0.4514(2)	0.0210(9)
C21	0.3085(3)	0.9381(8)	0.5018(3)	0.0229(10)
C22	0.3891(3)	0.0452(8)	0.4931(3)	0.0254(10)
C23	0.4292(3)	0.1752(9)	0.5416(3)	0.0289(11)
C24	0.3913(4)	0.2086(9)	0.6019(3)	0.0310(11)
C25	0.3145(3)	0.1037(9)	0.6124(3)	0.0285(11)
C26	0.2723(3)	0.9620(8)	0.5635(3)	0.0243(10)
C27	0.1961(3)	0.8472(8)	0.5745(3)	0.0238(10)
C28	0.1546(3)	0.7098(8)	0.5271(3)	0.0231(10)
C29	0.0761(3)	0.5858(8)	0.5381(3)	0.0250(10)
C30	0.0336(3)	0.5897(8)	0.6055(3)	0.0259(10)
C31	0.0809(3)	0.4330(9)	0.6563(3)	0.0266(11)
C32	0.0281(3)	0.3776(8)	0.7164(3)	0.0257(10)
C33	0.0861(3)	0.2754(9)	0.7759(3)	0.0282(11)
C34	0.0307(4)	0.1536(9)	0.8247(3)	0.0314(12)
C35	0.0843(4)	0.1112(10)	0.8935(3)	0.0354(13)
C36	0.0430(5)	0.9385(12)	0.9345(4)	0.0462(16)

Table S3-13. Bond lengths (Å) for Pu_XW4_2.

F1-C12	1.352(6)	F2-C12	1.362(6)

F3-C13	1.357(6)	F4-C13	1.344(6)
F5-C14	1.345(6)	F6-C14	1.345(6)
F7-C15	1.342(6)	F8-C15	1.351(6)
F9-C16	1.349(6)	F10-C16	1.334(7)
F11-C17	1.349(6)	F12-C17	1.338(7)
F13-C18	1.331(8)	F14-C18	1.319(9)
F15-C18	1.318(7)	F16-C30	1.347(6)
F17-C30	1.351(6)	F18-C31	1.347(6)
F19-C31	1.342(6)	F20-C32	1.340(6)
F21-C32	1.342(6)	F22-C33	1.332(7)
F23-C33	1.349(6)	F24-C34	1.342(7)
F25-C34	1.334(7)	F26-C35	1.335(7)
F27-C35	1.337(7)	F28-C36	1.339(9)
F29-C36	1.324(9)	F30-C36	1.317(8)
O1-C1	1.350(6)	O1-H1	0.92(8)
O2-C11	1.233(7)	O3-C19	1.356(6)
O3-H3	0.87(11)	O4-C29	1.227(7)
C1-C2	1.375(7)	C1-C10	1.437(7)
C2-C3	1.427(7)	C2-C20	1.491(7)
C3-C4	1.418(7)	C3-C8	1.432(7)
C4-C5	1.364(8)	C4-H4	0.95
C5-C6	1.426(8)	C5-H5	0.95
C6-C7	1.361(8)	C6-H6	0.95
C7-C8	1.432(7)	C7-H7	0.95
C8-C9	1.392(7)	C9-C10	1.392(7)

C9-H9	0.95	C10-C11	1.462(7)
C11-C12	1.565(7)	C12-C13	1.539(7)
C13-C14	1.572(7)	C14-C15	1.547(7)
C15-C16	1.559(7)	C16-C17	1.556(8)
C17-C18	1.544(9)	C19-C20	1.378(7)
C19-C28	1.442(7)	C20-C21	1.423(7)
C21-C22	1.414(7)	C21-C26	1.425(7)
C22-C23	1.368(8)	C22-H22	0.95
C23-C24	1.419(8)	C23-H23	0.95
C24-C25	1.367(8)	C24-H24	0.95
C25-C26	1.431(7)	C25-H25	0.95
C26-C27	1.393(7)	C27-C28	1.391(7)
C27-H27	0.95	C28-C29	1.453(7)
C29-C30	1.570(7)	C30-C31	1.545(7)
C31-C32	1.564(7)	C32-C33	1.550(7)
C33-C34	1.562(7)	C34-C35	1.556(8)
C35-C36	1.540(9)		

Table S3-14. Bond angles (°) for Pu_XW4_2.

C1-O1-H1	114.(4)	C19-O3-H3	106.(7)
O1-C1-C2	116.7(4)	O1-C1-C10	121.8(4)
C2-C1-C10	121.5(5)	C1-C2-C3	119.6(5)
C1-C2-C20	118.3(4)	C3-C2-C20	122.0(4)
C4-C3-C2	122.4(5)	C4-C3-C8	118.6(5)

C2-C3-C8	119.0(4)	C5-C4-C3	121.1(5)
C5-C4-H4	119.4	C3-C4-H4	119.4
C4-C5-C6	120.7(5)	C4-C5-H5	119.7
C6-C5-H5	119.7	C7-C6-C5	119.7(5)
C7-C6-H6	120.1	C5-C6-H6	120.1
C6-C7-C8	121.2(5)	C6-C7-H7	119.4
C8-C7-H7	119.4	C9-C8-C3	119.8(5)
C9-C8-C7	121.5(5)	C3-C8-C7	118.7(5)
C8-C9-C10	121.5(5)	C8-C9-H9	119.2
C10-C9-H9	119.2	C9-C10-C1	118.4(5)
C9-C10-C11	122.8(5)	C1-C10-C11	118.9(5)
O2-C11-C10	124.4(5)	O2-C11-C12	116.0(5)
C10-C11-C12	119.6(5)	F1-C12-F2	107.6(4)
F1-C12-C13	108.4(4)	F2-C12-C13	107.0(4)
F1-C12-C11	110.4(4)	F2-C12-C11	109.7(4)
C13-C12-C11	113.6(4)	F4-C13-F3	108.7(4)
F4-C13-C12	109.3(4)	F3-C13-C12	108.9(4)
F4-C13-C14	107.0(4)	F3-C13-C14	104.1(4)
C12-C13-C14	118.4(4)	F5-C14-F6	108.8(4)
F5-C14-C15	108.5(4)	F6-C14-C15	108.1(4)
F5-C14-C13	107.9(4)	F6-C14-C13	105.0(4)
C15-C14-C13	118.2(4)	F7-C15-F8	108.9(4)
F7-C15-C14	108.9(4)	F8-C15-C14	109.6(4)
F7-C15-C16	109.2(5)	F8-C15-C16	107.1(4)
C14-C15-C16	113.1(4)	F10-C16-F9	109.3(5)

F10-C16-C17	109.1(5)	F9-C16-C17	107.1(4)
F10-C16-C15	109.1(4)	F9-C16-C15	108.4(4)
C17-C16-C15	113.8(4)	F12-C17-F11	108.9(5)
F12-C17-C18	108.5(5)	F11-C17-C18	107.4(5)
F12-C17-C16	109.4(5)	F11-C17-C16	109.0(5)
C18-C17-C16	113.4(5)	F15-C18-F14	109.5(6)
F15-C18-F13	108.0(5)	F14-C18-F13	108.1(5)
F15-C18-C17	110.5(5)	F14-C18-C17	111.9(5)
F13-C18-C17	108.7(6)	O3-C19-C20	117.6(4)
O3-C19-C28	121.5(4)	C20-C19-C28	120.8(5)
C19-C20-C21	119.5(5)	C19-C20-C2	119.7(4)
C21-C20-C2	120.8(4)	C22-C21-C20	121.7(5)
C22-C21-C26	118.2(5)	C20-C21-C26	120.1(4)
C23-C22-C21	120.8(5)	C23-C22-H22	119.6
C21-C22-H22	119.6	C22-C23-C24	121.4(5)
C22-C23-H23	119.3	C24-C23-H23	119.3
C25-C24-C23	119.2(5)	C25-C24-H24	120.4
C23-C24-H24	120.4	C24-C25-C26	120.8(5)
C24-C25-H25	119.6	C26-C25-H25	119.6
C27-C26-C21	119.0(5)	C27-C26-C25	121.5(5)
C21-C26-C25	119.4(5)	C28-C27-C26	121.8(5)
C28-C27-H27	119.1	C26-C27-H27	119.1
C27-C28-C19	118.6(4)	C27-C28-C29	122.6(5)
C19-C28-C29	118.7(4)	O4-C29-C28	124.0(5)
O4-C29-C30	113.4(4)	C28-C29-C30	122.6(4)

F16-C30-F17	107.1(4)	F16-C30-C31	110.2(4)
F17-C30-C31	107.2(4)	F16-C30-C29	113.1(4)
F17-C30-C29	107.3(4)	C31-C30-C29	111.7(4)
F19-C31-F18	108.7(4)	F19-C31-C30	108.5(4)
F18-C31-C30	108.5(4)	F19-C31-C32	108.2(4)
F18-C31-C32	107.5(4)	C30-C31-C32	115.3(4)
F20-C32-F21	108.8(4)	F20-C32-C33	107.9(4)
F21-C32-C33	108.9(5)	F20-C32-C31	109.1(4)
F21-C32-C31	107.8(4)	C33-C32-C31	114.2(4)
F22-C33-F23	108.8(4)	F22-C33-C32	109.0(5)
F23-C33-C32	108.7(4)	F22-C33-C34	108.5(4)
F23-C33-C34	107.8(5)	C32-C33-C34	113.8(4)
F25-C34-F24	109.3(5)	F25-C34-C35	108.9(5)
F24-C34-C35	108.1(5)	F25-C34-C33	108.8(5)
F24-C34-C33	108.6(4)	C35-C34-C33	113.1(5)
F26-C35-F27	108.7(5)	F26-C35-C36	107.5(5)
F27-C35-C36	107.9(5)	F26-C35-C34	109.0(5)
F27-C35-C34	109.8(5)	C36-C35-C34	113.9(5)
F30-C36-F29	110.3(7)	F30-C36-F28	108.3(6)
F29-C36-F28	106.9(6)	F30-C36-C35	111.1(5)
F29-C36-C35	111.3(6)	F28-C36-C35	108.8(6)

Table 3-15. Torsion angles (°) for Pu_XW4_2.

O1-C1-C2-C3	-179.6(4)	C10-C1-C2-C3	2.9(7)

O1-C1-C2-C20	-1.3(7)	C10-C1-C2-C20	-178.9(4)
C1-C2-C3-C4	-177.7(5)	C20-C2-C3-C4	4.1(7)
C1-C2-C3-C8	1.1(7)	C20-C2-C3-C8	-177.1(4)
C2-C3-C4-C5	-178.4(5)	C8-C3-C4-C5	2.8(7)
C3-C4-C5-C6	-0.5(8)	C4-C5-C6-C7	-1.3(8)
C5-C6-C7-C8	0.7(8)	C4-C3-C8-C9	174.8(4)
C2-C3-C8-C9	-4.1(7)	C4-C3-C8-C7	-3.3(7)
C2-C3-C8-C7	177.9(4)	C6-C7-C8-C9	-176.5(5)
C6-C7-C8-C3	1.6(8)	C3-C8-C9-C10	3.0(7)
C7-C8-C9-C10	-179.0(5)	C8-C9-C10-C1	0.9(7)
C8-C9-C10-C11	-179.4(5)	O1-C1-C10-C9	178.6(5)
C2-C1-C10-C9	-4.0(7)	O1-C1-C10-C11	-1.0(7)
C2-C1-C10-C11	176.4(5)	C9-C10-C11-O2	-169.7(5)
C1-C10-C11-O2	10.0(8)	C9-C10-C11-C12	10.8(8)
C1-C10-C11-C12	-169.6(4)	O2-C11-C12-F1	-126.1(5)
C10-C11-C12-F1	53.4(6)	O2-C11-C12-F2	115.5(5)
C10-C11-C12-F2	-64.9(6)	O2-C11-C12-C13	-4.2(7)
C10-C11-C12-C13	175.4(5)	F1-C12-C13-F4	-173.4(4)
F2-C12-C13-F4	-57.7(5)	C11-C12-C13-F4	63.4(5)
F1-C12-C13-F3	67.9(5)	F2-C12-C13-F3	-176.4(4)
C11-C12-C13-F3	-55.2(5)	F1-C12-C13-C14	-50.6(6)
F2-C12-C13-C14	65.1(5)	C11-C12-C13-C14	-173.7(4)
F4-C13-C14-F5	-167.7(4)	F3-C13-C14-F5	-52.7(5)
C12-C13-C14-F5	68.4(6)	F4-C13-C14-F6	-51.8(5)
F3-C13-C14-F6	63.3(5)	C12-C13-C14-F6	-175.7(4)

F4-C13-C14-C15	68.9(6)	F3-C13-C14-C15	-176.1(4)
C12-C13-C14-C15	-55.0(6)	F5-C14-C15-F7	-45.5(5)
F6-C14-C15-F7	-163.4(4)	C13-C14-C15-F7	77.6(6)
F5-C14-C15-F8	-164.5(4)	F6-C14-C15-F8	77.6(5)
C13-C14-C15-F8	-41.4(6)	F5-C14-C15-C16	76.1(5)
F6-C14-C15-C16	-41.8(6)	C13-C14-C15-C16	-160.8(4)
F7-C15-C16-F10	-159.7(4)	F8-C15-C16-F10	-41.9(6)
C14-C15-C16-F10	79.0(6)	F7-C15-C16-F9	81.5(5)
F8-C15-C16-F9	-160.8(4)	C14-C15-C16-F9	-39.9(6)
F7-C15-C16-C17	-37.5(6)	F8-C15-C16-C17	80.2(6)
C14-C15-C16-C17	-158.9(5)	F10-C16-C17-F12	-164.0(4)
F9-C16-C17-F12	-45.8(6)	C15-C16-C17-F12	73.9(6)
F10-C16-C17-F11	77.0(6)	F9-C16-C17-F11	-164.9(5)
C15-C16-C17-F11	-45.2(6)	F10-C16-C17-C18	-42.7(6)
F9-C16-C17-C18	75.5(6)	C15-C16-C17-C18	-164.8(5)
F12-C17-C18-F15	72.3(7)	F11-C17-C18-F15	-170.0(6)
C16-C17-C18-F15	-49.5(7)	F12-C17-C18-F14	-165.4(5)
F11-C17-C18-F14	-47.7(7)	C16-C17-C18-F14	72.9(7)
F12-C17-C18-F13	-46.1(7)	F11-C17-C18-F13	71.6(6)
C16-C17-C18-F13	-167.9(5)	O3-C19-C20-C21	-178.0(4)
C28-C19-C20-C21	2.2(7)	O3-C19-C20-C2	-0.5(7)
C28-C19-C20-C2	179.6(4)	C1-C2-C20-C19	-79.5(6)
C3-C2-C20-C19	98.7(6)	C1-C2-C20-C21	97.8(6)
C3-C2-C20-C21	-84.0(6)	C19-C20-C21-C22	174.8(5)
C2-C20-C21-C22	-2.6(7)	C19-C20-C21-C26	-3.9(7)

C2-C20-C21-C26	178.8(4)	C20-C21-C22-C23	178.6(5)
C26-C21-C22-C23	-2.7(7)	C21-C22-C23-C24	-0.4(8)
C22-C23-C24-C25	1.9(8)	C23-C24-C25-C26	-0.1(8)
C22-C21-C26-C27	-176.0(5)	C20-C21-C26-C27	2.7(7)
C22-C21-C26-C25	4.4(7)	C20-C21-C26-C25	-176.9(5)
C24-C25-C26-C27	177.3(5)	C24-C25-C26-C21	-3.1(8)
C21-C26-C27-C28	0.1(8)	C25-C26-C27-C28	179.7(5)
C26-C27-C28-C19	-1.8(7)	C26-C27-C28-C29	178.8(5)
O3-C19-C28-C27	-179.2(4)	C20-C19-C28-C27	0.6(7)
O3-C19-C28-C29	0.1(7)	C20-C19-C28-C29	180.0(5)
C27-C28-C29-O4	-179.7(5)	C19-C28-C29-O4	0.9(8)
C27-C28-C29-C30	-2.4(8)	C19-C28-C29-C30	178.2(4)
O4-C29-C30-F16	-141.9(5)	C28-C29-C30-F16	40.5(6)
O4-C29-C30-F17	-24.1(6)	C28-C29-C30-F17	158.3(4)
O4-C29-C30-C31	93.1(5)	C28-C29-C30-C31	-84.5(6)
F16-C30-C31-F19	-168.6(4)	F17-C30-C31-F19	75.3(5)
C29-C30-C31-F19	-42.0(5)	F16-C30-C31-F18	-50.6(5)
F17-C30-C31-F18	-166.8(4)	C29-C30-C31-F18	76.0(5)
F16-C30-C31-C32	70.0(5)	F17-C30-C31-C32	-46.2(6)
C29-C30-C31-C32	-163.4(4)	F19-C31-C32-F20	-164.0(4)
F18-C31-C32-F20	78.8(5)	C30-C31-C32-F20	-42.4(6)
F19-C31-C32-F21	-45.9(5)	F18-C31-C32-F21	-163.2(4)
C30-C31-C32-F21	75.7(6)	F19-C31-C32-C33	75.2(5)
F18-C31-C32-C33	-42.1(6)	C30-C31-C32-C33	-163.2(5)
F20-C32-C33-F22	-43.6(5)	F21-C32-C33-F22	-161.6(4)

C31-C32-C33-F22	77.9(5)	F20-C32-C33-F23	-162.1(4)
F21-C32-C33-F23	79.9(5)	C31-C32-C33-F23	-40.6(6)
F20-C32-C33-C34	77.7(5)	F21-C32-C33-C34	-40.3(6)
C31-C32-C33-C34	-160.8(4)	F22-C33-C34-F25	-162.3(5)
F23-C33-C34-F25	-44.6(6)	C32-C33-C34-F25	76.2(6)
F22-C33-C34-F24	78.9(5)	F23-C33-C34-F24	-163.4(5)
C32-C33-C34-F24	-42.7(6)	F22-C33-C34-C35	-41.1(6)
F23-C33-C34-C35	76.6(6)	C32-C33-C34-C35	-162.7(5)
F25-C34-C35-F26	-161.8(5)	F24-C34-C35-F26	-43.2(6)
C33-C34-C35-F26	77.1(6)	F25-C34-C35-F27	79.2(6)
F24-C34-C35-F27	-162.1(5)	C33-C34-C35-F27	-41.8(7)
F25-C34-C35-C36	-41.8(7)	F24-C34-C35-C36	76.9(6)
C33-C34-C35-C36	-162.9(5)	F26-C35-C36-F30	69.5(7)
F27-C35-C36-F30	-173.4(6)	C34-C35-C36-F30	-51.3(8)
F26-C35-C36-F29	-167.2(6)	F27-C35-C36-F29	-50.1(8)
C34-C35-C36-F29	72.0(7)	F26-C35-C36-F28	-49.6(7)
F27-C35-C36-F28	67.5(7)	C34-C35-C36-F28	-170.4(5)

Table S3-16. Anisotropic atomic displacement parameters (Å^2) for Pu_XW4_2.

The anisotropic atomic displacement factor exponent takes the form: $-2\pi^2[h^2 a^{*2} U_{11} + ... + 2 h k a^* b^* U_{12}]$

	U_{11}	U_{22}	U_{33}	U_{23}	U_{13}	U_{12}
F1	0.0301(15)	0.0239(15)	0.0339(17)	0.0008(13)	0.0095(12)	-0.0007(12)
F2	0.0266(14)	0.0321(16)	0.0318(17)	-0.0052(13)	0.0025(11)	0.0042(12)
F3	0.0275(15)	0.0351(17)	0.0299(17)	-0.0031(13)	0.0015(11)	0.0034(12)

	U_{11}	U_{22}	U_{33}	U_{23}	U_{13}	U_{12}
F4	0.0280(15)	0.0224(15)	0.0397(17)	0.0001(13)	0.0084(12)	-0.0019(11)
F5	0.0272(15)	0.0394(18)	0.0367(18)	-0.0063(14)	0.0088(12)	-0.0091(13)
F6	0.0264(15)	0.0371(18)	0.0353(18)	0.0000(14)	0.0067(12)	0.0090(13)
F7	0.0360(16)	0.0318(17)	0.0390(19)	0.0011(15)	0.0059(13)	0.0097(14)
F8	0.0246(14)	0.0388(18)	0.0380(18)	-0.0062(15)	0.0044(12)	-0.0056(13)
F9	0.0222(15)	0.052(2)	0.0337(17)	-0.0020(15)	0.0053(12)	0.0001(14)
F10	0.0464(19)	0.0307(17)	0.0380(19)	-0.0010(15)	0.0122(14)	0.0088(15)
F11	0.0304(17)	0.065(3)	0.039(2)	-0.0023(18)	-0.0042(13)	0.0041(16)
F12	0.056(2)	0.0389(19)	0.041(2)	0.0053(16)	0.0099(16)	-0.0019(17)
F13	0.066(3)	0.070(3)	0.0296(19)	0.0006(19)	0.0078(16)	-0.001(2)
F14	0.077(3)	0.049(2)	0.040(2)	-0.0110(18)	0.0135(18)	0.003(2)
F15	0.042(2)	0.099(4)	0.043(2)	-0.010(2)	0.0098(16)	0.018(2)
F16	0.0290(14)	0.0256(15)	0.0325(16)	0.0001(13)	0.0110(11)	0.0019(12)
F17	0.0175(13)	0.0410(19)	0.0356(17)	0.0001(14)	0.0061(11)	-0.0042(12)
F18	0.0206(14)	0.049(2)	0.0393(18)	0.0098(15)	0.0032(12)	-0.0036(13)
F19	0.057(2)	0.0278(17)	0.0375(19)	-0.0008(15)	0.0135(15)	0.0127(15)
F20	0.0362(16)	0.0358(17)	0.0357(17)	0.0025(14)	0.0130(13)	0.0123(14)
F21	0.0377(18)	0.048(2)	0.0375(19)	0.0052(16)	-0.0007(14)	-0.0233(16)
F22	0.0373(17)	0.047(2)	0.0329(18)	0.0055(15)	-0.0026(13)	-0.0108(15)
F23	0.046(2)	0.044(2)	0.045(2)	0.0116(17)	0.0192(16)	0.0220(16)
F24	0.0300(17)	0.058(2)	0.046(2)	0.0106(18)	0.0144(14)	0.0097(16)
F25	0.074(3)	0.035(2)	0.044(2)	-0.0023(17)	0.0058(18)	-0.0220(19)
F26	0.066(2)	0.044(2)	0.033(2)	0.0013(16)	0.0012(16)	-0.0013(18)

	U_{11}	U_{22}	U_{33}	U_{23}	U_{13}	U_{12}
F27	0.0410(19)	0.062(3)	0.052(2)	0.020(2)	0.0104(16)	0.0168(19)
F28	0.089(4)	0.078(4)	0.043(3)	0.028(2)	0.011(2)	0.006(3)
F29	0.090(3)	0.034(2)	0.071(3)	0.012(2)	0.026(2)	0.006(2)
F30	0.061(3)	0.067(3)	0.065(3)	0.025(2)	0.031(2)	0.008(2)
O1	0.0318(18)	0.0263(19)	0.0271(19)	0.0054(15)	0.0078(14)	0.0055(15)
O2	0.038(2)	0.026(2)	0.036(2)	0.0038(17)	0.0125(16)	0.0057(16)
O3	0.0220(16)	0.0301(19)	0.0295(19)	-0.0041(16)	0.0046(13)	-0.0042(15)
O4	0.0259(17)	0.033(2)	0.031(2)	-0.0040(16)	0.0055(14)	-0.0071(15)
C1	0.019(2)	0.020(2)	0.030(3)	0.0012(19)	0.0032(17)	-0.0028(17)
C2	0.022(2)	0.022(2)	0.027(3)	0.001(2)	0.0056(18)	-0.0007(19)
C3	0.021(2)	0.023(2)	0.026(3)	-0.0007(19)	0.0033(17)	-0.0018(18)
C4	0.019(2)	0.025(2)	0.030(3)	0.002(2)	0.0051(18)	-0.0001(18)
C5	0.022(2)	0.026(3)	0.037(3)	0.000(2)	0.0054(19)	0.003(2)
C6	0.028(3)	0.030(3)	0.034(3)	0.007(2)	0.005(2)	0.002(2)
C7	0.028(2)	0.031(3)	0.029(3)	0.005(2)	0.0071(19)	0.003(2)
C8	0.023(2)	0.021(2)	0.024(2)	0.0003(19)	0.0037(18)	-0.0002(18)
C9	0.023(2)	0.023(2)	0.028(3)	-0.002(2)	0.0079(18)	0.0006(18)
C10	0.026(2)	0.023(2)	0.030(3)	0.002(2)	0.0062(18)	0.0004(19)
C11	0.026(2)	0.022(3)	0.033(3)	0.000(2)	0.010(2)	-0.0007(19)
C12	0.026(2)	0.021(2)	0.028(3)	0.000(2)	0.0057(19)	-0.0020(19)
C13	0.022(2)	0.025(2)	0.032(3)	0.001(2)	0.0042(19)	-0.0028(19)
C14	0.021(2)	0.026(3)	0.034(3)	-0.002(2)	0.005(2)	0.0004(19)
C15	0.021(2)	0.028(3)	0.034(3)	-0.002(2)	0.0028(19)	0.0035(19)

	U_{11}	U_{22}	U_{33}	U_{23}	U_{13}	U_{12}
C16	0.024(2)	0.031(3)	0.032(3)	-0.004(2)	0.005(2)	0.000(2)
C17	0.027(3)	0.039(3)	0.035(3)	0.002(2)	0.003(2)	-0.001(2)
C18	0.040(3)	0.054(4)	0.032(3)	0.000(3)	0.005(2)	0.008(3)
C19	0.022(2)	0.019(2)	0.030(3)	0.001(2)	0.0033(18)	0.0034(18)
C20	0.024(2)	0.018(2)	0.022(2)	0.0021(18)	0.0042(17)	0.0022(17)
C21	0.022(2)	0.016(2)	0.031(3)	0.0012(19)	0.0038(18)	0.0010(18)
C22	0.021(2)	0.021(2)	0.034(3)	0.004(2)	0.0015(18)	-0.0004(19)
C23	0.023(2)	0.027(3)	0.037(3)	0.006(2)	0.002(2)	-0.0038(19)
C24	0.032(3)	0.027(3)	0.033(3)	0.000(2)	-0.001(2)	-0.003(2)
C25	0.026(2)	0.028(3)	0.031(3)	-0.001(2)	-0.0007(19)	0.000(2)
C26	0.022(2)	0.021(2)	0.029(3)	-0.001(2)	0.0016(18)	-0.0014(19)
C27	0.023(2)	0.023(2)	0.026(3)	0.001(2)	0.0032(18)	0.0029(19)
C28	0.020(2)	0.023(2)	0.026(3)	0.0012(19)	0.0023(17)	-0.0005(18)
C29	0.020(2)	0.027(3)	0.028(3)	0.000(2)	0.0032(18)	-0.0029(19)
C30	0.020(2)	0.025(3)	0.034(3)	0.002(2)	0.0054(18)	-0.0005(19)
C31	0.023(2)	0.025(2)	0.033(3)	-0.002(2)	0.007(2)	-0.0003(19)
C32	0.022(2)	0.023(3)	0.033(3)	-0.003(2)	0.0062(19)	-0.0042(19)
C33	0.028(2)	0.028(3)	0.030(3)	-0.002(2)	0.0059(19)	0.001(2)
C34	0.033(3)	0.022(3)	0.040(3)	0.000(2)	0.008(2)	-0.002(2)
C35	0.040(3)	0.033(3)	0.035(3)	0.003(2)	0.011(2)	0.009(2)
C36	0.053(4)	0.041(4)	0.046(4)	0.012(3)	0.012(3)	0.009(3)

Table S3-17. Hydrogen atomic coordinates and isotropic atomic displacement parameters (Å^2) for Pu_XW4_2.

	x/a	y/b	z/c	U(eq)
H1	0.395(4)	0.346(13)	0.417(3)	0.033(17)
H3	0.113(7)	0.488(18)	0.433(5)	0.08(3)
H4	0.2098	1.1478	0.3830	0.029
H5	0.1756	1.3782	0.2959	0.034
H6	0.2247	1.3092	0.1906	0.037
H7	0.3113	1.0148	0.1759	0.035
H9	0.3940	0.7013	0.2228	0.029
H22	0.4158	1.0265	0.4531	0.03
H23	0.4835	1.2447	0.5347	0.035
H24	0.4190	1.3026	0.6345	0.037
H25	0.2888	1.1252	0.6527	0.034
H27	0.1718	0.8632	0.6156	0.029

Table S3-18. Hydrogen bond distances (Å) and angles (°) for Pu_XW4_2.

	Donor-H	Acceptor-H	Donor-Acceptor	Angle
O1-H1···O2	0.92(8)	1.88(7)	2.623(5)	136.(6)
O3-H3···O4	0.87(11)	1.80(10)	2.586(5)	149.(10)

Table S3-19. Sample and crystal data for Pu_XW_4rac2. [(*Rac*)-1]

Identification code	Pu_XW_4rac2	
Chemical formula	$C_{36}H_{12}F_{30}O_4$	
Formula weight	1078.46 g/mol	
Temperature	100(2) K	
Wavelength	0.71073 Å	
Crystal size	0.086 x 0.171 x 0.465 mm	
Crystal habit	orange plate	
Crystal system	triclinic	
Space group	P -1	
Unit cell dimensions	a = 11.0172(11) Å	α = 80.852(3)°
	b = 11.6711(11) Å	β = 82.349(3)°
	c = 16.1008(15) Å	γ = 69.610(3)°
Volume	1909.1(3) $Å^3$	
Z	2	
Density (calculated)	1.876 g/cm^3	
Absorption coefficient	0.220 mm^{-1}	
F(000)	1060	

Table S3-20. Data collection and structure refinement for Pu_XW_4rac2.

Diffractometer	Bruker Kappa APEXII Duo
Radiation source	fine-focus sealed tube (Mo K_α, λ = 0.71073 Å)
Theta range for data collection	1.88 to 25.77°
Index ranges	-13<=h<=8, -14<=k<=13, -19<=l<=19

Reflections collected	29117	
Independent reflections	7288 [R(int) = 0.0768]	
Coverage of independent reflections	99.5%	
Absorption correction	Multi-Scan	
Max. and min. transmission	0.9810 and 0.9050	
Structure solution technique	direct methods	
Structure solution program	SHELXT 2014/5 (Sheldrick, 2014)	
Refinement method	Full-matrix least-squares on F^2	
Refinement program	SHELXL-2018/3 (Sheldrick, 2018)	
Function minimized	$\Sigma\, w(F_o^2 - F_c^2)^2$	
Data / restraints / parameters	7288 / 0 / 639	
Goodness-of-fit on F^2	1.017	
Final R indices	3930 data; $I>2\sigma(I)$	R1 = 0.0603, wR2 = 0.1490
	all data	R1 = 0.1341, wR2 = 0.1901
Weighting scheme	$w=1/[\sigma^2(F_o^2)+(0.0990P)^2+0.2561P]$ where $P=(F_o^2+2F_c^2)/3$	
Largest diff. peak and hole	0.387 and -0.429 eÅ^{-3}	
R.M.S. deviation from mean	0.089 eÅ^{-3}	

Table S3-21. Atomic coordinates and equivalent isotropic atomic displacement parameters (Å^2) for Pu_XW_4rac2.

U(eq) is defined as one third of the trace of the orthogonalized U_{ij} tensor.

	x/a	**y/b**	**z/c**	**U(eq)**

O1	0.0739(3)	0.3027(3)	0.33030(18)	0.0292(7)
O2	0.8565(3)	0.3443(3)	0.42307(19)	0.0269(7)
O3	0.7565(3)	0.2455(3)	0.6258(2)	0.0266(7)
O4	0.6147(3)	0.3395(3)	0.75604(19)	0.0335(7)
F1	0.2792(3)	0.0962(3)	0.76644(18)	0.0620(9)
F2	0.4476(3)	0.9421(3)	0.80073(19)	0.0651(10)
F3	0.2904(3)	0.9151(3)	0.75013(19)	0.0676(10)
F4	0.2891(4)	0.8389(3)	0.9109(2)	0.0661(10)
F5	0.1263(3)	0.0080(3)	0.8835(2)	0.0636(10)
F6	0.2981(3)	0.1292(3)	0.92398(16)	0.0422(7)
F7	0.4123(3)	0.9471(3)	0.97879(16)	0.0448(7)
F8	0.1734(3)	0.9267(2)	0.06053(17)	0.0459(7)
F9	0.0875(2)	0.1225(3)	0.02001(16)	0.0423(7)
F10	0.3087(2)	0.1454(2)	0.08628(15)	0.0357(6)
F11	0.3389(3)	0.9585(2)	0.14781(16)	0.0413(7)
F12	0.0680(2)	0.2273(2)	0.15697(15)	0.0355(6)
F13	0.0687(2)	0.0399(2)	0.20052(15)	0.0350(6)
F14	0.2788(2)	0.1803(2)	0.25066(15)	0.0309(6)
F15	0.2541(2)	0.0068(2)	0.30615(14)	0.0297(6)
F16	0.3229(2)	0.3445(2)	0.76847(15)	0.0355(6)
F17	0.3108(2)	0.5356(2)	0.72808(15)	0.0329(6)
F18	0.4681(2)	0.5187(2)	0.85302(15)	0.0352(6)
F19	0.4513(2)	0.3375(2)	0.90181(15)	0.0375(6)
F20	0.2217(3)	0.6324(2)	0.87555(15)	0.0384(7)
F21	0.1741(2)	0.4645(3)	0.88907(17)	0.0446(8)

F22	0.3742(2)	0.5161(3)	0.01693(16)	0.0503(8)
F23	0.2700(3)	0.3854(2)	0.03367(17)	0.0521(8)
F24	0.1649(3)	0.7019(2)	0.03530(16)	0.0398(7)
F25	0.0398(2)	0.6026(2)	0.01380(15)	0.0328(6)
F26	0.2495(2)	0.5132(2)	0.17477(15)	0.0405(7)
F27	0.0825(3)	0.4621(2)	0.15748(16)	0.0395(7)
F28	0.0972(3)	0.7401(3)	0.19874(18)	0.0476(8)
F29	0.0188(3)	0.6098(3)	0.27311(17)	0.0484(8)
F30	0.9309(2)	0.7113(2)	0.16025(16)	0.0405(7)
C1	0.3197(5)	0.9794(5)	0.7998(3)	0.0445(13)
C2	0.2564(5)	0.9609(5)	0.8887(3)	0.0395(12)
C3	0.2925(4)	0.0179(4)	0.9573(3)	0.0325(11)
C4	0.1994(4)	0.0317(4)	0.0383(3)	0.0305(11)
C5	0.2504(4)	0.0627(4)	0.1147(3)	0.0269(10)
C6	0.1430(4)	0.1122(4)	0.1855(3)	0.0262(10)
C7	0.1907(4)	0.1217(4)	0.2698(3)	0.0266(10)
C8	0.0782(4)	0.1966(4)	0.3302(3)	0.0252(10)
C9	0.9836(4)	0.1443(4)	0.3781(3)	0.0214(9)
C10	0.8719(4)	0.2236(4)	0.4223(3)	0.0227(9)
C11	0.7756(4)	0.1803(4)	0.4637(2)	0.0220(9)
C12	0.7881(4)	0.0550(4)	0.4650(3)	0.0233(9)
C13	0.6913(4)	0.0051(4)	0.5049(3)	0.0249(10)
C14	0.7080(4)	0.8837(4)	0.5049(3)	0.0306(10)
C15	0.8203(4)	0.8037(4)	0.4648(3)	0.0303(10)
C16	0.9152(4)	0.8483(4)	0.4260(3)	0.0277(10)

C17	0.9013(4)	0.9743(4)	0.4241(3)	0.0246(10)
C18	0.9968(4)	0.0212(4)	0.3814(3)	0.0242(9)
C19	0.6528(4)	0.2658(4)	0.5032(3)	0.0227(9)
C20	0.6458(4)	0.2908(4)	0.5851(3)	0.0239(9)
C21	0.5245(4)	0.3597(4)	0.6267(3)	0.0218(9)
C22	0.4156(4)	0.4060(4)	0.5819(3)	0.0225(9)
C23	0.4202(4)	0.3868(4)	0.4975(3)	0.0230(9)
C24	0.3090(4)	0.4356(4)	0.4514(3)	0.0222(9)
C25	0.3131(4)	0.4118(4)	0.3710(3)	0.0260(10)
C26	0.4303(4)	0.3384(4)	0.3318(3)	0.0259(10)
C27	0.5411(4)	0.2917(4)	0.3742(3)	0.0249(10)
C28	0.5400(4)	0.3139(4)	0.4577(3)	0.0206(9)
C29	0.5194(4)	0.3736(4)	0.7156(3)	0.0272(10)
C30	0.3856(4)	0.4267(4)	0.7661(3)	0.0256(10)
C31	0.3948(4)	0.4469(4)	0.8570(3)	0.0267(10)
C32	0.2618(4)	0.5116(4)	0.9046(3)	0.0260(10)
C33	0.2665(4)	0.4999(4)	0.0014(3)	0.0285(10)
C34	0.1487(4)	0.5915(4)	0.0479(3)	0.0255(10)
C35	0.1325(4)	0.5542(4)	0.1433(3)	0.0298(10)
C36	0.0439(4)	0.6562(5)	0.1946(3)	0.0351(11)

Table S3-22. Bond lengths (Å) for Pu_XW_4rac2.

O1-C8	1.223(5)	O2-C10	1.361(5)
O2-H2	0.90(5)	O3-C20	1.360(5)

O3-H3	0.85(5)	O4-C29	1.222(5)
F1-C1	1.324(6)	F2-C1	1.324(6)
F3-C1	1.316(5)	F4-C2	1.341(6)
F5-C2	1.354(5)	F6-C3	1.343(5)
F7-C3	1.347(5)	F8-C4	1.338(5)
F9-C4	1.348(5)	F10-C5	1.330(5)
F11-C5	1.349(5)	F12-C6	1.352(5)
F13-C6	1.343(4)	F14-C7	1.350(5)
F15-C7	1.355(5)	F16-C30	1.357(4)
F17-C30	1.352(5)	F18-C31	1.342(5)
F19-C31	1.346(5)	F20-C32	1.346(5)
F21-C32	1.332(4)	F22-C33	1.326(5)
F23-C33	1.344(5)	F24-C34	1.342(5)
F25-C34	1.342(4)	F26-C35	1.347(5)
F27-C35	1.346(5)	F28-C36	1.319(5)
F29-C36	1.327(5)	F30-C36	1.335(5)
C1-C2	1.525(7)	C2-C3	1.535(6)
C3-C4	1.541(6)	C4-C5	1.558(6)
C5-C6	1.551(6)	C6-C7	1.552(6)
C7-C8	1.562(6)	C8-C9	1.460(6)
C9-C18	1.386(6)	C9-C10	1.435(6)
C10-C11	1.380(6)	C11-C12	1.418(6)
C11-C19	1.504(5)	C12-C13	1.421(6)
C12-C17	1.427(6)	C13-C14	1.364(6)
C13-H13	0.95	C14-C15	1.413(6)

C14-H14	0.95	C15-C16	1.362(6)
C15-H15	0.95	C16-C17	1.421(6)
C16-H16	0.95	C17-C18	1.402(6)
C18-H18	0.95	C19-C20	1.383(6)
C19-C28	1.421(6)	C20-C21	1.437(6)
C21-C22	1.381(6)	C21-C29	1.458(6)
C22-C23	1.403(6)	C22-H22	0.95
C23-C24	1.414(5)	C23-C28	1.429(5)
C24-C25	1.358(6)	C24-H24	0.95
C25-C26	1.408(6)	C25-H25	0.95
C26-C27	1.377(6)	C26-H26	0.95
C27-C28	1.407(6)	C27-H27	0.95
C29-C30	1.557(6)	C30-C31	1.540(6)
C31-C32	1.555(6)	C32-C33	1.548(6)
C33-C34	1.555(6)	C34-C35	1.534(6)
C35-C36	1.529(6)		

Table S3-23. Bond angles (°) for Pu_XW_4rac2.

C10-O2-H2	108.(3)	C20-O3-H3	107.(4)
F3-C1-F2	108.6(4)	F3-C1-F1	107.5(4)
F2-C1-F1	108.5(4)	F3-C1-C2	109.9(4)
F2-C1-C2	110.3(4)	F1-C1-C2	112.0(4)
F4-C2-F5	108.3(4)	F4-C2-C1	106.6(4)
F5-C2-C1	106.8(4)	F4-C2-C3	108.8(4)

F5-C2-C3	109.2(4)	C1-C2-C3	116.8(4)
F6-C3-F7	107.7(3)	F6-C3-C2	108.2(4)
F7-C3-C2	108.4(4)	F6-C3-C4	109.0(4)
F7-C3-C4	108.1(4)	C2-C3-C4	115.2(4)
F8-C4-F9	108.1(3)	F8-C4-C3	108.1(3)
F9-C4-C3	108.0(4)	F8-C4-C5	109.0(4)
F9-C4-C5	108.1(3)	C3-C4-C5	115.3(4)
F10-C5-F11	108.8(3)	F10-C5-C6	109.5(3)
F11-C5-C6	108.4(3)	F10-C5-C4	108.3(3)
F11-C5-C4	107.8(3)	C6-C5-C4	114.0(3)
F13-C6-F12	108.3(3)	F13-C6-C5	108.0(3)
F12-C6-C5	108.3(3)	F13-C6-C7	109.3(3)
F12-C6-C7	106.5(3)	C5-C6-C7	116.2(3)
F14-C7-F15	106.8(3)	F14-C7-C6	107.4(3)
F15-C7-C6	108.9(3)	F14-C7-C8	108.4(3)
F15-C7-C8	112.5(3)	C6-C7-C8	112.5(3)
O1-C8-C9	124.0(4)	O1-C8-C7	114.1(4)
C9-C8-C7	121.9(4)	C18-C9-C10	118.8(4)
C18-C9-C8	122.4(4)	C10-C9-C8	118.8(4)
O2-C10-C11	118.1(4)	O2-C10-C9	121.0(4)
C11-C10-C9	120.9(4)	C10-C11-C12	120.0(4)
C10-C11-C19	121.0(4)	C12-C11-C19	118.9(4)
C11-C12-C13	122.8(4)	C11-C12-C17	119.5(4)
C13-C12-C17	117.7(4)	C14-C13-C12	120.7(4)
C14-C13-H13	119.7	C12-C13-H13	119.7

C13-C14-C15	121.6(4)	C13-C14-H14	119.2
C15-C14-H14	119.2	C16-C15-C14	119.3(4)
C16-C15-H15	120.3	C14-C15-H15	120.3
C15-C16-C17	120.9(4)	C15-C16-H16	119.6
C17-C16-H16	119.6	C18-C17-C16	120.8(4)
C18-C17-C12	119.4(4)	C16-C17-C12	119.8(4)
C9-C18-C17	121.4(4)	C9-C18-H18	119.3
C17-C18-H18	119.3	C20-C19-C28	119.7(4)
C20-C19-C11	120.8(4)	C28-C19-C11	119.3(4)
O3-C20-C19	118.0(4)	O3-C20-C21	121.1(4)
C19-C20-C21	120.9(4)	C22-C21-C20	118.8(4)
C22-C21-C29	122.3(4)	C20-C21-C29	118.9(4)
C21-C22-C23	121.8(4)	C21-C22-H22	119.1
C23-C22-H22	119.1	C22-C23-C24	121.8(4)
C22-C23-C28	119.1(4)	C24-C23-C28	119.2(4)
C25-C24-C23	121.3(4)	C25-C24-H24	119.4
C23-C24-H24	119.4	C24-C25-C26	119.9(4)
C24-C25-H25	120.1	C26-C25-H25	120.1
C27-C26-C25	120.3(4)	C27-C26-H26	119.8
C25-C26-H26	119.8	C26-C27-C28	121.3(4)
C26-C27-H27	119.4	C28-C27-H27	119.4
C27-C28-C19	122.3(4)	C27-C28-C23	118.1(4)
C19-C28-C23	119.6(4)	O4-C29-C21	124.0(4)
O4-C29-C30	116.0(4)	C21-C29-C30	119.8(3)
F17-C30-F16	107.5(3)	F17-C30-C31	106.7(3)

F16-C30-C31	109.2(3)	F17-C30-C29	112.6(3)
F16-C30-C29	106.4(3)	C31-C30-C29	114.3(3)
F18-C31-F19	109.7(3)	F18-C31-C30	107.8(3)
F19-C31-C30	109.3(3)	F18-C31-C32	107.5(3)
F19-C31-C32	108.2(3)	C30-C31-C32	114.3(3)
F21-C32-F20	108.2(3)	F21-C32-C33	108.7(3)
F20-C32-C33	107.7(3)	F21-C32-C31	109.4(3)
F20-C32-C31	108.9(3)	C33-C32-C31	113.8(3)
F22-C33-F23	109.0(4)	F22-C33-C32	108.8(3)
F23-C33-C32	107.9(3)	F22-C33-C34	108.5(3)
F23-C33-C34	107.5(3)	C32-C33-C34	115.0(3)
F25-C34-F24	108.2(3)	F25-C34-C35	109.1(3)
F24-C34-C35	108.2(3)	F25-C34-C33	108.9(3)
F24-C34-C33	108.2(3)	C35-C34-C33	114.1(4)
F27-C35-F26	108.4(3)	F27-C35-C36	107.1(4)
F26-C35-C36	107.0(3)	F27-C35-C34	109.0(3)
F26-C35-C34	109.5(3)	C36-C35-C34	115.6(4)
F28-C36-F29	107.4(4)	F28-C36-F30	108.7(4)
F29-C36-F30	107.8(4)	F28-C36-C35	112.0(4)
F29-C36-C35	110.6(4)	F30-C36-C35	110.2(4)

Table S3-24. Torsion angles (°) for Pu_XW_4rac2.

F3-C1-C2-F4	51.6(5)	F2-C1-C2-F4	-68.1(5)
F1-C1-C2-F4	171.0(4)	F3-C1-C2-F5	-64.0(5)

F2-C1-C2-F5	176.2(4)	F1-C1-C2-F5	55.4(5)
F3-C1-C2-C3	173.5(4)	F2-C1-C2-C3	53.8(6)
F1-C1-C2-C3	-67.1(6)	F4-C2-C3-F6	161.1(4)
F5-C2-C3-F6	-80.9(5)	C1-C2-C3-F6	40.3(6)
F4-C2-C3-F7	44.6(5)	F5-C2-C3-F7	162.7(4)
C1-C2-C3-F7	-76.1(5)	F4-C2-C3-C4	-76.7(5)
F5-C2-C3-C4	41.4(6)	C1-C2-C3-C4	162.6(4)
F6-C3-C4-F8	167.0(3)	F7-C3-C4-F8	-76.2(4)
C2-C3-C4-F8	45.2(5)	F6-C3-C4-F9	50.3(4)
F7-C3-C4-F9	167.1(3)	C2-C3-C4-F9	-71.5(5)
F6-C3-C4-C5	-70.7(5)	F7-C3-C4-C5	46.0(5)
C2-C3-C4-C5	167.4(4)	F8-C4-C5-F10	163.1(3)
F9-C4-C5-F10	-79.7(4)	C3-C4-C5-F10	41.3(5)
F8-C4-C5-F11	45.5(5)	F9-C4-C5-F11	162.8(3)
C3-C4-C5-F11	-76.3(5)	F8-C4-C5-C6	-74.8(4)
F9-C4-C5-C6	42.5(5)	C3-C4-C5-C6	163.4(4)
F10-C5-C6-F13	167.3(3)	F11-C5-C6-F13	-74.1(4)
C4-C5-C6-F13	45.9(5)	F10-C5-C6-F12	50.2(4)
F11-C5-C6-F12	168.8(3)	C4-C5-C6-F12	-71.2(4)
F10-C5-C6-C7	-69.5(4)	F11-C5-C6-C7	49.2(4)
C4-C5-C6-C7	169.1(4)	F13-C6-C7-F14	171.6(3)
F12-C6-C7-F14	-71.6(4)	C5-C6-C7-F14	49.1(4)
F13-C6-C7-F15	56.3(4)	F12-C6-C7-F15	173.1(3)
C5-C6-C7-F15	-66.3(4)	F13-C6-C7-C8	-69.2(4)
F12-C6-C7-C8	47.6(4)	C5-C6-C7-C8	168.3(3)

F14-C7-C8-O1	17.8(5)	F15-C7-C8-O1	135.7(4)
C6-C7-C8-O1	-100.8(4)	F14-C7-C8-C9	-165.4(3)
F15-C7-C8-C9	-47.5(5)	C6-C7-C8-C9	76.0(5)
O1-C8-C9-C18	-175.2(4)	C7-C8-C9-C18	8.3(6)
O1-C8-C9-C10	5.8(6)	C7-C8-C9-C10	-170.7(4)
C18-C9-C10-O2	178.0(4)	C8-C9-C10-O2	-2.9(6)
C18-C9-C10-C11	-3.4(6)	C8-C9-C10-C11	175.6(4)
O2-C10-C11-C12	-179.6(3)	C9-C10-C11-C12	1.9(6)
O2-C10-C11-C19	4.3(6)	C9-C10-C11-C19	-174.3(4)
C10-C11-C12-C13	-178.7(4)	C19-C11-C12-C13	-2.5(6)
C10-C11-C12-C17	0.7(6)	C19-C11-C12-C17	176.9(4)
C11-C12-C13-C14	-179.7(4)	C17-C12-C13-C14	0.9(6)
C12-C13-C14-C15	-0.7(6)	C13-C14-C15-C16	0.8(7)
C14-C15-C16-C17	-1.2(6)	C15-C16-C17-C18	-177.6(4)
C15-C16-C17-C12	1.4(6)	C11-C12-C17-C18	-1.7(6)
C13-C12-C17-C18	177.7(4)	C11-C12-C17-C16	179.3(4)
C13-C12-C17-C16	-1.3(6)	C10-C9-C18-C17	2.4(6)
C8-C9-C18-C17	-176.6(4)	C16-C17-C18-C9	179.1(4)
C12-C17-C18-C9	0.1(6)	C10-C11-C19-C20	-87.8(5)
C12-C11-C19-C20	96.0(5)	C10-C11-C19-C28	96.8(5)
C12-C11-C19-C28	-79.4(5)	C28-C19-C20-O3	-178.5(3)
C11-C19-C20-O3	6.2(6)	C28-C19-C20-C21	3.3(6)
C11-C19-C20-C21	-172.1(4)	O3-C20-C21-C22	178.6(4)
C19-C20-C21-C22	-3.2(6)	O3-C20-C21-C29	-4.1(6)
C19-C20-C21-C29	174.1(4)	C20-C21-C22-C23	0.5(6)

C29-C21-C22-C23	-176.7(4)	C21-C22-C23-C24	-179.2(4)
C21-C22-C23-C28	2.0(6)	C22-C23-C24-C25	-177.0(4)
C28-C23-C24-C25	1.8(6)	C23-C24-C25-C26	-0.8(6)
C24-C25-C26-C27	-0.7(6)	C25-C26-C27-C28	1.1(6)
C26-C27-C28-C19	179.4(4)	C26-C27-C28-C23	0.0(6)
C20-C19-C28-C27	180.0(4)	C11-C19-C28-C27	-4.6(6)
C20-C19-C28-C23	-0.7(6)	C11-C19-C28-C23	174.8(3)
C22-C23-C28-C27	177.4(3)	C24-C23-C28-C27	-1.4(6)
C22-C23-C28-C19	-2.0(6)	C24-C23-C28-C19	179.2(3)
C22-C21-C29-O4	-176.1(4)	C20-C21-C29-O4	6.7(6)
C22-C21-C29-C30	8.2(6)	C20-C21-C29-C30	-169.0(4)
O4-C29-C30-F17	131.0(4)	C21-C29-C30-F17	-53.0(5)
O4-C29-C30-F16	-111.6(4)	C21-C29-C30-F16	64.5(5)
O4-C29-C30-C31	9.0(5)	C21-C29-C30-C31	-174.9(4)
F17-C30-C31-F18	-70.1(4)	F16-C30-C31-F18	174.0(3)
C29-C30-C31-F18	55.0(5)	F17-C30-C31-F19	170.7(3)
F16-C30-C31-F19	54.8(4)	C29-C30-C31-F19	-64.2(4)
F17-C30-C31-C32	49.3(4)	F16-C30-C31-C32	-66.6(4)
C29-C30-C31-C32	174.4(3)	F18-C31-C32-F21	162.0(3)
F19-C31-C32-F21	-79.6(4)	C30-C31-C32-F21	42.4(5)
F18-C31-C32-F20	43.9(4)	F19-C31-C32-F20	162.3(3)
C30-C31-C32-F20	-75.7(4)	F18-C31-C32-C33	-76.2(4)
F19-C31-C32-C33	42.2(4)	C30-C31-C32-C33	164.2(3)
F21-C32-C33-F22	164.0(3)	F20-C32-C33-F22	-79.0(4)
C31-C32-C33-F22	41.8(5)	F21-C32-C33-F23	45.8(4)

F20-C32-C33-F23	162.9(3)	C31-C32-C33-F23	-76.3(4)
F21-C32-C33-C34	-74.1(4)	F20-C32-C33-C34	42.9(4)
C31-C32-C33-C34	163.8(3)	F22-C33-C34-F25	161.9(3)
F23-C33-C34-F25	-80.4(4)	C32-C33-C34-F25	39.8(5)
F22-C33-C34-F24	44.4(5)	F23-C33-C34-F24	162.2(3)
C32-C33-C34-F24	-77.6(4)	F22-C33-C34-C35	-75.9(4)
F23-C33-C34-C35	41.8(4)	C32-C33-C34-C35	162.0(3)
F25-C34-C35-F27	46.3(4)	F24-C34-C35-F27	163.8(3)
C33-C34-C35-F27	-75.8(4)	F25-C34-C35-F26	164.8(3)
F24-C34-C35-F26	-77.7(4)	C33-C34-C35-F26	42.7(4)
F25-C34-C35-C36	-74.3(4)	F24-C34-C35-C36	43.2(4)
C33-C34-C35-C36	163.6(3)	F27-C35-C36-F28	167.5(4)
F26-C35-C36-F28	51.3(5)	C34-C35-C36-F28	-70.9(5)
F27-C35-C36-F29	47.7(4)	F26-C35-C36-F29	-68.4(4)
C34-C35-C36-F29	169.3(3)	F27-C35-C36-F30	-71.4(5)
F26-C35-C36-F30	172.5(4)	C34-C35-C36-F30	50.2(5)

Table S3-25. Anisotropic atomic displacement parameters (Å^2) for Pu_XW_4rac2.

The anisotropic atomic displacement factor exponent takes the form: $-2\pi^2[h^2 a^{*2} U_{11} + ... + 2 h k a^* b^* U_{12}]$

	U_{11}	U_{22}	U_{33}	U_{23}	U_{13}	U_{12}
O1	0.0319(17)	0.0264(18)	0.0327(18)	-0.0089(14)	0.0040(13)	-0.0141(14)
O2	0.0259(17)	0.0194(17)	0.0360(18)	-0.0075(13)	0.0051(14)	-0.0092(14)
O3	0.0192(16)	0.0291(18)	0.0303(19)	-0.0082(14)	-0.0028(14)	-0.0041(13)
O4	0.0258(17)	0.042(2)	0.0315(18)	-0.0094(14)	-0.0013(14)	-0.0082(15)

	U_{11}	U_{22}	U_{33}	U_{23}	U_{13}	U_{12}
F1	0.082(2)	0.058(2)	0.0372(18)	-0.0128(15)	-0.0024(16)	-0.0096(18)
F2	0.0354(18)	0.103(3)	0.0478(19)	-0.0197(18)	0.0065(15)	-0.0107(18)
F3	0.077(2)	0.081(2)	0.052(2)	-0.0409(18)	0.0037(17)	-0.026(2)
F4	0.105(3)	0.046(2)	0.059(2)	-0.0258(16)	0.0166(19)	-0.0396(19)
F5	0.0396(18)	0.107(3)	0.063(2)	-0.0459(19)	0.0059(15)	-0.0357(18)
F6	0.0563(18)	0.0432(17)	0.0345(16)	-0.0078(13)	0.0032(13)	-0.0270(14)
F7	0.0299(16)	0.0571(19)	0.0403(17)	-0.0170(14)	0.0028(12)	-0.0030(13)
F8	0.062(2)	0.0434(17)	0.0448(17)	-0.0173(13)	0.0137(14)	-0.0352(15)
F9	0.0275(15)	0.0550(18)	0.0418(17)	-0.0190(13)	-0.0036(12)	-0.0045(13)
F10	0.0395(16)	0.0415(16)	0.0345(15)	-0.0096(12)	0.0070(12)	-0.0255(13)
F11	0.0351(15)	0.0377(16)	0.0397(16)	-0.0112(13)	-0.0004(12)	0.0039(13)
F12	0.0327(14)	0.0300(15)	0.0379(15)	-0.0084(12)	-0.0057(12)	-0.0002(12)
F13	0.0337(15)	0.0465(16)	0.0352(15)	-0.0118(12)	0.0046(12)	-0.0262(13)
F14	0.0244(13)	0.0366(15)	0.0369(15)	-0.0115(11)	0.0030(11)	-0.0159(11)
F15	0.0256(13)	0.0262(14)	0.0349(15)	-0.0064(11)	0.0002(11)	-0.0053(11)
F16	0.0347(15)	0.0412(16)	0.0407(16)	-0.0184(12)	0.0088(12)	-0.0236(13)
F17	0.0305(14)	0.0348(15)	0.0287(14)	-0.0080(12)	-0.0026(11)	-0.0031(12)
F18	0.0289(14)	0.0468(17)	0.0377(15)	-0.0148(12)	0.0039(11)	-0.0204(12)
F19	0.0332(15)	0.0361(16)	0.0321(15)	-0.0008(12)	-0.0002(12)	0.0001(12)
F20	0.0438(16)	0.0296(16)	0.0337(15)	-0.0051(12)	0.0027(12)	-0.0038(12)
F21	0.0299(15)	0.070(2)	0.0487(17)	-0.0330(15)	0.0102(12)	-0.0287(14)
F22	0.0216(14)	0.094(2)	0.0368(16)	-0.0239(15)	0.0010(12)	-0.0164(15)
F23	0.068(2)	0.0272(16)	0.0420(17)	-0.0034(13)	0.0139(15)	0.0002(14)

	U_{11}	U_{22}	U_{33}	U_{23}	U_{13}	U_{12}
F24	0.0530(18)	0.0347(16)	0.0385(16)	-0.0121(12)	0.0082(13)	-0.0242(14)
F25	0.0213(13)	0.0421(16)	0.0349(15)	-0.0096(12)	-0.0034(11)	-0.0081(11)
F26	0.0260(14)	0.0561(18)	0.0313(15)	-0.0070(13)	-0.0036(11)	-0.0022(13)
F27	0.0461(17)	0.0305(15)	0.0419(16)	-0.0042(12)	0.0067(13)	-0.0166(13)
F28	0.0474(18)	0.0520(19)	0.0531(18)	-0.0272(15)	0.0033(14)	-0.0223(15)
F29	0.0479(18)	0.0549(19)	0.0329(17)	-0.0080(14)	0.0076(13)	-0.0081(15)
F30	0.0268(15)	0.0429(17)	0.0459(17)	-0.0125(13)	-0.0031(12)	-0.0010(12)
C1	0.050(3)	0.047(3)	0.040(3)	-0.018(3)	0.001(3)	-0.016(3)
C2	0.034(3)	0.039(3)	0.050(3)	-0.019(2)	0.001(2)	-0.014(2)
C3	0.027(3)	0.033(3)	0.041(3)	-0.011(2)	0.001(2)	-0.013(2)
C4	0.029(3)	0.028(3)	0.038(3)	-0.007(2)	0.001(2)	-0.014(2)
C5	0.026(2)	0.022(2)	0.032(3)	-0.0051(19)	0.0006(19)	-0.008(2)
C6	0.020(2)	0.020(2)	0.040(3)	-0.005(2)	-0.0024(19)	-0.0086(19)
C7	0.022(2)	0.024(2)	0.034(3)	-0.003(2)	0.0002(19)	-0.0084(19)
C8	0.023(2)	0.026(3)	0.029(2)	-0.0069(19)	-0.0011(18)	-0.0100(19)
C9	0.021(2)	0.016(2)	0.026(2)	-0.0021(17)	-0.0029(18)	-0.0048(17)
C10	0.024(2)	0.020(2)	0.025(2)	-0.0061(18)	-0.0024(18)	-0.0071(18)
C11	0.024(2)	0.021(2)	0.020(2)	-0.0023(18)	-0.0018(18)	-0.0068(18)
C12	0.023(2)	0.022(2)	0.026(2)	-0.0038(18)	-0.0008(18)	-0.0097(19)
C13	0.025(2)	0.024(2)	0.026(2)	-0.0052(19)	0.0027(18)	-0.0107(19)
C14	0.026(2)	0.029(3)	0.039(3)	-0.007(2)	0.001(2)	-0.013(2)
C15	0.030(3)	0.023(2)	0.038(3)	-0.004(2)	0.004(2)	-0.011(2)
C16	0.026(2)	0.023(2)	0.034(3)	-0.006(2)	0.001(2)	-0.0081(19)

	U_{11}	U_{22}	U_{33}	U_{23}	U_{13}	U_{12}
C17	0.023(2)	0.022(2)	0.028(2)	-0.0025(19)	-0.0014(18)	-0.0066(19)
C18	0.022(2)	0.021(2)	0.027(2)	-0.0035(18)	-0.0008(18)	-0.0048(18)
C19	0.020(2)	0.020(2)	0.028(2)	-0.0037(18)	0.0028(18)	-0.0081(18)
C20	0.024(2)	0.020(2)	0.028(2)	-0.0050(18)	-0.0019(18)	-0.0077(18)
C21	0.017(2)	0.018(2)	0.030(2)	-0.0048(18)	0.0017(18)	-0.0056(17)
C22	0.019(2)	0.019(2)	0.029(2)	-0.0077(18)	0.0027(18)	-0.0061(18)
C23	0.021(2)	0.020(2)	0.029(3)	-0.0042(18)	0.0013(18)	-0.0076(18)
C24	0.019(2)	0.021(2)	0.028(2)	-0.0020(18)	-0.0012(18)	-0.0089(18)
C25	0.026(2)	0.023(2)	0.030(3)	-0.0024(19)	-0.0031(19)	-0.0090(19)
C26	0.029(2)	0.026(2)	0.026(2)	-0.0054(19)	-0.0029(19)	-0.011(2)
C27	0.024(2)	0.022(2)	0.030(3)	-0.0094(19)	0.0020(19)	-0.0095(19)
C28	0.020(2)	0.019(2)	0.026(2)	-0.0052(18)	-0.0011(17)	-0.0090(18)
C29	0.023(2)	0.030(3)	0.033(3)	-0.009(2)	0.001(2)	-0.013(2)
C30	0.022(2)	0.026(2)	0.030(3)	-0.0070(19)	-0.0032(19)	-0.0077(19)
C31	0.023(2)	0.031(3)	0.027(2)	-0.004(2)	-0.0017(19)	-0.010(2)
C32	0.023(2)	0.026(3)	0.032(3)	-0.008(2)	0.0027(19)	-0.0106(19)
C33	0.022(2)	0.030(3)	0.032(3)	-0.006(2)	0.0001(19)	-0.008(2)
C34	0.020(2)	0.025(2)	0.034(3)	-0.0088(19)	-0.0002(19)	-0.0090(19)
C35	0.023(2)	0.030(3)	0.036(3)	-0.002(2)	-0.007(2)	-0.008(2)
C36	0.024(2)	0.044(3)	0.036(3)	-0.011(2)	-0.001(2)	-0.008(2)

Table S3-26. Hydrogen atomic coordinates and isotropic atomic displacement parameters (Å^2) for Pu_XW_4rac2.

	x/a	y/b	z/c	U(eq)
H2	0.927(5)	0.359(5)	0.394(3)	0.059(17)
H3	0.736(5)	0.265(5)	0.676(3)	0.054(18)
H13	0.6142	0.0568	0.5319	0.03
H14	0.6425	-0.1478	0.5326	0.037
H15	0.8296	-0.2804	0.4648	0.036
H16	0.9916	-0.2056	0.3998	0.033
H18	1.0720	-0.0326	0.3542	0.029
H22	0.3353	0.4521	0.6089	0.027
H24	0.2298	0.4860	0.4771	0.027
H25	0.2371	0.4446	0.3412	0.031
H26	0.4329	0.3210	0.2758	0.031
H27	0.6198	0.2435	0.3466	0.03

Table S3-27. Hydrogen bond distances (Å) and angles (°) for Pu_XW_4rac2.

	Donor-H	Acceptor-H	Donor-Acceptor	Angle
O2-H2···O1	0.90(5)	1.78(5)	2.583(4)	148.(5)
O3-H3···O4	0.85(5)	1.82(5)	2.590(4)	150.(5)

Appendix for Chapter 5

1 ^{1}H NMR, ^{13}C{^{1}H} NMR and HRMS spectra of compounds

^{1}H NMR spectrum of **4** in DMSO-d_6

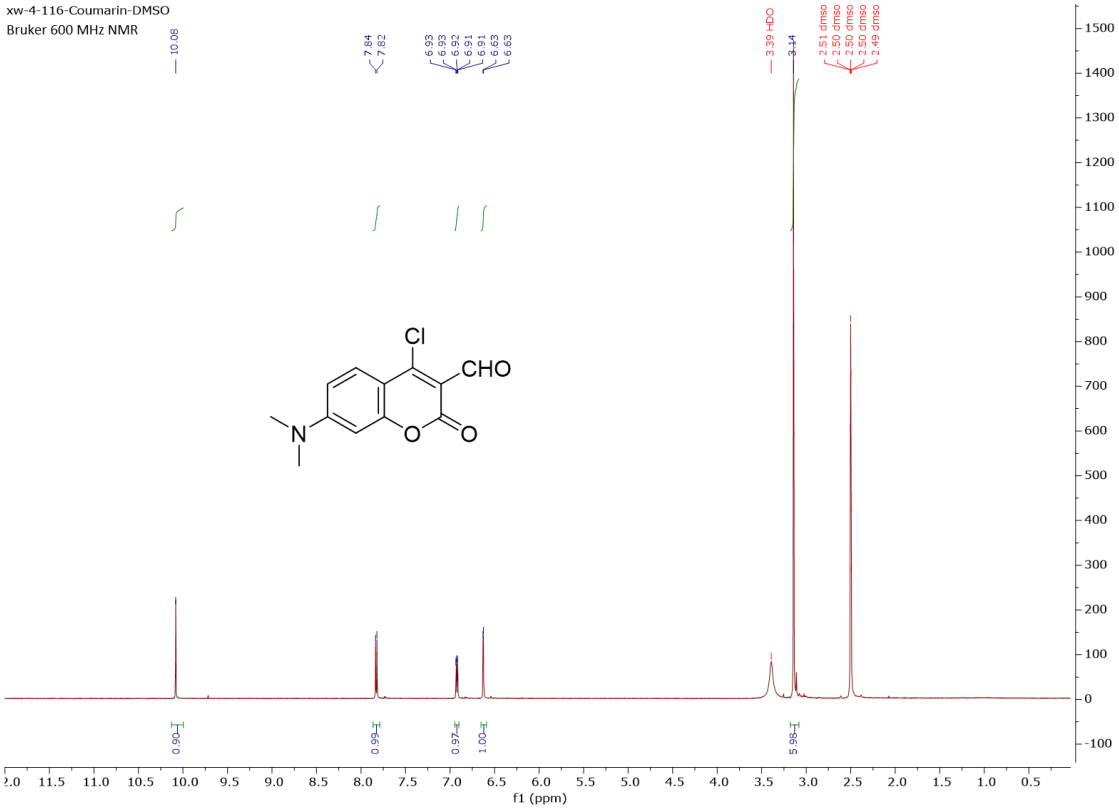

^{1}H NMR spectrum of (*S*)-**6** in DMSO-d_6

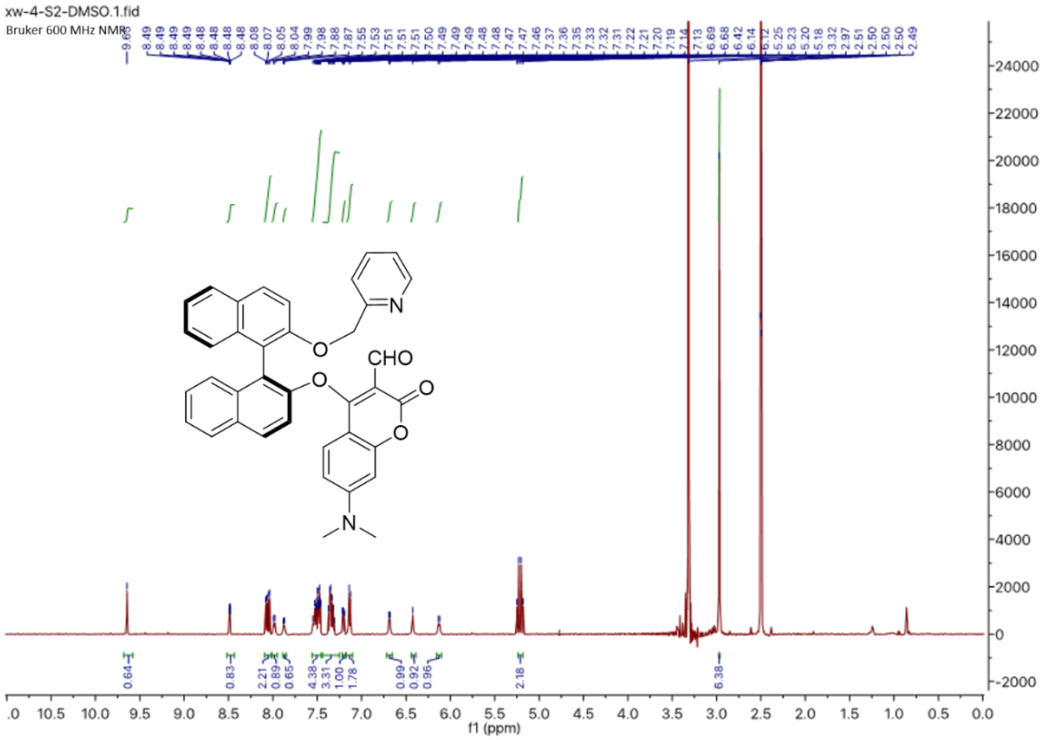

^{1}H NMR spectrum of (*S*)-**6** in $CDCl_3$

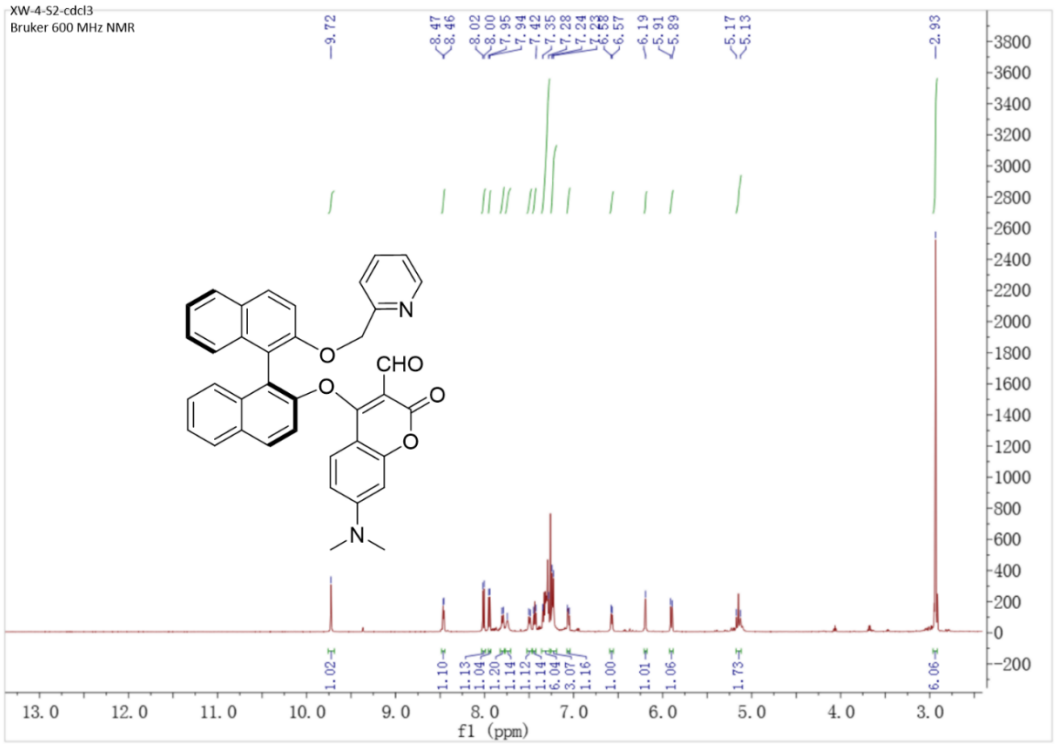

COSY NMR (Bruker 600MHz) spectrum of (*S*)-**6** in $CDCl_3$

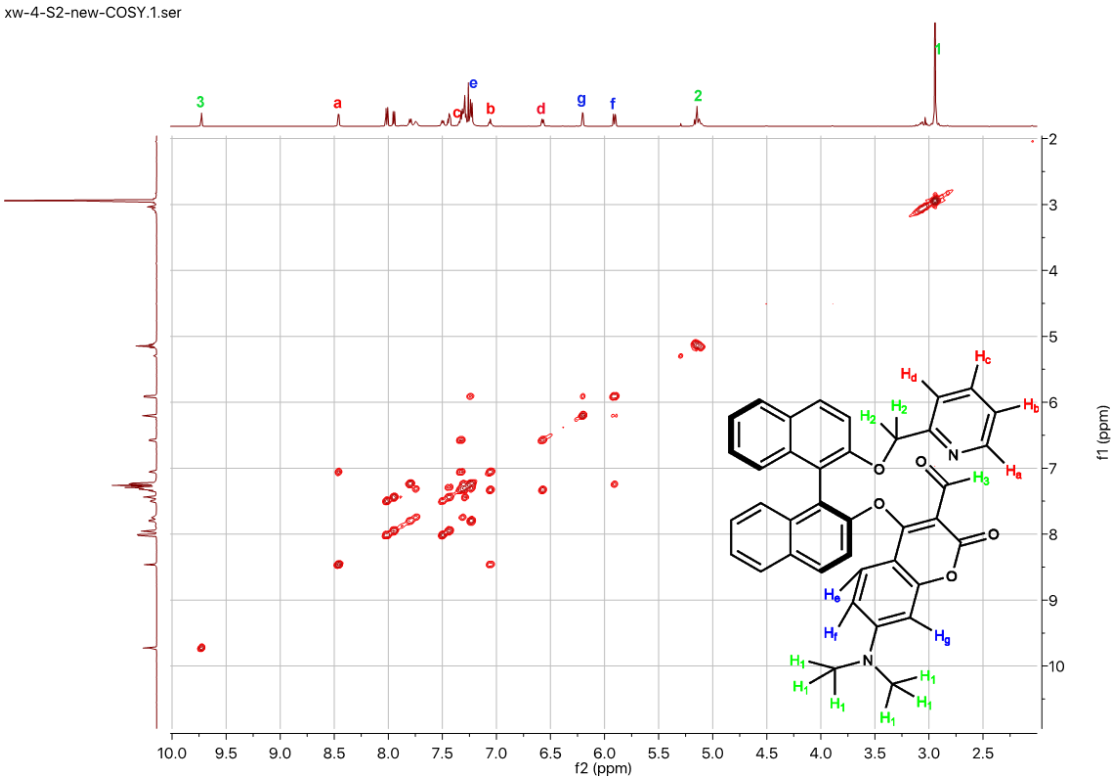

H_a δ 8.46, H_b δ 7.06, H_c δ 7.33, H_d δ 6.58

H_e δ 7.25, H_f δ 5.92, H_g δ 6.22

H_1 δ 2.95, H_2 δ 5.15, H_3 δ 9.73

$^{13}C\{^{1}H\}$ NMR spectrum of (*S*)-**6** in $CDCl_3$

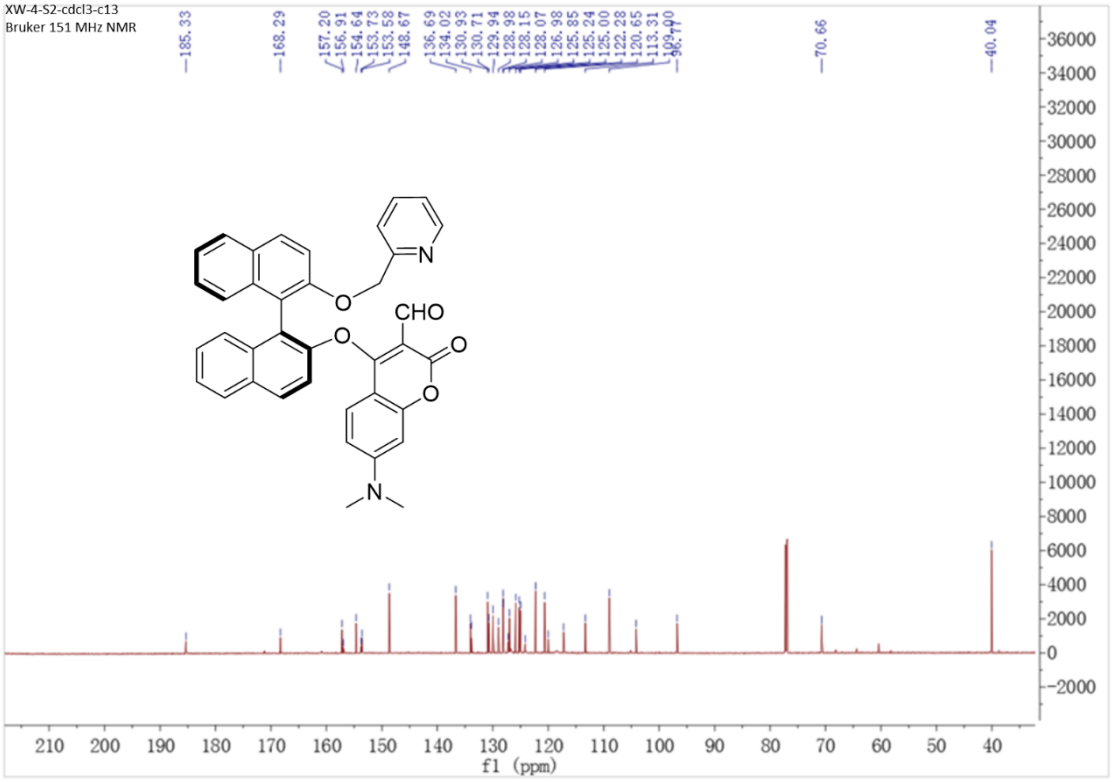

HRMS spectrum of (*S*)-**6**

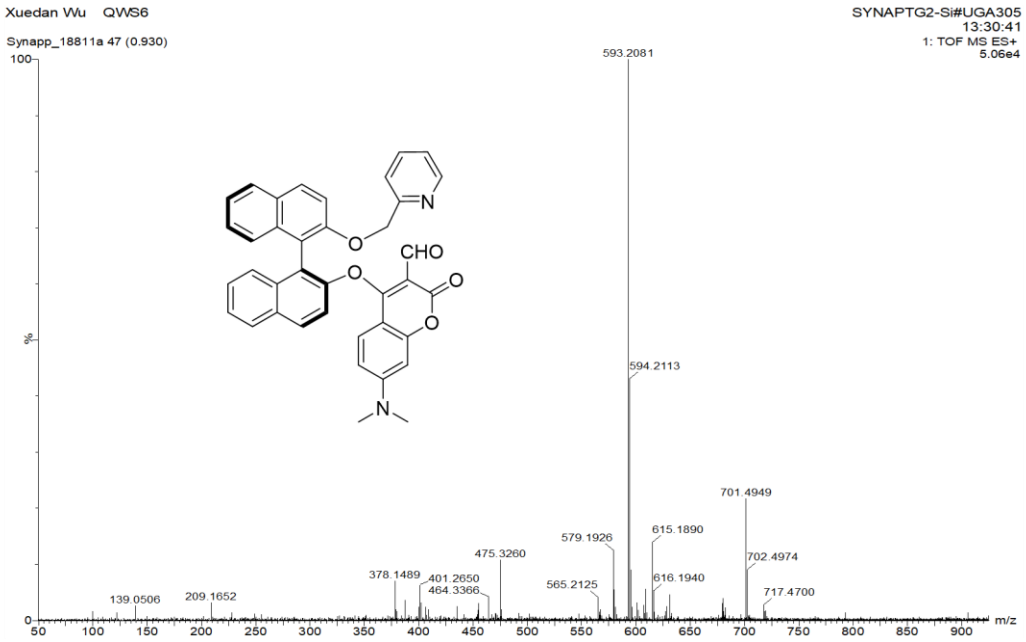

^{1}H NMR spectrum of (*R*)-**6** in DMSO-d6

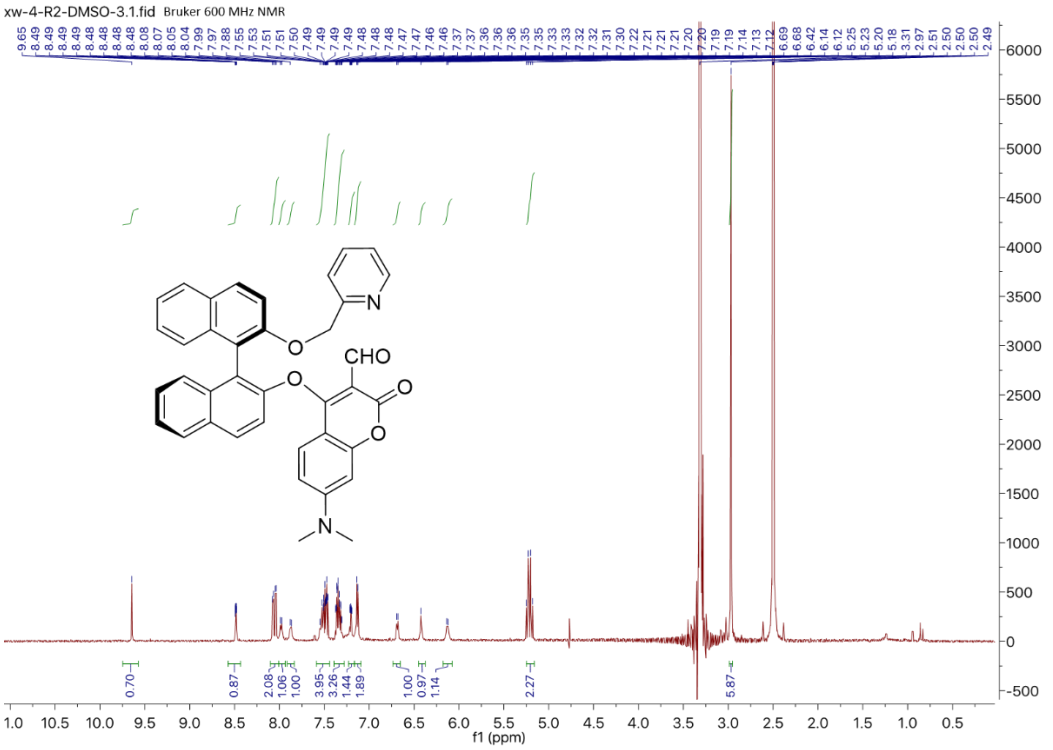

^{1}H NMR spectrum of (*R*)-**6** in $CDCl_3$

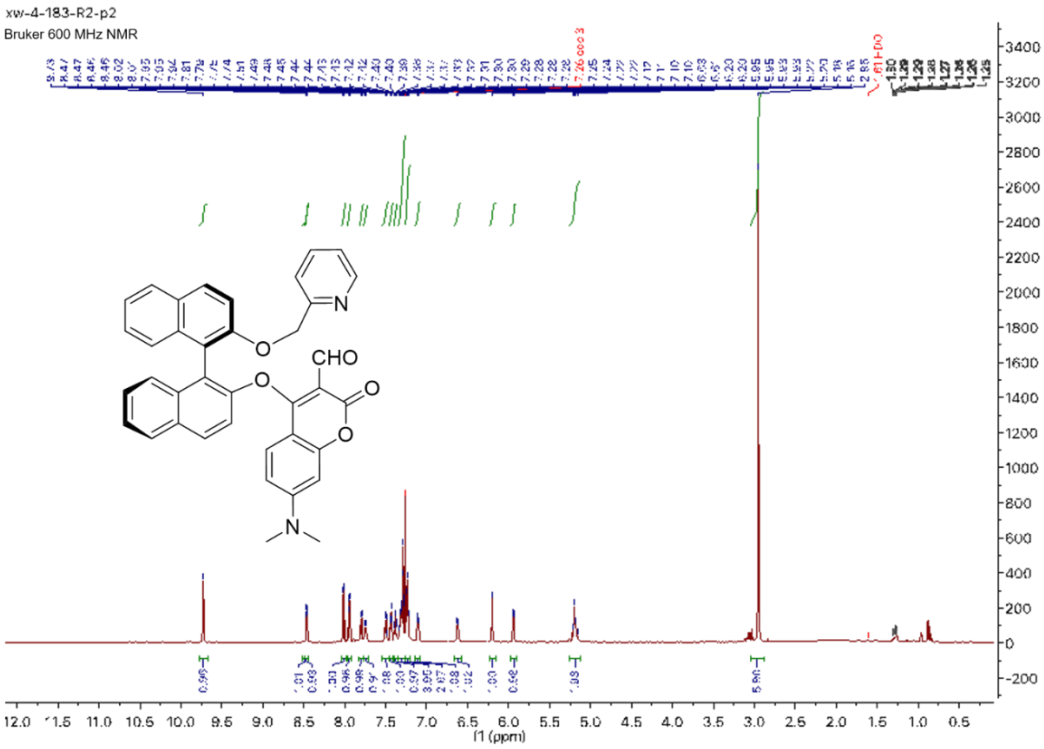

COSY NMR (Bruker 600MHz) spectrum of (*R*)-**6** in $CDCl_3$

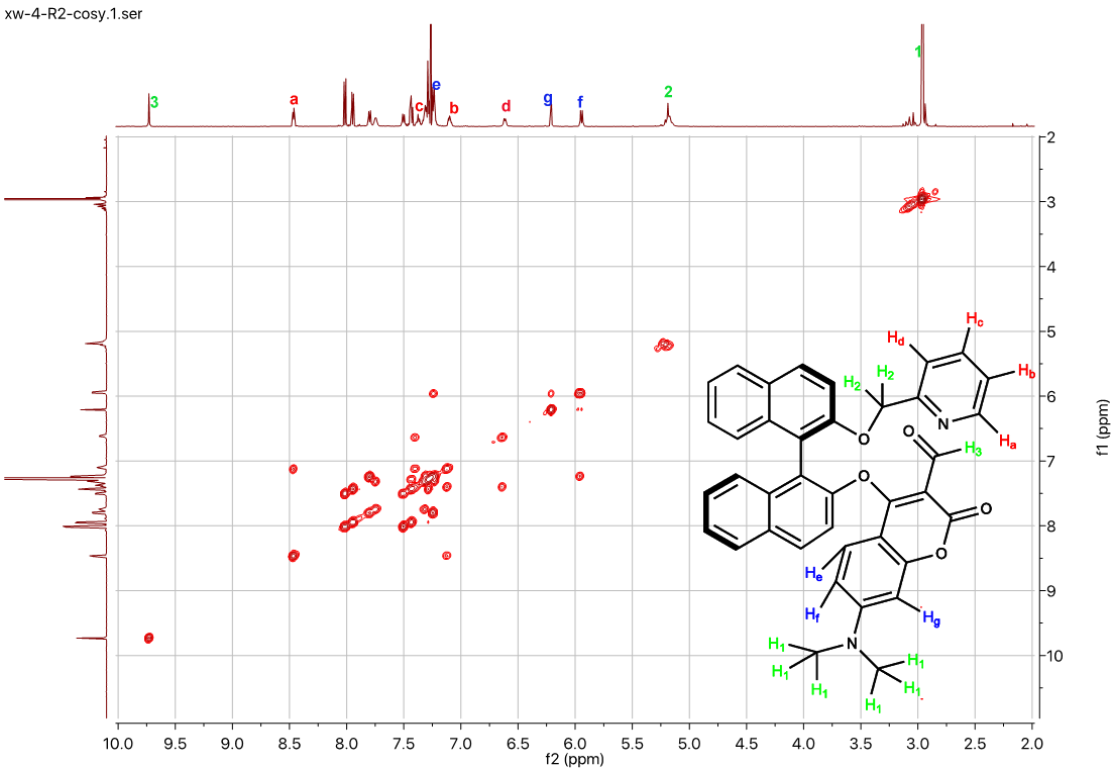

H_a δ 8.46, H_b δ 7.11, H_c δ 7.38, H_d δ 6.62

H_e δ 7.24, H_f δ 5.96, H_g δ 6.21

H_1 δ 2.95, H_2 δ 5.19, H_3 δ 9.73

$^{13}C\{^{1}H\}$ NMR spectrum of (*R*)-**6** in $CDCl_3$

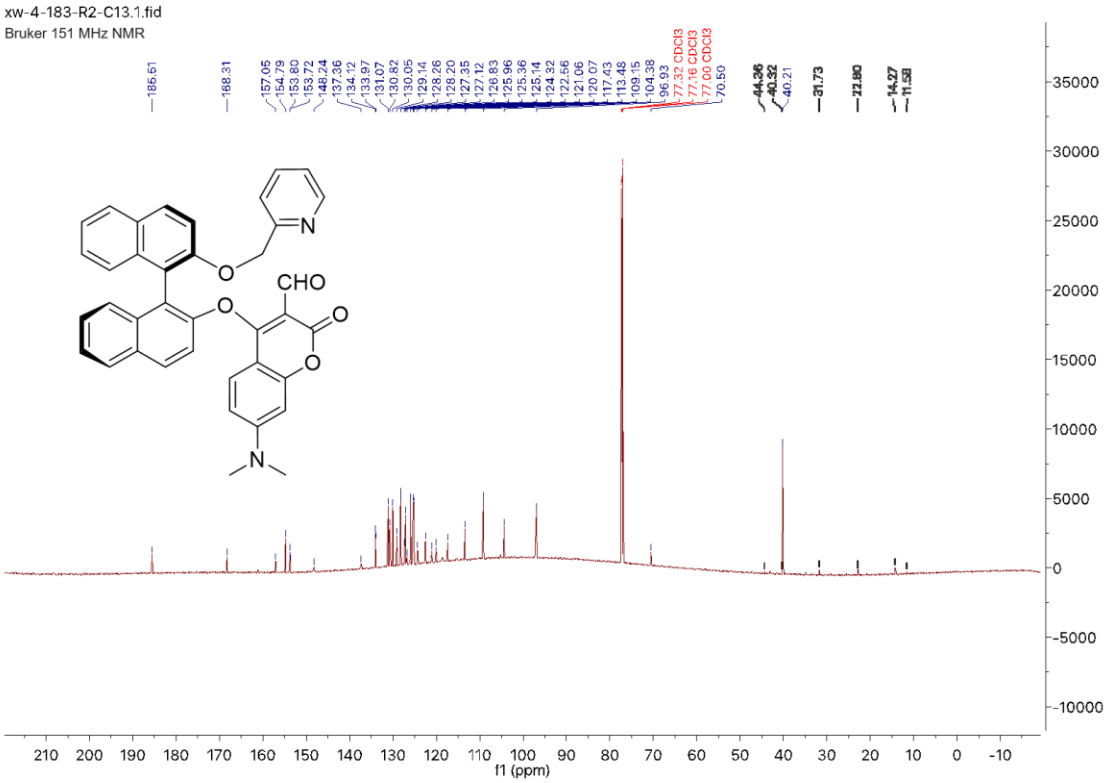

HRMS spectrum of (*R*)-**6**

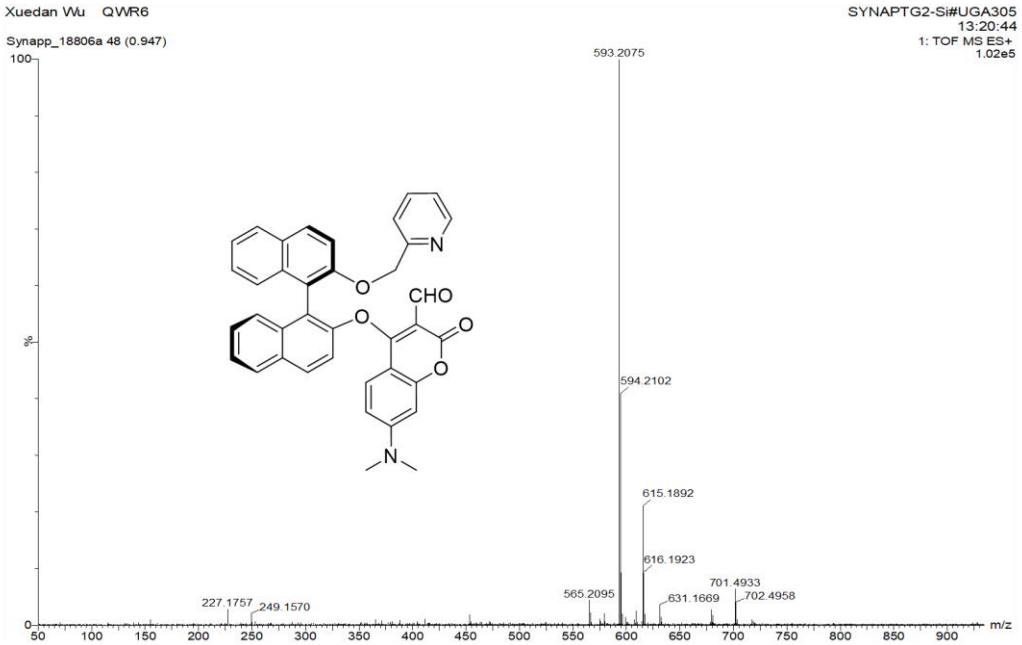

^{1}H NMR spectrum of (*S*)-**7** in $CDCl_3$

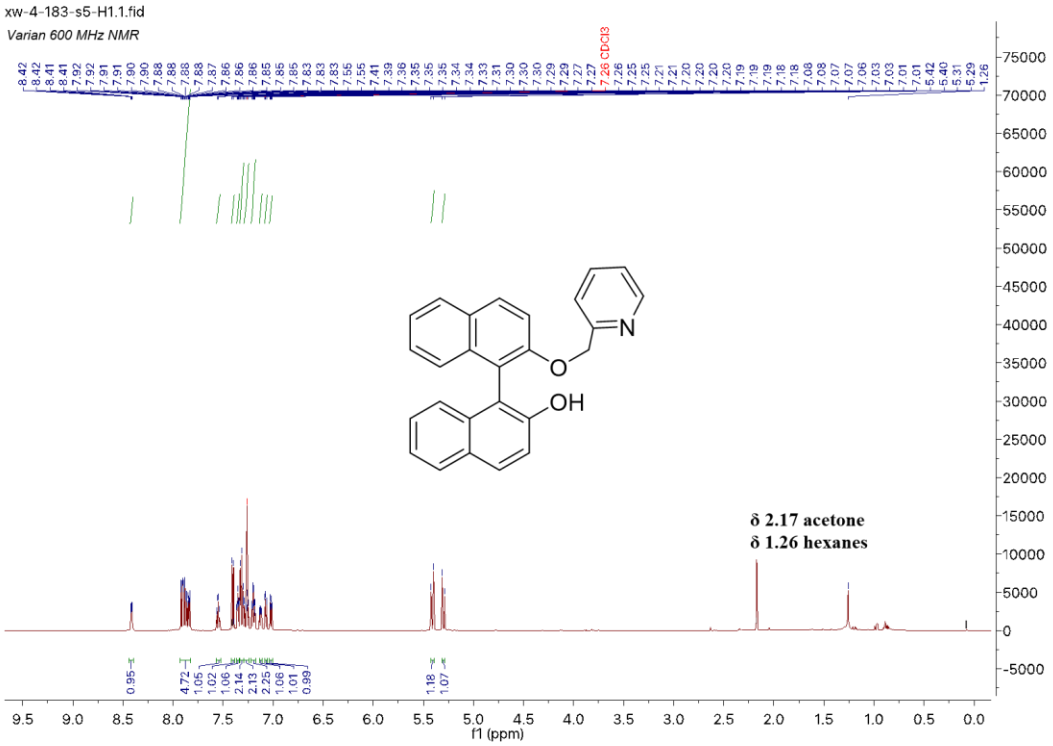

^{1}H NMR spectrum of (*S*)-**12** in $CDCl_3$

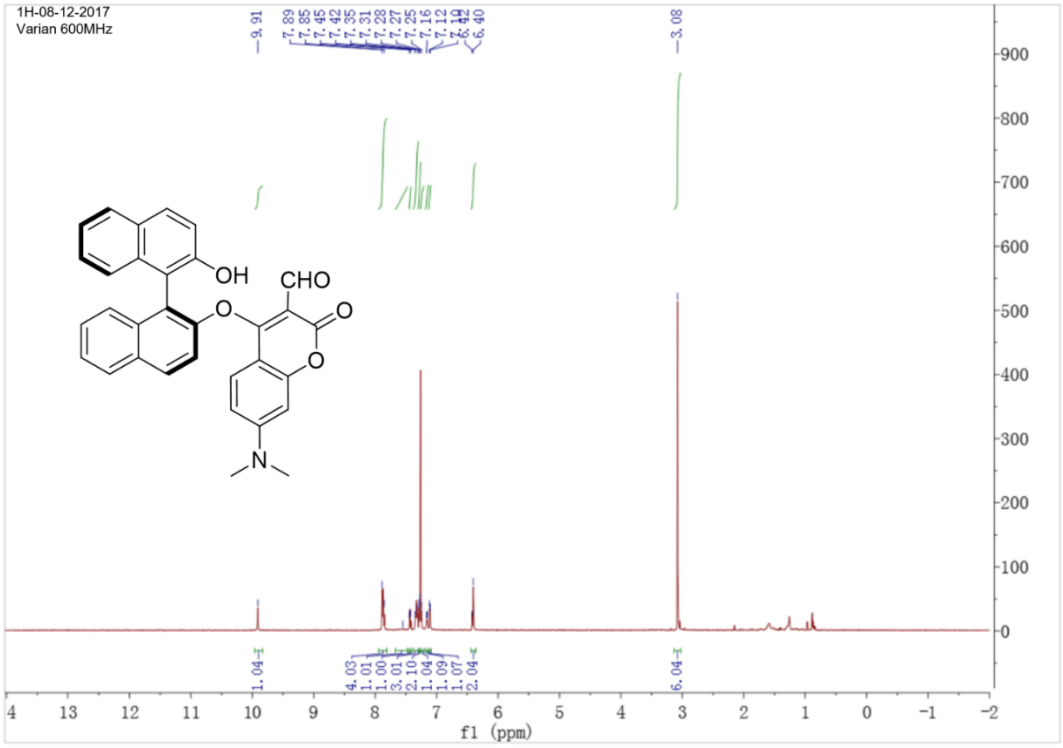

^{13}C NMR spectrum of (*S*)-**12** in $CDCl_3$

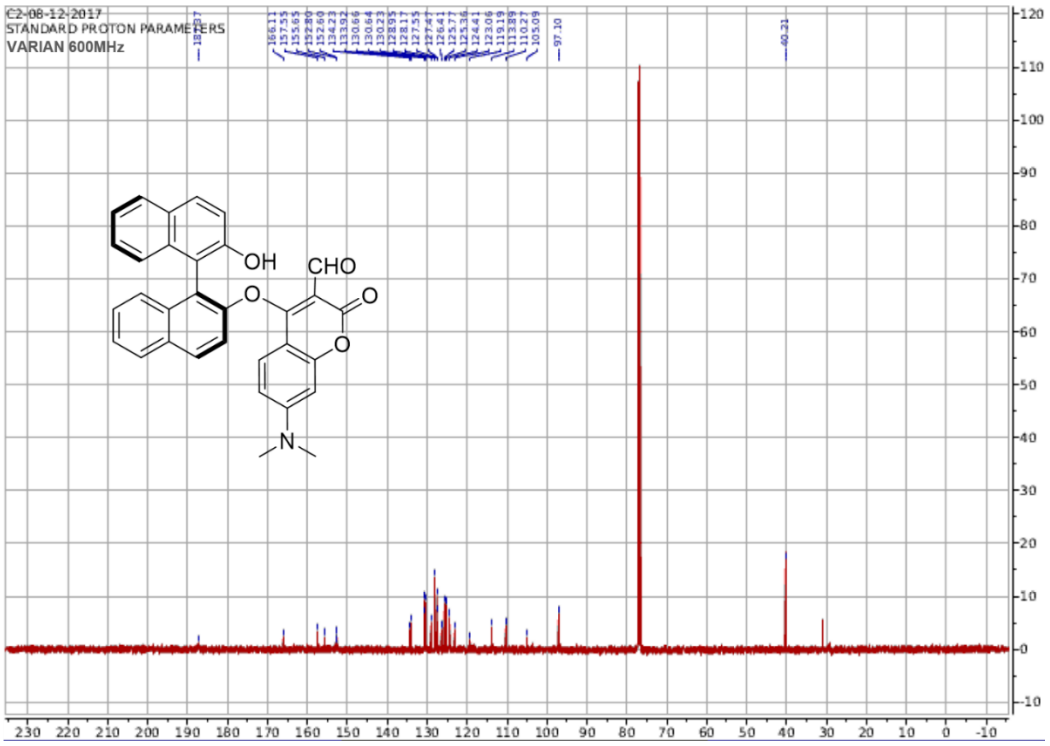

HRMS spectrum of (*S*)-**12**

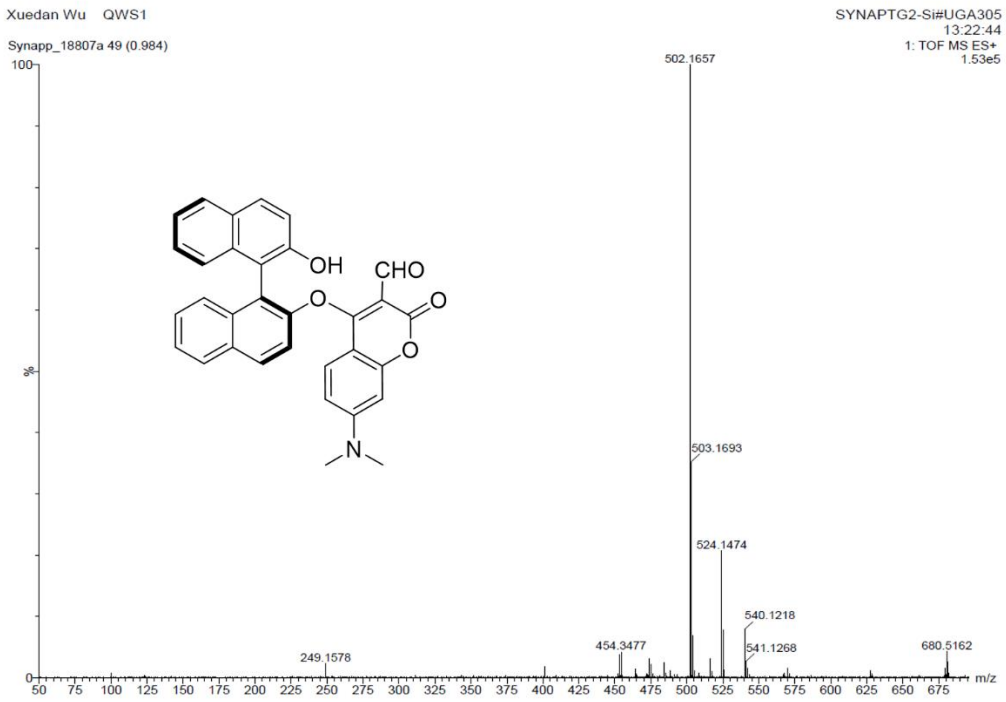

Figure S5-10a. ^{1}H NMR spectra of (*R*)-**6** (1.0 mM in DMSO-d_6) with D-Val (40 equiv) in HEPES (D_2O, 25 mM HEPES, 120 mM NaCl, pH=7.4). [reaction time: 0.5 – 36 h. DMSO: HEPES = 9:1 (v)]

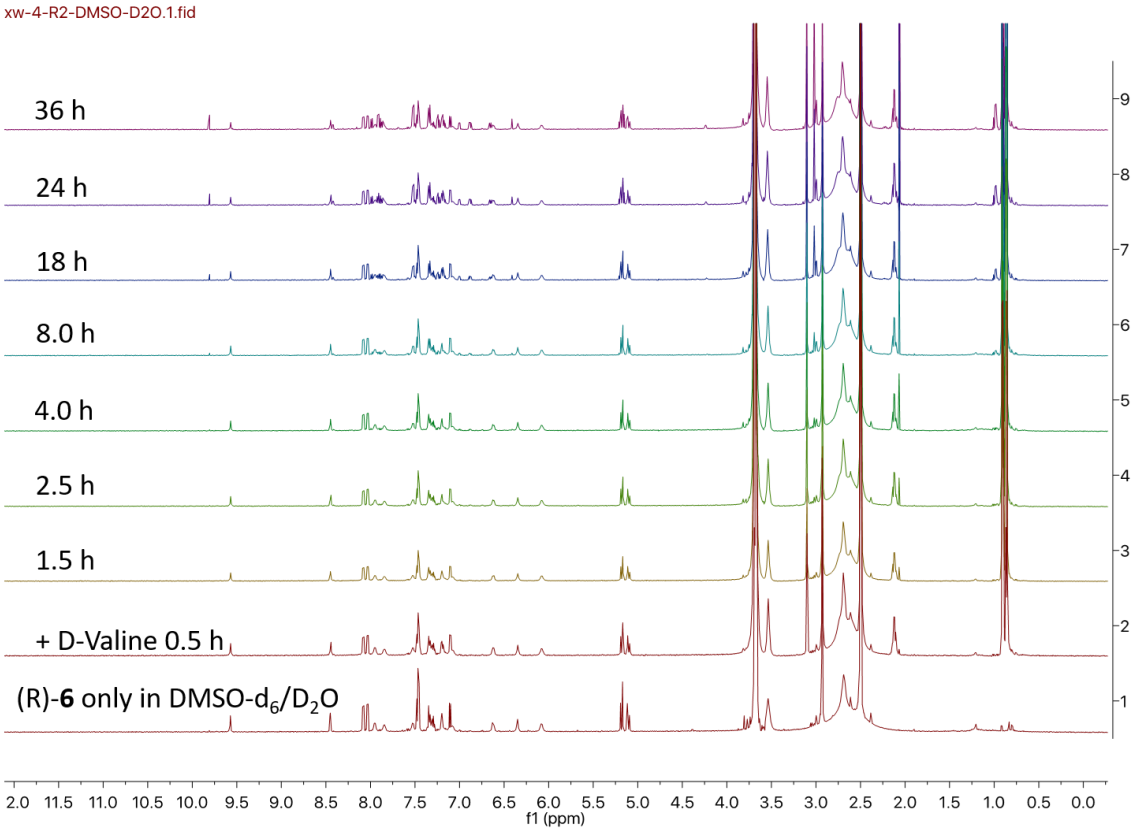

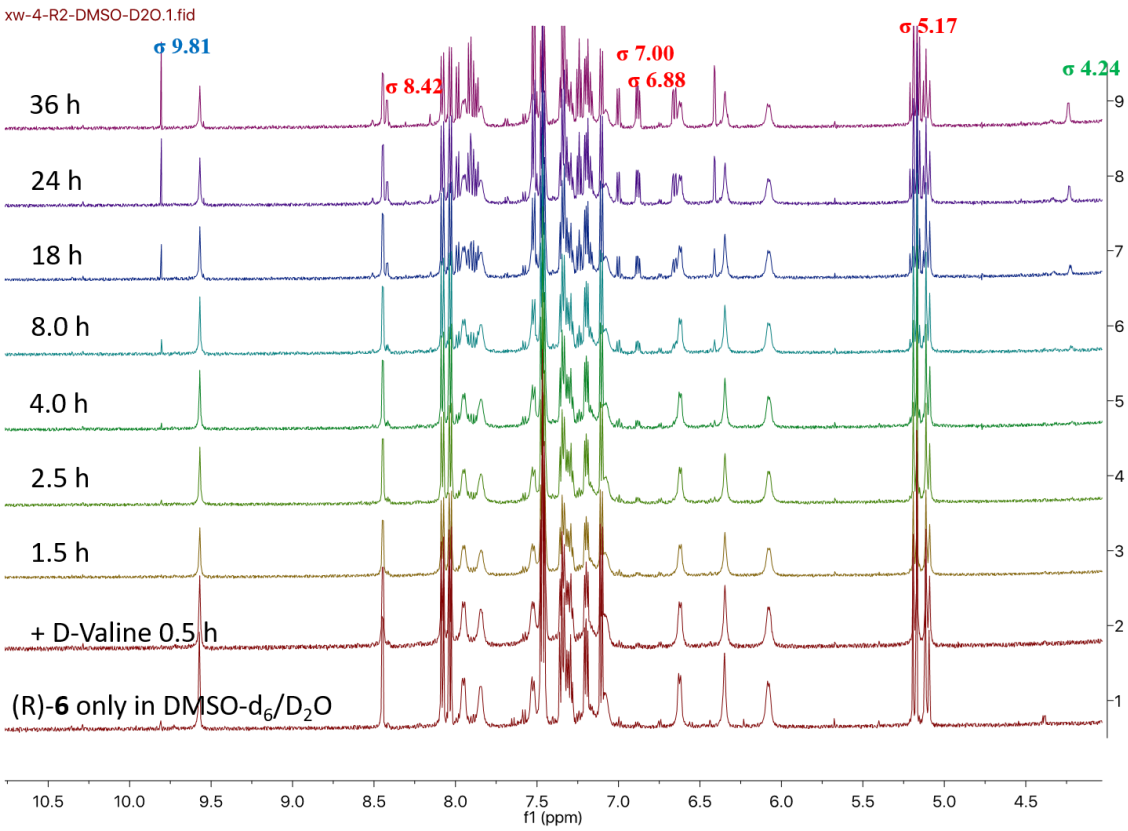
xw-4-R2-DMSO-D2O.1.fid
σ 9.81
σ 8.42
σ 7.00
σ 6.88
σ 5.17
σ 4.24
36 h
24 h
18 h
8.0 h
4.0 h
2.5 h
1.5 h
+ D-Valine 0.5 h
(R)-6 only in DMSO-d6/D2O
10.5
10.0
9.5
9.0
8.5
8.0
7.5
7.0
6.5
6.0
5.5
5.0
4.5
f1 (ppm)

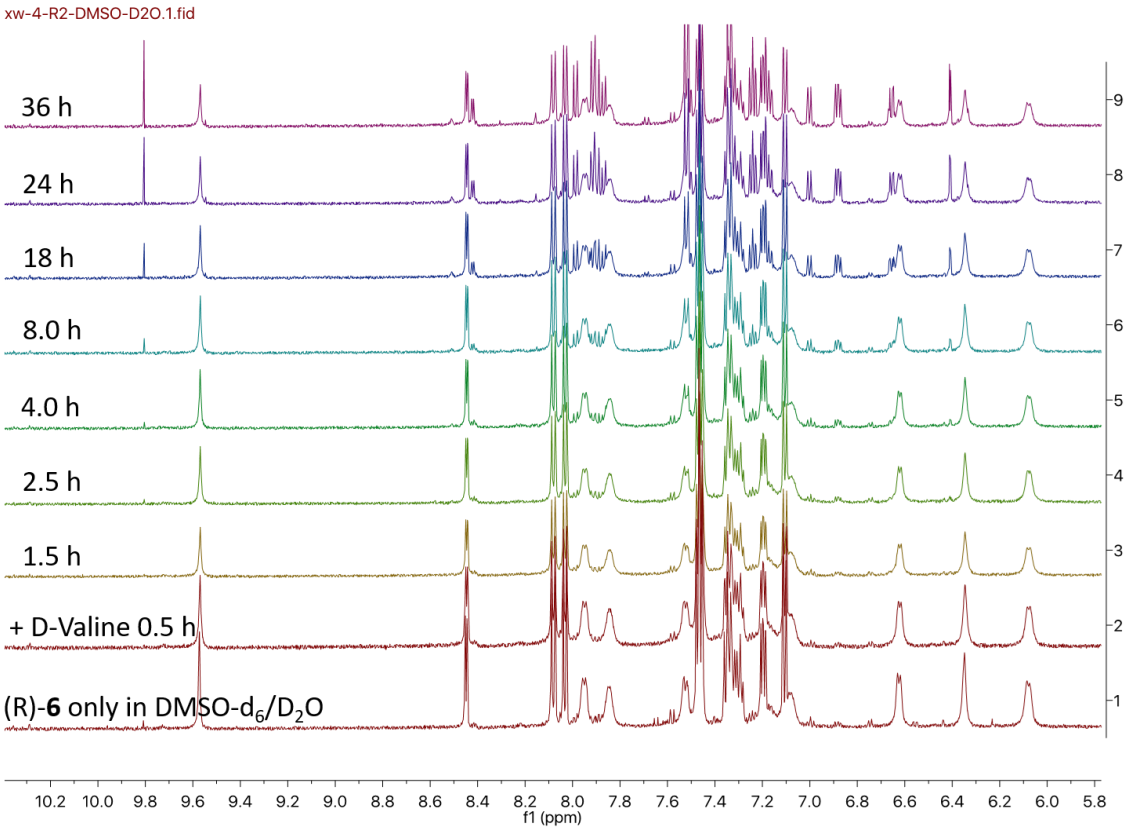
xw-4-R2-DMSO-D2O.1.fid
36 h
24 h
18 h
8.0 h
4.0 h
2.5 h
1.5 h
+ D-Valine 0.5 h
(R)-6 only in DMSO-d6/D2O
10.2 10.0 9.8 9.6 9.4 9.2 9.0 8.8 8.6 8.4 8.2 8.0 7.8 7.6 7.4 7.2 7.0 6.8 6.6 6.4 6.2 6.0 5.8
f1 (ppm)

Figure S5-10b. ^{1}H NMR spectra of (*R*)-**6** (1.0 mM in DMSO-d_6) with L-Val (40 equiv) in HEPES (D_2O, 25 mM HEPES, 120 mM NaCl, pD=7.4). [reaction time: 0.5 – 36 h. DMSO: HEPES = 9:1 (v)].

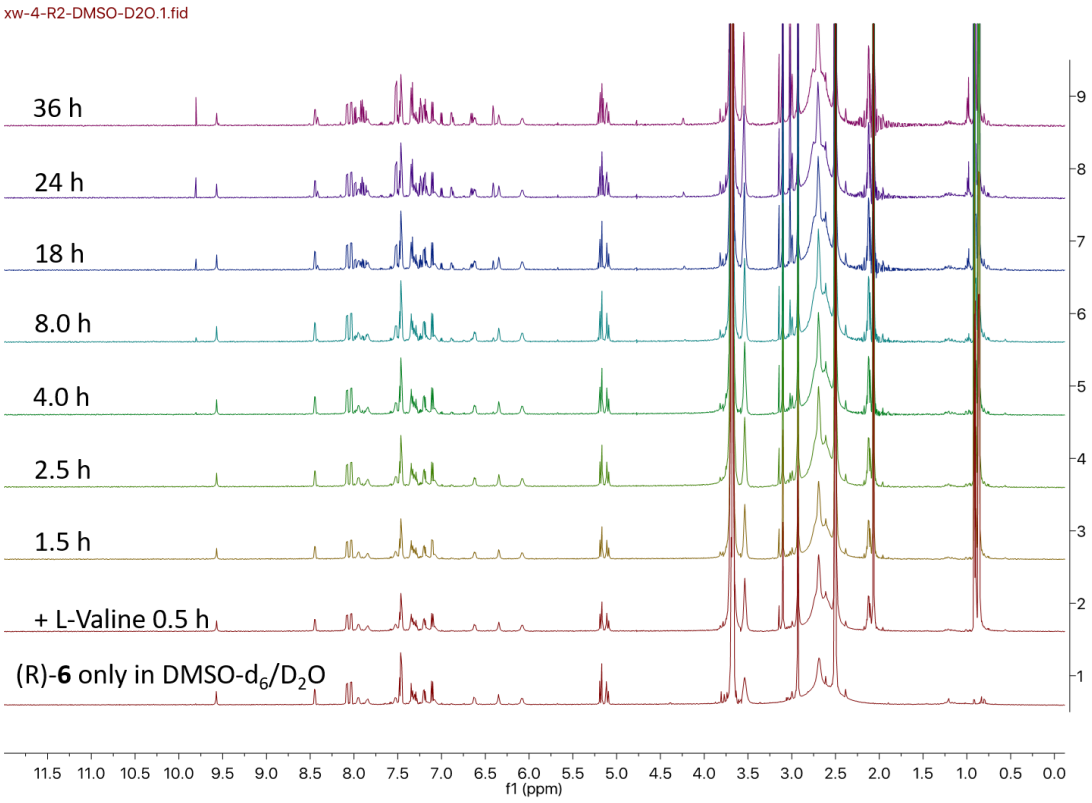

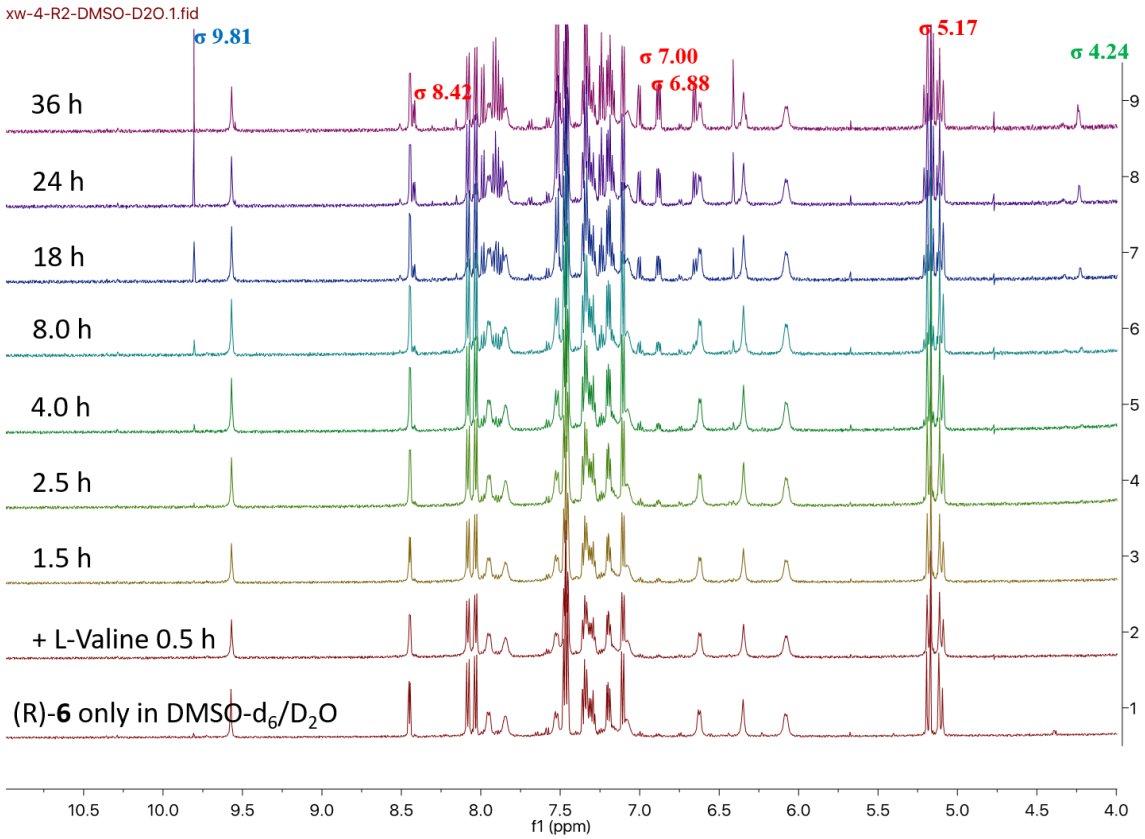
xw-4-R2-DMSO-D2O.1.fid
σ 9.81
σ 8.42
σ 7.00
σ 6.88
σ 5.17
σ 4.24
36 h
24 h
18 h
8.0 h
4.0 h
2.5 h
1.5 h
+ L-Valine 0.5 h
(R)-6 only in DMSO-d6/D2O
f1 (ppm)

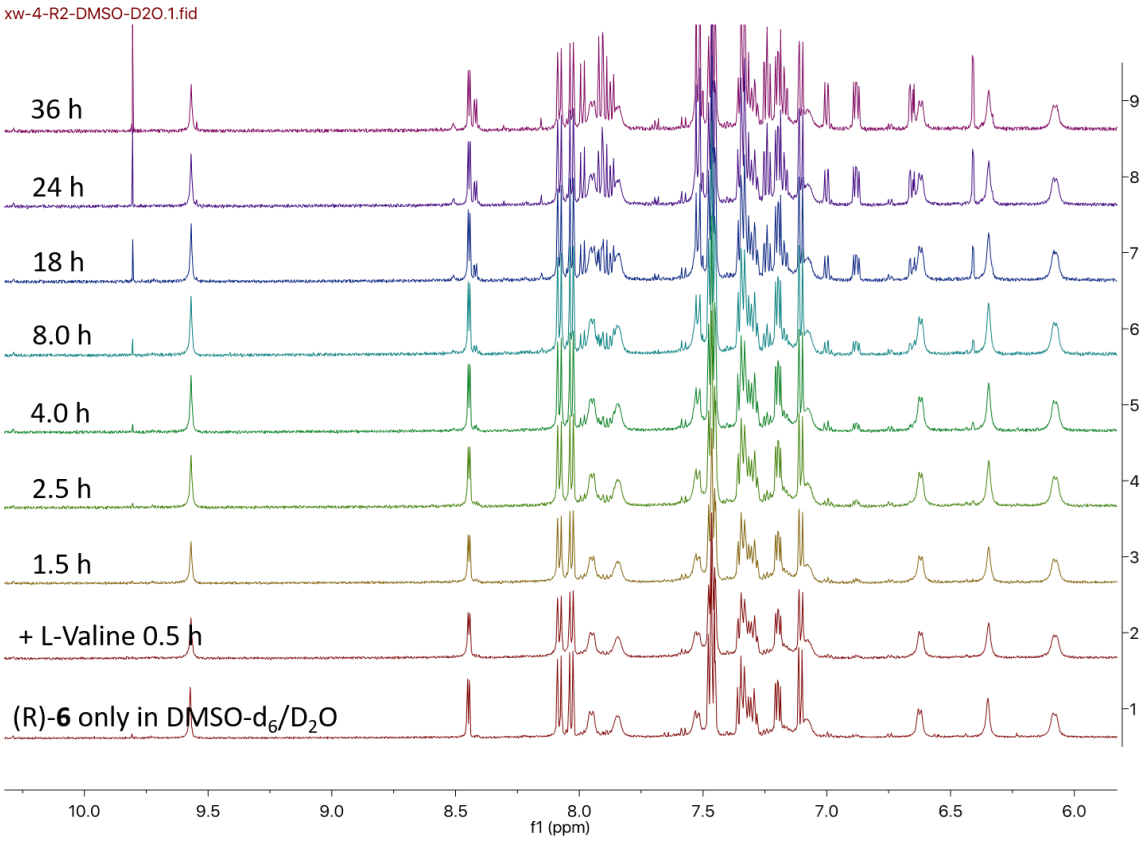
xw-4-R2-DMSO-D2O.1.fid
36 h
24 h
18 h
8.0 h
4.0 h
2.5 h
1.5 h
+ L-Valine 0.5 h
(R)-6 only in DMSO-d6/D2O
f1 (ppm)

Figure S5-11a. ^{1}H NMR spectra of (*S*)-**12** (1.0 mM in DMSO-d_6) with L-Val (20 equiv) in HEPES (D_2O, 25 mM HEPES, 120 mM NaCl, pD=7.4). [reaction time: 0.5 – 30 h. DMSO: HEPES = 9:1 (v).

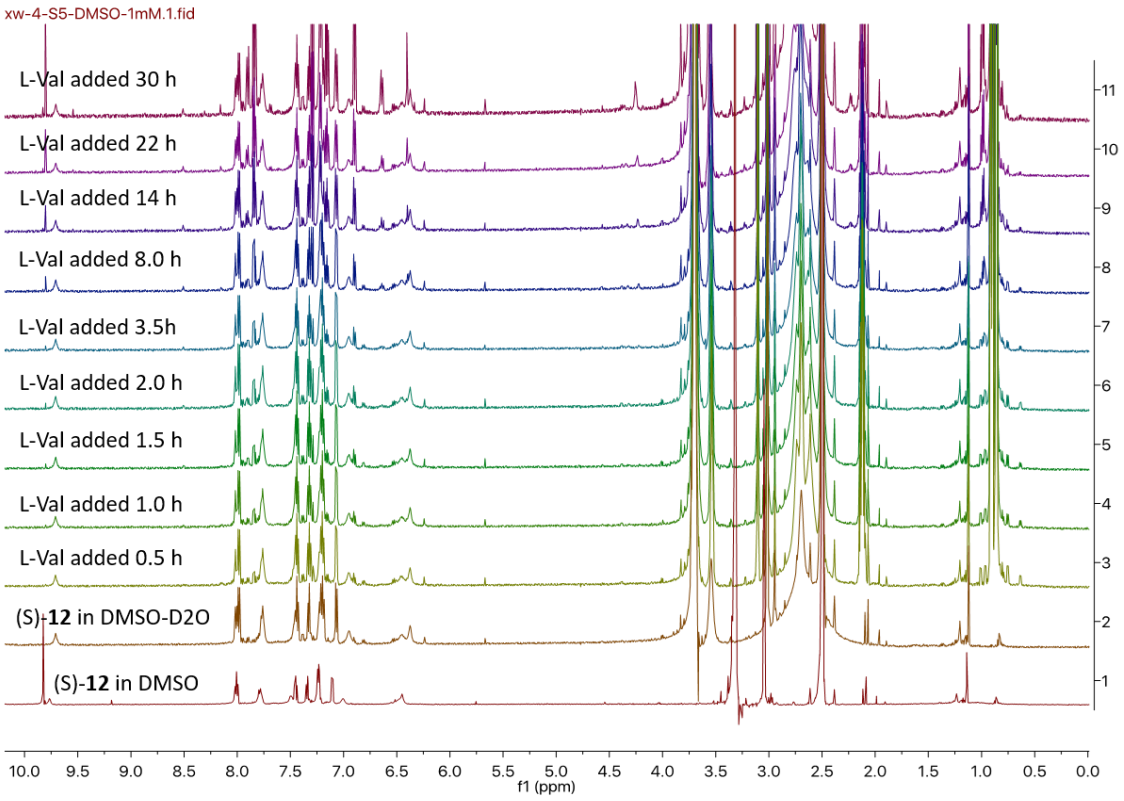

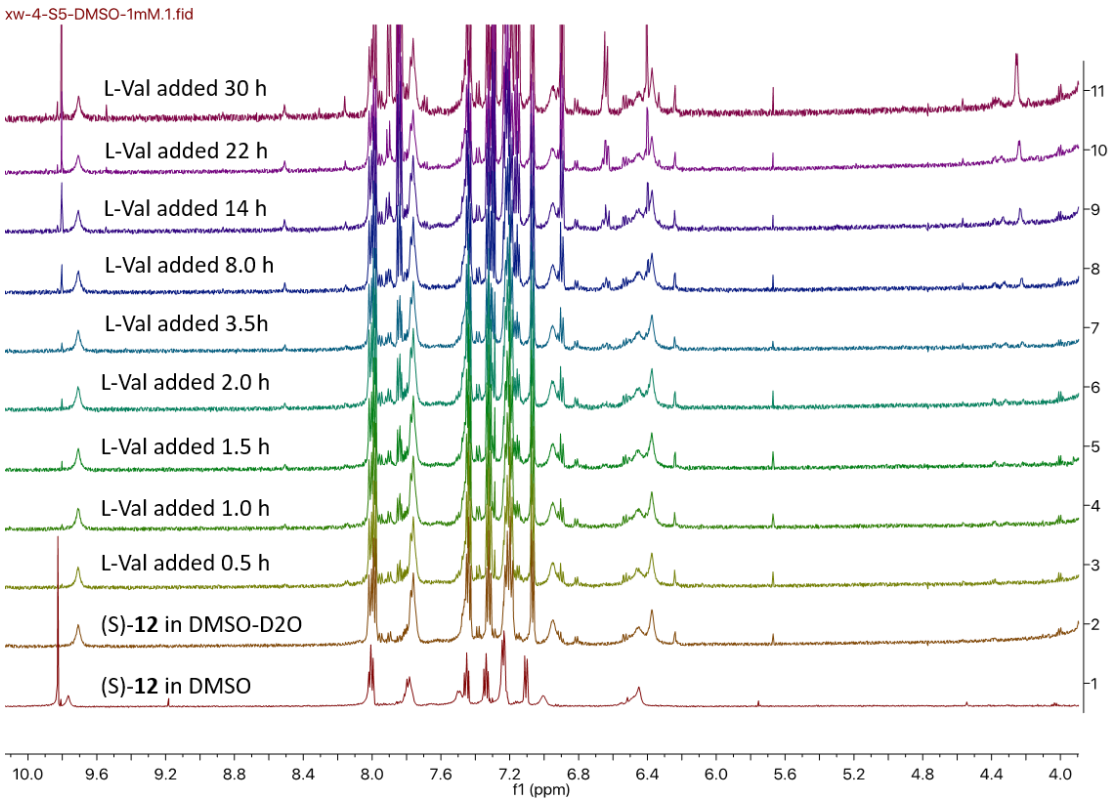
xw-4-S5-DMSO-1mM.1.fid
L-Val added 30 h
L-Val added 22 h
L-Val added 14 h
L-Val added 8.0 h
L-Val added 3.5h
L-Val added 2.0 h
L-Val added 1.5 h
L-Val added 1.0 h
L-Val added 0.5 h
(S)-12 in DMSO-D2O
(S)-12 in DMSO
10.0 9.6 9.2 8.8 8.4 8.0 7.6 7.2 6.8 6.4 6.0 5.6 5.2 4.8 4.4 4.0
f1 (ppm)

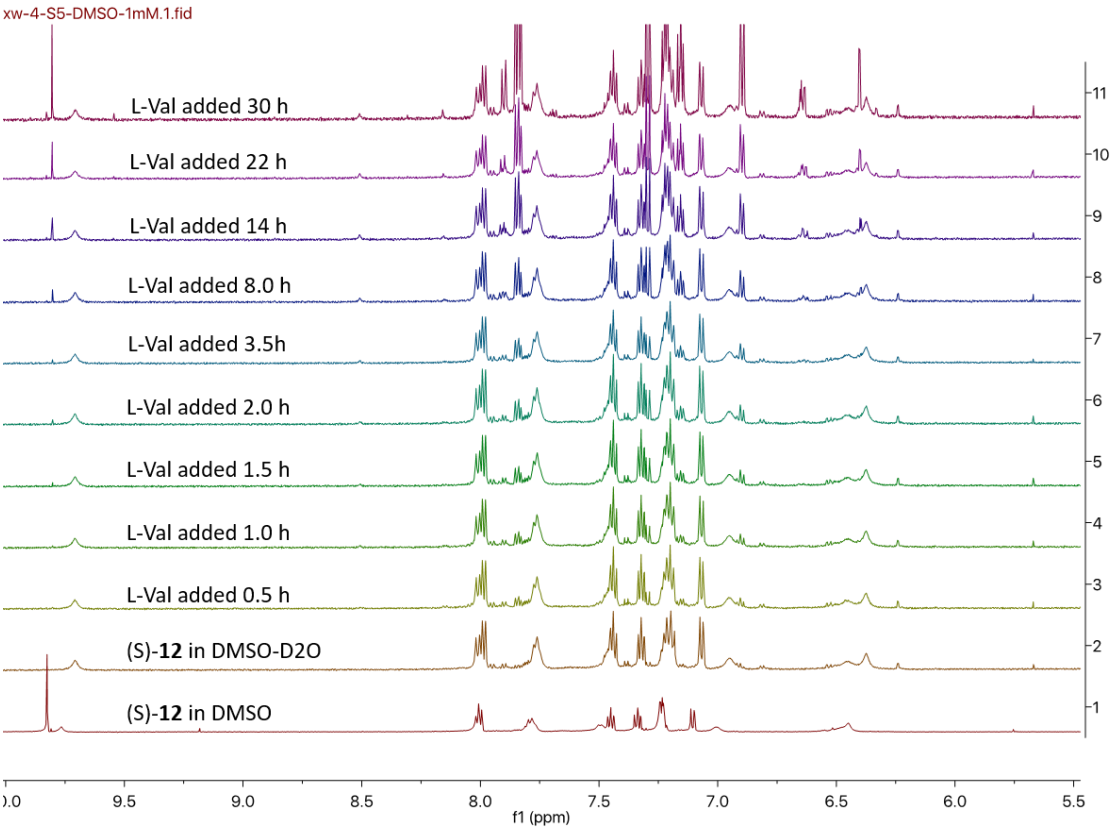
xw-4-S5-DMSO-1mM.1.fid
L-Val added 30 h
L-Val added 22 h
L-Val added 14 h
L-Val added 8.0 h
L-Val added 3.5h
L-Val added 2.0 h
L-Val added 1.5 h
L-Val added 1.0 h
L-Val added 0.5 h
(S)-12 in DMSO-D2O
(S)-12 in DMSO
9.5 9.0 8.5 8.0 7.5 7.0 6.5 6.0 5.5
f1 (ppm)

Figure S5-11b. ^{1}H NMR spectra of (*S*)-**12** (1.0 mM in DMSO-d6) with D-Val (20 equiv) in HEPES (D2O, 25 mM HEPES, 120 mM NaCl, pD=7.4). [reaction time: 0.5 – 30 h. DMSO: HEPES = 9:1 (v).

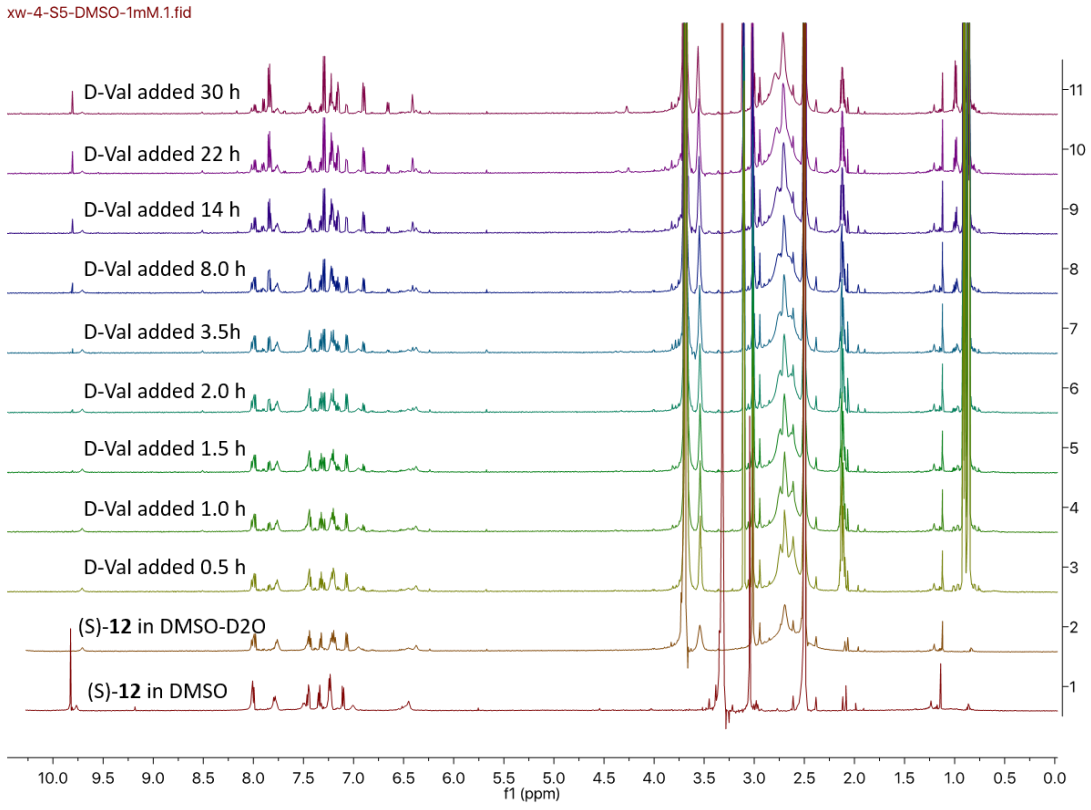

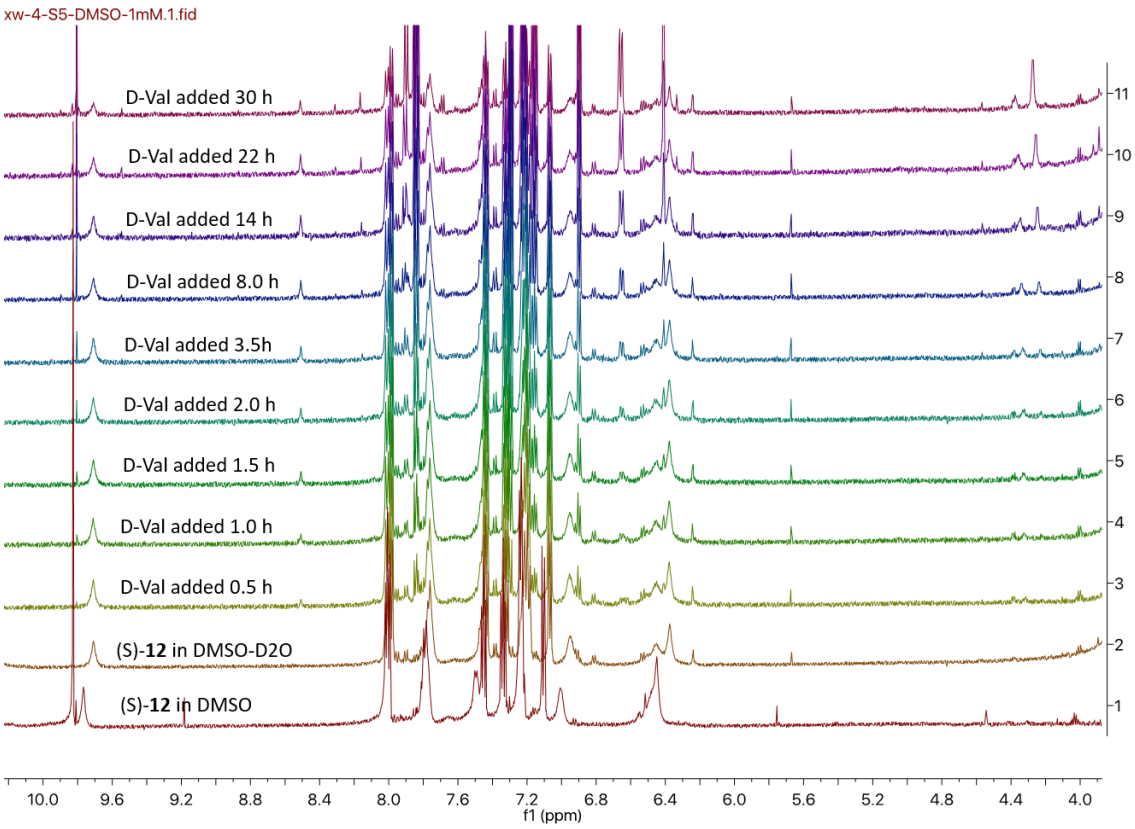
xw-4-S5-DMSO-1mM.1.fid
D-Val added 30 h
D-Val added 22 h
D-Val added 14 h
D-Val added 8.0 h
D-Val added 3.5h
D-Val added 2.0 h
D-Val added 1.5 h
D-Val added 1.0 h
D-Val added 0.5 h
(S)-12 in DMSO-D2O
(S)-12 in DMSO
11
10
9
8
7
6
5
4
3
2
1
10.0 9.6 9.2 8.8 8.4 8.0 7.6 7.2 6.8 6.4 6.0 5.6 5.2 4.8 4.4 4.0
f1 (ppm)

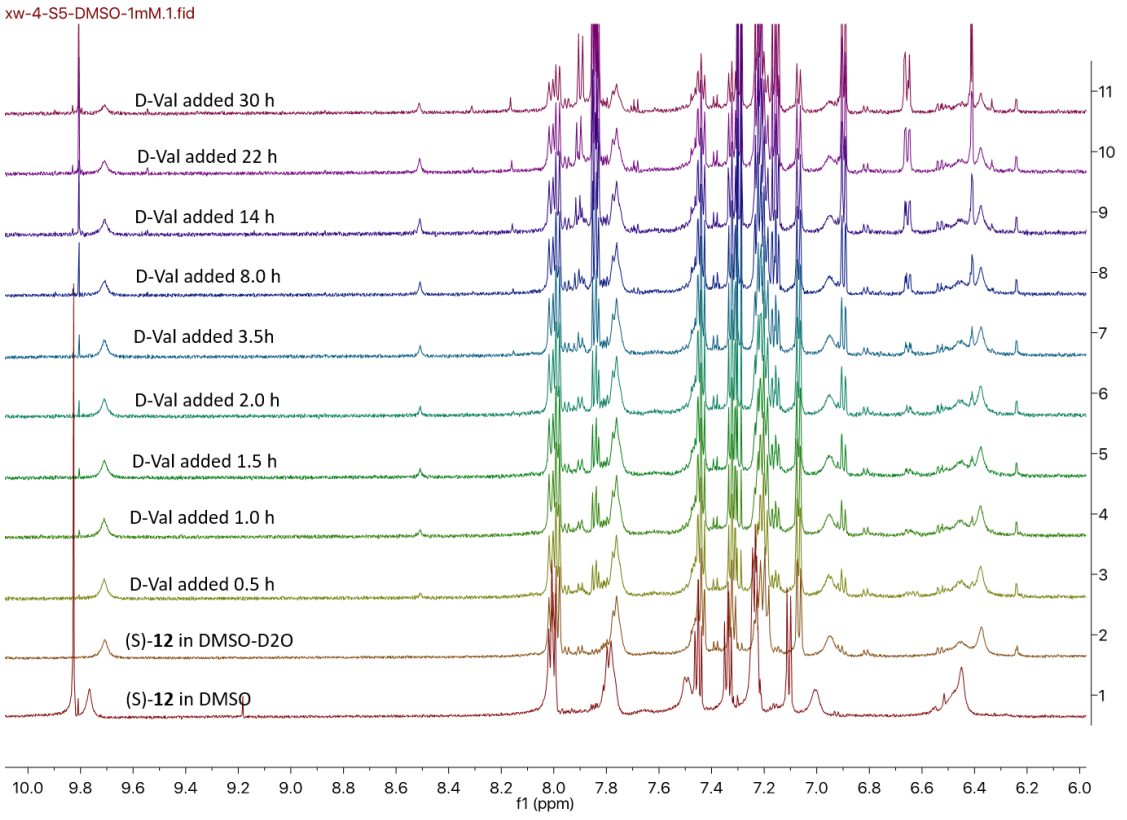
xw-4-S5-DMSO-1mM.1.fid
D-Val added 30 h
D-Val added 22 h
D-Val added 14 h
D-Val added 8.0 h
D-Val added 3.5h
D-Val added 2.0 h
D-Val added 1.5 h
D-Val added 1.0 h
D-Val added 0.5 h
(S)-12 in DMSO-D2O
(S)-12 in DMSO
11
10
9
8
7
6
5
4
3
2
1
10.0 9.8 9.6 9.4 9.2 9.0 8.8 8.6 8.4 8.2 8.0 7.8 7.6 7.4 7.2 7.0 6.8 6.6 6.4 6.2 6.0
f1 (ppm)

Figure S5-11c. ^{1}H NMR spectrum of (*S*)-**7** [1.0 mM in DMSO-d_6 and HEPES (D_2O), 25 mM HEPES, 120 mM NaCl, pD = 7.4, DMSO: HEPES = 9: 1 (v)].

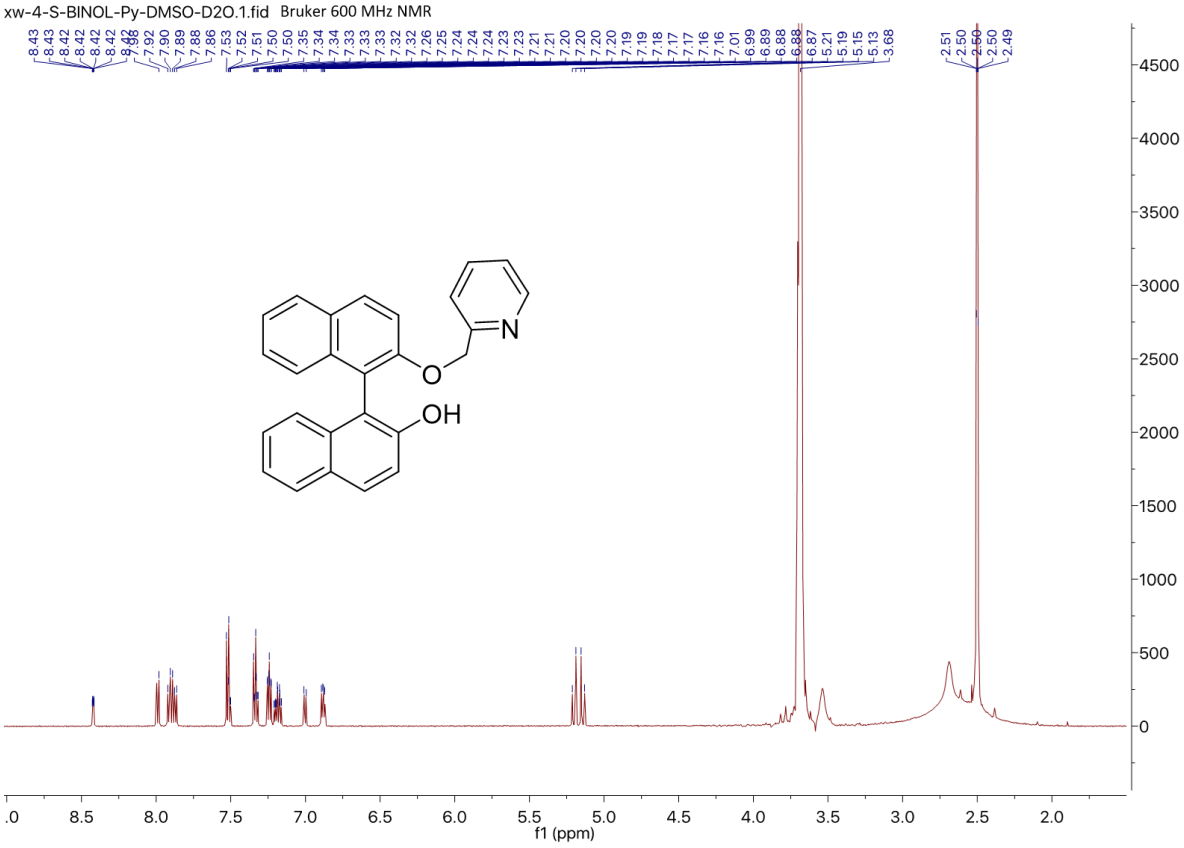

Figure S5-11d. ^{1}H NMR spectra of (S)-**7** (a), (*S*)-**6** with D-Valine (40 equiv, 36 h) (b), (*S*)-**6** with L-Valine (40 equiv, 36 h) (c), (*S*)-**12** with D-Val (20 equiv, 30h) (d), (*S*)-**12** with L-Val (20 equiv, 30h) (e), and product mixture of **8** and L-Val (40 equiv, 24h) (f) in (all 1.0 mM in DMSO-d_6 and HEPES [D_2O, 25 mM HEPES, 120 mM NaCl, pD = 7.4, DMSO:HEPES = 9:1 (v)].

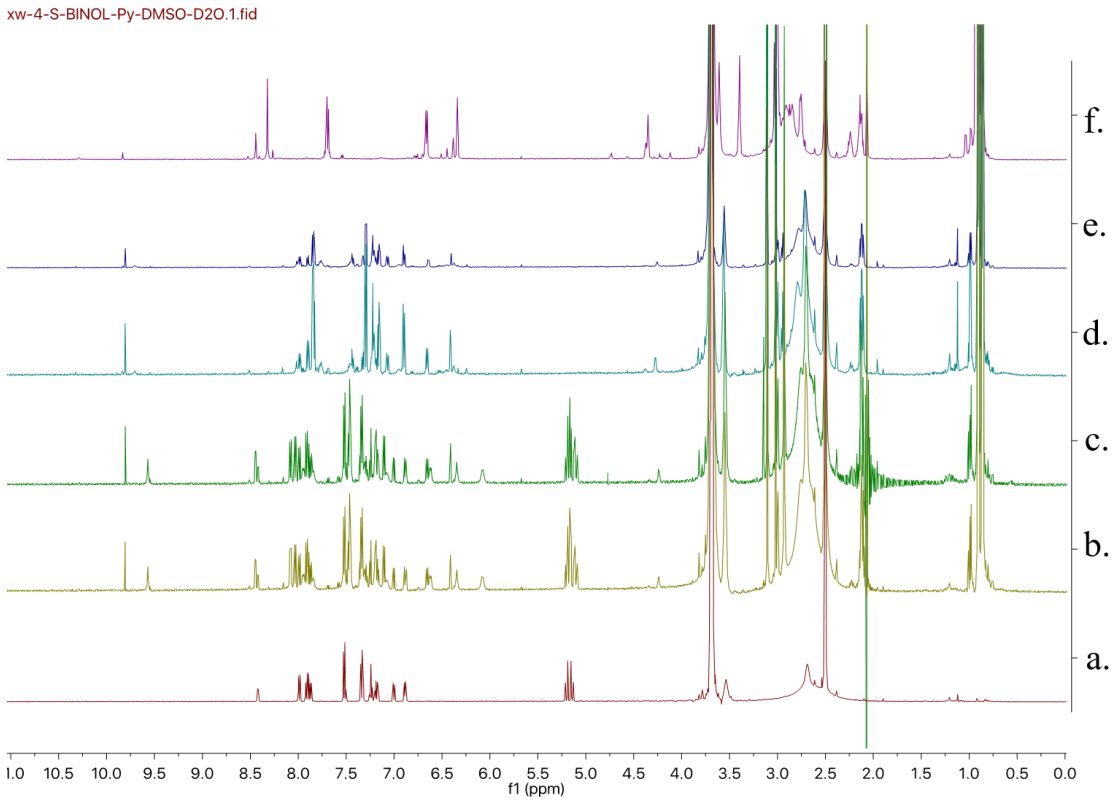
xw-4-S-BINOL-Py-DMSO-D2O.1.fid
f.
e.
d.
c.
b.
a.
f1 (ppm)

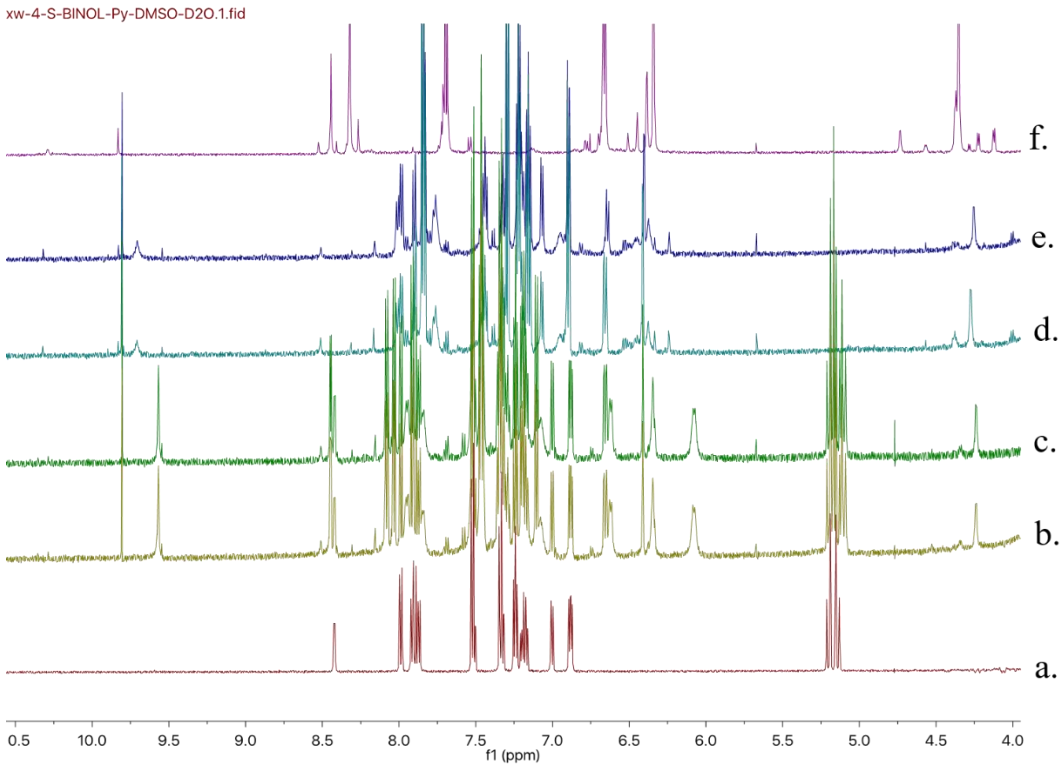
xw-4-S-BINOL-Py-DMSO-D2O.1.fid
f.
e.
d.
c.
b.
a.
f1 (ppm)

2 Synthesis and characterization of 8

Figure S5-12a. ^{1}H NMR spectrum of the products of **4** and L-Val (1.0 equiv, 1.0 mM in DMSO-d6, reaction time: 55 h.)

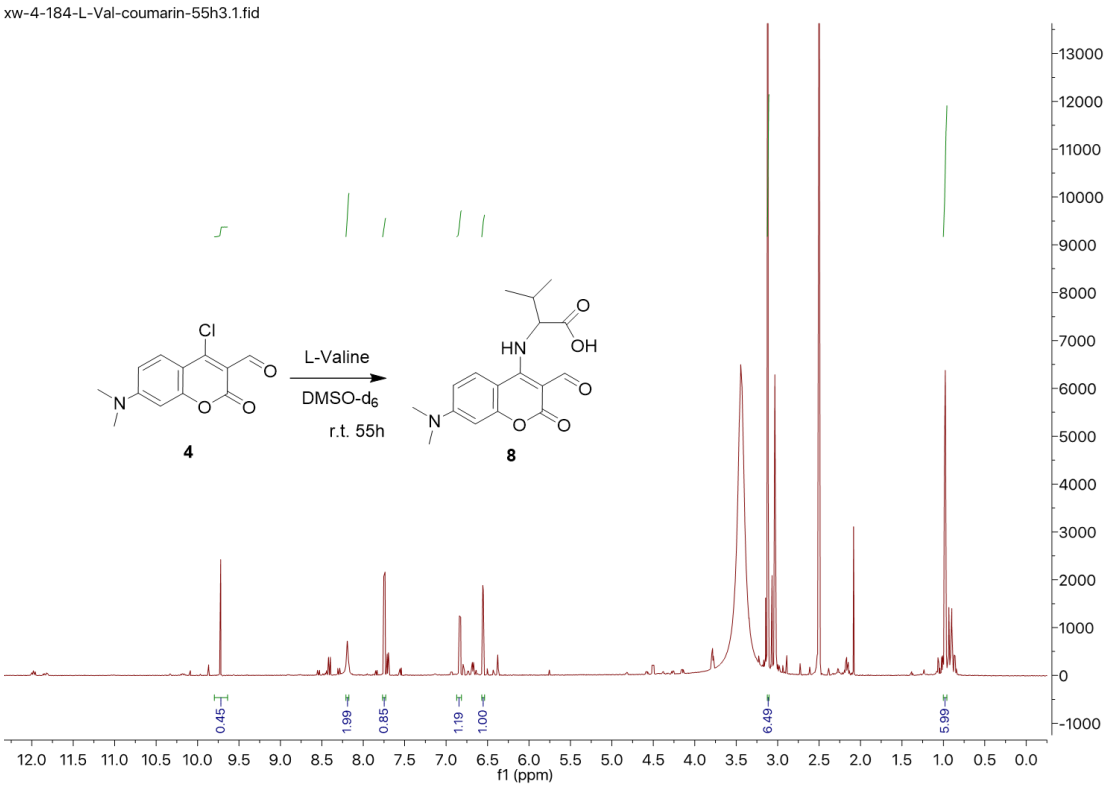

Figure S5-12b. ^{1}H NMR spectrum of **8** (generated by the reaction of **4** with L-Val, 1.0 equiv, 1.0 mM in DMSO-d6, reaction time: 55 h.) in DMSO-d6/D_2O, 9/1 (v).

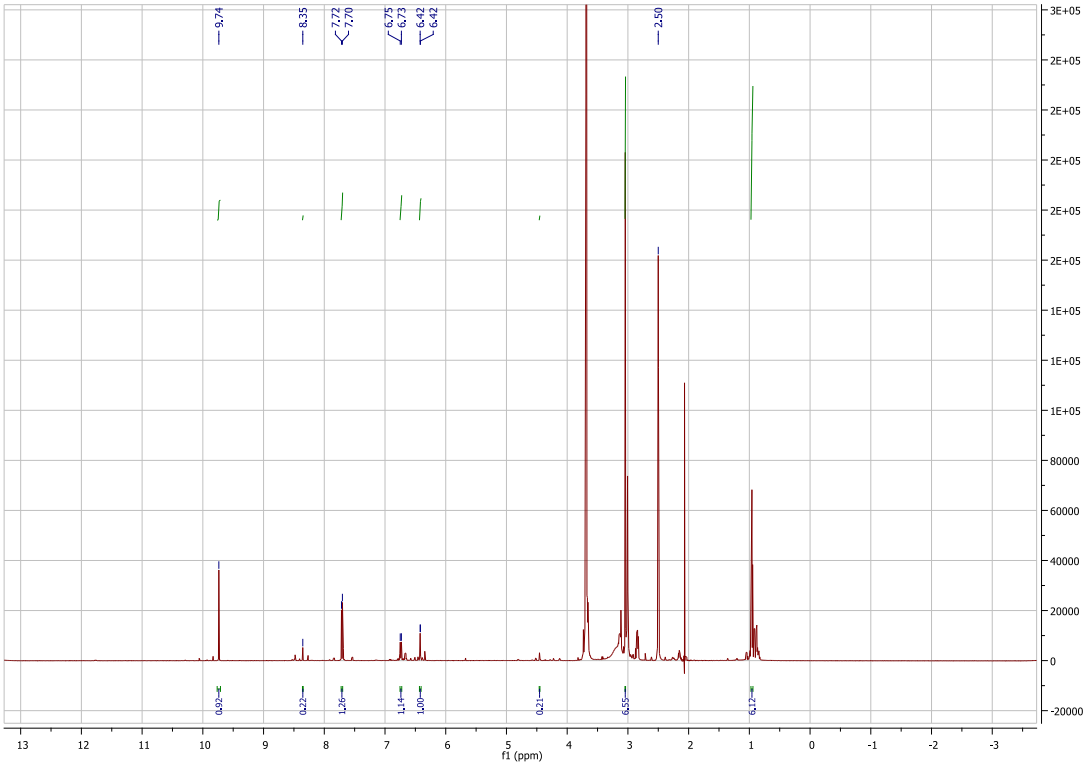

Figure S5-13a. HRMS spectrum of the major product **8** from the reaction above

Qualitative Analysis Report

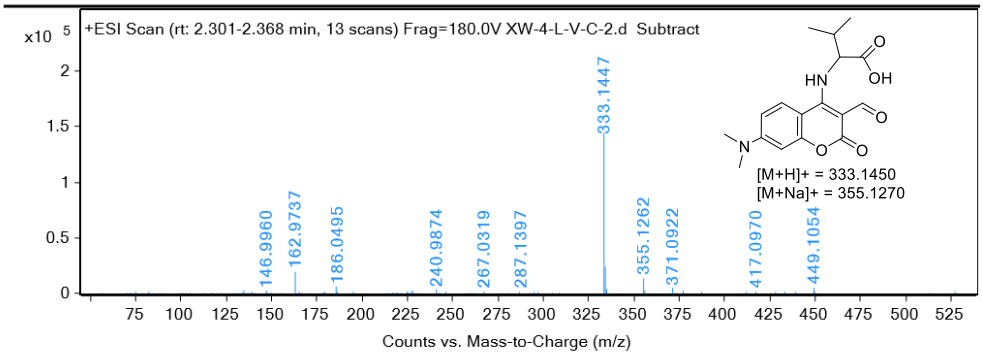

Peak List

m/z	z	Abund
134.9562		1861.23
146.996		2359
162.9737		19045.34
186.0495		5651.02
225.0099		1510.01
225.056		1812.08
228.0256		2169.99
240.9874		3088.29
267.0319		1784.47
287.1397		1556.72
333.1447	1	144377.58
334.1478	1	24260.56
335.1502	1	3328.23
355.1262	1	13439.72
356.1295	1	2422.26
371.0922		4618.07
377.1084		2179.67
417.097		1489.9
449.1054		5406.43

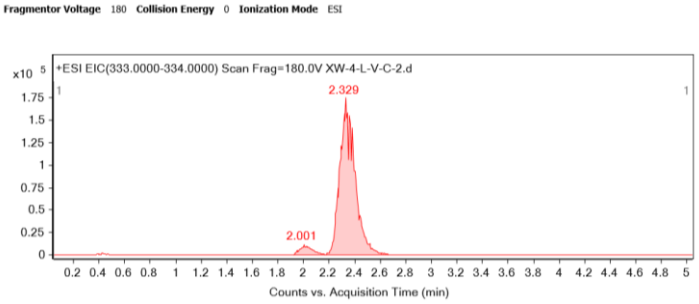

Integration Peak List

Peak	Start	RT	End	Height	Area	Area %
1	1.923	2.001	2.168	11176.54	71822.52	5.13
2	2.173	2.329	2.662	175632.3	1399393.24	100

Figure S5-13b. HRMS Spectra of the minor product **9** from the reaction above

Qualitative Analysis Report

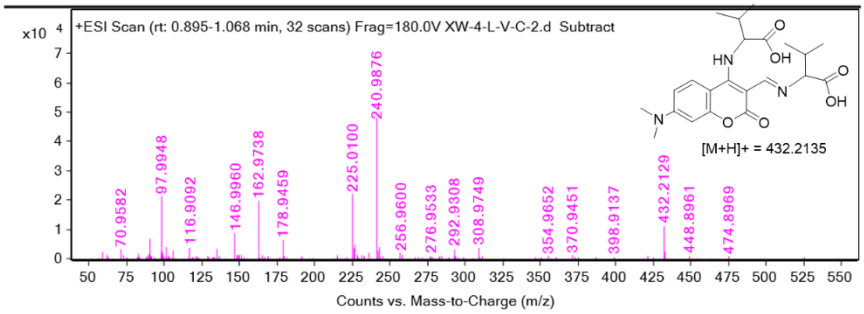

Peak List

m/z	z	Abund
70.9582		3008.81
90.4831	2	6782.57
97.9948	2	21254.31
98.4693	2	2618.42
101.0033		4059.57
105.9809		2859.36
116.9092		3686.07
134.9197		3057.14
146.996	1	8632.43
162.9738		19667.25
178.9459		6286.81
225.01	1	21979.41
226.0114	1	3602.78
227.0072	1	4657.5
240.9876	1	47939.37
241.9903	1	2795.13
242.9837	1	3784.74
292.9308	1	3356.78
308.9749		3559.83
432.2129	1	11084.9

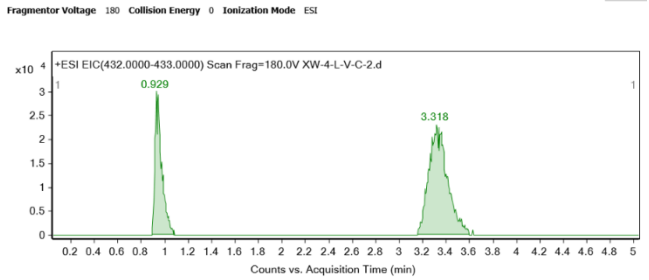

Integration Peak List

Peak	Start	RT	End	Height	Area	Area %
1	0.89	0.929	1.073	30047.1	116496.08	46.32
2	3.157	3.318	3.595	22997.02	251521.78	100

Qualitative Analysis Report

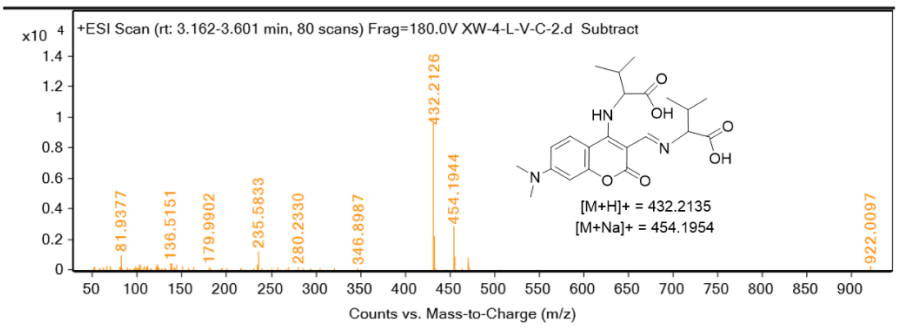

Peak List

m/z	z	Abund
68.9826		267.21
81.9377		966.89
97.9917		233.69
102.0131		322.88
103.9557		286.94
112.0062		223.67
121.062		223.65
122.9639		320.21
136.5151	2	399.21
138.9638		376.21
143.9967		280.9
234.0762		281.08
235.5833	2	1206.76
432.2126	1	9565.11
433.2157	1	2179.43
454.1944	1	2800.13
455.1942	1	847.81
470.1605		484.4
471.1159	1	788.2
922.0097		233.15

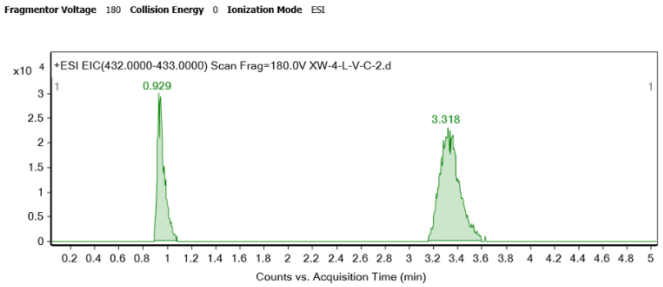

Integration Peak List

Peak	Start	RT	End	Height	Area	Area %
1	0.89	0.929	1.073	30047.1	116496.08	46.32
2	3.157	3.318	3.595	22997.02	251521.78	100

3 ^{1}H NMR and mass spectroscopic study of 8 with L-Val

Figure S5-14a. ^{1}H NMR spectra for the reaction of **8** (as the major compound, 1.0 mM in DMSO-d_6) with L-Val (40 equiv) in HEPES (D_2O, 25 mM HEPES, 120 mM NaCl, pH=7.4). [reaction time: 0.5 – 24 h. DMSO: HEPES = 9:1 (v)].

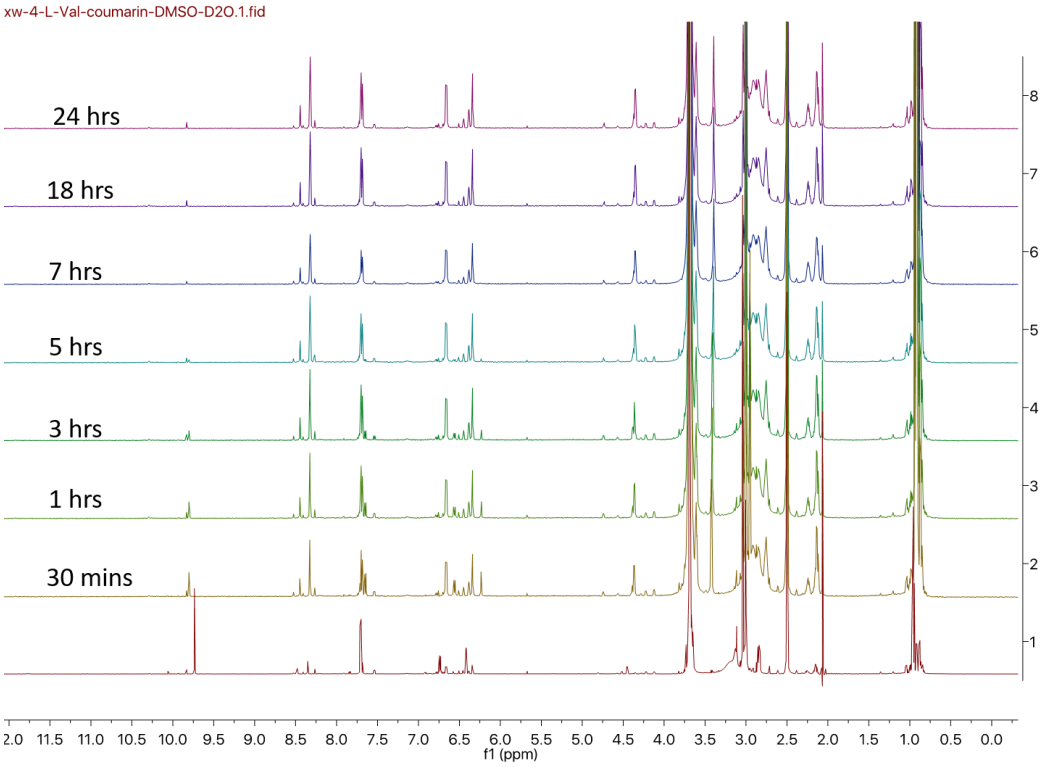

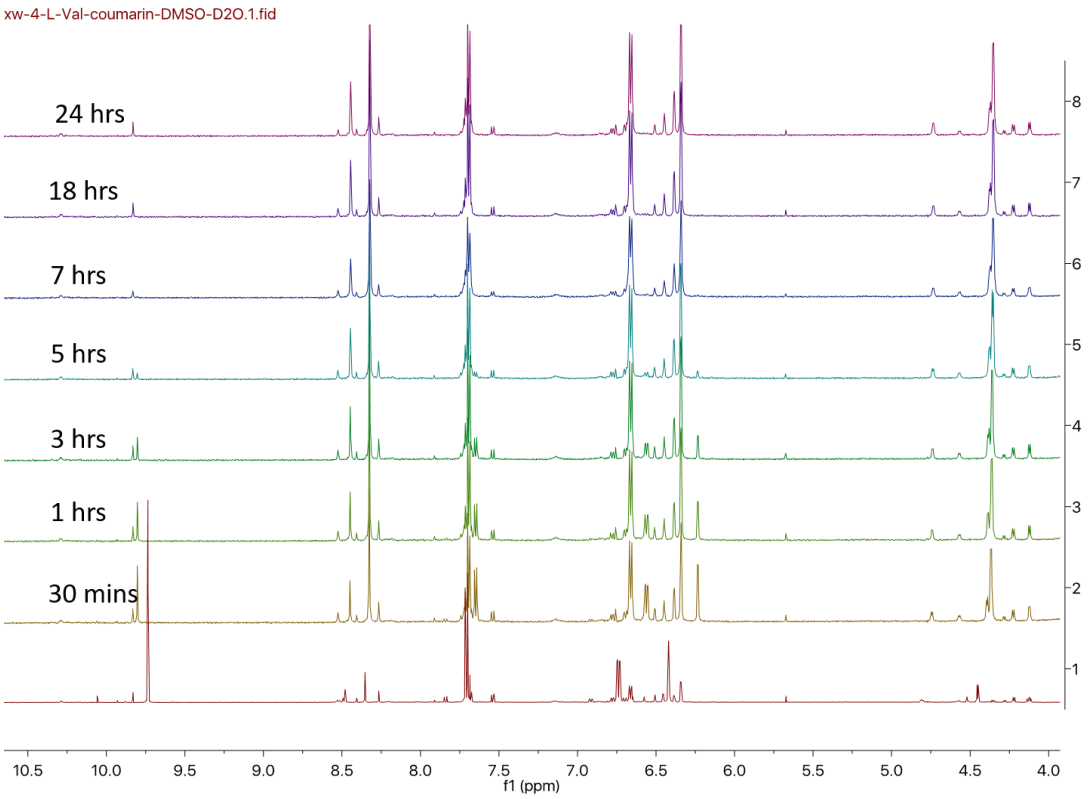
xw-4-L-Val-coumarin-DMSO-D2O.1.fid
24 hrs
18 hrs
7 hrs
5 hrs
3 hrs
1 hrs
30 mins
10.5
10.0
9.5
9.0
8.5
8.0
7.5
7.0
6.5
6.0
5.5
5.0
4.5
4.0
f1 (ppm)
8
7
6
5
4
3
2
1

Figure S5-14b. ^{1}H NMR spectrum of the product **9** from the reaction of **8** (as the major compound, 1.0 mM in DMSO-d_6) with L-Val (40 equiv) in HEPES (D_2O, 25 mM HEPES, 120 mM NaCl, pH=7.4). [reaction time: 24 h. DMSO: HEPES = 9:1 (v).

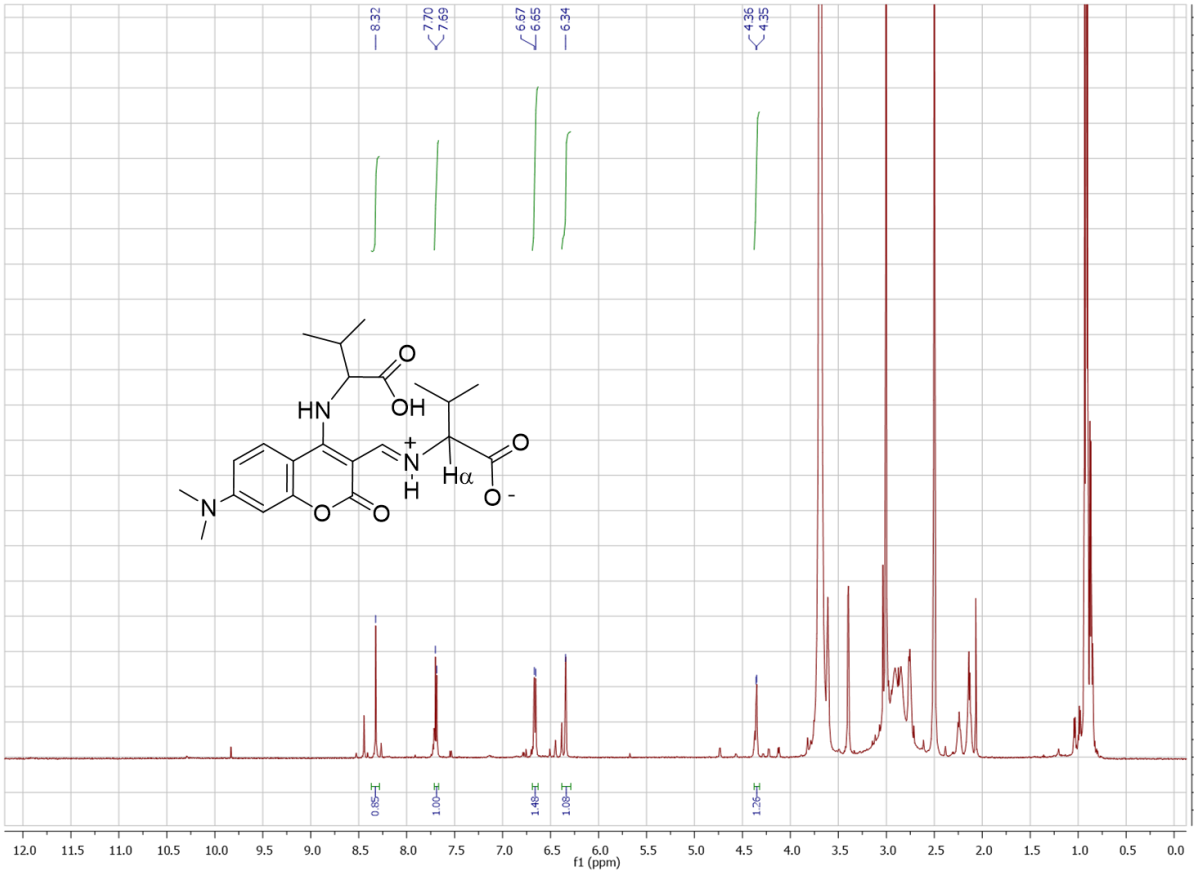

Figure S5-15a. HRMS spectrum of **9** in the above NMR experiment mixture after 24 h by reacting **8** (~1 mM) with L-valine (40 mM) in D_2O HEPES buffer.

Qualitative Plot Window Report

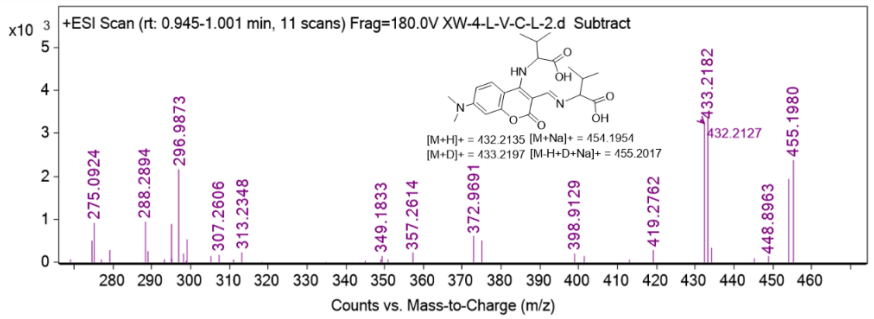

Peak List

m/z	z	Abund
71.9296		4487.88
81.9377		1580.01
112.9557		2169.97
116.9682		1247.3
120.9846		774.28
121.0509	1	2729.74
214.2523		1050.03
214.9174		1127.36
216.978		805.08
218.9734		829.18
250.1776		3352.22
261.1097	1	4357.44
288.2894		1633.56
294.9916		842.43
296.9872	1	2159.72
432.2129		2851.4
433.2183	1	2932.5
454.195		1666.93
455.1977		2113.43
922.0095	1	3169.82

Fragmentor Voltage 180 **Collision Energy** 0 **Ionization Mode** ESI

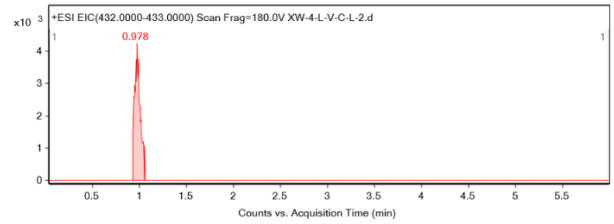

Integration Peak List

Peak	Start	RT	End	Height	Area	Area %
1	0.928	0.978	1.051	4269.18	17268.4	100

Figure S5-15b. HRMS spectrum of **8** in the above NMR experiment mixture after 24 h by reacting **8** (~1 mM) L-valine (40 mM) in D_2O HEPES buffer.

Qualitative Analysis Report

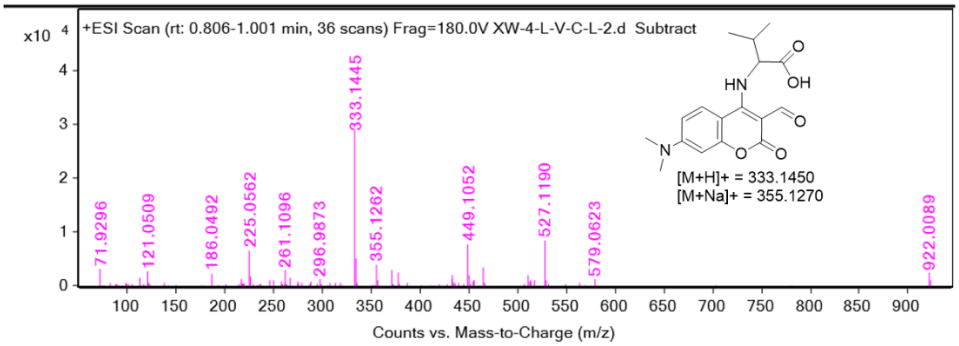

Peak List

m/z	z	Abund
71.9296		3096.6
112.9557		1393.93
121.0509		2556.8
186.0492		2184.08
225.0562	2	6549.12
225.5586	2	1601.9
261.1096		2824.88
333.1445	1	29020.36
334.1479	1	5094.58
355.1262	1	3914.95
371.0918	1	2789.1
377.1084	1	2509.93
433.1276	1	1900.77
449.1052	1	7737.98
450.1095	1	1903.07
465.0774	1	3248.68
511.1416	1	1882.74
527.119	1	8349.41
528.1219	1	1945.89
922.0089	1	2379.71

Qualitative Analysis Report

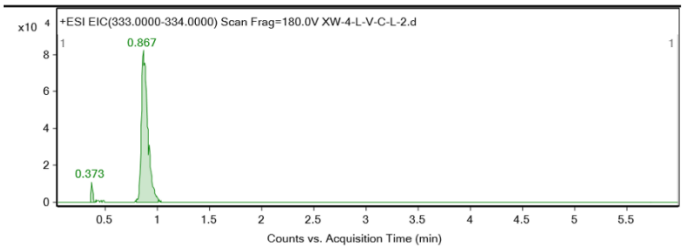

Integration Peak List

Peak	Start	RT	End	Height	Area	Area %
1	0.356	0.373	0.395	10745.99	12725.29	3.64
2	0.795	0.867	1.012	82420.13	350014.53	100

4 Fluorescence spectra of 8 and 9

Figure S5-16. Fluorescence spectra of the crude product mixtures of **8** and **9** [in DMSO-d_6 (90%) and HEPES in D_2O (10%) and diluted with HEPES buffer in H_2O to 1 - 10 µM, λ_{exc} = 365 nm, slits: 3/3 nm].

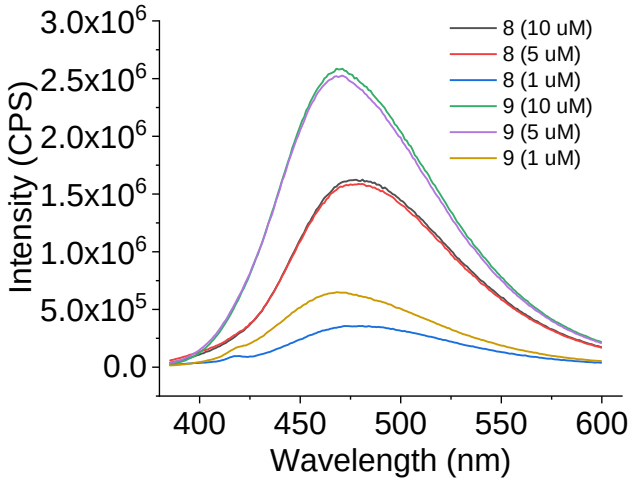

Figure S5-17. Fluorescence spectra of the crude product mixtures of **8** and **9** [in DMSO-d_6 (90%) and HEPES in D_2O (10%) and diluted with HEPES buffer in H_2O to 1 - 10 µM, λ_{exc} = 467 nm, slits: 3/3 nm].

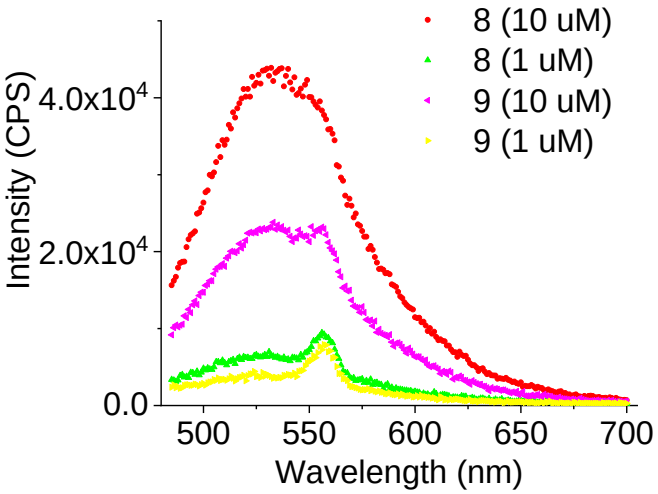

5 High-resolution mass spectroscopic study on the reaction of (*S*)-6 with valine

Figure S5-18a. HRMS spectra for the reaction of (*S*)-**6** (1.0 mM in DMSO) with L-Valine (100 equiv) in HEPES in a 1:1 volume ratio. (reaction time: 2 h, then diluted to 1×10^{-5} M probe with H_2O before direct flow injection)

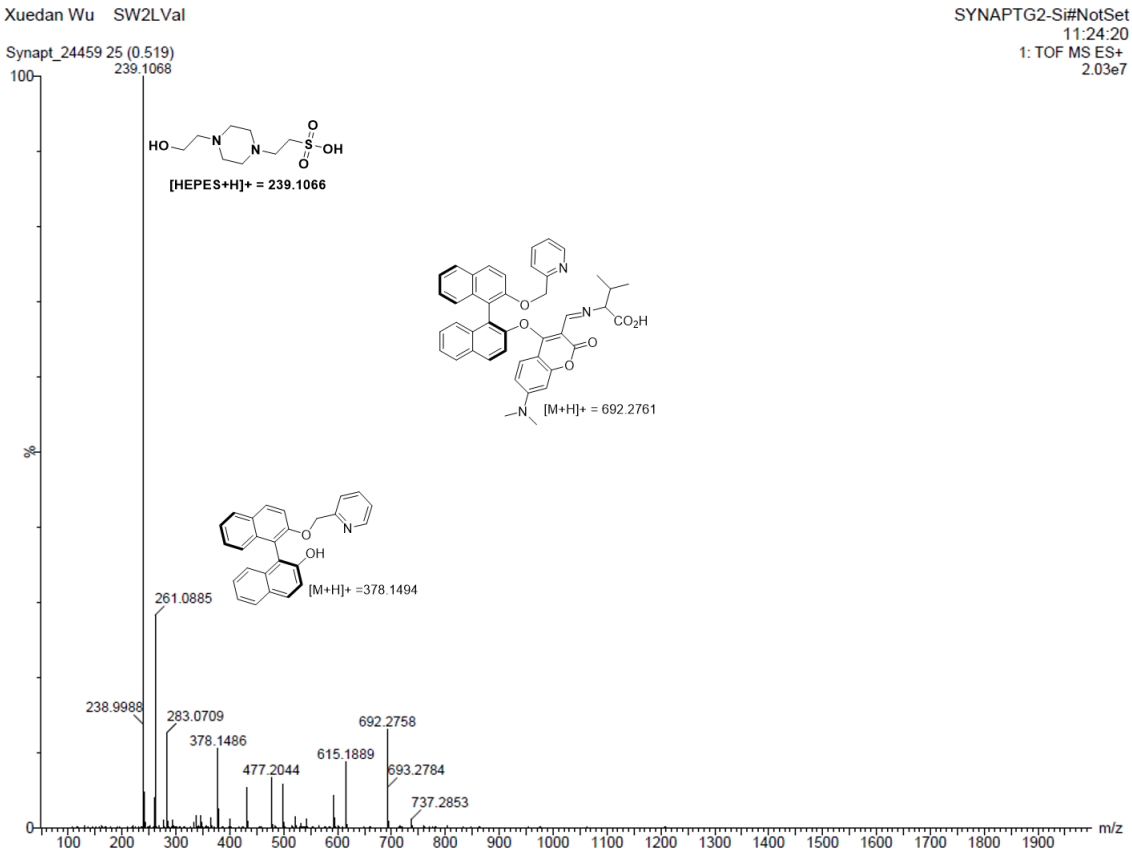

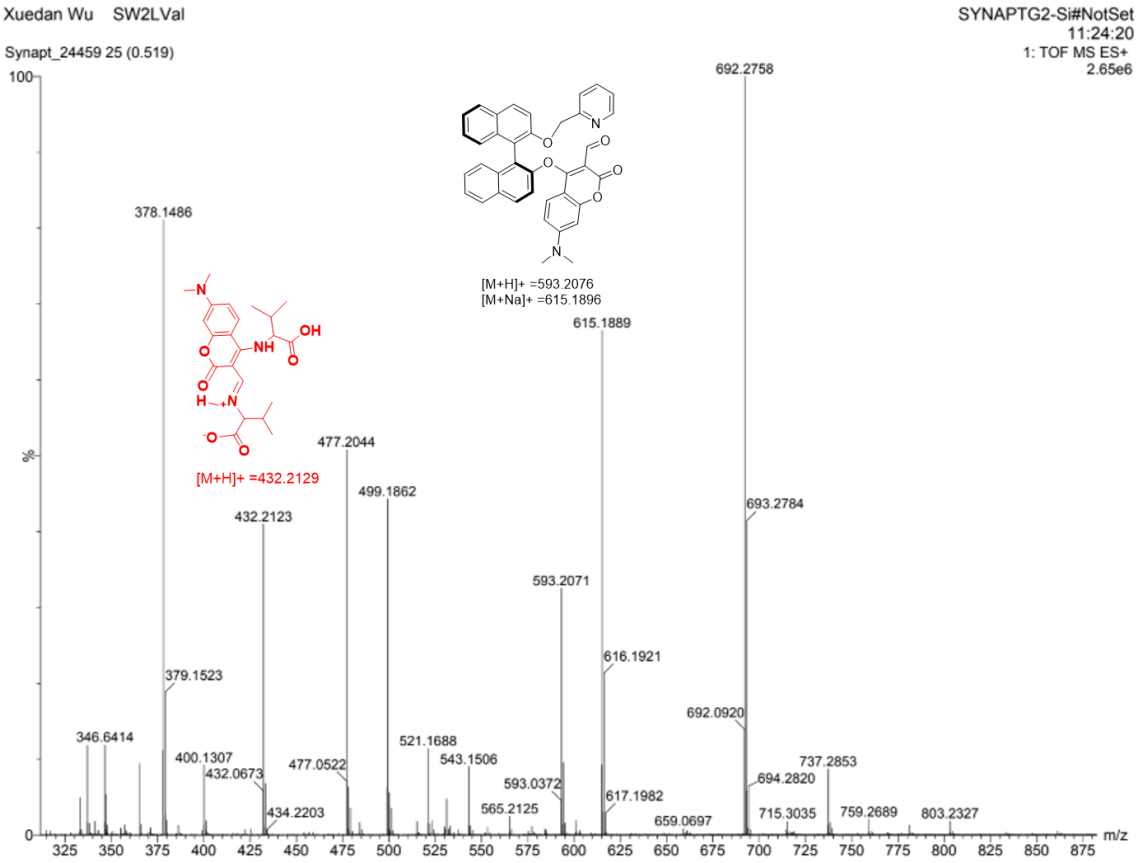
Xuedan Wu SW2LVal
Synapt_24459 25 (0.519)
SYNAPTG2-Si#NotSet
11:24:20
1: TOF MS ES+
2.65e6
100
%
0
[M+H]+ =593.2076
[M+Na]+ =615.1896
[M+H]+ =432.2129
692.2758
378.1486
615.1889
477.2044
499.1862
693.2784
432.2123
593.2071
616.1921
379.1523
692.0920
346.6414
521.1688
543.1506
737.2853
400.1307
432.0673
477.0522
694.2820
593.0372
617.1982
565.2125
715.3035
759.2689
803.2327
434.2203
659.0697
325 350 375 400 425 450 475 500 525 550 575 600 625 650 675 700 725 750 775 800 825 850 875
m/z

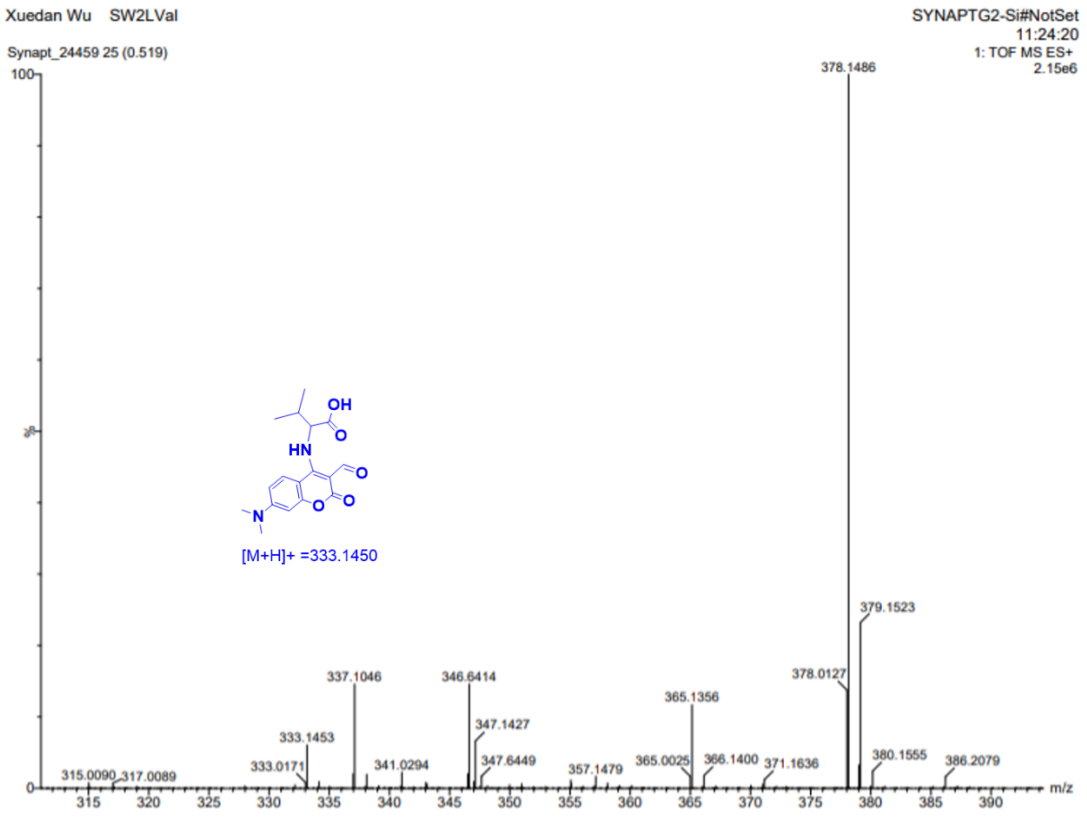
Xuedan Wu SW2LVal
SYNAPTG2-Si#NotSet
11:24:20
Synapt_24459 25 (0.519)
1: TOF MS ES+
2.15e6
100
%
0
OH
O
HN
O
O
O
N
[M+H]+ =333.1450
378.1486
379.1523
337.1046
346.6414
378.0127
365.1356
347.1427
333.1453
315.0090
317.0089
333.0171
341.0294
347.6449
357.1479
365.0025
366.1400
371.1636
380.1555
386.2079
315
320
325
330
335
340
345
350
355
360
365
370
375
380
385
390
m/z

Figure S5-18b. HRMS spectra for the reaction of (*S*)-**6** (1.0 mM in DMSO) with D-Valine (100 equiv) in HEPES in a 1:1 volume ratio. (reaction time: 2 h, then diluted to 1×10^{-5} M probe with H_2O before direct flow injection)

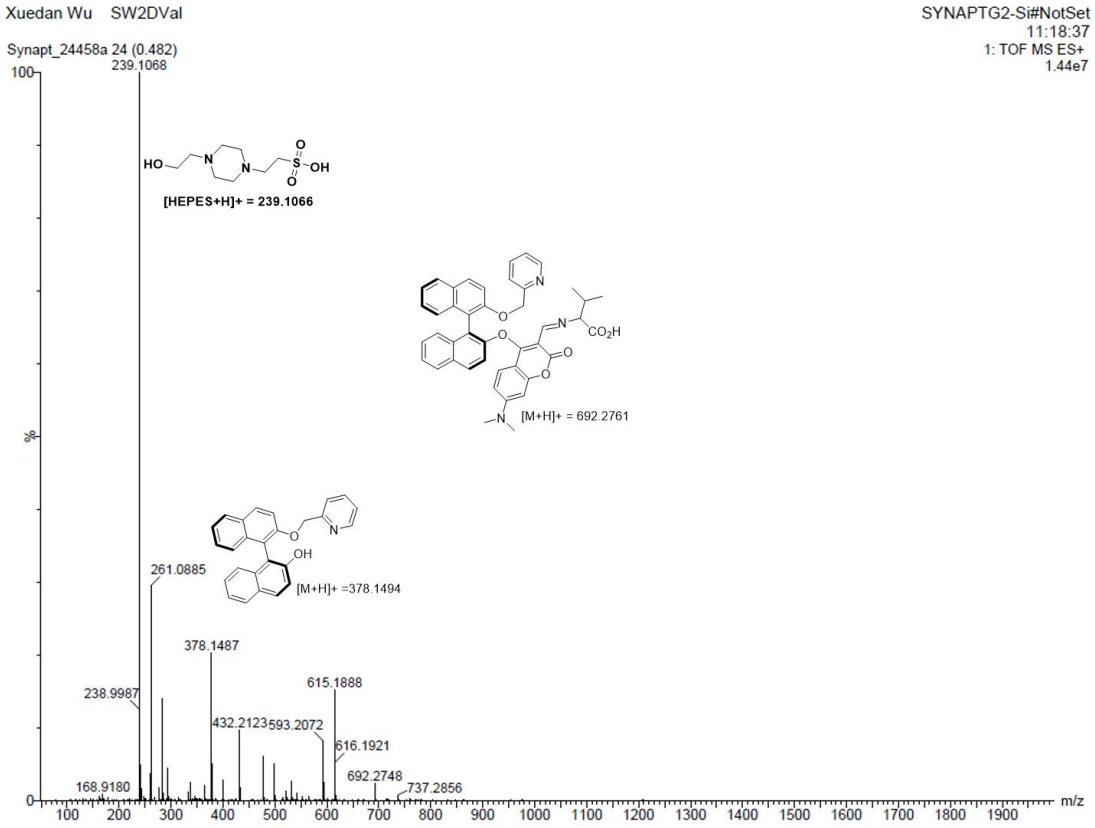

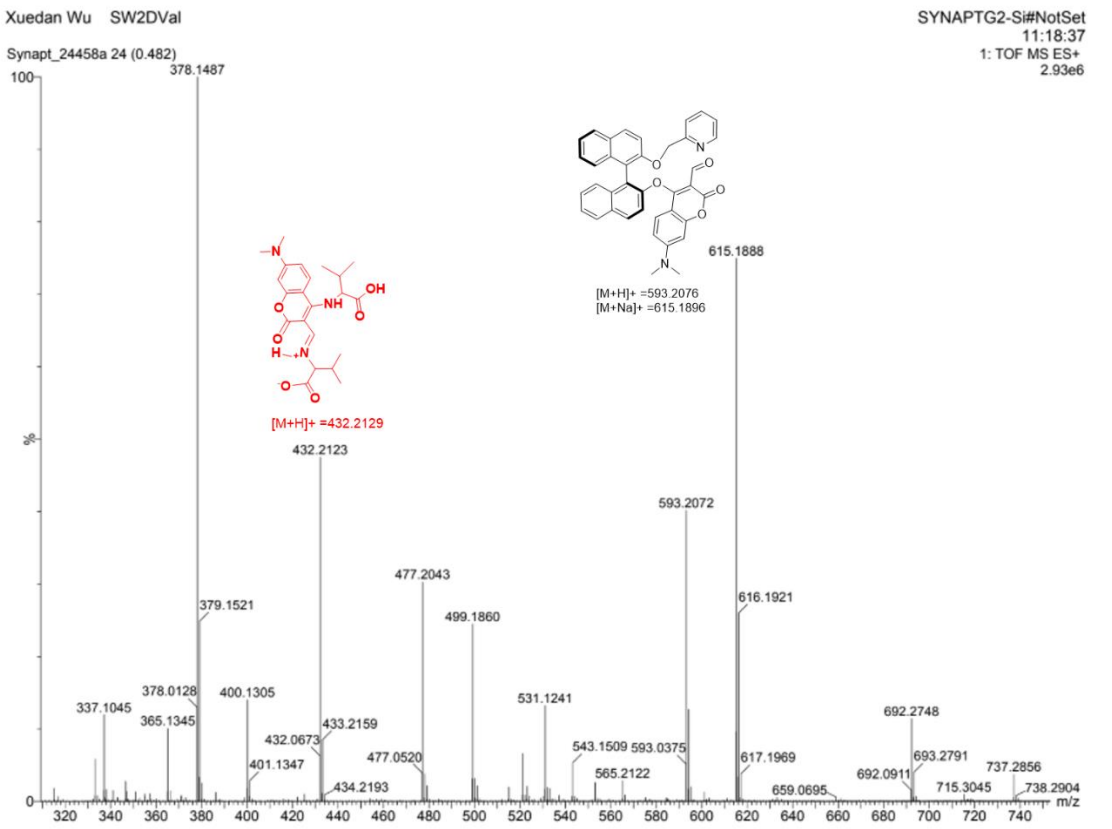
Xuedan Wu SW2DVal
Synapt_24458a 24 (0.482)
SYNAPTG2-Si#NotSet
11:18:37
1: TOF MS ES+
2.93e6
100
%
0
[M+H]+ =593.2076
[M+Na]+ =615.1896
[M+H]+ =432.2129
378.1487
615.1888
432.2123
593.2072
477.2043
379.1521
616.1921
499.1860
378.0128
400.1305
337.1045
531.1241
692.2748
365.1345
433.2159
432.0673
543.1509
593.0375
693.2791
737.2856
477.0520
617.1969
401.1347
565.2122
692.0911
715.3045
738.2904
434.2193
659.0695
320 340 360 380 400 420 440 460 480 500 520 540 560 580 600 620 640 660 680 700 720 740
m/z

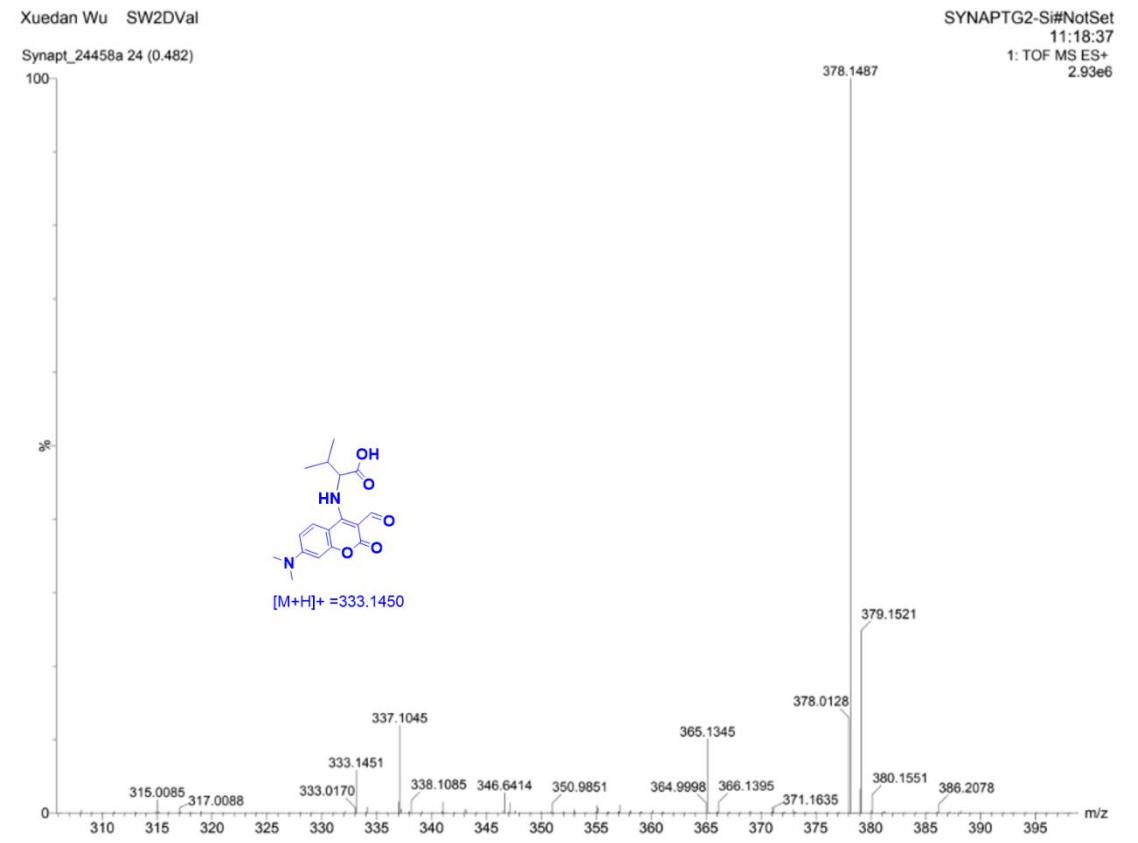
Xuedan Wu SW2DVal
SYNAPTG2-Si#NotSet
11:18:37
Synapt_24458a 24 (0.482)
1: TOF MS ES+
2.93e6
100
%
0
OH
O
HN
O
O
O
N
[M+H]+ =333.1450
378.1487
379.1521
378.0128
337.1045
365.1345
333.1451
315.0085
317.0088
333.0170
338.1085
346.6414
350.9851
364.9998
366.1395
371.1635
380.1551
386.2078
310
315
320
325
330
335
340
345
350
355
360
365
370
375
380
385
390
395
m/z

Figure S5-19. (a - c) High-resolution mass spectra of (*R*)-**6** with L-Valine-TBA (20 equiv) in DMSO

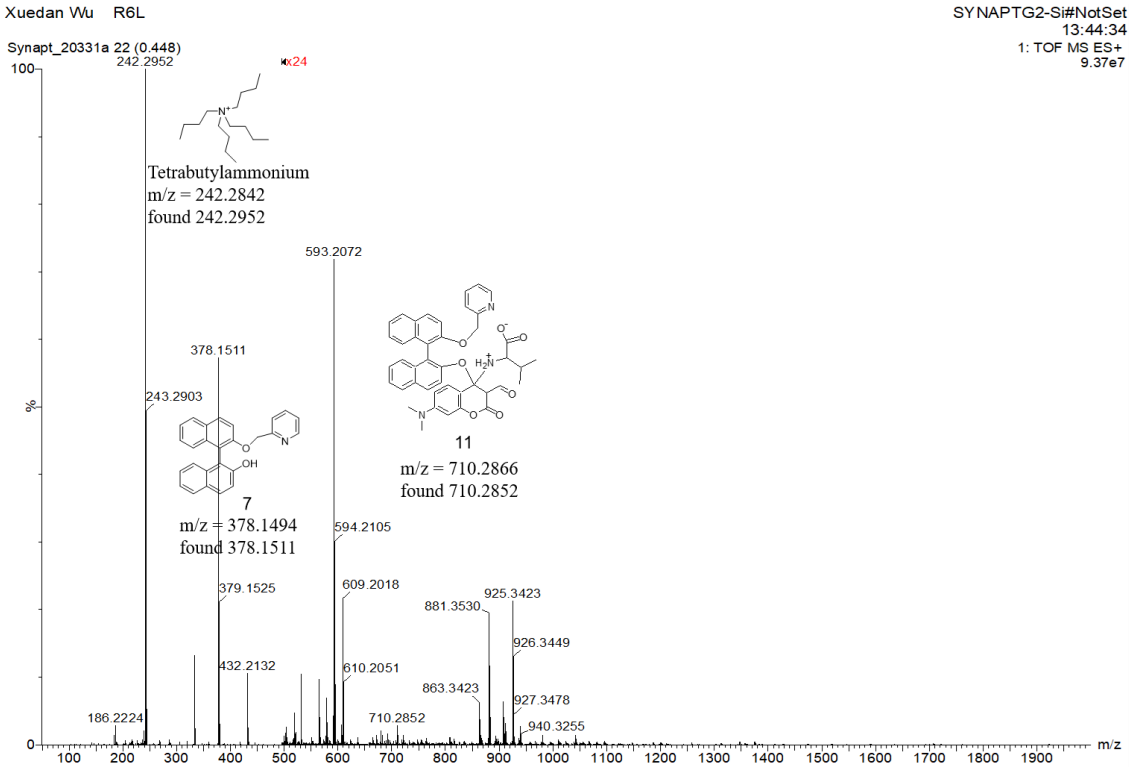

(a)

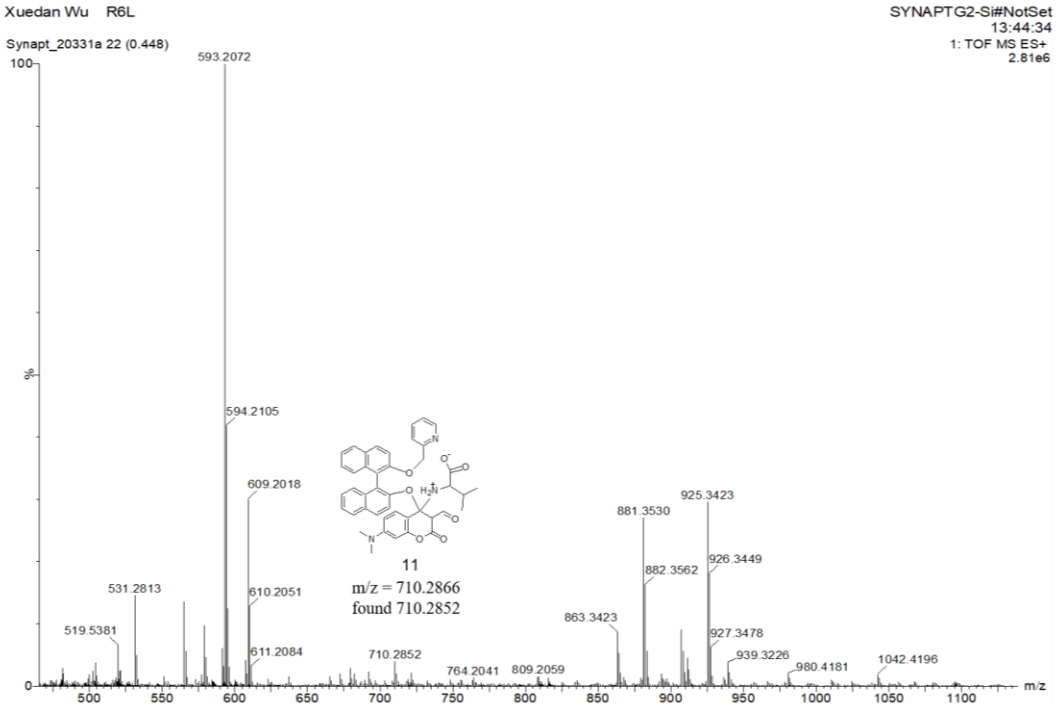
Xuedan Wu R6L
SYNAPTG2-Si#NotSet
13:44:34
1: TOF MS ES+
2.81e6
Synapt_20331a 22 (0.448)
593.2072
594.2105
609.2018
531.2813
610.2051
519.5381
611.2084
710.2852
764.2041
809.2059
863.3423
881.3530
882.3562
925.3423
926.3449
927.3478
939.3226
980.4181
1042.4196
11
m/z = 710.2866
found 710.2852
m/z

(b)

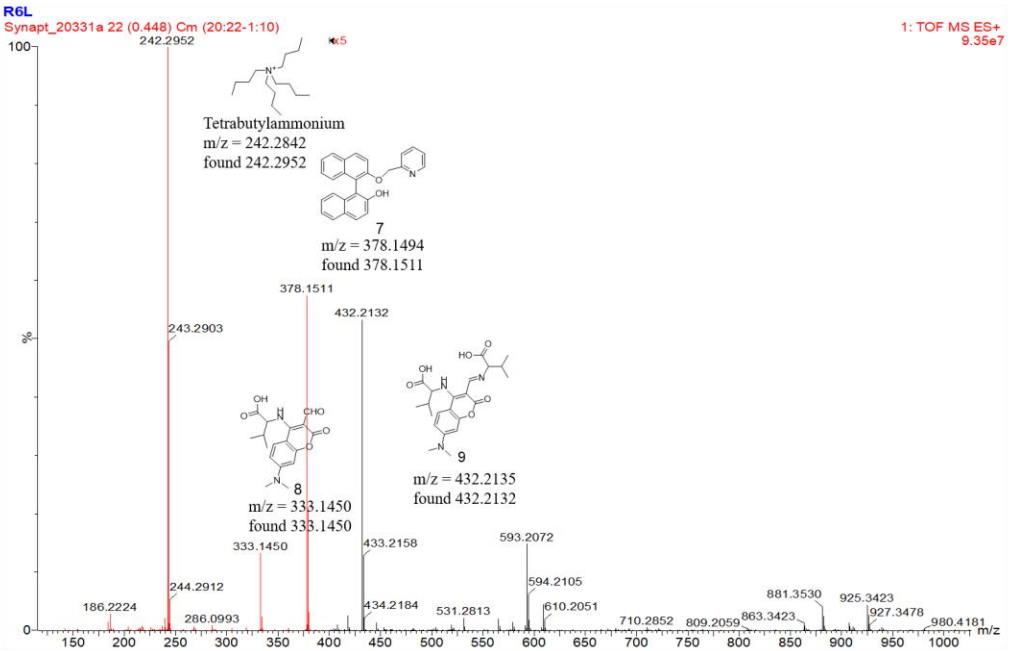
R6L
Synapt_20331a 22 (0.448) Cm (20:22-1:10)
1: TOF MS ES+
9.35e7
242.2952
Tetrabutylammonium
m/z = 242.2842
found 242.2952
7
m/z = 378.1494
found 378.1511
378.1511
432.2132
243.2903
8
m/z = 333.1450
found 333.1450
9
m/z = 432.2135
found 432.2132
333.1450
433.2158
593.2072
594.2105
244.2912
186.2224
434.2184
531.2813
610.2051
710.2852
809.2059
863.3423
881.3530
925.3423
927.3478
980.4181
286.0993
m/z

(c)

Figure S5-19. (d - f) High-resolution mass spectra of (*R*)-**6** with D-Valine-TBA (20 equiv) in DMSO.

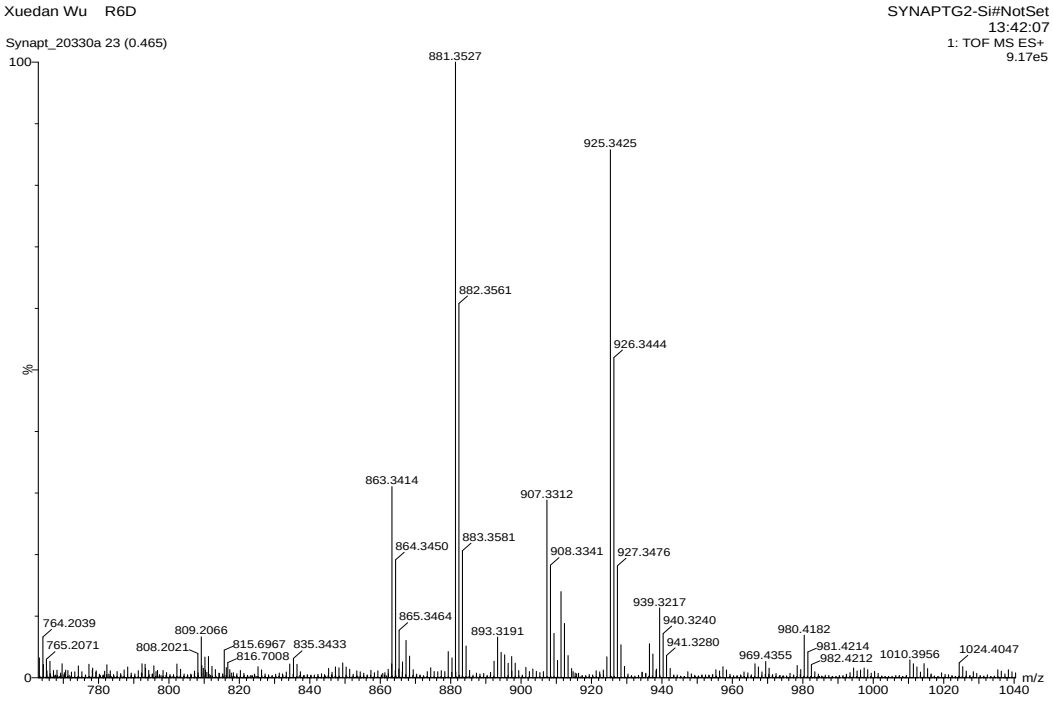

(d)

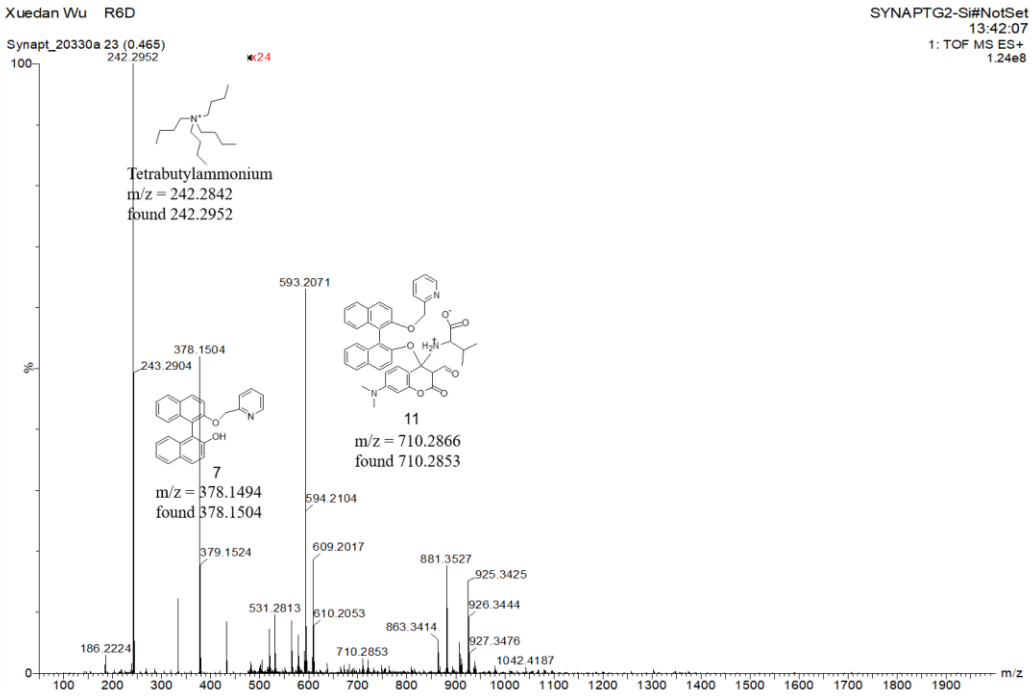
Xuedan Wu R6D
SYNAPTG2-Si#NotSet
13:42:07
1: TOF MS ES+
1.24e8
Synapt_20330a 23 (0.465)
Tetrabutylammonium
m/z = 242.2842
found 242.2952
7
m/z = 378.1494
found 378.1504
11
m/z = 710.2866
found 710.2853
m/z

(e)

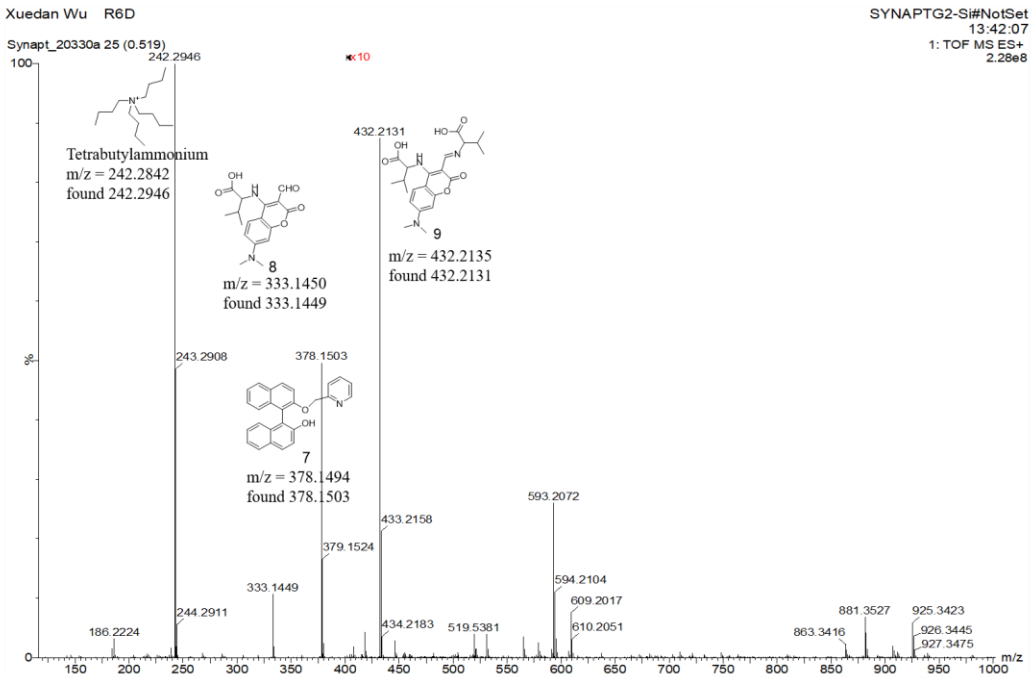
Xuedan Wu R6D
SYNAPTG2-Si#NotSet
13:42:07
1: TOF MS ES+
2.28e8
Synapt_20330a 25 (0.519)
Tetrabutylammonium
m/z = 242.2842
found 242.2946
8
m/z = 333.1450
found 333.1449
9
m/z = 432.2135
found 432.2131
7
m/z = 378.1494
found 378.1503
m/z

(f)

Molecule modeling

1,2-addition intermediates:

Figure S5-20a. Density functional calculation for the intermediate **10**-D from the reaction of (*R*)-**6** with D-valine.

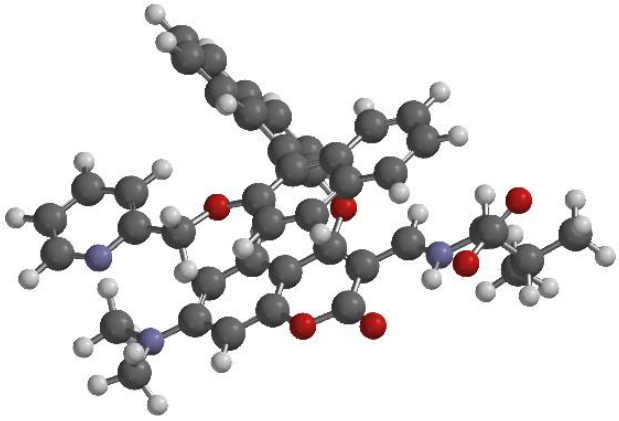

10-D

SPARTAN '18 (Win/64b) Release 1.4.2

Name:	M0001
Formula:	$C_{43}H_{37}N_3O_6$

Job type:	Equilibrium Geometry
Solvent:	Water
Method:	ωB97X-D
Basis set:	6-31G*
With Options:	PRINTCOORDS
Energy:	-2275.830783 hartrees

Cartesian Coordinates (Angstroms)

Atom	X	Y	Z
1 H H1	-5.0392146	-4.7872492	-0.9609607
2 C C1	-4.4050641	-3.9365116	-0.7311635
3 C C4	-2.7230031	-1.7573646	-0.1268687
4 C C2	-3.3838158	-4.0642518	0.2400001
5 C C6	-4.5946482	-2.7397755	-1.3730811
6 C C5	-3.7650791	-1.6231723	-1.0870713

7	C	C3	-2.5670567	-3.0030247	0.5380180
8	H	H2	-3.2453062	-5.0121251	0.7513169
9	H	H6	-5.3817910	-2.6261298	-2.1137491
10	H	H3	-1.7851295	-3.1091444	1.2829660
11	C	C7	-3.9553651	-0.3768143	-1.7410684
12	C	C8	-3.1215151	0.6772242	-1.4890650
13	C	C9	-2.0591879	0.5067130	-0.5795098
14	C	C10	-1.8493914	-0.6532723	0.1309168
15	H	H7	-4.7663306	-0.2733687	-2.4560746
16	H	H8	-3.2345194	1.6318295	-1.9916966
17	C	C11	-0.7916878	-0.0254206	2.3451116
18	C	C12	1.5307111	-1.4675119	1.6533619
19	C	C13	0.3490037	-0.0095606	3.1971770
20	C	C14	-0.7365953	-0.7451324	1.1158612
21	C	C15	0.3966122	-1.4805992	0.8056679
22	C	C16	1.5032190	-0.7351711	2.8110395
23	H	H13	2.3798888	-0.7082013	3.4522511
24	H	H14	2.4256115	-2.0140437	1.3793465
25	C	C17	0.3144879	0.7456636	4.3984390
26	C	C18	-0.8113141	1.4401349	4.7590476
27	C	C19	-1.9507131	1.4157213	3.9211293
28	C	C20	-1.9423352	0.7092406	2.7440342
29	H	H15	1.2026064	0.7692234	5.0242209
30	H	H16	-0.8182556	2.0394166	5.6627022
31	H	H17	-2.8395154	1.9692229	4.2096948
32	H	H18	-2.8235943	0.7016269	2.1103861
33	H	H4	-0.9196188	0.3483786	-2.7887539
34	C	C21	0.1309156	0.1702342	-2.5979941
35	C	C22	2.8600892	-0.2618883	-2.1682694
36	C	C23	0.8302054	-0.6127611	-3.4702361
37	C	C24	0.7498178	0.7589476	-1.4680117
38	C	C25	2.1371688	0.5503664	-1.3242287
39	C	C26	2.2124067	-0.9047190	-3.2491051
40	H	H5	0.3121262	-1.0363629	-4.3200620
41	H	H20	3.9168351	-0.3883076	-1.9741149
42	O	O1	2.8410894	1.1415814	-0.3185091
43	C	C28	2.2698220	1.9846457	0.5890142
44	C	C30	0.0981598	1.4973443	-0.4528557
45	O	O2	3.0132093	2.4846425	1.4137908
46	O	O4	-1.2385568	1.6239636	-0.3971856
47	H	H9	0.0873363	-6.1005599	-4.8617597
48	C	C31	0.2980611	-5.4540475	-4.0168059
49	C	C32	0.9468481	-3.8786027	-1.8852693
50	C	C33	1.5600005	-5.4536029	-3.4292110
51	C	C34	-0.6680868	-4.5999716	-3.4955566
52	C	C35	-0.3409852	-3.7932950	-2.4104028

53	N	N1	1.8893796	-4.6868108	-2.3853444
54	H	H10	2.3460854	-6.0984649	-3.8155125
55	H	H21	-1.6648426	-4.5605099	-3.9243905
56	H	H22	-1.0633606	-3.1142403	-1.9737363
57	O	O5	0.3675781	-2.1499238	-0.3678207
58	N	N2	2.8759193	-1.7658513	-4.0476642
59	C	C36	4.2501735	-2.1323217	-3.7408456
60	H	H12	4.5874616	-2.8792613	-4.4578054
61	H	H23	4.3220971	-2.5613756	-2.7344759
62	H	H24	4.9182490	-1.2660401	-3.8049681
63	C	C37	2.1990324	-2.3987916	-5.1714286
64	H	H19	1.8766174	-1.6542533	-5.9076271
65	H	H25	1.3251825	-2.9681083	-4.8386847
66	H	H28	2.8889589	-3.0872771	-5.6569522
67	C	C27	0.8369746	2.1756928	0.5191970
68	C	C38	1.3755831	-3.0941614	-0.6689503
69	H	H29	1.5165909	-3.7845403	0.1728916
70	H	H30	2.3312669	-2.5953210	-0.8687613
71	C	C29	0.1681716	2.9729059	1.4942073
72	H	H26	-0.9089300	3.0817736	1.4163616
73	N	N3	0.7527641	3.5961070	2.4636510
74	H	H11	1.7617629	3.4833696	2.6082017
75	C	C39	0.1160356	4.4512508	3.4579509
76	H	H32	-0.9156822	4.1150826	3.5969264
77	C	C40	0.1251382	5.9266012	2.9837407
78	H	H33	1.1784667	6.2239485	2.8902292
79	C	C41	-0.5519718	6.0931456	1.6207034
80	H	H27	-0.5749548	7.1519589	1.3423925
81	H	H35	-1.5875527	5.7315504	1.6549929
82	H	H36	-0.0274187	5.5572980	0.8233313
83	C	C42	-0.5496943	6.8297609	4.0199386
84	H	H34	-0.5092983	7.8723288	3.6878933
85	H	H37	-0.0703161	6.7528986	4.9978141
86	H	H38	-1.6046418	6.5531118	4.1385932
87	C	C43	0.9367072	4.2662825	4.7723247
88	O	O3	0.3235913	4.4381872	5.8457573
89	O	O6	2.1503205	3.9898407	4.6010156

Figure S5-20b. Density functional calculation for the intermediate **10**-L from the reaction of (*R*)-**6** with L-valine.

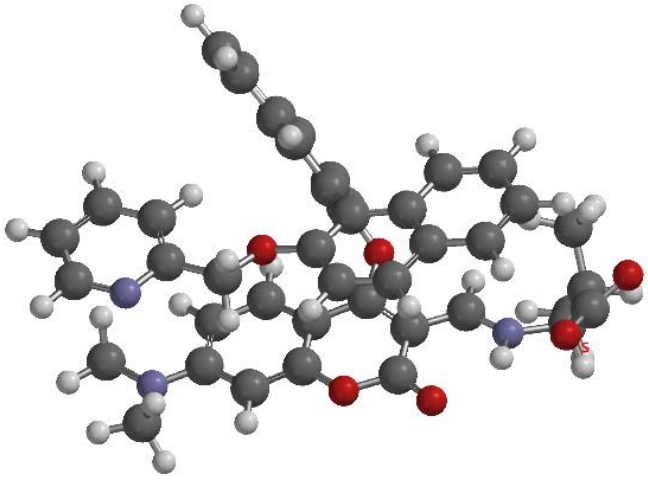

SPARTAN '18 (Win/64b) Release 1.4.2

Name:	M0001
Formula:	$C_{43}H_{37}N_3O_6$

Job type:	Equilibrium Geometry
Solvent:	Water
Method:	ωB97X-D
Basis set:	6-31G*
With Options:	PRINTCOORDS
Energy:	-2275.819222 hartrees

Cartesian Coordinates (Angstroms)

Atom	X	Y	Z
1 H H1	-4.8713658	4.7210520	-1.0060356
2 C C1	-4.0047735	4.1163126	-0.7569041
3 C C4	-1.7826990	2.5105874	-0.1029285
4 C C2	-4.1330208	3.0537194	0.1688468
5 C C6	-2.7879029	4.3834512	-1.3295659
6 C C5	-1.6495557	3.5944509	-1.0161856
7 C C3	-3.0513923	2.2737382	0.4908114
8 H H2	-5.0973325	2.8548936	0.6267142

9	H	H6	-2.6744791	5.2028979	-2.0343289
10	H	H3	-3.1574839	1.4604712	1.2014128
11	C	C7	-0.3816179	3.8675636	-1.5942416
12	C	C8	0.6976370	3.0765551	-1.3123349
13	C	C9	0.5333467	1.9749976	-0.4494130
14	C	C10	-0.6531767	1.6808532	0.1850630
15	H	H7	-0.2804612	4.7081896	-2.2744391
16	H	H8	1.6708290	3.2533739	-1.7576785
17	C	C11	-0.1056725	0.5986620	2.4043396
18	C	C12	-1.3543686	-1.7854492	1.5684559
19	C	C13	-0.0574091	-0.5658148	3.2218386
20	C	C14	-0.7425503	0.5344422	1.1309475
21	C	C15	-1.3950126	-0.6279451	0.7529806
22	C	C16	-0.6813661	-1.7518961	2.7614869
23	H	H13	-0.6299213	-2.6462292	3.3762442
24	H	H14	-1.8291332	-2.7026407	1.2398008
25	C	C17	0.6137923	-0.5154872	4.4711195
26	C	C18	1.1752030	0.6525470	4.9178413
27	C	C19	1.0901402	1.8208144	4.1257711
28	C	C20	0.4877099	1.7934683	2.8936018
29	H	H15	0.6767150	-1.4220359	5.0661127
30	H	H16	1.6952287	0.6826593	5.8699290
31	H	H17	1.5199103	2.7477225	4.4921125
32	H	H18	0.4425946	2.6957274	2.2919481
33	H	H4	0.5318845	0.8868688	-2.6911703
34	C	C21	0.3883557	-0.1737144	-2.5286324
35	C	C22	0.0528133	-2.9268770	-2.1741368
36	C	C23	-0.3155773	-0.8877031	-3.4551983
37	C	C24	0.9447615	-0.7909870	-1.3818970
38	C	C25	0.7882173	-2.1878837	-1.2748752
39	C	C26	-0.5590747	-2.2849607	-3.2759625
40	H	H5	-0.7136049	-0.3711175	-4.3181993
41	H	H20	-0.0408144	-3.9911382	-2.0038314
42	O	O1	1.3439869	-2.8842210	-0.2438131
43	C	C28	2.1274620	-2.2987675	0.7060533
44	C	C30	1.6220697	-0.1321031	-0.3290585
45	O	O2	2.5946297	-3.0346952	1.5581988
46	O	O4	1.6822856	1.2059993	-0.2344418
47	H	H9	-5.7866531	-0.4179950	-5.1028694
48	C	C31	-5.1676191	-0.6127596	-4.2338908
49	C	C32	-3.6537322	-1.2237718	-2.0470516
50	C	C33	-5.1157330	-1.8881717	-3.6786888
51	C	C34	-4.3996414	0.3884684	-3.6488988
52	C	C35	-3.6239429	0.0807675	-2.5355905
53	N	N1	-4.3786573	-2.1991914	-2.6082472
54	H	H10	-5.6912714	-2.7012539	-4.1152735

55	H	H21	-4.4028444	1.3974341	-4.0502096
56	H	H22	-3.0113246	0.8312159	-2.0507764
57	O	O5	-2.0084713	-0.6034419	-0.4517042
58	N	N2	-1.3493634	-2.9662027	-4.1311936
59	C	C36	-1.6755041	-4.3595118	-3.8683562
60	H	H12	-2.3722091	-4.7110374	-4.6279619
61	H	H23	-2.1511034	-4.4679579	-2.8864078
62	H	H24	-0.7812435	-4.9920991	-3.9008903
63	C	C37	-1.9544120	-2.2913619	-5.2711587
64	H	H19	-1.1901722	-1.9304977	-5.9684566
65	H	H25	-2.5673145	-1.4435744	-4.9488781
66	H	H28	-2.5969163	-2.9953217	-5.7979230
67	C	C27	2.3102899	-0.8655557	0.6409549
68	C	C38	-2.9017646	-1.6402618	-0.8063448
69	H	H29	-3.6185383	-1.8200986	0.0057840
70	H	H30	-2.3611177	-2.5737153	-1.0013073
71	C	C29	3.1919506	-0.2037200	1.5497567
72	H	H26	3.3804071	0.8493425	1.3865364
73	N	N3	3.8258388	-0.8022491	2.5038188
74	H	H11	3.5683824	-1.7749951	2.6940450
75	C	C39	4.8702823	-0.3316675	3.4180494
76	C	C43	4.4280917	-0.7918615	4.8566116
77	O	O3	4.8102870	-0.0977474	5.8189298
78	O	O6	3.7812292	-1.8663094	4.8729134
79	H	H40	5.7265259	-0.9807359	3.1824331
80	C	C40	5.3710952	1.1086093	3.2786133
81	H	H32	6.1279790	1.1558911	4.0692135
82	C	C41	6.0979813	1.3671673	1.9514508
83	H	H31	5.4205886	1.4062357	1.0917024
84	H	H33	6.8445531	0.5900468	1.7534152
85	H	H34	6.6163796	2.3308681	1.9959836
86	C	C42	4.3522983	2.2029929	3.6033235
87	H	H27	3.8880650	2.0096335	4.5728573
88	H	H35	3.5560085	2.2922152	2.8580517
89	H	H36	4.8615097	3.1718267	3.6512767

1,4-addition intermediates:

Figure S5-20c. Density functional calculation for the intermediate **11**-D from the reaction of (*R*)-**6** with D-valine.

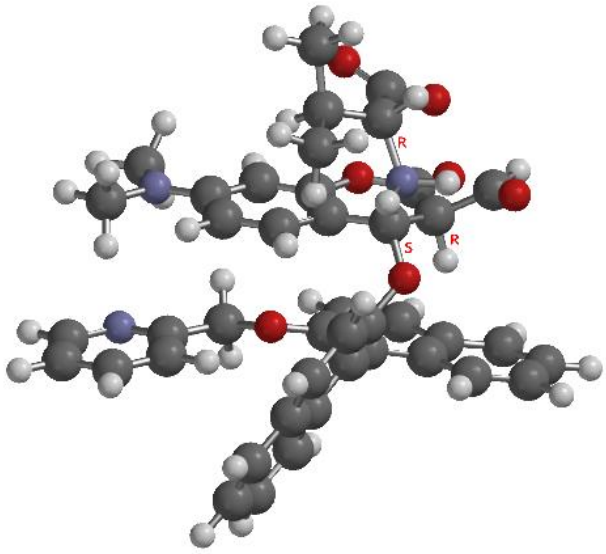

SPARTAN '18 (Win/64b) Release 1.4.2

Name:	M0001
Formula:	$C_{43}H_{39}N_3O_7$

Job type:	Equilibrium Geometry
Solvent:	Water
Method:	ωB97X-D
Basis set:	6-31G*
With Options:	PRINTCOORDS
Energy:	-2352.212772 hartrees

Cartesian Coordinates (Angstroms)

Atom	X	Y	Z
1 H H1	-5.1571152	-4.1726322	-0.9829053
2 C C1	-4.5606883	-3.3608523	-0.5777882
3 C C4	-2.9730010	-1.2844719	0.4842100
4 C C2	-3.8052768	-3.5641449	0.6011700
5 C C6	-4.5468284	-2.1372962	-1.1964051

6	C	C5	-3.7642100	-1.0708964	-0.6789033
7	C	C3	-3.0353080	-2.5543619	1.1192949
8	H	H2	-3.8335826	-4.5297888	1.0969619
9	H	H6	-5.1350326	-1.9621121	-2.0933085
10	H	H3	-2.4561433	-2.7218844	2.0214230
11	C	C7	-3.7589158	0.2066572	-1.2980998
12	C	C8	-2.9792411	1.2123651	-0.8007336
13	C	C9	-2.1400896	0.9729119	0.3122245
14	C	C10	-2.1241540	-0.2366129	0.9712695
15	H	H7	-4.3826728	0.3752478	-2.1712018
16	H	H8	-2.9666388	2.1966918	-1.2585038
17	C	C11	-1.4269306	0.1760825	3.3829706
18	C	C12	0.7843433	-1.5351484	3.0274336
19	C	C13	-0.4880153	-0.0223378	4.4369799
20	C	C14	-1.2216310	-0.4732560	2.1299305
21	C	C15	-0.1460158	-1.3340252	1.9788282
22	C	C16	0.6146741	-0.8855265	4.2210488
23	H	H13	1.3383836	-1.0241470	5.0193759
24	H	H14	1.6413356	-2.1821029	2.8796581
25	C	C17	-0.6603323	0.6656967	5.6674920
26	C	C18	-1.7197578	1.5146207	5.8541756
27	C	C19	-2.6632886	1.7020316	4.8148112
28	C	C20	-2.5253293	1.0513454	3.6154604
29	H	H15	0.0706826	0.5085387	6.4563662
30	H	H16	-1.8421298	2.0419275	6.7952006
31	H	H17	-3.5060478	2.3690654	4.9705669
32	H	H18	-3.2562183	1.2033170	2.8278535
33	H	H4	-0.6206581	0.9644038	-1.8070748
34	C	C21	0.3001440	0.6075392	-1.3617070
35	C	C22	2.6602892	-0.3458529	-0.2917884
36	C	C23	1.0014655	-0.3603019	-2.0431256
37	C	C24	0.7292451	1.1374021	-0.1352586
38	C	C25	1.9279766	0.6280409	0.3599608
39	C	C26	2.2104562	-0.8783163	-1.5157890
40	H	H5	0.6032048	-0.7259276	-2.9805766
41	H	H20	3.5769393	-0.6804076	0.1762103
42	O	O1	2.5004497	1.0462613	1.5433334
43	C	C28	1.8988416	1.9153132	2.3695335
44	O	O2	2.4130227	2.1420897	3.4369556
45	O	O4	-1.4054701	2.0571437	0.7671043
46	H	H9	-0.2467882	-5.7913906	-3.8079989
47	C	C31	-0.0719343	-5.1916035	-2.9214224
48	C	C32	0.4680647	-3.7617959	-0.6599495
49	C	C33	1.0233066	-5.4507095	-2.1022656
50	C	C34	-0.9182466	-4.1448894	-2.5718300
51	C	C35	-0.6428222	-3.4099767	-1.4236848

52	N	N1	1.2965412	-4.7597393	-0.9911630
53	H	H10	1.7153774	-6.2530821	-2.3481097
54	H	H21	-1.7827121	-3.9000818	-3.1817997
55	H	H22	-1.2716413	-2.5834978	-1.1185912
56	O	O8	-0.0228022	-1.9345467	0.7737351
57	N	N2	2.9072127	-1.8544474	-2.1595343
58	C	C36	4.1131282	-2.4006588	-1.5655889
59	H	H12	4.5179672	-3.1683510	-2.2242505
60	H	H23	3.9067535	-2.8628138	-0.5916477
61	H	H24	4.8804451	-1.6286823	-1.4270796
62	C	C37	2.4323194	-2.3665973	-3.4327706
63	H	H19	2.4055555	-1.5787172	-4.1957388
64	H	H25	1.4289582	-2.7969418	-3.3414997
65	H	H28	3.1069496	-3.1509448	-3.7746958
66	C	C38	0.8023292	-3.0727618	0.6408156
67	H	H29	0.6287916	-3.7704004	1.4710255
68	H	H30	1.8612359	-2.7886584	0.6473010
69	C	C29	0.4765135	3.9269753	2.4990624
70	H	H26	1.1683483	4.1564448	3.3195379
71	O	O3	-0.3645296	4.7233161	2.1295007
72	C	C30	-0.0052885	2.2284397	0.5731750
73	C	C27	0.5535686	2.4919598	1.9956580
74	H	H36	-0.1441295	1.9599374	2.6564426
75	C	C44	1.2198903	4.0134372	-1.0410797
76	C	C42	2.5126910	3.7504615	-0.2066730
77	O	O5	3.4956221	3.2556514	-0.7778243
78	H	H44	1.0698280	5.0992231	-1.0393175
79	C	C39	1.2512176	3.5496040	-2.5057272
80	H	H31	1.6314735	2.5244857	-2.5391541
81	C	C40	2.2244430	4.4526456	-3.2756840
82	H	H11	2.3226897	4.0994211	-4.3072498
83	H	H32	3.2111277	4.4499193	-2.8108804
84	H	H34	1.8490501	5.4833044	-3.3065311
85	C	C41	-0.1190327	3.6104042	-3.1930681
86	H	H27	0.0020850	3.4238454	-4.2644324
87	H	H35	-0.5730814	4.6027381	-3.0768435
88	H	H37	-0.8337767	2.8615771	-2.8332896
89	N	N3	0.0024267	3.5196109	-0.2752947
90	H	H40	-0.3161254	4.2560278	0.3746750
91	H	H41	-0.7725136	3.4204194	-0.9345680
92	O	O6	2.4287825	4.1091500	1.0016749

Point Group = C1 Order = 1 Nsymop = 1

Figure S5-20d. Density functional calculation for the intermediate **11**-L from the reaction of (*R*)-**6** with L-valine.

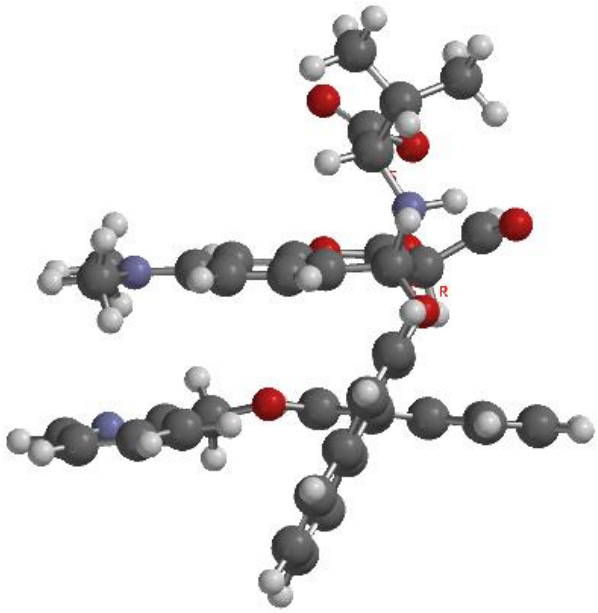

SPARTAN '18 (Win/64b) Release 1.4.2

Name:	M0001
Formula:	$C_{43}H_{39}N_3O_7$

Job type:	Equilibrium Geometry
Solvent:	Water
Method:	ωB97X-D
Basis set:	6-31G*
With Options:	PRINTCOORDS
Energy:	-2352.220149 hartrees

Cartesian Coordinates (Angstroms)

Atom	X	Y	Z
1 H H1	-5.2461083	-4.2408934	-1.4084274
2 C C1	-4.6409324	-3.4642291	-0.9508510
3 C C4	-3.0327443	-1.4791376	0.2470698
4 C C2	-3.8908207	-3.7520585	0.2139740
5 C C6	-4.6095514	-2.2040499	-1.4900772
6 C C5	-3.8162708	-1.1826047	-0.9030785

7	C	C3	-3.1109048	-2.7868358	0.7980813
8	H	H2	-3.9320156	-4.7472773	0.6463537
9	H	H6	-5.1925898	-1.9646127	-2.3755055
10	H	H3	-2.5372292	-3.0200168	1.6890254
11	C	C7	-3.7937863	0.1315297	-1.4392951
12	C	C8	-3.0057895	1.0949011	-0.8755394
13	C	C9	-2.1770840	0.7765141	0.2252506
14	C	C10	-2.1788950	-0.4724419	0.8064447
15	H	H7	-4.4116265	0.3627412	-2.3022929
16	H	H8	-2.9822726	2.1065264	-1.2684723
17	C	C11	-1.5100848	-0.2111830	3.2465123
18	C	C12	0.7066201	-1.8961437	2.8101021
19	C	C13	-0.5803012	-0.4700811	4.2956947
20	C	C14	-1.2932018	-0.7861958	1.9598487
21	C	C15	-0.2156791	-1.6358250	1.7673338
22	C	C16	0.5259525	-1.3175458	4.0384427
23	H	H13	1.2437756	-1.5013255	4.8329571
24	H	H14	1.5662592	-2.5317174	2.6312362
25	C	C17	-0.7640861	0.1462230	5.5621930
26	C	C18	-1.8258838	0.9827063	5.7876938
27	C	C19	-2.7604345	1.2292481	4.7524012
28	C	C20	-2.6110006	0.6492214	3.5189393
29	H	H15	-0.0399038	-0.0554115	6.3471883
30	H	H16	-1.9567270	1.4553550	6.7562312
31	H	H17	-3.6051727	1.8857466	4.9390850
32	H	H18	-3.3344109	0.8462436	2.7344450
33	H	H4	-0.6044297	0.9317446	-1.8961488
34	C	C21	0.2959566	0.5176484	-1.4544949
35	C	C22	2.6428940	-0.5129676	-0.4178204
36	C	C23	1.0094203	-0.3998163	-2.1915639
37	C	C24	0.6976129	0.9371455	-0.1762703
38	C	C25	1.9003345	0.4132771	0.2903101
39	C	C26	2.2027531	-0.9667897	-1.6768253
40	H	H5	0.6369583	-0.6859518	-3.1665307
41	H	H20	3.5604675	-0.8697463	0.0318074
42	O	O1	2.4715564	0.7759526	1.4944552
43	C	C28	1.8671874	1.6023992	2.3631104
44	O	O2	2.3909509	1.7928437	3.4323597
45	O	O4	-1.4391897	1.8241809	0.7553846
46	H	H9	-0.2255562	-5.7058307	-4.3024683
47	C	C31	-0.0669212	-5.1666003	-3.3748354
48	C	C32	0.4329724	-3.8882759	-1.0154885
49	C	C33	1.0179884	-5.4748994	-2.5591214
50	C	C34	-0.9241491	-4.1498841	-2.9681174
51	C	C35	-0.6694972	-3.4916564	-1.7695533
52	N	N1	1.2711421	-4.8583763	-1.4005932

53	H	H10	1.7179048	-6.2558704	-2.8478512
54	H	H21	-1.7815542	-3.8695617	-3.5728155
55	H	H22	-1.3074759	-2.6903613	-1.4192626
56	O	O8	-0.0812063	-2.1604519	0.5284535
57	N	N2	2.8986146	-1.9081711	-2.3708715
58	C	C36	4.0976845	-2.4939118	-1.8012938
59	H	H12	4.4901175	-3.2414702	-2.4900570
60	H	H23	3.8855870	-2.9907454	-0.8459845
61	H	H24	4.8765129	-1.7391304	-1.6340687
62	C	C37	2.4362609	-2.3351964	-3.6796367
63	H	H19	2.4461445	-1.5069027	-4.3992708
64	H	H25	1.4199295	-2.7408752	-3.6294817
65	H	H28	3.0952714	-3.1194538	-4.0507020
66	C	C38	0.7482985	-3.2861575	0.3322639
67	H	H29	0.5663819	-4.0369842	1.1127594
68	H	H30	1.8063860	-3.0013167	0.3698892
69	C	C29	0.3832013	3.5674653	2.6130849
70	H	H26	1.0590711	3.7704053	3.4539696
71	O	O3	-0.4781834	4.3559304	2.2760519
72	C	C30	-0.0372893	1.9894505	0.5870371
73	C	C27	0.5100465	2.1701847	2.0236646
74	H	H36	-0.1754414	1.5745413	2.6421997
75	C	C44	1.2593067	3.6788914	-0.9770361
76	C	C42	2.5140331	3.6931446	-0.0741933
77	O	O5	3.5936182	3.4792974	-0.6505088
78	N	N3	0.0184901	3.3095992	-0.2085701
79	H	H40	-0.2475498	4.0493723	0.4590524
80	H	H41	-0.7596106	3.2633135	-0.8722439
81	O	O6	2.3282286	3.9585240	1.1462054
82	H	H33	1.3759342	2.9087170	-1.7397625
83	C	C39	1.0073173	5.0364130	-1.6707246
84	H	H31	0.0179930	4.9655563	-2.1441475
85	C	C40	2.0339587	5.2574638	-2.7841861
86	H	H11	3.0436707	5.3322412	-2.3708732
87	H	H32	1.8065330	6.1848259	-3.3194065
88	H	H34	2.0198539	4.4327305	-3.5045548
89	C	C41	0.9907993	6.2222102	-0.6999462
90	H	H27	1.9764241	6.3707499	-0.2468054
91	H	H35	0.2650672	6.0991991	0.1113960
92	H	H37	0.7241184	7.1345668	-1.2423325

Point Group = C1 Order = 1 Nsymop = 1

6 X-Ray Analysis Data of (*S*)-6 (Pu_XW4_SW2)

Crystal Structure Report for Pu_XW4_SW2

A yellow needle-like specimen of $C_{38}H_{30}N_2O_6$, approximate dimensions 0.017 mm x 0.030 mm x 0.171 mm, was coated with Paratone oil and mounted on a MiTeGen MicroLoop. The X-ray intensity data were measured on a Bruker Kappa APEXII Duo system equipped with a Incoatec Microfocus IμS (Cu K_α, λ = 1.54178 Å) and a multi-layer mirror monochromator.

The total exposure time was 33.00 hours. The frames were integrated with the Bruker SAINT software package[1] using a narrow-frame algorithm. The integration of the data using a monoclinic unit cell yielded a total of 4191 reflections to a maximum θ angle of 44.48° (1.10 Å resolution), of which 2530 were independent (average redundancy 1.657, completeness = 99.8%, R_{int} = 34.11%, R_{sig} = 59.19%) and 630 (24.90%) were greater than 2σ(F^2). The final cell constants of a = 13.329(10) Å, b = 7.430(3) Å, c = 16.909(8) Å, β = 93.69(4)°, volume = 1671.1(17) $Å^3$, are based upon the refinement of the XYZ-centroids of 344 reflections above 20 σ(I) with 5.228° < 2θ < 79.68°. Data were corrected for absorption effects using the Multi-Scan method (SADABS).[1] The ratio of minimum to maximum apparent transmission was 0.722. The calculated minimum and maximum transmission coefficients (based on crystal size) are 0.6226 and 0.8627.

The structure was solved and refined using the Bruker SHELXTL Software Package[2] within APEX3 [1] and OLEX2,[3] using the space group P 2_1, with Z = 2 for the formula unit,

1 Bruker (2012). *Saint; SADABS; APEX3*. Bruker AXS Inc., Madison, Wisconsin, USA.
2 Sheldrick, G. M. (2015). *Acta Cryst.* A**71**, 3-8.
3 Dolomanov, O. V.; Bourhis, L. J.; Gildea, R. J.; Howard, J. A. K.; Puschmann, H. *J. Appl. Cryst.* (2009). **42**, 339-341.

$C_{38}H_{30}N_2O_6$. Non-hydrogen atoms were refined anisotropically. The OH hydrogen atoms were placed in sensible hydrogen bonding positions and refined isotropically with restraints on the O-H distances. All other hydrogen atoms were placed in geometrically calculated positions with U_{iso} = 1.2U_{equiv} of the parent atom (U_{iso} = 1.5U_{equiv} for methyl). A global RIGU restraint was used on the anisotropic displacement parameters of the atoms due to the extremely low resolution and redundancy of the diffraction from this crystals. During the refinement, some severely disordered solvent was located in the crystal lattice that could not be adequately modeled with or without restraints. Thus, the structure factors were modified using the PLATON SQUEEZE[4] technique, in order to produce a "solvate-free" structure factor set. PLATON reported a total electron density of 94 e^- and total solvent accessible volume of 258 $Å^3$. The final anisotropic full-matrix least-squares refinement on F^2 with 367 variables converged at R1 = 13.10%, for the observed data and wR2 = 47.21% for all data. The goodness-of-fit was 0.875. The largest peak in the final difference electron density synthesis was 0.256 $e^-/Å^3$ and the largest hole was -0.242 $e^-/Å^3$ with an RMS deviation of 0.059 $e^-/Å^3$. On the basis of the final model, the calculated density was 1.214 g/cm^3 and F(000), 640 e^-.

Table S5-1. Sample and crystal data for Pu_XW4_SW2.

Identification code	Pu_XW4_SW2
Chemical formula	$C_{38}H_{30}N_2O_6$
Formula weight	610.64 g/mol
Temperature	100(2) K

4 Spek, A. L. *Acta Crystallogr. Sect C: Struct. Chem.* **2015**, *C71*, 9-18.

Wavelength	1.54178 Å	
Crystal size	0.017 x 0.030 x 0.171 mm	
Crystal habit	yellow needle	
Crystal system	monoclinic	
Space group	P 2_1	
Unit cell dimensions	a = 13.329(10) Å	α = 90°
	b = 7.430(3) Å	β = 93.69(4)°
	c = 16.909(8) Å	γ = 90°
Volume	1671.1(17) $Å^3$	
Z	2	
Density (calculated)	1.214 g/cm^3	
Absorption coefficient	0.671 mm^{-1}	
F(000)	640	

Table 5S-2. Data collection and structure refinement for Pu_XW4_SW2.

Diffractometer	Bruker Kappa APEXII Duo
Radiation source	Incoatec Microfocus IμS (Cu K_α, λ = 1.54178 Å)
Theta range for data collection	2.62 to 44.48°
Index ranges	-11<=h<=12, -6<=k<=6, -14<=l<=15
Reflections collected	4191
Independent reflections	2530 [R(int) = 0.3411]
Coverage of independent reflections	99.8%
Absorption correction	Multi-Scan

Max. and min. transmission	0.8627 and 0.6226	
Structure solution technique	direct methods	
Structure solution program	SHELXT 2014/5 (Sheldrick, 2014)	
Refinement method	Full-matrix least-squares on F^2	
Refinement program	SHELXL-2018/3 (Sheldrick, 2018)	
Function minimized	$\Sigma\ w(F_o^2 - F_c^2)^2$	
Data / restraints / parameters	2530 / 375 / 367	
Goodness-of-fit on F^2	0.875	
Δ/σ_{max}	0.001	
Final R indices	630 data; $I>2\sigma(I)$	R1 = 0.1310, wR2 = 0.3238
	all data	R1 = 0.3066, wR2 = 0.4721
Weighting scheme	$w=1/[\sigma^2(F_o^2)]$ where $P=(F_o^2+2F_c^2)/3$	
Absolute structure parameter	0.(3)	
Largest diff. peak and hole	0.256 and -0.242 eÅ^{-3}	
R.M.S. deviation from mean	0.059 eÅ^{-3}	

Table S5-3. Atomic coordinates and equivalent isotropic atomic displacement parameters (Å²) for Pu_XW4_SW2.

U(eq) is defined as one third of the trace of the orthogonalized U_{ij} tensor.

	x/a	y/b	z/c	U(eq)
O1	0.344(2)	0.499(4)	0.2792(18)	0.064(11)
O2	0.550(2)	0.857(4)	0.2003(15)	0.042(7)

	x/a	y/b	z/c	U(eq)
O3	0.500(2)	0.884(5)	0.4376(16)	0.057(10)
O4	0.665(3)	0.844(6)	0.471(2)	0.068(11)
O5	0.789(2)	0.798(5)	0.344(2)	0.070(12)
O6	0.124(3)	0.549(6)	0.534(2)	0.086(14)
N2	0.159(3)	0.041(6)	0.394(2)	0.053(11)
C5	0.1738(17)	0.538(5)	0.3090(16)	0.063(7)
C4	0.146(2)	0.537(5)	0.2283(15)	0.063(7)
C3	0.049(2)	0.582(5)	0.2015(13)	0.063(7)
C2	0.9787(18)	0.628(5)	0.2554(16)	0.063(7)
C1	0.0062(19)	0.630(5)	0.3361(15)	0.063(7)
N1	0.104(2)	0.585(5)	0.3629(13)	0.068(13)
C6	0.278(3)	0.493(9)	0.347(3)	0.072(17)
C7	0.446(4)	0.445(7)	0.291(3)	0.055(14)
C8	0.474(4)	0.381(7)	0.367(3)	0.059(14)
C9	0.575(4)	0.313(7)	0.372(3)	0.056(13)
C10	0.646(4)	0.337(7)	0.311(3)	0.053(13)
C11	0.747(4)	0.282(7)	0.316(3)	0.047(12)
C12	0.807(4)	0.290(7)	0.259(3)	0.062(15)
C13	0.763(4)	0.376(7)	0.188(3)	0.059(15)
C14	0.670(3)	0.455(7)	0.177(3)	0.046(11)
C15	0.610(4)	0.425(6)	0.243(3)	0.044(11)
C16	0.506(4)	0.475(8)	0.233(3)	0.056(12)
C17	0.460(3)	0.565(7)	0.157(3)	0.041(5)

	x/a	y/b	z/c	U(eq)
C18	0.398(3)	0.486(7)	0.096(3)	0.041(5)
C19	0.370(3)	0.306(6)	0.116(3)	0.041(5)
C20	0.303(3)	0.232(7)	0.049(3)	0.050(11)
C21	0.274(4)	0.319(7)	0.981(3)	0.053(11)
C22	0.305(4)	0.490(8)	0.967(3)	0.071(14)
C23	0.369(4)	0.575(8)	0.026(3)	0.062(12)
C24	0.402(3)	0.758(7)	0.020(3)	0.048(10)
C25	0.462(4)	0.843(9)	0.076(3)	0.061(12)
C26	0.485(3)	0.750(7)	0.147(3)	0.041(5)
C27	0.536(4)	0.863(8)	0.279(3)	0.054(13)
C28	0.435(4)	0.902(8)	0.301(3)	0.061(15)
C29	0.345(3)	0.941(7)	0.250(3)	0.054(14)
C30	0.261(4)	0.973(7)	0.283(3)	0.048(13)
C31	0.248(4)	0.979(7)	0.365(3)	0.045(12)
C32	0.330(4)	0.959(7)	0.419(3)	0.057(14)
C33	0.423(3)	0.911(6)	0.386(3)	0.041(11)
C34	0.606(4)	0.856(9)	0.417(3)	0.060(15)
C35	0.616(3)	0.854(7)	0.332(3)	0.044(11)
C36	0.713(4)	0.813(8)	0.308(3)	0.060(16)
C37	0.067(3)	0.081(8)	0.341(3)	0.056(14)
C38	0.147(4)	0.022(8)	0.487(3)	0.073(17)

Table 4. Bond lengths (Å) for Pu_XW4_SW2.

O1-C7	1.43(6)	O1-C6	1.49(5)
O2-C27	1.36(5)	O2-C26	1.46(5)
O3-C33	1.33(5)	O3-C34	1.49(6)
O4-C34	1.17(5)	O5-C36	1.15(5)
O6-H6C	1.056	O6-H6D	0.7506
N2-C31	1.39(6)	N2-C37	1.50(6)
N2-C38	1.61(6)	C5-C4	1.39
C5-N1	1.39	C5-C6	1.53(6)
C4-C3	1.39	C4-H4	0.95
C3-C2	1.39	C3-H3	0.95
C2-C1	1.39	C2-H2	0.95
C1-N1	1.39	C1-H1	0.95
C6-H6A	0.99	C6-H6B	0.99
C7-C16	1.33(6)	C7-C8	1.39(6)
C8-C9	1.43(7)	C8-H8	0.95
C9-C10	1.46(7)	C9-H9	0.95
C10-C15	1.38(6)	C10-C11	1.40(6)
C11-C12	1.31(6)	C11-H11	0.95
C12-C13	1.45(7)	C12-H12	0.95
C13-C14	1.37(6)	C13-H13	0.95
C14-C15	1.43(6)	C14-H14	0.95
C15-C16	1.43(7)	C16-C17	1.53(7)
C17-C18	1.41(6)	C17-C26	1.43(6)
C18-C23	1.38(7)	C18-C19	1.43(7)

C19-C20	1.50(7)	C19-H19	0.95
C20-C21	1.36(6)	C20-H20	0.95
C21-C22	1.36(7)	C21-H21	0.95
C22-C23	1.41(8)	C22-H22	0.95
C23-C24	1.44(7)	C24-C25	1.35(7)
C24-H24	0.95	C25-C26	1.39(6)
C25-H25	0.95	C27-C35	1.34(6)
C27-C28	1.45(6)	C28-C33	1.45(6)
C28-C29	1.47(6)	C29-C30	1.30(6)
C29-H29	0.95	C30-C31	1.41(6)
C30-H30	0.95	C31-C32	1.39(6)
C32-C33	1.43(6)	C32-H32	0.95
C34-C35	1.45(6)	C35-C36	1.42(7)
C36-H36	0.95	C37-H37A	0.98
C37-H37B	0.98	C37-H37C	0.98
C38-H38A	0.98	C38-H38B	0.98
C38-H38C	0.98		

Table S5-5. Bond angles (°) for Pu_XW4_SW2.

C7-O1-C6	119.(4)	C27-O2-C26	121.(3)
C33-O3-C34	125.(3)	H6C-O6-H6D	127.8
C31-N2-C37	123.(4)	C31-N2-C38	117.(4)
C37-N2-C38	118.(4)	C4-C5-N1	120.0
C4-C5-C6	126.(2)	N1-C5-C6	114.(2)

C5-C4-C3	120.0	C5-C4-H4	120.0
C3-C4-H4	120.0	C4-C3-C2	120.0
C4-C3-H3	120.0	C2-C3-H3	120.0
C3-C2-C1	120.0	C3-C2-H2	120.0
C1-C2-H2	120.0	N1-C1-C2	120.0
N1-C1-H1	120.0	C2-C1-H1	120.0
C1-N1-C5	120.0	O1-C6-C5	103.(4)
O1-C6-H6A	111.1	C5-C6-H6A	111.1
O1-C6-H6B	111.1	C5-C6-H6B	111.1
H6A-C6-H6B	109.1	C16-C7-C8	127.(5)
C16-C7-O1	117.(4)	C8-C7-O1	115.(4)
C7-C8-C9	112.(4)	C7-C8-H8	123.9
C9-C8-H8	123.9	C8-C9-C10	124.(5)
C8-C9-H9	118.2	C10-C9-H9	118.2
C15-C10-C11	118.(4)	C15-C10-C9	117.(4)
C11-C10-C9	125.(5)	C12-C11-C10	125.(5)
C12-C11-H11	117.5	C10-C11-H11	117.5
C11-C12-C13	113.(5)	C11-C12-H12	123.3
C13-C12-H12	123.3	C14-C13-C12	128.(4)
C14-C13-H13	115.9	C12-C13-H13	115.9
C13-C14-C15	112.(4)	C13-C14-H14	124.1
C15-C14-H14	124.1	C10-C15-C14	123.(4)
C10-C15-C16	120.(4)	C14-C15-C16	117.(4)
C7-C16-C15	119.(5)	C7-C16-C17	118.(4)
C15-C16-C17	123.(4)	C18-C17-C26	116.(4)

C18-C17-C16	128.(5)	C26-C17-C16	116.(4)
C23-C18-C17	123.(5)	C23-C18-C19	126.(5)
C17-C18-C19	111.(5)	C18-C19-C20	108.(5)
C18-C19-H19	125.8	C20-C19-H19	125.8
C21-C20-C19	126.(5)	C21-C20-H20	117.0
C19-C20-H20	117.0	C20-C21-C22	121.(6)
C20-C21-H21	119.5	C22-C21-H21	119.5
C21-C22-C23	118.(6)	C21-C22-H22	120.9
C23-C22-H22	120.9	C18-C23-C22	121.(5)
C18-C23-C24	116.(5)	C22-C23-C24	123.(5)
C25-C24-C23	124.(5)	C25-C24-H24	118.0
C23-C24-H24	118.0	C24-C25-C26	117.(6)
C24-C25-H25	121.5	C26-C25-H25	121.5
C25-C26-C17	123.(5)	C25-C26-O2	111.(4)
C17-C26-O2	126.(4)	C35-C27-O2	120.(4)
C35-C27-C28	123.(4)	O2-C27-C28	117.(4)
C27-C28-C33	116.(4)	C27-C28-C29	129.(4)
C33-C28-C29	115.(4)	C30-C29-C28	119.(4)
C30-C29-H29	120.5	C28-C29-H29	120.5
C29-C30-C31	126.(5)	C29-C30-H30	116.8
C31-C30-H30	116.8	C32-C31-N2	117.(4)
C32-C31-C30	120.(4)	N2-C31-C30	121.(4)
C31-C32-C33	115.(4)	C31-C32-H32	122.5
C33-C32-H32	122.5	O3-C33-C32	115.(4)
O3-C33-C28	120.(4)	C32-C33-C28	124.(4)

O4-C34-C35	133.(5)	O4-C34-O3	114.(4)
C35-C34-O3	113.(4)	C27-C35-C36	122.(4)
C27-C35-C34	122.(4)	C36-C35-C34	115.(5)
O5-C36-C35	131.(5)	O5-C36-H36	114.5
C35-C36-H36	114.5	N2-C37-H37A	109.5
N2-C37-H37B	109.5	H37A-C37-H37B	109.5
N2-C37-H37C	109.5	H37A-C37-H37C	109.5
H37B-C37-H37C	109.5	N2-C38-H38A	109.5
N2-C38-H38B	109.5	H38A-C38-H38B	109.5
N2-C38-H38C	109.5	H38A-C38-H38C	109.5
H38B-C38-H38C	109.5		

Table S5-6. Torsion angles (°) for Pu_XW4_SW2.

N1-C5-C4-C3	0	C6-C5-C4-C3	-180.(5)
C5-C4-C3-C2	0	C4-C3-C2-C1	0
C3-C2-C1-N1	0	C2-C1-N1-C5	0
C4-C5-N1-C1	0	C6-C5-N1-C1	180.(4)
C7-O1-C6-C5	-173.(4)	C4-C5-C6-O1	15.(6)
N1-C5-C6-O1	-165.(3)	C6-O1-C7-C16	-171.(5)
C6-O1-C7-C8	3.(7)	C16-C7-C8-C9	-12.(8)
O1-C7-C8-C9	174.(4)	C7-C8-C9-C10	11.(7)
C8-C9-C10-C15	-3.(7)	C8-C9-C10-C11	176.(5)
C15-C10-C11-C12	-8.(8)	C9-C10-C11-C12	174.(5)
C10-C11-C12-C13	5.(8)	C11-C12-C13-C14	4.(8)

C12-C13-C14-C15	-8.(8)	C11-C10-C15-C14	2.(7)
C9-C10-C15-C14	-179.(5)	C11-C10-C15-C16	177.(5)
C9-C10-C15-C16	-4.(7)	C13-C14-C15-C10	5.(7)
C13-C14-C15-C16	-170.(5)	C8-C7-C16-C15	6.(9)
O1-C7-C16-C15	179.(5)	C8-C7-C16-C17	-174.(5)
O1-C7-C16-C17	-1.(7)	C10-C15-C16-C7	3.(8)
C14-C15-C16-C7	178.(5)	C10-C15-C16-C17	-177.(5)
C14-C15-C16-C17	-2.(7)	C7-C16-C17-C18	-77.(6)
C15-C16-C17-C18	104.(6)	C7-C16-C17-C26	105.(5)
C15-C16-C17-C26	-74.(6)	C26-C17-C18-C23	5.(6)
C16-C17-C18-C23	-173.(4)	C26-C17-C18-C19	-175.(3)
C16-C17-C18-C19	7.(5)	C23-C18-C19-C20	-1.(5)
C17-C18-C19-C20	179.(3)	C18-C19-C20-C21	1.(6)
C19-C20-C21-C22	-1.(7)	C20-C21-C22-C23	1.(7)
C17-C18-C23-C22	-179.(4)	C19-C18-C23-C22	2.(7)
C17-C18-C23-C24	-2.(6)	C19-C18-C23-C24	178.(4)
C21-C22-C23-C18	-1.(7)	C21-C22-C23-C24	-178.(4)
C18-C23-C24-C25	3.(6)	C22-C23-C24-C25	179.(5)
C23-C24-C25-C26	-6.(6)	C24-C25-C26-C17	9.(6)
C24-C25-C26-O2	180.(4)	C18-C17-C26-C25	-9.(6)
C16-C17-C26-C25	169.(4)	C18-C17-C26-O2	-178.(3)
C16-C17-C26-O2	1.(5)	C27-O2-C26-C25	139.(4)
C27-O2-C26-C17	-51.(5)	C26-O2-C27-C35	138.(5)
C26-O2-C27-C28	-50.(6)	C35-C27-C28-C33	-7.(8)
O2-C27-C28-C33	-179.(4)	C35-C27-C28-C29	171.(6)

O2-C27-C28-C29	-1.(9)	C27-C28-C29-C30	180.(6)
C33-C28-C29-C30	-2.(7)	C28-C29-C30-C31	2.(8)
C37-N2-C31-C32	175.(5)	C38-N2-C31-C32	-19.(7)
C37-N2-C31-C30	8.(8)	C38-N2-C31-C30	173.(4)
C29-C30-C31-C32	3.(8)	C29-C30-C31-N2	170.(5)
N2-C31-C32-C33	-175.(4)	C30-C31-C32-C33	-7.(7)
C34-O3-C33-C32	-172.(5)	C34-O3-C33-C28	4.(7)
C31-C32-C33-O3	-177.(4)	C31-C32-C33-C28	7.(7)
C27-C28-C33-O3	0.(7)	C29-C28-C33-O3	-178.(4)
C27-C28-C33-C32	176.(5)	C29-C28-C33-C32	-2.(7)
C33-O3-C34-O4	176.(5)	C33-O3-C34-C35	-2.(7)
O2-C27-C35-C36	-9.(8)	C28-C27-C35-C36	179.(5)
O2-C27-C35-C34	-179.(5)	C28-C27-C35-C34	9.(9)
O4-C34-C35-C27	177.(7)	O3-C34-C35-C27	-4.(8)
O4-C34-C35-C36	6.(11)	O3-C34-C35-C36	-175.(5)
C27-C35-C36-O5	-179.(7)	C34-C35-C36-O5	-8.(10)

Table S5-7. Anisotropic atomic displacement parameters (Å^2) for Pu_XW4_SW2.

The anisotropic atomic displacement factor exponent takes the form: $-2\pi^2[h^2 a^{*2} U_{11} + ... + 2 h k a^* b^* U_{12}]$

	U_{11}	U_{22}	U_{33}	U_{23}	U_{13}	U_{12}
O1	0.070(15)	0.08(3)	0.046(19)	0.009(19)	0.033(14)	0.02(2)
O2	0.053(17)	0.037(17)	0.039(11)	-0.006(15)	0.016(9)	0.019(14)
O3	0.056(13)	0.09(3)	0.027(15)	0.005(19)	0.016(10)	-0.002(18)

	U_{11}	U_{22}	U_{33}	U_{23}	U_{13}	U_{12}
O4	0.058(16)	0.11(3)	0.040(15)	-0.01(2)	0.010(12)	0.01(2)
O5	0.049(16)	0.11(3)	0.06(2)	0.00(2)	0.008(17)	0.01(2)
O6	0.08(3)	0.11(3)	0.07(3)	0.04(3)	0.04(2)	0.03(3)
N2	0.054(16)	0.07(3)	0.030(16)	-0.02(2)	0.007(12)	0.00(2)
C5	0.051(11)	0.090(18)	0.053(12)	-0.003(17)	0.030(11)	-0.012(15)
C4	0.051(11)	0.090(18)	0.053(12)	-0.003(17)	0.030(11)	-0.012(15)
C3	0.051(11)	0.090(18)	0.053(12)	-0.003(17)	0.030(11)	-0.012(15)
C2	0.051(11)	0.090(18)	0.053(12)	-0.003(17)	0.030(11)	-0.012(15)
C1	0.051(11)	0.090(18)	0.053(12)	-0.003(17)	0.030(11)	-0.012(15)
N1	0.052(15)	0.10(4)	0.053(17)	0.00(2)	0.030(13)	-0.01(2)
C6	0.057(16)	0.12(5)	0.05(2)	-0.02(3)	0.027(13)	-0.01(2)
C7	0.063(17)	0.06(4)	0.05(2)	0.02(2)	0.023(16)	0.01(2)
C8	0.07(2)	0.06(4)	0.04(2)	0.02(3)	0.025(18)	0.00(3)
C9	0.08(2)	0.05(4)	0.04(2)	0.00(2)	0.009(17)	0.01(2)
C10	0.069(19)	0.04(3)	0.05(2)	0.01(2)	0.009(16)	0.00(2)
C11	0.063(19)	0.06(3)	0.02(2)	-0.01(2)	-0.008(15)	0.00(2)
C12	0.07(3)	0.08(4)	0.04(2)	0.00(2)	0.007(18)	0.01(3)
C13	0.05(2)	0.08(4)	0.04(2)	0.02(3)	0.020(19)	0.00(2)
C14	0.044(19)	0.05(3)	0.04(2)	0.00(2)	0.004(17)	-0.02(2)
C15	0.047(15)	0.04(3)	0.05(2)	0.01(2)	0.003(13)	-0.019(18)
C16	0.053(15)	0.08(3)	0.039(16)	0.013(19)	0.014(11)	0.00(2)
C17	0.035(12)	0.055(13)	0.035(9)	0.001(10)	0.023(7)	0.009(11)
C18	0.035(12)	0.055(13)	0.035(9)	0.001(10)	0.023(7)	0.009(11)

	U_{11}	U_{22}	U_{33}	U_{23}	U_{13}	U_{12}
C19	0.035(12)	0.055(13)	0.035(9)	0.001(10)	0.023(7)	0.009(11)
C20	0.05(3)	0.05(2)	0.046(19)	0.002(18)	0.011(16)	0.01(2)
C21	0.05(3)	0.07(2)	0.04(2)	0.00(2)	0.013(17)	0.02(2)
C22	0.09(4)	0.07(3)	0.05(2)	0.01(2)	0.005(19)	0.01(2)
C23	0.07(3)	0.07(2)	0.045(18)	0.013(16)	0.012(15)	0.012(19)
C24	0.05(3)	0.06(2)	0.033(19)	0.006(18)	0.015(15)	0.02(2)
C25	0.07(3)	0.08(3)	0.035(16)	0.006(17)	0.011(14)	0.01(2)
C26	0.035(12)	0.055(13)	0.035(9)	0.001(10)	0.023(7)	0.009(11)
C27	0.051(14)	0.07(4)	0.040(12)	-0.012(19)	0.013(10)	0.00(2)
C28	0.045(14)	0.09(4)	0.045(15)	0.00(2)	0.010(12)	0.00(2)
C29	0.051(16)	0.07(4)	0.041(18)	0.00(3)	0.015(12)	0.01(2)
C30	0.048(18)	0.05(3)	0.045(17)	-0.01(2)	0.015(15)	0.00(2)
C31	0.056(16)	0.04(3)	0.044(17)	0.00(2)	0.012(13)	0.00(2)
C32	0.058(16)	0.08(4)	0.04(2)	0.01(3)	0.017(13)	0.01(2)
C33	0.049(14)	0.03(3)	0.046(15)	0.00(2)	0.013(11)	0.00(2)
C34	0.052(15)	0.09(4)	0.039(14)	0.00(3)	0.012(11)	0.00(2)
C35	0.043(14)	0.05(3)	0.039(13)	0.01(2)	0.015(10)	-0.02(2)
C36	0.044(15)	0.09(4)	0.04(3)	0.02(3)	0.016(15)	-0.01(2)
C37	0.05(2)	0.09(4)	0.03(2)	-0.01(3)	0.015(16)	0.00(3)
C38	0.08(4)	0.10(5)	0.035(18)	-0.02(3)	0.017(19)	-0.03(4)

Table S5-8. Hydrogen atomic coordinates and isotropic atomic displacement parameters ($Å^2$) for Pu_XW4_SW2.

	x/a	y/b	z/c	U(eq)
H6C	0.0728	0.5141	0.4861	0.129
H6D	0.1399	0.4926	0.5694	0.129
H4	0.1942	0.5046	0.1915	0.076
H3	0.0300	0.5806	0.1464	0.076
H2	-0.0879	0.6593	0.2371	0.076
H1	-0.0416	0.6619	0.3730	0.076
H6A	0.2993	0.5827	0.3883	0.086
H6B	0.2785	0.3717	0.3717	0.086
H8	0.4317	0.3828	0.4095	0.071
H9	0.5970	0.2475	0.4186	0.068
H11	0.7730	0.2355	0.3657	0.057
H12	0.8739	0.2433	0.2628	0.075
H13	0.8032	0.3770	0.1434	0.071
H14	0.6486	0.5229	0.1312	0.055
H19	0.3910	0.2440	0.1631	0.049
H20	0.2790	0.1125	0.0549	0.06
H21	0.2323	0.2589	-0.0585	0.064
H22	0.2832	0.5519	-0.0799	0.085
H24	0.3807	0.8240	-0.0262	0.057
H25	0.4882	0.9598	0.0673	0.073
H29	0.3472	0.9423	0.1944	0.064
H30	0.2036	0.9934	0.2486	0.058
H32	0.3256	0.9763	0.4746	0.068

	x/a	y/b	z/c	U(eq)
H36	0.7167	0.7955	0.2526	0.072
H37A	0.0816	1.1805	0.3052	0.083
H37B	0.0117	1.1155	0.3731	0.083
H37C	0.0480	0.9742	0.3095	0.083
H38A	0.1776	0.9096	0.5065	0.109
H38B	0.0751	1.0220	0.4975	0.109
H38C	0.1799	1.1241	0.5149	0.109

Table 9. Hydrogen bond distances (Å) and angles (°) for Pu_XW4_SW2.

	Donor-H	Acceptor-H	Donor-Acceptor	Angle
O6-H6C···N1	1.06	2.21	2.90(4)	120.8
O6-H6D···O5#1	0.75	2.22	2.96(5)	166.6

Symmetry transformations used to generate equivalent atoms:

#1 -x+1, y-1/2, -z+1

Appendix for Chapter 6

Fluorescence excitation spectra of (*S*)-2 with L-cysteine

Figure S6-1. Fluorescence excitation spectra of (*S*)-**2** (1.0×10^{-5} M in HEPES/ 1% DMSO, pH = 7.4) with L-Cys (30 equiv) (reaction time: 8 h, room temperature, λ_{em1} = 462 nm, λ_{em2} = 570 nm slits: 3/3 nm).

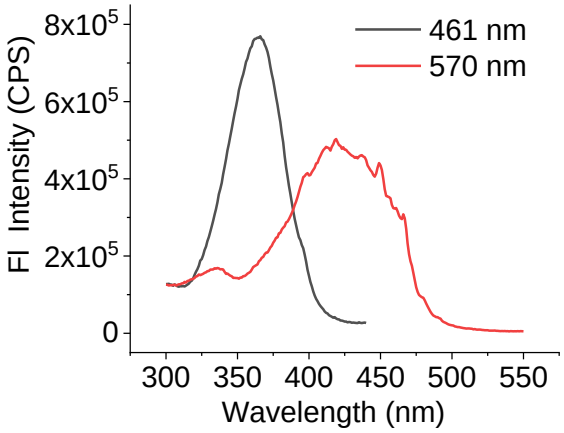

Effect of NEM on the fluorescent response of (*S*)-2 toward thiols

Figure S6-2. The fluorescence spectra of (*S*)-**2** (1.0×10^{-5} M in HEPES/ 1% DMSO, pH = 7.4) with various substrates (30 equiv. additionally with or without 30 equiv. NEM or 4equiv. GSH) at the excitation wavelength of 362 nm (a) and 415 nm (b) (reaction time: 8h, at room temperature, slits: 3/3 nm).

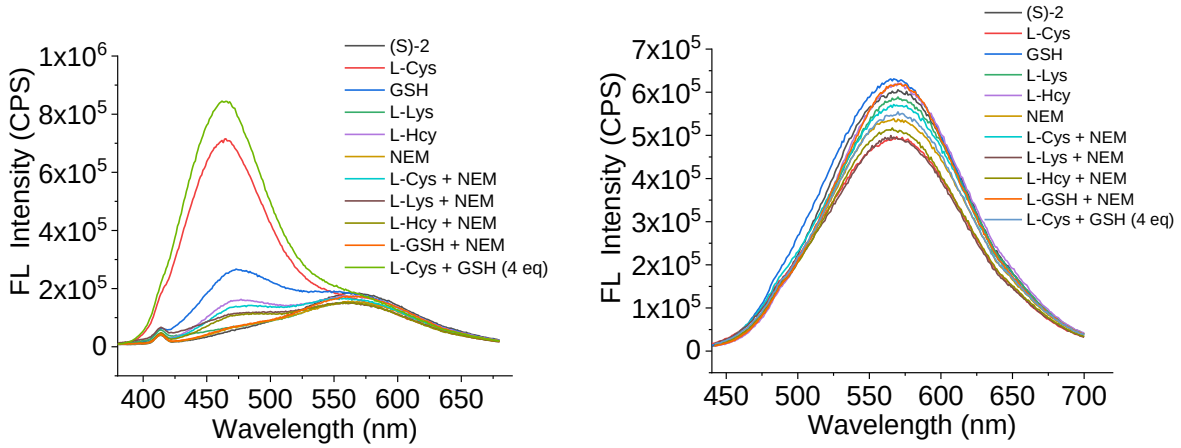

(a) (b)

Fluorescent enantioselective exploration of (*S*)-2 with Cys and Lys

Figure S6-3. The fluorescence spectra of (*S*)-**2** (1.0×10^{-5} M in HEPES/ 1% DMSO, pH = 7.4) with the enantiomers of Cys and Lys (30 equiv) at the excitation wavelength of 362 nm (a) and 415 nm (b) (reaction time: 8h, at room temperature, slits: 3/3 nm).

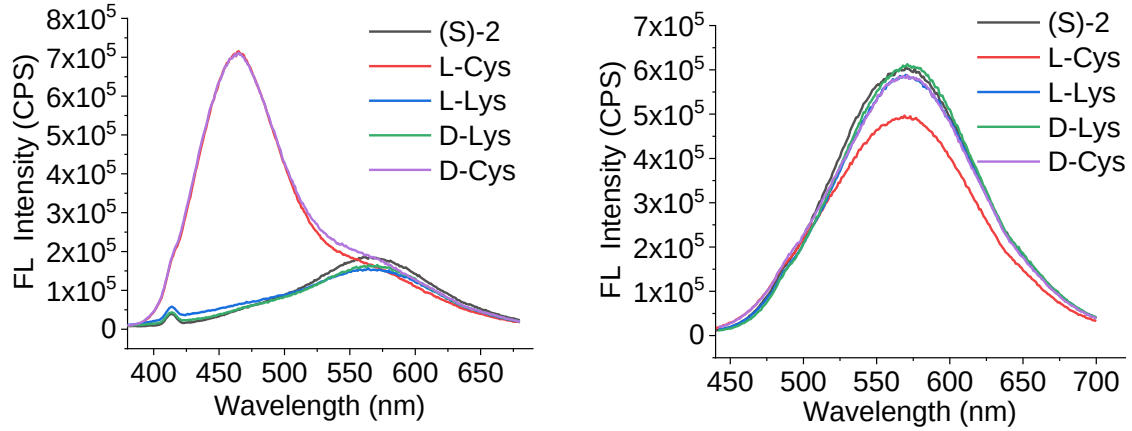

(a) (b)

Fluorescent response of (*S*)-2 with analytes at different temperature and time

Figure S6-4. The fluorescence spectra of (*S*)-**2** (1.0×10^{-5} M in HEPES/ 1% DMSO, pH = 7.4) with 30 equiv. of L-Cys (a), L-Hcy (b), L-His (c), L-Lys (d) as well as the fluorescent intensities at 461 nm when incubated at 37 °C (e) and cooled in an ice bath (f) (37 °C reaction time: 0-3h, ice bath cooling time: 0-120 mins, slits: 3/3 nm).

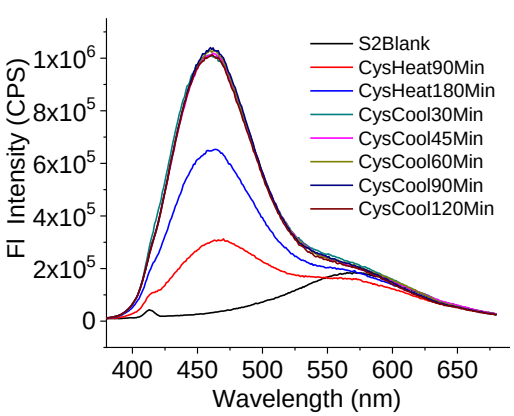

(a)

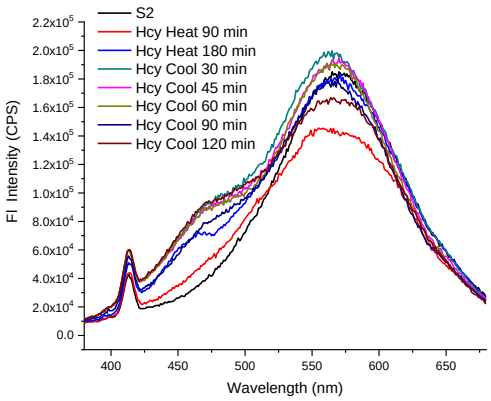

(b)

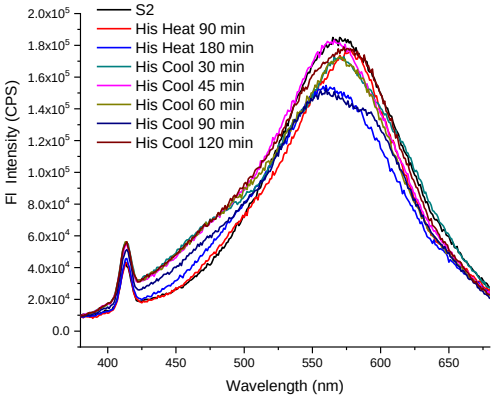

(c)

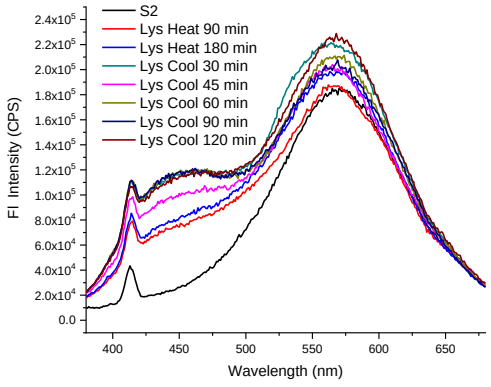

(d)

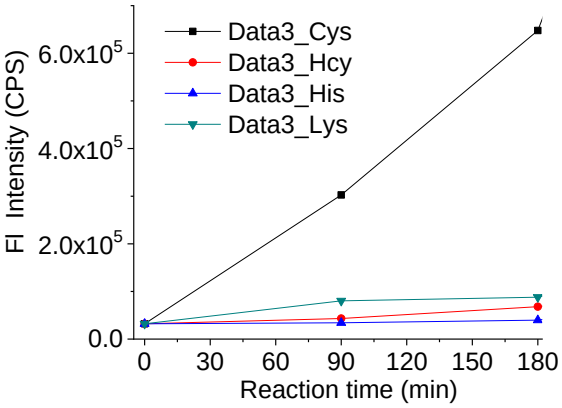
Data3_Cys
Data3_Hcy
Data3_His
Data3_Lys
Fl Intensity (CPS)
6.0x10^5
4.0x10^5
2.0x10^5
0.0
0
30
60
90
120
150
180
Reaction time (min)

(e)

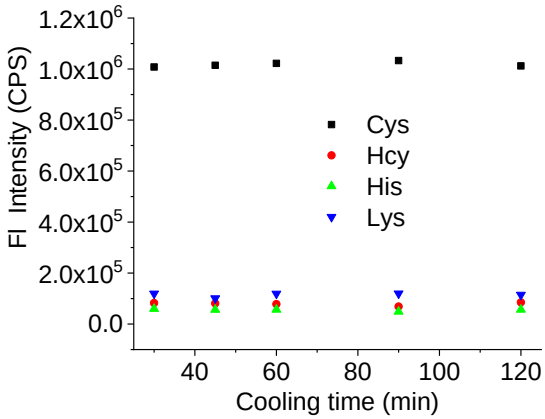
Cys
Hcy
His
Lys
Fl Intensity (CPS)
1.2x10^6
1.0x10^6
8.0x10^5
6.0x10^5
4.0x10^5
2.0x10^5
0.0
40
60
80
100
120
Cooling time (min)

(f)

Determination of detection limit for cysteine by (*S*)-2

Figure S6-5. The fluorescence intensities at 461 nm versus the L-Cys concentrations from 0-200 μM of three independent experiments (a-c) and the averaged curve (d) (reaction time: 3h, at 37 °C, λ_{exc} = 362 nm, slits: 3/3 nm).

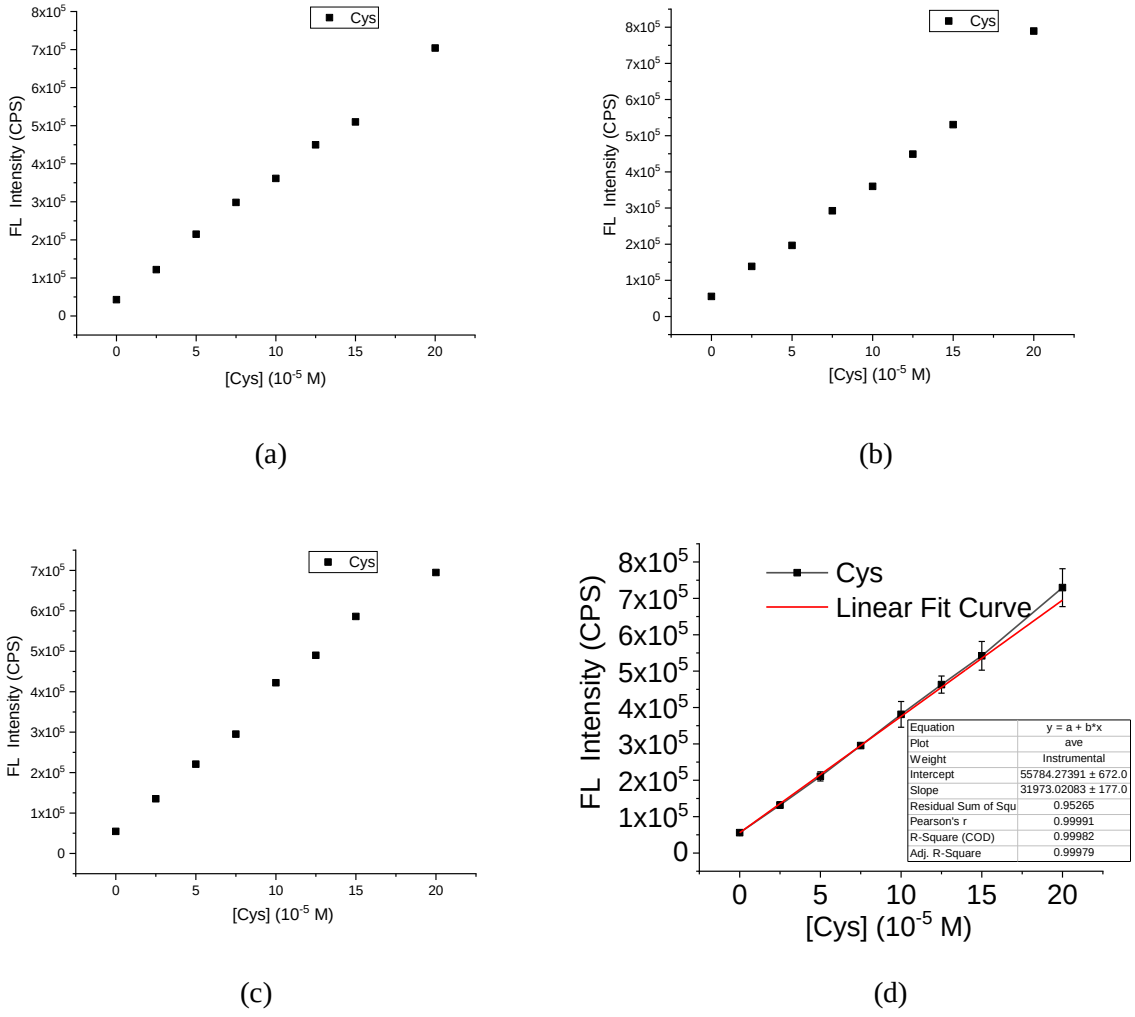

The detection limit was evaluated based on the fluorescence titration. Under the heating-cooling conditions, a good linear relationship between the fluorescence intensity and the Cys concentration could be obtained from 0 to 200 μmol/L (R^2 = 0.99979). The detection limit was then calculated

with the equation: detection limit=3δ/m, where δ is the standard deviation of blank measurements; m is the averaged slope between intensity versus sample concentrations (n=3).

LOD = 3×δ/m ×10^{-5} M= (3×1708.40/31973.02) ×10^{-5} M = 0.16×10^{-5} M = 1.60 μM

Fluorescence response of (*S*)-2 with various amino acids

Figure S6-6. The fluorescence response of (*S*)-**2** (1.0 × 10^{-5} M in HEPES/ 1% DMSO, pH = 7.4) with various amino acids [10 equiv. (a), 30 equiv. (c)] as well as the fluorescence intensities at 461 nm of all spectra in graph a (b) and graph c (d). (reaction time: 3h, at 37 °C, λ_{exc} = 362 nm, slits: 3/3 nm, the saturated concentrations were applied to calculate the reacted concentrations for Tyr and Cst since both tyrosine and cystine had very low solubilities)

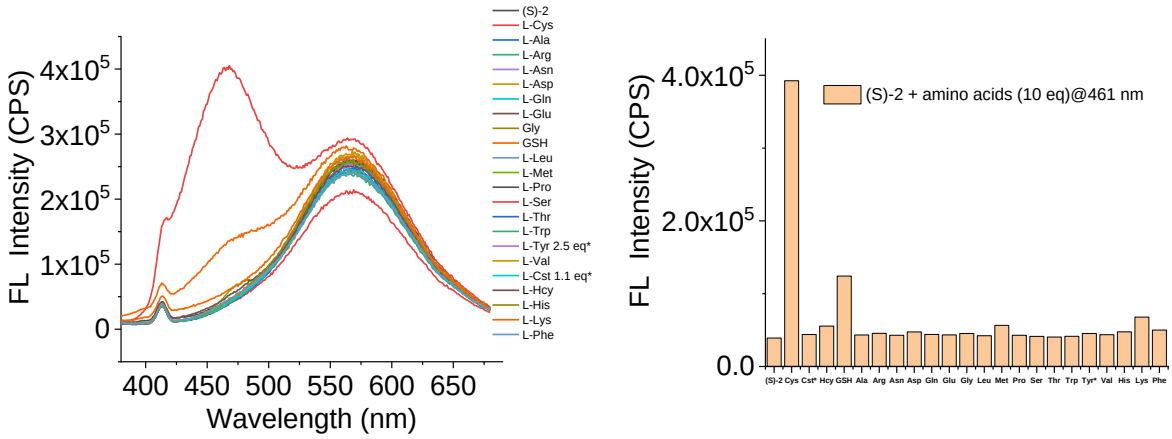

(a) (b)

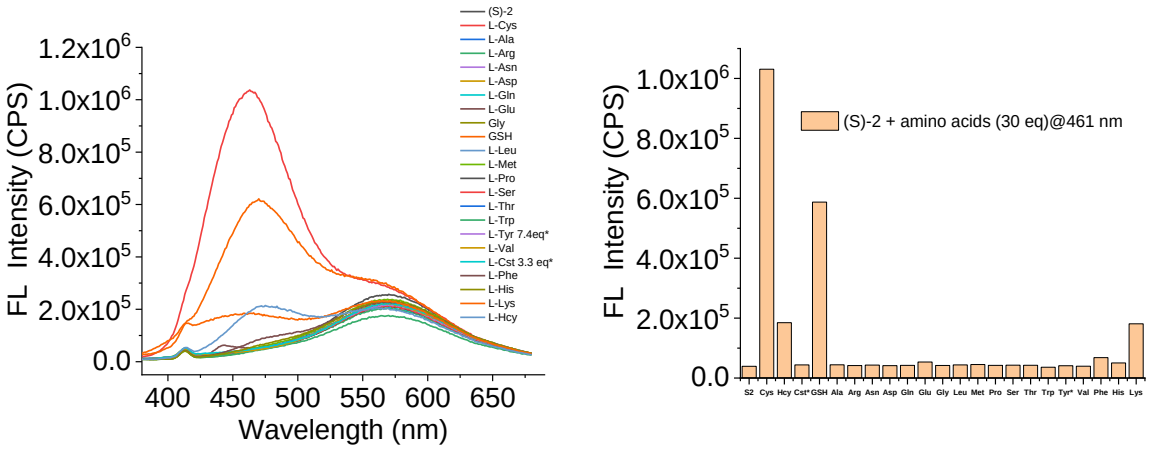

(c) (d)

Competing experiments of (*S*)-2 and L-Cys with various other competing analytes

Figure S6-7. The fluorescence spectra of (*S*)-**2** (1.0×10^{-5} M in HEPES/ 1% DMSO, pH = 7.4) and L-Cys (10 equiv) in the presence of various competing analytes (2-30 equiv) (a) as well as the changes of the fluorescence intensities at 461 nm of (*S*)-**2** (1.0×10^{-5} M) towards L-Cys (10 equiv) in the presence of the competing analytes (b). (reaction time: 3h, at 37 ^{o}C, λ_{exc} = 362 nm, slits: 3/3 nm, the saturated concentrations were applied to calculate the reacted concentrations for Tyr and Cst since both tyrosine and cystine had very low solubilities)

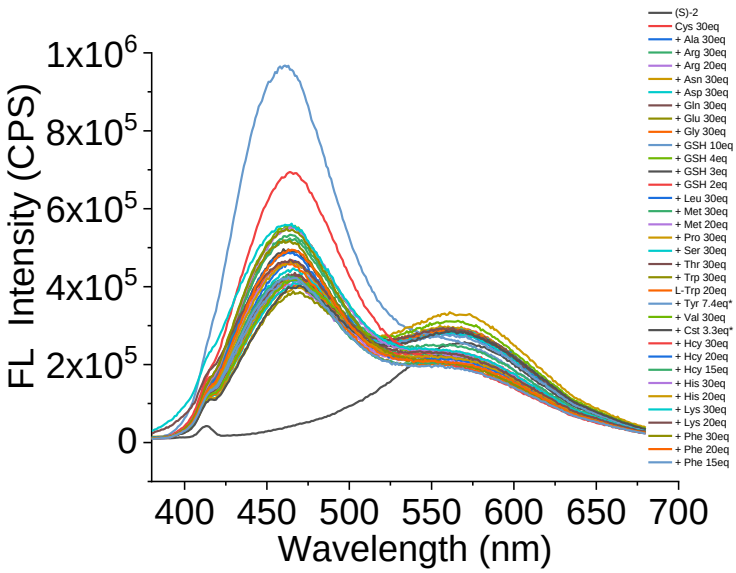
FL Intensity (CPS)
1x10^6
8x10^5
6x10^5
4x10^5
2x10^5
0
400 450 500 550 600 650 700
Wavelength (nm)
(S)-2
Cys 30eq
+ Ala 30eq
+ Arg 30eq
+ Arg 20eq
+ Asn 30eq
+ Asp 30eq
+ Gln 30eq
+ Glu 30eq
+ Gly 30eq
+ GSH 10eq
+ GSH 4eq
+ GSH 3eq
+ GSH 2eq
+ Leu 30eq
+ Met 30eq
+ Met 20eq
+ Pro 30eq
+ Ser 30eq
+ Thr 30eq
+ Trp 30eq
L-Trp 20eq
+ Tyr 7.4eq*
+ Val 30eq
+ Cst 3.3eq*
+ Hcy 30eq
+ Hcy 20eq
+ Hcy 15eq
+ His 30eq
+ His 20eq
+ Lys 30eq
+ Lys 20eq
+ Phe 30eq
+ Phe 20eq
+ Phe 15eq

(a)

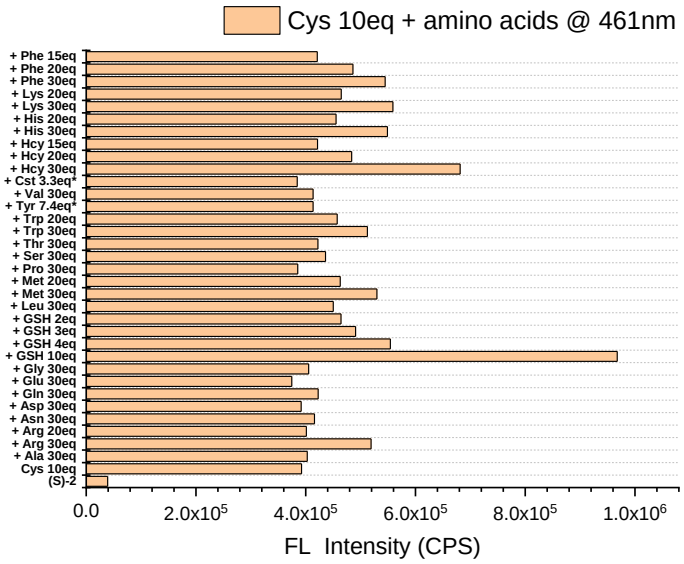
Cys 10eq + amino acids @ 461nm
+ Phe 15eq
+ Phe 20eq
+ Phe 30eq
+ Lys 20eq
+ Lys 30eq
+ His 20eq
+ His 30eq
+ Hcy 15eq
+ Hcy 20eq
+ Hcy 30eq
+ Cst 3.3eq*
+ Val 30eq
+ Tyr 7.4eq*
+ Trp 20eq
+ Trp 30eq
+ Thr 30eq
+ Ser 30eq
+ Pro 30eq
+ Met 20eq
+ Met 30eq
+ Leu 30eq
+ GSH 2eq
+ GSH 3eq
+ GSH 4eq
+ GSH 10eq
+ Gly 30eq
+ Glu 30eq
+ Gln 30eq
+ Asp 30eq
+ Asn 30eq
+ Arg 20eq
+ Arg 30eq
+ Ala 30eq
Cys 10eq
(S)-2
0.0
2.0x10^5
4.0x10^5
6.0x10^5
8.0x10^5
1.0x10^6
FL Intensity (CPS)

(b)

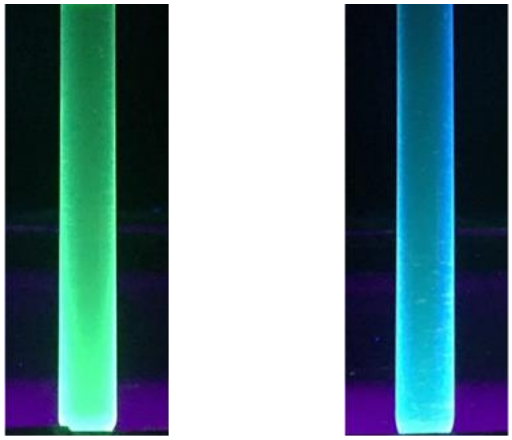

(a) (b)

Figure S6-8. The photo images observed under a 365 nm UV lamp of the fluorescence response of (*S*)-**2** (1.0×10^{-3} M in HEPES/ 1% DMSO, pH = 7.4) without amino acids (a) and with 3 equiv of Cys (b). (reaction undergoes for 3h at 37 ^{o}C, photos taken at room temperature)

UV-Vis spectroscopic study

Figure S6-9. (a) UV-Vis spectrum of (*S*)-**2**, (*S*)-BINOL, (*S*)-**6**, and **4** (All 10 □M in DMSO). (b) UV-Vis spectrum of (*S*)-**2**, (*S*)-**6**, **7'** and **8+8'** (**7'** with 3 equiv Cys, product mixture of Figure S16 in SI) (All 10 μM in 99% HEPES and 1% DMSO).

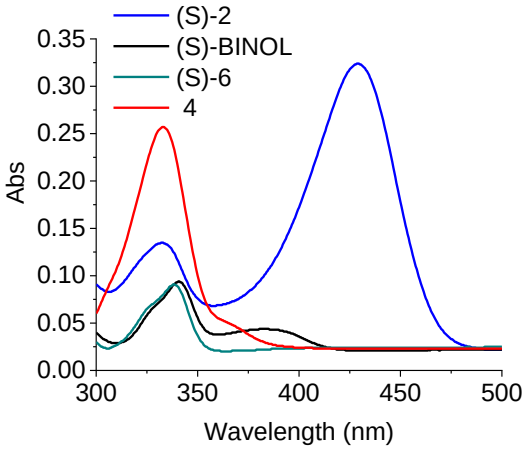

(a)

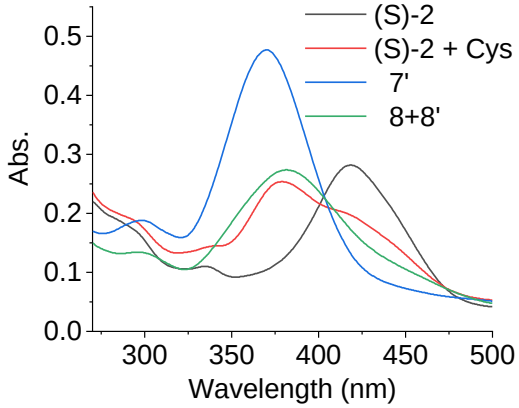

(b)

^{1}H NMR spectroscopic study

Figure S6-10. ^{1}H NMR spectra of (*S*)-**2** (1.0 mM in DMSO-d_6) with L-Cys (3 equiv) in HEPES (H_2O, 25 mM HEPES, 120 mM NaCl, pH=7.4). [reaction time: 10 min – 20 h. DMSO: HEPES = 9:1 (v)]

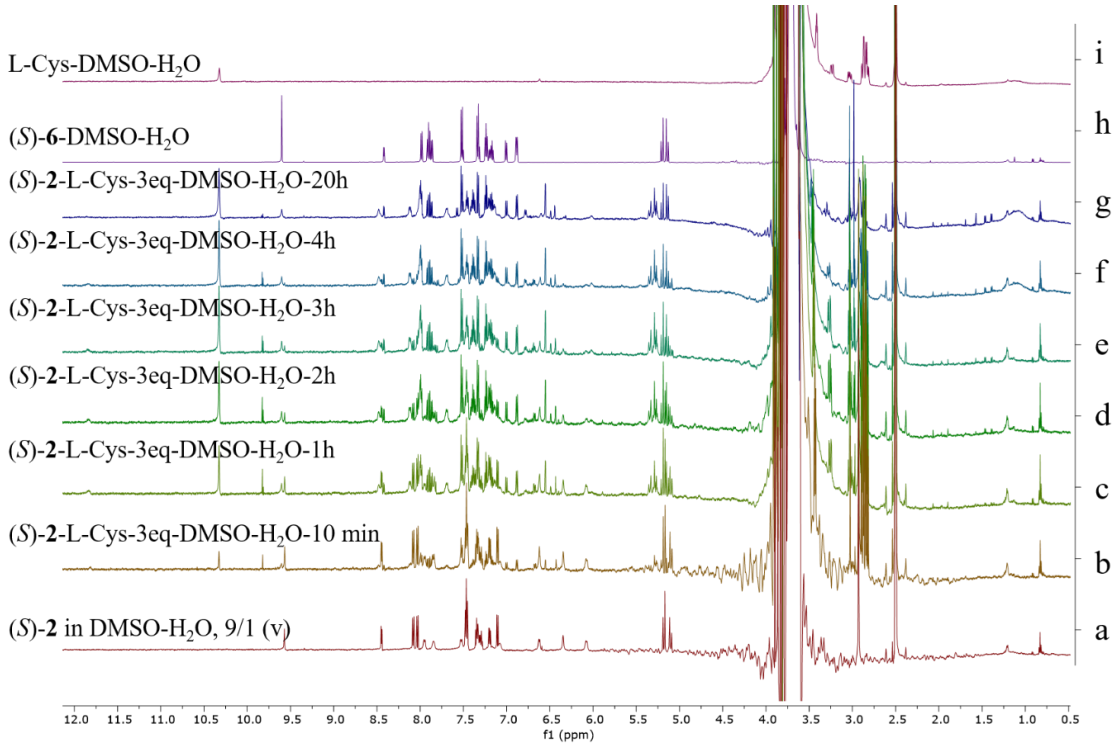

(1)

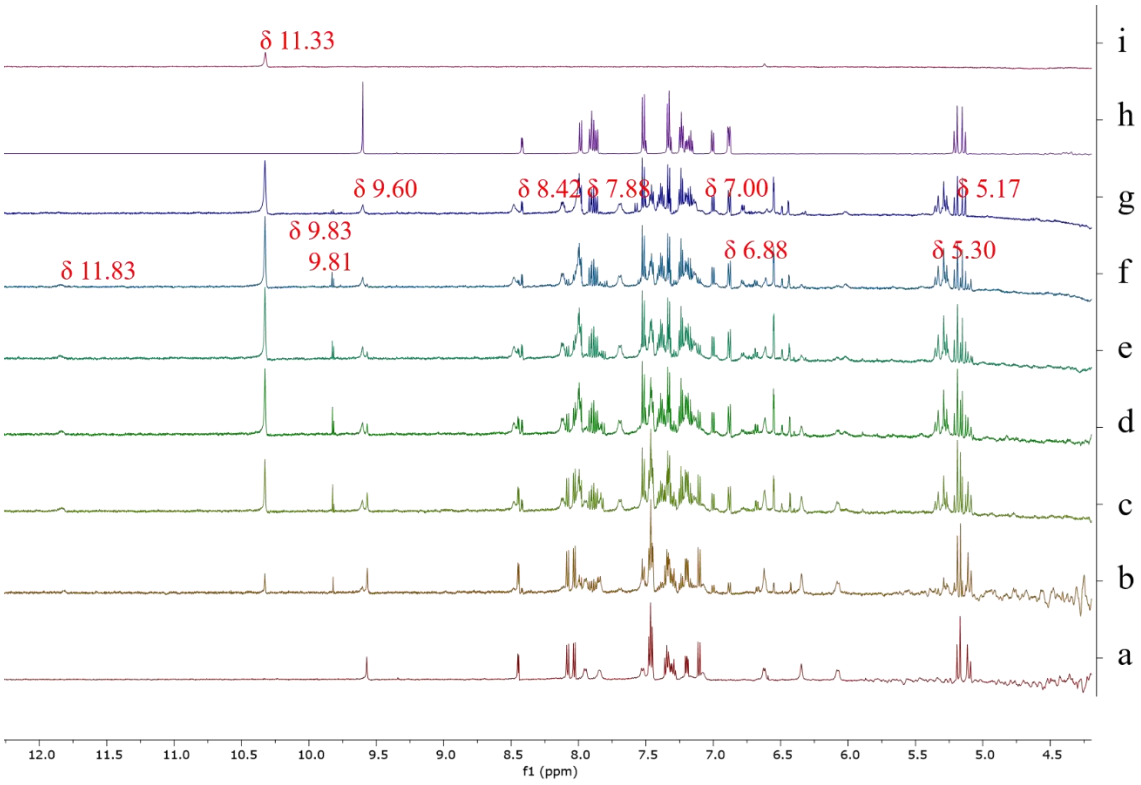
δ 11.33
δ 9.60
δ 8.42
δ 7.88
δ 7.00
δ 5.17
δ 9.83
9.81
δ 11.83
δ 6.88
δ 5.30
i
h
g
f
e
d
c
b
a
12.0 11.5 11.0 10.5 10.0 9.5 9.0 8.5 8.0 7.5 7.0 6.5 6.0 5.5 5.0 4.5
f1 (ppm)

(2)

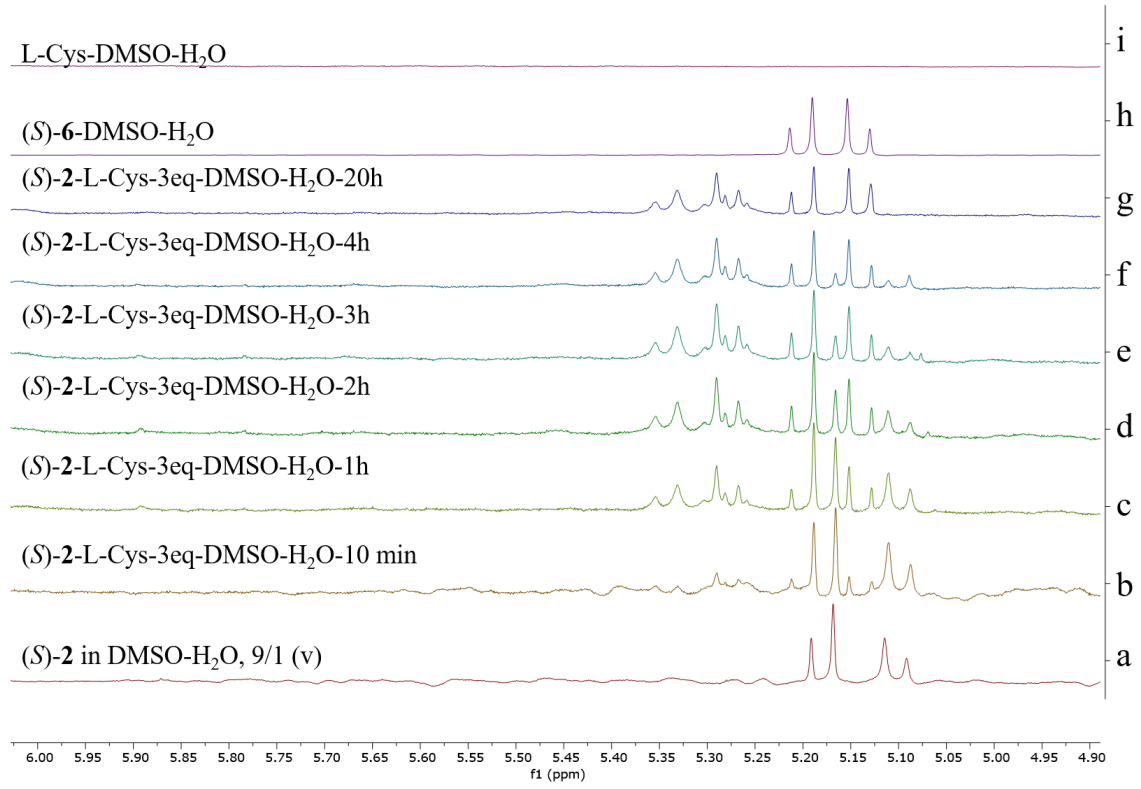
L-Cys-DMSO-H2O
(S)-6-DMSO-H2O
(S)-2-L-Cys-3eq-DMSO-H2O-20h
(S)-2-L-Cys-3eq-DMSO-H2O-4h
(S)-2-L-Cys-3eq-DMSO-H2O-3h
(S)-2-L-Cys-3eq-DMSO-H2O-2h
(S)-2-L-Cys-3eq-DMSO-H2O-1h
(S)-2-L-Cys-3eq-DMSO-H2O-10 min
(S)-2 in DMSO-H2O, 9/1 (v)
i
h
g
f
e
d
c
b
a
6.00 5.95 5.90 5.85 5.80 5.75 5.70 5.65 5.60 5.55 5.50 5.45 5.40 5.35 5.30 5.25 5.20 5.15 5.10 5.05 5.00 4.95 4.90
f1 (ppm)

(3)

Figure S6-11. ^{1}H NMR spectra of (*S*)-**2** (1.0 mM in DMSO-d_6) with 2 equiv of L-Cys (a-d), 2 equiv of GSH (e-h), 1 equiv of Hcy (i-k), 1 equiv of Cys (l-n) in H_2O [reaction time: 10 min – 20 h. DMSO: H_2O = 9:1 (v)]

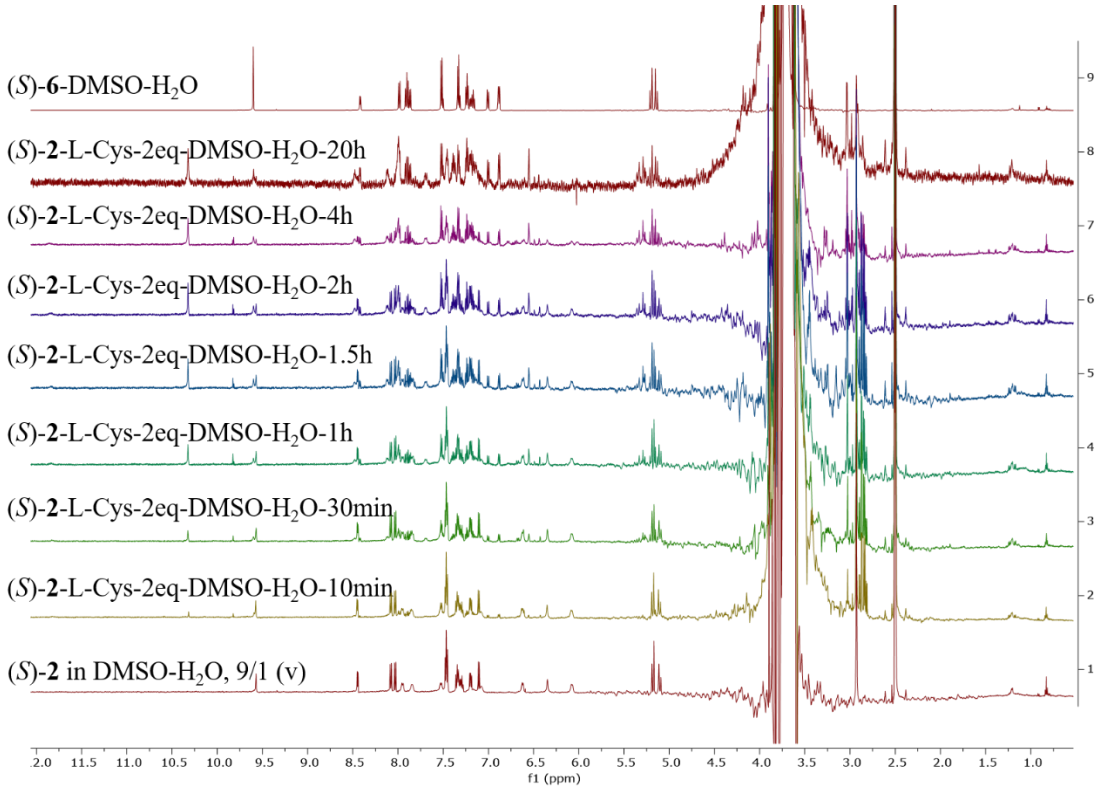

(a)

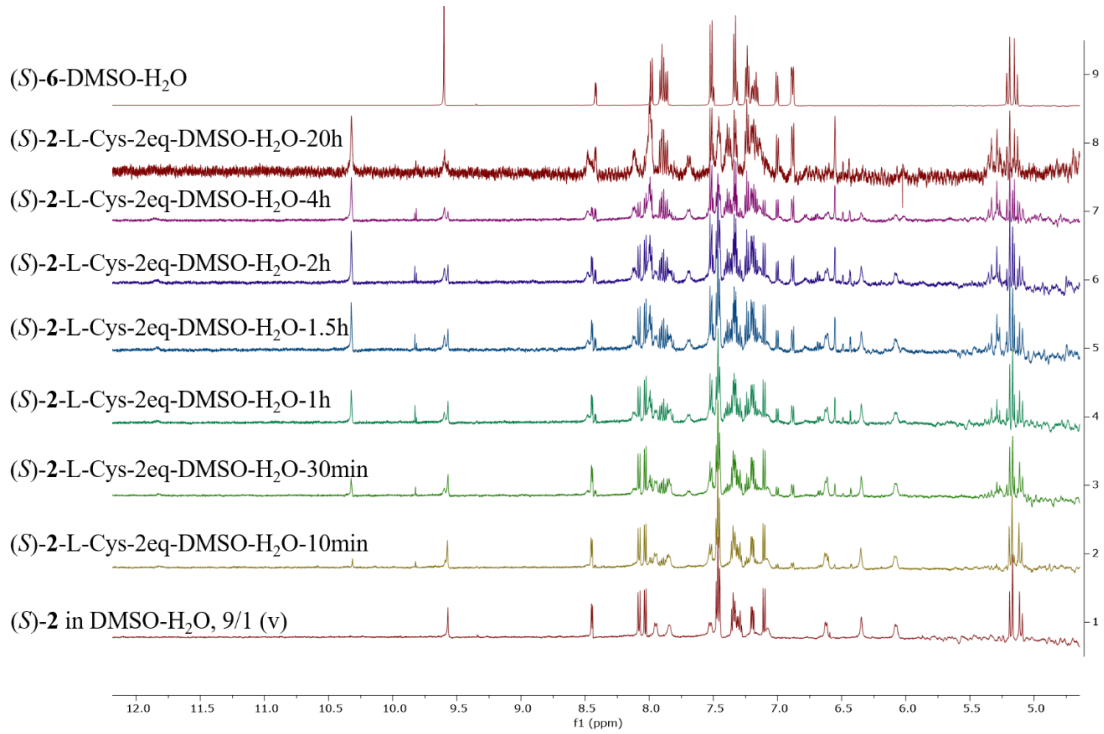
(S)-6-DMSO-H2O
(S)-2-L-Cys-2eq-DMSO-H2O-20h
(S)-2-L-Cys-2eq-DMSO-H2O-4h
(S)-2-L-Cys-2eq-DMSO-H2O-2h
(S)-2-L-Cys-2eq-DMSO-H2O-1.5h
(S)-2-L-Cys-2eq-DMSO-H2O-1h
(S)-2-L-Cys-2eq-DMSO-H2O-30min
(S)-2-L-Cys-2eq-DMSO-H2O-10min
(S)-2 in DMSO-H2O, 9/1 (v)
12.0 11.5 11.0 10.5 10.0 9.5 9.0 8.5 8.0 7.5 7.0 6.5 6.0 5.5 5.0
f1 (ppm)

(b)

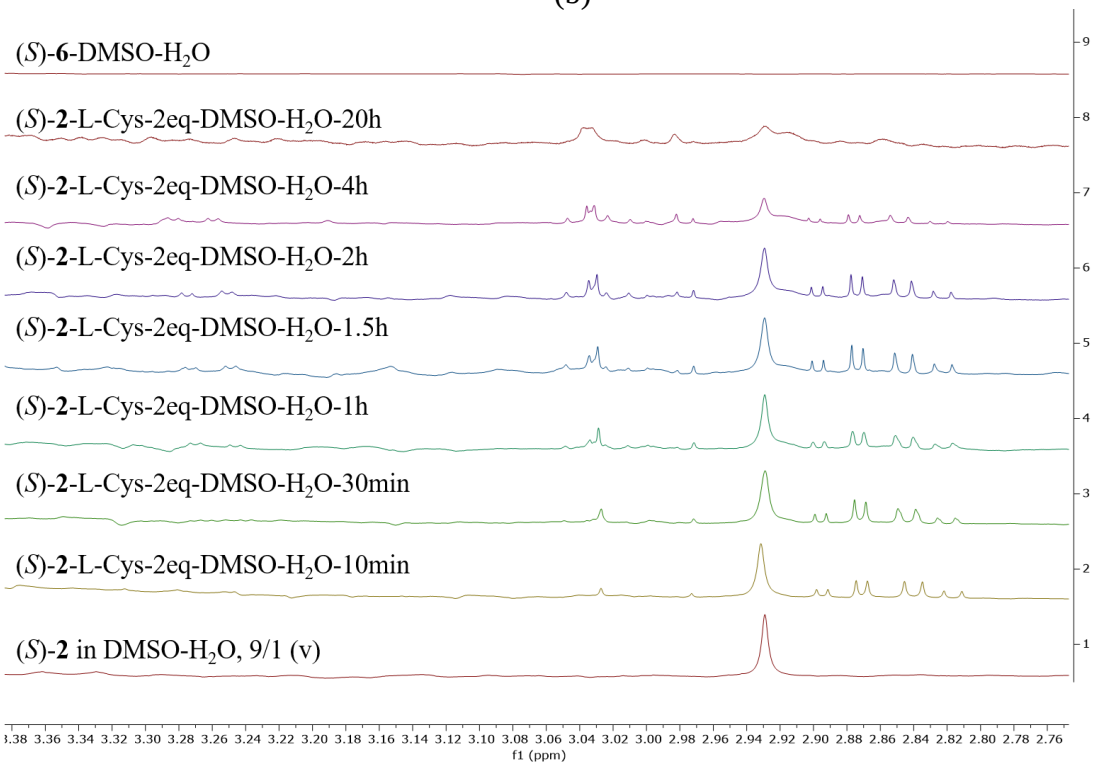
(S)-6-DMSO-H2O
(S)-2-L-Cys-2eq-DMSO-H2O-20h
(S)-2-L-Cys-2eq-DMSO-H2O-4h
(S)-2-L-Cys-2eq-DMSO-H2O-2h
(S)-2-L-Cys-2eq-DMSO-H2O-1.5h
(S)-2-L-Cys-2eq-DMSO-H2O-1h
(S)-2-L-Cys-2eq-DMSO-H2O-30min
(S)-2-L-Cys-2eq-DMSO-H2O-10min
(S)-2 in DMSO-H2O, 9/1 (v)
3.38 3.36 3.34 3.32 3.30 3.28 3.26 3.24 3.22 3.20 3.18 3.16 3.14 3.12 3.10 3.08 3.06 3.04 3.02 3.00 2.98 2.96 2.94 2.92 2.90 2.88 2.86 2.84 2.82 2.80 2.78 2.76
f1 (ppm)

(c)

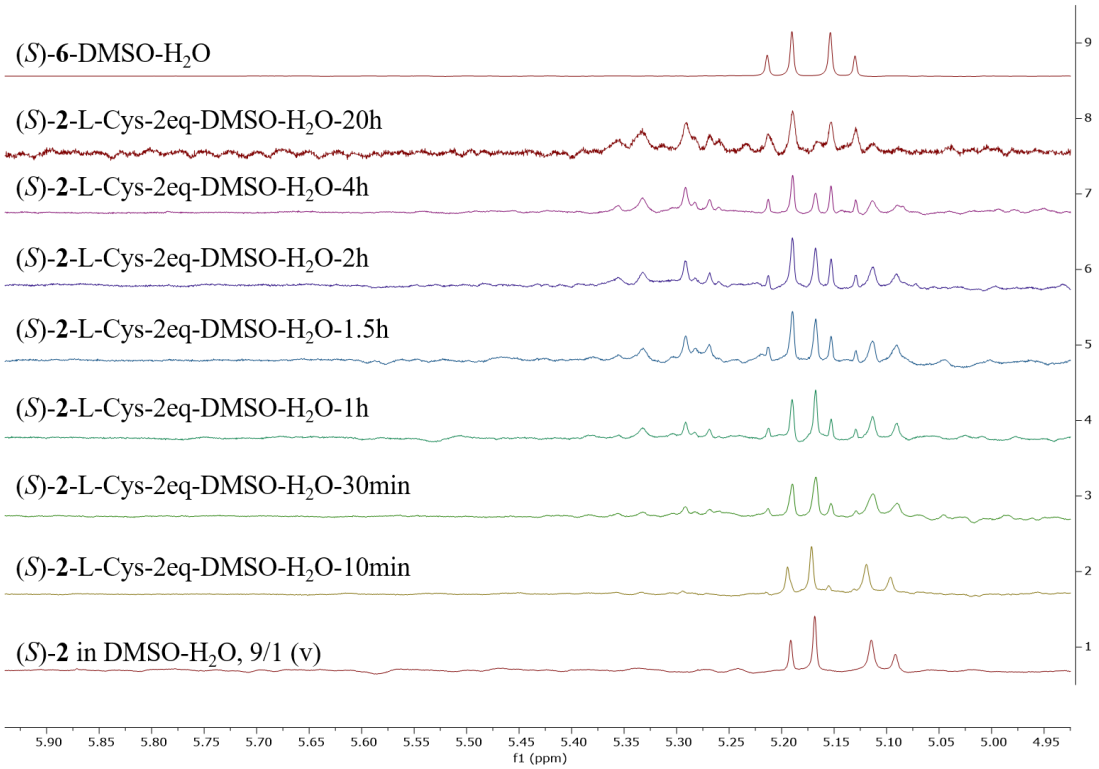
(S)-6-DMSO-H2O
(S)-2-L-Cys-2eq-DMSO-H2O-20h
(S)-2-L-Cys-2eq-DMSO-H2O-4h
(S)-2-L-Cys-2eq-DMSO-H2O-2h
(S)-2-L-Cys-2eq-DMSO-H2O-1.5h
(S)-2-L-Cys-2eq-DMSO-H2O-1h
(S)-2-L-Cys-2eq-DMSO-H2O-30min
(S)-2-L-Cys-2eq-DMSO-H2O-10min
(S)-2 in DMSO-H2O, 9/1 (v)
5.90 5.85 5.80 5.75 5.70 5.65 5.60 5.55 5.50 5.45 5.40 5.35 5.30 5.25 5.20 5.15 5.10 5.05 5.00 4.95
f1 (ppm)

(d)

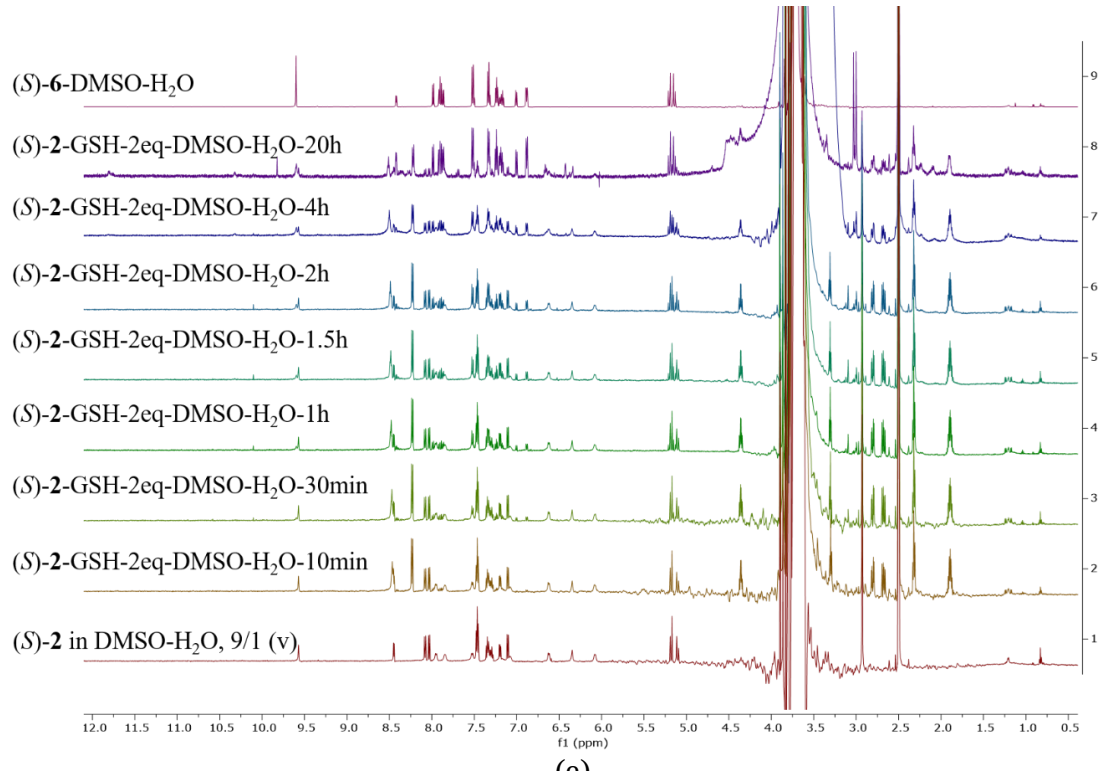
(S)-6-DMSO-H2O
(S)-2-GSH-2eq-DMSO-H2O-20h
(S)-2-GSH-2eq-DMSO-H2O-4h
(S)-2-GSH-2eq-DMSO-H2O-2h
(S)-2-GSH-2eq-DMSO-H2O-1.5h
(S)-2-GSH-2eq-DMSO-H2O-1h
(S)-2-GSH-2eq-DMSO-H2O-30min
(S)-2-GSH-2eq-DMSO-H2O-10min
(S)-2 in DMSO-H2O, 9/1 (v)
12.0 11.5 11.0 10.5 10.0 9.5 9.0 8.5 8.0 7.5 7.0 6.5 6.0 5.5 5.0 4.5 4.0 3.5 3.0 2.5 2.0 1.5 1.0 0.5
f1 (ppm)

(e)

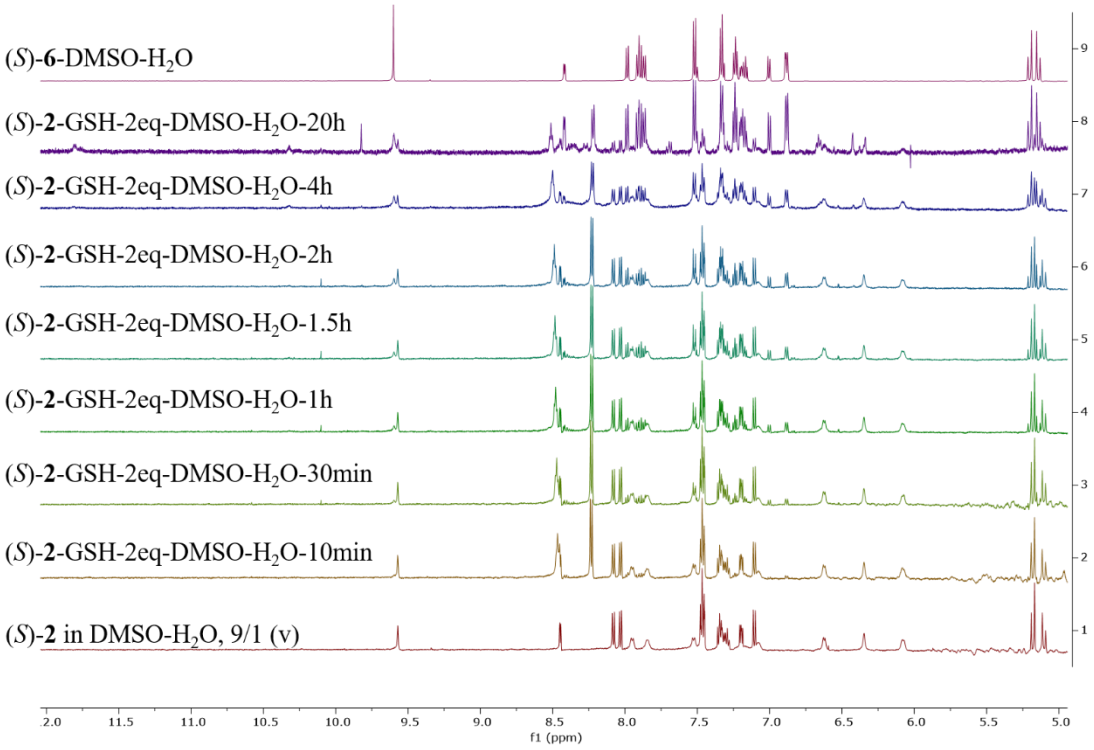
(S)-6-DMSO-H2O
(S)-2-GSH-2eq-DMSO-H2O-20h
(S)-2-GSH-2eq-DMSO-H2O-4h
(S)-2-GSH-2eq-DMSO-H2O-2h
(S)-2-GSH-2eq-DMSO-H2O-1.5h
(S)-2-GSH-2eq-DMSO-H2O-1h
(S)-2-GSH-2eq-DMSO-H2O-30min
(S)-2-GSH-2eq-DMSO-H2O-10min
(S)-2 in DMSO-H2O, 9/1 (v)
f1 (ppm)

(f)

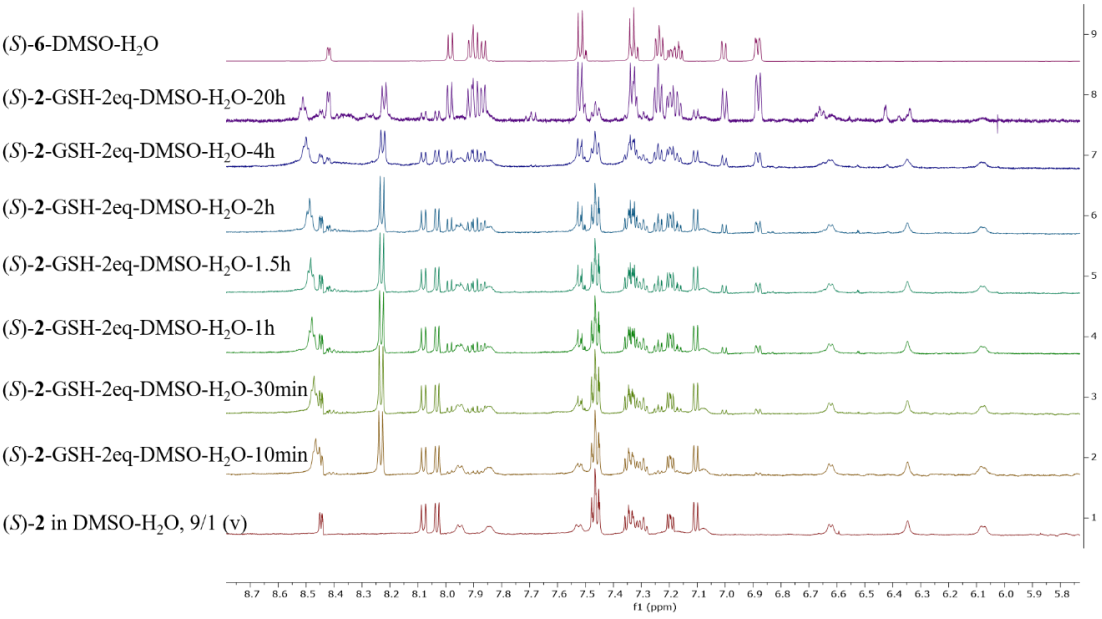
(S)-6-DMSO-H2O
(S)-2-GSH-2eq-DMSO-H2O-20h
(S)-2-GSH-2eq-DMSO-H2O-4h
(S)-2-GSH-2eq-DMSO-H2O-2h
(S)-2-GSH-2eq-DMSO-H2O-1.5h
(S)-2-GSH-2eq-DMSO-H2O-1h
(S)-2-GSH-2eq-DMSO-H2O-30min
(S)-2-GSH-2eq-DMSO-H2O-10min
(S)-2 in DMSO-H2O, 9/1 (v)
f1 (ppm)

(g)

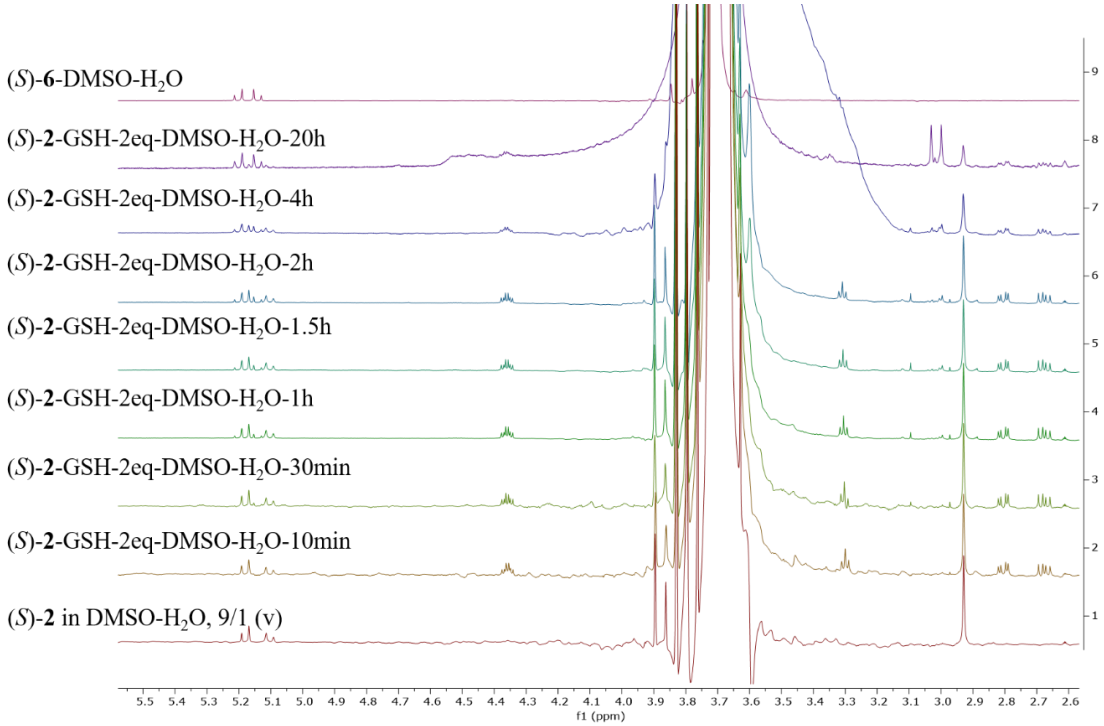
(S)-6-DMSO-H2O
(S)-2-GSH-2eq-DMSO-H2O-20h
(S)-2-GSH-2eq-DMSO-H2O-4h
(S)-2-GSH-2eq-DMSO-H2O-2h
(S)-2-GSH-2eq-DMSO-H2O-1.5h
(S)-2-GSH-2eq-DMSO-H2O-1h
(S)-2-GSH-2eq-DMSO-H2O-30min
(S)-2-GSH-2eq-DMSO-H2O-10min
(S)-2 in DMSO-H2O, 9/1 (v)
f1 (ppm)

(h)

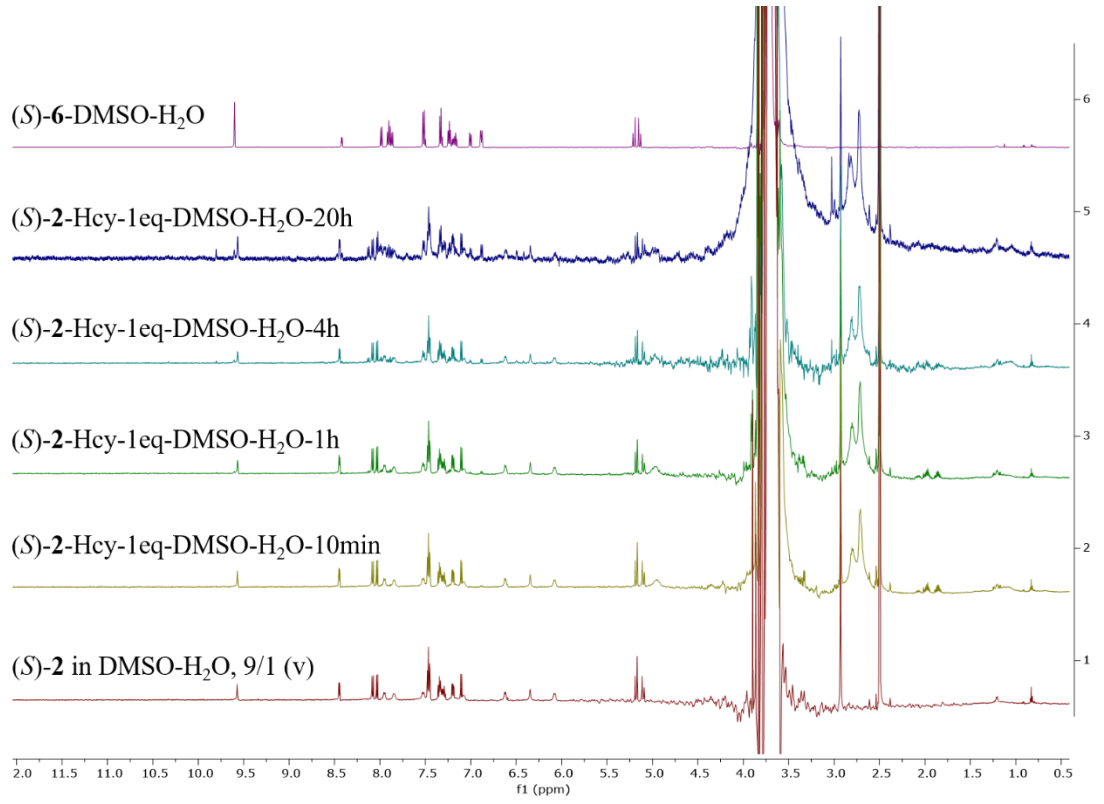
(S)-6-DMSO-H2O
(S)-2-Hcy-1eq-DMSO-H2O-20h
(S)-2-Hcy-1eq-DMSO-H2O-4h
(S)-2-Hcy-1eq-DMSO-H2O-1h
(S)-2-Hcy-1eq-DMSO-H2O-10min
(S)-2 in DMSO-H2O, 9/1 (v)
f1 (ppm)

(i)

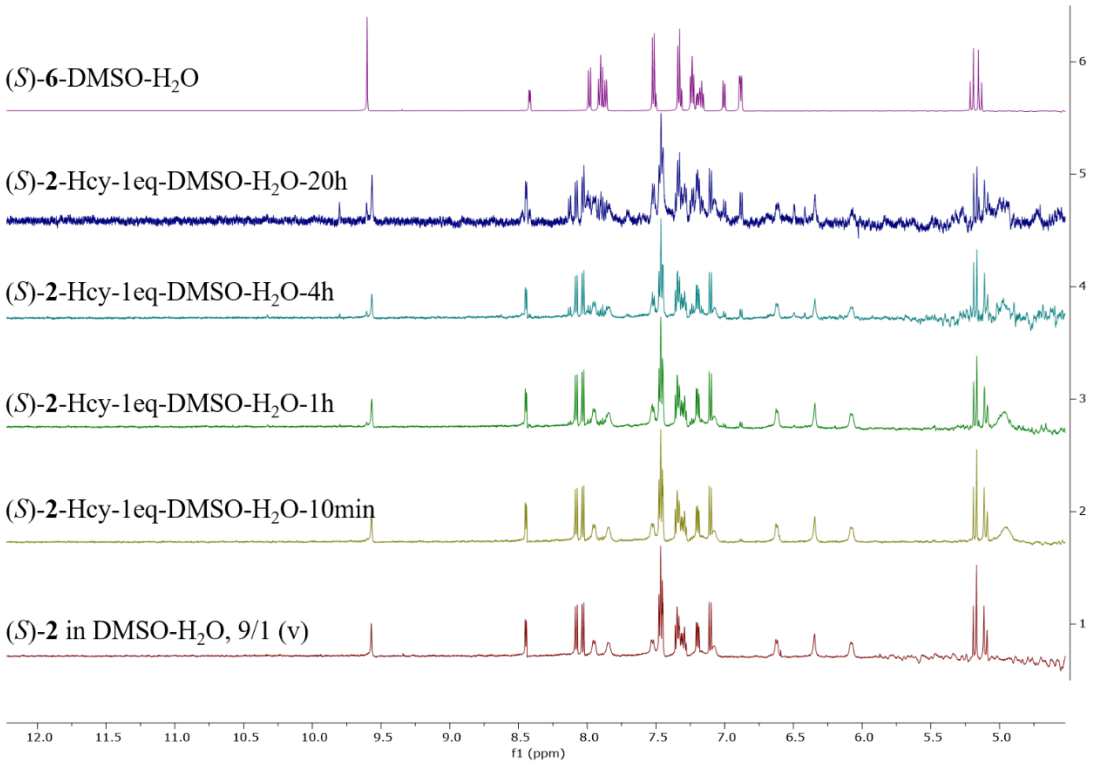
(S)-6-DMSO-H2O
(S)-2-Hcy-1eq-DMSO-H2O-20h
(S)-2-Hcy-1eq-DMSO-H2O-4h
(S)-2-Hcy-1eq-DMSO-H2O-1h
(S)-2-Hcy-1eq-DMSO-H2O-10min
(S)-2 in DMSO-H2O, 9/1 (v)
12.0 11.5 11.0 10.5 10.0 9.5 9.0 8.5 8.0 7.5 7.0 6.5 6.0 5.5 5.0
f1 (ppm)
6 5 4 3 2 1

(j)

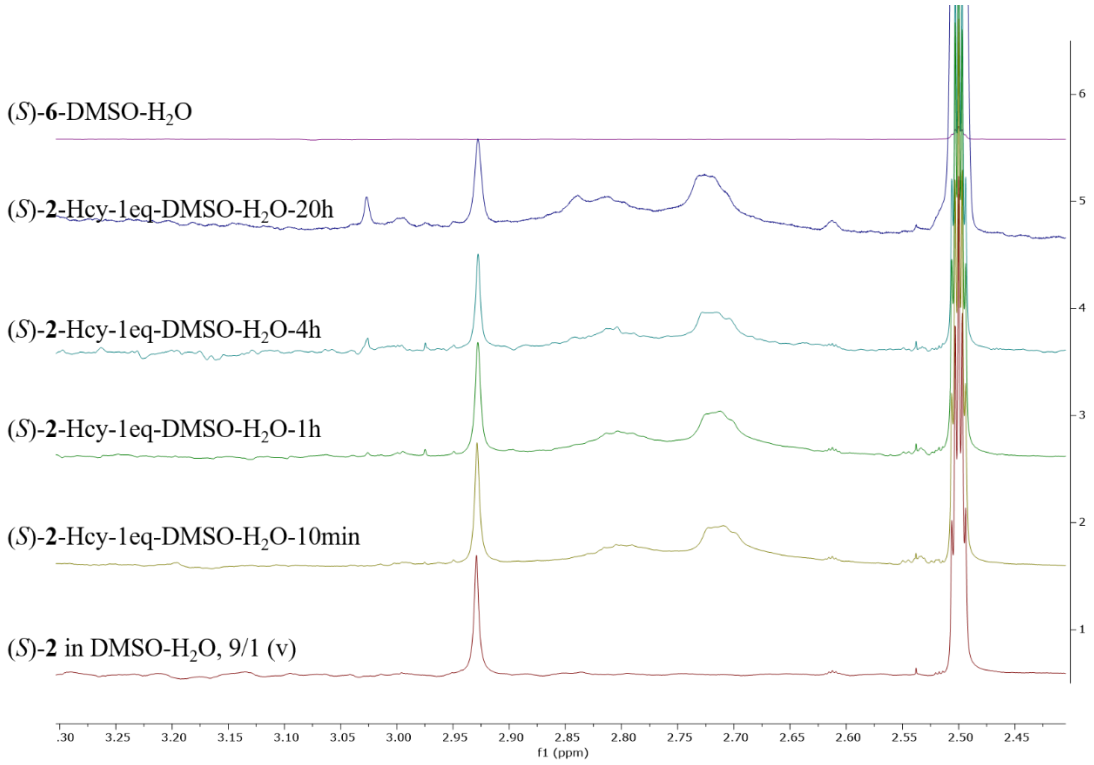
(S)-6-DMSO-H2O
(S)-2-Hcy-1eq-DMSO-H2O-20h
(S)-2-Hcy-1eq-DMSO-H2O-4h
(S)-2-Hcy-1eq-DMSO-H2O-1h
(S)-2-Hcy-1eq-DMSO-H2O-10min
(S)-2 in DMSO-H2O, 9/1 (v)
.30 3.25 3.20 3.15 3.10 3.05 3.00 2.95 2.90 2.85 2.80 2.75 2.70 2.65 2.60 2.55 2.50 2.45
f1 (ppm)
6 5 4 3 2 1

(k)

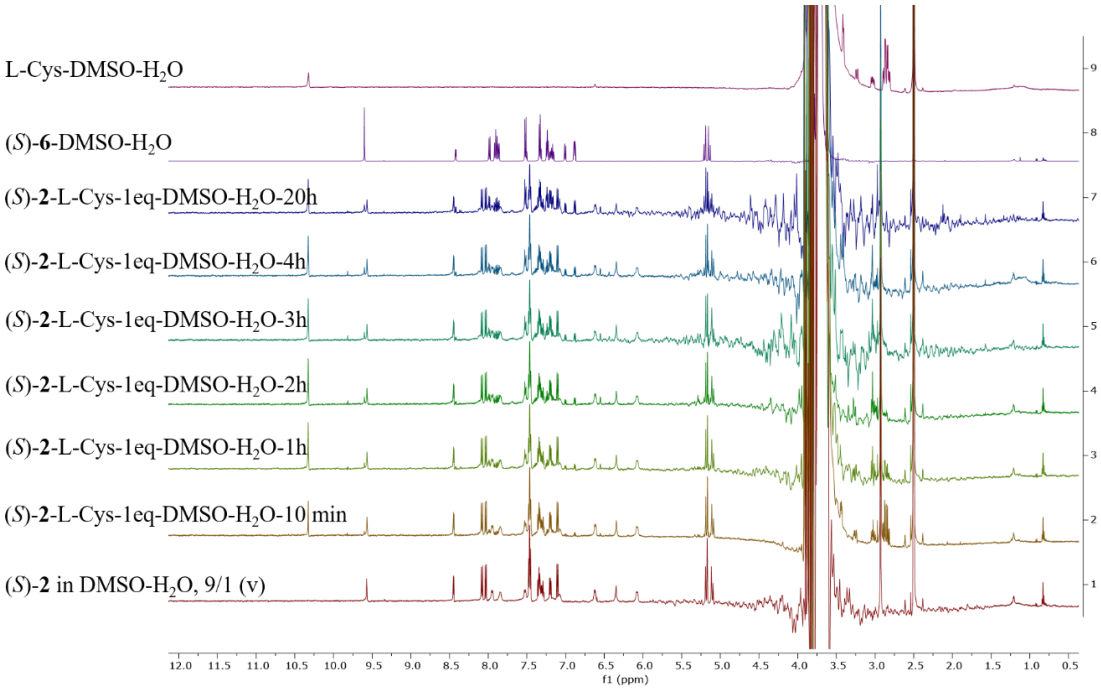
L-Cys-DMSO-H2O
(S)-6-DMSO-H2O
(S)-2-L-Cys-1eq-DMSO-H2O-20h
(S)-2-L-Cys-1eq-DMSO-H2O-4h
(S)-2-L-Cys-1eq-DMSO-H2O-3h
(S)-2-L-Cys-1eq-DMSO-H2O-2h
(S)-2-L-Cys-1eq-DMSO-H2O-1h
(S)-2-L-Cys-1eq-DMSO-H2O-10 min
(S)-2 in DMSO-H2O, 9/1 (v)
f1 (ppm)

(l)

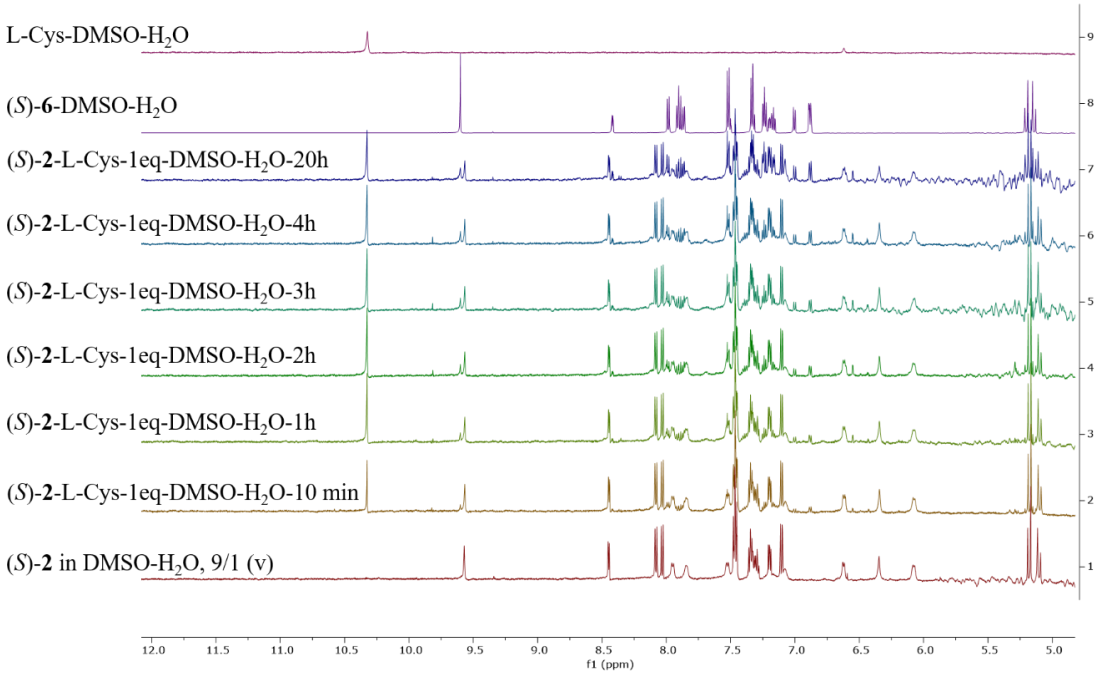
L-Cys-DMSO-H2O
(S)-6-DMSO-H2O
(S)-2-L-Cys-1eq-DMSO-H2O-20h
(S)-2-L-Cys-1eq-DMSO-H2O-4h
(S)-2-L-Cys-1eq-DMSO-H2O-3h
(S)-2-L-Cys-1eq-DMSO-H2O-2h
(S)-2-L-Cys-1eq-DMSO-H2O-1h
(S)-2-L-Cys-1eq-DMSO-H2O-10 min
(S)-2 in DMSO-H2O, 9/1 (v)
f1 (ppm)

(m)

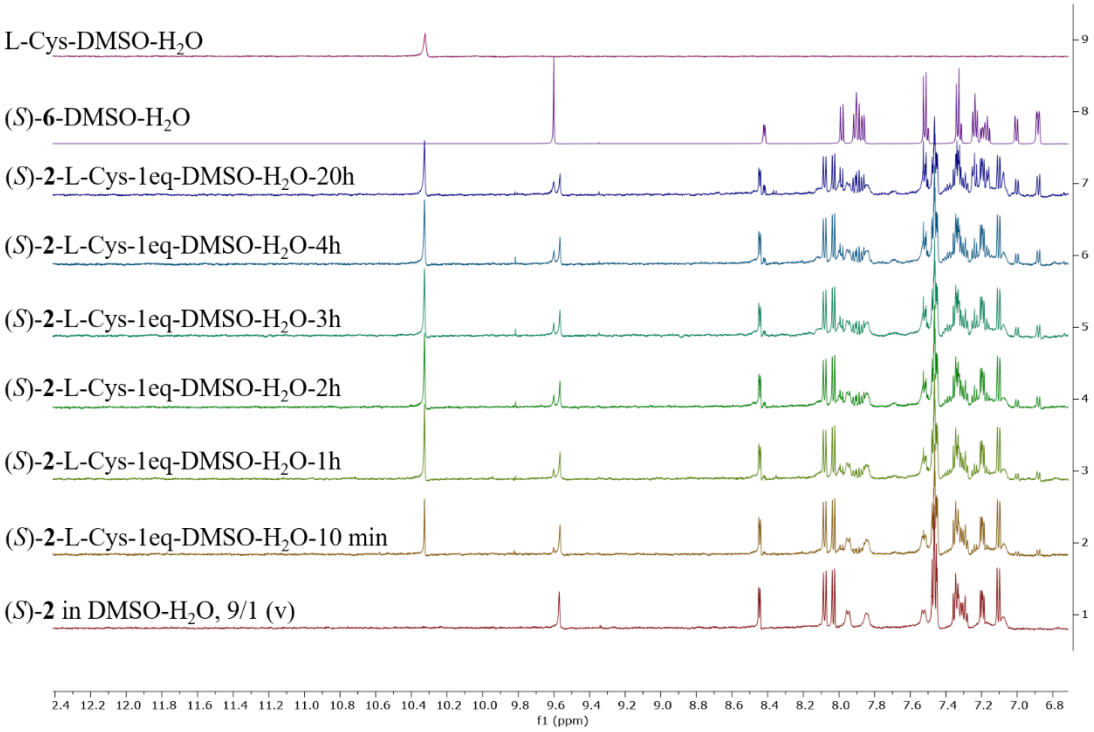
L-Cys-DMSO-H2O
(S)-6-DMSO-H2O
(S)-2-L-Cys-1eq-DMSO-H2O-20h
(S)-2-L-Cys-1eq-DMSO-H2O-4h
(S)-2-L-Cys-1eq-DMSO-H2O-3h
(S)-2-L-Cys-1eq-DMSO-H2O-2h
(S)-2-L-Cys-1eq-DMSO-H2O-1h
(S)-2-L-Cys-1eq-DMSO-H2O-10 min
(S)-2 in DMSO-H2O, 9/1 (v)
9
8
7
6
5
4
3
2
1
2.4 12.2 12.0 11.8 11.6 11.4 11.2 11.0 10.8 10.6 10.4 10.2 10.0 9.8 9.6 9.4 9.2 9.0 8.8 8.6 8.4 8.2 8.0 7.8 7.6 7.4 7.2 7.0 6.8
f1 (ppm)

(n)

Figure S6-12. ^{1}H NMR spectra of (*S*)-**2** (1.0 mM in DMSO-d_6) with L-Cys (3 equiv) in HEPES (D_2O, 25 mM HEPES, 120 mM NaCl, pD=7.4). [reaction time: 0 – 3 h. DMSO: HEPES = 9:1 (v)] (1)-(4), **7'** (1.0 mM in DMSO-d6 and HEPES) added in to the mixture (5)-(6).

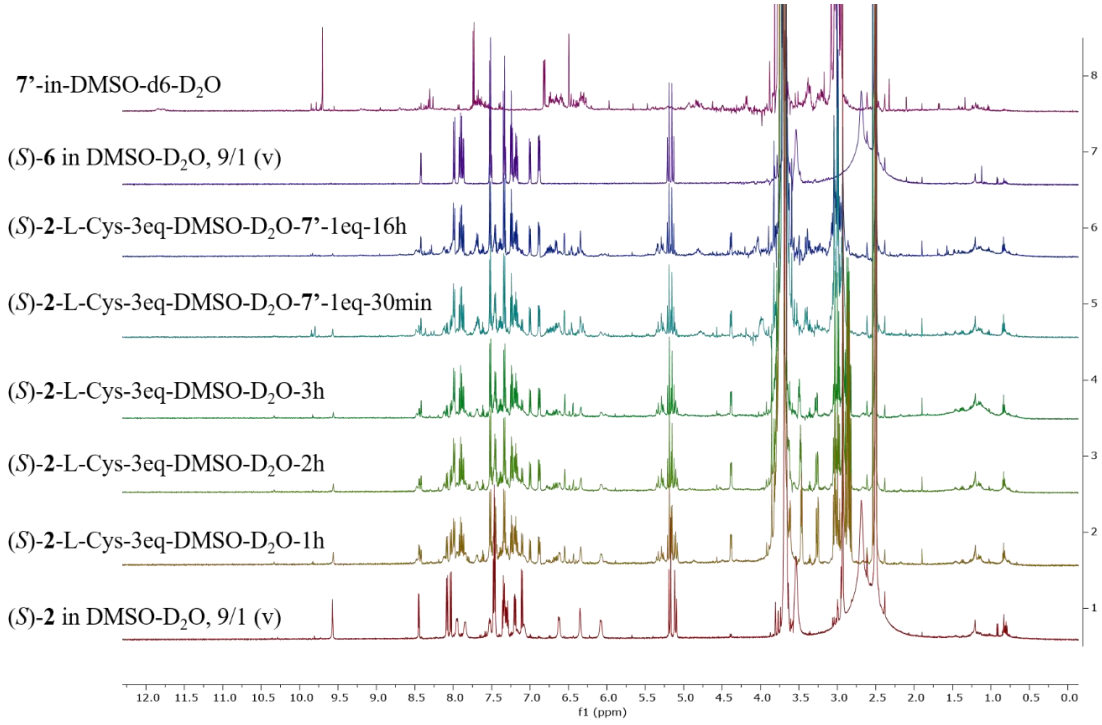

(a)

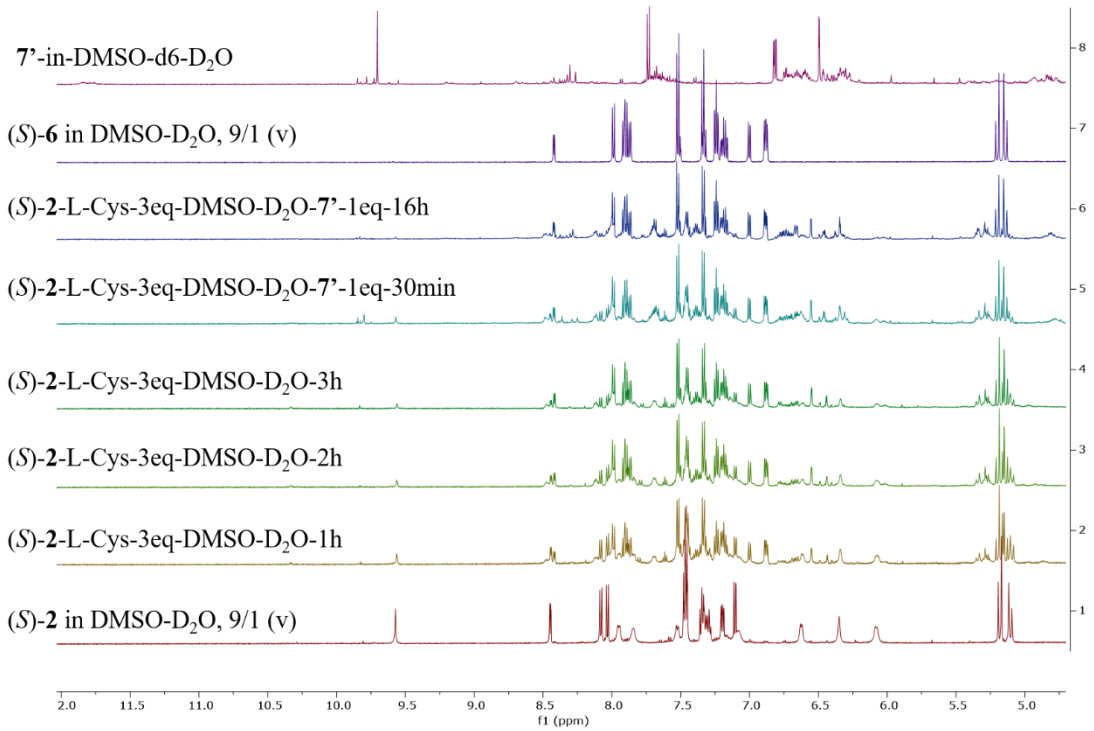
7'-in-DMSO-d6-D2O
(S)-6 in DMSO-D2O, 9/1 (v)
(S)-2-L-Cys-3eq-DMSO-D2O-7'-1eq-16h
(S)-2-L-Cys-3eq-DMSO-D2O-7'-1eq-30min
(S)-2-L-Cys-3eq-DMSO-D2O-3h
(S)-2-L-Cys-3eq-DMSO-D2O-2h
(S)-2-L-Cys-3eq-DMSO-D2O-1h
(S)-2 in DMSO-D2O, 9/1 (v)
f1 (ppm)

(b)

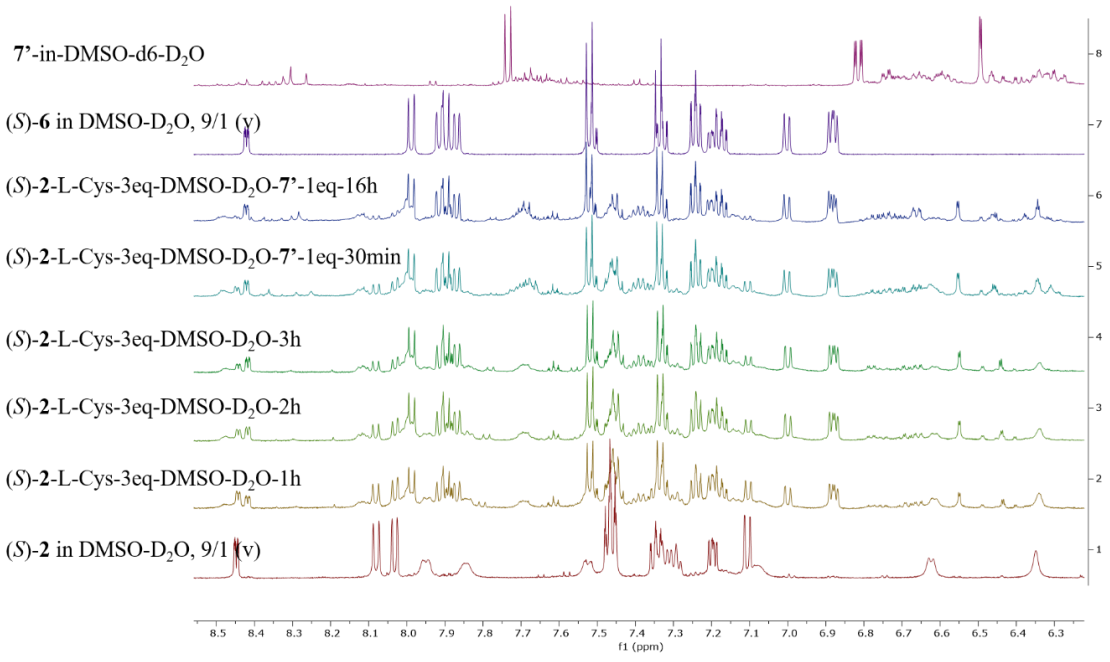
7'-in-DMSO-d6-D2O
(S)-6 in DMSO-D2O, 9/1 (v)
(S)-2-L-Cys-3eq-DMSO-D2O-7'-1eq-16h
(S)-2-L-Cys-3eq-DMSO-D2O-7'-1eq-30min
(S)-2-L-Cys-3eq-DMSO-D2O-3h
(S)-2-L-Cys-3eq-DMSO-D2O-2h
(S)-2-L-Cys-3eq-DMSO-D2O-1h
(S)-2 in DMSO-D2O, 9/1 (v)
f1 (ppm)

(c)

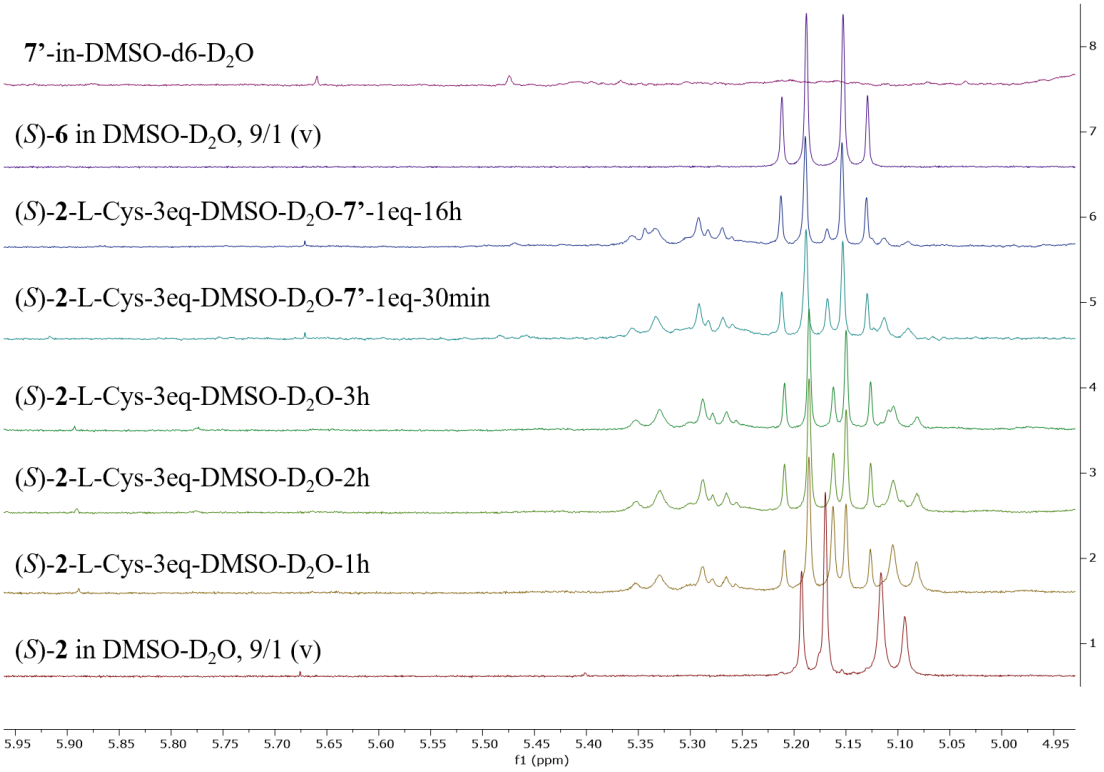
7'-in-DMSO-d6-D2O
(S)-6 in DMSO-D2O, 9/1 (v)
(S)-2-L-Cys-3eq-DMSO-D2O-7'-1eq-16h
(S)-2-L-Cys-3eq-DMSO-D2O-7'-1eq-30min
(S)-2-L-Cys-3eq-DMSO-D2O-3h
(S)-2-L-Cys-3eq-DMSO-D2O-2h
(S)-2-L-Cys-3eq-DMSO-D2O-1h
(S)-2 in DMSO-D2O, 9/1 (v)
8
7
6
5
4
3
2
1
5.95 5.90 5.85 5.80 5.75 5.70 5.65 5.60 5.55 5.50 5.45 5.40 5.35 5.30 5.25 5.20 5.15 5.10 5.05 5.00 4.95
f1 (ppm)

(d)

Figure S6-13. ^{1}H NMR spectra of (*S*)-**2** (1.0 mM in DMSO-d_6) with GSH (3 equiv) in HEPES (D_2O, 25 mM HEPES, 120 mM NaCl, pD=7.4). [reaction time: 0 – 26 h. DMSO: HEPES = 9:1 (v)].

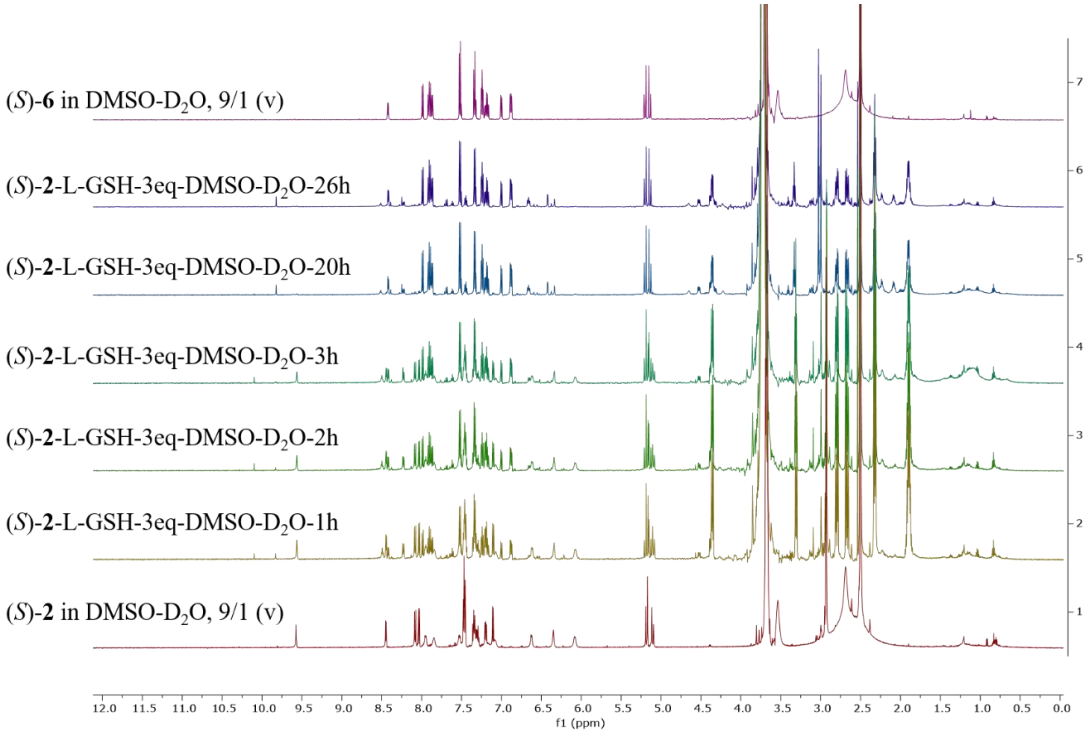

(a)

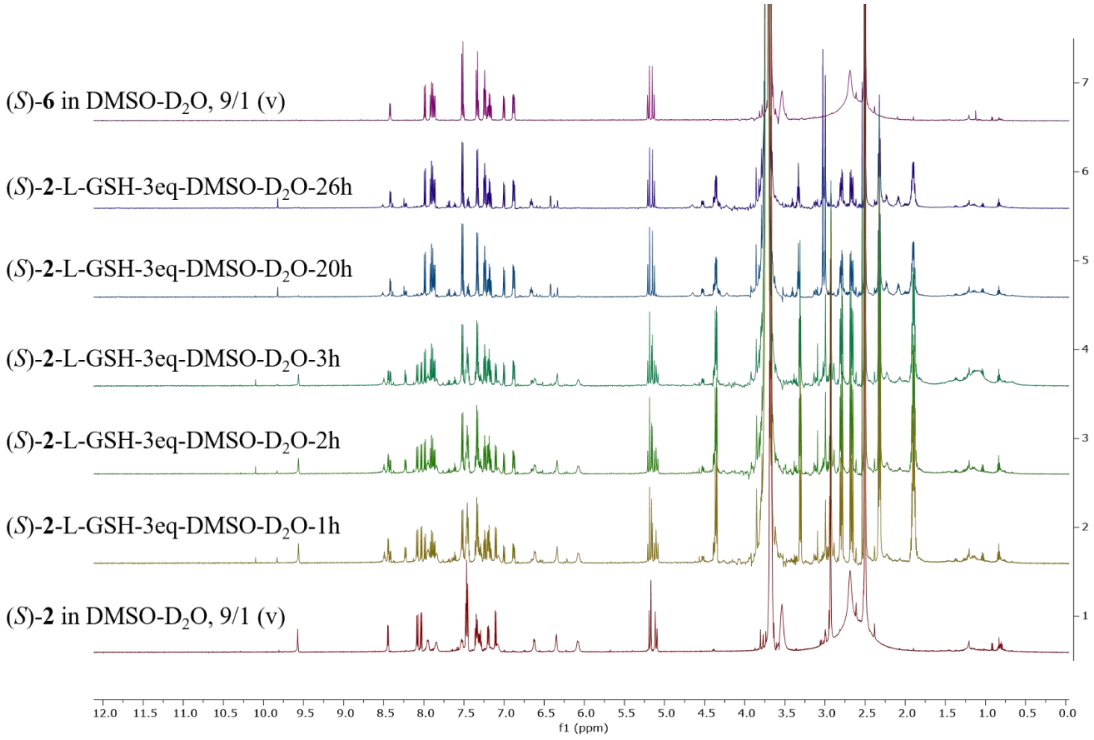
(S)-6 in DMSO-D2O, 9/1 (v)
(S)-2-L-GSH-3eq-DMSO-D2O-26h
(S)-2-L-GSH-3eq-DMSO-D2O-20h
(S)-2-L-GSH-3eq-DMSO-D2O-3h
(S)-2-L-GSH-3eq-DMSO-D2O-2h
(S)-2-L-GSH-3eq-DMSO-D2O-1h
(S)-2 in DMSO-D2O, 9/1 (v)
f1 (ppm)

(b)

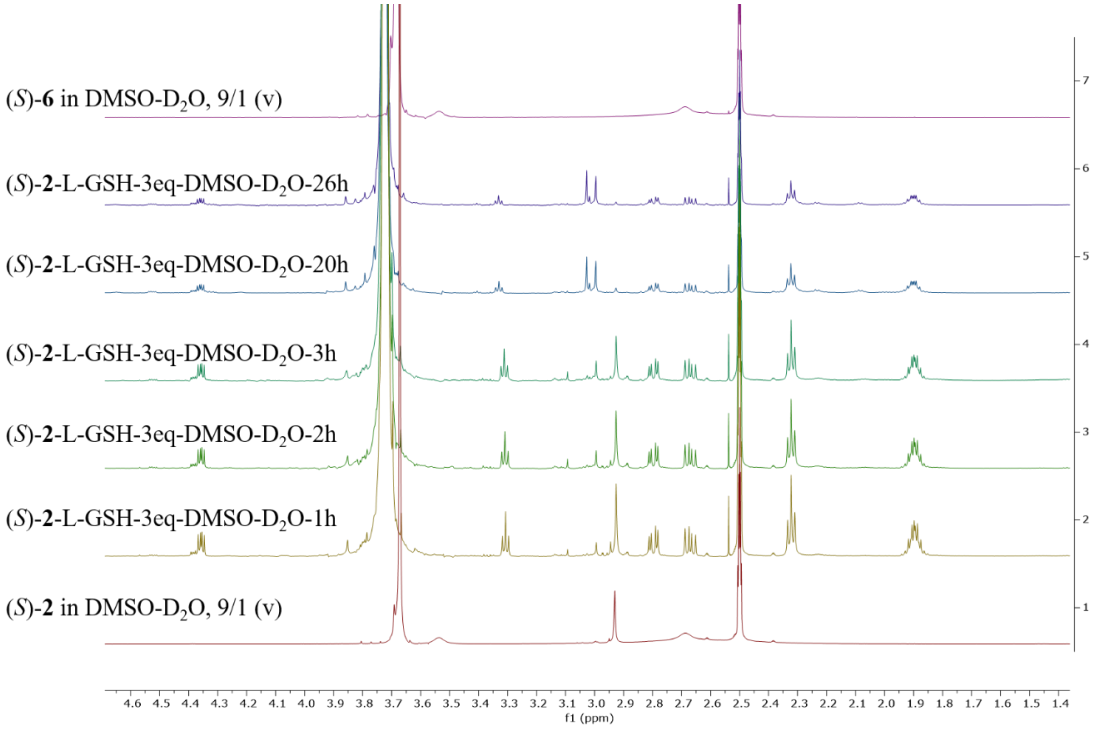
(S)-6 in DMSO-D2O, 9/1 (v)
(S)-2-L-GSH-3eq-DMSO-D2O-26h
(S)-2-L-GSH-3eq-DMSO-D2O-20h
(S)-2-L-GSH-3eq-DMSO-D2O-3h
(S)-2-L-GSH-3eq-DMSO-D2O-2h
(S)-2-L-GSH-3eq-DMSO-D2O-1h
(S)-2 in DMSO-D2O, 9/1 (v)
f1 (ppm)

(c)

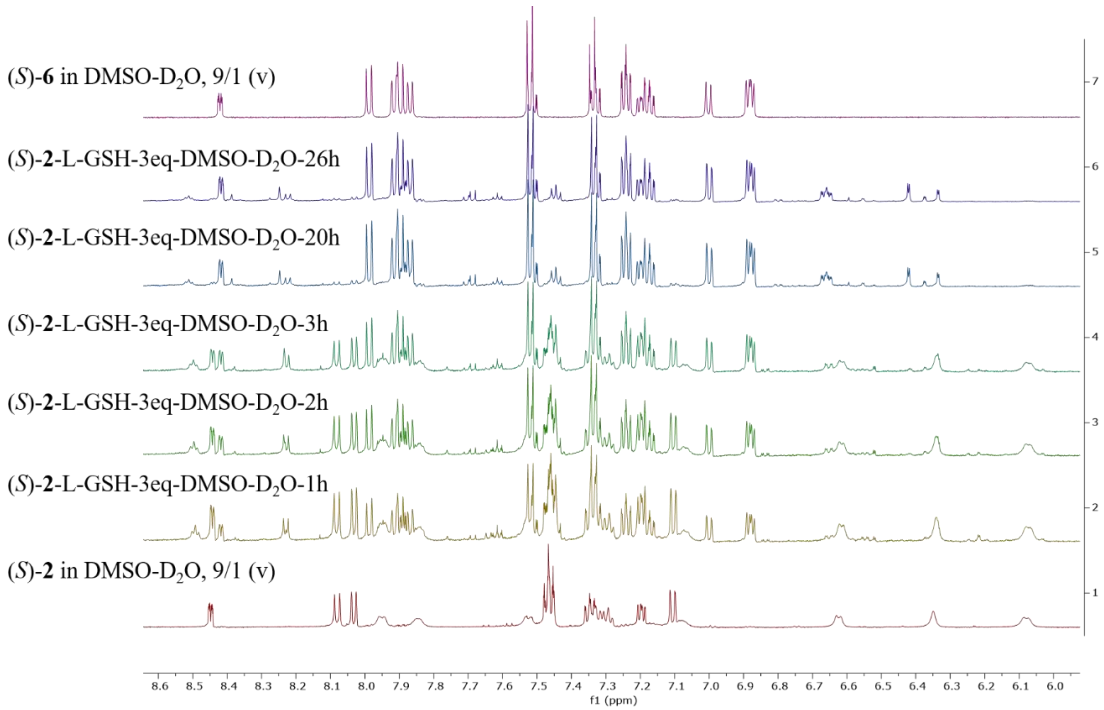

(d)

Figure S6-14. ^{1}H NMR spectra of (*S*)-**2** (1.0 mM in DMSO-d_6) with L-Cys (1-3 equiv) in H_2O [reaction time: 10 min (a-b), 1h (c-d), 4h(e-g). DMSO: H_2O = 9:1 (v)]

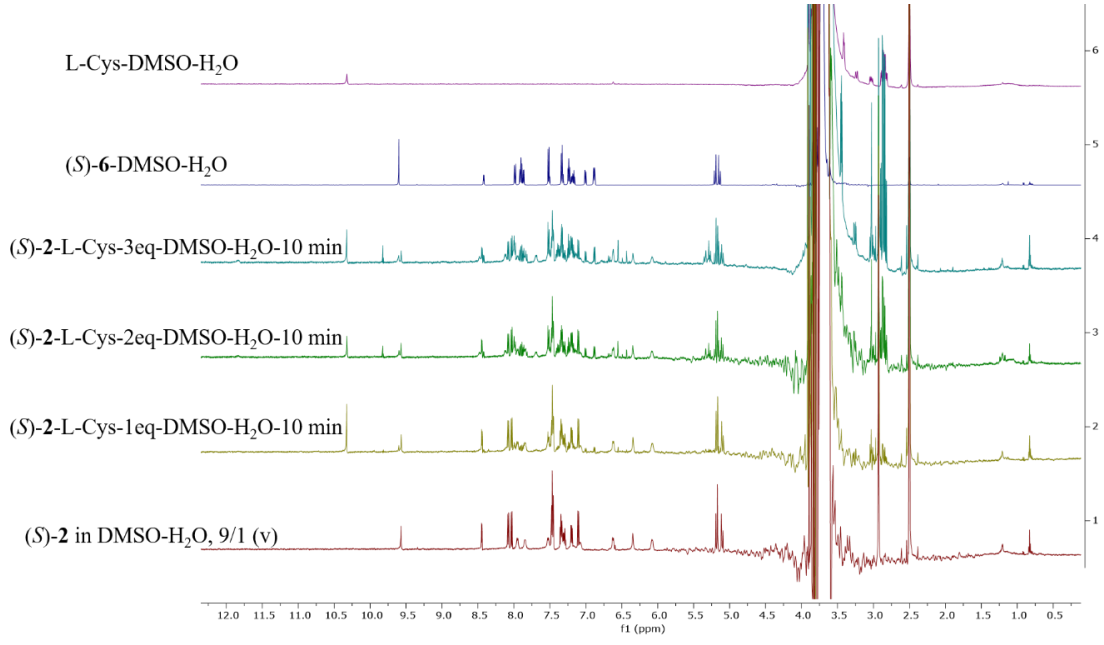

(a)

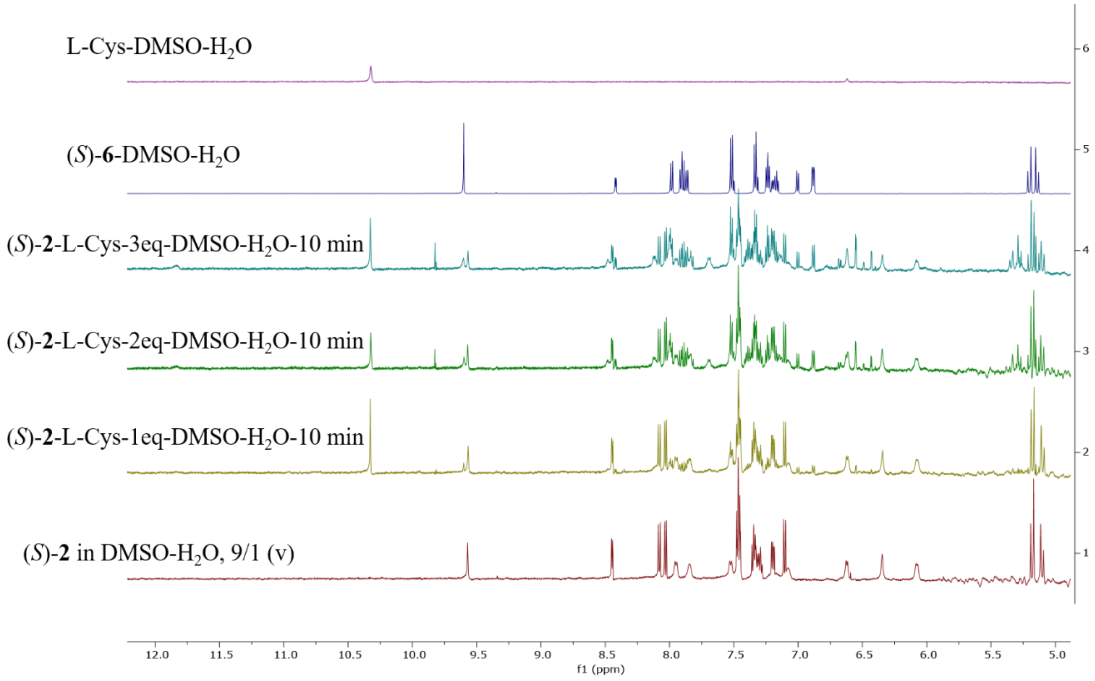
L-Cys-DMSO-H2O
(S)-6-DMSO-H2O
(S)-2-L-Cys-3eq-DMSO-H2O-10 min
(S)-2-L-Cys-2eq-DMSO-H2O-10 min
(S)-2-L-Cys-1eq-DMSO-H2O-10 min
(S)-2 in DMSO-H2O, 9/1 (v)
f1 (ppm)

(b)

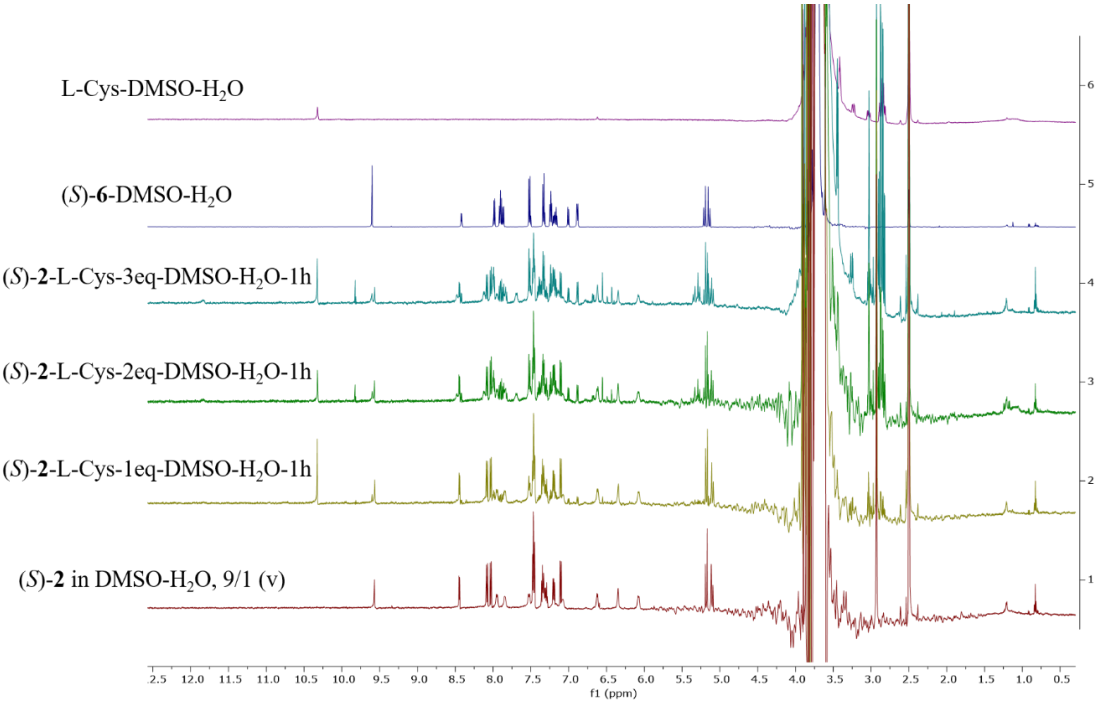
L-Cys-DMSO-H2O
(S)-6-DMSO-H2O
(S)-2-L-Cys-3eq-DMSO-H2O-1h
(S)-2-L-Cys-2eq-DMSO-H2O-1h
(S)-2-L-Cys-1eq-DMSO-H2O-1h
(S)-2 in DMSO-H2O, 9/1 (v)
f1 (ppm)

(c)

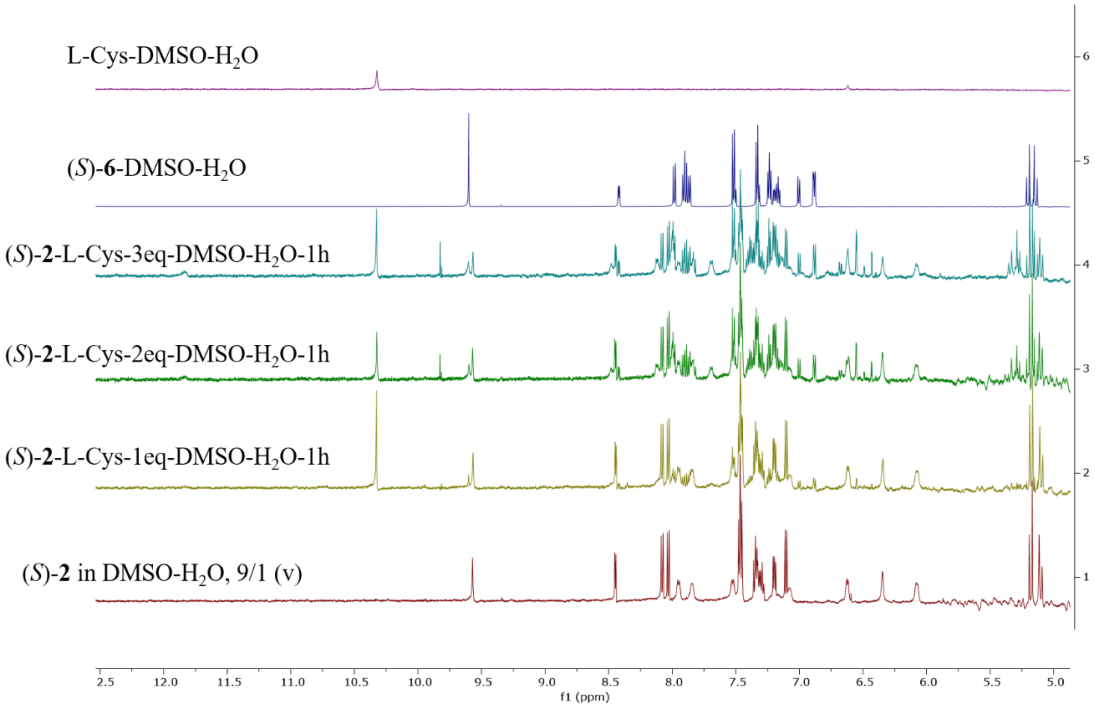
L-Cys-DMSO-H2O
(S)-6-DMSO-H2O
(S)-2-L-Cys-3eq-DMSO-H2O-1h
(S)-2-L-Cys-2eq-DMSO-H2O-1h
(S)-2-L-Cys-1eq-DMSO-H2O-1h
(S)-2 in DMSO-H2O, 9/1 (v)
f1 (ppm)

(d)

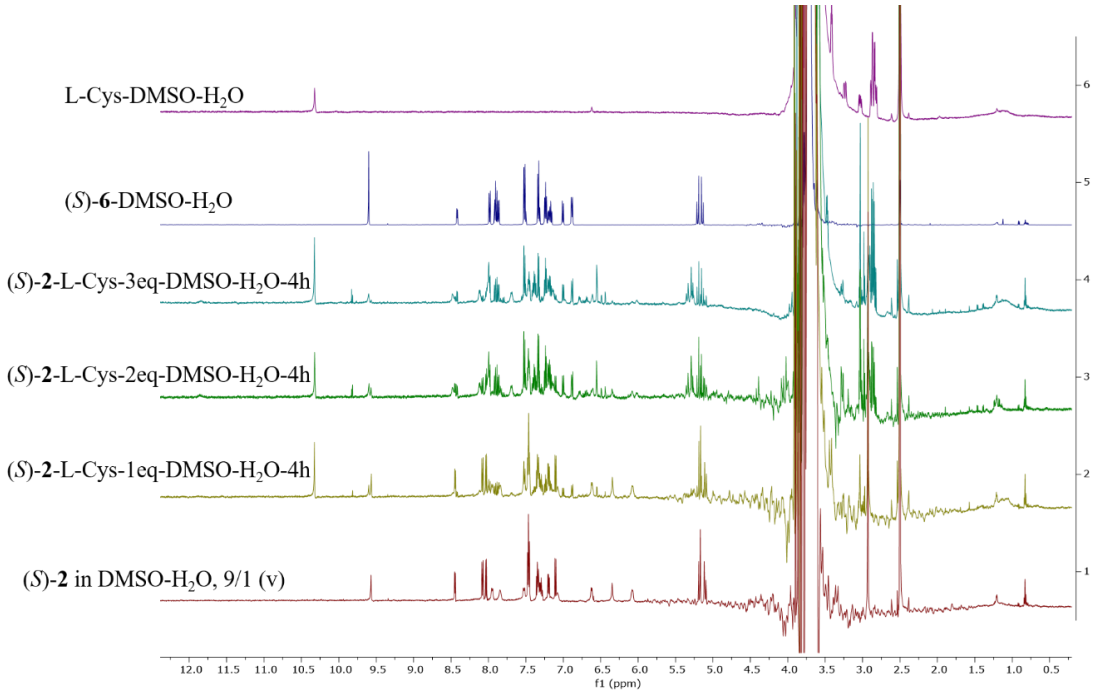
L-Cys-DMSO-H2O
(S)-6-DMSO-H2O
(S)-2-L-Cys-3eq-DMSO-H2O-4h
(S)-2-L-Cys-2eq-DMSO-H2O-4h
(S)-2-L-Cys-1eq-DMSO-H2O-4h
(S)-2 in DMSO-H2O, 9/1 (v)
f1 (ppm)

(e)

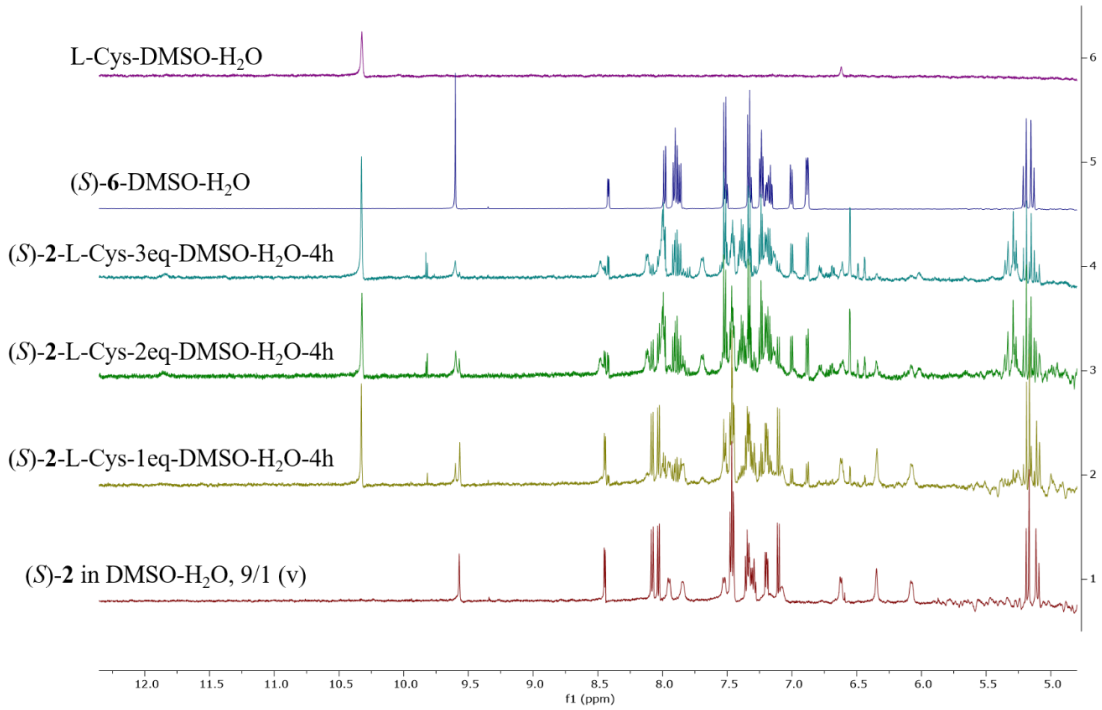

(f)

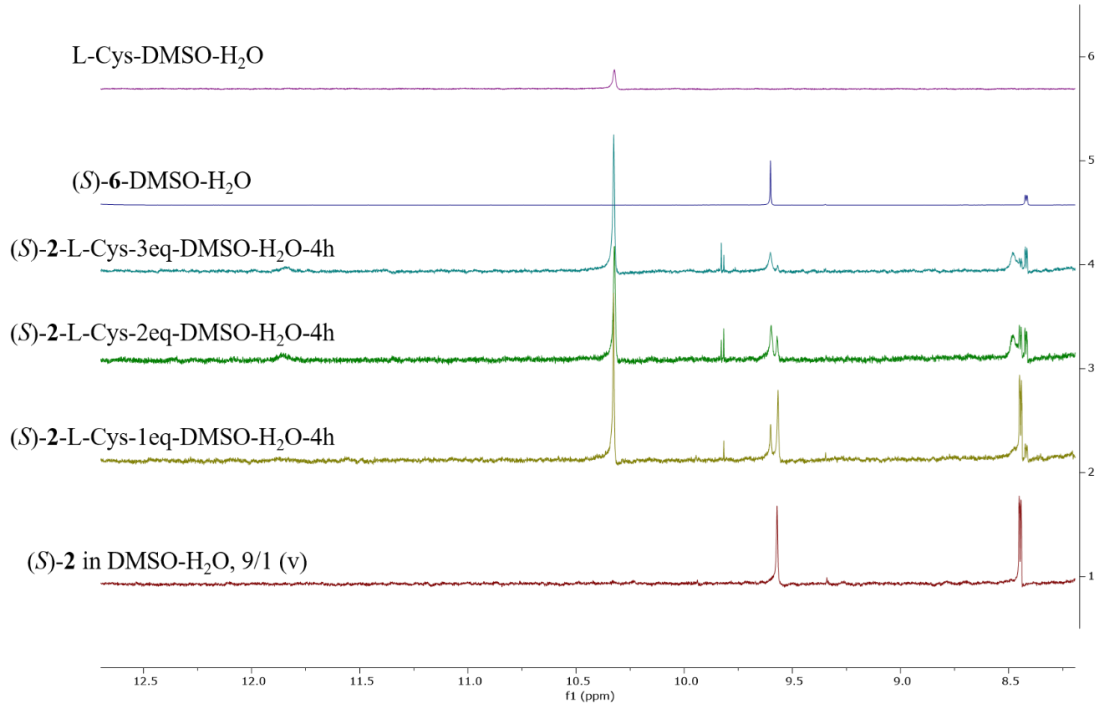

(g)

Study the reaction of 4 with L-Cys

Figure S6-15. ^{1}H NMR spectrum of the products of **4** and L-Cys [0.9 equiv, 1.0 mM in DMSO-d6 (a), 1.0 mM in DMSO-d6-D_2O (9-1, v) (b), reaction time: 0-50 h (c)].

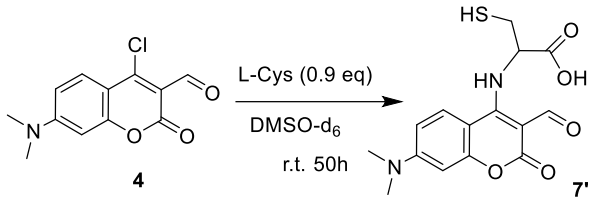

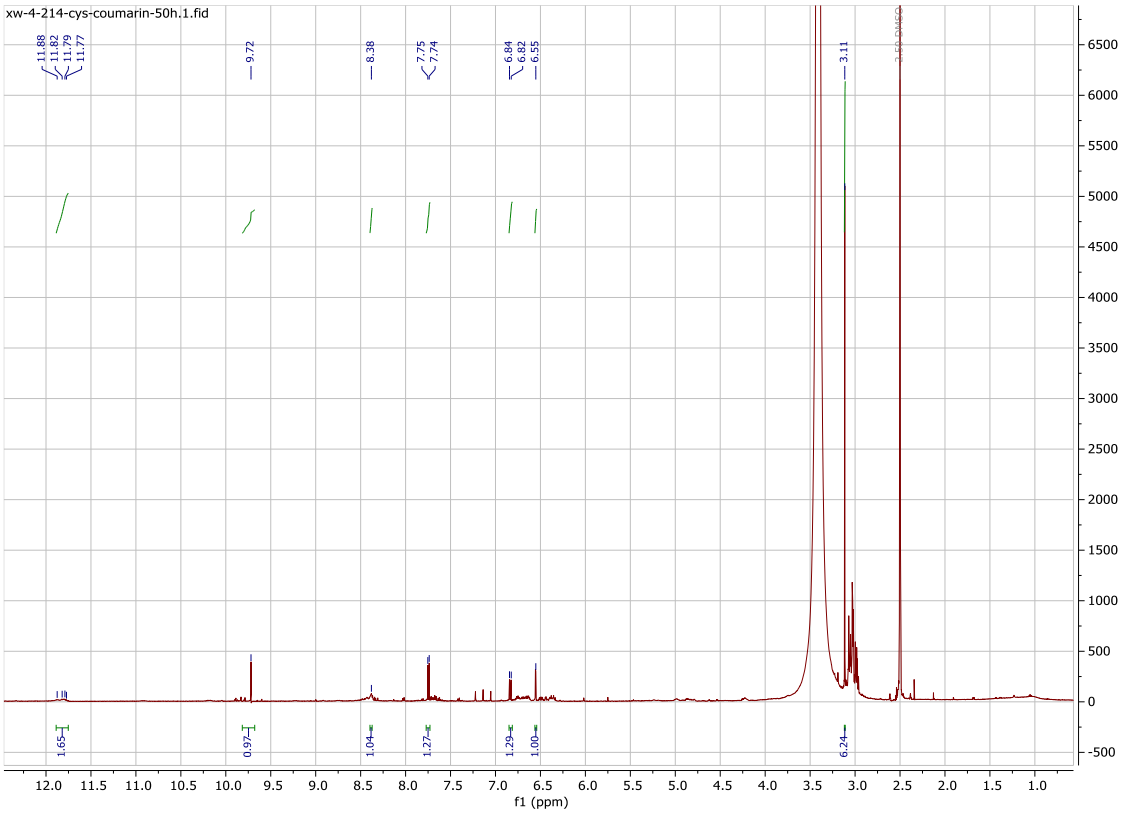

(a)

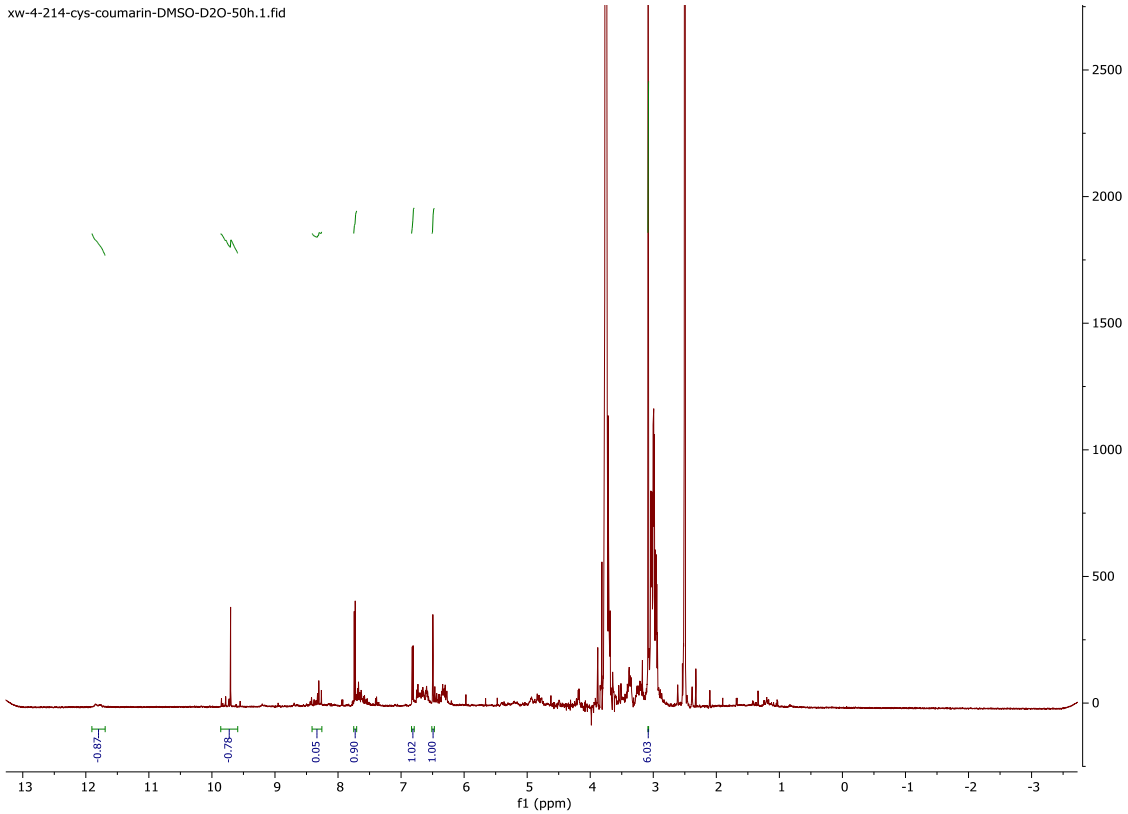
xw-4-214-cys-coumarin-DMSO-D2O-50h.1.fid
2500
2000
1500
1000
500
0
-0.87
-0.78
0.05
0.90
1.02
1.00
6.03
13 12 11 10 9 8 7 6 5 4 3 2 1 0 -1 -2 -3
f1 (ppm)

(b)

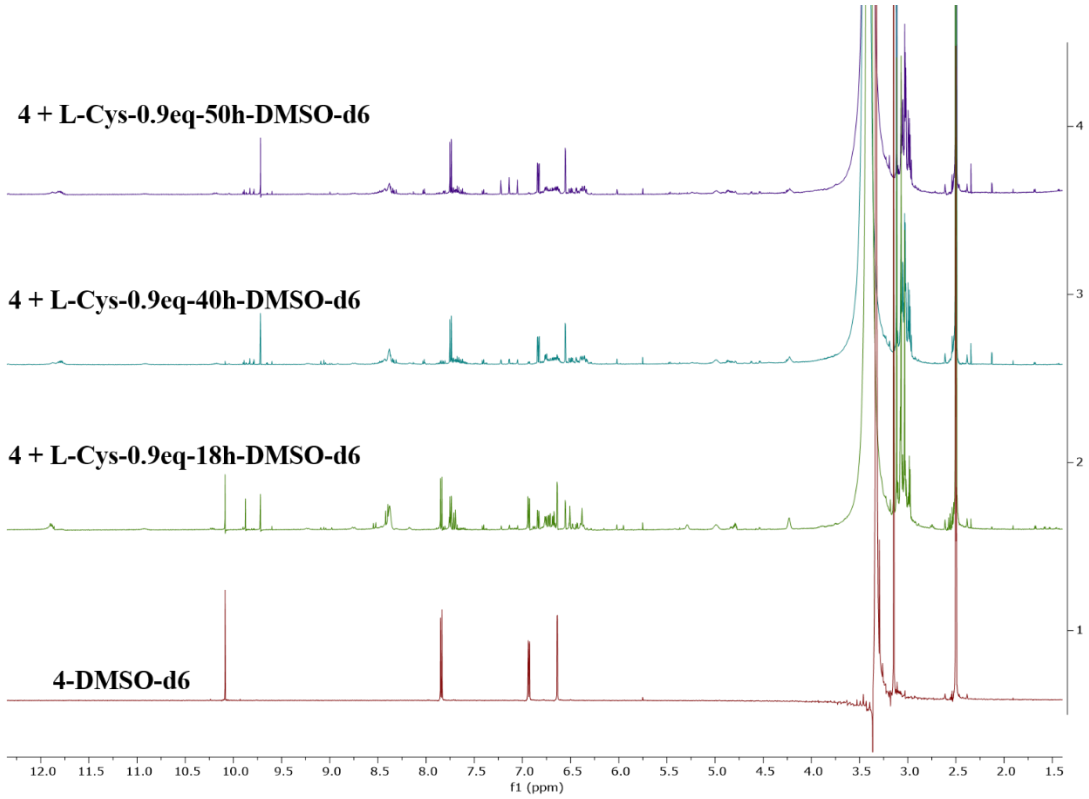
4 + L-Cys-0.9eq-50h-DMSO-d6
4 + L-Cys-0.9eq-40h-DMSO-d6
4 + L-Cys-0.9eq-18h-DMSO-d6
4-DMSO-d6
4
3
2
1
12.0 11.5 11.0 10.5 10.0 9.5 9.0 8.5 8.0 7.5 7.0 6.5 6.0 5.5 5.0 4.5 4.0 3.5 3.0 2.5 2.0 1.5
f1 (ppm)

(c)

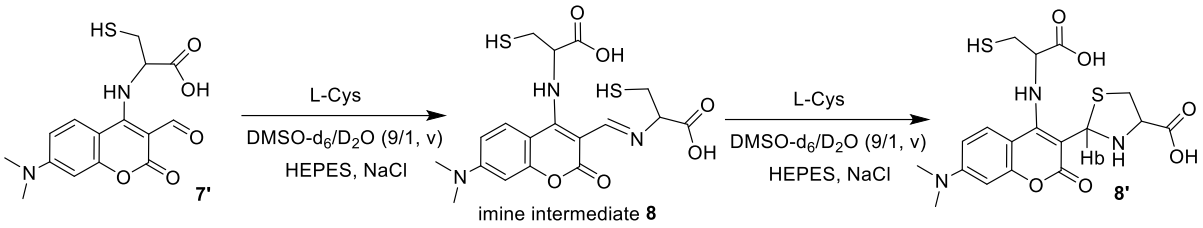

Figure S6-16. ^{1}H NMR spectra for the reaction of **7'** (as the major compound, 1.0 mM in DMSO-d_6) with L-Cys (3 equiv) in HEPES (D_2O, 25 mM HEPES, 120 mM NaCl, pH=7.4). [reaction time: 20 h. DMSO: HEPES = 9:1 (v)].

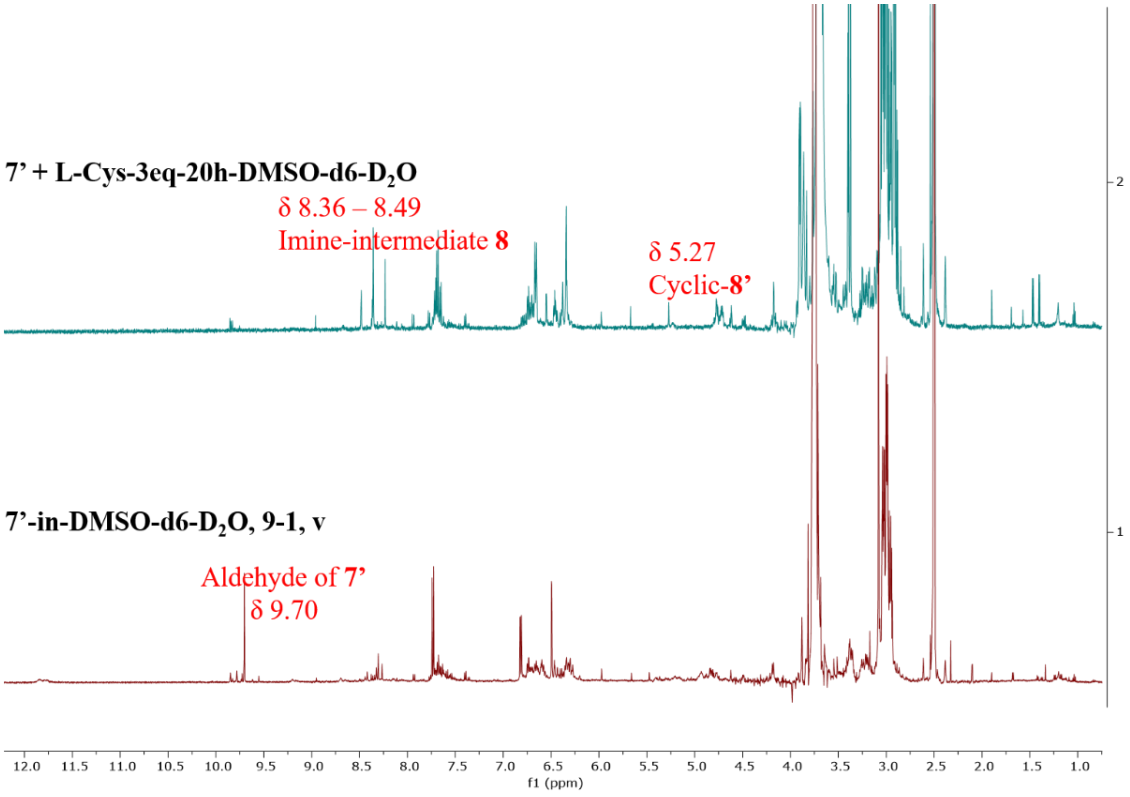

Figure S6-17. ^{1}H NMR spectra for the reaction of **4** (as the major compound, 1.0 mM in DMSO-d_6) with L-Cys (3 equiv) in DMSO-d6. And HEPES (D_2O, 25 mM HEPES, 120 mM NaCl, pH=7.4) was added into DMSO-d6 before recording the spectrum. [reaction time: 20-22h. DMSO: HEPES = 9:1 (v)].

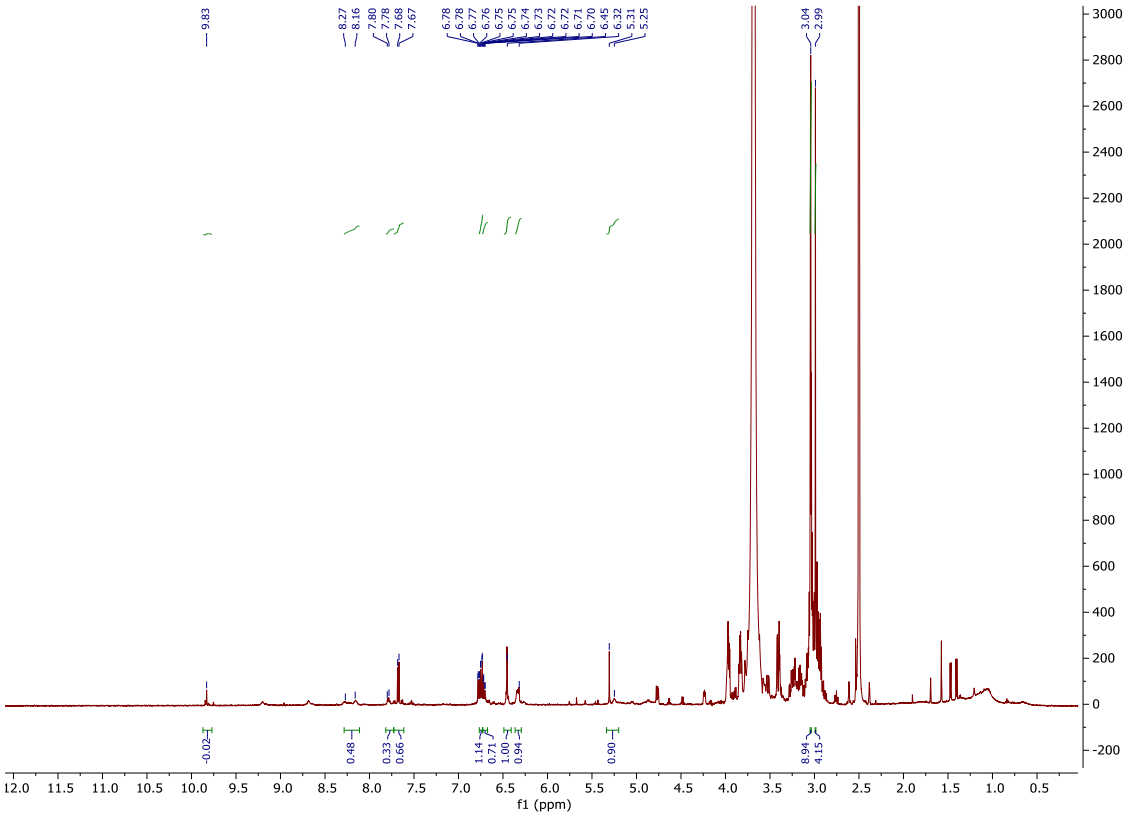

(a)

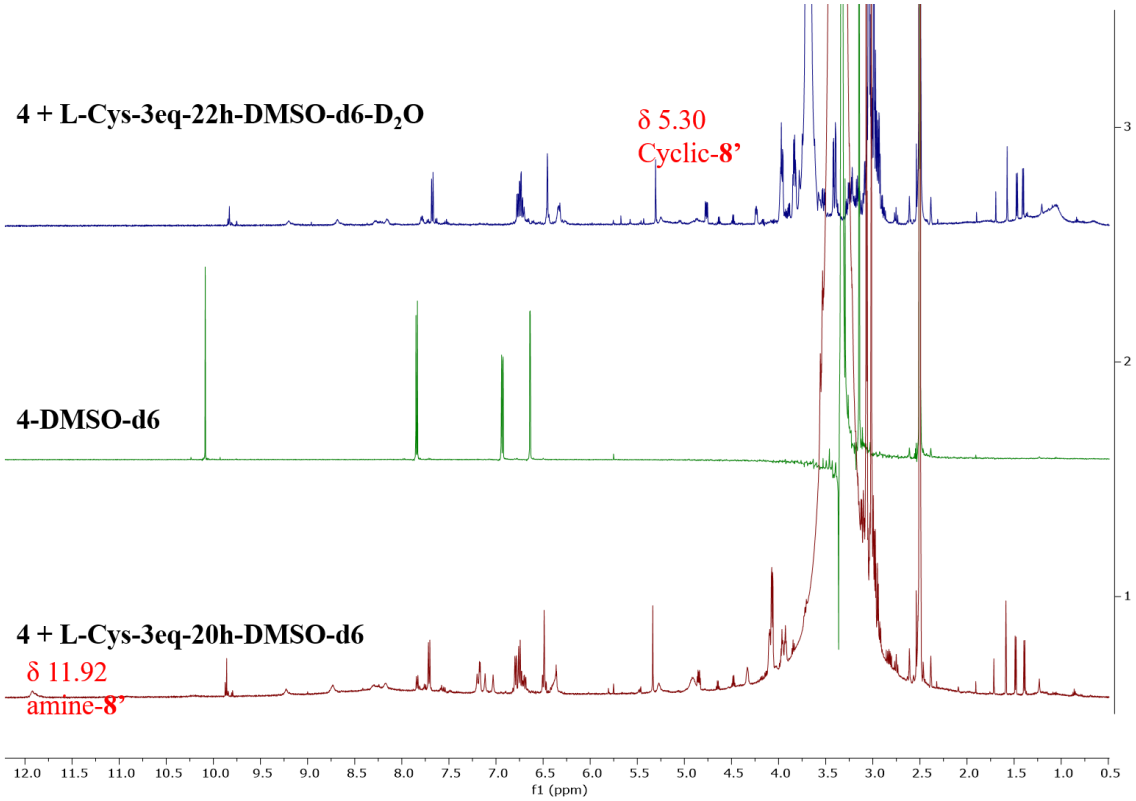
4 + L-Cys-3eq-22h-DMSO-d6-D2O
δ 5.30
Cyclic-8'
4-DMSO-d6
4 + L-Cys-3eq-20h-DMSO-d6
δ 11.92
amine-8'
12.0 11.5 11.0 10.5 10.0 9.5 9.0 8.5 8.0 7.5 7.0 6.5 6.0 5.5 5.0 4.5 4.0 3.5 3.0 2.5 2.0 1.5 1.0 0.5
f1 (ppm)
3
2
1

(b)

Fluorescence spectra of 7' and 7' with Cys

Figure S6-18. Fluorescence spectra of the crude product mixtures of **7'** and **7'** with Cys (3 equiv) [in DMSO-d_6 (90%) and HEPES in D_2O (10%) and diluted with HEPES buffer in H_2O to 2 - 10 μM, λ_{exc} = 362 nm, slits: 3/3 nm].

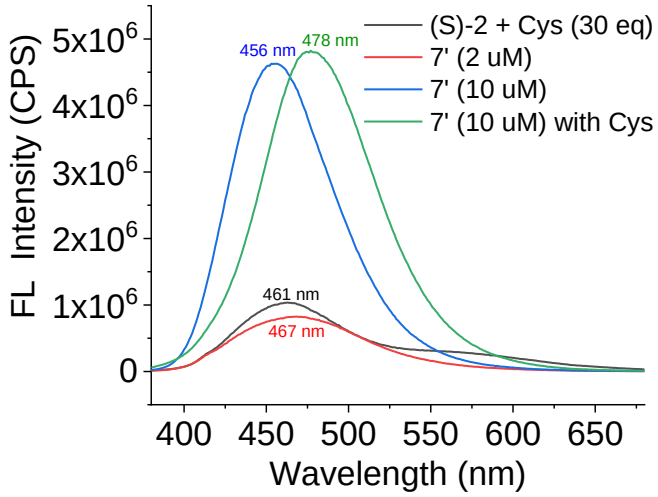

Figure S6-19. Fluorescence spectra of the crude product mixtures of **7'** and **8'** [in DMSO-d_6 (90%) and HEPES in D_2O (10%) and diluted with HEPES buffer in H_2O to 10 μM, λ_{exc} = 415 nm, slits: 3/3 nm].

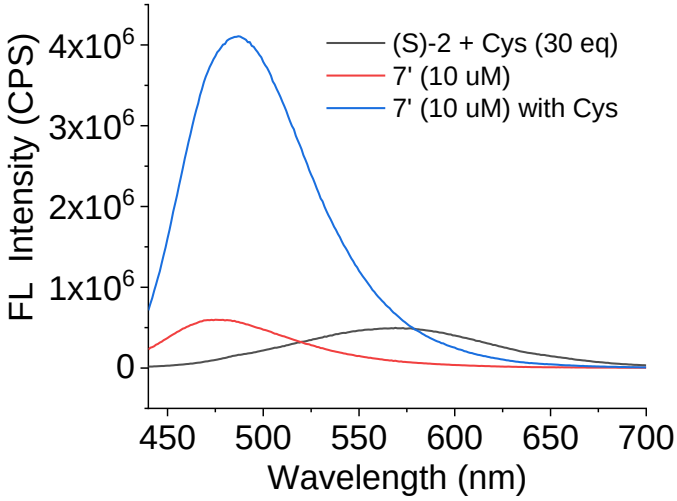

High-resolution mass spectroscopic study on the reaction of (*S*)-2 with Cys and GSH

Figure S6-20. HRMS spectra for the reaction of (*S*)-**2** (1.9 mM in DMSO) with L-Cysteine (5 mM in HEPES, pH=7.4) in a 1:1 volume ratio. (reaction time: 20 h.)

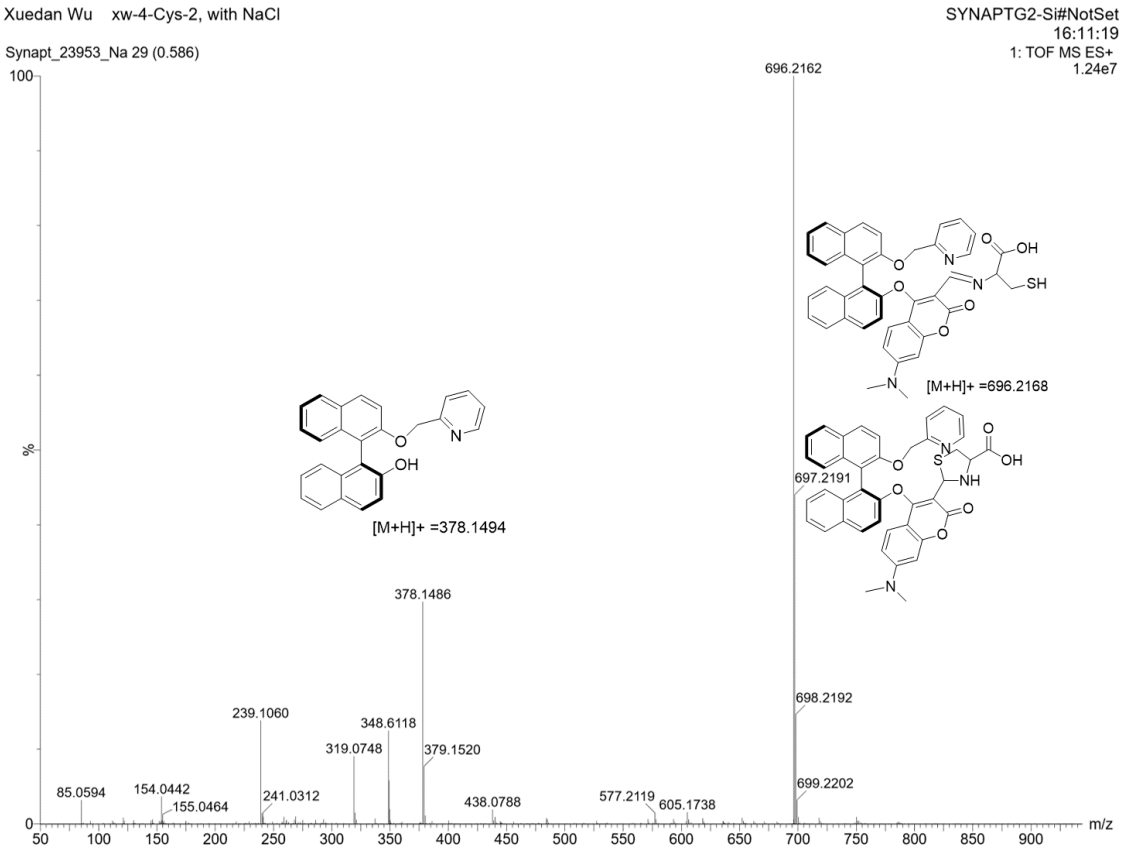

(a)

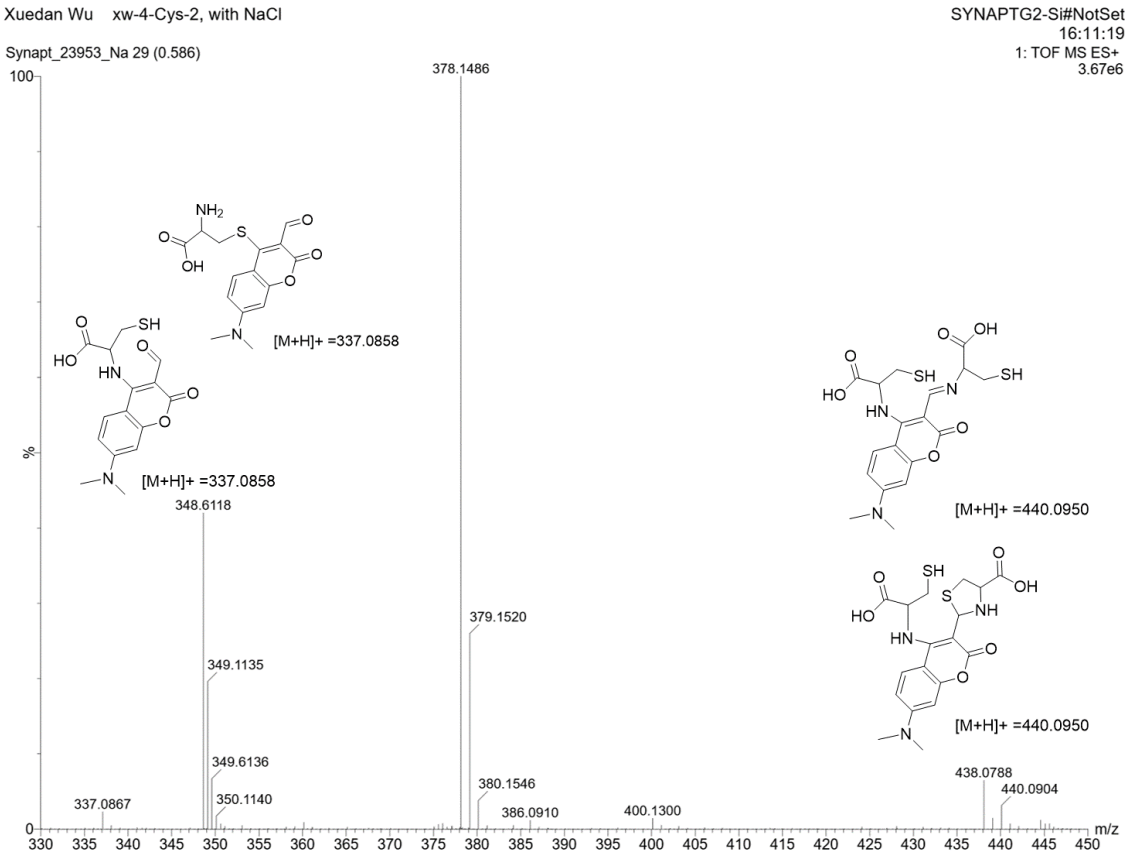
Xuedan Wu xw-4-Cys-2, with NaCl
SYNAPTG2-Si#NotSet
16:11:19
1: TOF MS ES+
3.67e6
Synapt_23953_Na 29 (0.586)
100
%
0
378.1486
348.6118
379.1520
349.1135
349.6136
350.1140
337.0867
380.1546
386.0910
400.1300
438.0788
440.0904
[M+H]+ =337.0858
[M+H]+ =337.0858
[M+H]+ =440.0950
[M+H]+ =440.0950
330 335 340 345 350 355 360 365 370 375 380 385 390 395 400 405 410 415 420 425 430 435 440 445 450
m/z

(b)

Figure S6-21. HRMS spectra for the reaction of (*S*)-**2** (1.9 mM in DMSO) with GSH (5 equiv mM in HEPES, pH=7.4) in a 1:1 volume ratio. (reaction time: 20 h)

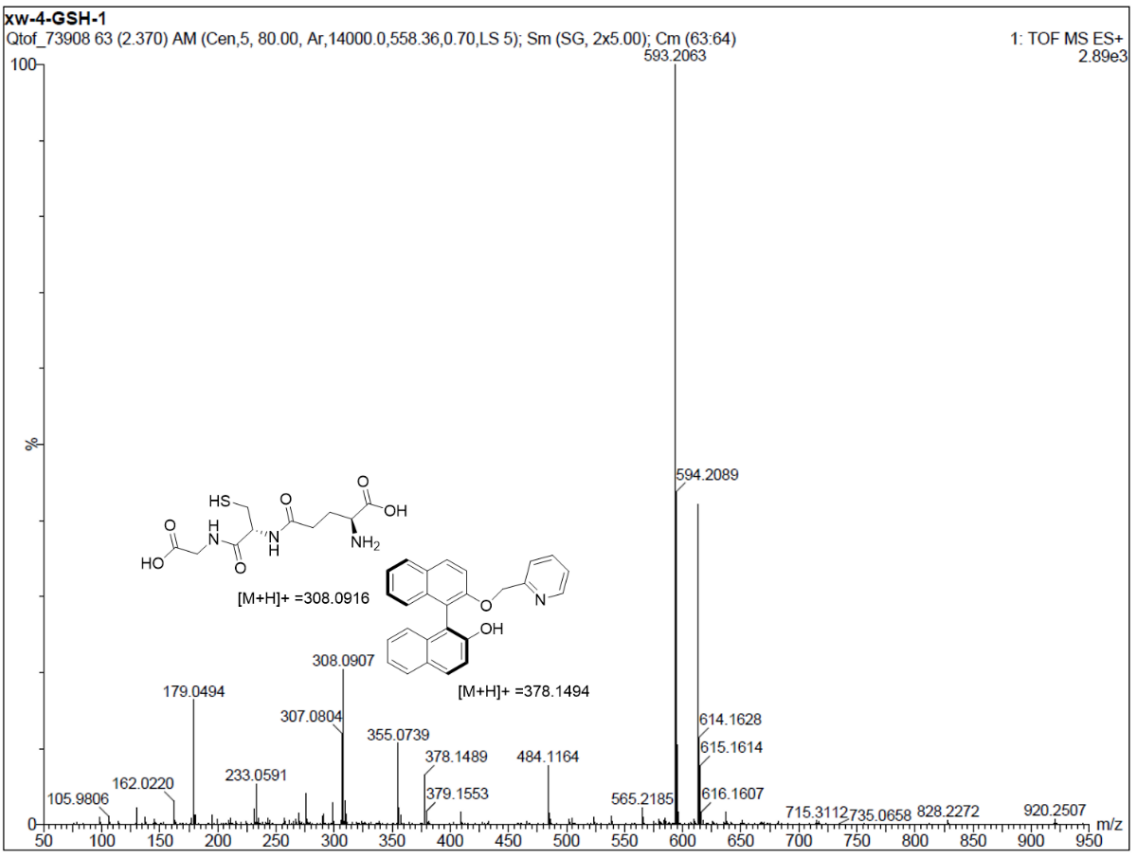

(a)

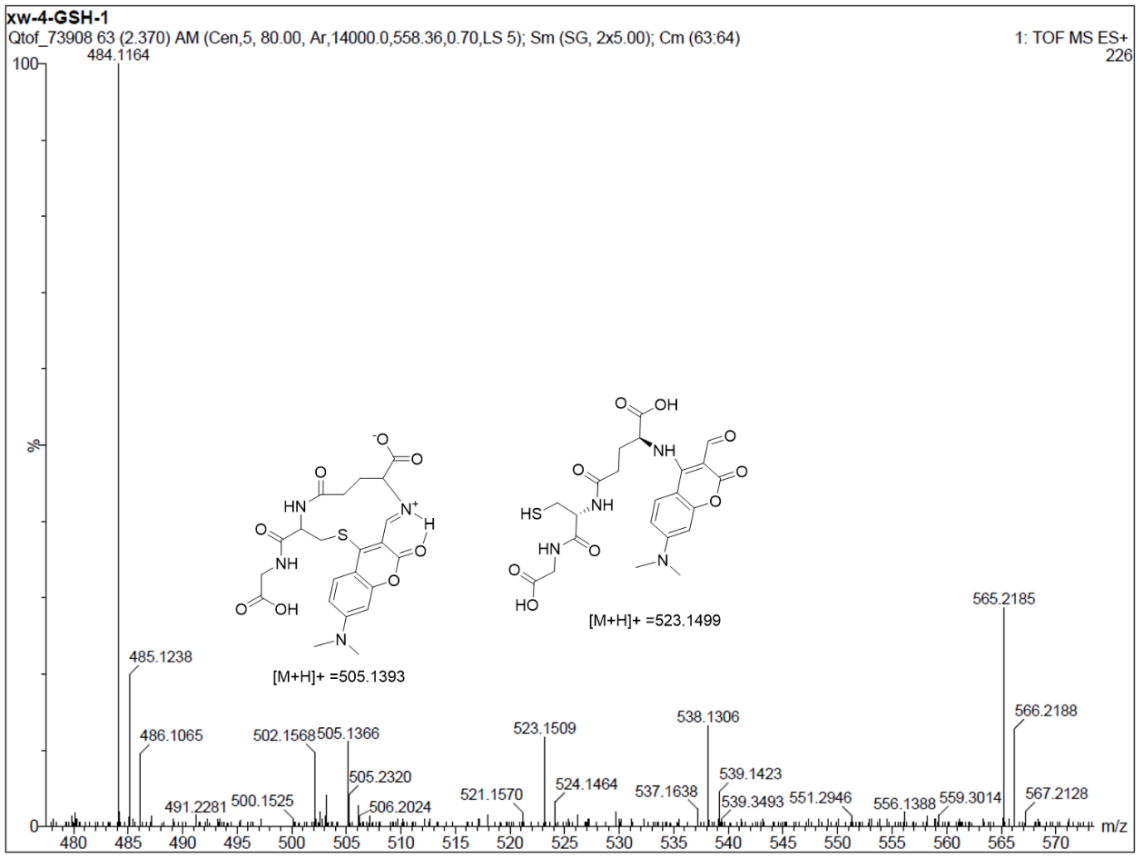
xw-4-GSH-1
Qtof_73908 63 (2.370) AM (Cen,5, 80.00, Ar,14000.0,558.36,0.70,LS 5); Sm (SG, 2x5.00); Cm (63:64)
1: TOF MS ES+
226
484.1164
100
%
0
[M+H]+ =505.1393
[M+H]+ =523.1499
485.1238
486.1065
491.2281
500.1525
502.1568
505.1366
505.2320
506.2024
521.1570
523.1509
524.1464
537.1638
538.1306
539.1423
539.3493
551.2946
556.1388
559.3014
565.2185
566.2188
567.2128
480 485 490 495 500 505 510 515 520 525 530 535 540 545 550 555 560 565 570
m/z

(b)

Figure S6-22. Proposed reaction pathways of **2** with Hcy.